Cheaper, portable scanners promise MRI for all p. 748

War in Ukraine may spark a global land grab p. 752

Growth rate and duration contributed to size in dinosaurs p. 811

Science

$15
24 FEBRUARY 2023
science.org

AAAS

SPECIAL ISSUE

ASTEROID SAMPLES

Lab analysis reveals Ryugu's history p. 782

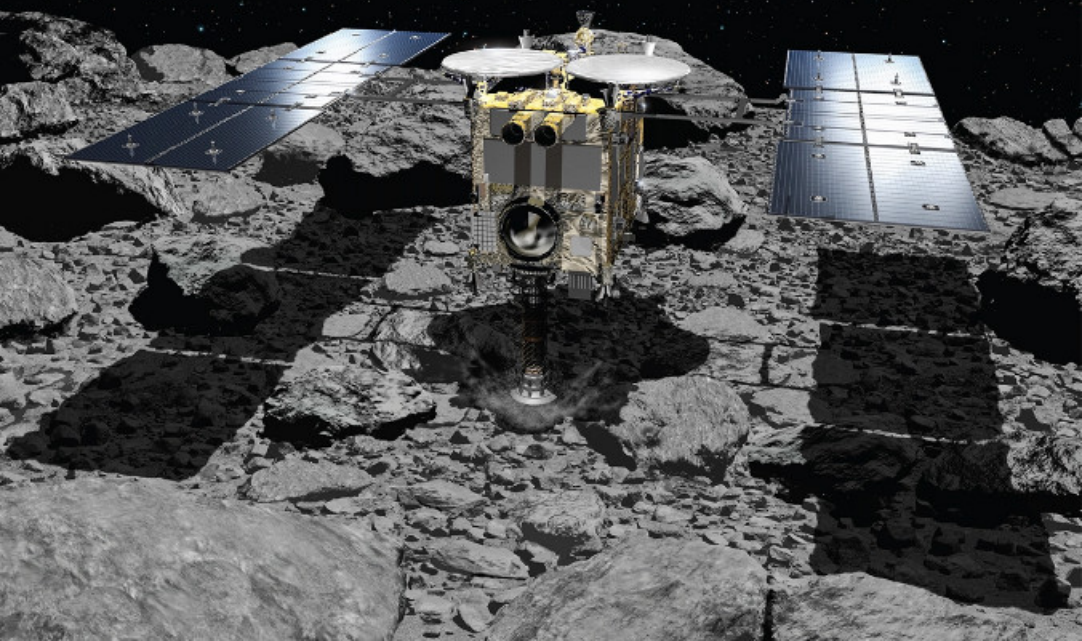

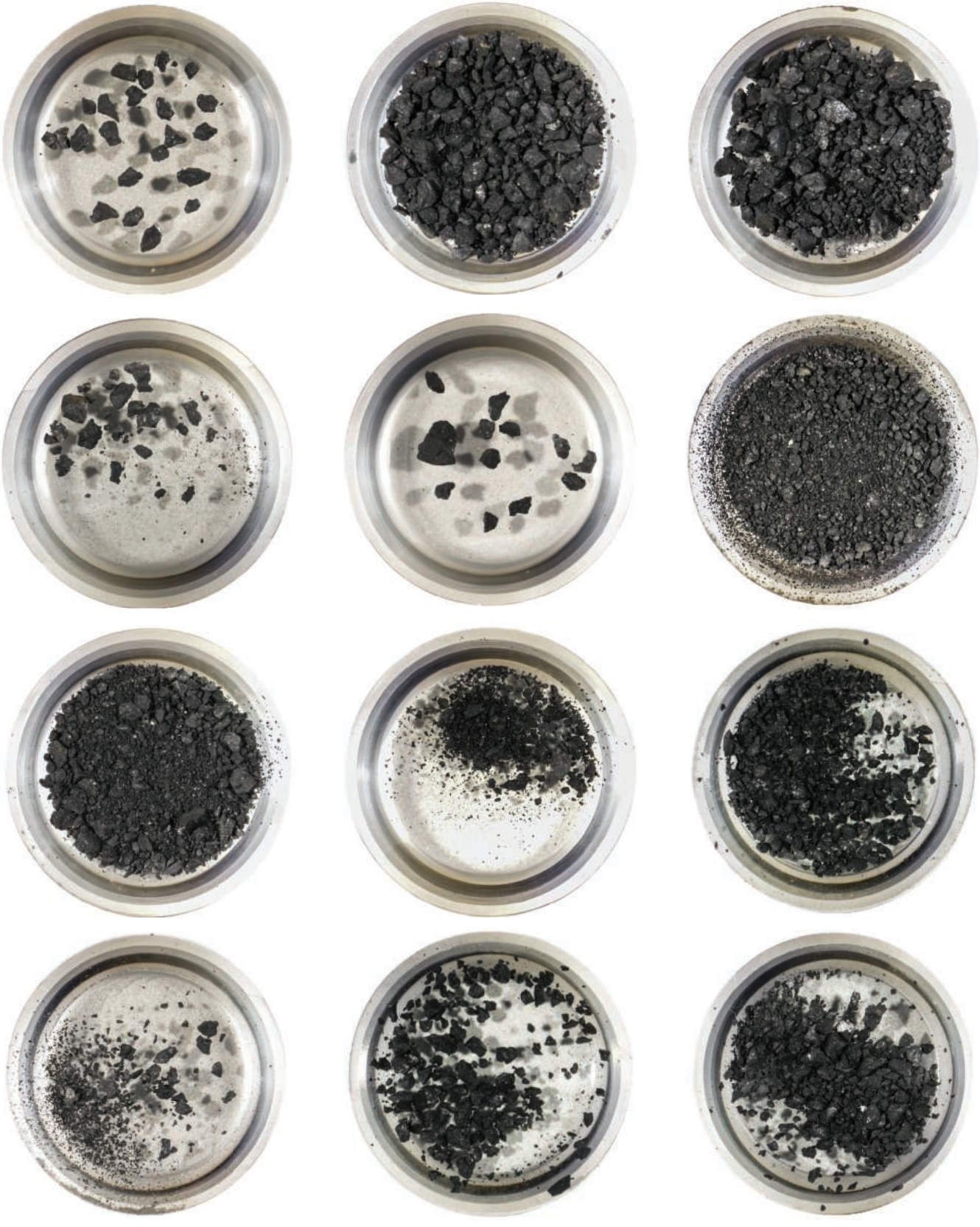

Optical microscope images of 12 particle aggregates that were selected from the Hayabusa2 samples of asteroid Ryugu

IMAGES: JAPAN AEROSPACE EXPLORATION AGENCY (JAXA)

PERSPECTIVE

Analyzing asteroid Ryugu p. 784

RESEARCH ARTICLES

Samples returned from the asteroid Ryugu are similar to Ivuna-type carbonaceous meteorites p. 786

Formation and evolution of carbonaceous asteroid Ryugu: Direct evidence from returned samples p. 787

Noble gases and nitrogen in samples of asteroid Ryugu record its volatile sources and recent surface evolution p. 788

Soluble organic molecules in samples of the carbonaceous asteroid (162173) Ryugu p. 789

Macromolecular organic matter in samples of the asteroid (162173) Ryugu p. 790

AN ASTEROID IN THE LABORATORY

By **Keith T. Smith**

Small asteroids are leftover material from the formation of the Solar System, so samples of them could provide information on processes that occurred during that early period. The Hayabusa2 spacecraft collected about 5 grams of material from the nearby asteroid (162173) Ryugu and brought it to Earth, where scientists have access to more techniques and can collect data with far greater sensitivity than is possible with spacecraft instruments.

In this issue, the results of laboratory analyses of the Ryugu samples are reported in five studies that investigate elemental abundances, isotope ratios, mineralogy, organic molecules, and more. The samples have similar composition to a class of meteorites known as Ivuna-type carbonaceous (CI) chondrites. However, there are indications that the Ryugu material is more pristine, perhaps because it has undergone less modification on Earth than CI meteorites have experienced. The Ryugu samples contain thousands of different types of organic molecules, including amino acids.

Together, these studies constrain the history of the Ryugu material. Some of the organic molecules formed in the interstellar medium, so they predate the Solar System. About 2 million years (Myr) after the Solar System began to form, some material in its outer region collapsed under gravity to form a planetesimal, known as Ryugu's parent body. About 3 Myr later, the decay of radioactive elements raised its internal temperature high enough to melt frozen water. The water reacted with the rock for a few million years, until the temperature fell again. Those aqueous alteration reactions modified the mineralogy and formed additional organic molecules. After about a billion years, an impact on the parent body ejected material into space; some of that rubble reaccumulated under gravity to form Ryugu. About 5 Myr ago, gravitational perturbations caused Ryugu to migrate into its current near-Earth orbit. A lot can be learned from just a few grams.

A long-exposure image shows the light trail of the Hayabusa2 reentry capsule, with Ryugu samples on board, as it entered Earth's atmosphere early on 6 December 2020, as seen from Coober Pedy in South Australia.

PHOTO: MORGAN SETTE/AFP/GETTY IMAGES

COSMOCHEMISTRY

Analyzing asteroid Ryugu

Samples returned by the Hayabusa2 mission provide context for the world's meteorites

By **Christopher D. K. Herd**

There are more than 70,000 meteorites worldwide. Owing to spectroscopic measurements, most of these meteorites are linked to asteroids, which largely orbit in the main asteroid belt between Mars and Jupiter. In a few tens of cases, observations of a meteorite's fall to Earth enable the calculation of an orbit that links it to part of the main asteroid belt. Rarely, however, have specific meteorite types been linked to specific asteroids. Asteroid sample return missions have changed that. On pages 786 to 790 of this issue, Yokoyama *et al.* (*1*), Nakamura *et al.* (*2*), Okazaki *et al.* (*3*), Naraoka *et al.* (*4*), and Yabuta *et al.* (*5*) report that samples of asteroid Ryugu returned to Earth by the Hayabusa2 mission closely resemble a meteorite that is classified as carbonaceous, Ivuna-like (CI), with some notable differences between asteroid and meteorite. These findings elucidate the joint history of Ryugu and CI chondrites, providing new context for meteorites in the world's collections.

The Hayabusa2 mission, operated by the Japan Aerospace Exploration Agency (JAXA), launched 3 December 2014 and spent most of 2018 and 2019 exploring the 900-m-diameter, near-Earth asteroid (162173) Ryugu. The goal of the mission was the investigation and sampling of a carbonaceous (Cb-type) asteroid—a type that likely contains water and primitive organic matter (*6*). The compositions of these asteroids are difficult to constrain, in part because they are so dark—reflecting only a small percentage of the sunlight falling on their surface, which limits spectroscopic measurements. Hayabusa2 used a suite of remote sensing instruments to provide detailed maps of the asteroid (*7*). The mission collected samples of Ryugu through two touchdowns on the asteroid: one on the raw, space-exposed surface and a second after a projectile from the spacecraft was used to uncover fresh material (*8*). The sample capsule was returned to Earth on 6 December 2020, and the sample container was subsequently transferred to the JAXA Extraterrestrial Sample Curation Center, where it was opened and the sample cataloged. A total of 5.4 g was collected from Ryugu, consisting of rock fragments up to 10 mm in size (*1*).

Department of Earth and Atmospheric Sciences, University of Alberta, Edmonton, AB, Canada. Email: herd@ualberta.ca

Yokoyama *et al.* report that the Ryugu samples contain fragments of rock that are dominated by clay-like minerals, such as serpentine and saponite, as well as carbonates, sulfides, and magnetite. The Ryugu samples date to the earliest stages of the Solar System, some 4.565 billion years ago, when warm, water-rich fluid percolated through the parent asteroid, converting primordial Solar System components into the minerals now found within them (*1*).

Meteorite classification reveals possible relationships between meteorites with similar origins or formation histories and are thus from the same parent asteroid. If a piece of Ryugu had fallen to Earth as a meteorite instead of being returned by spacecraft, meteorite scientists would classify it as a carbonaceous, Ivuna-like (CI) chondrite type 2, where Ivuna is the location in Tanzania where the prototype of this class of meteorite was recovered in 1938. CI chondrites are both fundamentally important and enigmatic: Their bulk compositions in terms of all elements (except those that remain in the gas phase) most closely match the Sun's photosphere (*9*), but their formation requires the involvement of water-rich fluid to produce the minerals within them. That the ratios of elements in CI chondrites are unchanged relative to those in the Sun implies that they represent the starting materials for everything in the entire Solar System. For this reason, CI chondrites are a baseline for all of geochemistry: Trace elements within rocks from Earth are commonly reported as CI chondrite normalized (or simply, chondrite normalized). Conversely, the alteration by water does not separate elements from one another, at least at the scale of the samples analyzed, which implies that water on the parent asteroid did not percolate more than a few centimeters.

The fall of meteorites to Earth is not a gentle journey, especially for the carbonaceous types, which tend to be very friable. The high relative velocity of the meter-scale asteroid fragments that enter Earth's atmosphere (called meteoroids) coupled with Earth's atmosphere result in friction, which slows and fragments them and causes substantial ablation (>90% of carbonaceous meteoroids), as was observed, for example, with the meteoroid fall of Tagish Lake, Canada (*10*). Once on the ground, Earth's surface is an inhospitable, alien place for these types of meteorites: In addition to the oxidizing and moisture-rich nature of Earth's atmosphere, there are organic molecules everywhere. These aspects can rapidly influence the preservation of intrinsic components in carbonaceous meteorites, including organic matter that formed on the parent asteroid (*11*). This is why the comparison of the Ryugu samples from the Hayabusa2 mission to meteorites found on Earth is so important.

The analyses reveal the link between Ryugu and CI meteorites, with important differences. Nakamura *et al.* document the various minerals within the Ryugu samples, constraining the conditions under which water percolated through their parent body. Yokoyama *et al.* determine that the altering water on the Ryugu parent asteroid was ~40°C and that the samples have since never experienced temperatures greater than 100°C. Nakamura *et al.* address the observation that spectra of reflected light from Ryugu samples are darker and flatter than those of their CI chondrite counterparts, likely a result of mineralogical changes that have occurred to CI chondrites in Earth's environment. The growth of very small sulfate crystals within Ryugu samples since their recovery suggests that similar processes in meteorites could have changed meteorite reflectance properties. Furthermore, measurements of physical properties show that Ryugu samples are distinct from any known meteorite and are a lot weaker in strength: A Ryugu-type meteoroid would not likely survive a fall to Earth's surface. Okazaki *et al.* use noble gas analyses to show that Ryugu's orbit changed ~5 million years ago, interpreted as the time when the asteroid migrated from the main belt to its current orbit near Earth.

Yabuta *et al.* and Naraoka *et al.* elucidate the composition, structure, and nature of organic matter in the samples. Macromolecular organic carbon in the Ryugu samples shows little sign of substantial heating, nor has it been affected by irradiation from exposure to cosmic rays and solar ultraviolet rays (*5*). Soluble organic matter, including proteinogenic amino acids, is preserved (*4*), suggesting that compounds of prebiotic relevance are retained and perhaps protected within mineral grains, even within the irradiated, harsh surface of Ryugu. This may also support the concept that such asteroids were sources of prebiotic molecules to the surface of early Earth (the first billion years). A general conclusion from these studies is that Ryugu is clearly linked to CI chondrites. A primordial ~100-km body (*2*), upon disruption, gave rise to the Polana or Eulalia asteroid families (*1*), from which Ryugu and all CI chondrites may be derived.

Beyond the insights into Ryugu's history, these studies emphasize the primary justification for sample return missions: Analyses in laboratories on Earth can provide far more detailed information than even the most advanced, space-qualified instrumentation. The studies have provided an unprecedented look at the mineralogy, petrology, and organic geochemistry of Ryugu from just a few tens of milligrams of material, with sequential analysis carried out to maximize the scientific return on the least amount of sample. In effect, they have defined what "the least amount of sample" is. State-of-the-art instrumentation was developed in advance of the return of the sample, and instrumentation with greater spatial sensitivity and ability to measure elements, isotopes, and compounds will continue to be developed to help answer as-yet-undefined questions generated from its study, supported by advanced curation to preserve material for future work (*11*). Hayabusa2 joins the ranks of other sample return missions, including Apollo and Luna from the Moon and Hayabusa from the asteroid Itokawa. These missions have revolutionized the scientific understanding of the planetary bodies from which the samples were collected and point the way for future missions, including OSIRIS-REx—on its way back with samples of carbonaceous asteroid Bennu—and the international effort to return samples from Mars. ■

An image captured by the Hayabusa2 spacecraft immediately after the first sampling event on 22 February 2019 shows the location of touchdown sampling on the asteroid Ryugu.

PHOTO: JAXA, UNIVERSITY OF TOKYO, KOCHI UNIVERSITY, RIKKYO UNIVERSITY, NAGOYA UNIVERSITY, CHIBA INSTITUTE OF TECHNOLOGY, MEIJI UNIVERSITY, UNIVERSITY OF AIZU, AIST

REFERENCES AND NOTES

1. T. Yokoyama *et al.*, *Science* **379**, eabn7850 (2023).
2. T. Nakamura *et al.*, *Science* **379**, eabn8671 (2023).
3. R. Okazaki *et al.*, *Science* **379**, eabo0431 (2023).
4. H. Naraoka *et al.*, *Science* **379**, eabn9033 (2023).
5. H. Yabuta *et al.*, *Science* **379**, eabn9057 (2023).
6. S.-I. Watanabe *et al.*, *Space Sci. Rev.* **208**, 3 (2017).
7. S. Sugita *et al.*, *Science* **364**, eaaw0422 (2019).
8. T. Morota *et al.*, *Science* **368**, 654 (2020).
9. H. Palme, K. Lodders, A. Jones, in *Treatise on Geochemistry (Second Edition)*, H. D. Holland, K. K. Turekian, Eds. (Elsevier, 2014), pp. 15–36.
10. P. G. Brown *et al.*, *Meteorit. Planet. Sci.* **37**, 661 (2002).
11. F. M. McCubbin *et al.*, *Space Sci. Rev.* **215**, 48 (2019).

10.1126/science.ade4188

RESEARCH ARTICLE SUMMARY

COSMOCHEMISTRY

Samples returned from the asteroid Ryugu are similar to Ivuna-type carbonaceous meteorites

Tetsuya Yokoyama† and Kazuhide Nagashima† *et al.*

INTRODUCTION: The Hayabusa2 spacecraft made two landings on the asteroid (162173) Ryugu in 2019, during which it collected samples of the surface material. Those samples were delivered to Earth in December 2020. The colors, shapes, and morphologies of the returned samples are consistent with those observed on Ryugu by Hayabusa2, indicating that they are representative of the asteroid. Laboratory analysis of the samples can determine the chemical composition of Ryugu and provide information on its formation and history.

RATIONALE: We used laboratory analysis to inform the following questions: (i) What are the elemental abundances of Ryugu? (ii) What are the isotopic compositions of Ryugu? (iii) Does Ryugu consist of primary materials produced in the disk from which the Solar System formed or of secondary materials produced in the asteroid or on a parent asteroid? (iv) When were Ryugu's constituent materials formed? (v) What, if any, relationship does Ryugu have with meteorites?

RESULTS: We quantified the abundances of 66 elements in the Ryugu samples: H, Li, Be, C, O, Na, Mg, Al, Si, P, S, Cl, K, Ca, Sc, Ti, V, Cr, Mn, Fe, Co, Ni, Cu, Zn, Ga, Ge, As, Se, Rb, Sr, Y, Zr, Nb, Mo, Ru, Rh, Pd, Ag, Cd, In, Sn, Te, Cs, Ba, La, Ce, Pr, Nd, Sm, Eu, Gd, Tb, Dy, Ho, Er, Tm, Yb, Lu, Hf, Ta, W, Tl, Pb, Bi, Th, and U. There is a slight variation in chemical compositions between samples from the first and second touchdown sites, but the variations could be due to heterogeneity among the samples that were analyzed.

The Cr-Ti isotopes and abundance of volatile elements are similar to those of carbonaceous meteorites in the CI (Ivuna-like) chondrite group. The Ryugu samples consist of the minerals magnetite, breunnerite, dolomite, and pyrrhotite as grains embedded in a matrix composed of serpentine and saponite. This mineral assemblage and the texture are also similar to those of CI meteorites. Anhydrous silicates are almost absent, which indicates extensive liquid water–rock reactions (aqueous alteration) in the material. We conclude that the samples mainly consist of secondary materials that were formed by aqueous alteration in a parent body, from which Ryugu later formed.

The oxygen isotopes in the bulk Ryugu samples are also similar to those in CI chondrites. We used oxygen isotope thermometry to determine the temperature at which the dolomite and magnetite precipitated from an aqueous solution, which we found to be 37° ± 10°C. The ^{53}Mn-^{53}Cr isotopes date the aqueous alteration at $5.2^{+0.8}_{-0.7}$ million (statistical) or $5.2^{+1.6}_{-2.1}$ million (systematic) years after the birth of the Solar System.

Phyllosilicate minerals are the main host of water in the Ryugu samples. The amount of structural water in Ryugu is similar to that in CI chondrites, but interlayer water is largely absent in Ryugu, which suggests a loss of interlayer water to space. The abundance of structural water and results from dehydration experiments indicate that the Ryugu samples remained below ~100°C from the time of aqueous alteration until the present. We ascribe the removal of interlayer water to a combination of impact heating, solar heating, solar wind irradiation, and long-term exposure to the ultrahigh vacuum of space. The loss of interlayer water from phyllosilicates could be responsible for the comet-like activity of some carbonaceous asteroids and the ejection of solid material from the surface of asteroid Bennu.

CONCLUSION: The Ryugu samples are most similar to CI chondrite meteorites but are more chemically pristine. The chemical composition of the Ryugu samples is a closer match to the Sun's photosphere than to the composition of any other natural samples studied in laboratories. CI chondrites appear to have been modified on Earth or during atmospheric entry. Such modification of CI chondrites could have included the alteration of the structures of organics and phyllosilicates, the adsorption of terrestrial water, and the formation of sulfates and ferrihydrites. Those issues do not affect the Ryugu samples. Those modifications might have changed the albedo, porosity, and density of the CI chondrites, causing the observed differences between CI meteorites, Hayabusa2 measurements of Ryugu's surface, and the Ryugu samples returned to Earth. ■

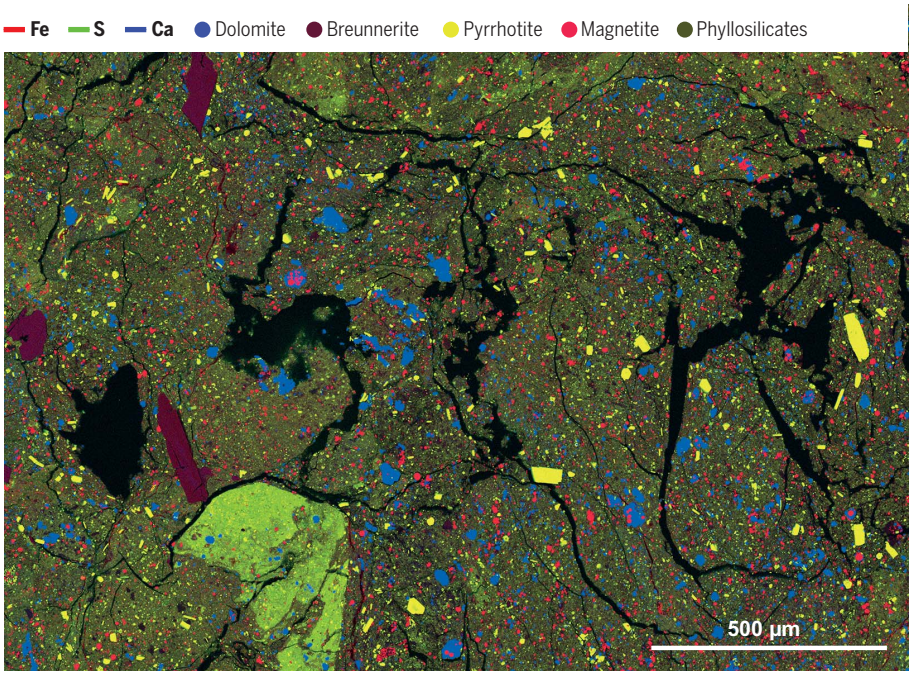

Representative petrography of a Ryugu sample, designated C0002-C1001. Colors indicate elemental abundances determined from x-ray spectroscopy. Lines of iron, sulfur, and calcium are shown as red, green, and blue (RGB) color channels in that order. Combinations of these elements are assigned to specific minerals, as indicated in the legend. All visible minerals were formed by aqueous alteration on Ryugu's parent body.

The complete list of authors and their affiliations is available in the full article online.
*Corresponding author: Hisayoshi Yurimoto (yuri@ep.sci.hokudai.ac.jp)
†These authors contributed equally to this work.
Cite this article as T. Yokoyama *et al.*, *Science* **379**, eabn7850 (2023). DOI: 10.1126/science.abn7850

READ THE FULL ARTICLE AT
https://doi.org/10.1126/science.abn7850

RESEARCH ARTICLE

COSMOCHEMISTRY

Samples returned from the asteroid Ryugu are similar to Ivuna-type carbonaceous meteorites

Tetsuya Yokoyama[1]†, Kazuhide Nagashima[2]†, Izumi Nakai[3], Edward D. Young[4], Yoshinari Abe[5], Jérôme Aléon[6], Conel M. O'D. Alexander[7], Sachiko Amari[8], Yuri Amelin[9], Ken-ichi Bajo[10], Martin Bizzarro[11], Audrey Bouvier[12], Richard W. Carlson[7], Marc Chaussidon[13], Byeon-Gak Choi[14], Nicolas Dauphas[15], Andrew M. Davis[15], Tommaso Di Rocco[16], Wataru Fujiya[17], Ryota Fukai[18], Ikshu Gautam[1], Makiko K. Haba[1], Yuki Hibiya[19], Hiroshi Hidaka[20], Hisashi Homma[21], Peter Hoppe[22], Gary R. Huss[2], Kiyohiro Ichida[23], Tsuyoshi Iizuka[24], Trevor R. Ireland[25], Akira Ishikawa[1], Motoo Ito[26], Shoichi Itoh[27], Noriyuki Kawasaki[10], Noriko T. Kita[28], Kouki Kitajima[28], Thorsten Kleine[29], Shintaro Komatani[23], Alexander N. Krot[2], Ming-Chang Liu[4], Yuki Masuda[1], Kevin D. McKeegan[4], Mayu Morita[23], Kazuko Motomura[30], Frédéric Moynier[13], Ann Nguyen[31], Larry Nittler[7], Morihiko Onose[23], Andreas Pack[16], Changkun Park[32], Laurette Piani[33], Liping Qin[34], Sara S. Russell[35], Naoya Sakamoto[36], Maria Schönbächler[37], Lauren Tafla[4], Haolan Tang[4], Kentaro Terada[38], Yasuko Terada[39], Tomohiro Usui[18], Sohei Wada[10], Meenakshi Wadhwa[40], Richard J. Walker[41], Katsuyuki Yamashita[42], Qing-Zhu Yin[43], Shigekazu Yoneda[44], Hiroharu Yui[45], Ai-Cheng Zhang[46], Harold C. ConnollyJr.[47], Dante S. Lauretta[48], Tomoki Nakamura[49], Hiroshi Naraoka[50], Takaaki Noguchi[27], Ryuji Okazaki[50], Kanako Sakamoto[18], Hikaru Yabuta[51], Masanao Abe[18], Masahiko Arakawa[52], Atsushi Fujii[18], Masahiko Hayakawa[18], Naoyuki Hirata[52], Naru Hirata[53], Rie Honda[54], Chikatoshi Honda[53], Satoshi Hosoda[18], Yu-ichi Iijima[18]‡, Hitoshi Ikeda[18], Masateru Ishiguro[14], Yoshiaki Ishihara[18], Takahiro Iwata[18,55], Kosuke Kawahara[18], Shota Kikuchi[56], Kohei Kitazato[53], Koji Matsumoto[57], Moe Matsuoka[18]§, Tatsuhiro Michikami[58], Yuya Mimasu[18], Akira Miura[18], Tomokatsu Morota[24], Satoru Nakazawa[18], Noriyuki Namiki[57], Hirotomo Noda[57], Rina Noguchi[59], Naoko Ogawa[18], Kazunori Ogawa[18], Tatsuaki Okada[18,60], Chisato Okamoto[52]‡, Go Ono[18], Masanobu Ozaki[18,55], Takanao Saiki[18], Naoya Sakatani[61], Hirotaka Sawada[18], Hiroki Senshu[56], Yuri Shimaki[18], Kei Shirai[18], Seiji Sugita[24], Yuto Takei[18], Hiroshi Takeuchi[18], Satoshi Tanaka[18], Eri Tatsumi[62], Fuyuto Terui[63], Yuichi Tsuda[18], Ryudo Tsukizaki[18], Koji Wada[56], Sei-ichiro Watanabe[20], Manabu Yamada[56], Tetsuya Yamada[18], Yukio Yamamoto[18], Hajime Yano[18], Yasuhiro Yokota[18], Keisuke Yoshihara[18], Makoto Yoshikawa[18], Kent Yoshikawa[18], Shizuho Furuya[18], Kentaro Hatakeda[64], Tasuku Hayashi[18], Yuya Hitomi[64], Kazuya Kumagai[64], Akiko Miyazaki[18], Aiko Nakato[18], Masahiro Nishimura[18], Hiromichi Soejima[64], Ayako Suzuki[64], Toru Yada[18], Daiki Yamamoto[18], Kasumi Yogata[18], Miwa Yoshitake[18], Shogo Tachibana[65], Hisayoshi Yurimoto[10,36]*

Carbonaceous meteorites are thought to be fragments of C-type (carbonaceous) asteroids. Samples of the C-type asteroid (162173) Ryugu were retrieved by the Hayabusa2 spacecraft. We measured the mineralogy and bulk chemical and isotopic compositions of Ryugu samples. The samples are mainly composed of materials similar to those of carbonaceous chondrite meteorites, particularly the CI (Ivuna-type) group. The samples consist predominantly of minerals formed in aqueous fluid on a parent planetesimal. The primary minerals were altered by fluids at a temperature of 37° ± 10°C, about $5.2^{+0.8}_{-0.7}$ million (statistical) or $5.2^{+1.6}_{-2.1}$ million (systematic) years after the formation of the first solids in the Solar System. After aqueous alteration, the Ryugu samples were likely never heated above ~100°C. The samples have a chemical composition that more closely resembles that of the Sun's photosphere than other natural samples do.

Meteorites are fragments of asteroids, but identifications of the specific parent asteroid are rarely available. Samples of asteroid (25143) Itokawa that were returned by the Hayabusa mission showed that S-type (stony, in a remote sensing classification) asteroids are composed of materials that are consistent with those of ordinary chondrite meteorites (*1*, *2*). The Hayabusa2 (*3*) spacecraft was launched on 2014 December 3 to collect samples of the near-Earth asteroid (162173) Ryugu, which is Cb-type [a subclass of C-type (carbonaceous) asteroid in the remote sensing classification]. A mission goal was to determine the relationship between C-type asteroids and the carbonaceous chondrite meteorites. Observations of Ryugu from Hayabusa2 after rendezvous showed that (i) Ryugu is darker than every meteorite group (*4*, *5*), (ii) Ryugu contains ubiquitous phyllosilicate minerals (*4*, *6*), (iii) Ryugu's surface experienced heating above 300°C (*6*), and (iv) Ryugu materials are probably more porous than carbonaceous chondrites (*7*, *8*). These results indicated that carbonaceous chondrites are plausible analogs of Ryugu but do not completely match the spacecraft observations. Laboratory analysis of the samples of Ryugu returned by Hayabusa2 is required to explain these results.

During 2019, the Hayabusa2 spacecraft made two landings on Ryugu to collect materials (*9*); it then delivered the collected samples to Earth on 2020 December 6. The returned samples are rock fragments that range in size up to ~10 mm in length, with a total mass of 5.4 g. Their colors, shapes, and morphologies are consistent with those observed on the surface by Hayabusa2, indicating that the returned samples are representative of Ryugu's surface (*10*, *11*). The samples were recovered in a nondestructive manner and examined under contamination-controlled conditions at the Japan Aerospace Exploration Agency (JAXA) Extraterrestrial Sample Curation Center before delivery to initial analysis teams in June 2021 (*10*). Our team was allocated ~125 mg of samples, which contained both powder and particles from the first and the second touchdown sites (*12*). We used ~95 mg for this paper.

Petrology and mineralogy

We prepared polished sections of particle samples that were retrieved from the first touchdown site (particle designation A0058) and from the second touchdown site (C0002) (*12*). The petrography, mineralogy, and chemical composition of the minerals were determined using electron microscopy (*12*).

The Ryugu samples are mixtures of mechanical fragments—composed of fine-grained materials of phyllosilicate minerals, predominantly serpentine and saponite—and coarser grains dominated by carbonates, magnetite, and sulfides (Fig. 1, A, B, and D). No Ca-Al–rich inclusions (CAIs) or chondrules, which are characteristic constituents of most chondrite meteorites, were evident in the allocated samples. The serpentine-to-saponite molar ratio is about 3:2 on the basis of the chemical compositions of the phyllosilicate minerals (Fig. 1C). The coarser-grained minerals in the polished sections are dolomite [$CaMg(CO_3)_2$], breunnerite [$(Mg, Fe, Mn)CO_3$], pyrrhotite ($Fe_{1-x}S$, where x = 0 to 0.17), and magnetite (Fe_3O_4) (Fig. 1B). These are distributed throughout the sections (Fig. 1D) and in small veins (Fig. 1A). Calcite ($CaCO_3$), pentlandite [$(Fe,Ni)_9S_8$], cubanite ($CuFe_2S_3$), ilmenite ($FeTiO_3$), apatite [$(Ca_5(PO_4)_3(OH,F,Cl)$], and Mg-Na-phosphate are present as accessory minerals. Anhydrous silicates, such as olivine and pyroxene, are common in chondrites but are very rare in our Ryugu samples, occurring only as discrete grains smaller than ~10 μm across. No metal grains were identified. Overall, the petrology and mineralogy of the Ryugu samples most closely resemble those of the CI (Ivuna-like) group of chondrite

meteorites, which have experienced extensive aqueous alteration (*13*). However, sulfates and ferrihydrite, which are commonly observed in CI chondrites, were not identified in the Ryugu samples that we studied.

Bulk chemical and isotopic compositions

Bulk chemical compositions were determined using ~25 mg of small-grain aggregate samples from each site: particles A0106 and A0107 from the first touchdown site and C0108 from the second touchdown site (*12*). Elemental abundances were determined using x-ray fluorescence (XRF) analysis and inductively coupled plasma mass spectrometry (ICP-MS). After chemical analysis, the same samples, ICP-MS analysis, and thermal ionization mass spectrometry (TIMS) were used to determine isotopic compositions of titanium and chromium.

We found no systematic differences in chemical composition between the samples from the first and second touchdown sites (Fig. 2). We did find variations in bulk composition within each of those samples, which are most likely due to heterogeneity at small scales (*12*). The masses of the samples that were analyzed were less than 30 mg; coarser-grained water-precipitated minerals might not be uniformly distributed at that scale (a cross section of an ~10-mg block is shown in Fig. 1D). Spatial heterogeneity in the mineral distributions is observed for carbonates (dolomite) and sulfides (pyrrhotite), which both precipitate from aqueous solution and probably occurred during aqueous alteration on Ryugu's parent planetesimal (Fig. 1). We found different concentrations of rare earth elements (REEs) between samples from the first touchdown site and the second touchdown site (*12*), with both being higher than the REE abundance in CI chondrites (Fig. 2). These variable enrichments could be due to depletion of H_2O, relative to CI chondrites (see next paragraph and the section H_2O and CO_2 sources), and the heterogeneous distribution of REE-rich Ca-phosphate grains (*14*, *15*). Heterogeneity at similar scales has been observed in CI chondrites (*16*, *17*) and in the ungrouped carbonaceous chondrite Tagish Lake (*18*).

We did not observe systematic depletions of elemental abundances, relative to CI chondrites, as a function of the 50% condensation temperatures of each element (their volatility) (Fig. 2). This is unlike other groups of carbonaceous chondrites, which show various degrees of depletion with volatility (*19*). The high abundance of moderately and highly volatile elements in the Ryugu samples indicates that Ryugu is composed of materials related to the CI chondrite group. However, the elemental abundances of hydrogen and oxygen are highly depleted in the Ryugu samples compared with CI chondrites, which we interpret as being due to the removal of H_2O.

Previous studies have found a dichotomy in the isotopic compositions of titanium and chromium between noncarbonaceous (NC)–like and carbonaceous (CC)–like isotope ratios (*20*–*23*). The bulk titanium and chromium isotopic ratios we measured for the Ryugu samples are similar to the CB (Bencubbin-like) and CI chondrite values (*12*), which are both CC (Fig. 3). CB chondrites are metal rich (*24*), unlike the Ryugu samples, and so are unlikely to be directly related.

Oxygen isotopic composition

Bulk oxygen isotopic compositions of the Ryugu samples from the first (~4 mg of aggregate sample A0107) and the second (~1 mg of fragment from particle sample C0002) touchdown sites were determined using laser-fluorination isotope-ratio mass spectrometry (LF-IRMS) (*12*). Oxygen isotopic compositions of secondary minerals from the first touchdown site were determined by secondary ion mass spectrometry (SIMS) using the polished section used for petrology and mineralogy (*12*).

Oxygen isotopes measured in the bulk Ryugu samples overlap with those of the bulk samples of the Orgueil CI chondrite (Fig. 4). We interpret the variation in $\delta^{18}O$ (defined as the permille deviation from the $^{18}O/^{16}O$ ratio of standard mean ocean water) as being due to the heterogeneous distributions of the constituent minerals, which may have very different isotopic compositions, including phyllosilicates, carbonates, and magnetite. Two ~2-mg Ryugu samples from the first touchdown site have consistent $\Delta^{17}O$ values (defined as the permille deviation from

[1]Department of Earth and Planetary Sciences, Tokyo Institute of Technology, Tokyo 152-8551, Japan. [2]Hawai'i Institute of Geophysics and Planetology, University of Hawai'i at Mānoa, Honolulu, HI 96822, USA. [3]Department of Applied Chemistry, Tokyo University of Science, Tokyo 162-8601, Japan. [4]Department of Earth, Planetary, and Space Sciences, University of California, Los Angeles, CA 90095, USA. [5]Graduate School of Engineering Materials Science and Engineering, Tokyo Denki University, Tokyo 120-8551, Japan. [6]Institut de Minéralogie, de Physique des Matériaux et de Cosmochimie, Sorbonne Université, Museum National d'Histoire Naturelle, Centre National de la Recherche Scientifique Unité Mixte de Recherche 7590, Institut de recherche pour le développement, 75005 Paris, France. [7]Earth and Planets Laboratory, Carnegie Institution for Science, Washington, DC 20015, USA. [8]McDonnell Center for the Space Sciences and Physics Department, Washington University, St. Louis, MO 63130, USA. [9]Guangzhou Institute of Geochemistry, Chinese Academy of Sciences, Guangzhou, GD 510640, China. [10]Department of Natural History Sciences, Hokkaido University, Sapporo 001-0021, Japan. [11]Centre for Star and Planet Formation, Globe Institute, University of Copenhagen, K 1350 Copenhagen, Denmark. [12]Bayerisches Geoinstitut, Universität Bayreuth, 95447 Bayreuth, Germany. [13]Université de Paris, Institut de physique du globe de Paris, Centre National de la Recherche Scientifique, 75005 Paris, France. [14]Department of Physics and Astronomy, Seoul National University, Seoul 08826, Republic of Korea. [15]Department of the Geophysical Sciences and Enrico Fermi Institute, University of Chicago, Chicago, IL 60637, USA. [16]Faculty of Geosciences and Geography, University of Göttingen, D-37077 Göttingen, Germany. [17]Faculty of Science, Ibaraki University, Mito 310-8512, Japan. [18]Institute of Space and Astronautical Science/Jaxa Space Exploration Center, Japan Aerospace Exploration Agency, Sagamihara 252-5210, Japan. [19]Department of General Systems Studies, University of Tokyo, Tokyo 153-0041, Japan. [20]Department of Earth and Planetary Sciences, Nagoya University, Nagoya 464-8601, Japan. [21]Osaka Application Laboratory, Rigaku Corporation, Osaka 569-1146, Japan. [22]Max Planck Institute for Chemistry, Mainz 55128, Germany. [23]Analytical Technology Division, Horiba Techno Service Co. Ltd., Kyoto 601-8125, Japan. [24]Department of Earth and Planetary Science, University of Tokyo, Tokyo 113-0033, Japan. [25]School of Earth and Environmental Sciences, University of Queensland, St Lucia, QLD 4072, Australia. [26]Kochi Institute for Core Sample Research, Japan Agency for Marine-Earth Science and Technology, Kochi 783-8502, Japan. [27]Department of Earth and Planetary Sciences, Kyoto University, Kyoto 606-8502, Japan. [28]Department of Geoscience, University of Wisconsin, Madison, WI 53706, USA. [29]Max Planck Institute for Solar System Research, 37077 Göttingen, Germany. [30]Thermal Analysis Division, Rigaku Corporation, Tokyo 196-8666, Japan. [31]Astromaterials Research and Exploration Science Division, National Aeronautics and Space Administration Johnson Space Center, Houston, TX 77058, USA. [32]Division of Earth-System Sciences, Korea Polar Research Institute, Incheon 21990, Korea. [33]Centre de Recherches Pétrographiques et Géochimiques, Centre National de la Recherche Scientifique–Université de Lorraine, 54500 Nancy, France. [34]School of Earth and Space Sciences, University of Science and Technology of China, Anhui 230026, China. [35]Department of Earth Sciences, Natural History Museum, London SW7 5BD, UK. [36]Isotope Imaging Laboratory, Hokkaido University, Sapporo 001-0021, Japan. [37]Institute for Geochemistry and Petrology, Department of Earth Sciences, ETH Zurich, Zurich, Switzerland. [38]Department of Earth and Space Science, Osaka University, Osaka 560-0043, Japan. [39]Spectroscopy and Imaging Division, Japan Synchrotron Radiation Research Institute, Hyogo 679-5198, Japan. [40]School of Earth and Space Exploration, Arizona State University, Tempe, AZ 85281, USA. [41]Department of Geology, University of Maryland, College Park, MD 20742, USA. [42]Graduate School of Natural Science and Technology, Okayama University, Okayama 700-8530, Japan. [43]Department of Earth and Planetary Sciences, University of California, Davis, CA 95616, USA. [44]Department of Science and Engineering, National Museum of Nature and Science, Tsukuba 305-0005, Japan. [45]Department of Chemistry, Tokyo University of Science, Tokyo 162-8601, Japan. [46]School of Earth Sciences and Engineering, Nanjing University, Nanjing 210023, China. [47]Department of Geology, School of Earth and Environment, Rowan University, Glassboro, NJ 08028, USA. [48]Lunar and Planetary Laboratory, University of Arizona, Tucson, AZ 85705, USA. [49]Department of Earth Science, Tohoku University, Sendai 980-8578, Japan. [50]Department of Earth and Planetary Sciences, Kyushu University, Fukuoka 819-0395, Japan. [51]Earth and Planetary Systems Science Program, Hiroshima University, Higashi-Hiroshima 739-8526, Japan. [52]Graduate School of Science, Kobe University, Kobe 657-8501, Japan. [53]Department of Computer Science and Engineering, University of Aizu, Aizu-Wakamatsu 965-8580, Japan. [54]Faculty of Science and Technology, Kochi University, Kochi 780-8520, Japan. [55]Graduate University for Advanced Studies, Sokendai, Kanagawa 240-0193, Japan. [56]Planetary Exploration Research Center, Chiba Institute of Technology, Narashino 275-0016, Japan. [57]National Astronomical Observatory of Japan, Mitaka 181-8588, Japan. [58]Faculty of Engineering, Kinki University, Higashi-Hiroshima 739-2116, Japan. [59]Academic Assembly Institute of Science and Technology, Niigata University, Niigata 950-2181, Japan. [60]Department of Chemistry, University of Tokyo, Tokyo 113-0033, Japan. [61]College of Science Department of Physics, Rikkyo University, Tokyo 171-8501, Japan. [62]Instituto de Astrofísica de Canarias, University of La Laguna, Tenerife, Spain. [63]Graduate School of Engineering, Kanagawa Institute of Technology, Atsugi 243-0292, Japan. [64]Marine Works Japan Ltd., Yokosuka 237-0063, Japan. [65]UTokyo Organization for Planetary and Space Science, University of Tokyo, Tokyo 113-0033, Japan.

***Corresponding author. Email: yuri@ep.sci.hokudai.ac.jp** †These authors contributed equally to this work. ‡Deceased. §Present address: Laboratoire d'études spatiales et d'instrumentation en astrophysique, Observatoire de Paris, 92195 Meudon, France.

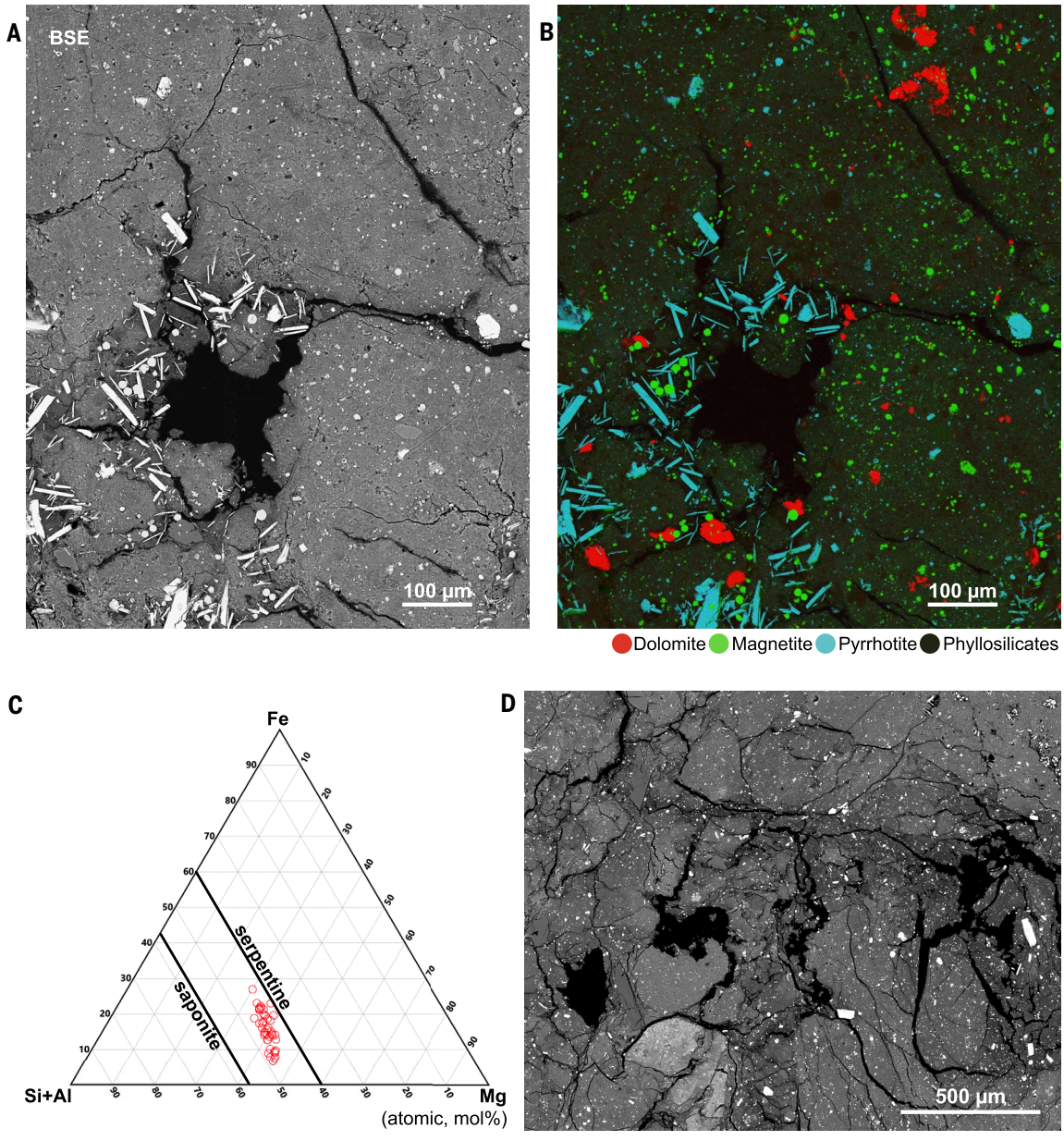

Fig. 1. Petrography of the Ryugu sample. (**A**) Backscattered electron (BSE) image of Ryugu sample A0058-C1001 (*12*). The black space in the figure is a pore. (**B**) Combined elemental map of the same sample, with characteristic x-rays of Ca Kα, Fe Kα, and S Kα lines assigned to red, green, and blue (RGB) color channels. Carbonate (dolomite), sulfide (pyrrhotite), and iron oxide (magnetite) minerals are embedded in a matrix of phyllosilicates and, in some cases, precipitated in small veins. The sulfide texture is similar to that in the ungrouped chondrite Flensburg (*52*). (**C**) Ternary diagram between Fe, Mg, and Si with Al (Si+Al) showing bulk chemical compositions of phyllosilicates in A0058-C1001. Black lines are compositions of solid solution for serpentine and saponite. Each open red circle shows the bulk chemical composition of phyllosilicates that were measured in various locations of the areas shown in (A) and (B), with each location being a 5- to 10-μm square. We chose each size to exclude minerals other than phyllosilicates in the area. The bulk compositions differ from location to location, with a distribution that indicates that the phyllosilicates consist of serpentine and saponite with variable Fe/Mg ratios. Uncertainties on each measurement are smaller than the symbol size. (**D**) BSE image of Ryugu sample C0002-C1001 showing brecciated matrix. The texture is similar to that of CI chondrites (*53*).

the terrestrial fractionation line) (*12*), with an average $\Delta^{17}O$ of 0.68 ± 0.05 per mil (‰) (uncertainty of 2 SD). These are higher $\Delta^{17}O$ values than those of the three samples of Orgueil that were analyzed in the same laboratory session, which have $\Delta^{17}O$ values of 0.42 to 0.53‰. Another Ryugu sample from the second touchdown site that was analyzed in a different laboratory has a lower $\Delta^{17}O$ value of 0.44 ± 0.05‰, which is consistent with values for Orgueil that were analyzed with the same equipment ($\Delta^{17}O$ = 0.39 to 0.57‰). We therefore ascribe the differences between the Ryugu samples as being due to heterogeneity on small scales or different sampling sites on Ryugu and not as systematic differences between the laboratories. The average $\Delta^{17}O$ value of the three Ryugu samples, 0.61 ± 0.28‰ (2 SD), is slightly higher than the average for the Orgueil samples of 0.48 ± 0.15‰ (2 SD, five samples); a single measurement of the CI chondrite Ivuna,

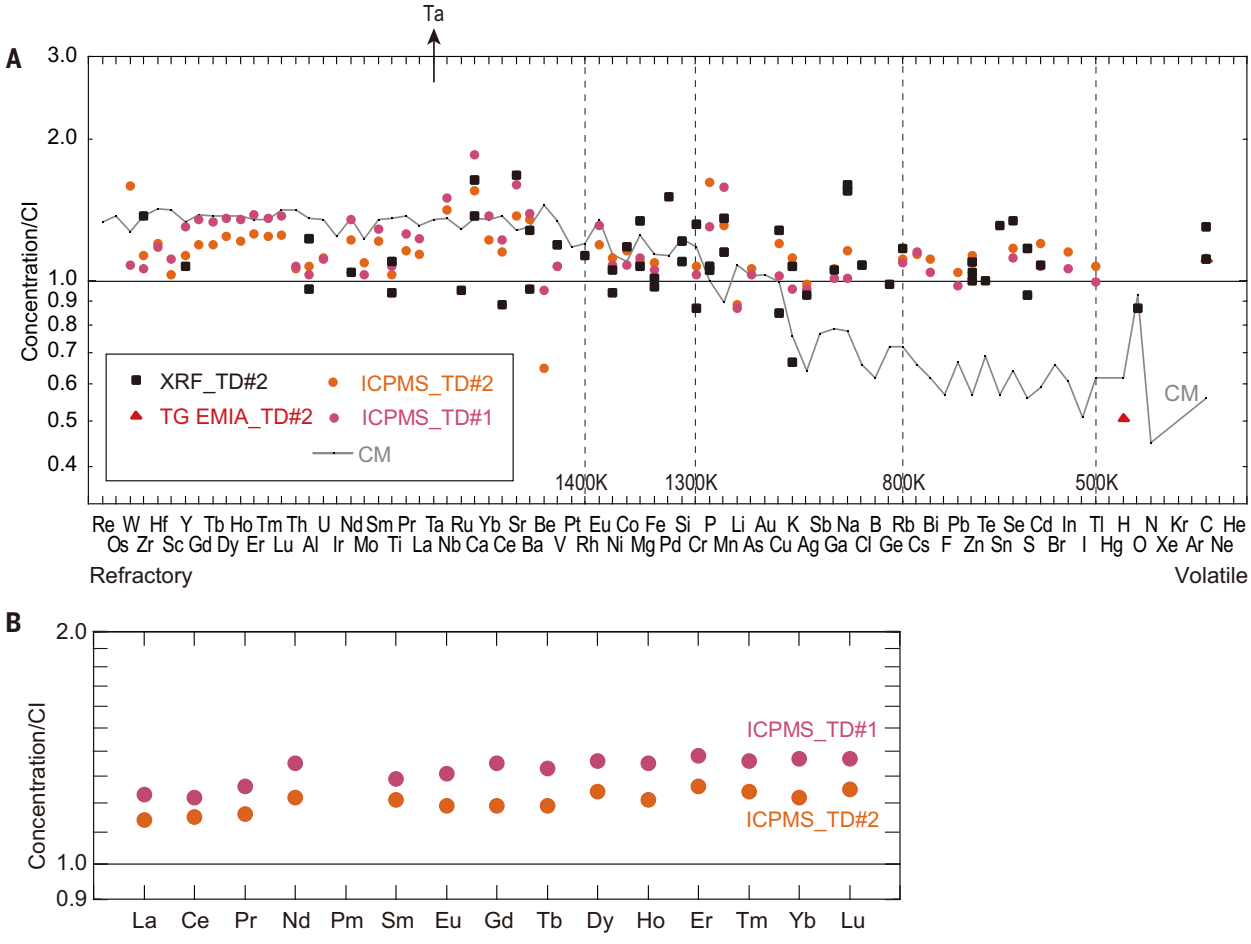

Fig. 2. Elemental abundances of Ryugu. (**A**) Measured abundances of elements in Ryugu normalized to CI chondrite values (*49*) and plotted on a logarithmic scale and as a function of 50% condensation temperature (i.e., volatility) (*49*). There is no systematic trend with condensation temperature. Black squares are results from our XRF analysis (*12*). Pink and orange circles are results from our ICP-MS analysis (*12*). Red triangles are results from our TG-MS and EMIA-Step analyses (*12*). In the legend, TD#1 and TD#2 indicate samples from the first and second touchdown sites, respectively. The high abundance of tantalum is indicated by an upward arrow, which is due to contamination by the tantalum projectiles used in the sampling process (*12*). The gray line shows representative values for CM (Mighei-type) chondrites (*49*). The horizontal black line is the 1:1 ratio. The vertical dashed lines show specific condensation temperature thresholds, as labeled. (**B**) REE abundances, plotted in order of atomic number and on a logarithmic scale. For both (A) and (B), numeric values and uncertainties are provided in data S2. Uncertainties are mostly much smaller than the variations between the samples and techniques.

which was 0.41 ± 0.05‰; and prior measurements of CI chondrites [0.39 to 0.47‰ (*25*)]. The difference may either reflect original heterogeneity between small samples or result from contamination of the meteorite samples by terrestrial water that was incorporated by the phyllosilicates, sulfates, iron oxides, and iron hydroxides. The discrepancy in the $\Delta^{17}O$ values between Ryugu and Orgueil (~0.15‰ offset) persists despite heating both groups of samples to ~116°C for 2 to 4 hours to remove adsorbed water, which indicates that any terrestrial contamination in the Orgueil samples is part of the structure of the minerals and not adsorbed to surfaces.

Dolomite grains in the Ryugu samples are enriched in ^{18}O, relative to the whole-rock values, but have $\Delta^{17}O$ values consistent with those of the whole rock (Fig. 4). The constituent minerals are generally consistent with mass-dependent fractionation. The oxygen isotope ratios of dolomite in Ryugu overlap with those of dolomite from Ivuna (Fig. 4). Ryugu magnetite is depleted in ^{18}O, relative to the whole-rock value, with all but one measurement being consistent with mass fractionation. The oxygen isotope ratios of Ryugu magnetite grains are consistent with those of Ivuna (*26*, *27*). The distributions of $^{18}O/^{16}O$ ratios and the consistency of $\Delta^{17}O$ values indicate isotopic equilibrium during the growth of the minerals that were produced during aqueous alteration.

In one polished section, dolomite and magnetite grains are located within ~100 μm of each other (fig. S1). The dolomite $\Delta^{17}O$ value is −0.7 ± 0.9‰ (2 SD) (*12*), whereas the magnetite grains have consistent $\Delta^{17}O$ values, with a mean of −0.1 ± 0.4‰ (2 SE). Because the $\Delta^{17}O$ values of dolomite and magnetite grains are within their mutual uncertainties, they might have precipitated from the same fluid. Assuming isotopic equilibrium, we used oxygen isotope thermometry (*28*–*31*) to estimate the temperature at which the dolomite-magnetite pair precipitated. The $\delta^{18}O$ values of the dolomite and magnetite are 29.9 ± 0.9‰ (2 SD) and −3.0 ± 1.1‰ (2 SD), respectively. The difference in $\delta^{18}O$ values between the dolomite and magnetite is 32.9 ± 1.4‰, which corresponds to an equilibration temperature of 37° ± 10°C (fig. S2). The temperature is in the range (10° to 150°C) of previous estimates for aqueous alteration of CI chondrites (*25*, *32*–*34*). We also estimated (*12*) the oxygen isotope ratios of the water and serpentine that would have been in

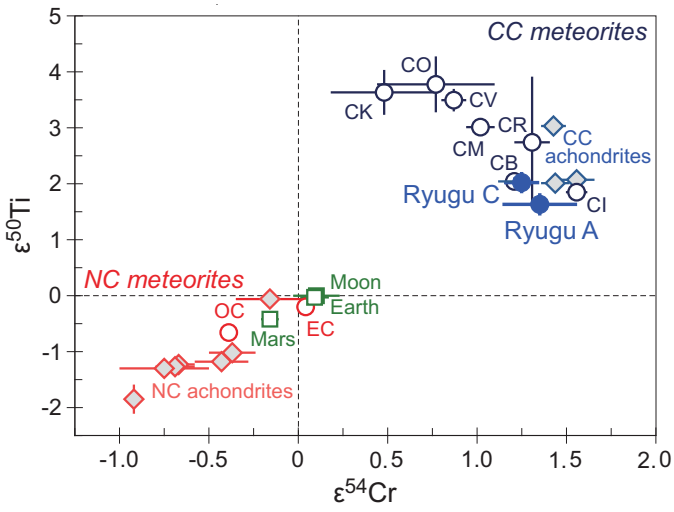

Fig. 3. Ti and Cr isotopes for Ryugu and other Solar System materials. Data are shown in epsilon notation, as defined by eqs. S1 and S2. The Ryugu samples (filled blue circles) are most similar to the CB and CI chondrites, in the CC meteorites region. Abbreviations are as follows: CC, carbonaceous (dark blue symbols); NC, noncarbonaceous (red symbols); CI, CM, CO, CV, CK, CR, and CB, named groups of carbonaceous chondrite meteorites; OC, ordinary chondrite meteorites; and EC, enstatite chondrite meteorites (all empty circles). The CC achondrites and NC achondrites (filled diamonds) are differentiated stony meteorites that have Ti and Cr isotopic compositions similar to those of CC and NC meteorites, respectively. Values for Earth, the Moon, and Mars are shown for comparison (empty green squares). Error bars are 2 SD of the mean. Data are from (*21*, *54*, *55*), except Ryugu (this work). Numeric values are provided in data S3.

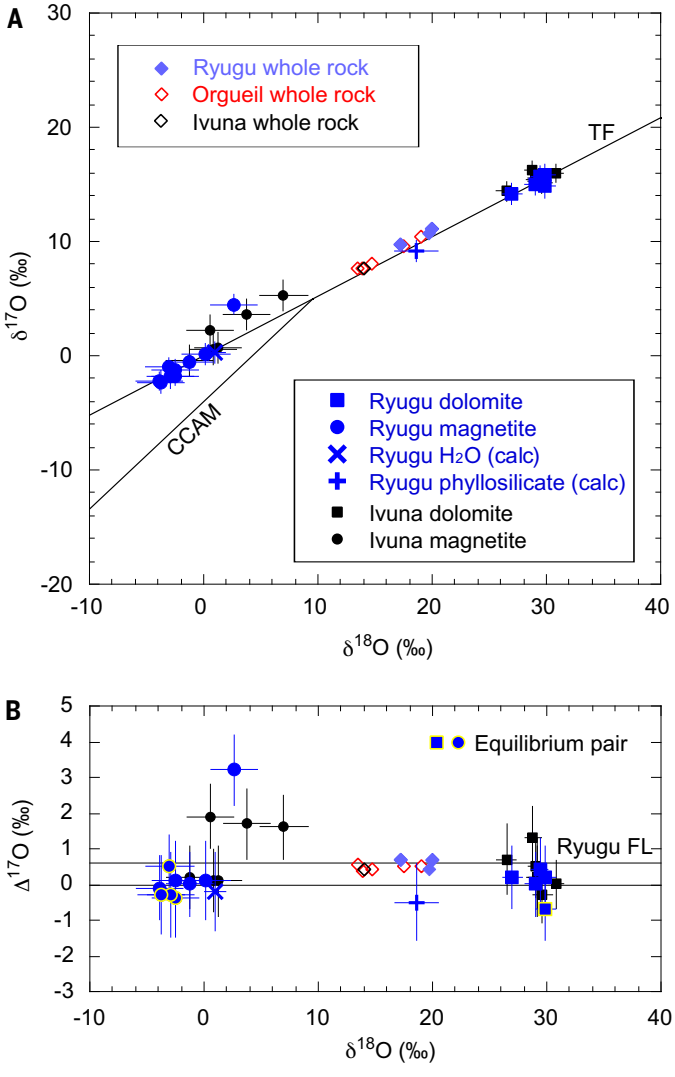

Fig. 4. Oxygen isotopes in Ryugu, Ivuna, and Orgueil. (**A**) $\delta^{17}O$ as a function of $\delta^{18}O$. Data are shown in δ notation, which is defined as the permille deviation from standard mean ocean water; see eq. S3. TF indicates the terrestrial mass fractionation line, which corresponds to mass-dependent isotope fractionations on Earth. CCAM indicates the carbonaceous chondrite anhydrous mineral line, which corresponds to the mass-independent isotope fractionations observed in refractory inclusions in chondrite meteorites. The Ryugu samples (solid blue symbols) are similar to the CI chondrites (black symbols for Ivuna and red for Orgueil). Oxygen isotopic compositions of H_2O (cross symbol) and phyllosilicates (plus symbol) in samples of Ryugu were calculated from values of dolomite and magnetite [blue symbols outlined in yellow in (B)] from the locations shown in fig. S1. (**B**) $\Delta^{17}O$ as a function of $\delta^{18}O$. The Δ notation is defined as the permille deviation from the TF line; see eq. S4. Ryugu FL indicates the mass-dependent fractionation line of Ryugu, which is derived by fitting a linear model to the Ryugu whole-rock data (*12*). In both (A) and (B), the error bars are 2 SD. Numeric values are provided in data S4.

equilibrium with those of the magnetite and dolomite grains and found ($\delta^{18}O$, $\delta^{17}O$) = (1.0 ± 1.0‰, 0.3 ± 1.0‰) for the water and (18.6 ± 2.0‰, 9.2 ± 1.0‰) for the serpentine (Fig. 4 and fig. S2). The value for serpentine is consistent with that of the whole rock, which is what we expected because of the high abundance of serpentine in the samples. These measurements indicate that oxygen isotopes were in equilibrium, or close to it, during aqueous alteration of the Ryugu samples.

^{53}Mn-^{53}Cr dating

The precipitation of dolomite and magnetite during aqueous alteration was dated using the ^{53}Mn-^{53}Cr system (*12*), which is based on the decay of the short-lived radionuclide ^{53}Mn to ^{53}Cr (half-life of 3.7 million years). The ^{53}Mn-^{53}Cr systems for dolomite in the Ryugu and Ivuna samples (Fig. 5) were measured from the polished section used for petrology and mineralogy using SIMS (*12*).

The slopes of linear models fitted to the data indicate initial ^{53}Mn/^{55}Mn ratios of $(2.55 \pm 0.35) \times 10^{-6}$ (2 SD) for Ryugu and $(3.14 \pm 0.28) \times 10^{-6}$ (2 SD) for Ivuna (*12*). Both initial values are consistent with those of CI dolomites that were obtained in previous studies (*35*, *36*). We compared the initial ^{53}Mn/^{55}Mn ratio to that of the D'Orbigny meteorite (*37*), an angrite that has been precisely dated and can be related to the ages of the oldest CAIs from CV (Vigarano-type) chondrites (*38*–*40*). We found that dolomite precipitation in the Ryugu sample occurred at $5.2^{+0.8}_{-0.7}$ million years after the oldest CAI formation, which is conventionally used to represent the formation of the Solar System. However, there is additional systematic uncertainty in this dolomite precipitation date because the initial Solar System ratio of ^{53}Mn/^{55}Mn is not precisely constrained. If we adopt different initial ^{53}Mn/^{55}Mn ratios than those found for D'Orbigny, the dolomite precipitation date changes to 4.8 million years [using the value in (*41*)] or 6.8 million years [for the value in (*42*)] after CAI formation. There may be additional systematic uncertainty in the ^{53}Mn-^{53}Cr age due to inherent analytical limitations of the measurement technique (*12*). We conclude that the Ryugu precipitation date is in the range of 3.1 million to 6.8 million years after CAI formation.

H_2O and CO_2 sources

Gas-release curves were measured for Ryugu samples from the first touchdown site (particle samples of A0040 and A0094) and Ivuna. Gas release was measured by increasing heating temperatures using thermogravimetric analysis coupled with mass spectrometry (TG-MS) and combination analyses of pyrolysis and combustion (EMIA-Step) (*12*). The mass decrease of the samples during heating (mass loss) was measured simultaneously.

The mass loss and differential mass loss [derivative thermogravimetric (DTG)] curves (*12*) for our Ryugu and Ivuna samples are shown in Fig. 6 [see also (*12*)]. The results for Ivuna are similar to those reported in previous studies (*43*). For Ryugu, we found a total mass loss of 15.38 ± 0.50 wt %, which is ~30% smaller than that of Ivuna (data S6). The species responsible for the mass loss are mainly H_2O and CO_2 for both Ivuna and Ryugu (Fig. 6). SO_2 might also contribute substantially, but we were unable to quantify it because of a lack of an appropriate standard (*12*).

The total weight fractions of H_2O and CO_2 gases released from the Ryugu sample that were measured using TG-MS are larger (20.78 ± 1.40 wt %) than the total mass loss (15.38 ± 0.50 wt %) that was measured using TG alone (*12*). We interpret this as indicating that carbonates were not the only sources of CO_2 during the TG-MS measurement, with organic carbon being oxidized to CO_2 by residual O_2 in the He gas flow used for the experiment, which produced a spurious excess of CO_2 in the mass spectrometry. Because decomposition of carbonates occurs within a small temperature range (*43*), we assigned the sharp CO_2 peaks at 600° to 800°C (Fig. 6) to carbonates. We observed two carbonate peaks for the Ryugu samples, which, according to the petrographic results above, contain three types of carbonate (dolomite, breunnerite, and calcite). We were unable to attribute specific peaks to specific carbonates. The double peaks might arise from sealed pore spaces because we analyzed intact chips and not powders.

The remaining broad continuum in Fig. 6 is probably due to the oxidation of organic carbon by the indigenous oxygen that is contained in organics in the sample or by residual O_2 in the He gas flow. Therefore, we assigned the CO_2 peak to carbonates and the remainder to organics (Fig. 6). The organic carbon content values are lower limits, because TG-MS leaves some organic carbon in the sample. The organic carbon and total carbon concentrations that we found using TG-MS were lower than those measured using EMIA-Step (*12*) (data S6). We estimate that 74 ± 3% of Ryugu organic carbon was released in TG-MS, as the broad organic carbon continuum, and 93 ± 4% for Ivuna. The profiles of the broad organic carbon continuum are different for both samples, which indicates differing organic components in Ryugu and Ivuna.

Many peaks are apparent in the H_2O release curves (Fig. 6). We identified adsorbed H_2O from sulfates released at ~250°C and a larger amount of H_2O from phyllosilicates

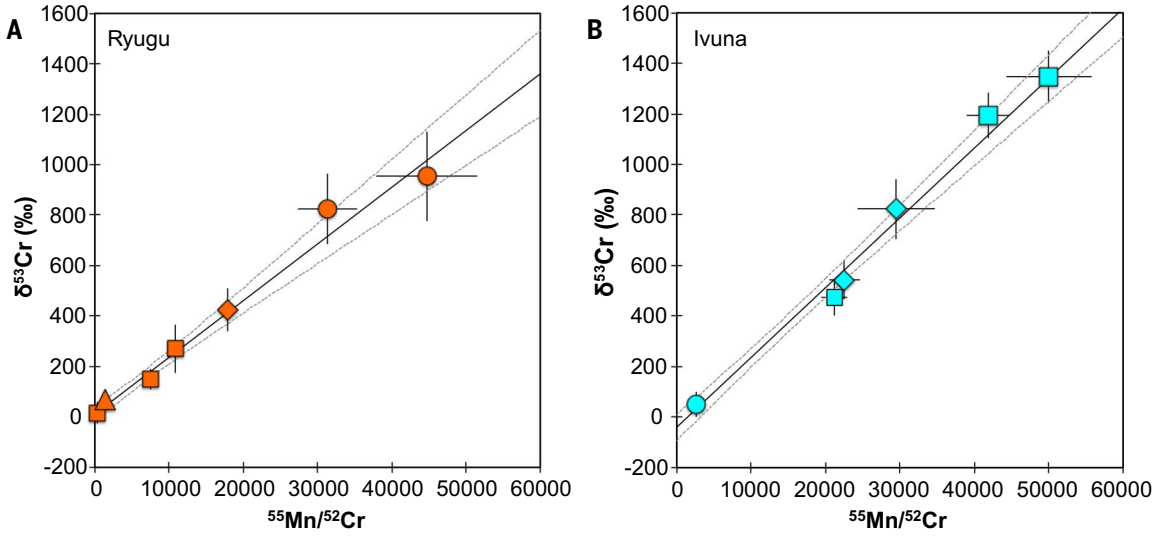

Fig. 5. ^{53}Mn-^{53}Cr isotopes measured from dolomite. (**A** and **B**) Data are shown for samples of (A) Ryugu and (B) Ivuna. Each symbol shape corresponds to measurements of a single crystal. The solid straight lines are least squares regression lines fitted to the data, and the dashed curves show 2σ confidence limits (*12*). The regression for Ryugu (*12*) indicates that dolomite precipitation occurred $5.2^{+0.8}_{-0.7}$ million years after the birth of the Solar System (there are additional systematic uncertainties on this value; see the text). Error bars are 2 SD. Numeric values are provided in data S5.

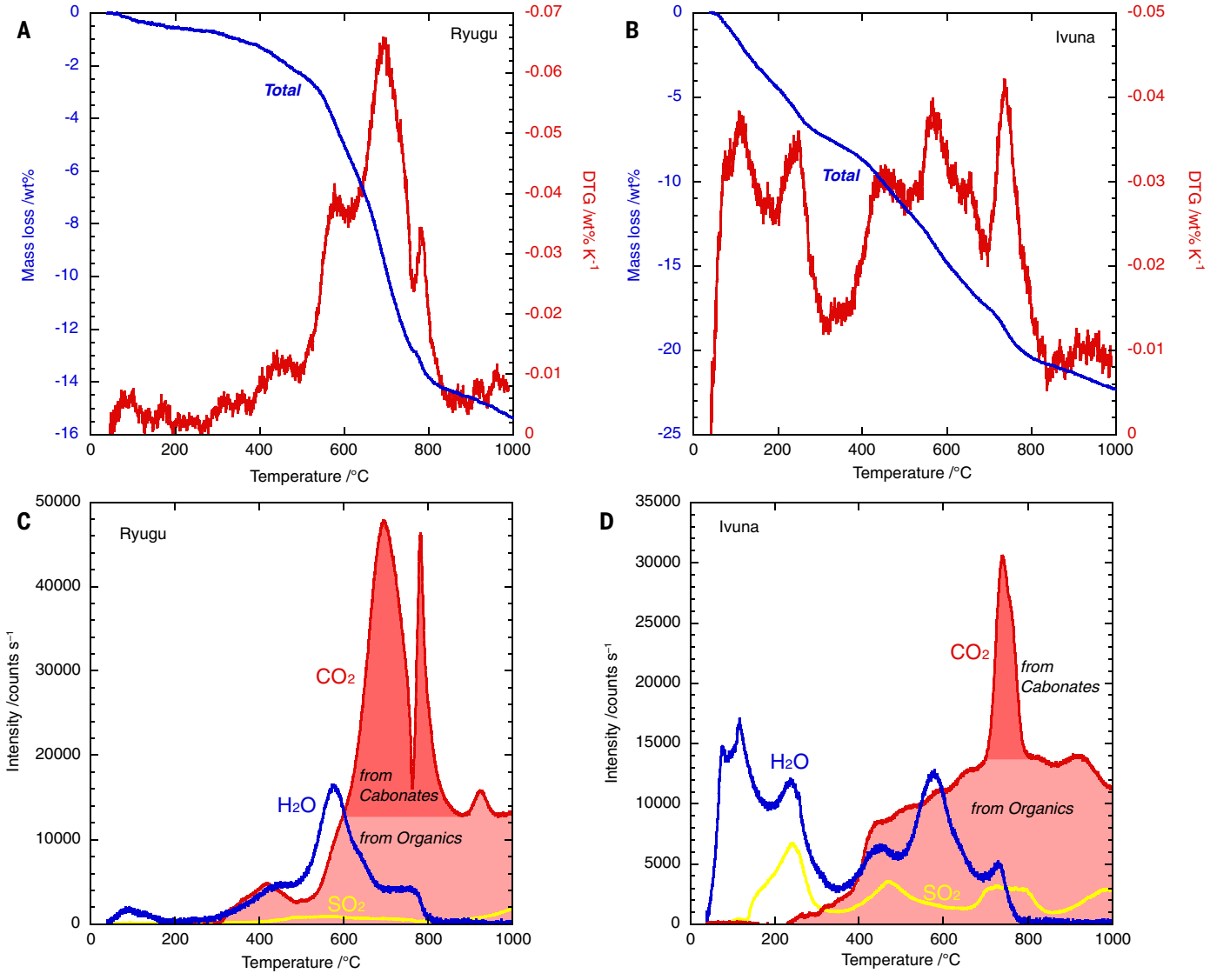

Fig. 6. TG-MS for Ryugu and Ivuna. (**A** to **D**) Mass loss (blue, left axis) and differential of mass-loss (DTG; red, right axis) curves are shown for (A) Ryugu and (B) Ivuna. Derived mass intensity curves are shown for (C) Ryugu and (D) Ivuna. The H_2O trace (blue) is for mass-to-charge ratio (m/z) = 18, CO_2 (red line) for m/z = 44, and SO_2 (yellow) for m/z = 64. Contributions of CO_2 are assigned to carbonates (red shading) and organics (pink shading). Numeric values are provided in data S7 (*12*).

at ~600°C. The phyllosilicates consist of serpentine and saponite (Fig. 1C). Serpentine contains structural OH sites in the crystal structure, whereas saponite contains interlayer H_2O in addition to structural OH sites. The petrologic and mineralogic observations suggest that the sulfate contribution is negligible for Ryugu but not for Ivuna. The SO_2 and H_2O peak releases coincide in Ivuna (at both 250° and 450°C) but not in Ryugu. We conclude that phyllosilicates are the dominant source of the H_2O that is released from the Ryugu sample.

Dehydration of the interlayer H_2O of saponite is complete at 170°C (peaking at 90°C) for Ryugu and complete at 350°C (peaking at 100°C) for Ivuna. Dehydroxylation of structural OH in saponite and serpentine occurs at 300° to 800°C for Ryugu and at 350° to 800°C for Ivuna. The structural OH is dominant (6.54 ± 0.32 wt % H_2O) in the Ryugu sample, with smaller amounts of interlayer H_2O (0.30 ± 0.01 wt % H_2O). Both forms of H_2O are present at similar levels in Ivuna (data S6).

Organic-inorganic fractions for hydrogen and carbon

We performed an EMIA-Step analysis of the Ryugu and Ivuna samples (*12*). For Ivuna, the results showed that the total carbon concentration is 3.31 ± 0.33 wt % (*12*), of which 90% is organic carbon (Fig. 7 and data S6). The total hydrogen in Ivuna is 1.59 ± 0.08 wt %, of which 89% is inorganic hydrogen. All these values are consistent with previous measurements of the same meteorite (*44*). The total H_2O for Ivuna is 12.73 ± 0.63 wt %, distributed as 6.58 ± 0.32 wt % interlayer H_2O and 6.15 ± 0.30 wt % structural OH or H_2O in the phyllosilicate minerals.

The Ryugu samples contain less H_2O than Ivuna. The total H_2O is 6.84 ± 0.34 wt %, including 0.30 ± 0.01 wt % interlayer H_2O and 6.54 ± 0.32 wt % structural OH or H_2O (data S6). The structural value is similar to that of Ivuna, but the interlayer water value is substantially lower. The total hydrogen is 0.94 ± 0.05 wt % for Ryugu, and the inorganic hydrogen (i.e., H_2O) makes up 81% of the total hydrogen. The amount of organic

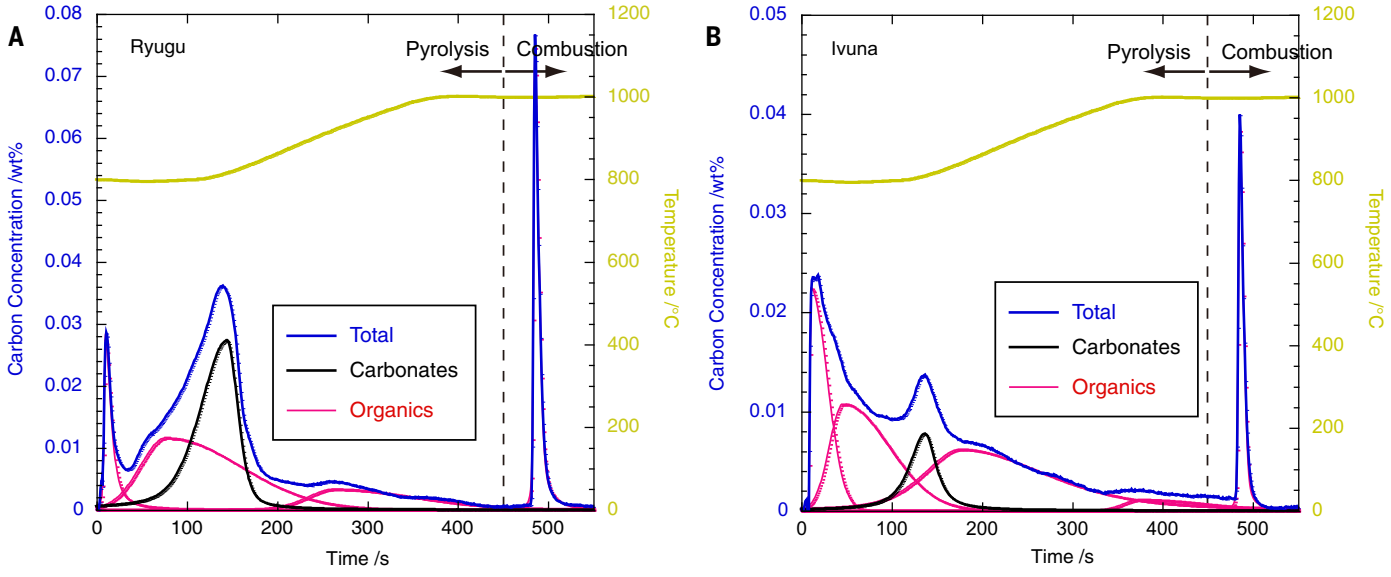

Fig. 7. Combination analyses of pyrolysis and combustion (EMIA-Step) for Ryugu and Ivuna. (**A** and **B**) Carbon release curves are shown for (A) Ryugu and (B) Ivuna. The carbon concentration (blue, left axis) is plotted as a function of the sample heating time (*x* axis). The sample temperature (yellow, right axis) changes nonlinearly with time. The dashed line at 450 s shows the boundary between conditions of pyrolysis and combustion (*12*). The integration under each blue curve corresponds to the total carbon released from the sample. These contributions are deconvolved and assigned to different carbonates (black) and organics (pink) in the sample (*12*); the integration under these curves corresponds to inorganic and organic carbon concentrations, respectively. Numeric values are provided in data S8.

carbon in Ryugu is 3.08 ± 0.30 wt %, which is indistinguishable from that in Ivuna (2.97 ± 0.29 wt %) (Fig. 7 and data S6). This implies that the inorganic matter/organic matter ratio is similar in the Ryugu and Ivuna samples that were studied, excluding a previous proposal that Ryugu's low albedo is due to Ryugu having higher organic carbon contents than CI chondrites (*45*). However, the total carbon is higher in Ryugu (4.63 ± 0.23 wt %) than in Ivuna, owing to the higher abundances of carbonates in the Ryugu samples.

Formation history of Ryugu

Ryugu is thought to have formed through the reaccumulation of material ejected from a parent body by an impact (*5*). The aqueous alteration of the samples must have occurred on the parent body because aqueous fluid is not stable in the current Ryugu asteroid. The CI-like elemental abundances of Ryugu suggest that the parent body accreted all elements with 50% condensation temperatures higher than 500 K that were present at the formation of the Solar System, along with some ice-forming elements (Fig. 2). Ryugu's parent body was probably closely related to the parent body (or bodies) of the CI chondrites. We assume that the accreted material was mainly anhydrous dust and ice. Physical modeling of the thermal evolution of a water ice–bearing CI-like planetesimal (*35*), compared with the results of our oxygen-isotope thermometry, suggests that the Ryugu parent body accreted 2 million to 4 million years after the formation of the Solar System (as defined by the ages of the oldest CAIs).

About 1 million to 2 million years later, roughly 5 million years after the formation of the Solar System (Fig. 5), the material that would later be incorporated into Ryugu experienced aqueous alteration. This caused the precipitation of dolomite and magnetite from an aqueous solution at about 37°C. The aqueous alteration of the primary minerals was very extensive. The saponite produced by this fluid-assisted alteration in the parent body must have contained large amounts of interlayer water (~7 wt %) in its crystal structure when it formed under saturated water activity, as observed in Ivuna (data S6). The low abundance of interlayer water in the Ryugu samples (0.3 wt %) indicates that much of this water later escaped to space, most likely after disruption of the parent body and formation of the rubble-pile asteroid Ryugu. We cannot definitively identify the dehydration mechanism but suggest that it may have included some combination of impact heating, solar heating, space weathering, and long-term exposure of the asteroid surface to the ultrahigh vacuum of space.

We estimate the dehydration temperature as 170°C, the temperature at which interlayer water that is now in the Ryugu samples completely dehydrates. The dehydration speed of the interlayer water in our experiments is 20% of the total interlayer water per minute, around the peak temperature of 90°C (data S7) (*12*). The ambient space pressure in Ryugu, which is much lower than the experimental pressure of 10^5 Pa, would accelerate this dehydration speed. Such high dehydration rates are sufficient to completely dehydrate the interlayer water for any plausible geological heating events that occurred in Ryugu. Because a small peak of interlayer water is still emitted at 90°C in our experiments, it is possible that, since their aqueous alteration, the Ryugu samples have never been heated above ~100°C (Fig. 6). These temperatures rule out the previously proposed thermal history of Ryugu (*6*), which was based on laboratory heating experiments of carbonaceous chondrites. The temperatures that we estimate are consist with Hayabusa2 observations of the surface temperature at the present orbit of Ryugu (*7*).

Some asteroids show comet-like activity, the origin of which is uncertain and could involve several mechanisms (*46*). This activity can be subtle, as in the B-type (bluish and spectroscopically similar to C-type) asteroid Bennu, where small ejections of dust particles and rocks have been observed (*47*). Thermal fracturing, phyllosilicate dehydration, and micrometeoroid impacts have been proposed (*47*) as explanations for the ejection of solid particles from Bennu. Our finding that saponite in Ryugu is partially dehydrated supports the possibility that volatile release from phyllosilicates can induce comet-like activity at the surface of inner Solar System

carbonaceous asteroids. Possible mechanisms to lift dust and rocks from asteroid surfaces include (i) anisotropic release of water molecules from phyllosilicate-rich dust particles, which imparts a net momentum to those particles, or (ii) buildup of vapor pressure in sealed pore spaces, which leads to pore bursting that propels dust particles away from the surface. Phyllosilicate dehydration could also play a role in the production of interplanetary dust particles and micrometeorites. The thermal release pattern of Ivuna (Fig. 6) shows that interlayer water is lost from saponite at a temperature between ~0° and 200°C. The observed maximum current surface temperatures of ~100°C for Ryugu (*7*) and ~170°C for Bennu (*48*) would therefore be sufficient for such devolatilization to take place. If so, the devolatilization must be largely complete for surface particles on Ryugu because no particle ejections were observed by the Hayabusa2 spacecraft.

Implications for CI chondrites and cosmochemistry

The elemental compositions of CI chondrites more closely match measurements of the solar photosphere than those of other types of meteorites (*49*); CIs differ from the Sun in the abundances of the noble gases, hydrogen, carbon, nitrogen, oxygen, and lithium. CI chondrites experienced pervasive aqueous alteration during water-rock interactions in the early Solar System. Fewer than a dozen CI chondrites are known, and they have all been on Earth for decades to centuries (the most recent fall was in 1965). It is therefore unknown how much handling and exposure to atmospheric moisture has modified their mineralogies and elemental compositions. Unlike CI chondrites, the Ryugu samples are nearly free of sulfates, ferrihydrite, and interlayer water. This could be due to CI chondrites either having originated on parent asteroids with higher water contents than Ryugu or having been contaminated by terrestrial moisture during their residence on Earth (*50*, *51*). The lower abundance of anhydrous silicates, and the small but measurable offset in $\Delta^{17}O$ between Ryugu and the Orgueil CI chondrite (Fig. 4), supports the terrestrial contamination explanation. The slightly higher $\Delta^{17}O$ values of Orgueil in this study compared with those in earlier studies could be explained if O-isotope exchange in the structural OH water of CI chondrites occurred under room-temperature conditions. The gas emission patterns measured in the TG-MS and EMIA-Step analyses of Ryugu differ from those of the Ivuna CI chondrite (Figs. 6 and 7). This suggests that the structures of the organic matter differ between Ryugu samples and Ivuna, possibly because of modification during their residence on Earth.

We conclude that the Ryugu samples are more chemically pristine than other Solar System materials that have been analyzed in laboratories, including CI meteorites. The materials observed in CI chondrites may have been modified on Earth and thus no longer reflect their states in space. Possible causes are phyllosilicate hydration, organic matter transformation and contamination, adsorption or reaction of atmospheric components, and oxidation. These modifications might have changed the albedo, porosity, and density of the CI chondrites, which could explain the differences between CIs and the observations of Ryugu by Hayabusa2 (*5*, *7*) and between CIs and the Ryugu samples returned to Earth (*10*).

REFERENCES AND NOTES

1. H. Yurimoto *et al*., Oxygen isotopic compositions of asteroidal materials returned from Itokawa by the Hayabusa mission. *Science* **333**, 1116–1119 (2011). doi: 10.1126/science.1207776; pmid: 21868668
2. T. Nakamura *et al*., Itokawa dust particles: A direct link between S-type asteroids and ordinary chondrites. *Science* **333**, 1113–1116 (2011). doi: 10.1126/science.1207758; pmid: 21868667
3. S. Tachibana *et al*., Hayabusa2: Scientific importance of samples returned from C-type near-Earth asteroid (162173) 1999 JU_3. *Geochem. J.* **48**, 571–587 (2014). doi: 10.2343/geochemj.2.0350
4. K. Kitazato *et al*., The surface composition of asteroid 162173 Ryugu from Hayabusa2 near-infrared spectroscopy. *Science* **364**, 272–275 (2019). doi: 10.1126/science.aav7432; pmid: 30890589
5. S. Sugita *et al*., The geomorphology, color, and thermal properties of Ryugu: Implications for parent-body processes. *Science* **364**, 252 (2019). doi: 10.1126/science.aaw0422; pmid: 30890587
6. K. Kitazato *et al*., Thermally altered subsurface material of asteroid (162173) Ryugu. *Nat. Astron.* **5**, 246–250 (2021). doi: 10.1038/s41550-020-01271-2
7. T. Okada *et al*., Highly porous nature of a primitive asteroid revealed by thermal imaging. *Nature* **579**, 518–522 (2020). doi: 10.1038/s41586-020-2102-6; pmid: 32214245
8. M. Grott *et al*., Low thermal conductivity boulder with high porosity identified on C-type asteroid (162173) Ryugu. *Nat. Astron.* **3**, 971–976 (2019). doi: 10.1038/s41550-019-0832-x
9. T. Morota *et al*., Sample collection from asteroid (162173) Ryugu by Hayabusa2: Implications for surface evolution. *Science* **368**, 654–659 (2020). doi: 10.1126/science.aaz6306; pmid: 32381723
10. T. Yada *et al*., Preliminary analysis of the Hayabusa2 samples returned from C-type asteroid Ryugu. *Nat. Astron.* **6**, 214–220 (2021). doi: 10.1038/s41550-021-01550-6
11. S. Tachibana *et al*., Pebbles and sand on asteroid (162173) Ryugu: In situ observation and particles returned to Earth. *Science* **375**, 1011–1016 (2022). doi: 10.1126/science.abj8624; pmid: 35143255
12. See supplementary materials.
13. A. J. Brearley, in *Meteorites and the Early Solar System II*, D. S. Lauretta, H. Y. McSween, Eds. (Univ. of Arizona Press, 2006), pp. 587–624.
14. N. Dauphas, A. Pourmand, Thulium anomalies and rare earth element patterns in meteorites and Earth: Nebular fractionation and the nugget effect. *Geochim. Cosmochim. Acta* **163**, 234–261 (2015). doi: 10.1016/j.gca.2015.03.037
15. A.-C. Zhang *et al*., Young asteroidal fluid activity revealed by absolute age from apatite in carbonaceous chondrite. *Nat. Commun.* **7**, 12844 (2016). doi: 10.1038/ncomms12844; pmid: 27682449
16. A. Morlok *et al*., Brecciation and chemical heterogeneities of CI chondrites. *Geochim. Cosmochim. Acta* **70**, 5371–5394 (2006). doi: 10.1016/j.gca.2006.08.007
17. J. A. Barrat *et al*., Geochemistry of CI chondrites: Major and trace elements, and Cu and Zn isotopes. *Geochim. Cosmochim. Acta* **83**, 79–92 (2012). doi: 10.1016/j.gca.2011.12.011
18. C. M. O'D. Alexander, R. Bowden, M. L. Fogel, K. T. Howard, Carbonate abundances and isotopic compositions in chondrites. *Meteorit. Planet. Sci.* **50**, 810–833 (2015). doi: 10.1111/maps.12410
19. J. T. Wasson, G. W. Kallemeyn, Compositions of chondrites. *Philos. Trans. R. Soc. Lond. A* **325**, 535–544 (1988). doi: 10.1098/rsta.1988.0066
20. P. H. Warren, Stable-isotopic anomalies and the accretionary assemblage of the Earth and Mars: A subordinate role for carbonaceous chondrites. *Earth Planet. Sci. Lett.* **311**, 93–100 (2011). doi: 10.1016/j.epsl.2011.08.047
21. A. Trinquier *et al*., Origin of nucleosynthetic isotope heterogeneity in the solar protoplanetary disk. *Science* **324**, 374–376 (2009). doi: 10.1126/science.1168221; pmid: 19372428
22. T. Kleine *et al*., The non-carbonaceous–carbonaceous meteorite dichotomy. *Space Sci. Rev.* **216**, 55 (2020). doi: 10.1007/s11214-020-00675-w
23. I. Leya, M. Schönbächler, U. Wiechert, U. Krähenbühl, A. N. Halliday, Titanium isotopes and the radial heterogeneity of the solar system. *Earth Planet. Sci. Lett.* **266**, 233–244 (2008). doi: 10.1016/j.epsl.2007.10.017
24. A. N. Krot, K. Keil, E. R. D. Scott, C. A. Goodrich, M. K. Weisberg, in *Treatise on Geochemistry*, H. D. Holland, K. K. Turekian, Eds. (Elsevier, ed. 2, 2014), pp. 1–63.
25. R. N. Clayton, T. K. Mayeda, Oxygen isotope studies of carbonaceous chondrites. *Geochim. Cosmochim. Acta* **63**, 2089–2104 (1999). doi: 10.1016/S0016-7037(99)00090-3
26. M. W. Rowe, R. N. Clayton, T. K. Mayeda, Oxygen isotopes in separated components of CI and CM meteorites. *Geochim. Cosmochim. Acta* **58**, 5341–5347 (1994). doi: 10.1016/0016-7037(94)90317-4
27. M. Piralla *et al*., Primordial water and dust of the Solar System: Insights from in situ oxygen measurements of CI chondrites. *Geochim. Cosmochim. Acta* **269**, 451–464 (2020). doi: 10.1016/j.gca.2019.10.041
28. Y. Zheng, Calculation of oxygen isotope fractionation in metal oxides. *Geochim. Cosmochim. Acta* **55**, 2299–2307 (1991). doi: 10.1016/0016-7037(91)90105-E
29. Y.-F. Zheng, Oxygen isotope fractionation in carbonate and sulfate minerals. *Geochem. J.* **33**, 109–126 (1999). doi: 10.2343/geochemj.33.109
30. Y.-F. Zheng, On the theoretical calculations of oxygen isotope fractionation factors for carbonate-water systems. *Geochem. J.* **45**, 341–354 (2011). doi: 10.2343/geochemj.1.0125
31. Y.-F. Zheng, Calculation of oxygen isotope fractionation in hydroxyl-bearing silicates. *Earth Planet. Sci. Lett.* **120**, 247–263 (1993). doi: 10.1016/0012-821X(93)90243-3
32. W. Guo, thesis, California Institute of Technology (2009).
33. R. Visser, T. John, M. Menneken, M. Patzek, A. Bischoff, Temperature constraints by Raman spectroscopy of organic matter in volatile-rich clasts and carbonaceous chondrites. *Geochim. Cosmochim. Acta* **241**, 38–55 (2018). doi: 10.1016/j.gca.2018.08.037
34. M. E. Zolensky, W. L. Bourcier, J. L. Gooding, Aqueous alteration on the hydrous asteroids: Results of EQ3/6 computer simulations. *Icarus* **78**, 411–425 (1989). doi: 10.1016/0019-1035(89)90188-7
35. W. Fujiya, N. Sugiura, Y. Sano, H. Hiyagon, Mn-Cr ages of dolomites in CI chondrites and the Tagish Lake ungrouped carbonaceous chondrite. *Earth Planet. Sci. Lett.* **362**, 130–142 (2013). doi: 10.1016/j.epsl.2012.11.057
36. R. Visser, T. John, M. J. Whitehouse, M. Patzek, A. Bischoff, A short-lived ^{26}Al induced hydrothermal alteration event in the outer solar system: Constraints from Mn/Cr ages of carbonates. *Earth Planet. Sci. Lett.* **547**, 116440 (2020). doi: 10.1016/j.epsl.2020.116440
37. D. P. Glavin, A. Kubny, E. Jagoutz, G. W. Lugmair, Mn-Cr isotope systematics of the D'Orbigny angrite. *Meteorit. Planet. Sci.* **39**, 693–700 (2004). doi: 10.1111/j.1945-5100.2004.tb00112.x
38. G. A. Brennecka, M. Wadhwa, Uranium isotope compositions of the basaltic angrite meteorites and the chronological implications for the early Solar System. *Proc. Natl. Acad. Sci. U.S.A.* **109**, 9299–9303 (2012). doi: 10.1073/pnas.1114043109; pmid: 22647606
39. J. N. Connelly *et al*., The absolute chronology and thermal processing of solids in the solar protoplanetary disk. *Science* **338**, 651–655 (2012). doi: 10.1126/science.1226919; pmid: 23118187
40. F. L. H. Tissot, N. Dauphas, T. L. Grove, Distinct $^{238}U/^{235}U$ ratios and REE patterns in plutonic and volcanic angrites: Geochronologic implications and evidence for U isotope fractionation during magmatic processes. *Geochim. Cosmochim. Acta* **213**, 593–617 (2017). doi: 10.1016/j.gca.2017.06.045

41. A. Trinquier, J. L. Birck, C. J. Allègre, C. Göpel, D. Ulfbeck, ^{53}Mn–^{53}Cr systematics of the early Solar System revisited. *Geochim. Cosmochim. Acta* **72**, 5146–5163 (2008). doi: 10.1016/j.gca.2008.03.023
42. L. E. Nyquist, T. Kleine, C. Y. Shih, Y. D. Reese, The distribution of short-lived radioisotopes in the early solar system and the chronology of asteroid accretion, differentiation, and secondary mineralization. *Geochim. Cosmochim. Acta* **73**, 5115–5136 (2009). doi: 10.1016/j.gca.2008.12.031
43. A. J. King, J. R. Solomon, P. F. Schofield, S. S. Russell, Characterising the CI and CI-like carbonaceous chondrites using thermogravimetric analysis and infrared spectroscopy. *Earth Planets Space* **67**, 198 (2015). doi: 10.1186/s40623-015-0370-4
44. C. M. O'D. Alexander *et al*., The provenances of asteroids, and their contributions to the volatile inventories of the terrestrial planets. *Science* **337**, 721–723 (2012). doi: 10.1126/science.1223474; pmid: 22798405
45. C. Potiszil, R. Tanaka, K. Kobayashi, T. Kunihiro, E. Nakamura, The albedo of Ryugu: Evidence for a high organic abundance, as inferred from the Hayabusa2 touchdown maneuver. *Astrobiology* **20**, 916–921 (2020). doi: 10.1089/ast.2019.2198; pmid: 32543220
46. D. Jewitt, H. Hsieh, J. Agarwal, in *Asteroids IV*, P. Michel, F. E. DeMeo, W. F. Bottke, Eds. (Univ. of Arizona Press, 2015), pp. 221–241.
47. D. S. Lauretta *et al*., Episodes of particle ejection from the surface of the active asteroid (101955) Bennu. *Science* **366**, eaay3544 (2019). doi: 10.1126/science.aay3544; pmid: 31806784
48. D. N. DellaGiustina *et al*., Properties of rubble-pile asteroid (101955) Bennu from OSIRIS-REx imaging and thermal analysis. *Nat. Astron.* **3**, 341–351 (2019). doi: 10.1038/s41550-019-0731-1
49. K. Lodders, Relative atomic solar system abundances, mass fractions, and atomic masses of the elements and their isotopes, composition of the solar photosphere, and compositions of the major chondritic meteorite groups. *Space Sci. Rev.* **217**, 44 (2021). doi: 10.1007/s11214-021-00825-8
50. M. Gounelle, M. E. Zolensky, The Orgueil meteorite: 150 years of history. *Meteorit. Planet. Sci.* **49**, 1769–1794 (2014). doi: 10.1111/maps.12351
51. L. Baker, I. A. Franchi, I. P. Wright, C. T. Pillinger, The oxygen isotopic composition of water from Tagish Lake: Its relationship to low-temperature phases and to other carbonaceous chondrites. *Meteorit. Planet. Sci.* **37**, 977–985 (2002). doi: 10.1111/j.1945-5100.2002.tb00870.x
52. A. Bischoff *et al*., The old, unique C1 chondrite Flensburg – Insight into the first processes of aqueous alteration, brecciation, and the diversity of water-bearing parent bodies and lithologies. *Geochim. Cosmochim. Acta* **293**, 142–186 (2021). doi: 10.1016/j.gca.2020.10.014
53. J. Alfing, M. Patzek, A. Bischoff, Modal abundances of coarse-grained (>5 μm) components within CI-chondrites and their individual clasts – Mixing of various lithologies on the CI parent body(ies). *Chem. Erde* **79**, 125532 (2019). doi: 10.1016/j.chemer.2019.08.004
54. N. Dauphas, E. A. Schauble, Mass Fractionation Laws, Mass-Independent Effects, and Isotopic Anomalies. *Annu. Rev. Earth Planet. Sci.* **44**, 709–783 (2016). doi: 10.1146/annurev-earth-060115-012157
55. C. Burkhardt *et al*., In search of the Earth-forming reservoir: Mineralogical, chemical, and isotopic characterizations of the ungrouped achondrite NWA 5363/NWA 5400 and selected chondrites. *Meteorit. Planet. Sci.* **52**, 807–826 (2017). doi: 10.1111/maps.12834

ACKNOWLEDGMENTS

We thank D. Rogers, M. Spicuzza, and J. Valley for their help with the carbonate standards for the SIMS analyses. We thank SPring-8 for allowing us to use their facilities. Hayabusa2 was developed and built under the leadership of the Japan Aerospace Exploration Agency (JAXA), with contributions from the German Aerospace Center (DLR) and the Centre National d'Études Spatiales (CNES) and in collaboration with NASA and other universities, institutes, and companies in Japan. The curation system was developed by JAXA in collaboration with companies in Japan. **Funding:** H.Yu., T.Yo., I.N., T.U., T.No., S.W., and S.Tac. acknowledge funding from Japan Society for the Promotion of Science (JSPS) KAKENHI grants. E.D.Y., L.N., and A.Ng. acknowledge funding from NASA grants. T.R.I. acknowledges an Australian Research Council grant. **Author contributions:** H.Yu. coordinated coauthor contributions and wrote the paper, with contributions from members of the Hayabusa2-initial-analysis chemistry team. H.Yu. led the TG-MS and EMIA-Step analyses, with contributions from Ho.H., S.Ko., and S.Tac. T.Yo. led the ICP-MS and TIMS analysis. K.N. led the SIMS analysis. I.N. led the XRF analysis. E.D.Y. led the LF-IRMS analysis. Y.Ab., J.A., C.M.O.A., S.A., Y.Am., K.B., M.B., A.B., R.W.C., M.C., B.-G.C., N.D., A.M.D., T.D.R., W.F., R.F., I.G., M.H., Y.Hib., H.Hi., H.Ho., P.H., G.R.H., K.I., T.Ii., T.R.I., A.I., M.It., S.I., N.K., N.T.K., K.Kitaj., T.K., S.Ko., A.N.K., M.-C.L., Y.Ma., K.D.M., M.Mo., K.Mo., F.M., A.Ng., L.N., M. On., A.P., C.P., L.P., L.Q., S.S.R., N.Sakam., M.S., L.T., H.Tan., K.T., Y.Te., T.U., S.Wad., M.W., R.J.W., K.Ya., Q.-Z.Y., S.Y., H.Yu., A.-C.Z., and S.Tac. assisted with the analyses. All authors discussed the results and commented on the manuscript. **Competing interests:** We declare no competing interests. **Data and materials availability:** Measurement values from each of our experiments are tabulated in data S1 to S9. All images and data tables used in this study are also available at the JAXA Data Archives and Transmission System (DARTS) at https://data.darts.isas.jaxa.jp/pub/hayabusa2/paper/sample/Yokoyama_2022/. Further data on the Hayabusa2 samples are available at the DARTS archive www.darts.isas.jaxa.jp/curation/hayabusa2. The samples of Ryugu are curated by the JAXA Astromaterials Science Research Group; distribution for analysis is through announcements of opportunity available at https://jaxa-ryugu-sample-ao.net. Details of the Orgueil and Ivuna samples that we used for comparison are provided in the supplementary materials. **License information:** Copyright © 2023 the authors, some rights reserved; exclusive licensee American Association for the Advancement of Science. No claim to original US government works. https://www.science.org/about/science-licenses-journal-article-reuse

SUPPLEMENTARY MATERIALS

science.org/doi/10.1126/science.abn7850
Materials and Methods
Supplementary Text
Figs. S1 to S4
References (*56*–*82*)
Data S1 to S9

Submitted 20 December 2021; accepted 25 May 2022
10.1126/science.abn7850

RESEARCH ARTICLE SUMMARY

COSMOCHEMISTRY

Formation and evolution of carbonaceous asteroid Ryugu: Direct evidence from returned samples

T. Nakamura* *et al.*

INTRODUCTION: Observations of asteroid Ryugu by the Hayabusa2 spacecraft found that it is a rubble pile, formed from fragments of a parent asteroid. Samples retrieved from Ryugu by the spacecraft were expected to contain a record of this history, including the formation and early evolution of the parent body, the subsequent impact destruction and partial reaccretion, and later space weathering. The composition of Ryugu was expected to be similar to that of Ivuna-type carbonaceous chondrite meteorites (CI chondrites).

RATIONALE: We investigated the formation history of Ryugu through laboratory analysis of the samples. Specifically, we sought to determine (i) when and where in the Solar System the parent asteroid formed; (ii) the original mineralogy, elemental abundances as a whole, and chemical compositions of the accreted materials, including their ice content; (iii) how these materials evolved through chemical reactions; and (iv) how the material was ejected from the parent body in an impact. To address these issues, we analyzed 17 Ryugu particles of 1 to ~8 mm in size.

RESULTS: We found carbon dioxide (CO_2)–bearing water in an iron-nickel (Fe–Ni) sulfide crystal, indicating that the parent body formed in the outer Solar System. Remanent magnetization was detected, implying that the solar nebula might still have been present when magnetite crystals formed on the parent body.

We used muon analysis to determine the abundances of light elements, including carbon (C), nitrogen (N), sodium (Na), and magnesium (Mg), whose abundances relative to silicon (Si) are similar to those in CI chondrites, whereas oxygen (O) is deficient compared with that in CI chondrites. X-ray computed tomography analysis shows that all our Ryugu samples consist of fine-grained material. There are only rare objects of high-temperature origin, such as melted silicate-rich particles, all being smaller than 100 μm.

Electron microscope observations showed that the samples are breccias, assemblies of numerous small rock fragments with different compositions, mineralogies, and histories. The most common mineralogy contains Mg-rich hydrous silicates, MgCa and MgFe carbonates, hydroxyapatite, Fe sulfides, and Fe oxides. The mineralogy of this major lithology is consistent with classification as a CI chondrite. It also indicates widespread aqueous alteration (reactions with liquid water) on the parent body.

Some Ryugu fragments have a different mineralogy, containing anhydrous silicates (olivine and pyroxene), amorphous silicates, Ca carbonate, phosphides, Fe–Ni sulfide, Fe oxide, and poorly crystalline phyllosilicates. Some small objects (<~30 μm) that formed at high temperatures were also found. This mineralogy suggests that these fragments experienced less aqueous alteration.

We measured mechanical and thermal properties from the Ryugu samples. We found that they are similar, but not identical, to hydrated CI chondrites. Numerical simulations of the thermal history and impact disruption processes of the Ryugu parent asteroid were performed by incorporating the physical and mineralogical properties and appropriate water/rock ratios.

CONCLUSION: We propose that Ryugu's parent asteroid formed ~1.8 million to 2.9 million years after the beginning of Solar System formation, in the outer Solar System, where water and CO_2 were present as ice. It acquired a water ice/rock mass ratio in the range of 0.2 to 0.9. In this region, material formed at low temperatures is dominant, whereas material of high temperature origin is rare. In the interior of the parent asteroid, radioactive heating caused the water ice to melt at ~3 million years; water-rock reactions then gradually changed the initial anhydrous mineralogy to a largely hydrous mineralogy. At shallow depths, the original material was less altered, at a low water/rock ratio of <0.2. At ~5 million years, all material in the parent asteroid experienced its peak temperature, and aqueous alteration continued. An impact occurred ~1 billion years ago, disrupting the parent asteroid. Some fragments, originating away from the impact point, then reassembled to form Ryugu. ■

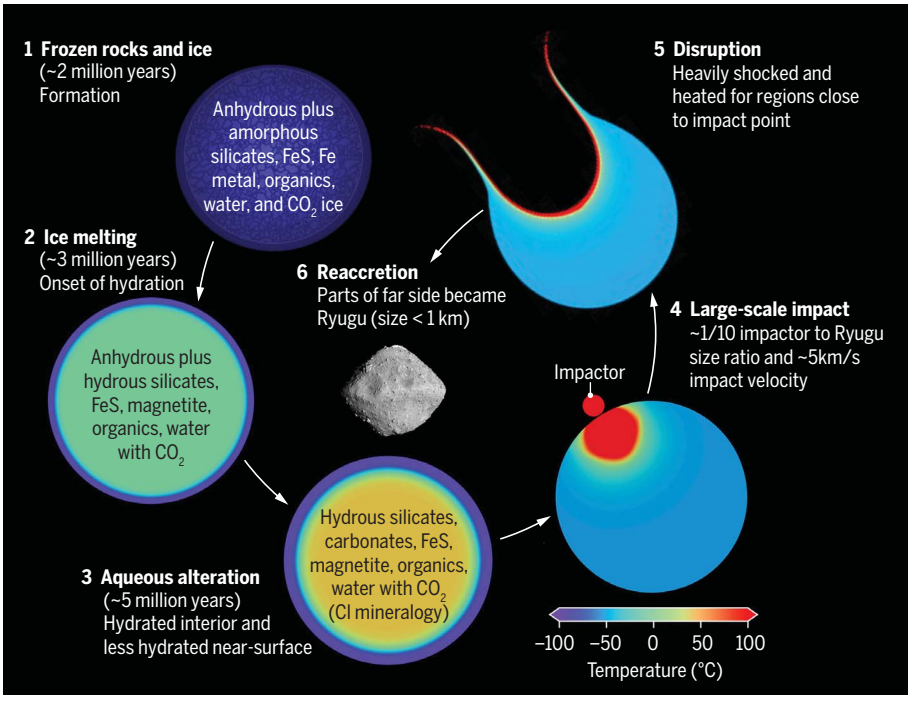
1 Frozen rocks and ice
(~2 million years)
Formation
Anhydrous plus amorphous silicates, FeS, Fe metal, organics, water, and CO2 ice
2 Ice melting
(~3 million years)
Onset of hydration
Anhydrous plus hydrous silicates, FeS, magnetite, organics, water with CO2
3 Aqueous alteration
(~5 million years)
Hydrated interior and less hydrated near-surface
Hydrous silicates, carbonates, FeS, magnetite, organics, water with CO2 (CI mineralogy)
5 Disruption
Heavily shocked and heated for regions close to impact point
6 Reaccretion
Parts of far side became Ryugu (size < 1 km)
4 Large-scale impact
~1/10 impactor to Ryugu size ratio and ~5km/s impact velocity
Impactor
−100 −50 0 50 100
Temperature (°C)

Proposed model of Ryugu's formation history. (1) A parent body asteroid forms in the outer Solar System, containing abundant ice. (2 and 3) Radioactive heating causes the ice to melt, which modifies the mineralogy through aqueous alteration reactions. (4 and 5) An impact then disrupts the parent body but does not cause widespread heating. (6) Ryugu formed from reaccumulation of ejected material that originated away from the impact point. All times were measured from the start of Solar System formation. Colors indicate estimated temperatures from our thermal interior and impact models.

The complete list of authors and their affiliations is available in the full article online.
*Corresponding author. Email: tomoki.nakamura.a8@tohoku.ac.jp
Cite this article as T. Nakamura *et al.*, *Science* **379**, eabn8671 (2023). DOI: 10.1126/science.abn8671

READ THE FULL ARTICLE AT
https://doi.org/10.1126/science.abn8671

RESEARCH ARTICLE

COSMOCHEMISTRY

Formation and evolution of carbonaceous asteroid Ryugu: Direct evidence from returned samples

T. Nakamura[1]*, M. Matsumoto[1], K. Amano[1], Y. Enokido[1], M. E. Zolensky[2], T. Mikouchi[3], H. Genda[4], S. Tanaka[5,6], M. Y. Zolotov[7], K. Kurosawa[8], S. Wakita[9], R. Hyodo[5], H. Nagano[10], D. Nakashima[1], Y. Takahashi[11,12], Y. Fujioka[1], M. Kikuiri[1], E. Kagawa[1], M. Matsuoka[13,14], A. J. Brearley[15], A. Tsuchiyama[16,17,18], M. Uesugi[19], J. Matsuno[16], Y. Kimura[20], M. Sato[11], R. E. Milliken[21], E. Tatsumi[22,11], S. Sugita[11,8], T. Hiroi[21], K. Kitazato[23], D. Brownlee[24], D. J. Joswiak[24], M. Takahashi[1], K. Ninomiya[25], T. Takahashi[26,27], T. Osawa[28], K. Terada[29], F. E. Brenker[30], B. J. Tkalcec[30], L. Vincze[31], R. Brunetto[32], A. Aléon-Toppani[32], Q. H. S. Chan[33], M. Roskosz[34], J.-C. Viennet[34], P. Beck[35], E. E. Alp[36], T. Michikami[37], Y. Nagaashi[38,1], T. Tsuji[39,40], Y. Ino[41,5], J. Martinez[2], J. Han[42], A. Dolocan[43], R. J. Bodnar[44], M. Tanaka[45], H. Yoshida[11], K. Sugiyama[46], A. J. King[47], K. Fukushi[48], H. Suga[49], S. Yamashita[50,51], T. Kawai[11], K. Inoue[48], A. Nakato[5], T. Noguchi[52,53], F. Vilas[54], A. R. Hendrix[54], C. Jaramillo-Correa[55], D. L. Domingue[54], G. Dominguez[56], Z. Gainsforth[57], C. Engrand[58], J. Duprat[34], S. S. Russell[47], E. Bonato[59], C. Ma[60], T. Kawamoto[61], T. Wada[1], S. Watanabe[5,26], R. Endo[62], S. Enju[63], L. Riu[64], S. Rubino[32], P. Tack[31], S. Takeshita[65], Y. Takeichi[50,51,66], A. Takeuchi[19], A. Takigawa[11], D. Takir[2], T. Tanigaki[67], A. Taniguchi[68], K. Tsukamoto[1], T. Yagi[69], S. Yamada[70], K. Yamamoto[71], Y. Yamashita[69], M. Yasutake[19], K. Uesugi[19], I. Umegaki[72,65], I. Chiu[25], T. Ishizaki[5], S. Okumura[52], E. Palomba[73], C. Pilorget[32,74], S. M. Potin[13,75], A. Alasli[10], S. Anada[71], Y. Araki[76], N. Sakatani[70,5], C. Schultz[21], O. Sekizawa[49], S. D. Sitzman[77], K. Sugiura[4], M. Sun[17,18,78], E. Dartois[79], E. De Pauw[31], Z. Dionnet[32], Z. Djouadi[32], G. Falkenberg[80], R. Fujita[10], T. Fukuma[81], I. R. Gearba[43], K. Hagiya[82], M. Y. Hu[36], T. Kato[71], T. Kawamura[83], M. Kimura[50,51], M. K. Kubo[84], F. Langenhorst[85], C. Lantz[32], B. Lavina[86], M. Lindner[30], J. Zhao[36], B. Vekemans[31], D. Baklouti[32], B. Bazi[31], F. Borondics[87], S. Nagasawa[26, 27], G. Nishiyama[11], K. Nitta[49], J. Mathurin[88], T. Matsumoto[52], I. Mitsukawa[52], H. Miura[89], A. Miyake[52], Y. Miyake[65], H. Yurimoto[90], R. Okazaki[91], H. Yabuta[92], H. Naraoka[91], K. Sakamoto[5], S. Tachibana[11,5], H. C. Connolly Jr.[93], D. S. Lauretta[94], M. Yoshitake[5], M. Yoshikawa[5,6], K. Yoshikawa[95], K. Yoshihara[5], Y. Yokota[5], K. Yogata[5], H. Yano[5,6], Y. Yamamoto[5,6], D. Yamamoto[5], M. Yamada[8], T. Yamada[5], T. Yada[5], K. Wada[8], T. Usui[5,11], R. Tsukizaki[5], F. Terui[96], H. Takeuchi[5,6], Y. Takei[5], A. Iwamae[97], H. Soejima[5,97], K. Shirai[5], Y. Shimaki[5], H. Senshu[8], H. Sawada[5], T. Saiki[5], M. Ozaki[5,6], G. Ono[95] T. Okada[5,98], N. Ogawa[5], K. Ogawa[5], R. Noguchi[99], H. Noda[100], M. Nishimura[5], N. Namiki[100,6], S. Nakazawa[5], T. Morota[11], A. Miyazaki[5], A. Miura[5], Y. Mimasu[5], K. Matsumoto[100,6], K. Kumagai[5,97], T. Kouyama[101], S. Kikuchi[8,100], K. Kawahara[5], S. Kameda[70,5], T. Iwata[5,6], Y. Ishihara[102], M. Ishiguro[103], H. Ikeda[95], S. Hosoda[5], R. Honda[104,105], C. Honda[23], Y. Hitomi[5,97], N. Hirata[38], N. Hirata[23], T. Hayashi[5], M. Hayakawa[5], K. Hatakeda[5,97], S. Furuya[11], R. Fukai[5], A. Fujii[5], Y. Cho[11], M. Arakawa[38], M. Abe[5,6], S. Watanabe[106], Y. Tsuda[5]

Samples of the carbonaceous asteroid Ryugu were brought to Earth by the Hayabusa2 spacecraft. We analyzed 17 Ryugu samples measuring 1 to 8 millimeters. Carbon dioxide–bearing water inclusions are present within a pyrrhotite crystal, indicating that Ryugu's parent asteroid formed in the outer Solar System. The samples contain low abundances of materials that formed at high temperatures, such as chondrules and calcium- and aluminum-rich inclusions. The samples are rich in phyllosilicates and carbonates, which formed through aqueous alteration reactions at low temperature, high pH, and water/rock ratios of <1 (by mass). Less altered fragments contain olivine, pyroxene, amorphous silicates, calcite, and phosphide. Numerical simulations, based on the mineralogical and physical properties of the samples, indicate that Ryugu's parent body formed ~2 million years after the beginning of Solar System formation.

The carbonaceous asteroid (162173) Ryugu is a rubble pile formed by the reaccumulation of material ejected from a parent asteroid by a large impact (*1*). Remote sensing observations have shown that Ryugu is related to hydrous carbonaceous chondrite meteorites (*2*). However, there are some differences with those meteorites, suggesting later heating and partial dehydration of Ryugu (*2*, *3*). Reflectance spectra are nearly uniform across Ryugu's surface, indicating minimal compositional diversity at its surface (*2*, *3*), except for some boulders (*3*–*5*).

We expect samples of Ryugu to retain a record of the formation and early evolution of the parent body and Ryugu itself. We analyzed samples collected by the Hayabusa2 spacecraft (*6*), seeking to determine (i) when and where in the solar nebula Ryugu's parent asteroid formed, (ii) the initial mineralogy and water ice content, (iii) how these original materials evolved through water-rock reactions, (iv) how the asteroid was heated by the decay of short-lived radionuclides, and (v) how the material was ejected from the parent body by an impact and reaccumulated to form Ryugu.

We analyzed 17 Ryugu particles ranging from 1 to 8 mm in size (the largest particle, C0002, is shown in Fig. 1A, and all particles are shown in fig. S1), consisting of seven particles from chamber A, collected at the first touchdown site (TD1), and 10 particles from chamber C, collected at the second touchdown site (TD2) (*6*). We refer to these millimeter-sized particles as coarse samples. Finer-grained powder samples (<1 mm in size) (fig. S2) obtained from TD1 and TD2 were also used for reflectance spectroscopy.

Reflectance spectra

Visible (Vis), near-infrared (NIR), and mid-infrared (MIR) reflectance spectra (wavelength range, 0.4 to 18 μm) were measured from coarse Ryugu samples packed together (seven particles from TD1 and seven particles from TD2) (fig. S2), from the powder samples (fig. S2), and from samples of the meteorites Orgueil and Tagish Lake. The samples were not exposed to air in the entire analysis procedure (*7*). MIR and far-infrared (FIR; 17 to 100 μm) reflectance spectra were also measured in air for sample A0026 and samples of the meteorites Orgueil, Alais, Tagish Lake, and Murchison.

All analyzed Ryugu samples exhibit similar Vis-NIR spectra (Fig. 2A). They have ~2.0 to 2.5% reflectance (at 550 nm), with a slightly red slope of ~0.1 to 0.3% μm^{-1} (0.48 to 0.86 μm) and ~0.2 to 0.3% μm^{-1} (2.0 to 2.5 μm). There are no strong absorption features blueward of 2.7 μm (Fig. 2A). No 0.7 μm absorption, because of Fe^{3+}-rich phyllosilicates (*8*), was detected. The Ryugu samples have an absorption band (~20% in depth) centered at ~2.71 μm (Fig. 2B), which is due to O–H stretching vibrations in Mg-rich phyllosilicates (*9*, *10*). A weaker absorption band at ~3.1 μm is possibly due to ammoniated salts or other nitrogen (N)–bearing compounds (*11*). Absorptions at ~3.4 to 3.5 μm are due to aliphatic organics and carbonates, and those at ~3.8 to 3.95 μm are due to carbonates. In the MIR-FIR, the Christiansen feature (a reflectance minimum characteristic of the chemical composition) is present at ~9.1 μm. Reststrahlen bands (reflectance peaks associated with Si–O stretching and bending modes) appear as strong peaks at ~9.8 μm, with a shoulder at ~10.75 μm, and as a doublet at ~22.3 μm (Fig. 2C).

Visible spectra of the touchdown sites were previously obtained with the Optical Navigation Camera Telescope (ONC-T) (*3*) on the Hayabusa2 spacecraft, at spatial resolution of 0.3 to 0.5 m per pixel, before and after the sample collection. The location of TD1 showed higher reflectance than that of TD2 (Fig. 2D). We found similar results: The coarse and powder Ryugu samples from TD1 both exhibit higher reflectance than those from TD2 (Fig. 2A). The surface reflectance decreased after

the touchdowns because the spacecraft thrusters removed powder from the surface of Ryugu during ascent (Fig. 2D) (*12*). Visible spectra of the coarse and powder Ryugu samples have similar reflectance values to those of the ONC-T spectra of the landing sites (*7*) and to the global average (Fig. 2A); the reflectance ratios of ONC-T to the powder samples at 0.55 μm are ~0.9 for both TD1 and TD2 (Fig. 2D). This indicates that the samples are representative of the global reflectance properties of Ryugu.

Spectra of the Ryugu samples are generally consistent with Ryugu average spectra measured with Hayabusa2's ONC-T (*3*) and Near Infrared Spectrometer (NIRS3) (*2*) instruments. There are some differences between the NIRS3 and laboratory spectra (Fig. 2A), even after converting both to the same wavelength resolution (Fig. 2B). The NIRS3 spectra have lower reflectance R relative to sample (R_{NIRS3}/R_{sample} = 0.7 at 2.0 μm) and a shallower 2.7 μm absorption depth (ratio of ~0.5 at 2.7 μm), which is consistent with analysis of other Ryugu samples (*13*). This could be due to differences in particle size distribution and porosity between the laboratory samples and Ryugu's surface or to the much larger field of view of NIRS3 (*13*).

Spectra of Ryugu and the laboratory samples have similar reflectances to that of asteroid Bennu (*14*) at visible wavelengths, but opposite spectral slopes (Fig. 2A). The 2.7 μm feature (Fig. 2B) and the bands in the MIR-FIR spectrum (Fig. 2C) of Bennu (*15*) also differ from Ryugu.

The Ryugu samples are much darker and have a flatter spectral slope than the meteorites Orgueil and Tagish Lake (Fig. 2A). Orgueil is classified as a CI1 meteorite, meaning an aqueously altered (modified by reactions with water) Ivuna-type carbonaceous chondrite, whereas Tagish Lake is a C2, a carbonaceous chondrite that was less altered so retains anhydrous minerals. The position of the OH absorption band in the Ryugu sample spectra is consistent with that in Orgueil, Tagish Lake, and Flensburg. Flensburg is an ungrouped C1 chondrite, in which chondrules (submillimeter anhydrous aggregates made of silicate and glass) are totally replaced by phyllosilicates (*16*). The same feature appears at longer wavelengths in Murchison, which is classified as CM2 (carbonaceous chondrite meteorites of Mighei type), and in asteroid Bennu (Fig. 2B) (*2*, *14*). The position of this band is known to correlate with the Mg/Fe ratio in phyllosilicates, so we infer that Ryugu, Orgueil, Tagish Lake, and Flensburg contain Mg-rich phyllosilicates, whereas Murchison and Bennu contain Fe-rich phyllosilicates (*9*, *10*).

Three-dimensional structure and density

All but one of our coarse Ryugu samples (the exception was sample A0058) were characterized by using synchrotron x-ray computed tomography (SR-CT) (*7*), with a resolution of 0.85 μm per voxel (table S1). Most of the

[1]Department of Earth Sciences, Tohoku University, Sendai 980-8578, Japan. [2]NASA Johnson Space Center; Houston, TX 77058, USA. [3]The University Museum, The University of Tokyo, Tokyo 113-0033, Japan. [4]Earth-Life Science Institute, Tokyo Institute of Technology, Tokyo 152-8550, Japan. [5]Institute of Space and Astronautical Science, Japan Aerospace Exploration Agency (JAXA), Sagamihara 252-5210, Japan. [6]Department of Space and Astronautical Science, The Graduate University for Advanced Studies (SOKENDAI), Hayama 240-0193, Japan. [7]School of Earth and Space Exploration, Arizona State University, Tempe, AZ 85287, USA. [8]Planetary Exploration Research Center, Chiba Institute of Technology, Narashino 275-0016, Japan. [9]Department of Earth, Atmospheric and Planetary Sciences, Massachusetts Institute of Technology, Cambridge, MA 02139, USA. [10]Department of Mechanical Systems Engineering, Nagoya University, Nagoya 464-8603, Japan. [11]Department of Earth and Planetary Science, The University of Tokyo, Tokyo 113-0033, Japan. [12]Isotope Science Center, The University of Tokyo, Tokyo 113-0032, Japan. [13]Laboratoire d'Etudes Spatiales et d'Instrumentation en Astrophysique (LESIA), Observatoire de Paris, Meudon 92195 France. [14]Geological Survey of Japan, National Institute of Advanced Industrial Science and Technology (AIST), Tsukuba, 305-8567, Japan. [15]Department of Earth and Planetary Sciences, University of New Mexico, Albuquerque, NM 87131, USA. [16]Research Organization of Science and Technology, Ritsumeikan University, Kusatsu 525-8577, Japan. [17]Key Laboratory of Mineralogy and Metallogeny, Guangdong Provincial Key Laboratory of Mineral Physics and Materials, Guangzhou Institute of Geochemistry, Chinese Academy of Sciences (CAS), Guangzhou 510640, China. [18]Center for Excellence in Deep Earth Science, CAS, Guangzhou 510640, China. [19]Scattering and Imaging Division, Japan Synchrotron Radiation Research Institute, Sayo 679-5198, Japan. [20]Institute of Low Temperature Science, Hokkaido University, Sapporo 060-0819, Japan. [21]Department of Earth, Environmental, and Planetary Sciences, Brown University, Providence, RI 02912, USA. [22]Instituto de Astrofísica de Canarias, University of La Laguna, Tenerife 38205, Spain. [23]Aizu Research Center for Space Informatics, The University of Aizu, Aizu-Wakamatsu 965-8580, Japan. [24]Department of Astronomy, University of Washington, Seattle, WA 98195 USA. [25]Institute for Radiation Sciences, Osaka University, Toyonaka 560-0043, Japan. [26]Kavli Institute for the Physics and Mathematics of the Universe, The University of Tokyo, Kashiwa 277-8583, Japan. [27]Department of Physics, The University of Tokyo, Tokyo 113-0033, Japan. [28]Materials Sciences Research Center, Japan Atomic Energy Agency, Tokai 319-1195, Japan. [29]Department of Earth and Space Science, Osaka University, Toyonaka 560-0043, Japan. [30]Institute of Geoscience, Goethe University, Frankfurt, 60438 Frankfurt am Main, Germany. [31]Department of Chemistry, Ghent University, Krijgslaan 281 S12, Ghent, Belgium. [32]Institut d'Astrophysique Spatiale, Université Paris-Saclay, Orsay 91405, France. [33]Department of Earth Sciences, Royal Holloway, University of London, Egham TW20 0EX, UK. [34]Institut de Minéralogie, Physique des Matériaux et Cosmochimie, Muséum National d'Histoire Naturelle, Centre national de la recherche scientifique (CNRS), Sorbonne Université, Paris, France. [35]Institut de Planétologie et d'Astrophysique de Grenoble, CNRS, Université Grenoble Alpes, 38000 Grenoble, France. [36]Advanced Photon Source, Argonne National Laboratory, Argonne, IL 60439, USA. [37]Faculty of Engineering, Kindai University, Higashi-Hiroshima 739-2116, Japan. [38]Department of Planetology, Kobe University, Kobe 657-8501, Japan. [39]Department of Earth Resources Engineering, Kyushu University, Fukuoka 819-0395, Japan. [40]School of Engineering, The University of Tokyo, Tokyo 113-0033, Japan. [41]Department of Physics, Kwansei Gakuin University, Sanda 669-1330, Japan. [42]Department of Earth and Atmospheric Sciences, University of Houston, Houston, TX 77204, USA. [43]Texas Materials Institute, The University of Texas at Austin, Austin, TX 78712, USA. [44]Department of Geoscience, Virginia Tech, Blacksburg, VA 24061, USA. [45]Materials Analysis Station, National Institute for Materials Science, Tsukuba 305-0047, Japan. [46]Institute for Materials Research, Tohoku University, Sendai 980-8577, Japan. [47]Department of Earth Science, Natural History Museum, London SW7 5BD, UK. [48]Institute of Nature and Environmental Technology, Kanazawa University, Kanazawa 920-1192, Japan. [49]Spectroscopy Division, Japan Synchrotron Radiation Research Institute, Sayo 679-5198, Japan. [50]Department of Materials Structure Science, The Graduate University for Advanced Studies (SOKENDAI), Tsukuba, Ibaraki 305-0801, Japan. [51]Institute of Materials Structure Science, High-Energy Accelerator Research Organization, Tsukuba 305-0801, Japan. [52]Division of Earth and Planetary Sciences, Kyoto University, Kyoto 606-8502, Japan [53]Faculty of Arts and Science, Kyushu University, Fukuoka 819-0395, Japan. [54]Planetary Science Institute, Tucson, AZ 85719, USA. [55]The Pennsylvania State University, University Park, PA 16802, USA. [56]Department of Physics, California State University, San Marcos, CA 92096, USA. [57]Space Sciences Laboratory, University of California, Berkeley, CA 94720, USA. [58]Laboratoire de Physique des 2 Infinis Irène Joliot-Curie, Université Paris-Saclay, CNRS, 91405 Orsay, France. [59]Institute for Planetary Research, Deutsches Zentrum für Luftund Raumfahrt, Rutherfordstraße 2 12489 Berlin, Germany. [60]Division of Geological and Planetary Sciences, California Institute of Technology, Pasadena CA 91125, USA. [61]Department of Geosciences, Shizuoka University, Shizuoka 422-8529, Japan. [62]Department of Materials Science and Engineering, Tokyo Institute of Technology, Tokyo 152-8550, Japan. [63]Graduate School of Science and Engineering, Ehime University, Matsuyama 790-8577, Japan. [64]European Space Astronomy Centre, 28692 Villanueva de la Cañada, Spain. [65]High Energy Accelerator Research Organization, Tokai 319-1106, Japan. [66]Department of Applied Physics, Osaka University, Suita 565-0871, Japan [67]Hitachi, Hatoyama 350-0395, Japan. [68]Institute for Integrated Radiation and Nuclear Science, Kyoto University, Kumatori 590-0494, Japan. [69]National Metrology Institute of Japan, AIST, Tsukuba 305-8565, Japan. [70]Department of Physics, Rikkyo University, Tokyo 171-8501, Japan. [71]Japan Fine Ceramics Center, Nagoya 456-8587, Japan. [72]Toyota Central Research and Development Laboratories, Nagakute 480-1192, Japan. [73]Istituto di Astrofisica e Planetologia Spaziali, Istituto Nazionale di Astrofisica, Rome 00133, Italy. [74]Institut Universitaire de France, Paris, France. [75]Faculty of Aerospace Engineering, Delft University of Technology, Delft, Netherlands. [76]Department of Physical Sciences, Ritsumeikan University, Shiga 525-0058, Japan. [77]Physical Sciences Laboratory, The Aerospace Corporation, CA 90245, USA. [78]University of Chinese Academy of Sciences, Beijing 100049, China. [79]Institut des Sciences Moléculaires d'Orsay, Université Paris-Saclay, CNRS, 91405 Orsay, France. [80]Deutsches Elektronen-Synchrotron Photon Science, 22603 Hamburg, Germany. [81]Nano Life Science Institute, Kanazawa University, Kanazawa 920-1192, Japan. [82]Graduate School of Life Science, University of Hyogo, Hyogo 678-1297, Japan. [83]Institut de Physique du Globe de Paris, Université de Paris, Paris 75205, France. [84]Division of Natural Sciences, International Christian University, Mitaka 181-8585, Japan. [85]Institute of Geosciences, Friedrich-Schiller-Universität Jena, 07745 Jena, Germany. [86]Center for Advanced Radiation Sources, University of Chicago, Chicago, IL 60637, USA. [87]Optimized Light Source of Intermediate Energy to LURE (SOLEIL) L'Orme des Merisiers, Gif sur Yvette F-91192, France. [88]Institut Chimie Physique, Université Paris-Saclay, CNRS, 91405 Orsay, France. [89]Graduate School of Science, Nagoya City University, Nagoya 467-8501, Japan. [90]Department of Natural History Sciences, Hokkaido University, Sapporo 060-0810, Japan. [91]Department of Earth and Planetary Sciences, Kyushu University, Fukuoka 819-0395, Japan. [92]Graduate School of Advanced Science and Engineering, Hiroshima University, Higashi-Hiroshima 739-8526, Japan. [93]Department of Geology, Rowan University, Glassboro, NJ 08028, USA. [94]Lunar and Planetary Laboratory, University of Arizona, Tucson, AZ 85721, USA. [95]Research and Development Directorate, JAXA, Sagamihara 252-5210, Japan. [96]Department of Mechanical Engineering, Kanagawa Institute of Technology, Atsugi 243-0292, Japan. [97]Marine Works Japan, Yokosuka 237-0063, Japan. [98]Department of Chemistry, The University of Tokyo, Tokyo 113-0033, Japan. [99]Faculty of Science, Niigata University, Niigata 950-2181, Japan. [100]National Astronomical Observatory of Japan, Mitaka 181-8588, Japan. [101]Digital Architecture Research Center, National Institute of Advanced Industrial Science and Technology, Tokyo 135-0064, Japan. [102]JAXA Space Exploration Center, JAXA, Sagamihara 252-5210, Japan. [103]Department of Physics and Astronomy, Seoul National University, Seoul 08826, Korea. [104]Department of Information Science, Kochi University, Kochi 780-8520, Japan. [105]Center for Data Science, Ehime University, Matsuyama 790-8577, Japan. [106]Department of Earth and Environmental Sciences, Nagoya University, Nagoya 464-8601, Japan.
***Corresponding author. Email: tomoki.nakamura.a8@tohoku.ac.jp**

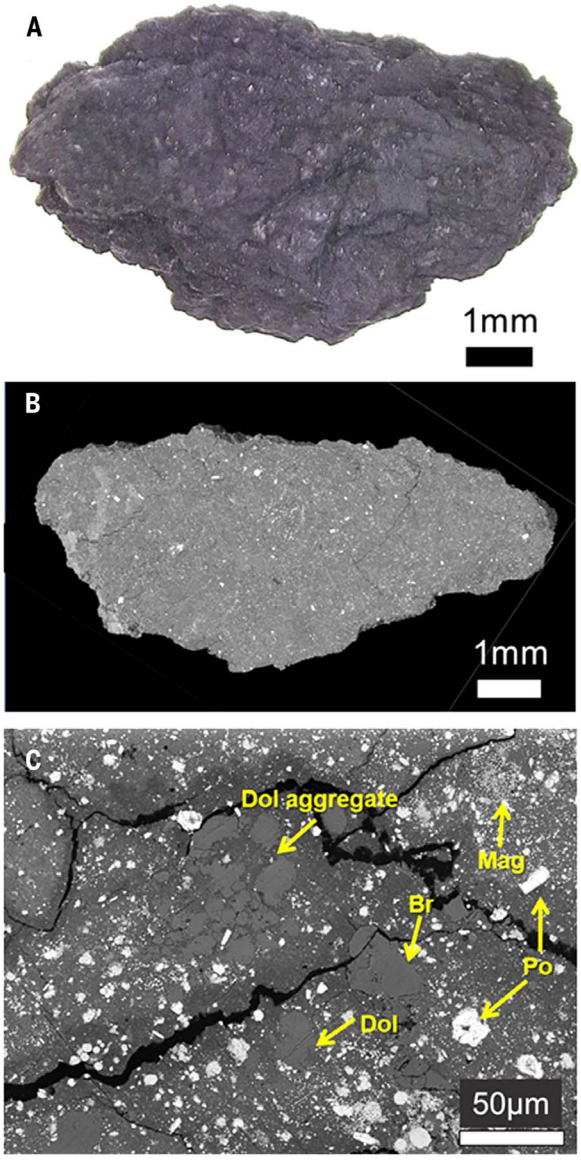

Fig. 1. Morphology and internal texture of C0002. (**A**) Optical micrograph of entire C0002 sample. (**B**) CT image of the largest cross section, showing the absence of chondrules and CAIs. (**C**) Back-scattered electron (BSE) image of typical internal texture. Dolomite (Dol), breunnerite (Br), pyrrhotite (Po), and magnetite framboids (Mag) are labeled; these are embedded in a fine-grained phyllosilicate matrix.

samples had an irregular shape, but some exhibited one or two broad flat surfaces. Particles with flat surfaces were also observed during the sample collection process (*6*). The particle interiors have cracks; most are irregular, but some particles (such as C0055) contain parallel cracks with spacings of tens to hundreds of micrometers (fig. S3).

The mass of each coarse sample particle was measured under dry conditions in a glove box, and the density was calculated from the sample volume determined by using SR-CT (table S1). The bulk density (mass per total volume, including cracks and pores) ranged from 1.7 to 1.9 g cm^{-3} with an average of 1.79 ± 0.08 g cm^{-3} (table S1), which is higher than was estimated from earlier measurements in the curation facility (1.3 g cm^{-3}) (*17*), which did not consider the full three-dimensional (3D) structure. These densities are higher than the measured average density of Ryugu (1.2 g cm^{-3}) (*1*), indicating that the asteroid has high internal macroporosity. The average bulk densities of CI (Ivuna-type) and CM (Mighei-type) chondrite meteorites are 2.12 and 2.21 g cm^{-3}, respectively (*18*), whereas the ungrouped C1 chondrite Flensburg has a density of 1.98 g cm^{-3} (*16*). Because Ryugu has mineralogical similarities to CI chondrites, the lower density of the Ryugu samples indicates a higher porosity than that of CI chondrites.

Mechanical, thermal, electrical, and magnetic properties

The Ryugu samples A0026 (TD1) and C0002 (TD2; our largest particle) were measured (*7*) to determine mechanical, thermal, electrical, and magnetic properties (Table 1) to compare with carbonaceous chondrites (table S2) and for use in numerical simulations.

The resulting physical properties of the Ryugu samples are not identical to any known meteorite. Most properties are similar to hydrous CI and CM chondrites but differ from anhydrous CV (Vigarano-type) and CO (Ornans-type) chondrites (Table 1 and table S2). The mechanical properties show that Ryugu samples are weaker in strength, especially their Young's modulus and Poisson's ratio, than hydrous carbonaceous chondrites (table S2) and have a larger volume change upon deformation (such as compression or impact). The thermal expansivity of the Ryugu samples differs from the nonlinear temperature-dependent results measured for some carbonaceous chondrites (*19*) but is linear in the temperature range of 220 to 370 K (fig. S4).

The thermal properties (Table 1) could be responsible for the low thermal inertia of Ryugu (*20*, *21*). The thermal diffusivity (Table 1) and the bulk density of sample C0002 (table S1) were used to calculate the thermal conductivity of 0.5 W m^{-1} K^{-1} and thermal inertia of 890 J m^{-2} s$^{-0.5}$ K^{-1} [hereafter thermal inertia units (TIU)] at a temperature of 298 K. The thermal inertia of the sample is higher than the mean of the asteroid surface observed by Hayabusa2 [225 ± 45 TIU (*22*)] and measured in situ by the Mobile Asteroid Surface Scout (MASCOT) [295 ± 18 TIU (*21*)]. Remote sensing is sensitive to a thermal skin depth of ~10 mm, whereas the thickness of the sample measured in the laboratory is <1 mm, so a thermal shielding effect could arise on intermediate scales (for example, cracks of several millimeters in length).

Thin sections of magnetite framboids (aggregates of equidimensional microcrystals of magnetite) with diameters of 300 to 1100 nm were observed with electron holography at a spatial resolution of 14 nm (*7*). These magnetite inclusions have vortex magnetic structures and magnetic flux leakage out of the particles (Fig. 3, A to C, and fig. S5). The externally leaking magnetic flux was detected as remanent magnetization in macroscopic measurements. Mössbauer spectra showed that half of the iron in these samples is in magnetite, and the magnetic hysteresis parameter values (Table 1) are similar to those of carbonaceous chondrites that contain submicrometer magnetite framboids (*23*, *24*). Therefore, the magnetite framboids dominate the natural remanent magnetization (NRM) of asteroid Ryugu. Two Ryugu particles from different sampling sites (A0026 from TD1 and C0002 from TD2) record magnetic fields of 31 to 260 μT and 18 to 704 μT (fig. S6), respectively. We suggest that the source magnetic field was homogeneous on Ryugu's parent body.

Elemental abundances

We used muon x-ray emission spectroscopy to measure the abundances of major chemical elements in 10 coarse Ryugu samples, including the largest sample C0002 (126.6 mg in total)

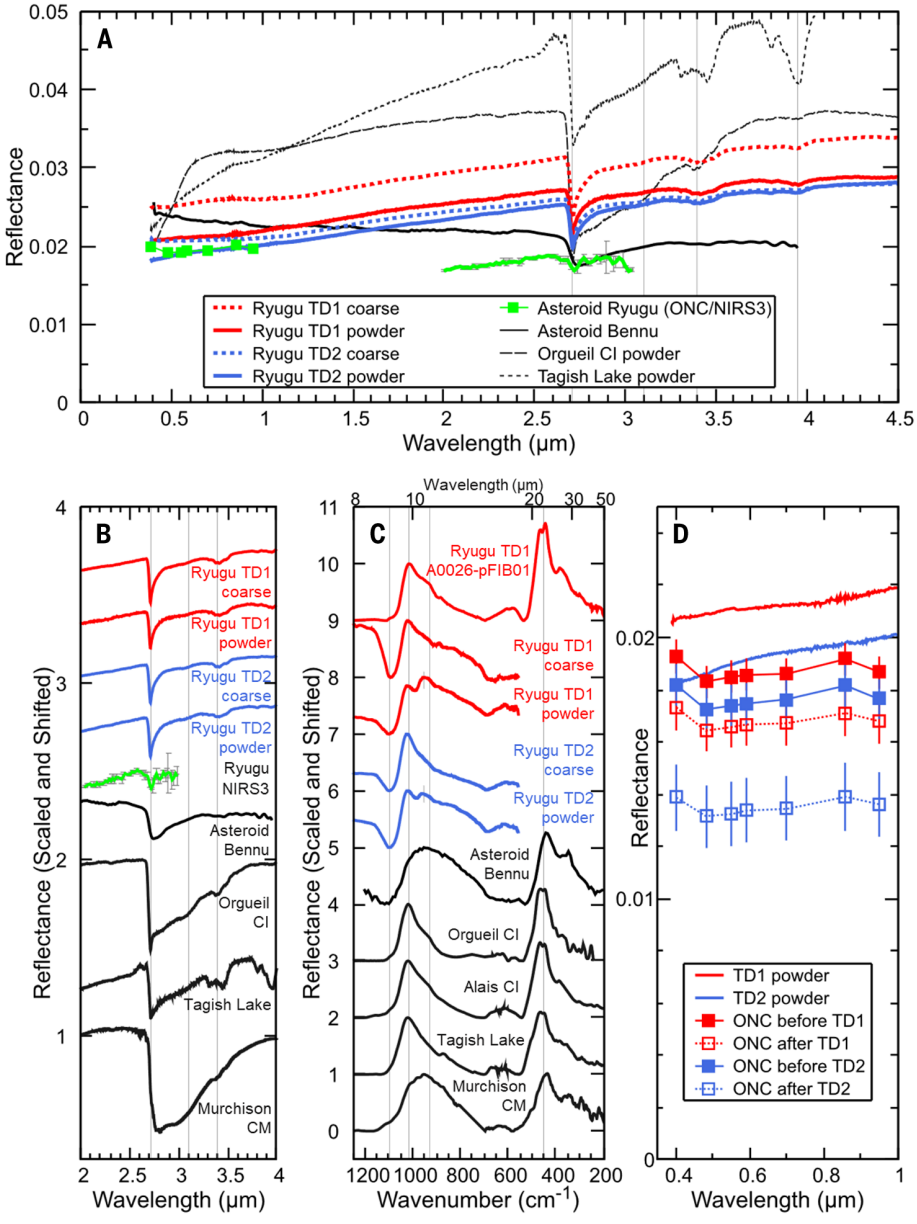

Fig. 2. Reflectance spectra of coarse and powder samples of Ryugu. (**A**) Vis-NIR reflectance spectra of coarse (dotted lines) and powder (solid lines) samples from the TD1 (red) and TD2 (blue) sites on Ryugu, compared with hydrated carbonaceous chondrites (dashed and dotted black lines), Hayabusa2 remote sensing observations of Ryugu (solid green lines) (*2*, *3*), and remote sensing observations of Bennu (solid black line) (*14*). The vertical gray lines are at 2.71, 3.1, 3.4, and 3.95 μm. (**B**) Same data as (A), but normalized at 2.595 μm and shifted arbitrarily in the NIR wavelength region to aid comparison. (**C**) MIR-FIR spectra of TD1 and TD2 coarse and powder samples, the flat surface of sample A0026, remote sensing observations of Bennu (*95*), pressed powders of meteorites (Alais and Tagish Lake), and meteorite coarse samples (Orgueil and Murchison). All spectra are scaled to have the same difference between reflectance minimum and maximum, then shifted arbitrarily for comparison. The vertical gray lines at 9.1, 9.8, 10.75, and 22.3 μm indicate, respectively, the Christiansen feature, an Si–O stretching peak, an additional shoulder of the main Si-O peak, and a peak of the doublet from saponite (*96*). The peaks at 10.5 μm in the powder samples are scattered light from the sample dish (*7*). (**D**) Visible reflectance spectra of Ryugu TD1 and TD2 powder samples measured in the laboratory compared with the TD1 and TD2 sites before and after the touchdowns (*7*).

(*7*, *25*, *26*). Because the muon beam is >3 cm in diameter, we analyzed all 10 samples together to obtain a mean bulk elemental abundance. Pellets of the meteorites Murray (type CM2; 306.5 mg) and Orgueil (type CI1; 195 mg) were measured for comparison.

We detected carbon (C), N, oxygen (O), sodium (Na), magnesium (Mg), silicon (Si), sulfur (S), iron (Fe), and nickel (Ni) (Fig. 4A). The Ryugu and Orgueil spectra are very similar, indicating similar major elemental abundances. However, the Ryugu samples contain less O than that in Orgueil.

We calculated elemental mass ratios M/Si (M = C, N, O, Na, Mg, S, and Fe) from the muon x-ray data (*7*). M/Si has previously been measured for the Murray meteorite (table S3), so it was used as a standard. We determined Ryugu mass ratios of C/Si = 0.338 ± 0.008, N/Si = 0.019 ± 0.009, O/Si = 3.152 ± 0.099, Na/Si = 0.039 ± 0.006, Mg/Si = 0.890 ± 0.021, S/Si = 0.510 ± 0.019, and Fe/Si = 1.620 ± 0.040. These elemental ratios are consistent with those of CI chondrites (*27*) and the Sun (*28*), except O/Si is 25% lower in Ryugu than in CIs (table S3 and fig. S7). These abundances are nevertheless sufficiently similar to classify Ryugu as a CI chondrite, which is consistent with other lines of evidence (*29*).

CI chondrites contain 45 wt % oxygen (*27*); Ryugu is therefore depleted in oxygen by 11.3 wt %, given its similar Si concentration to CI chondrites (*29*). The Ryugu samples were prepared and analyzed in low-oxygen conditions (<0.1%) and in dry atmosphere (dew points < −50°C), so the results indicate the indigenous oxygen abundance of Ryugu. The lower water content and sulfate abundance of Ryugu samples than CI chondrites (*29*) are probably the cause of the low oxygen abundance.

Nitrogen-bearing molecules such as NH_3, CN, and N_2 have low freezing points and could only have been incorporated into asteroids in the outer Solar System (*30*). The N/C ratio can therefore be used to infer the distance from the Sun of Ryugu's parent body during its formation. We measured an average N/C atomic ratio of 0.047 ± 0.022 from the 10 coarse samples. This is higher than that of primitive anhydrous chondrites (N/C = 0.001 to 0.02), which is consistent with hydrated chondrites such CM and CI (N/C = 0.02 to 0.06) and lower than ultracarbonaceous micrometeorites of probable cometary origin (N/C = 0.06 to 0.2) (*30*). We conclude that Ryugu's parent body formed at heliocentric distances similar to those of hydrated carbonaceous chondrites.

Mineralogy and mineral chemistry

The SR-CT image of C0002 (Fig. 1B) shows that it consists almost entirely of fine-grained matrix material. We searched for distinct objects formed at high temperatures (>1000°C) in the early solar nebula, such as chondrules (formed by melting of precursor silicate-rich dust) or Ca-, aluminum (Al)–rich inclusions (CAIs; formed through condensation from hot nebular gas and the earliest solids to form in the Solar System). We found no examples more than 100 μm in diameter in any of the

Table 1. Summary of the physical properties measured from the Ryugu samples (7).

	Value	Uncertainty	Unit	Measurement condition	Measured sample(s)
Mechanical properties					
Compressive hardness	0.18	0.1	GPa	Ambient	C0002 plate 3*
Young's modulus	5.3	1.6	GPa	Ambient	C0002 plate 3*
Bending strength	4.9	1.9	MPa	Ambient	C0002 plate 3 and 4
Longitudinal velocity	2.08	0.13	km/s	Ambient	Average of C0002 plate 3 and 4†
Shear velocity	1.37	0.15	km/s	Ambient	Average of C0002 plate 3 and 4†
Thermal expansivity	2.6×10^{-5}	2×10^{-6}	/K	210 to 400 K, nitrogen gas	C0002 plate 3
Cohesive force	0.17	0.02	μN	Ambient	C0002 plate 4
Thermal properties					
Heat capacity at 298K	865	16	J/kg/K	213 to 373 K, nitrogen gas	Average of C0002 plate 4 and A0026
Thermal diffusivity	3.2×10^{-7}	0.3×10^{-7}	m^2/s	300 K, vacuum	Average of C0002 plate 3 and 4
Electrical properties					
Resistivity	2.5×10^{6}	0.3×10^{-6}	ohm·m	300 K, vacuum	Average of C0002 plate 3 and 4
Relative permittivity	6.8	0.8	—	300 K, vacuum	Average of C0002 plate 3 and 4
Magnetic properties					
Magnetic susceptibility	8.39×10^{-5}	4.0×10^{-6}	m^3/kg	300 K, direct current, alternating current (1 to 1000 Hz)	Average of C0002 and A0026
Saturation magnetization	11.6	5.1×10^{-3}	Am^2/kg	300 K	Average of C0002 and A0026
Saturation remanence	1.05	6.3×10^{-3}	Am^2/kg	300 K	Average of C0002 and A0026
Coercivity	12.2	9.3×10^{-2}	mT	300 K	Average of C0002 and A0026
Coercivity of remanence	61.3	4.1×10^{-1}	mT	300 K	Average of C0002 and A0026

*Average is of 26 analyses of fine-grained matrix. †Two fragments from plate 4 were used.

coarse samples, but there are smaller examples. CI chondrites also lack large chondrules.

We produced 31 polished sections cut from 11 samples (table S4), including two plates from the largest sample C0002. Observations with field-emission electron microscopes show that most of the coarse samples are breccias—rocks that consist of fragments ranging in size from ~10 to ~500 μm. Elemental abundance maps of Na and Mg show compositional differences between fragments (fig. S8), usually with sharp boundaries. Most of the fragments consist primarily of fine-grained matrix material, with similar (although not identical) mineralogy and mineral chemistry, which we refer to as Ryugu's major lithology. CI1 chondrites have similar properties, with Orgueil being the most brecciated (31, 32). The Ryugu samples have similar levels of brecciation to that of Orgueil.

The major lithology of Ryugu (Fig. 1C) consists of minerals formed through aqueous alteration: The dominant phase is a phyllosilicate-rich matrix that contains minerals including abundant iron sulfides (pyrrhotite and pentlandite), carbonates (breunnerite and dolomite), magnetite, and hydroxyapatite. The phyllosilicates consist of the minerals saponite and serpentine. Chlorite was only detected in a limited area in C0076. Mg–Na phosphate occurs in some places and appears to have shrunk in volume since its formation, probably owing to degassing of volatile species, such as water (fig. S9). Dolomite is the most abundant carbonate mineral; breunnerite is less abundant but occurs as larger crystals, with one in C0002 measuring 940 by 450 by 262 μm (movie S1). Ca carbonate is rare. Pyrrhotite crystals with a pseudohexagonal shape (1 to 100 μm) are abundant and sometimes include pentlandite. Nano- to submicrometer-size pyrrhotite and pentlandite crystals occur ubiquitously in the phyllosilicate matrix (fig. S10). Magnetite is present in diverse morphologies (fig. S11), which is typical of CI1 chondrites (31). The carbonates often contain small (<10 μm) crystals of magnetite and pyrrhotite. Small (<10 μm) olivine and low-Ca pyroxene crystals are present but rare; they are completely absent from some of the coarse samples.

Ferrihydrite was not observed, despite being a major component of Orgueil (33, 34). Nor was magnesium sulfate. Calcium sulfate [gypsum; $CaSO_4 2(H_2O)$] was detected only as very small grains around larger crystals of calcite (fig. S12); it probably formed after sample recovery on Earth, through reactions of calcite with sulfuric acid, produced by oxidation of small pyrrhotite crystals within the Ryugu samples (35, 36). Small crystals of sodium sulfate grew on the surface of polished sections of Ryugu samples (fig. S13) so are of terrestrial origin. We infer that sulfates are likely absent on Ryugu, implying that sulfates in CI1 chondrites are terrestrial contamination (37). Additional minor minerals include chromite, manganese (Mn)–rich ilmenite, spinel, zinc sulfide (ZnS), cubanite, and daubréelite. Carbonaceous material occurs as globules and diffuse objects embedded in the matrix.

Phyllosilicates in the major lithology have Mg# [defined as the atomic ratio Mg/(Mg+Fe) × 100)] mostly in the range of 75 to 90, which is similar to that in Orgueil. However, Ryugu phyllosilicates have more Mg-rich varieties than in Orgueil, with some locations having Mg# > 85 (Fig. 4B). The compositions of the carbonates are very similar to those of CI1 chondrites (Fig. 4C). Breunnerite and dolomite contain 1 to 10 wt % and 2 to 5 wt % MnO, respectively. Hydroxyapatite contains a small amount of fluorine (<1 wt %), which is typical of chondrites (38). We performed high-energy synchrotron x-ray fluorescence (XRF) tomographic analysis (39) and found enrichment of rare-earth elements (REEs) in hydroxyapatite, with mutually consistent levels of each REE (fig. S14). This is unlike apatite grains in ordinary chondrites (40) and Orgueil (32), which have higher levels of europium (Eu) and gadolinium (Gd), respectively, than thosse of other REEs. Ordinary chondrites and CK (Karoonda-type carbonaceous) chondrites have REE abundances that decrease from light to heavy atomic masses (40), unlike Ryugu. The magnetite does not contain detectable trace elements, whereas ilmenite contains various concentrations of MnO up to 10 wt %, both of which are typical of CIs (34, 41). Pyrrhotite

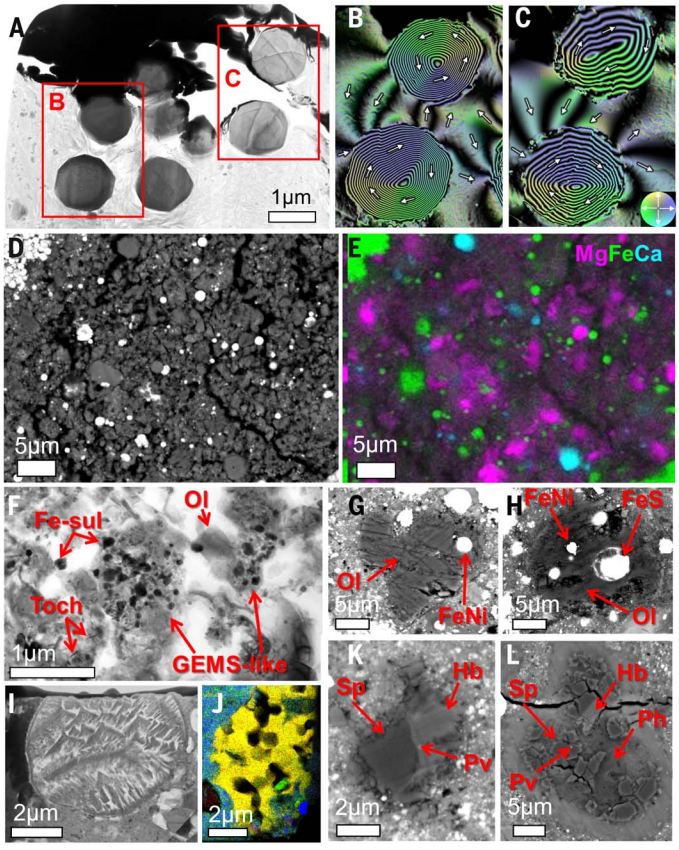

Fig. 3. Characteristic textures, magnetic structures, and embedded objects in the Ryugu samples. (**A**) TEM image of typical magnetite framboids (dark gray rounded objects) from A0064. The light gray area is phyllosilicate from the major lithology, and the upper black area is tungsten contamination. (**B** and **C**) Color maps of the magnetic flux direction obtained from the reconstruction of remanent magnetism, for the magnetite framboids in red boxes in (A) observed by using electron holography (*7*). Each particle has a concentric circular magnetic field (vortex structure) indicated with white arrows, which show the direction of the magnetic flux as shown in the color-wheel in (C). The composition and electron diffraction data for this region are shown in fig. S5. (**D**) Enlarged view of the least-altered fragment 4 in sample C0002, showing high porosity. (**E**) Compositional map of (D), showing high abundances of Mg-rich olivine and Mg-rich, low-Ca pyroxene (magenta); magnetite and pyrrhotite (green); and minor Ca carbonate (light blue). (**F**) TEM image of a part of the least-altered fragment 5 in C0002, showing a very porous aggregate with labeled GEMS-like objects, Fe sulfide (Fe-sul), Mg-rich olivine (Ol), and tochilinite (Toch). (**G** to **I**) Chondrule-like objects. Objects in (G) and (H), both from C0002, show textures similar to those of type I chondrules, consisting of Mg-rich olivine (Ol) and an FeNi metal inclusion. An FeS inclusion occurs only in (H). The object in (I), from C0076, shows a barred-olivine texture, consisting of several sets of parallel olivine bars and an olivine rim. (**J**) TEM–energy-dispersive spectrometer (EDS) color map of a porous olivine (yellow) from C0076, including a small Al-, Ti-rich diopside crystal (green). Red-green-blue (RGB) colors indicate the concentrations of Mg, Si, and Fe, respectively. (**K** and **L**) Small CAI-like objects. The object in (K), from C0040, consists of Al spinel (Sp), hibonite (Hb), and a small inclusion of perovskite (Pv). The object in (L), from C0002, consists of Al spinel (Sp), hibonite (Hb), a small inclusion of perovskite (Pv), and phyllosilicate (Ph). (A), (F), and (I) are bright-field TEM images, and (D), (G), (H), (K), and (L) are BSE images.

contains Ni up to 2 wt %. The Ni/Fe atomic ratios of pentlandite range from 1 to 1.2 in most cases. Representative compositions are listed in table S5.

Relative mineral abundances were estimated from two element maps of C0002 (~9.0 and ~8.6 mm^2 area) composed primarily of the major lithology. The abundances (table S6) are broadly consistent with those of Orgueil (*31*, *32*, *42*).

We performed x-ray diffraction (XRD) analysis of a whole sample of C0002 (fig. S15) and found a large, broad peak at ~10 Å and a distinct peak at 7.45 Å, which we identified as being due to saponite and serpentine, respectively. The 10-Å peak indicates a low abundance of interlayer H_2O in saponite, as previously inferred from use of other techniques (*29*). To characterize the phyllosilicates, we applied ethylene glycol to 10 small particles separated from several coarse samples (*7*) and observed peak shifts in the XRD patterns, indicating expansion of interlayer spacings due to incorporation of glycol (fig. S16). We identified reflections at 16.8 and 13.3 Å as being due to saponite-serpentine mixed-layer minerals, and at 7.28 Å as being due to pure serpentine (*7*). The saponite-rich mixed-layer mineral is the most abundant, followed by serpentine, but the relative abundances differ between samples. Similar results have previously been obtained for Orgueil (*43*).

Although the bulk mineralogy of Ryugu samples is similar to that of Orgueil, we found that the Ryugu samples are much darker. Possible explanations are the presence of bright Mg-sulfate epsomite in Orgueil (*37*), or a lower Fe^{3+} abundance in phyllosilicates in the Ryugu samples (Fe^{3+}/Fe_{total} is 0.4 for Ryugu and 0.9 for Orgueil). Mg-rich smectite becomes brighter as Fe^{3+}/Fe_{total} increases from 0.40 to 0.97 (*44*). The oxidation of phyllosilicates and the formation of epsomite can occur on Earth because of weathering, which we infer is the likely origin of the brightness of Orgueil. Ryugu samples also contain a high abundance of opaque, nano-size pyrrhotite (fig. S10), which acts as a darkening agent; Orgueil lacks these (*34*), possibly also because of oxidation on Earth (*45*).

The mineralogy, mineral chemistry, and relative mineral abundances of the major lithology indicate that Ryugu (or its parent body) experienced pervasive aqueous alteration. Except for the lack of sulfate and ferrihydrite, the petrological and mineralogical properties of Ryugu are consistent with the five CI chondrites (*31*, *32*, *34*, *46*–*48*); we therefore classified the Ryugu samples as CI chondrites.

Less altered fragments

Although most Ryugu fragments have experienced extensive aqueous alteration, some fragments in samples of C0002, C0033, C0023, C0025, C0040, C0046, C0076, and C0103 show considerably lesser degrees of alteration. Electron-microprobe analysis (*7*) indicates that these fragments contain higher abundances of olivine and pyroxene (table S6). Electron diffraction (fig. S17) shows that they also contain calcite or aragonite (not dolomite or breunnerite) and phosphides [schreibersite $(Fe, Ni)_3P$ and allabogdanite $(Fe, Ni)_2P$], not hydroxyapatite. These are characteristic features of a less-altered lithology. These less-altered fragments are enriched in Na, with Na/Si ratios roughly twice that of the Sun (table S7).

We identified five less altered fragments in one of the thin sections of C0002. The Mg map of C0002 (fig. S8B, fragment 1 to 5) indicates a high abundance of olivine and low-Ca pyroxene only in the fragments. These minerals are rich in Mg relative to the surrounding phyllosilicates; we confirmed their presence using an electron microprobe. We also identified spinel

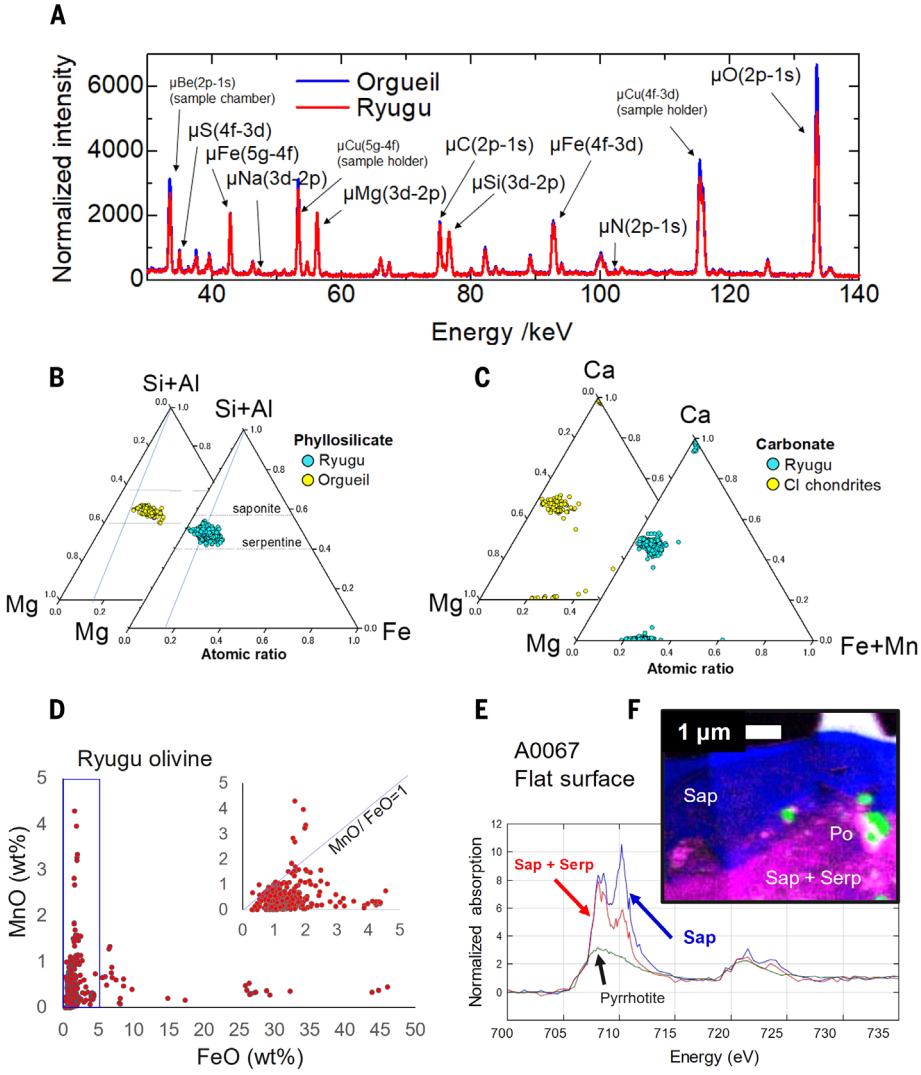

Fig. 4. Results of chemical analyses using muon, electron, and x-ray spectroscopy. (**A**) Muonic x-ray spectra for Ryugu (red) and Orgueil (blue), normalized by means of μSi 3d-2p x-ray (76 keV) intensities (the muonic Si x-ray emitted by transition of 3d to 2p muon atomic orbit). (**B**) Ternary diagrams of Mg, Fe, and Si+Al, showing the chemical composition of Ryugu phyllosilicates (cyan; 774 analyses), compared with Orgueil (yellow). The blue line corresponds to Mg# = 85. The contribution from FeS was corrected according to S content (*7*). (**C**) Ternary diagrams of Mg, Ca, and Fe+Mn showing the chemical composition of Ryugu carbonates (653 analyses), compared with CI chondrites (*48*, *52*). (**D**) MnO and FeO abundances measured from Ryugu olivine (611 analyses). (Inset) An enlargement of the blue box area in the range from 0 to 5 FeO wt %. The blue line indicates MnO/FeO = 1; most olivine data have MnO/FeO < 1. (**E**) XANES spectra [at Fe L_2-edge (706.8 eV) and L_3-edge (719.9 eV) regions] of a saponite-rich layer (blue), phyllosilicates of the major lithology (red), and pyrrhotite (green). (**F**) XANES color map of the region shown in Fig. 6B. Three Fe species were identified by means of decomposition analysis (*97*), including Fe in saponite (blue), in serpentine-saponite (pink), and in pyrrhotite (green).

grains with sizes of <30 μm (fig. S18 and table S6). Most olivine in the Ryugu samples occurs in these less altered fragments; the olivine has Mg# > 97 (corresponding to FeO < 3 wt % in Fig. 4D), which is similar to the olivine in CI chondrites (*49*–*51*). A similar, but more altered, fragment has previously been reported in Orgueil [(*52*), their clast 1].

We identified the two fragments that exhibit the least alteration among our samples, labeled fragments 4 and 5 in fig. S8B. The fragments are small (130 by 50 μm and 200 by 90 μm for fragments 4 and 5, respectively) (fig. S19) and embedded within the major lithology. They have a very porous texture, dominated by submicrometer particles of olivine, pyroxene, and other smaller silicate phases with numerous iron sulfide inclusions (Fig. 3, D and E). They also contain micrometer-sized Ca carbonate, pyrrhotite, Al spinel, magnetite spherules, small quantities of phosphides, Mg-Na phosphate, pentlandite, chromium (Cr) spinel, and tochilinite [a hydrous sulfide that is abundant in CM2 chondrites (*53*)] (fig. S20). These mineral assemblages are similar to fragment 1 (fig. S18), but the abundance of olivine and pyroxene is much higher (12.8 and 14.1 vol % for olivine in fragments 4 and 5, respectively) (table S6). Most of the olivine and pyroxene is enriched in Mg, but examples of Fe-rich olivine (Mg# < 44) are also present. Several small areas in fragment 4 contain Na-rich phyllosilicate, indicating that aqueous alteration fluids were enriched in Na. The high abundance of anhydrous silicates leads us to classify the least altered fragments as CI2 (a CI chondrite that was altered but still retains anhydrous minerals) rather than CI1 (in which almost all anhydrous silicates are replaced with phyllosilicates).

We observed the least-altered fragments using transmission electron microscopy (TEM) (*7*) and found that the least-altered fragments also contain numerous partially rounded, mostly 100 to 500 nm, amorphous silicate objects that contain abundant Fe sulfides (mainly <50 nm pyrrhotite and minor pentlandite) (Fig. 3F and fig. S21A). These objects are similar in texture and composition (fig. S21, A and B) to glass with embedded metal and sulfides (GEMS) that occur in anhydrous chondritic interplanetary dust particles (IDPs) of probable cometary origin (*54*). The silicates are mostly amorphous or very poorly crystalline material (the latter possibly phyllosilicates), with lattice spacings close to 2.6 and 1.5 Å (fig. S21A). This is similar to fine-grained fibrous material reported in the GEMS-like objects in the Paris CM chondrite (*55*, *56*).

However, there are differences between the least-altered Ryugu fragments and GEMS in IDPs. The GEMS-like objects we identified in Ryugu lack Fe metal, instead containing pyrrhotite, pentlandite, and tochilinite. The silicates have signs of incipient alteration to phyllosilicates (fig. S21A). The Mg-rich silicate composition of the GEMS-like objects in Ryugu is similar to that of the silicates in GEMS in IDPs (fig. S21B) but also to the phyllosilicate composition in the major lithology (Fig. 4B). This indicates that the GEMS-like objects in Ryugu are at least partially altered, which is similar to the primitive clasts in the Paris CM chondrite (*55*–*57*).

Chondrules, CAIs, and porous olivine

We did not identify any normal-sized chondrules (100 to 1000 μm) in the Ryugu samples analyzed by using SR-CT. However, some smaller objects and fragments (Fig. 3, G to I) have features characteristic of chondrules. Some of these (Fig. 3, G and H) contain FeNi metal spheres embedded in Mg-rich olivine (Mg# > 98), which is indicative of melting in very chemically reduced conditions. This is typical of type-I

chondrules, which are defined as those that consist mainly of olivine with Mg# >90. One object has a barred olivine texture in TEM observations (Fig. 3I)—a thin rim and many bars constituting a single crystal of Mg-rich olivine—so we classified this object as a type-I barred olivine chondrule. No glass is present between the olivine bars, only pores, which probably indicates that glass was originally present but dissolved during the early stages of aqueous alteration. We also identified a small (~30 μm in size) chondrule that has been completely replaced by phyllosilicates (fig. S22 and movie S2). Similar completely altered chondrules have previously been found in the ungrouped C1 chondrite Flensburg, although they are larger (>300 μm) (*16*). The small sizes and low abundance of the chondrules in Ryugu are similar to those found in samples of the short-period comet 81P/Wild2 (*58*).

We also identified a few small (<30 μm) CAIs in the Ryugu samples (Fig. 3, K and L). Their sizes are smaller than CAIs in the Ivuna CI1 chondrite (~100 μm) (*59*). One of the CAIs (Fig. 3K) consists of half hibonite and half Al-rich Fe-free spinel, with a small perovskite inclusion. Another (Fig. 3L) consists of Al-rich Fe-free spinel, with a small hibonite and a perovskite inclusion, and phyllosilicates. We interpreted this as evidence that CAI material that is susceptible to aqueous alteration, such as melilite (*60*), was replaced with phyllosilicates. Several CAI-related spinel-rich aggregates, together with forsteritic olivine, were also observed (fig. S18).

Forsterite (Mg# 98 to 99) grains occur in the less-altered lithology, being <30 μm in size with numerous micrometer-size pores. One (Fig. 3J) contains diopside, an Al-, titanium (Ti)–bearing and Ca-, Mg-rich pyroxene. We analyzed 20 grains of porous forsterite by use of an electron microprobe and found that they all contain ~0.5 wt % MnO. Atomic ratios of Mn/Fe do not exceed 1 in most cases, so the grains are not low-iron manganese-enriched (LIME) olivine (*61*). The pores suggest partial dissolution during aqueous alteration. The origin of this porous olivine is unclear; they could be condensation products, similar to amoeboid olivine aggregates (AOAs) found in carbonaceous chondrites (*62*), although the texture of the olivine crystals in Ryugu is different from AOAs (*63*).

Fluid inclusions in pyrrhotite

We performed higher-resolution (~50 nm per voxel) synchrotron nano-computed tomography (SR-nanoCT) of a large pyrrhotite crystal taken from sample C0002. This crystal showed probable fluid inclusions in the center (Fig. 5, A and B), which suggests that the fluids were trapped in the early stages of crystal growth. These inclusions were completely encapsulated in pyrrhotite and filled with a light-element

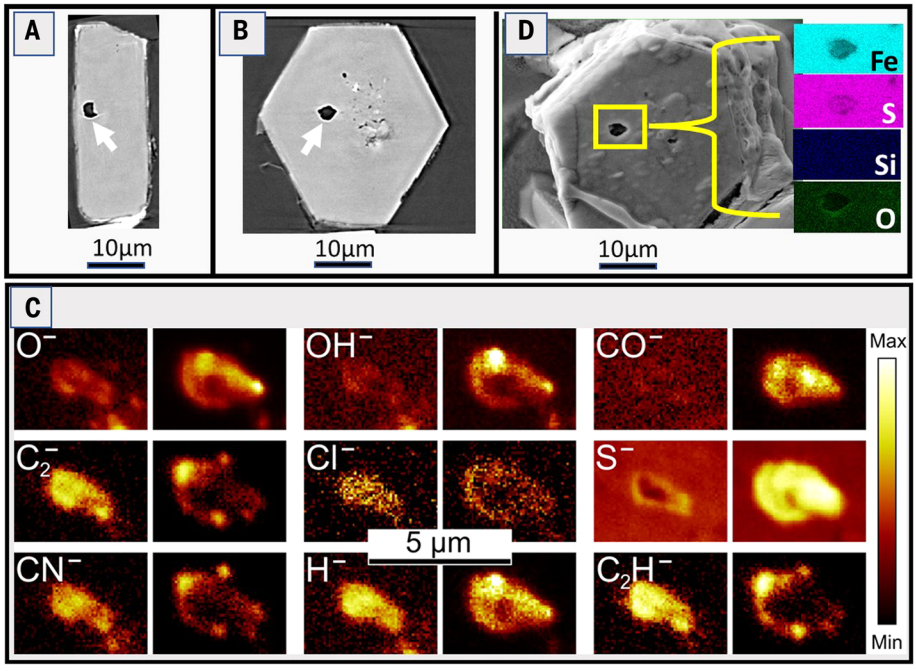

Fig. 5. A fluid inclusion in a Ryugu pyrrhotite crystal. TOF-SIMS and SR-nanoCT measurements were performed on a crystal separated from sample C0002. (**A** and **B**) Slices through the SR-nanoCT scan, showing that the fluid inclusion (indicated with arrows) is unconnected to the surface, with a minimum depth of ~1.5 μm in (A). (**C**) TOF-SIMS maps (arbitrary color scale) of the fluid inclusion after being frozen (−120°C) and opened. Representative secondary ion species are labeled on each image pair, which are measured at the top (left images) and the mid-plane (right images) of the fluid inclusion. OH^- and CO^- are secondary ions of water and CO_2, respectively. S^- is an ion in the aqueous solution. The presence of CN^- indicates N-bearing organic compounds in the fluid, and Cl^- indicates that the trapped fluid was a brine. Differences in the distribution of each species within the inclusion, both within each map and between the top and midplane maps, are a result of the distribution of the various fluid components between the different solid phases (solid carbon dioxide, carbon dioxide clathrate, and H_2O ice) that form during cooling of the fluid inclusion to −120°C. (**D**) BSE image of the final surface following the TOF-SIMS measurements, with the opened fluid inclusion in the yellow box. (Insets) Fe, S, Si, and O element maps, measured with EDS, of the region within the box. These indicate that FeS is the host phase.

material (fig. S23). We performed time-of-flight–secondary ion mass spectrometry (TOF-SIMS) depth profiling and lateral mapping (<80 nm per pixel) at a temperature of −120°C to expose and measure, respectively, the composition of the (now frozen) fluids in five inclusions.

The TOF-SIMS measurements show that the trapped fluids were solutions containing H_2O, CO_2, sulfur species, and N- and chlorine (Cl)–bearing organic compounds. These were identified by their representative secondary ion species, including O^-, OH^-, CO^-, C_2^-, C_2H^-, Cl^-, S^-, and CN^- (Fig. 5C). The detection of CO^-, C_2^-, C_2H^-, and C_3^- indicates that organic molecules were dissolved in the aqueous solution. Electron microscope observations of the largest inclusion show no phyllosilicates or other OH^-–bearing phases that could have contributed to the signal (Fig. 5D). The presence of CO_2–bearing water in a crystal of pyrrhotite indicates that the Ryugu parent body formed beyond the CO_2 and H_2O snow lines (boundaries between gas and ice in the early Solar System), which were >3 to 4 astronomical units (au) from the Sun (*64*).

Flat surfaces and CuS tabular coral-shaped object

We identified some features of the Ryugu samples that have not been observed in meteorites. These include the very flat surfaces of some coarse samples (Fig. 6A). We cut five slices (each 10 by 10 by 0.1 μm) from the flat surface of A0067 to perform depth profiles. TEM observations show a 2-μm-thick saponite-rich layer with high Mg# ~90 running along the flat surface (Fig. 6B). The saponite layer is superposed on an irregular surface of the major lithology, indicating that it formed later. All five slices show similar features, which we infer are present across the whole flat surface. The formation of the saponite layer requires that fluids were present. Pyrrhotite crystals on the flat surface are aligned with their pseudohexagonal facets parallel to the saponite

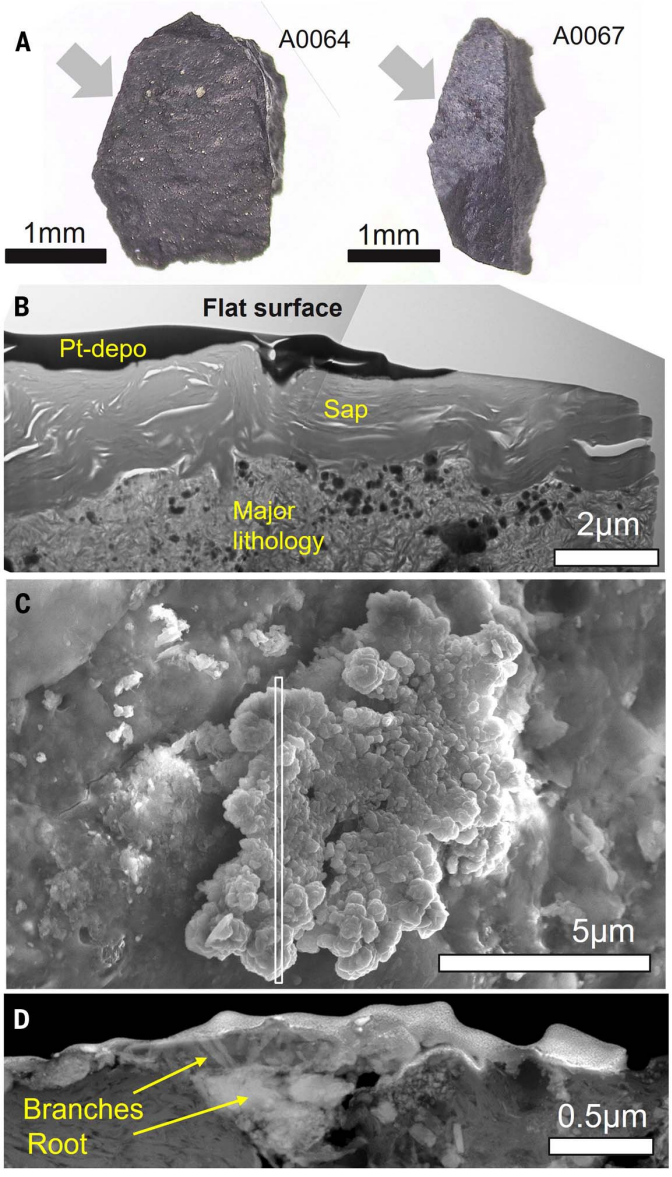

Fig. 6. Flat surface structures and a CuS table coral–shaped object. (**A**) Optical microscope images of flat surfaces (arrows) from two Ryugu samples. (**B**) Depth profile from a TEM image of a slice cut from the flat surface of A0067 to 5 μm depth. The black layer is contamination from Pt coating. A layer of saponite (interlayer spacing d = ~10 Å) makes the surface flat. (**C**) Secondary-electron image of a tabular coral–shaped CuS object on the flat surface of A0067, formed of a stack of submicrometer-sized disk-like crystals. (**D**) Scanning TEM dark-field image of a slice taken from the white box in (C), perpendicular to the surface to a depth of 10 μm by use of a focused-ion beam. The object has morphologies similar to that of a root, several branches, and a stack of disk-like crystals on top. The thin white layer on the top surface of the object is contamination from a Pt coating.

layer (fig. S24), which implies a compressive force during formation. One possible explanation is ice lensing, the formation and growth of subsurface ice crystals (*65*, *66*), as occurs in permafrost soils. At the final stage of aqueous alteration, fluids could have been segregated in thin cracks as they froze. Ice in the cracks could then have grown to form ice lenses. The pressure exerted by the expanding ice lens could have squeezed the adjacent regolith, compacting and aligning phyllosilicates, especially expandable clays such as saponite (*66*).

We also identified table coral–shaped growths of a copper sulfide (CuS) phase on the flat surface of A0067 (Fig. 6C). A thin section was made by cutting the CuS object perpendicular to the flat surface, which was then observed with TEM. The CuS has a morphology that resembles a table coral, with a root, several branches, and many disk-shaped crystals on top (Fig. 6D). Electron diffraction measurements indicate that the CuS phase is probably digenite (Cu_9S_5), which is of hydrothermal origin (*67*). We cannot determine the formation mechanism, but it might have grown from a solution that filled a crack exposed on the flat surface.

Shock effects

Most of our samples show no features that indicate strong deformation or shock melting, indicating that the collected material generally did not experience any intense shock. However, C0055 shows evidence of uniaxial compression and sets of parallel fractures perpendicular to the compaction axis (fig. S3). Such features are common in shocked hydrous carbonaceous chondrites (*68*) and appear in experiments that shocked the Murchison CM2 chondrite to a pressure of 20 GPa (*69*). Therefore, C0055 experienced a shock, whereas the other 16 samples contain no evidence of shock effects.

Aqueous alteration conditions

The low abundance of Mg-chlorite suggests that aqueous alteration occurred at low temperature, below the ~100°C (*70*) required to stabilize Mg-chlorite. All 10 pyrrhotite crystals observed with x-ray and electron diffraction have a monoclinic 4C structure (one of the crystal structures of pyrrhotite, having three unequal crystal axes with one oblique intersection), which indicates that they formed below 254°C (*71*). The Ryugu pentlandite and pyrrhotite compositions are most consistent with formation at 25°C (fig. S25) (*67*, *72*, *73*). The site occupancy by Fe and Ni in pentlandite and its lattice constants are a function of temperature (*74*). We measured the pentlandite lattice constant of 10.0643 ± 0.0009 Å; using XRD analysis of a single pentlandite crystal, 5 μm in size, which was separated from sample C0040, following established methods (*75*). This lattice spacing and the chemical composition indicate an equilibrium temperature of 20 ± 29.5°C (table S9). O isotopes in dolomite indicate formation at 37 ± 10°C (*29*). All of these temperature estimates are consistent.

Mössbauer spectra (conventional and synchrotron) were collected from 1-mm-size fragments, taken from C0061 and A0026 under N_2 gas. These show that magnetite is not oxidized (table S9). The Fe^{2+}/Fe_{total} ratios measured from the phyllosilicates are approximately 0.61 for C0061 and 0.48 for A0026 (fig. S26). Magnetite, pyrrhotite, and silicates contain 40 to 50%, 15 to 30%, and 25 to 40% total iron, respectively (by atom) (table S9). We performed micro-x-ray fluorescence x-ray absorption near-edge structure (μ-XRF-XANES) analysis of the Fe K-edge (a sudden increase of x-ray absorption just beyond the binding energy of the K-shell electrons of the Fe atom), using a 1.0- by 1.0-μm x-ray beam (*76*). Measurements were

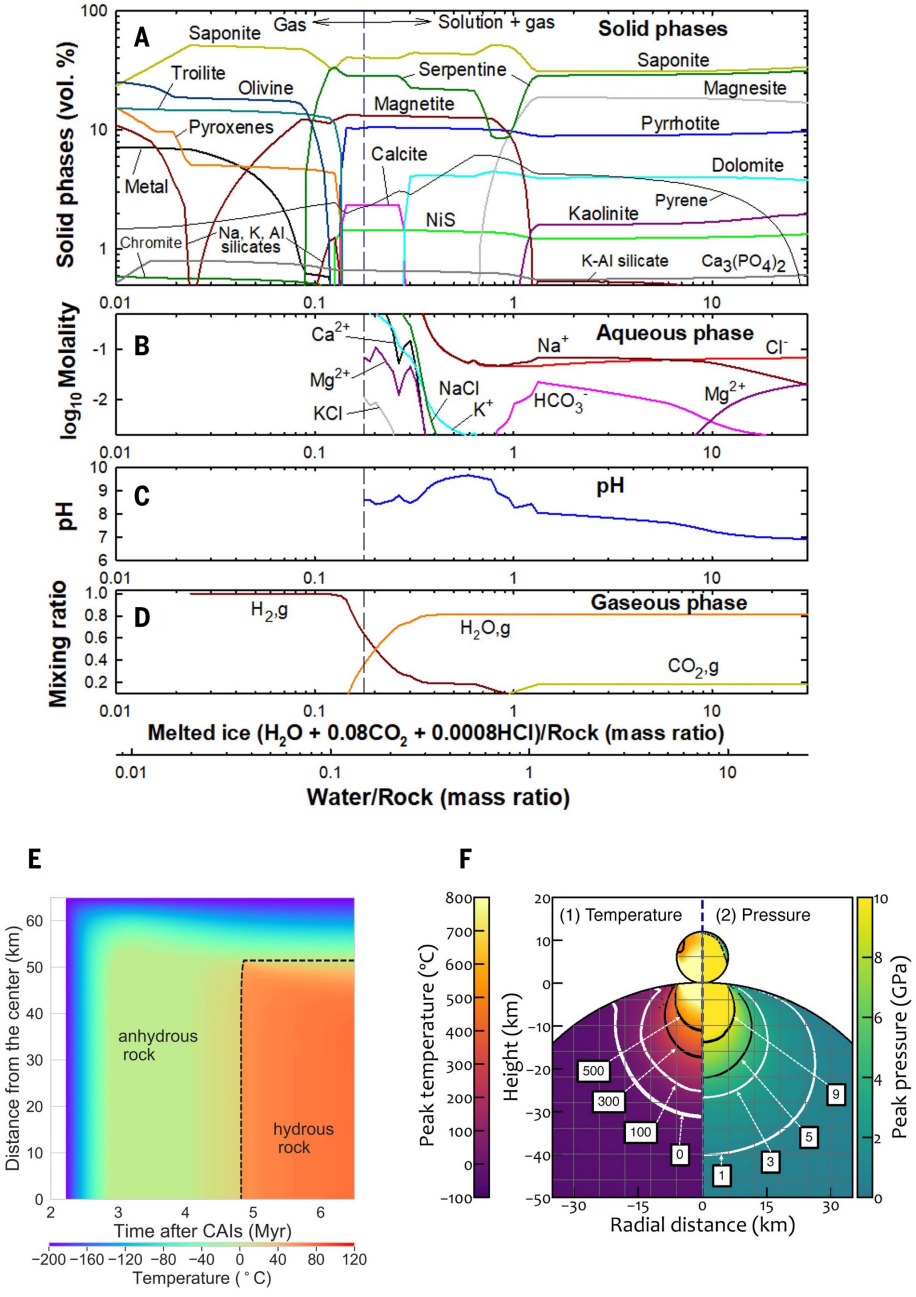

Fig. 7. Calculated models of the aqueous alteration, thermal history, and impact. (**A** to **D**) Model chemical equilibrium of solid, solution, and gas phases during aqueous alteration on the Ryugu parent body at 40°C, assuming the pressure of water saturation (7.4×10^{-2} bar), and 10% chemically active organic matter. Each line indicates a different species or the pH, as labeled. The vertical dashed lines indicate boundaries between aqueous and water-free conditions. The two horizontal scales indicate ratios of melted ice/rock and *W/R*. The ice includes CO_2 and HCl in addition to water, so *W/R* is smaller than melted ice/rock by a factor of 0.835. (**E**) Temperature evolution of the Ryugu parent body. The calculation assumes a 65-km radius with *W/R* = 0.6 and formation time 2.23 million years after CAI formation. The color scale shows the temperature at each location and time. The black dashed line indicates the boundary between hydrous rock and anhydrous rock, where the highly altered lithology shifts to the less altered lithology. (**F**) Impact shock model (*7*), with coordinates measured from the center of the impact point. The images show peak temperature (left) and peak pressure (right) during the impact. The grid of tracer points, placed at multiples of the impactor radius, is shown as gray lines. Isotherms of the peak temperatures are shown as colored curves at 500°, 300°, 100°, and 0°C. Isobaric lines of the peak pressures are shown at 9, 5, 3, and 1 GPa. We infer that the material that later accumulated to form Ryugu was further from the impact than the 100°C isotherm and the 1 GPa isobar.

performed under N_2 gas, using a 150-μm-size particle separated from sample C0025. They showed that the Fe^{2+}/Fe_{total} ratio in phyllosilicates is 0.6 to 0.7 (fig. S27), which is consistent with the Mössbauer data.

The determination of Fe^{2+}/Fe_{total} ratio in other minerals, specifically saponite and serpentine, is required to determine the redox conditions during formation because the stability of Fe^{2+} in each phase can be different. We used scanning transmission x-ray microscopy (STXM) (*77*) analysis with a ~50-nm spatial resolution to measure Fe^{2+}/Fe_{total} in the saponite layers in A0067 (Fig. 6B), finding 0.68 ± 0.05 (Fig. 4, E and F). The sample must have been oxidized to some degree during its storage in a desiccator for more than 5 months, so we regard this ratio as a lower limit. On the basis of (i) the relationship between Fe^{2+}/Fe_{total} ratio and oxidation reduction potential E_h determined for the minerals nontronite and high-Fe-bearing montmorillonite (*78*) and (ii) a reduction experiment we performed on terrestrial saponite with Fe^{2+}/Fe^{3+} ratio determined by means of XANES (fig. S28), we infer that the Fe^{2+}/Fe_{total} (> 0.68) obtained from A0067 indicates that the E_h of saponite formation was likely lower than −0.45 V. If we assume that this E_h value is valid at neutral to alkaline pH conditions and combine it with other μ-XRF-XANES data on a dominant oxidized arsenic form (As^{3+}) in As-bearing species in A0067 (fig. S29), we infer fluid pH > ~9 on the basis of the E_h-pH diagram of As compounds at 25°C (*79*). The presence of saponite on Ryugu also indicates an alkaline fluid (pH > 8) on the basis of (i) the stability field of saponite in the Eh-pH diagram of Fe and (ii) the pH condition of terrestrial lakes where saponite has been found (*80*). We conclude that aqueous alteration proceeded at ~25°C in alkaline conditions.

Chemical equilibrium modeling of aqueous alteration

Aqueous alteration cannot have begun until accreted ices melted in the interior of Ryugu's parent body and likely continued until temperatures reached ~40°C [this study and (*29*)]. We therefore performed chemical equilibrium modeling of a water-gas-solid system at 0° to 40°C (*7*). Consistent with the muon analysis (table S3), we assumed the initial accreted rock had the elemental composition of CI chondrites, but with modified amounts of H, C, O, S, and Cl. Our model mixes this rock in different proportions with a water-ice–rich component, which contains CO_2 and HCl, reflecting the presence of CO_2 and Cl in the fluid inclusion (Fig. 5) and the inferred C and Cl sources in carbonaceous chondrites (*81*, *82*). Although Ryugu material might not have reached chemical equilibrium during alteration, we ran our calculations to that stage.

Our calculated equilibrium composition of the water-gas-solid system at 40°C is shown in Fig. 7, A to D, as a function of the initial melted ice/rock and the water/rock (*W*/*R*) mass ratios. Only 10% of organic matter is allowed to react (*7*). The modeled mineralogy (Fig. 7A) at initial *W*/*R* of 0.06 to 0.1 reproduces the least-altered lithology we found in the Ryugu samples (table S6). These (and lower) *W*/*R* ratios permit stable reduced phases (such as Fe-rich metal, and phosphides), which could remain unaltered or form through alteration under water-poor and H_2-rich conditions. A higher *W*/*R* ratio of 0.1 to 0.2 matches the less-altered lithology, and *W*/*R* of 0.2 to 0.9 with pH > ~8.5 (Fig. 7C) matches with the more extensively altered major lithology (table S6). Analogous calculations were performed at temperatures below 40°C (0° and 20°C), and the results are similar to those at 40°C (*7*).

Our calculations show high Na concentrations at lower *W*/*R*, both in the fluid and in saponite (Fig. 7, A and B), which are consistent with the Na-rich composition of the least- and less-altered lithologies of Ryugu (table S7). The modeling suggests an initial Mg–Na–Cl solution with H_2O–CO_2 in the gas phase, which evolved toward a more reduced and Na–Cl alkaline brine that coexisted with a H_2-rich gas phase (Fig. 7, B to D). No sulfates formed in the model because of the reduced conditions, which is consistent with our observations of the Ryugu samples. The formation of sulfates requires strong oxidants—such as O_2, H_2O_2, and H_2SO_4—in ices accreted on asteroids (*83*).

Formation of Ryugu's parent asteroid

Ryugu's parent body formed in a different orbit than Ryugu's current near-Earth orbit. Orbital dynamics calculations have shown that the most likely origin of Ryugu is two asteroid families (Eulalia or Polana) in the inner main asteroid belt (*3*, *4*, *84*, *85*). However, our observation of CO_2-bearing aqueous fluid in Ryugu pyrrhotite is consistent with the parent asteroid having formed beyond the H_2O and CO_2 snow lines of the early Solar System, more than 3 to 4 au from the Sun. This must have been followed by scattering inward, to the current orbit of the Polana and Eulalia families (<2.5 au). We found many similarities between the Ryugu samples and CI chondrites, which suggests that CI chondrites might have a similar origin.

The Ryugu samples record a magnetic field (fig. S6), which could have arisen from the nebular magnetic field or the dynamo fields generated by differentiated objects (such as Jupiter), although magnetization effects on Earth are to be corrected. The homogeneous global reflectance spectra of Ryugu indicate that its parent body was not differentiated (*2*, *3*). The stable component of NRM is likely carried by the framboidal magnetite (Fig. 3, A to C). If the source was the nebular field (*86*), then the solar nebula had not yet dispersed when magnetite formed on Ryugu's parent body.

Our interpretation that Ryugu's parent asteroid formed far from the Sun is supported by (i) the rarity and very small size of chondrules and CAIs in the samples (Fig. 3, G to L), which are similar to those observed in comets (*58*); (ii) the high abundance of carbonate (table S6); and (iii) the presence of GEMS-like objects (Fig. 3F). However, the C/Si abundance ratio is not as high as those of comets (table S3), according to measurements of cometary IDPs and ultracarbonaceous micrometeorites (*30*, *87*, *88*). This indicates that the parent body of Ryugu did not originate from comets themselves but formed in the same region as CI chondrites, at a large heliocentric distance, possibly outside the orbit of Jupiter (*89*).

Thermal model of Ryugu's parent asteroid

We used the physical properties obtained from the sample analysis (Table 1) to calculate a thermal model of Ryugu's parent body. The radius of the parent body was chosen on the basis of an estimate of the total mass of the Eulalia family (*85*). We set a radius of 50 km for the rocky part of the parent body then added additional size according to the amount of water ice in each model. The initial internal and surface temperatures were set to −200°C [70 K; rationale provided in (*7*)]. The temperature was then allowed to increase through heating by radioactive decay of ^{26}Al, which melted the water ice at 0°C. Subsequent formation of hydrous minerals (assumed to occur at 20°C) released energy that caused further heating. We ran simulations for ranges of formation age (t_s) and initial *W*/*R* ratio.

Mn-Cr dating of Ryugu samples has indicated that carbonates formed at 37 ± 10°C, 5.2 million years after the formation of the first solid materials in the solar system (CAIs) (*29*). That temperature is consistent with our mineralogical constraints (mostly ≲50°C). Our chemical modeling of the aqueous alteration found that a *W*/*R* ratio of 0.2 to 0.9 reproduces the mineralogy of the major lithology (Fig. 7A). An example thermal model that satisfies these constraints (t_s ~2.2 million years and *W*/*R* = 0.6) is shown in Fig. 7E. Inside the parent body (~51 km radius from the center), the ice melts, hydrous minerals form, and carbonate minerals precipitate at ~4.8 million years. Although hydrous and carbonate minerals form throughout, the subsequent temperature increase is limited (reaching a peak of ~75°C), and therefore, dehydration of the hydrous minerals does not occur. Within 14 km of the cold surface, ice melting is limited, so the initial mineralogy experiences very little alteration at low *W*/*R* ratios and low temperature (~0°C). Therefore, the least-altered lithology (Fig. 3, D to F) that we found in the Ryugu samples might have been located close to the surface of Ryugu's parent body.

The formation age in the model required to satisfy the constraints from the sample analysis varies depending on the initial *W*/*R*. The major lithology is consistent with *W*/*R* = 0.2 to 0.9 (Fig. 7A), which corresponds to a range of formation ages from 1.8 million years (*W*/*R* = 0.9) to 2.9 million years (*W*/*R* = 0.2) after CAI formation (conventionally taken to be the beginning of Solar System formation) (fig. S30). We assume instantaneous accretion of the parent body at the time of formation; if the parent body accreted slowly, then the formation must have started earlier.

Impact on Ryugu's parent body

Ryugu's parent body was disrupted by a large-scale impact to form the Eulalia or Polana asteroid family, including Ryugu itself (*3*, *90*). Using the physical properties measured from the samples (Table 1), we constructed an equation of state consistent with the Ryugu material and used it to calculate a destructive collision with the parent body (*7*) by use of the impact-simplified arbitrary Lagrangian Eulerian (iSALE) software (*91*–*93*). Shown in Fig. 7F is the head-on collision of a 6-km-radius impactor onto a 50-km-radius parent body at an impact speed of 5 km s^{-1}, which is typical for the main asteroid belt (*94*). In this simulation, the parent body is mostly destroyed, with the diameter (*D*) of the largest surviving body being ~50 km (fig. S31). This is consistent with the measured sizes of Eulalia (*D* = 40 km) or Polana (*D* = 55 km) (*85*).

Only limited volumes experienced high shock pressure and temperature during the impact (Fig. 7F); we found that 10 and 0.2 vol % of the parent body experienced pressures higher than 1 and 10 GPa, respectively. The temperature near the impact site (approximated as the size of the impactor) rises above 700°C,

whereas regions away from the impact site do not rise above 90°C. The latter temperature is consistent with the amount of interlayer water found in Ryugu saponite (*29*). With this temperature limitation and the absence of evidence for shocks in most of our samples, we propose that Ryugu might have formed from fragments excavated from areas far from the impact site, such as on the far side. It is likely that some of the reaccumulated material originated from the surface and subsurface layer of the parent body; such material would have experienced limited degrees of aqueous alteration at low temperature and low W/R ratio, which is consistent with the least-altered and the less-altered fragments found in our samples.

We conclude that the samples collected by the Hayabusa2 mission originated from multiple depths within Ryugu's parent body, which formed beyond the H_2O and CO_2 snow lines, possibly beyond the orbit of Jupiter.

REFERENCES AND NOTES

1. S. Watanabe *et al*., Hayabusa2 arrives at the carbonaceous asteroid 162173 Ryugu-A spinning top-shaped rubble pile. *Science* **364**, 268–272 (2019). doi: 10.1126/science.aav8032; pmid: 30890588
2. K. Kitazato *et al*., The surface composition of asteroid 162173 Ryugu from Hayabusa2 near-infrared spectroscopy. *Science* **364**, 272–275 (2019). doi: 10.1126/science.aav7432; pmid: 30890589
3. S. Sugita *et al*., The geomorphology, color, and thermal properties of Ryugu: Implications for parent-body processes. *Science* **364**, 252 (2019). doi: 10.1126/science.aaw0422; pmid: 30890587
4. E. Tatsumi *et al*., Spectrally blue hydrated parent body of asteroid (162173) Ryugu. *Nat. Commun.* **12**, 5837 (2021). doi: 10.1038/s41467-021-26071-8; pmid: 34611167
5. E. Tatsumi *et al*., Collisional history of Ryugu's parent body from bright surface boulders. *Nat. Astron.* **5**, 39–45 (2021). doi: 10.1038/s41550-020-1179-z
6. S. Tachibana *et al*., Pebbles and sand on asteroid (162173) Ryugu: In situ observation and particles returned to Earth. *Science* **375**, 1011–1016 (2022). doi: 10.1126/science.abj8624; pmid: 35143255
7. Materials and methods are available as supplementary materials.
8. F. Vilas, M. J. Gaffey, Phyllosilicate absorption features in main-belt and outer-belt asteroid reflectance spectra. *Science* **246**, 790–792 (1989). doi: 10.1126/science.246.4931.790; pmid: 17748705
9. P. Beck *et al*., Hydrous mineralogy of CM and CI chondrites from infrared spectroscopy and their relationship with low albedo asteroids. *Geochim. Cosmochim. Acta* **74**, 4881–4892 (2010). doi: 10.1016/j.gca.2010.05.020
10. D. Takir *et al*., Nature and degree of aqueous alteration in CM and CI carbonaceous chondrites. *Meteorit. Planet. Sci.* **48**, 1618–1637 (2013). doi: 10.1111/maps.12171
11. O. Poch *et al*., Ammonium salts are a reservoir of nitrogen on a cometary nucleus and possibly on some asteroids. *Science* **367**, eaaw7462 (2020). doi: 10.1126/science.aaw7462; pmid: 32165559
12. T. Morota *et al*., Sample collection from asteroid (162173) Ryugu by Hayabusa2: Implications for surface evolution. *Science* **368**, 654–659 (2020). doi: 10.1126/science.aaz6306; pmid: 32381723
13. C. Pilorget *et al*., First compositional analysis of Ryugu samples by the MicrOmega hyperspectral microscope. *Nat. Astron.* **6**, 221–225 (2021). doi: 10.1038/s41550-021-01549-z
14. A. A. Simon *et al*., Widespread carbon-bearing materials on near-Earth asteroid (101955) Bennu. *Science* **370**, eabc3522 (2020). doi: 10.1126/science.abc3522; pmid: 33033153
15. V. E. Hamilton *et al*., Evidence for limited compositional and particle size variation on asteroid (101955) Bennu from thermal infrared spectroscopy. *Astron. Astrophys.* **650**, A120 (2021). doi: 10.1051/0004-6361/202039728
16. A. Bischoff *et al*., The old, unique C1 chondrite Flensburg–insight into the first processes of aqueous alteration, brecciation, and the diversity of water-bearing parent bodies and lithologies. *Geochim. Cosmochim. Acta* **293**, 142–186 (2021). doi: 10.1016/j.gca.2020.10.014
17. T. Yada *et al*., Preliminary analysis of the Hayabusa2 samples returned from C-type asteroid Ryugu. *Nature Astron.* **6**, 214–220 (2021). doi: 10.1038/s41550-021-01550-6
18. D. T. Britt, D. Yeomans, K. Housen, G. Consolmagno, "Asteroid density, porosity and structure" in *Asteroids III*, W. F. Bottke, A. Cellino, P. Paolicchi, R. P. Binzel, Eds. (Univ. Arizona Press, 2002), pp. 485–500.
19. C. P. Opeil, D. T. Britt, R. J. Macke, G. J. Consolmagno, The surprising thermal properties of CM carbonaceous chondrites. *Meteorit. Planet. Sci.* **55**, maps.13556 (2020). doi: 10.1111/maps.13556
20. T. Okada *et al*., Highly porous nature of a primitive asteroid revealed by thermal imaging. *Nature* **579**, 518–522 (2020). doi: 10.1038/s41586-020-2102-6; pmid: 32214245
21. M. Hamm, I. Pelivan, M. Grott, T. de Wiljes, Thermophysical parameter estimation of small Solar system bodies via data assimilation. *Mon. Not. R. Astron. Soc.* **496**, 2776–2785 (2020). doi: 10.1093/mnras/staa1755
22. Y. Shimaki *et al*., Thermophysical modelling and properties of the surface of asteroid 162173 Ryugu: Infrared observations and thermal inertia mapping. *Icarus* **348**, 113835 (2020). doi: 10.1016/j.icarus.2020.113835
23. S. Sridhar, J. F. Bryson, A. J. King, R. J. Harrison, Constraints on the ice composition of carbonaceous chondrites from their magnetic mineralogy. *Earth Planet. Sci. Lett.* **576**, 117243 (2021). doi: 10.1016/j.epsl.2021.117243
24. Ö. Özdemir, D. J. Dunlop, Effect of crystal defects and internal stress on the domain structure and magnetic properties of magnetite. *J. Geophys. Res.* **102** (B9), 20211–20224 (1997). doi: 10.1029/97JB01779
25. K. Shimomura *et al*., Superconducting muon channel at J-PARC. *Nucl. Instrum. Methods Phys. Res. A* **600**, 192–194 (2009). doi: 10.1016/j.nima.2008.11.029
26. K. Terada *et al*., A new X-ray fluorescence spectroscopy for extraterrestrial materials using a muon beam. *Sci. Rep.* **4**, 5072 (2014). doi: 10.1038/srep05072; pmid: 24861282
27. K. Lodders, Relative atomic solar system abundances, mass fractions, and atomic masses of the elements and their isotopes, composition of the solar photosphere, and compositions of the major chondritic meteorite groups. *Space Sci. Rev.* **217**, 44 (2021). doi: 10.1007/s11214-021-00825-8
28. M. Asplund, A. M. Amarsi, N. Grevesse, The chemical make-up of the Sun: A 2020 vision. *Astron. Astrophys.* **653**, A141 (2021). doi: 10.1051/0004-6361/202140445
29. T. Yokoyama *et al*., Samples returned from the asteroid Ryugu are similar to Ivuna-type carbonaceous meteorites. *Science* **379**, eabn7850 (2023).
30. E. Dartois *et al*., Dome C ultracarbonaceous Antarctic micrometeorites. *Astron. Astrophys.* **609**, A65 (2018). doi: 10.1051/0004-6361/201731322
31. J. Alfing, M. Patzek, A. Bischoff, Modal abundances of coarse-grained (>5 μm) components within CI-chondrites and their individual clasts – Mixing of various lithologies on the CI parent body(ies). *Chem. Erde* **79**, 125532 (2019). doi: 10.1016/j.chemer.2019.08.004
32. A. Morlok *et al*., Brecciation and chemical heterogeneities of CI chondrites. *Geochim. Cosmochim. Acta* **70**, 5371–5394 (2006). doi: 10.1016/j.gca.2006.08.007
33. A. J. King, P. F. Schofield, K. T. Howard, S. S. Russell, Modal mineralogy of CI and CI-like chondrites by X-ray diffraction. *Geochim. Cosmochim. Acta* **165**, 148–160 (2015). doi: 10.1016/j.gca.2015.05.038
34. K. Tomeoka, P. R. Buseck, Matrix mineralogy of the Orgueil CI carbonaceous chondrite. *Geochim. Cosmochim. Acta* **52**, 1627–1640 (1988). doi: 10.1016/0016-7037(88)90231-1
35. R. G. Burns, D. S. Fisher, Rates of oxidative weathering on the surface of Mars. *J. Geophys. Res.* **98**, 3365–3372 (1993). doi: 10.1029/92JE02055
36. J. Booth, Q. Hong, R. G. Compton, K. Prout, R. M. Payne, Gypsum overgrowths passivate calcite to acid attack. *J. Colloid Interface Sci.* **192**, 207–214 (1997). doi: 10.1006/jcis.1997.4978; pmid: 9268560
37. M. Gounelle, M. E. Zolensky, A terrestrial origin for sulfate veins in CI1 chondrites. *Meteorit. Planet. Sci.* **36**, 1321–1329 (2001). doi: 10.1111/j.1945-5100.2001.tb01827.x
38. M. Piralla, R. Tartèse, Y. Marrocchi, K. H. Joy, Apatite halogen and hydrogen isotope constraints on the conditions of hydrothermal alteration in carbonaceous chondrites. *Meteorit. Planet. Sci.* **56**, 809–828 (2021). doi: 10.1111/maps.13639
39. E. De Pauw *et al*., High energy synchrotron X-ray fluorescence trace element study of a millimeter-sized asteroidal particle in preparation for the Hayabusa2 return sample analyses. *Spectrochim. Acta B At. Spectrosc.* **188**, 106346 (2022). doi: 10.1016/j.sab.2021.106346
40. D. Ward, A. Bischoff, J. Roszjar, J. Berndt, M. J. Whitehouse, Trace element inventory of meteoritic Ca-phosphates. *Am. Mineral.* **102**, 1856–1880 (2017). doi: 10.2138/am-2017-6056
41. M. Endreß, Mineralogische und chemische Untersuchungen an CI Chondriten – Ein Modell zur mineralogisch-kosmochemischen Evolution der(s) CI-Mutterkörper(s), thesis, University of Muenster (1994).
42. P. A. Bland, G. Cressey, O. N. Menzies, Modal mineralogy of carbonaceous chondrites by X-ray diffraction and Mössbauer spectroscopy. *Meteorit. Planet. Sci.* **39**, 3–16 (2004). doi: 10.1111/j.1945-5100.2004.tb00046.x
43. M. N. Bass, Montmorillonite and serpentine in Orgueil meteorite. *Geochim. Cosmochim. Acta* **35**, 139–147 (1971). doi: 10.1016/0016-7037(71)90053-6
44. S. M. Chemtob, R. D. Nickerson, R. V. Morris, D. G. Agresti, J. G. Catalano, Oxidative alteration of ferrous smectites and implications for the redox evolution of early Mars. *J. Geophys. Res. Planets* **122**, 2469–2488 (2017). doi: 10.1002/2017JE005331; pmid: 32802700
45. S. Boursiquot, M. Mullet, M. Abdelmoula, J.-M. Génin, J.-J. Ehrhardt, The dry oxidation of tetragonal FeS_{1-x} mackinawite. *Phys. Chem. Miner.* **28**, 600–611 (2001). doi: 10.1007/s002690100193
46. J. F. Kerridge, Major element composition of phyllosilicates in the Orgueil carbonaceous meteorite. *Earth Planet. Sci. Lett.* **29**, 194–200 (1976). doi: 10.1016/0012-821X(76)90039-X
47. M. E. Zolensky, R. Barrett, L. Browning, Mineralogy and composition of matrix and chondrule rims in carbonaceous chondrites. *Geochim. Cosmochim. Acta* **57**, 3123–3148 (1993). doi: 10.1016/0016-7037(93)90298-B
48. M. Endress, A. Bischoff, Carbonates in CI chondrites: Clues to parent body evolution. *Geochim. Cosmochim. Acta* **60**, 489–507 (1996). doi: 10.1016/0016-7037(95)00399-1; pmid: 11539921
49. A. M. Reid, M. N. Bass, H. Fujita, J. F. Kerridge, K. Fredriksson, Olivine and pyroxene in the Orgueil meteorite. *Geochim. Cosmochim. Acta* **34**, 1253–1255 (1970). doi: 10.1016/0016-7037(70)90063-3
50. I. M. Steele, Minor elements in forsterites of Orgueil (C1), Alais (C1) and two interplanetary dust particles compared to C2-C3-UOC forsterites. *Meteoritics* **25**, 301–307 (1990). doi: 10.1111/j.1945-5100.1990.tb00714.x
51. D. R. Frank, M. E. Zolensky, L. Le, Olivine in terminal particles of Stardust aerogel tracks and analogous grains in chondrite matrix. *Geochim. Cosmochim. Acta* **142**, 240–259 (2014). doi: 10.1016/j.gca.2014.05.037
52. M. R. Lee, K. Nicholson, Ca-carbonate in the Orgueil (CI) carbonaceous chondrite: Mineralogy, microstructure and implications for parent body history. *Earth Planet. Sci. Lett.* **280**, 268–275 (2009). doi: 10.1016/j.epsl.2009.01.038
53. I. D. R. Mackinnon, M. E. Zolensky, Proposed structures for poorly characterized phases in C2M carbonaceous chondrite meteorites. *Nature* **309**, 240–242 (1984). doi: 10.1038/309240a0
54. J. P. Bradley, Chemically anomalous, preaccretionally irradiated grains in interplanetary dust from comets. *Science* **265**, 925–929 (1994). doi: 10.1126/science.265.5174.925; pmid: 17782142
55. H. Leroux, P. Cuvillier, B. Zanda, R. H. Hewins, GEMS-like material in the matrix of the Paris meteorite and the early stages of alteration of CM chondrites. *Geochim. Cosmochim. Acta* **170**, 247–265 (2015). doi: 10.1016/j.gca.2015.09.019
56. K. K. Ohtaki *et al*., Search for meteoritic GEMS I: Comparison of amorphous silicates in Paris and Acfer 094 chondrite matrices and in anhydrous chondritic interplanetary dust particles. *Geochim. Cosmochim. Acta* **310**, 320–345 (2021). doi: 10.1016/j.gca.2021.05.042
57. K. L. Villalon *et al*., Search for meteoritic GEMS II: Comparison of inclusions in amorphous silicates from the Paris chondrite and from anhydrous chondritic interplanetary dust particles. *Geochim. Cosmochim. Acta* **310**, 346–362 (2021). doi: 10.1016/j.gca.2021.05.041
58. T. Nakamura *et al*., Chondrulelike objects in short-period comet 81P/Wild 2. *Science* **321**, 1664–1667 (2008). doi: 10.1126/science.1160995; pmid: 18801994
59. D. R. Frank *et al*., A CAI in the Ivuna CI1 chondrite, *Proceedings of the 42nd Lunar and Planetary Science Conference*, abstract 2785, JSC-CN-22691 (2011).

60. T. J. Fagan, Y. Guan, G. J. MacPherson, Al-Mg isotopic evidence for episodic alteration of Ca-Al-rich inclusions from Allende. *Meteorit. Planet. Sci.* **42**, 1221–1240 (2007). doi: 10.1111/j.1945-5100.2007.tb00570.x
61. W. Klöck, K. L. Thomas, D. S. McKay, H. Palme, Unusual olivine and pyroxene composition in interplanetary dust and unequilibrated ordinary chondrites. *Nature* **339**, 126–128 (1989). doi: 10.1038/339126a0
62. L. Grossman, I. M. Steele, Amoeboid olivine aggregates in the Allende meteorite. *Geochim. Cosmochim. Acta* **40**, 149–155 (1976). doi: 10.1016/0016-7037(76)90172-1
63. J. Han, A. J. Brearley, Microstructural evidence for complex formation histories of amoeboid olivine aggregates from the ALHA77307 CO3.0 chondrite. *Meteorit. Planet. Sci.* **50**, 904–925 (2015). doi: 10.1111/maps.12439
64. A. Tsuchiyama *et al*., Discovery of primitive CO_2-bearing fluid in an aqueously altered carbonaceous chondrite. *Sci. Adv.* **7**, eabg9707 (2021). doi: 10.1126/sciadv.abg9707; pmid: 33883146
65. M. E. Zolensky, Cyclical regolith processes on hydrous asteroids. *Meteoritics* **30**, 606–607 (1995).
66. L. Zhang, F. Ren, H. Li, D. Cheng, B. Sun, The influence mechanism of freeze-thaw on soil erosion: A review. *Water* **13**, 1010 (2021). doi: 10.3390/w13081010
67. D. J. Vaughan, *Mineral Chemistry of Metal Sulfides* (Cambridge Earth Science Services, 1978).doi: 10.1016/0012-8252(80)90122-1
68. T. Nakamura *et al*., Irradiation-energy dependence on the spectral changes of hydrous C-type asteroids based on 4keV and 20keV He exposure experiments of Murchison CM chondrite, *Proceedings of the 51st Lunar and Planetary Science Conference*, abstract 1310 (2020).
69. K. Tomeoka, Y. Yamahana, T. Sekine, Experimental shock metamorphism of the Murchison CM carbonaceous chondrite. *Geochim. Cosmochim. Acta* **63**, 3683–3703 (1999). doi: 10.1016/S0016-7037(99)00149-0
70. D. Beaufort *et al*., Chlorite and chloritization processes through mixed-layer mineral series in low-temperature geological systems—A review. *Clay Miner.* **50**, 497–523 (2015). doi: 10.1180/claymin.2015.050.4.06
71. S. A. Kissin, S. D. Scott, Phase relations involving pyrrhotite below 350 degrees C. *Econ. Geol.* **77**, 1739–1754 (1982). doi: 10.2113/gsecongeo.77.7.1739
72. E. L. Berger, D. S. Lauretta, T. J. Zega, L. P. Keller, Heterogeneous histories of Ni-bearing pyrrhotite and pentlandite grains in the CI chondrites Orgueil and Alais. *Meteorit. Planet. Sci.* **51**, 1813–1829 (2016). doi: 10.1111/maps.12721
73. R. Visser, T. John, M. Patzek, A. Bischoff, M. J. Whitehouse, Sulfur isotope study of sulfides in CI, CM, $C2_{ung}$ chondrites and volatile-rich clasts—Evidence for different generations and reservoirs of sulfide formation. *Geochim. Cosmochim. Acta* **261**, 210–223 (2019). doi: 10.1016/j.gca.2019.06.046
74. K. Tsukimura, H. Nakazawa, T. Endo, O. Fukunaga, Cation distribution in pentlandites $(Fe,Ni)_9S_8$: Dependence on pressure and temperature and kinetics of the cation exchange reaction. *Phys. Chem. Miner.* **19**, 203–212 (1992). doi: 10.1007/BF00202309
75. K. Sugiyama, T. Kawamata, T. Kuribayashi, Structure refinement of prehnite from Passaic County, New Jersey, USA. *J. Mineral. Petrol. Sci.* **116**, 272–276 (2021). doi: 10.2465/jmps.210318
76. H.-B. Qin, Y. Takeichi, H. Nitani, Y. Terada, Y. Takahashi, Tellurium distribution and speciation in contaminated soils from abandoned mine tailings: Comparison with selenium. *Environ. Sci. Technol.* **51**, 6027–6035 (2017). doi: 10.1021/acs.est.7b00955; pmid: 28426210
77. Y. Takeichi *et al*., Design and performance of a compact scanning transmission x-ray microscope at the Photon Factory. *Rev. Sci. Instrum.* **87**, 013704 (2016). doi: 10.1063/1.4940409; pmid: 26827325
78. C. A. Gorski, L. E. Klüpfel, A. Voegelin, M. Sander, T. B. Hofstetter, Redox properties of structural Fe in clay minerals: 3. Relationships between smectite redox and structural properties. *Environ. Sci. Technol.* **47**, 13477–13485 (2013). doi: 10.1021/es403824x; pmid: 24219773
79. P. Lu, C. Zhu, Arsenic Eh-pH diagrams at 25°C and 1 bar. *Environ. Earth Sci.* **62**, 1673–1683 (2011). doi: 10.1007/s12665-010-0652-x
80. K. Fukushi, Y. Sekine, H. Sakuma, K. Morida, R. Wordsworth, Semiarid climate and hyposaline lake on early Mars inferred from reconstructed water chemistry at Gale. *Nat. Commun.* **10**, 4896 (2019). doi: 10.1038/s41467-019-12871-6; pmid: 31653859
81. C. M. O. D. Alexander, R. Bowden, M. L. Fogel, K. T. Howard, Carbonate abundances and isotopic compositions in chondrites. *Meteorit. Planet. Sci.* **50**, 810–833 (2015). doi: 10.1111/maps.12410
82. M. Yu. Zolotov, Aqueous fluid composition in CI chondritic materials: Chemical equilibrium assessments in closed systems. *Icarus* **220**, 713–729 (2012). doi: 10.1016/j.icarus.2012.05.036
83. M. Yu. Zolotov, Formation of sulfates on parent bodies of carbonaceous chondrites, Ceres, Europa, and other icy bodies, *Proceedings of the 47th Lunar and Planetary Science Conference*, abstract 1778 (2016).
84. H. Campins *et al*., The origin of asteroid 162173 (1999 JU_3). *Astron. J.* **146**, 26 (2013). doi: 10.1088/0004-6256/146/2/26
85. K. J. Walsh, M. Delbó, W. F. Bottke, D. Vokrouhlický, D. S. Lauretta, Introducing the Eulalia and new Polana asteroid families: Re-assessing primitive asteroid families in the inner Main Belt. *Icarus* **225**, 283–297 (2013). doi: 10.1016/j.icarus.2013.03.005
86. H. Wang *et al*., Lifetime of the solar nebula constrained by meteorite paleomagnetism. *Science* **355**, 623–627 (2017). doi: 10.1126/science.aaf5043; pmid: 28183977
87. K. L. Thomas, G. E. Blanford, L. P. Keller, W. Klöck, D. S. McKay, Carbon abundance and silicate mineralogy of anhydrous interplanetary dust particles. *Geochim. Cosmochim. Acta* **57**, 1551–1566 (1993). doi: 10.1016/0016-7037(93)90012-L; pmid: 11539451
88. M. J. Mumma, S. B. Charnley, The chemical composition of comets—Emerging taxonomies and natal heritage. *Annu. Rev. Astron. Astrophys.* **49**, 471–524 (2011). doi: 10.1146/annurev-astro-081309-130811
89. S. J. Desch, A. Kalyaan, C. M. O. D. Alexander, The effect of Jupiter's formation on the distribution of refractory elements and inclusions in meteorites. *Astrophys. J. Suppl. Ser.* **238**, 11 (2018). doi: 10.3847/1538-4365/aad95f
90. P. Michel *et al*., Collisional formation of top-shaped asteroids and implications for the origins of Ryugu and Bennu. *Nat. Commun.* **11**, 2655 (2020). doi: 10.1038/s41467-020-16433-z; pmid: 32461569
91. A. A. Amsden, H. M. Ruppel, C. W. Hirt, "SALE: a simplified ALE computer program for fluid flow at all speeds," technical report (Office of Scientific and Technical Information, 1980); doi: 10.2172/5176006
92. B. A. Ivanov, D. Deniem, G. Neukum, Implementation of dynamic strength models into 2D hydrocodes: Applications for atmospheric breakup and impact cratering. *Int. J. Impact Eng.* **20**, 411–430 (1997). doi: 10.1016/S0734-743X(97)87511-2
93. K. Wünnemann, G. S. Collins, H. J. Melosh, A strain-based porosity model for use in hydrocode simulations of impacts and implications for transient crater growth in porous targets. *Icarus* **180**, 514–527 (2006). doi: 10.1016/j.icarus.2005.10.013
94. W. F. BottkeJr.., M. C. Nolan, R. Greenberg, R. A. Kolvoord, Velocity distributions among colliding asteroids. *Icarus* **107**, 255–268 (1994). doi: 10.1006/icar.1994.1021
95. V. E. Hamilton *et al*., Evidence for widespread hydrated minerals on asteroid (101955) Bennu. *Nat. Astron.* **3**, 332–340 (2019). doi: 10.1038/s41550-019-0722-2; pmid: 31360777
96. P. Beck *et al*., Transmission infrared spectra (2-25μm) of carbonaceous chondrites (CI, CM, CV-CK, CR, C2 ungrouped): Mineralogy, water, and asteroidal processes. *Icarus* **229**, 263–277 (2014). doi: 10.1016/j.icarus.2013.10.019
97. I. N. Koprinarov, A. P. Hitchcock, C. T. McCrory, R. F. Childs, Quantitative mapping of structured polymeric systems using singular value decomposition analysis of soft X-ray images. *J. Phys. Chem. B* **106**, 5358–5364 (2002). doi: 10.1021/jp013281l

ACKNOWLEDGMENTS

Synchrotron time for XRD and STXM analyses was allocated by the Photon Factory Advisory Committee (proposals 2020S2-002 and 2018S1-001). The SR-CT, SR-nanoCT, and μ-XRF-XANES analyses were conducted under SPring-8 proposals 2019A-2021A0165, 2019A-2021A0166, 2021B0185, 2021B0188, and 2022A0180. Technical support of the SR experiments at SPring-8 was provided by RIKEN. The negative muon analysis at MLF, J-PARC was conducted under proposal 2019MS01. Numerical computations for the thermal modeling were carried out on the PC cluster and analysis servers at the Center for Computational Astrophysics of the National Astronomical Observatory of Japan. We thank the developers of iSALE, including G. Collins, K. Wünnemann, B. Ivanov, J. Melosh, D. Elbeshausen, and T. Davison. We acknowledge the ESRF for provision of beamtime at beamline ID15A (proposal ES-1017). This research used resources of the Advanced Photon Source, a US Department of Energy (DOE) Office of Science User Facility at Argonne National Laboratory. We thank A. Simon and V. Hamilton for providing the spectra of asteroid Bennu, and Toyo Corporation for the use of the pFIB system for sample preparation. We also thank many researchers who have contributed to the various experiments and measurements, especially H. Nakao, R. Watanabe, S. Kobayashi, K. Mogi, Y. Kousaka, E. Tomosada, T. Morita, M. Nakamura, O. Sasaki, K. Saito, T. Konno, T. Miyazaki, Y. Ito, K. Onodera, S. Hasegawa, G. Nishikawa, T. Kobayashi, S. Murakoshi, K. Goto, Y. Tanaka, K. Hattori, M. Yoshioka, K. Tomioka, T. Kawahara, S. Tachikawa, T. Nishi, H. Ohta, M. Susa, T. Sunagawa, O. Nishizawa, K. Kitamura, K. Sawayama, T. Hatakeyama, S. Steve, S. Sutton, R. Jones, R. Yoshida, H. Kasai, T. Akashi, I. Hitachi, A. Dazzi, A. Deniset-Besseau, L. Bejach, J. Garrevoat, M. Michiel, T. Azuma, K. Mizumoto, T. Minami, K. Shimomura, S. Takeda, M. Katsuragawa, A. Yamaguchi, T. Yomogida, D. Wakabayashi, S. Lefrançois, E. Heripré, D. Troadec, J. Garrevoet, M. di Michiel, O. Mivumbi, C. Sandt, Z. Rahman, L. Le, F. Capitani, and Shimazu Corporation for their technical support. **Funding:** This work was supported by KAKENHI from the Japanese Society for Promotion of Science (JSPS); grants JP20H00188 and 19H05183 to T.Na.; JP19K14776 to M.Matsum.; 21K18645 to T.Mik. and K.Sugiy.; JP20H00205 to A.Ts., M.Matsum., A.Miyak., and J.Mats.; 17H06458 to K.F., Y.Taka., S.Yamas., and M.Kim.; JP17H06459 to T.Na., T.U., S.Wat., M.Matsuo., N.N., T.Mo., T.Ok., Y.S., N.S., and R.N.; JP15H05695 to A.Ts. and K.U.; 20H05846 to S.Tac.; JP17H06457 to H.G.; JP19H00726 to K.Kur., H. G., and T.Mik.; JP21J13337 to K.A.; JP18H05456 and JP20H00189 to K.Sugiy.; 18H05463 to T.Tak., S.Nakas., and S.Wat.; 18H05460 to K.Nin. and T.Os.; 18H05464 to Y.Miy.; 18H05457 to K.Nin., T.Tak., S.Wat., and Y.Miy.; and JP18H05479 to M.U. This work was also supported by the JSPS Core-to-Core program "International Network of Planetary Sciences" and the Ministry of Education, Culture, Sports, Science and Technology (MEXT) (grants JPMXS0450200421 and JPMXS0450200521 to S.S.); A.J.K. acknowledges funding support from UK Research and Innovation (UKRI) grant MR/T020261/1. A.J.B. acknowledges funding support from NASA Emerging Worlds grant 80NSSC18K0731. P.B. acknowledges funding from the European Research Council (ERC) under grant agreement 771691 (Solarys) and the CNES. R.B. and F.B. acknowledge support by Region Ile-de-France (DIM-ACAV) and SOLEIL for the FTIR micro-spectroscopy measurements. F.E.B and B.J.T. acknowledge funding from German Research Foundation DFG grant BR2015/38-1 and Dr. Ralph Schwieter Foundation. L.V. and B.B. acknowledge support from Ghent University Special Research Fund Grants BOF-01GC1517 and Research Foundation Flanders grants G0D5221N and 1205322N. B.V. acknowledges funding from BOF17-GOA-015. P.T. acknowledges funding from Ghent University Special Research Fund Grants BOF20/PDO/037 and Research Foundation Flanders grants G0D5221N and 1205322N. M.R. acknowledges the French PICS-CNRS funding program, the French ANR (CLASSY) and the FACCTS program, and funding from the DOE Office of Science Basic Energy Sciences, under contract DE-AC02-06CH11357. M.R. and J.C.V. benefited from the Ile de France DIM ACAV+ funding (PARYUGU). M.Y.Z. is supported by NASA grants 80NSSC19K0786 and 80NSSC19K0313. A.Ts. is supported by Chinese Academy of Sciences President's International Fellowship Initiative, grant 2019VCA0004. D.L.D. is supported by NASA grants NNX16AL34G and 80ARC017M00005. E.P. acknowledges funding from Italian Space Agency (ASI) through contract 2018-27-HH-0. F.V., A.R.H., and C.J. acknowledge funding from NASA's TREX node of the Solar System Exploration Research Virtual Institute 2016 (SSERVI16) Cooperative Agreement (NNH16ZDA001N). G.D. acknowledges NASA LARS funding of NanoIR technique development (80NSSC19K1051). M.E.Z. is supported by NASA Hayabusa2 Mission Participating Scientist Program. M.Tan. is supported by JSPS KAKENHI grant 21K03654. C.E., J.D., E.Da., and J.Math. acknowledge funding from CNES (MIAMI2), DIM-ACAV+ (C3E), LabEx P2IO, and ANR (COMETOR ANR-18-CE31-0011). R.B., A.Alé., Z.Di., C.L., Z.Dj., D.Ba., L.R., S.R., and C.P. acknowledge support by the CNES. K.A. is supported an GP-EES Research Grant. Z.G. acknowledges the Molecular Foundry, supported by the Office of Science, Office of Basic Energy Sciences, of the U.S. Department of Energy under Contract No. DE-AC02-05CH11231. **Author contributions:** Organizing the research, writing the manuscript, main sample analysis: T.Na. Writing the manuscript, main sample analysis: M.Matsum., Y.E., K.A., and M.E.Z. Electron microscopy: M.Matsum., Y.E., M.E.Z., T.Mik., D.N., M.Kik., A.J.B., Y.K., D.Br., D.J.J., J.Mar., J.H., H.Yo., A.N., T.No., C.E., J.D., S.S.R., C.M., T.Tan., K.Ts., S.Yamad., K.Ya., S.A., Y.A., S.D.S., T.F., T.Kat, F.L., T.Ma., H.M., and A.Miyak., Synchrotron experiments: Y.Tak., Y.F., A.Ts., M.U., J.Mats., M.Tak., F.E.B., B.J.T., L.V., M.R., J.-C.V., P.B., E.E.A., M.Tan., K.F., H.Su., S.Yamas., T.Kawai., K.I., E.B., S.E., P.T., Y.Takeic., A.Take., A.Taki., M.Yas., K.U., S.O., O.S., M.Su., E.Da., E.De., Z.Di., Z.Dj., G.F., K.Hag., M.Y.H., M.Kim., B.L., M.L., J.Z., B.V., D.Ba., B.B., F.B., K.Nit., J.Math., I.M., R.B., A.Alé., C.L., and

S.R. Muon analysis: K.Nin., T.Tak., T.Os., K.Te., T.W., S.Wat., S.Tak., A.Tan., I.U., I.C., M.K.K., S.Nag., and Y.Miy. Physical property measurements: S.Tan., H.Nag., M.Sa., T.Mic., Y.N., T.Ts., Y.In., R.E., T.Yag., T.Is., A.Ala., N.S., R.Fuj., T.Kawamu, and Y.Yamas. Numerical simulations: H.G., M.Y.Z., K.Kur., S.Wak., and R.Hy. Reflectance spectra: K.A., E.K., M.Matsuo., R.E.M., E.T., S.S., T.Hi., K.Ki., Q.H.S.C., F.V., A.R.H., C.J., D.L.D., G.D., Z.G., T.Kawamo., L.R., S.R., D.T., Y.Yamas., E.P., C.P., S.M.P., C.S., C.L., R.B., A.Alé., K.Sugiu., and G.N. TOF SIMS analysis: A.D., R.J.B., and I.R.G. XRD analysis: K.Sugiy., and A.J.K. Interdiscipline science discussion: H.Yu., R.O., H.Yab., H.Nar., K.Sa., S.Tac., H.C.C., and D.S.L. Hayabusa2 mission sample collection: M.Yoshit., M.Yoshik., K.Yoshik., K.Yoshih., Y.Yo., K.Yo., H.Ya., Y.Yamam., D.Y., M.Yam., T.Yam., T.Yad., K.W., T.U., R.T., F.T., H.T., Y.Takei., A.I., H.So., K.Sh., Y.S., H.Se., H.Sa., T.S., M.O., G.O., T.Ok., N.O., K.O., R.N., H.No., M.N., N.N., S.Nak., T.Mo., A.Miyaz., A.Miu., Y.Mim., K.M., K.Kum., T.Ko., S.Ki., K.Ka., S.Ka., T.Iw., Y.Is., M.I., H.I., S.H., R.Ho., C.H., Y.H., Nar.H., Nao.H., T.Ha., M.H., K.Hat., S.F., R.Fuk., A.F., Y.C., M.Ar., M.Ab., S.Wat., and Y.Ts. All authors discussed the results and commented on the manuscript. **Competing interests:** We declare no competing interests. **Data and materials availability:** All images and raw data used in this study are available at the JAXA Data Archives and Transmission System (DARTS) at https://data.darts.isas.jaxa.jp/pub/hayabusa2/paper/sample/Nakamura_2022. Software code, scripts, and input files for the thermal modeling, chemical modeling, and impact simulations are also available at the same URL. Other data on the Ryugu sample and from the Hayabusa2 mission are available at the DARTS archive at https://www.darts.isas.jaxa.jp/curation/hayabusa2 and https://www.darts.isas.jaxa.jp/planet/project/hayabusa2, respectively. The returned samples are curated by JAXA Astromaterials Science Research Group, who distribute them through an Announcement of Opportunity available at https://jaxa-ryugu-sample-ao.net.

License information: Copyright © 2023 the authors, some rights reserved; exclusive licensee American Association for the Advancement of Science. No claim to original US government works. https://www.science.org/about/science-licenses-journal-article-reuse

SUPPLEMENTARY MATERIALS

science.org/doi/10.1126/science.abn8671
Materials and Methods
Supplementary Text
Figs. S1 to S47
Tables S1 to S15
References (*98*–*189*)
Movies S1 and S2

Submitted 25 December 2021; accepted 5 September 2022
Published online 22 September 2022
10.1126/science.abn8671

RESEARCH ARTICLE SUMMARY

COSMOCHEMISTRY

Noble gases and nitrogen in samples of asteroid Ryugu record its volatile sources and recent surface evolution

Ryuji Okazaki* ***et al.***

INTRODUCTION: The Hayabusa2 spacecraft retrieved surface and subsurface samples from the carbonaceous near-Earth asteroid (162173) Ryugu, which was expected to be enriched in volatile species. The samples were collected from two locations, one undisturbed surface and the other including material excavated by an artificial impact. Unlike meteorites, these samples have experienced minimal alteration by Earth's atmosphere. Ryugu is thought to have formed from material ejected (by an impact) from a parent body, which had experienced aqueous alteration (reactions with liquid water) ~4.56 billion years (Gyr) ago. Ryugu's orbit later migrated from the main asteroid belt to become a near-Earth asteroid.

RATIONALE: Noble gases and nitrogen isotopes in Ryugu grains are inherited from Ryugu's parent body and potentially provide information about the source of Earth's volatile elements. Noble gas isotopes can also be used to assess the orbital evolution and recent surface activities of Ryugu.

We pelletized ~0.8-mm-diameter Ryugu grains and investigated their mineralogy before carrying out isotope measurements. We measured the concentrations and isotopic compositions of noble gases and nitrogen, extracted by stepped heating, with mass spectrometers.

RESULTS: The mineralogy of the Ryugu grains is similar to Ivuna-type carbonaceous (CI) chondrite meteorites. Fine-grained hydrous silicates (phyllosilicates), produced through aqueous alteration of primary minerals, compose the major fraction of the samples. This is consistent with infrared spectroscopic observations of the asteroid. Iron oxide, iron sulfides, and carbonates are also found within the matrix.

Noble gas isotopes are dominated by primordially trapped gases. Their abundances are mostly similar to the highest found in a CI chondrite, with some grains having several times higher concentrations than the highest CI value.

Isotopic compositions and concentrations of nitrogen vary between the Ryugu grains, with divergence from the CI chondrite composition. The nitrogen concentrations in four Ryugu grains are one-half to one-third the CI values, and the $^{15}N/^{14}N$ ratio is also lower. The Ryugu grains with compositions farthest from the CI values are similar to the composition of a dehydrated CI chondrite.

Only two surface samples, out of the 16 Ryugu grains measured, have clear signs of noble gases derived from solar wind (SW). Their abundances correspond to SW exposure durations of $\gtrsim$3500 and $\gtrsim$250 years at the current orbit, whereas most of the grains were exposed for $\gtrsim$1 to $\gtrsim$50 years. Cosmic ray–produced ^{21}Ne concentrations vary, with no systematic difference between the sample collection sites. The estimated cosmic ray exposure (CRE) ages for the surface and subsurface samples are 5.3 ± 0.9 and 5.2 ± 0.8 million years (Myr), assuming irradiations at 2 to 5 g cm^{-2} and 150 g cm^{-2}, respectively. This is consistent with the expected surface residence time under near-Earth impact rates. We infer that Ryugu's orbit migrated from the main asteroid belt to the near-Earth region ~5 Myr ago.

About 30% of cosmogenic ^{21}Ne, corresponding to a CRE age of ~1 Myr, was released in gas-extraction steps at 100°C, indicating that the Ryugu samples have not experienced heating above 100°C within the past 1 Myr. Previous studies have suggested that Ryugu experienced an orbital excursion much closer to the Sun. If this is the case, this excursion must have occurred $\gtrsim$1 Myr ago.

CONCLUSION: The mineralogical and noble gas measurements show that the Ryugu samples are similar to CI chondrites. The nitrogen data indicate a heterogeneous distribution of nitrogen-carrying materials with different compositions, one of which has been lost from Ryugu grains to varying degrees. The CRE age of ~5 Myr and the implanted SW are records of the recent irradiation at the current near-Earth orbit of Ryugu. ■

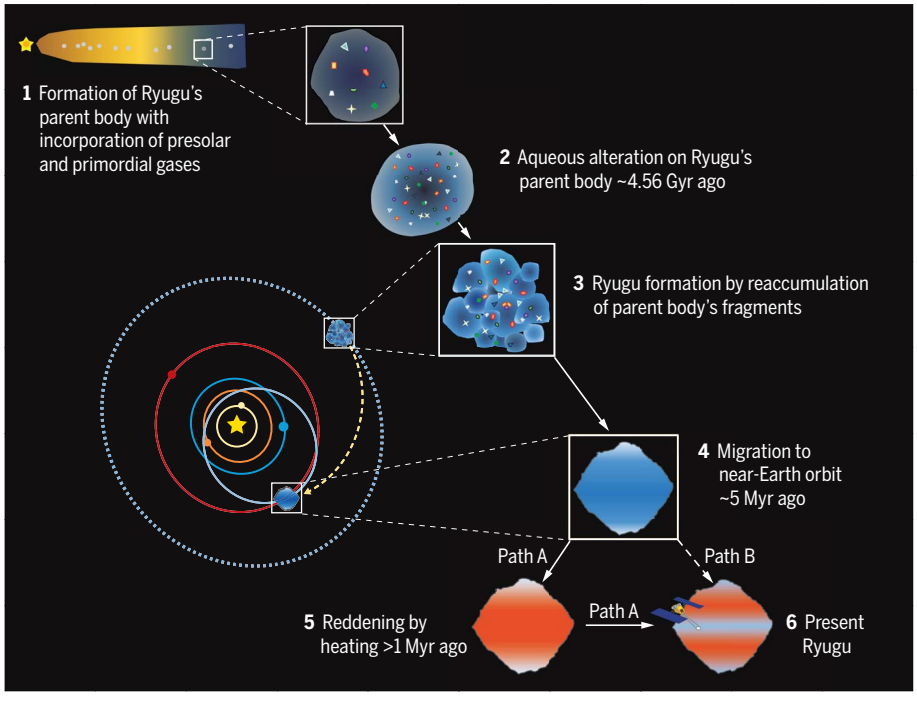
1 Formation of Ryugu's parent body with incorporation of presolar and primordial gases
2 Aqueous alteration on Ryugu's parent body ~4.56 Gyr ago
3 Ryugu formation by reaccumulation of parent body's fragments
4 Migration to near-Earth orbit ~5 Myr ago
Path A
Path B
5 Reddening by heating >1 Myr ago
Path A
6 Present Ryugu

Inferred formation and history of Ryugu. Ryugu's parent body formed in the early Solar System, incorporating primordial noble gases and nitrogen, followed by aqueous alteration ~4.56 Gyr ago. Ryugu formed from the accumulation of fragments of the parent body ejected by an impact, at an unknown date. Ryugu migrated to its current near-Earth orbit ~5 Myr ago. Ryugu might have experienced another change in orbit, bringing it closer to the Sun ("Path A"), or remained in the same near-Earth orbit ("Path B").

The complete list of authors and their affiliations is available in the full article online.
*Corresponding author. Email: okazaki.ryuji.703@m.kyushu-u.ac.jp
Cite this article as R. Okazaki *et al.*, *Science* **379**, eabo0431 (2023). DOI: 10.1126/science.abo0431

READ THE FULL ARTICLE AT
https://doi.org/10.1126/science.abo0431

RESEARCH ARTICLE

COSMOCHEMISTRY

Noble gases and nitrogen in samples of asteroid Ryugu record its volatile sources and recent surface evolution

Ryuji Okazaki[1]*, Bernard Marty[2], Henner Busemann[3], Ko Hashizume[4], Jamie D. Gilmour[5], Alex Meshik[6], Toru Yada[7], Fumio Kitajima[1], Michael W. Broadley[2], David Byrne[2], Evelyn Füri[2], My E. I. Riebe[3], Daniela Krietsch[3], Colin Maden[3], Akizumi Ishida[8], Patricia Clay[5], Sarah A. Crowther[5], Lydia Fawcett[5], Thomas Lawton[5], Olga Pravdivtseva[6], Yayoi N. Miura[9], Jisun Park[10,11], Ken-ichi Bajo[12], Yoshinori Takano[13], Keita Yamada[14], Shinsuke Kawagucci[15,16], Yohei Matsui[15,16], Mizuki Yamamoto[1], Kevin Righter[17], Saburo Sakai[13], Naoyoshi Iwata[18], Naoki Shirai[19,20], Shun Sekimoto[21], Makoto Inagaki[21], Mitsuru Ebihara[19], Reika Yokochi[22], Kunihiko Nishiizumi[23], Keisuke Nagao[24], Jong Ik Lee[24], Akihiro Kano[25], Marc W. Caffee[26,27], Ryu Uemura[28], Tomoki Nakamura[8], Hiroshi Naraoka[1], Takaaki Noguchi[29], Hikaru Yabuta[30], Hisayoshi Yurimoto[12], Shogo Tachibana[31], Hirotaka Sawada[7], Kanako Sakamoto[7], Masanao Abe[7,32], Masahiko Arakawa[33], Atsushi Fujii[7], Masahiko Hayakawa[7], Naoyuki Hirata[33], Naru Hirata[34], Rie Honda[35], Chikatoshi Honda[34], Satoshi Hosoda[7], Yu-ichi Iijima[7]†, Hitoshi Ikeda[7], Masateru Ishiguro[36], Yoshiaki Ishihara[37], Takahiro Iwata[7], Kosuke Kawahara[7], Shota Kikuchi[38,39], Kohei Kitazato[34], Koji Matsumoto[32,39], Moe Matsuoka[40], Tatsuhiro Michikami[41], Yuya Mimasu[7], Akira Miura[7], Tomokatsu Morota[25], Satoru Nakazawa[7], Noriyuki Namiki[32,39], Hirotomo Noda[32,39], Rina Noguchi[42], Naoko Ogawa[7], Kazunori Ogawa[37], Tatsuaki Okada[7,43], Chisato Okamoto[33]†, Go Ono[44], Masanobu Ozaki[7,32], Takanao Saiki[7,32], Naoya Sakatani[45], Hiroki Senshu[38], Yuri Shimaki[7], Kei Shirai[7,33], Seiji Sugita[25], Yuto Takei[7], Hiroshi Takeuchi[7], Satoshi Tanaka[7], Eri Tatsumi[25,46], Fuyuto Terui[47], Ryudo Tsukizaki[7], Koji Wada[38], Manabu Yamada[38], Tetsuya Yamada[7], Yukio Yamamoto[7], Hajime Yano[7,32], Yasuhiro Yokota[7], Keisuke Yoshihara[7], Makoto Yoshikawa[7,32], Kent Yoshikawa[7], Shizuho Furuya[7], Kentaro Hatakeda[48], Tasuku Hayashi[7], Yuya Hitomi[48], Kazuya Kumagai[48], Akiko Miyazaki[7], Aiko Nakato[7], Masahiro Nishimura[7], Hiromichi Soejima[48], Ayako Iwamae[48], Daiki Yamamoto[7,49], Kasumi Yogata[7], Miwa Yoshitake[7], Ryota Fukai[7], Tomohiro Usui[7], Harold C. Connolly Jr.[50], Dante Lauretta[51], Sei-ichiro Watanabe[28], Yuichi Tsuda[7]

The near-Earth carbonaceous asteroid (162173) Ryugu is expected to contain volatile chemical species that could provide information on the origin of Earth's volatiles. Samples of Ryugu were retrieved by the Hayabusa2 spacecraft. We measured noble gas and nitrogen isotopes in Ryugu samples and found that they are dominated by presolar and primordial components, incorporated during Solar System formation. Noble gas concentrations are higher than those in Ivuna-type carbonaceous (CI) chondrite meteorites. Several host phases of isotopically distinct nitrogen have different abundances among the samples. Our measurements support a close relationship between Ryugu and CI chondrites. Noble gases produced by galactic cosmic rays, indicating a ~5 million year exposure, and from implanted solar wind record the recent irradiation history of Ryugu after it migrated to its current orbit.

The Hayabusa2 spacecraft returned to Earth on 6 December 2020, after collecting surface and subsurface samples from asteroid (162173) Ryugu (*1*). Ryugu is a carbonaceous (C-type) asteroid thought to have a chemical and mineralogical composition similar to that of carbonaceous chondrites (*2*), which are primitive stony meteorites. Carbonaceous chondrites contain high abundances of volatile elements and molecules, including hydrogen, carbon, nitrogen, noble gases, and organic compounds, making them a potential source of volatiles delivered to Earth and the other terrestrial planets (*3*, *4*). Nitrogen and noble gases in different carbonaceous chondrites vary in their chemical abundances and isotopic ratios. This diversity is thought to be primarily inherited from primordial (prior to Solar System formation) source materials but could also reflect processes that occurred in the interior of asteroids after their accretion, such as thermal metamorphism and aqueous alteration (reactions with liquid water) (*5*, *6*). Ryugu is thought to have originated from a ~100-km-diameter parent body (*7*) that experienced variable amounts of aqueous alteration (*7*, *8*). The aqueous alteration on Ryugu's parent body occurred ~3 to 7 million years (Myr) after Solar System formation [~4.56 billion years (Gyr) ago], as determined using radioactive isotopes (*7*, *8*). After aqueous alteration, the parent body was catastrophically disrupted by an impact; part of the material reaccumulated to form a rubble pile asteroid, Ryugu (*9*, *10*).

Noble gas isotopes can be used to assess surface activities on rocky Solar System bodies, such as modification by impacts (heating, cratering, mixing, and rock fragmentation) and irradiation by solar wind (SW) and cosmic rays (*11*). Remote-sensing observations of Ryugu by Hayabusa2 showed signs of impacts, space weathering, and surface heating (*9*, *12*–*15*). Energetic particle irradiation could alter susceptible surface materials, such as organic molecules. Determining the effects of SW and cosmic ray irradiation requires distinguishing characteristic noble gas signatures originating from SW implantation, galactic cosmic rays (GCRs, from outside the Solar System), and solar cosmic rays (SCRs, from the Sun).

Ryugu grains

Samples of Ryugu were collected during the first and second Hayabusa2 touchdown (TD) operations by firing a 5-g tantalum projectile at a velocity of ~300 m s^{-1} (*1*, *16*, *17*). We were assigned samples from the first TD, which were collected from the surface of Ryugu at an equatorial region (*1*, *16*) and stored in Chamber A of the sample collection instrument (*18*) (hereafter denoted Ryugu-A samples, A0105-series). We also received second TD samples, collected from a site near a crater (*1*) generated by an artificial impact (*19*) and stored in Chamber C (*16*–*18*) (denoted Ryugu-C samples, C0106-series). Given that the depth of the artificial crater was ~1.7 m (*20*), the Ryugu-C samples were expected to include a mix of subsurface materials excavated by the impact and surface materials similar to the Ryugu-A samples. Because asteroid surface materials are generally fragmented rocks (breccias) consisting of different lithologies, we performed a combination of nondestructive analyses before destructive (high-precision) isotope measurements of pelletized samples (*21*) (fig. S1). Fourier transform infrared (FTIR) spectroscopy, field-emission scanning electron microscopy (FESEM) observations, and energy-dispersive x-ray spectroscopy (EDS) measurements were performed for nondestructive analyses (*21*). After these nondestructive examinations, abundances and isotopic compositions of noble gases and nitrogen were destructively measured in 21 individual Ryugu samples (fig. S1 and table S1). The pelletized samples were analyzed without exposure to Earth's atmosphere at any point, including during sample preparation, transportation, weighing, and introduction into the instruments for all analyses (*21*). The fragments of material generated during pelletization were also collected and used for noble gas analyses (*21*) (table S1). The masses of the pelletized samples were between 0.05 and 0.1729 mg, whereas those of the fragment samples were between 0.0006 and 0.0115 mg (table S1).

Mineralogy and petrography

The FESEM observations and EDS measurements showed that the pelletized Ryugu grains are mainly composed of fine-grained matrices, in which the major mineral phase consists of phyllosilicates (Fig. 1 and figs. S2 and S3). We measured modal abundances of magnetite and sulfide grains in 16 Ryugu-A samples, finding 5 ± 1% and 2 ± 1%, respectively, consistent with 5 ± 2% and 3 ± 1% we measured from eight Ryugu-C samples (*21*). These values are also consistent (within the uncertainties) with the 4.3 and 1.1% found in Ivuna-type carbonaceous (CI) chondrites (*22*) but distinct from Mighei-type carbonaceous (CM) (2.2 and 2.0%) and dehydrated CI-like carbonaceous (1.0 and 21.0%) chondrites (*23*).

The FTIR spectra of our Ryugu samples show absorption bands at 3698.8 cm^{-1} (2.70 μm) resulting from O-H stretching modes of phyllosilicates (*24*) and at 2968.4 cm^{-1} (3.37 μm) resulting from C-H stretching modes (*24*) (Fig. 2), which are consistent with earlier results for the Ryugu samples (*18*). A close relationship between Ryugu and CI chondrites has previously been reported using other techniques (*7*, *8*, *25*, *26*). Further spectral features are shown in figs. S4 and S5. These nondestructive results indicate that our samples are typical Ryugu grains with a CI-like lithology, containing no clasts with CM or dehydrated CI-like chondrite characteristics (*23*).

Noble gas isotopes

We measured noble gases (stable isotopes of helium, neon, argon, krypton, and xenon) in the Ryugu samples by stepped heating (*21*). On the basis of their isotopic ratios, we interpret the He in the Ryugu samples as superpositions of two components: one is primordially trapped He, designated P1 [also known as Q gas, residing in an unknown (likely carbonaceous) phase; Q stands for quintessence (*27*, *28*)], and the other is presolar gas designated HL [hosted by presolar nanodiamonds and named after its Xe isotopic composition, which is enriched in heavy (^{134}Xe and ^{136}Xe) and light (^{124}Xe and ^{126}Xe) isotopes compared with solar Xe (*28*)]. In addition to P1 and HL gases, there are contributions of SW (*11*, *29*), and SCR- and/or GCR-produced (cosmogenic) components (fig. S6). Most of the samples contain Ne from the major components HL-Ne and P1-Ne (Fig. 3A), although their relative abundances are uncertain, which affects our estimation of SW-Ne abundances. Although we cannot rule out implantation-fractionated SW (FSW) (*30*), the elemental abundances of the Ryugu samples (fig. S7A) are consistent with mixing between just HL and P1. Two samples (A0105-01 and C0106-06) record contributions from presolar Ne components, almost-pure ^{22}Ne carried by presolar graphite and/or SiC [referred to as G (from the He burning shells of giant stars) and R (radiogenic origin, the decay product of ^{22}Na) components (*28*)]. The sign of a G or R component appears at the higher temperatures (>900°C) of our stepped-heating Ne measurements (Fig. 3B and data S1). Only samples A0105-06 and A0105-15 lie on a mixing line between SW and P1 (Fig. 3A), which is evidence for a contribution of SW-Ne in their compositions. The rest of the samples have only a minor

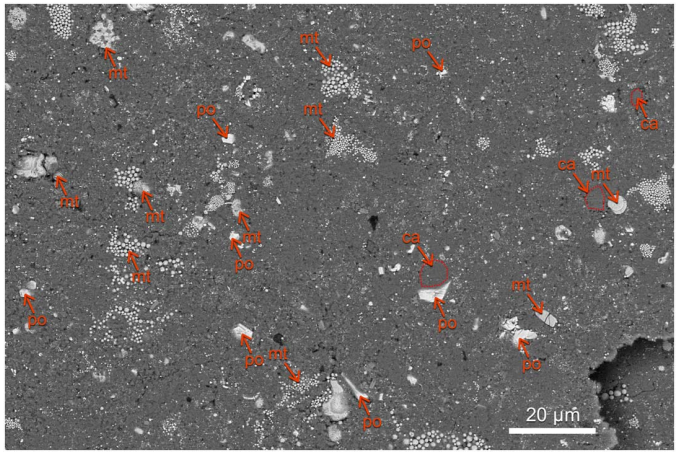

Fig. 1. Backscattered electron image of a Ryugu pellet sample (A0105-10). The sample is mainly composed of phyllosilicates (dark-gray regions). Spherical magnetite aggregates, thin magnetite plates, and iron sulfide grains are also present. Carbonates are found close to magnetites and sulfides. Red arrows indicate minerals, labeled "mt" for magnetite, "po" for pyrrhotite (iron sulfide), and "ca" for carbonate (rimmed with red dotted ovals), respectively.

[1]Department of Earth and Planetary Sciences, Kyushu University, Fukuoka 819-0395, Japan. [2]Université de Lorraine, CNRS, CRPG, F-54000 Nancy, France. [3]Institute of Geochemistry and Petrology, Eidgenössische Technische Hochschule Zürich, 8092 Zürich, Switzerland. [4]Faculty of Science, Ibaraki University, Mito 310-8512, Japan. [5]Department of Earth and Environmental Sciences, The University of Manchester, Manchester M13 9PL, UK. [6]Department of Physics, Washington University in St. Louis, St. Louis, MO 63130, USA. [7]Institute of Space and Astronautical Science, Japan Aerospace Exploration Agency (JAXA), Sagamihara 252-5210, Japan. [8]Department of Earth Science, Tohoku University, Sendai 980-8578, Japan. [9]Earthquake Research Institute, The University of Tokyo, Tokyo 113-0032, Japan. [10]Department of Physical Sciences, Kingsborough Community College, The City University of New York, Brooklyn, NY 11235, USA. [11]Department of Earth and Planetary Sciences, American Museum of Natural History, New York, NY 10024, USA. [12]Department of Earth and Planetary Sciences, Hokkaido University, Sapporo 060-0810, Japan. [13]Biogeochemistry Research Center, Japan Agency for Marine-Earth Science and Technology (JAMSTEC), Yokosuka 237-0061, Japan. [14]Department of Chemical Science and Engineering, Tokyo Institute of Technology, Yokohama 226-8503, Japan. [15]Research Institute for Global Change, JAMSTEC, Yokosuka 237-0061, Japan. [16]Institute for Extra-cutting-edge Science and Technology Avant-garde Research (X-star), JAMSTEC, Yokosuka 237-0061, Japan. [17]Astromaterials Research and Exploration Science, NASA Johnson Space Center, Houston, TX 77058, USA. [18]Faculty of Science, Yamagata University, Yamagata 990-8560, Japan. [19]Graduate School of Science and Engineering, Tokyo Metropolitan University, Hachioji 192-0397, Japan. [20]Department of Chemistry, Faculty of Science, Kanagawa University, Hiratsuka, Kanagawa 259-1293, Japan. [21]Institute for Integrated Radiation and Nuclear Science, Kyoto University, Osaka 590-0494, Japan. [22]Department of the Geophysical Sciences, The University of Chicago, Chicago, IL 60637, USA. [23]Space Sciences Laboratory, University of California, Berkeley, CA 94720, USA. [24]Division of Earth Sciences, Korea Polar Research Institute, Incheon 21990, Korea. [25]School of Science, The University of Tokyo, Tokyo 113-0033, Japan. [26]Department of Physics and Astronomy, Purdue University, West Lafayette, IN 47907, USA. [27]Department of Earth, Atmospheric, and Planetary Sciences, Purdue University, West Lafayette, IN 47907, USA. [28]Department of Earth and Environmental Sciences, Nagoya University, Nagoya 464-8601, Japan. [29]Division of Earth and Planetary Sciences, Kyoto University, Kyoto 606-8502, Japan. [30]Department of Earth and Planetary Systems Science, Hiroshima University, Higashi-Hiroshima 739-8526, Japan. [31]UTokyo Organization for Planetary and Space Science, The University of Tokyo, Tokyo 113-0033, Japan. [32]Department of Space and Astronautical Science, The Graduate University for Advanced Studies, Hayama 240-0193, Japan. [33]Department of Planetology, Kobe University, Kobe 657-8501, Japan. [34]Aizu Research Cluster for Space Science, University of Aizu, Aizu-Wakamatsu 965-8580, Japan. [35]Center of Data Science, Ehime University, Matsuyama 790-8577, Japan. [36]Department of Physics and Astronomy, Seoul National University, Seoul 08826, Republic of Korea. [37]JAXA Space Exploration Center, JAXA, Sagamihara 252-5210, Japan. [38]Planetary Exploration Research Center, Chiba Institute of Technology, Narashino 275-0016, Japan. [39]National Astronomical Observatory of Japan, Mitaka 181-8588, Japan. [40]Geological Survey of Japan, National Institute of Advanced Industrial Science and Technology, Ibaraki 305-8567, Japan. [41]Faculty of Engineering, Kindai University, Higashi-Hiroshima 739-2116, Japan. [42]Faculty of Science, Niigata University, Niigata 950-2181, Japan. [43]Department of Chemistry, The University of Tokyo, Tokyo 113-0033, Japan. [44]Research and Development Directorate, JAXA, Sagamihara 252-5210, Japan. [45]Department of Physics, Rikkyo University, Tokyo 171-8501, Japan. [46]Instituto de Astrofísica de Canarias, University of La Laguna, 38205 La Laguna, Santa Cruz de Tenerife, Spain. [47]Department of Mechanical Engineering, Kanagawa Institute of Technology, Atsugi 243-0292, Japan. [48]Marine Works Japan Ltd., Yokosuka 237-0063, Japan. [49]Department of Earth and Planetary Science, Tokyo Institute of Technology, Ookayama, Tokyo 152-8550, Japan. [50]Department of Geology, School of Earth and Environment, Rowan University, Glassboro, NJ 08028, USA. [51]Lunar and Planetary Laboratory, University of Arizona, Tucson, AZ 85705, USA.

***Corresponding author. Email: okazaki.ryuji.703@m.kyushu-u.ac.jp**

†Deceased.

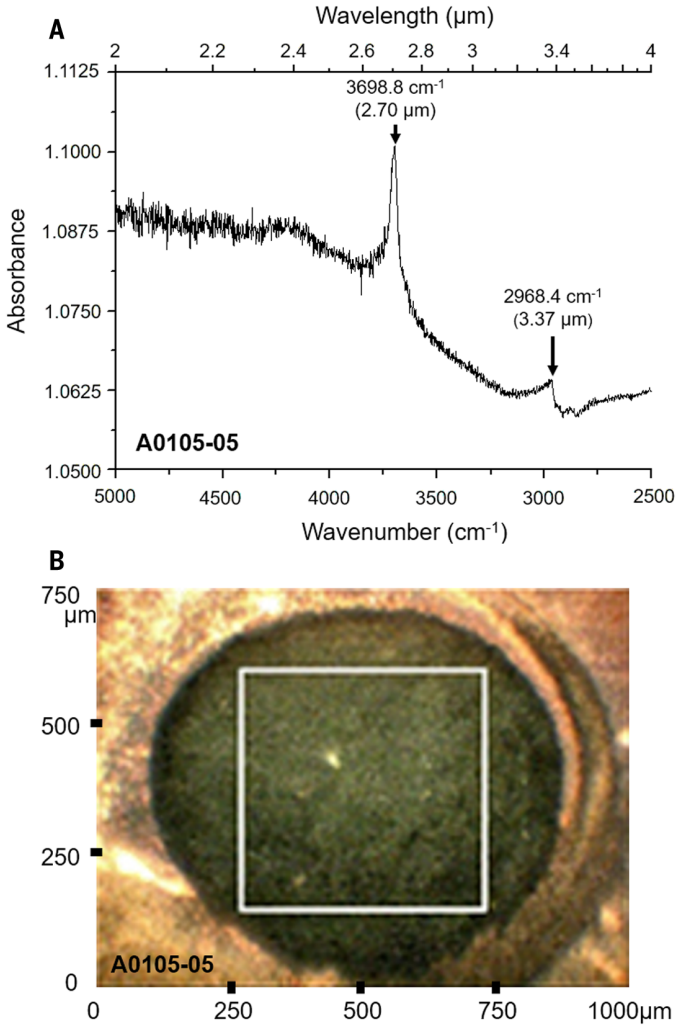

Fig. 2. Infrared spectroscopy of a Ryugu pelletized sample (A0105-05). (**A**) FT-IR spectrum of this sample. The absorption band at 3698.8 cm^{-1} (2.70 μm), resulting from the O-H stretching mode of phyllosilicates, was observed in all samples. The band at 2968.4 cm^{-1} (3.37 μm) aliphatic C-H stretching was also observed in all samples, although with weak intensity for A0105-06 and A0105-10. (**B**) An image of the sample under FT-IR spectroscopy. The white square indicates the analyzed area (aperture size: 450 μm by 450 μm).

contribution from SW, apparent at lower temperatures in their step-heating data (Fig. 3B).

The $^{38}Ar/^{36}Ar$ ratios of the Ryugu samples range between 0.186 ± 0.001 and 0.194 ± 0.007 (data S1), similar to the values expected for P1 [0.1873 ± 0.0007 (*27*, *28*)] or other trapped components (*28*). The SW-rich samples also fall within this $^{38}Ar/^{36}Ar$ range (data S1). The higher $^{38}Ar/^{36}Ar$ ratios (>0.187) are not correlated with cosmogenic ^{21}Ne concentrations, which could be attributed to higher concentrations of the target elements for cosmogenic ^{38}Ar production, such as K and Ca, in some of the samples. The $^{40}Ar/^{36}Ar$ ratios range from 4 to 70, probably with substantial instrumental contamination, owing to the small amounts of ^{40}Ar in the Ryugu samples. Concentrations of ^{40}Ar vary from 5×10^{-6} to 2×10^{-4} cm^3 g^{-1} at standard temperature and pressure (STP), suggesting heterogeneously distributed K in the samples and variable atmospheric contamination from the instrument.

We interpret the isotopic ratios of Xe as dominated by P1, with variable contributions from HL and SW components (figs. S7B and S8 and data S1), although we cannot exclude a small contamination by Earth-atmosphere Xe. Some samples could have cosmogenic contributions, but large uncertainties and the dominant presence of trapped Xe prevent us from unambiguously identifying its presence. Sample A0105-15 (which has abundant SW-Ne) has a Xe composition similar to that of SW-Xe in its ^{130}Xe to ^{136}Xe isotopes (fig. S8) but is depleted in ^{124}Xe and ^{126}Xe isotopes (data S1). Excesses in ^{129}Xe, which formed from the decay of short-lived ^{129}I, are observed in some samples with $^{129}Xe/^{132}Xe$ ratios higher than that for P1-Xe (1.042) (*27*). Isotopic ratios of Kr are dominated by the P1 and SW components (fig. S9). Some variations from P1 are observed for Kr and Xe isotopes, likely owing to interference with hydrocarbons, which can substantially affect the less-abundant Kr and Xe isotopes when measuring such small sample masses (figs. S8 and S9).

Nitrogen abundances and isotopes

Nitrogen isotopes were extracted by stepped heating of four pelletized samples (table S1). The total (organic and inorganic) carbon content was also determined for two of the samples (A0105-07 and C0106-07) (*21*). The $\delta^{15}N$ values [the difference from the atmospheric $^{15}N/^{14}N$ ratio (*31*)] of A0105-07 and C0106-07 are +1.7 ± 0.5 per mil (‰) and 0.0 ± 0.4‰, respectively (table S2). Other Ryugu samples have been reported to have higher values, in the range +39 to +43‰ [observed range in C-rich grains (*25*)] or +43.0 ± 9.0‰ [average value of milligram-sized aggregates of Ryugu-A (*26*)], consistent with the $\delta^{15}N$ values of CI chondrites between +31 and +52‰ (*32*–*36*). The two lowest ratios in our Ryugu samples are more similar to the dehydrated CI chondrite Yamato 980115 (hereafter Y-980115) of −2.8‰ (*37*) (Fig. 4). The $\delta^{15}N$ values for A0105-05 and C0106-06 are +18.1 ± 0.9‰ and +19.5 ± 0.9‰, respectively (table S2), between two other samples (A0105-07 and C0106-07) and CI chondrites (Fig. 4). The nitrogen abundances of our samples are between 700 and 900 parts per million (table S2), one-half to one-third that of CIs (*32*–*36*) but similar to Y-980115 (*37*) and the highly altered CM chondrite Meteorite Hills 01070 (hereafter MET 01070) (*36*) (Fig. 4). We find an inverse linear trend between the nitrogen isotope ratios and the nitrogen abundances (Fig. 4), indicating the presence of at least two phases: one with $\delta^{15}N$ up to +70‰, and the other with $\delta^{15}N$ close to zero (Earth atmosphere).

The lighter $\delta^{15}N$ value observed in some of our samples cannot be attributed to a fractionation process, which would result in enrichment of heavier isotopes relative to the lighter ones in the nitrogen-poor fractions. Atmospheric contamination would increase the nitrogen abundance and shift the $\delta^{15}N$ value closer to zero. Hence, the variation in $\delta^{15}N$ among our samples cannot be attributed to atmospheric contamination or diffusive loss of nitrogen (Fig. 4).

Ryugu's parent body

Our Ryugu samples have lower abundances of ^{15}N than do CI chondrites (*32*–*36*). Insoluble organic material (IOM) extracted from CI chondrites has lower $\delta^{15}N$ values than do bulk samples of CI chondrites (*38*), which could indicate that nitrogen in IOM is also ^{15}N-poor. Hence, a possible ^{15}N-rich material in CIs is soluble organic or inorganic phases, which could have been lost from the Ryugu samples to a variable extent.

The dehydrated CI chondrite Y-980115 resembles our Ryugu samples in nitrogen compositions (*37*) but, unlike the Ryugu samples, has mineralogy and lithology indicative of heating after aqueous alteration (*23*). Therefore, the ^{15}N-rich phase in Y-980115 is likely to have been lost through a devolatilization process, and the remaining ^{15}N-poor phase in Y-980115 is different from that in our Ryugu samples.

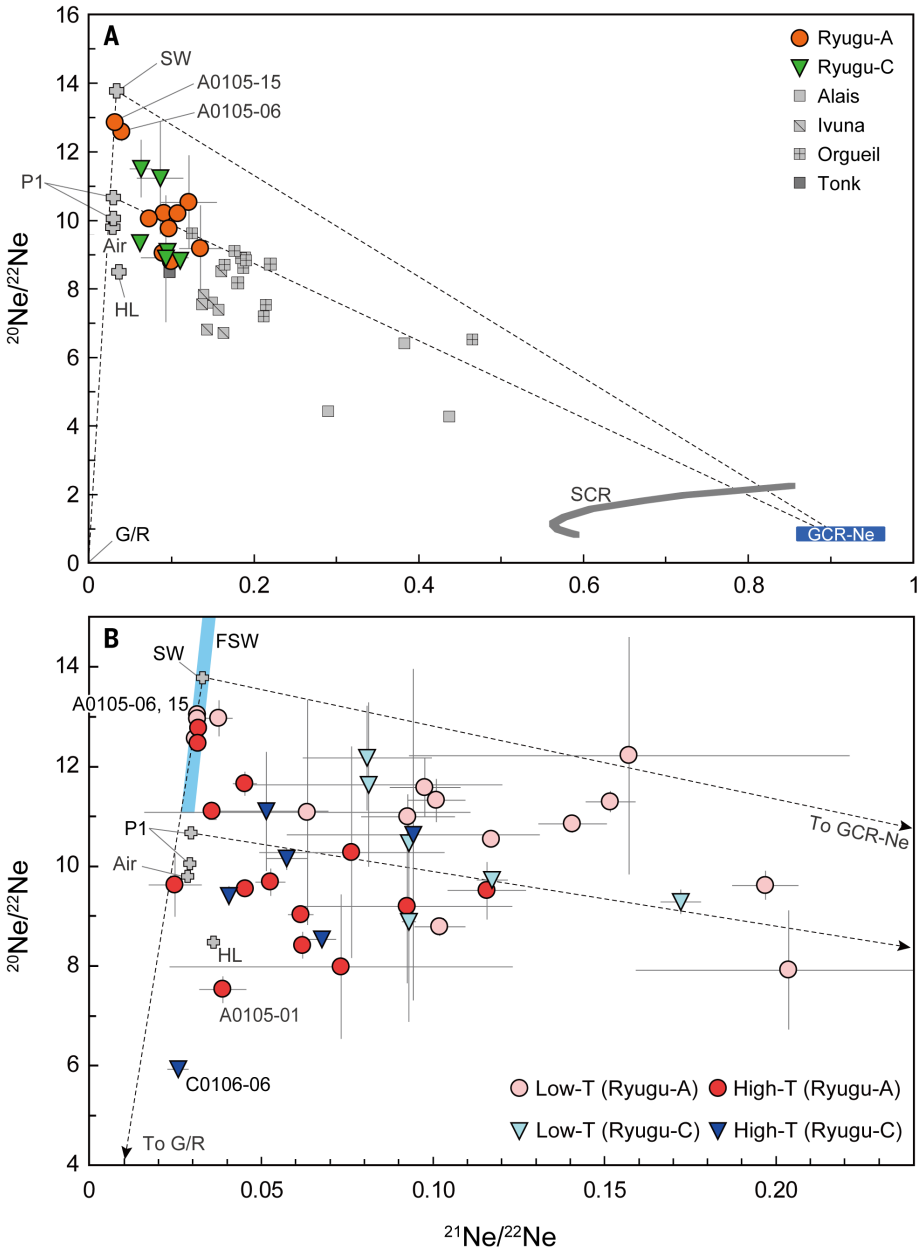

Fig. 3. Isotopic ratios of Ne in the Ryugu samples. (**A**) Ne isotope ratios measured from Ryugu-A samples (orange circles) and Ryugu-C samples (green inverted triangles). The CI chondrites Alais, Ivuna, Orgueil, and Tonk (gray squares) are shown for comparison. The dark-blue box is the expected composition of GCR-Ne. The gray solid curve shows the composition range expected for SCR-Ne. Compositions of SW, P1, HL, air, and G/R are shown as labeled gray crosses. Dashed lines are mixing lines for SW-G/R, SW-GCR, and P1-GCR. The Ryugu values are consistent with mixing of Ne with P1, HL, and GCR-Ne; two samples (labeled) also require a contribution from SW. (**B**) Isotope ratios of Ne extracted by stepped heating. The light-blue box is the compositional range of fractionated SW (FSW). Ne compositions for Ryugu-A and Ryugu-C samples are shown in red circles and blue inverted triangles, respectively. Low-temperature fractions (Low-T, ≤200°C or the first laser-heating extractions) are shown in light shading, and high-temperature fractions (High-T, >900°C fractions or the later laser-heating extractions) are shown in dark shading. The isotopic compositions of Ne released at low temperature indicate a contribution from SW in most of the samples, whereas those at high temperature exhibit contributions from P1 or HL, and G or R components. Isotopic compositions expected for GCR- and SCR-Ne were calculated using the GCR- and SCR-Ne production rates (*57*, *72*) and the CI chondrite composition (*55*). The composition of FSW (*30*) was for penetration depths between 20 and 100 nm, calculated (*21*) using simulation software (*73*), assuming CI elemental abundances (*55*). Data sources: CI chondrites (*23*, *56*); P1, HL, G, and R components (*27*, *28*); SW (*29*); and Earth atmosphere (*74*).

The measured total carbon abundances of the samples A0105-07 and C0106-07 are 6.8 ± 0.2 and 6.4 ± 0.1 wt %, respectively. The atomic C/N ratios are 112 ± 5 and 88 ± 3, respectively (table S2). This carbon content is 50% higher than that in CI chondrites [C/N ranging between 17 and 32 (*32*–*36*)], other Ryugu samples (*7*, *8*, *25*, *26*), and Y-980115 (*37*). The variable C/N ratios indicate that decoupling between nitrogen and carbon host phases could have occurred. We attribute the observed variations in the δ^{15}N, nitrogen, and carbon abundances to sample heterogeneity at a small spatial scale (table S2). Given this heterogeneity, we suggest that various host phases of nitrogen with distinct isotopic ratios are likely still present in Ryugu grains. The heterogeneous effects of aqueous alteration and dehydration or devolatilization on Ryugu materials could be responsible for the variation. The similarity of those two samples to the dehydrated CI chondrite Y-980115 indicates that some devolatilization process could be responsible for the depletion of the ^{15}N-rich phase from our samples. This is consistent with the results of thermogravimetric analysis of a Ryugu-A sample [A0040 (*8*)], in which the release of interlayer water was found only above 90°C. Such devolatilization could occur on the surface of Ryugu or in its subsurface layers. It is unlikely to have occurred in the interior of the Ryugu parent body, because thermal modeling (*7*) has shown that the internal heating did not reach 50°C. Devolatilization more likely occurred on Ryugu by some heating mechanism, such as solar radiation heating (*8*). However, the total carbon content in Y-980115 (*37*) is lower than that in our Ryugu samples, so we suggest that whatever devolatilization mechanism affected Y-980115, it differs from the one that occurred on Ryugu, which is more enriched in carbon than are CI chondrites. In addition to devolatilization, variable degrees of aqueous alteration could also be responsible. This could be attributed to a temperature increase at the subsurface layer of Ryugu's parent body, or a low amount of available water to drive alteration reactions (*7*). The least-altered materials in Ryugu samples are found as clasts (*7*), which could contain a ^{15}N-rich host phase.

The Ne and Xe isotope ratios in individual Ryugu samples show that Ryugu materials

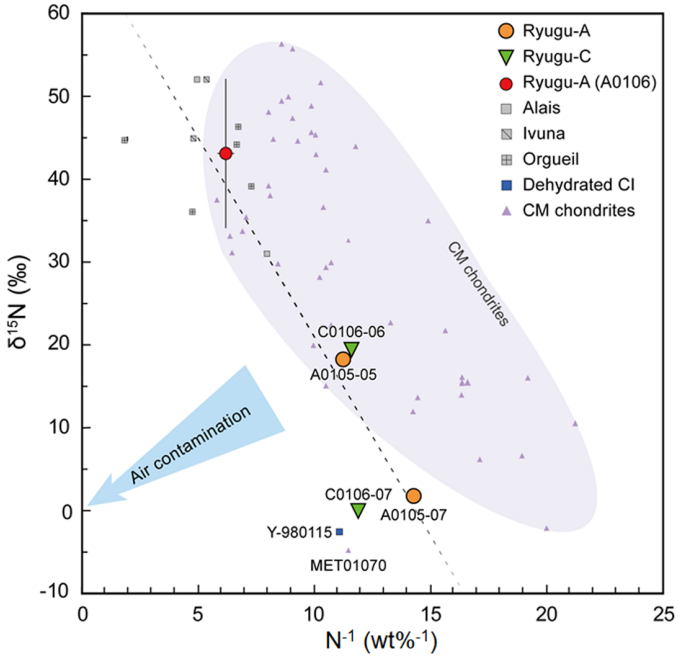

Fig. 4. Nitrogen isotopic compositions and inverse concentrations of the Ryugu pellet samples. Nitrogen compositions of each of the pelletized Ryugu-A samples (A0105-series, orange circles) and Ryugu-C samples (C0106-series, green inverted triangles) are shown. Uncertainties (1σ) for our data are smaller than the symbol sizes. An average composition of Ryugu-A aggregates (A0106, a red circle) (*26*), CI chondrite (Alais, Ivuna, and Orgueil) compositions (gray squares) (*32*–*34*, *36*), a dehydrated CI chondrite (Y-980115) composition (dark-blue square) (*37*), and CM chondrite compositions (purple triangles) (*34*–*36*) are also shown for comparison. The dashed line is a linear model fitted to the Ryugu samples and CI chondrites. The $\delta^{15}N$ values of A0105-07 and C0106-07 are ~0 and ~+20‰, respectively, lower than those of CI chondrites, but are close to Y-980115 and the highly altered CM chondrite MET 01070 (*36*). Two other samples (A0105-05 and C0106-06) have values intermediate between A0105-07 or C0106-07 and A0106 compositions.

contain the host phases of primordial and presolar components, thought to be phase Q, presolar diamonds, SiC, and graphite (*27*, *28*). These components were present in the early Solar System (*28*) before the formation of Ryugu's parent body and are commonly present in other CI chondrites (Fig. 3 and data S1). The elemental ratios of the heavy noble gases ^{36}Ar, ^{84}Kr, and ^{132}Xe are closest to the P1 noble gas component (fig. S7B), and hence their abundances reflect mainly the P1 abundance. With the exception of the SW-rich sample (A0105-15), the weighted mean values of the heavy noble gas concentrations in Ryugu samples are 1.5×10^{-6}, 2.0×10^{-8}, and 1.9×10^{-8} cm^3 STP g^{-1} for ^{36}Ar, ^{84}Kr, and ^{132}Xe, respectively. These averages are similar to the highest value found in a CI chondrite (*39*). Some individual grains have about two- to threefold higher concentrations than the highest CI chondrite value (Fig. 5), also above the highest concentrations observed in bulk CM and other chondritic materials (*39*–*41*).

In contrast to the low nitrogen abundances, the P1 gas in the Ryugu samples shows no evidence of having been lost during aqueous alteration episodes. The P1 gas in the Ningqiang ungrouped carbonaceous chondrite has been shown to be resistant to aqueous alteration (*42*), which is consistent with the high P1 abundances in the Ryugu samples. However, abundances of P1 gas in CM chondrites are correlated with their petrologic types, with lower P1 in CMs that experienced higher degrees of aqueous alteration (*41*). Mineralogical studies have found that the degree and condition of alteration differs between CI, CM, and Renazzo-type (CR) chondrite parent bodies (*6*). We hypothesize that the difference in the degree (or conditions) of aqueous alteration controls the P1 gas abundances. If this is correct, the degree of aqueous alteration experienced by the Ryugu parent body is similar to that for CI chondrites.

In addition to P1 and presolar noble gas components, Ningqiang (like many other nonhydrated meteorites) contains another noble gas component, referred to as Ar-rich gas (*28*), which is lost during hydrothermal experiments (*42*, *43*). The Ar-rich gas is also found in some less-altered CR and CM chondrites (*41*, *44*). It has been suggested that the host phase of Ar-rich gas is susceptive to aqueous alteration, with amorphous silicate being one of its host phases (*41*, *43*, *44*). Our measurements of the Ryugu samples do not show the presence of Ar-rich gas, but they do indicate the presence of SW gas—likely acquired recently, during surface exposure on Ryugu. Even if the Ryugu source material originally contained such amorphous silicates, the Ar-rich gas would have been easily lost during the decomposition of amorphous silicates. The absence of Ar-rich gas in the Ryugu samples is consistent with it appearing only in the least aqueously altered carbonaceous chondrites. All these lines of evidence indicate that Ryugu's parent body formed from similar volatile components as, and experienced similar aqueous alteration processes to, CI chondrites.

Cosmic ray and SW irradiations

Concentrations of ^4He in the individual Ryugu samples vary from 9×10^{-5} to 6×10^{-3} cm^3 STP g^{-1}, and concentrations of ^{22}Ne vary from 5×10^{-8} to 1×10^{-5} cm^3 STP g^{-1} (data S1), which we interpret as variable contributions of SW-derived gases. On the basis of the Ne isotopic ratios, we calculated the SW-derived ^{20}Ne and cosmogenic ^{21}Ne concentrations by subtracting contributions of the other Ne components (table S3). The smallest cosmogenic ^{21}Ne concentration is found in a SW-^{20}Ne–rich grain (A0105-15). No systematic differences in the cosmogenic ^{21}Ne concentrations are observed between the Ryugu-A and Ryugu-C samples (Fig. 6), although the high SW-^{20}Ne concentrations were observed only in two surface (Ryugu-A) samples.

We expected the SW-^{20}Ne and cosmogenic ^{21}Ne concentrations to be positively correlated, because this has been observed in all classes of regolithic meteorites (those originating from asteroid surface layers of fragmented incoherent rocky debris) (*45*, *46*). The correlation between SW and cosmogenic Ne concentrations requires grains to have been well mixed through the surface layer of the meteorites' parent bodies and to have experienced negligible grain-surface modification. However, we do not observe such a correlation (Fig. 6). Most of the Ryugu samples have lower ^{21}Ne than the trend observed in lunar soils and regolithic meteorites (*45*–*49*), implying a shorter exposure to SW. We calculated SW exposure ages of ≳3500 years for A0105-15 and ≳250 years for A0105-06, whereas the other samples range from ≳1 to ≳50 years. We calculated the SW-^{20}Ne flux at the current orbit of Ryugu [orbital semimajor axis of 1.19 astronomical units (au) (*50*, *51*)] using SW implantation rates measured by the Genesis mission (*52*), finding 4×10^{-9} cm^3 STP cm^{-2} $year^{-1}$. This calculation assumes spherical grains with a diameter of 0.8 mm (equivalent to the measured sizes) and a density of 1.8 g cm^{-3} (*7*), and that the samples did not experience any grain-surface modification by pulverization or fragmentation. We therefore regard the resulting SW exposure ages as lower limits.

The concentrations of cosmogenic ^{21}Ne in our samples, excluding the SW-rich sample A0105-15, range from 3×10^{-9} to 8×10^{-9} cm^3 STP g^{-1}. This variation is smaller than observed in the SW-^{20}Ne concentrations. We calculated the weighted means of the cosmogenic ^{21}Ne concentrations for each of the Ryugu-A and Ryugu-C samples using the sample mass as the weighting factor. The cosmogenic ^{21}Ne concentrations are $(4.8 \pm 0.8) \times 10^{-9}$ and $(4.1 \pm 0.7) \times 10^{-9}$ cm^3 STP g^{-1} for the Ryugu-A and Ryugu-C samples (excluding A0105-15), respectively. The

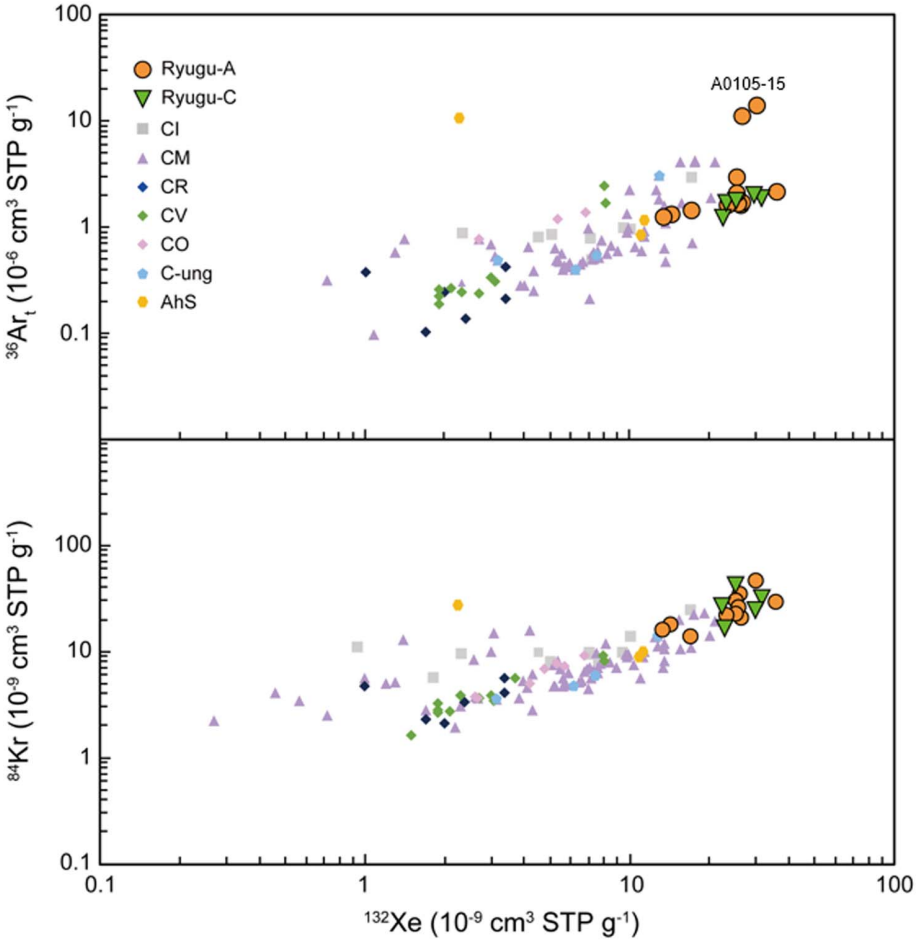

Fig. 5. Concentrations of the dominant isotopes of trapped argon, krypton, and xenon. Concentrations of ^{36}Ar, ^{84}Kr, and ^{132}Xe in Ryugu-A samples (orange circles) and Ryugu-C samples (green inverted triangles) are shown. Uncertainties (1σ) are 0.5 to 7% (data S1), smaller than the symbol sizes. Abundances are plotted for CI (gray squares), CM (purple triangles), CR (dark-blue diamonds), Vigarano-type (CV, green diamonds), and Ornans-type (CO, purple diamonds) chondrites; ungrouped carbonaceous chondrites (C-ung, blue pentagons); and a carbonaceous chondrite–like clast from the Almahata Sitta polymict ureilite (AhS, orange hexagon). The Ryugu grains contain higher abundances of noble gases than other chondritic materials. Data sources: CI, CM, CR, CV, and CO chondrites (*39*, *41*); C-ung (*41*); and AhS (*40*).

different sampling condition between the Ryugu-A and Ryugu-C samples explains their different exposure to SW and/or cosmic rays, brecciation, and meteoroid impacts. Abundances of the cosmogenic radionuclide ^{10}Be were reported to be ~12.8 and ~7.3 decays (or disintegrations) per minute per kilogram for the Ryugu-A and Ryugu-C samples, respectively (*53*), reflecting their different shielding conditions.

The low concentrations of SW in the Ryugu samples led us to conclude that the samples have not been transported vertically (mixed to shallower and deeper levels) by meteoroid impacts but instead remained at a specific shielding. A shielding of 150 g cm^{-2} is applied for the Ryugu-C samples on the basis of the ^{10}Be abundances (*53*), which corresponds to a physical depth of 1.3 m [assuming a Ryugu surface layer density of 1.2 g cm^{-3} (*50*)] and is close to the artificial crater depth of 1.7 m (*20*). The calculated production rate of ^{21}Ne (P_{21}) at 150 g cm^{-2} shielding is 0.79 × 10^{-9} cm^3 STP g^{-1} Myr^{-1} (*54*) assuming 2π steradian exposure on a 1.19-au orbit (*50*, *51*) and CI chondrite composition (*55*). For the Ryugu-A samples, we assumed that they had a lower shielding of 2 to 5 g cm^{-2}, appropriate for material just below the surface. At this shielding, cosmogenic ^{21}Ne can be produced by GCRs and SCRs, but SW-implanted Ne is expected to be rare. The calculated P_{21} at this shielding is 0.90 × 10^{-9} cm^3 STP g^{-1} Myr^{-1}. Using these production rates, we obtained cosmic ray exposure (CRE) ages of 5.3 ± 0.9 and 5.2 ± 0.8 Myr for the Ryugu-A and Ryugu-C samples, respectively. These CRE ages are averaged values for each sampling site; individual grains show some variation in their cosmogenic ^{21}Ne concentrations. This variation can be explained by variable shielding conditions and chemical compositions. For the SW-rich sample A0105-15, its CRE age is >100,000 years, obtained using a P_{21} of ~3 × 10^{-9} cm^3 STP g^{-1} Myr^{-1} for a shielding of 0 to 1 g cm^{-2} (*54*), where SW and SCR can be implanted at the grain surface. The CRE age of A0105-15 is longer than its SW exposure age, indicating that the SW-rich sample was temporarily brought to the surface but was mostly buried at a deeper depth, similar to the other Ryugu-A samples. Because only a small fraction of surface materials (~10 vol %, estimated from two SW-rich grains out of the 16 grains studied) seem to be mixed with subsurface material, a large fraction of surface layer materials down to several centimeters could have been ejected to space or shifted across the surface to lower-gravitational-potential regions, such as the mid-latitude region (*50*, *51*), in the past ~5 Myr (the CRE ages of the samples).

We compare Ryugu's CRE ages to those of meteorites, which primarily reflect their duration of exposure in interplanetary space (during transit to Earth), rather than exposure on the surface of their parent bodies (as is the case for Ryugu). We calculated expected cosmogenic ^{21}Ne concentrations in CI chondrites of (11 to 25) × 10^{-9} (Alais), (3 to 6) × 10^{-9}(Ivuna), (6 to 11) × 10^{-9} (Orgueil), and 3 × 10^{-9} cm^3 STP g^{-1} (Tonk), using previous measurements of Ne isotopes (*23*, *56*). Using a production rate of 1.5 × 10^{-9} cm^3 STP g^{-1} Myr^{-1}, calculated for a 100-cm-diameter body irradiated from 4π steradians (*57*), these concentrations correspond to CRE ages of 2 to 17 Myr. These calculations assume no SCR contribution and a constant GCR flux. Similar CRE ages for CI chondrites have previously been obtained on the basis of cosmogenic radionuclides (*58*), indicating that the CRE ages of CI chondrites reflect their space exposure histories, with little contribution from additional parent body exposures. In the case of such multistage irradiations, the abundances of cosmogenic radionuclides should be lower than those of stable isotopes owing to their decay during intervals between exposures. Only Ivuna is thought to have experienced multistage irradiation (*58*).

Two of five CI chondrites are known to have short CRE ages, 0.1 to 0.2 Myr (*58*), and more than half of CM chondrites also have short (<10 Myr) CRE ages (*41*, *59*, *60*), indicating similar transport times to Earth. Although many CM chondrites are regolithic and contain SW noble gases (*41*), which necessitates cosmic-ray exposure on the CM parent body, the duration of that exposure is not well determined. The Ryugu surface layer must have been irradiated by GCRs for a duration similar to the space exposure of CI (and possibly CM) chondrites. The lower collision frequency at the near-Earth orbit of Ryugu than at the main asteroid belt (MAB) (*61*, *62*) could be responsible for the surface residence time of Ryugu dust and grains. However, the parent bodies of CI and CM

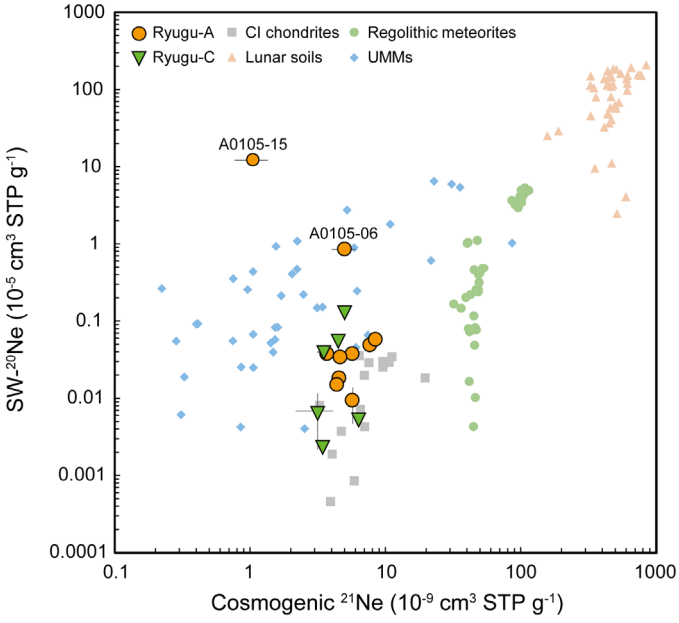

Fig. 6. Concentrations of SW ^{20}Ne and cosmogenic ^{21}Ne. Concentrations of SW-^{20}Ne and cosmogenic ^{21}Ne in Ryugu-A samples (orange circles) and Ryugu-C samples (green inverted triangles) are shown. These concentrations in CI chondrites (gray squares) (*23*, *56*), regolithic meteorites (light-green circles) (*45*, *46*), lunar soils (pink triangles) (*47*–*49*), and UMMs (light-blue diamonds) (*64*–*67*) are also shown for comparison. Two Ryugu samples (A0105-06 and A0105-15) have high SW-^{20}Ne. No correlation between SW-^{20}Ne and cosmogenic ^{21}Ne is evident.

chondrites could have experienced frequent collisions in the MAB, causing shorter surface residence times. Lunar surface materials likewise record a low-frequency collision history, because the Moon is also a near-Earth object. The higher concentrations of SW-^{20}Ne and cosmogenic ^{21}Ne in lunar soils reflect their longer surface and subsurface residence times (*47*–*49*) as compared with samples of Ryugu (Fig. 6).

The CRE ages of our samples constrain the orbital evolution of Ryugu, which is thought to have migrated from the MAB into its current near-Earth orbit (*9*, *13*–*15*). Because the crater production rate within the MAB is ~30 times higher than that in near-Earth orbits (*61*, *62*), the regolith residence time in the top 1-m layer of Ryugu's surface was previously reported to be 2 to 8 Myr for near-Earth bombardment rates, or ~0.1 to 0.3 Myr for MAB bombardment rates (*9*, *13*, *14*). Our derived surface residence time of ~5 Myr is more consistent with the near-Earth bombardment rate, indicating that Ryugu's orbit changed ~5 Myr ago.

After migration from the MAB to near-Earth orbit, Ryugu could have experienced other surface evolution processes in addition to impact bombardment. The spectral variations (red and blue material) observed across Ryugu's surface have been interpreted as indicating a temporary orbital excursion near the Sun, which could have produced the red material by intense heating and faster migration of surface materials (*9*, *13*). Our stepped-heating measurements show that ~30% of cosmogenic ^{21}Ne, corresponding to ~1 Myr of GCR exposure at 150 g cm^{-2} shielding, is released at 100°C, at least from some samples (Fig. 3B and data S1). This supports the suggestion (*8*) that Ryugu samples have not experienced heating above 100°C and demonstrates that the heating could not have occurred in the past ~1 Myr. Therefore, our data indicate surface alteration and migration more than 1 Myr ago—rather than more recent processes—as being responsible for the spectral-color distribution, if surface heating produced the red material.

The absence of a correlation between SW-^{20}Ne and cosmogenic ^{21}Ne, and the scarcity of SW in the Ne isotopic ratios, indicate that only a limited number of the Ryugu grains were exposed to SW. However, we cannot rule out the possibility that the fraction of SW-rich grains was previously higher, before some grains escaped to space or migrated to other regions of Ryugu. Thermal and/or mechanical effects, such as atmospheric heating of the Hayabusa2 reentry capsule or fragmentation and pulverization in the sample catcher during the return to Earth, could also have altered the SW inventory. The CRE ages of the Ryugu samples are shorter than those of lunar soils and regolithic meteorites (*45*–*49*), which could be explained by higher mechanical vulnerability on Ryugu. Particle ejections have been observed on the C-type asteroid (101955) Bennu (*63*), which could be related to grain-surface modification processes on Ryugu. Grain destruction by impact bombardment and/or phyllosilicate dehydration is predicted to be efficient on Ryugu (*8*, *63*).

Comparison with micrometeorites

Meteoroids and micrometeorites are exposed to SW, SCRs, and GCRs during their transit from their parent bodies to Earth. SW signatures are also commonly observed in unmelted micrometeorites (UMMs) collected from Antarctic snow and ice, most of which have similar composition and mineralogy to CI and CM chondrites (*64*–*67*). Unlike the Ryugu samples, the SW-^{20}Ne concentrations in UMMs are correlated with cosmogenic ^{21}Ne concentrations (Fig. 6). Some SW-^{20}Ne and cosmogenic ^{21}Ne must have been lost from UMMs by heating during atmospheric entry (*68*) and recoil effects (*69*), which could disturb the correlation between the SW and cosmogenic Ne concentrations. Still, most UMMs contain higher SW-^{20}Ne concentrations than do the Ryugu samples (Fig. 6). This indicates that UMMs acquired most of their SW and cosmogenic Ne in interplanetary space, not on the surface of their parent bodies. Unlike UMMs, only a small fraction of the Ryugu samples were exposed on the surface to SW, whereas cosmogenic ^{21}Ne was produced in both the surface and subsurface layers. Therefore, Ryugu's (and possibly other near-Earth asteroids') surface material cannot be the major source of UMMs. Short exposure (~250 years for ~1-mm-diameter grains, as observed in A0105-06) of Ryugu grains to SW in interplanetary space (e.g., after ejection from Ryugu by impact) would increase the SW implantation but could not produce the correlation between SW and cosmogenic Ne concentrations.

Survival of pristine Ryugu material

Although the nitrogen data indicate that some devolatilization has occurred, low-temperature gas-extraction steps (<200°C) released 35 to 70% of ^{22}Ne, and the Ne isotopic composition was consistent with mixing of SW and cosmogenic components (Fig. 3B and data S1). CI chondrites release smaller fractions (20 to 30%) of the total Ne content below 300°C (*70*). It is possible that CI chondrites have lost some fraction of their easily released noble gases during (or after) falling to Earth, whereas the Ryugu grains retain highly volatile noble gases acquired during surface evolution. Any temperature increase beyond 100°C on Ryugu's surface has not occurred within the past 1 Myr. The primordial and presolar noble gases in the Ryugu samples are released at higher temperatures (>900°C) (data S1). Atmospheric entry heating or terrestrial weathering could be responsible for the difference (*71*).

Conclusions

We measured noble gas and nitrogen abundances and isotopic compositions in individual grains returned from the surface and subsurface layers of near-Earth asteroid Ryugu. Ne and Xe are enriched in primordial and presolar noble gases, specifically the P1 and HL components. These isotopic compositions and the elemental abundances are similar to those in CI chondrites. Nitrogen in Ryugu exhibits

differences from that in CI chondrites: Some of the samples are depleted in nitrogen and have lower $\delta^{15}N$ values. These results indicate that Ryugu contains several host phases that have not lost their volatiles and are not mixed with each other.

We used the Ne isotopes to determine the amount of SW, GCR, and SCR irradiations after the formation of Ryugu. The CRE ages of ~5 Myr for the grains are compatible with near-surface residence times estimated for near-Earth bombardment rates, indicating that Ryugu left the MAB at least several million years ago. The current surface and subsurface materials on Ryugu have not experienced heating above 100°C within the past ~1 Myr.

REFERENCES AND NOTES

1. Y. Tsuda *et al*., Hayabusa2 mission status: Landing, roving and cratering on asteroid Ryugu. *Acta Astronaut.* **171**, 42–54 (2020). doi: 10.1016/j.actaastro.2020.02.035
2. S. Watanabe *et al*., *Hayabusa2* mission overview. *Space Sci. Rev.* **208**, 3–16 (2017). doi: 10.1007/s11214-017-0377-1
3. B. Marty, The origins and concentrations of water, carbon, nitrogen and noble gases on Earth. *Earth Planet. Sci. Lett.* **313–314**, 56–66 (2012). doi: 10.1016/j.epsl.2011.10.040
4. M. W. Broadley *et al*., Identification of chondritic krypton and xenon in Yellowstone gases and the timing of terrestrial volatile accretion. *Proc. Natl. Acad. Sci. U.S.A.* **117**, 13997–14004 (2020). doi: 10.1073/pnas.2003907117; pmid: 32513744
5. G. R. Huss, A. E. Rubin, J. N. Grossman, "Thermal metamorphism in chondrites" in *Meteorites and the Early Solar System II*, D. S. Lauretta, H. Y. McSween Jr., Eds. (Univ. of Arizona Press, 2006), pp. 567–586.
6. A. J. Brearley, "The action of water" in *Meteorites and the Early Solar System II*, D. S. Lauretta, H. Y. McSween Jr., Eds. (Univ. of Arizona Press, 2006), pp. 587–624.
7. T. Nakamura *et al*., Formation and evolution of carbonaceous asteroid Ryugu: Direct evidence from returned samples. *Science* **379**, eabn8671 (2023). doi: 10.1126/science.abn8671; pmid: 36137011
8. T. Yokoyama *et al*., Samples returned from the asteroid Ryugu are similar to Ivuna-type carbonaceous meteorites. *Science* **379**, eabn7850 (2023). doi: 10.1126/science.abn7850; pmid: 35679354
9. S. Sugita *et al*., The geomorphology, color, and thermal properties of Ryugu: Implications for parent-body processes. *Science* **364**, eaaw0422 (2019). doi: 10.1126/science.aaw0422; pmid: 30890587
10. P. Michel *et al*., Collisional formation of top-shaped asteroids and implications for the origins of Ryugu and Bennu. *Nat. Commun.* **11**, 2655 (2020). doi: 10.1038/s41467-020-16433-z; pmid: 32461569
11. D. D. Bogard, L. E. Nyquist, W. C. Hirsch, D. R. Moore, Trapped solar and cosmogenic noble gas abundances in Apollo 15 and 16 deep drill samples. *Earth Planet. Sci. Lett.* **21**, 52–69 (1973). doi: 10.1016/0012-821X(73)90225-2
12. N. Hirata *et al*., The spatial distribution of impact craters on Ryugu. *Icarus* **338**, 113527 (2020). doi: 10.1016/j.icarus.2019.113527
13. T. Morota *et al*., Sample collection from asteroid (162173) Ryugu by Hayabusa2: Implications for surface evolution. *Science* **368**, 654–659 (2020). doi: 10.1126/science.aaz6306; pmid: 32381723
14. Y. Cho *et al*., Geologic history and crater morphology of Asteroid (162173) Ryugu. *J. Geophys. Res. Planets* **126**, e2020JE006572 (2021). doi: 10.1029/2020JE006572
15. N. Takaki *et al*., Resurfacing processes constrained by crater distribution on Ryugu. *Icarus* **377**, 114911 (2022). doi: 10.1016/j.icarus.2022.114911
16. S. Tachibana *et al*., Pebbles and sand on asteroid (162173) Ryugu: In situ observation and particles returned to Earth. *Science* **375**, 1011–1016 (2022). doi: 10.1126/science.abj8624; pmid: 35143255
17. H. Sawada *et al*., Hayabusa2 sampler: Collection of asteroidal surface material. *Space Sci. Rev.* **208**, 81–106 (2017). doi: 10.1007/s11214-017-0338-8
18. T. Yada *et al*., Preliminary analysis of the Hayabusa2 samples returned from C-type asteroid Ryugu. *Nat. Astron.* **6**, 214–220 (2022). doi: 10.1038/s41550-021-01550-6
19. T. Saiki *et al*., Small carry-on impactor of Hayabusa2 mission. *Acta Astronaut.* **84**, 227–236 (2013). doi: 10.1016/j.actaastro.2012.11.010
20. M. Arakawa *et al*., An artificial impact on the asteroid (162173) Ryugu formed a crater in the gravity-dominated regime. *Science* **368**, 67–71 (2020). doi: 10.1126/science.aaz1701; pmid: 32193363
21. Materials and methods are available as supplementary materials.
22. J. Alfing, M. Patzek, A. Bischoff, Modal abundances of coarse-grained (>5 μm) components within CI-chondrites and their individual clasts – Mixing of various lithologies on the CI parent body(ies). *Chem. Erde* **79**, 125532 (2019). doi: 10.1016/j.chemer.2019.08.004
23. A. J. King *et al*., The Yamato-type (CY) carbonaceous chondrite group: Analogues for the surface of asteroid Ryugu? *Chem. Erde* **79**, 125531 (2019). doi: 10.1016/j.chemer.2019.08.003
24. G. Matrajt *et al*., FTIR and Raman analyses of the Tagish Lake meteorite: Relationship with the aliphatic hydrocarbons observed in the Diffuse Interstellar Medium. *Astron. Astrophys.* **416**, 983–990 (2004). doi: 10.1051/0004-6361:20034526
25. H. Yabuta *et al*., Macromolecular organic matter in samples of the asteroid (162173) Ryugu. *Science* **379**, eabn9057 (2023). doi: 10.1126/science.abn9057
26. H. Naraoka *et al*., Soluble organic molecules in samples of the carbonaceous asteroid (162173) Ryugu. *Science* **379**, eabn9033 (2023). doi: 10.1126/science.abn9033
27. H. Busemann, H. Baur, R. Wieler, Primordial noble gases in "phase Q" in carbonaceous and ordinary chondrites studied by closed-system stepped etching. *Meteorit. Planet. Sci.* **35**, 949–973 (2000). doi: 10.1111/j.1945-5100.2000.tb01485.x
28. U. Ott, Planetary and pre-solar noble gases in meteorites. *Chem. Erde* **74**, 519–544 (2014). doi: 10.1016/j.chemer.2014.01.003
29. V. S. Heber *et al*., Noble gas composition of the solar wind as collected by the Genesis mission. *Geochim. Cosmochim. Acta* **73**, 7414–7432 (2009). doi: 10.1016/j.gca.2009.09.013
30. A. Grimberg *et al*., Solar wind neon from Genesis: Implications for the lunar noble gas record. *Science* **314**, 1133–1135 (2006). doi: 10.1126/science.1133568; pmid: 17110575
31. T. B. Coplen, H. R. Krouse, J. K. Böhlke, Reporting of nitrogen-isotope abundances (technical report). *Pure Appl. Chem.* **64**, 907–908 (1992). doi: 10.1351/pac199264060907
32. C.-C. Kung, R. N. Clayton, Nitrogen abundances and isotopic compositions in stony meteorites. *Earth Planet. Sci. Lett.* **38**, 421–435 (1978). doi: 10.1016/0012-821X(78)90117-6
33. F. Robert, S. Epstein, The concentration and isotopic composition of hydrogen, carbon and nitrogen in carbonaceous meteorites. *Geochim. Cosmochim. Acta* **46**, 81–95 (1982). doi: 10.1016/0016-7037(82)90293-9
34. J. F. Kerridge, Carbon, hydrogen and nitrogen in carbonaceous chondrites: Abundances and isotopic compositions in bulk samples. *Geochim. Cosmochim. Acta* **49**, 1707–1714 (1985). doi: 10.1016/0016-7037(85)90141-3; pmid: 11539652
35. V. K. Pearson, M. A. Sephton, I. A. Franchi, J. M. Gibson, I. Gilmour, Carbon and nitrogen in carbonaceous chondrites: Elemental abundances and stable isotopic composition. *Meteorit. Planet. Sci.* **41**, 1899–1918 (2006). doi: 10.1111/j.1945-5100.2006.tb00459.x
36. C. M. O.'D. Alexander *et al*., The provenances of asteroids, and their contributions to the volatile inventories of the terrestrial planets. *Science* **337**, 721–723 (2012). doi: 10.1126/science.1223474; pmid: 22798405
37. Q. H. S. Chan, Y. Chikaraishi, Y. Takano, N. O. Ogawa, N. Ohkouchi, Amino acid compositions in heated carbonaceous chondrites and their compound-specific nitrogen isotopic ratios. *Earth Planets Space* **68**, 7 (2016). doi: 10.1186/s40623-016-0382-8
38. C. M. O.'D. Alexander, M. Fogel, H. Yabuta, G. D. Cody, The origin and evolution of chondrites recorded in the elemental and isotopic compositions of their macromolecular organic matter. *Geochim. Cosmochim. Acta* **71**, 4380–4403 (2007). doi: 10.1016/j.gca.2007.06.052
39. E. Mazor, D. Heymann, E. Anders, Noble gases in carbonaceous chondrites. *Geochim. Cosmochim. Acta* **34**, 781–824 (1970). doi: 10.1016/0016-7037(70)90031-1
40. C. A. Goodrich *et al*., The first samples from Almahata Sitta showing contacts between ureilitic and chondritic lithologies: Implications for the structure and composition of asteroid 2008 TC_3. *Meteorit. Planet. Sci.* **54**, 2769–2813 (2019). doi: 10.1111/maps.13390; pmid: 33716489
41. D. Krietsch *et al*., Noble gases in CM carbonaceous chondrites: Effect of parent body aqueous and thermal alteration and cosmic ray exposure ages. *Geochim. Cosmochim. Acta* **310**, 240–280 (2021). doi: 10.1016/j.gca.2021.05.050
42. Y. Yamamoto, R. Okazaki, T. Nakamura, Effects of experimental aqueous alteration on the abundances of argon-rich noble gases in the Ningqiang carbonaceous chondrite. *Meteorit. Planet. Sci.* **41**, 541–551 (2006). doi: 10.1111/j.1945-5100.2006.tb00481.x
43. T. Nakamura, M. Zolensky, M. Sekiya, R. Okazaki, K. Nagao, Acid-susceptive material as a host phase of argon-rich noble gas in the carbonaceous chondrite Ningqiang. *Meteorit. Planet. Sci.* **38**, 243–250 (2003). doi: 10.1111/j.1945-5100.2003.tb00262.x
44. T. Obase *et al*., Water-susceptible primordial noble gas components in less-altered CR chondrites: A possible link to cometary materials. *Geochim. Cosmochim. Acta* **312**, 75–105 (2021). doi: 10.1016/j.gca.2021.08.012
45. R. Wieler, H. Baur, A. Pedroni, P. Signer, P. Pellas, Exposure history of the regolithic chondrite Fayetteville: I. Solar-gas-rich matrix. *Geochim. Cosmochim. Acta* **53**, 1441–1448 (1989). doi: 10.1016/0016-7037(89)90076-8
46. T. E. Ferko *et al*., The irradiation history of the Ghubara (L5) regolith breccia. *Meteorit. Planet. Sci.* **37**, 311–327 (2002). doi: 10.1111/j.1945-5100.2002.tb00819.x
47. J. K. Agrawal, K. Gopalan, M. N. Rao, Solar wind and cosmogenic rare gases in Luna 16 and 20 soils and their correlation with cosmic ray produced fossil tracks in lunar samples. *Pramana* **3**, 176–185 (1974). doi: 10.1007/BF02875072
48. J. L. Jordan, D. Heymann, S. Lakatos, Inert gas patterns in the regolith at the Apollo 15 landing site. *Geochim. Cosmochim. Acta* **38**, 65–78 (1974). doi: 10.1016/0016-7037(74)90195-1
49. N. B. Bhai, K. Gopalan, J. N. Goswami, M. N. Rao, T. R. Venkatesan, Solar cosmic ray produced neon and xenon isotopes and particle tracks in feldspars from lunar fines 14148 and 24087. *Proc. Lunar Planet. Sci. Conf.* **9**, 1629–1645 (1978).
50. S. Watanabe *et al*., Hayabusa2 arrives at the carbonaceous asteroid 162173 Ryugu-A spinning top-shaped rubble pile. *Science* **364**, 268–272 (2019). doi: 10.1126/science.aav8032; pmid: 30890588
51. S. Kikuchi *et al*., Hayabusa2 pinpoint touchdown near the artificial crater on Ryugu: Trajectory design and guidance performance. *Adv. Space Res.* **68**, 3093–3140 (2021). doi: 10.1016/j.asr.2021.07.031
52. A. Grimberg, H. Baur, F. Bühler, P. Bochsler, R. Wieler, Solar wind helium, neon, and argon isotopic and elemental composition: Data from the metallic glass flown on NASA's Genesis mission. *Geochim. Cosmochim. Acta* **72**, 626–645 (2008). doi: 10.1016/j.gca.2007.10.017
53. K. Nishiizumi *et al*., Exposure conditions of samples collected on Ryugu's two touchdown sites determined by cosmogenic nuclides, Hayabusa Symposium 2021, #S3-1 (2021).
54. C. M. Hohenberg, K. Marti, F. A. Podosek, R. C. Reedy, J. R. Shirck, Comparisons between observed and predicted cosmogenic noble gases in lunar samples. *Proc. Lunar Planet. Sci. Conf.* **9**, 2311–2344 (1978).
55. K. Lodders, B. Fegley Jr., *The Planetary Scientist's Companion* (Oxford Univ. Press, 1998).
56. L. Schultz, L. Franke, Helium, neon, and argon in meteorites: A data collection. *Meteorit. Planet. Sci.* **39**, 1889–1890 (2004). doi: 10.1111/j.1945-5100.2004.tb00083.x
57. I. Leya, J. Masarik, Cosmogenic nuclides in stony meteorites revisited. *Meteorit. Planet. Sci.* **44**, 1061–1086 (2009). doi: 10.1111/j.1945-5100.2009.tb00788.x
58. K. Nishiizumi, M. W. Caffee, Exposure histories of CI1 and CM1 carbonaceous chondrites. *Proc. Lunar Planet. Sci. Conf.* **43**, 2758 (2012).
59. G. F. Herzog, M. W. Caffee, "Cosmic-ray exposure ages of meteorites" in *Treatise on Geochemistry, Volume 1: Meteorites and Cosmochemical Processes*, A. M. Davis, Ed. (Elsevier, ed. 2, 2014), pp. 419–454.
60. E. R. D. Scott, G. F. Herzog, Short cosmic-ray exposure ages of CI and CM chondrites may reflect disintegration of volatile-rich asteroids at perihelion. *Proc. Lunar Planet. Sci. Conf.* **52**, 1833 (2021).
61. W. F. Bottke Jr. *et al*., Linking the collisional history of the main asteroid belt to its dynamical excitation and depletion. *Icarus* **179**, 63–94 (2005). doi: 10.1016/j.icarus.2005.05.017
62. D. P. O'Brien, R. Greenberg, The collisional and dynamical evolution of the main-belt and NEA size distributions. *Icarus* **178**, 179–212 (2005). doi: 10.1016/j.icarus.2005.04.001

63. D. S. Lauretta *et al*., Episodes of particle ejection from the surface of the active asteroid (101955) Bennu. *Science* **366**, eaay3544 (2019). doi: 10.1126/science.aay3544 pmid: 31806784
64. T. Osawa, K. Nagao, Noble gas compositions of Antarctic micrometeorites collected at the Dome Fuji Station in 1996 and 1997. *Meteorit. Planet. Sci.* **37**, 911–936 (2002). doi: 10.1111/j.1945-5100.2002.tb00867.x
65. T. Osawa, T. Nakamura, K. Nagao, Noble gas isotopes and mineral assemblages of Antarctic micrometeorites collected at the meteorite ice field around the Yamato Mountains. *Meteorit. Planet. Sci.* **38**, 1627–1640 (2003). doi: 10.1111/j.1945-5100.2003.tb00005.x
66. K. Bajo *et al*., Single grain noble gas analysis of Antarctic micrometeorites by stepwise heating method with a newly constructed miniature furnace. *Earth Planets Space* **63**, 1097–1111 (2011). doi: 10.5047/eps.2011.08.001
67. R. Okazaki *et al*., Mineralogy and noble gas isotopes of micrometeorites collected from Antarctic snow. *Earth Planets Space* **67**, 90 (2015). doi: 10.1186/s40623-015-0261-8
68. E. Füri, A. Aléon-Toppani, B. Marty, G. Libourel, L. Zimmermann, Effects of atmospheric entry heating on the noble gas and nitrogen content of micrometeorites. *Earth Planet. Sci. Lett.* **377–378**, 1–12 (2013). doi: 10.1016/j.epsl.2013.07.031
69. R. Trappitsch, I. Leya, Cosmogenic production rates and recoil loss effects in micrometeorites and interplanetary dust particles. *Meteorit. Planet. Sci.* **48**, 195–210 (2013). doi: 10.1111/maps.12051
70. D. C. Black, On the origins of trapped helium, neon and argon isotopic variations in meteorites–II. Carbonaceous meteorites. *Geochim. Cosmochim. Acta* **36**, 377–394 (1972). doi: 10.1016/0016-7037(72)90029-4
71. A. J. King, K. J. H. Phillips, S. Strekopytov, C. Vita-Finzi, S. S. Russell, Terrestrial modification of the Ivuna meteorite and a reassessment of the chemical composition of the CI type specimen. *Geochim. Cosmochim. Acta* **268**, 73–89 (2020). doi: 10.1016/j.gca.2019.09.041
72. R. C. Reedy, Solar-proton production of neon and argon. *Proc. Lunar Planet. Sci. Conf.* **23**, 1133–1134 (1992).
73. J. F. Ziegler, SRIM-2003. *Nucl. Instrum. Methods Phys. Res. B* **219–220**, 1027–1036 (2004). doi: 10.1016/j.nimb.2004.01.208
74. M. Honda *et al*., Redetermination of the ^{21}Ne relative abundance of the atmosphere, using a high resolution, multi-collector noble gas mass spectrometer (HELIX-MC Plus). *Int. J. Mass Spectrom.* **387**, 1–7 (2015). doi: 10.1016/j.ijms.2015.05.012

ACKNOWLEDGMENTS

We thank the anonymous reviewers for their helpful comments and suggestions. Hayabusa2 was developed by JAXA, in collaboration with the German Aerospace Center, the Centre National d'Études Spatiales, NASA, and other universities, institutes, and companies in Japan. The sampler system was developed by JAXA, the University of Tokyo, Hokkaido University, Kyushu University, the Japan Agency for Marine-Earth Science and Technology, and other universities, institutes, and companies in Japan. **Funding:** R.O. was supported by JSPS KAKENHI (grants JP19H01959 and JP20H05846). B.M., E.F., M.W.B., and D.B. were supported by the European Research Council (PHOTONIS Advanced Grant 695618 and VOLATILIS Starting Grant 715028) and by the Centre National d'Etudes Spatiales (CNES). The work by D.K., M.E.I.R., and H.B. was carried out within the framework of the NCCR Planets and the Ambizione program supported by the Swiss NSF (grants 200020_182649, 51NF40-182901, and PZ00P2_193331). J.D.G., S.A.C., T.L., and L.F. were funded by STFC grants ST/R000751/1 and ST/V000675/1. P.C. was supported by UKRI FLF grant MR/S03465X/1. K.Has. and A.Is. were supported by JSPS KAKENHI Grant JP20H00190. **Author contributions:** R.O. led the sample preparation and noble gas mass spectrometry (NG-MS) analysis at Kyushu Univeristy with Y.N.M. R.O. wrote the paper, with contributions from B.M., H.B., K.Has., J.D.G., A.Me., T.Yad., F.K., M.W.B., D.B., E.F., M.E.I.R., D.K., C.M., A.Is., P.C., S.A.C., L.F., T.L., O.P., Y.N.M., J.P., K.B., Y.Taka., K.Ya., S.Ka., Y.Ma., M.Yamam., K.R., S.Sa., N.I., N.Sh., S.Se., M.In., M.E., R.Y., K.Ni., K.Na., J.I.L., A.K., M.W.C., and R.U. Hayabusa2 capsule recovery and curation was led by H.Sa., S.Tac., Y.N.M., K.Sa., Y.Taka., H.Yan., and R.O. FESEM and EDS analyses at JAXA were led by T.Yad. FTIR spectroscopy at JAXA was led by F.K. Nitrogen and NG-MS analyses at CRPG Nancy were led by M.W.B., B.M., D.B., and E.F. Xe-MS analysis at the University of Manchester was led by J.D.G., T.L., S.A.C., and L.F. NG-MS analysis at Washington University in St. Louis was led by A.Me. and O.P. NG-MS analysis at ETH Zürich was performed by H.B., D.K., C.M., and M.E.I.R. Nitrogen and NG-MS analyses at Ibaraki University were led by K.Has. and A.Is. All authors discussed the results and commented on the manuscript. **Competing interests:** The authors declare that they have no competing interests. **Data and materials availability:** Our numerical measurements are listed in tables S2 and S3 and data S1. The images and simulation results used in this paper are available on the JAXA Data Archives and Transmission System (DARTS) at https://data.darts.isas.jaxa.jp/pub/hayabusa2/paper/sample/Okazaki_2022a. The input parameters used in the simulation are provided in the supplementary materials (*21*). Data for all Hayabusa2 samples and other data from the mission are available at https://www.darts.isas.jaxa.jp/curation/hayabusa2 and https://www.darts.isas.jaxa.jp/planet/project/hayabusa2/, respectively. The samples of Ryugu are curated by the JAXA Astromaterials Science Research Group; distribution for analysis is through an Announcement of Opportunity available at https://jaxa-ryugu-sample-ao.net. The samples we used are listed in table S1. **License information:** Copyright © 2023 the authors, some rights reserved; exclusive licensee American Association for the Advancement of Science. No claim to original US government works. https://www.science.org/about/science-licenses-journal-article-reuse

SUPPLEMENTARY MATERIALS

science.org/doi/10.1126/science.abo0431
Materials and Methods
Supplementary Text
Figs. S1 to S9
Tables S1 to S3
References (*75*–*96*)
Data S1

Submitted 10 January 2022; accepted 5 October 2022
Published online 20 October 2022
10.1126/science.abo0431

RESEARCH ARTICLE SUMMARY

COSMOCHEMISTRY

Soluble organic molecules in samples of the carbonaceous asteroid (162173) Ryugu

Hiroshi Naraoka *et al.*

INTRODUCTION: Surface material from the near-Earth carbonaceous (C-type) asteroid (162173) Ryugu was collected and brought to Earth by the Hayabusa2 spacecraft. Ryugu is a dark, primitive asteroid containing hydrous minerals that are similar to the most hydrated carbonaceous meteorites. C-type asteroids are common in the asteroid belt and have been proposed as the parent bodies of carbonaceous meteorites. The samples of Ryugu provide an opportunity to investigate organic compounds for comparison with those from carbonaceous meteorites. Unlike meteorites, the Ryugu samples were collected and delivered for study under controlled conditions, reducing terrestrial contamination and the effects of atmospheric entry.

RATIONALE: Primitive carbonaceous chondrite meteorites are known to contain a variety of soluble organic molecules (SOMs), including prebiotic molecules such as amino acids. Meteorites might have delivered amino acids and other prebiotic organic molecules to the early Earth and other rocky planets. Organic matter in the Ryugu samples is the product of physical and chemical processes that occurred in the interstellar medium, the protosolar nebula, and/or on the planetesimal that became Ryugu's parent body. We investigated SOMs in Ryugu samples principally using mass spectrometry coupled with liquid or gas chromatography.

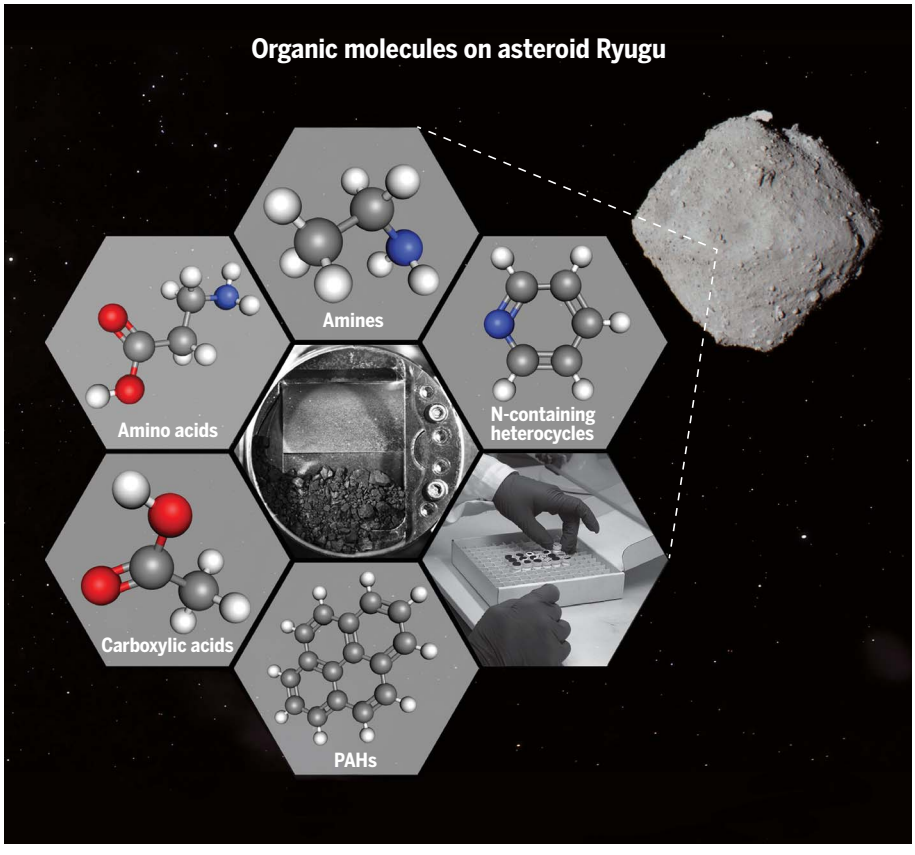

SOMs detected in surface samples of asteroid Ryugu. Chemical structural models are shown for example molecules from several classes identified in the Ryugu samples. Gray balls are carbon, white are hydrogen, red are oxygen, and blue are nitrogen. Clockwise from top: amines (represented by ethylamine), nitrogen-containing heterocycles (pyridine), a photograph of the sample vials for analysis, polycyclic aromatic hydrocarbons (PAHs) (pyrene), carboxylic acids (acetic acid), and amino acids (β-alanine). The central hexagon shows a photograph of the Ryugu sample in the sample collector of the Hayabusa2 spacecraft. The background image shows Ryugu in a photograph taken by Hayabusa2.

RESULTS: We identified numerous organic molecules in the Ryugu samples. Mass spectroscopy detected hundreds of thousands of ion signals, which we assigned to ~20,000 elementary compositions consisting of carbon, hydrogen, nitrogen, oxygen, and/or sulfur. Fifteen amino acids, including glycine, alanine, and α-aminobutyric acid, were identified. These were present as racemic mixtures (equal right- and left-handed abundances), consistent with an abiotic origin. Aliphatic amines (such as methylamine) and carboxylic acids (such as acetic acid) were also detected, likely retained on Ryugu as organic salts.

The presence of aromatic hydrocarbons, including alkylbenzenes, fluoranthene, and pyrene, implies hydrothermal processing on Ryugu's parent body and/or presolar synthesis in the interstellar medium. Nitrogen-containing heterocyclic compounds were identified as their alkylated homologs, which could have been synthesized from simple aldehydes and ammonia. In situ analysis of a grain surface showed heterogeneous spatial distribution of alkylated homologs of nitrogen- and/or oxygen-containing compounds.

CONCLUSION: The wide variety of molecules identified indicates that prolonged chemical processes contributed to the synthesis of soluble organics on Ryugu or its parent body. The highly diverse mixture of SOMs in the samples resembles that seen in some carbonaceous chondrites. However, the SOM concentration in Ryugu is less than that in moderately aqueously altered CM (Mighei-type) chondrites, being more similar to that seen in warm aqueously altered CI (Ivuna-type) chondrites. The chemical diversity with low SOM concentration in Ryugu is consistent with aqueous organic chemistry at modest temperatures on Ryugu's parent asteroid.

The samples collected from the surface of Ryugu were exposed to the hard vacuum of space, energetic particle irradiation, heating by sunlight, and micrometeoroid impacts, but the SOM is still preserved, likely by being associated with minerals. The presence of prebiotic molecules on the asteroid surface suggests that these molecules can be transported throughout the Solar System. ■

The complete list of authors and their affiliations is available in the full article online.
*Corresponding author. Email: naraoka@geo.kyushu-u.ac.jp
Cite this article as H. Naraoka *et al.*, *Science* **379**, eabn9033 (2023). DOI: 10.1126/science.abn9033

READ THE FULL ARTICLE AT
https://doi.org/10.1126/science.abn9033

CREDIT: JAXA, UNIVERSITY OF TOKYO, KOCHI UNIVERSITY, RIKKYO UNIVERSITY, NAGOYA UNIVERSITY, CHIBA INSTITUTE OF TECHNOLOGY, MEIJI UNIVERSITY, UNIVERSITY OF AIZU, AIST, NASA, DAN GALLAGHER

RESEARCH ARTICLE

COSMOCHEMISTRY

Soluble organic molecules in samples of the carbonaceous asteroid (162173) Ryugu

Hiroshi Naraoka[1]*, Yoshinori Takano[2], Jason P. Dworkin[3], Yasuhiro Oba[4], Kenji Hamase[5], Aogu Furusho[5]†, Nanako O. Ogawa[2], Minako Hashiguchi[6], Kazuhiko Fukushima[7], Dan Aoki[7], Philippe Schmitt-Kopplin[8,9,10], José C. Aponte[3], Eric T. Parker[3], Daniel P. Glavin[3], Hannah L. McLain[3,11,12], Jamie E. Elsila[3], Heather V. Graham[3], John M. Eiler[13], Francois-Regis Orthous-Daunay[14], Cédric Wolters[14], Junko Isa[15,16], Véronique Vuitton[14], Roland Thissen[17], Saburo Sakai[2], Toshihiro Yoshimura[2], Toshiki Koga[2], Naohiko Ohkouchi[2], Yoshito Chikaraishi[4], Haruna Sugahara[18], Hajime Mita[19], Yoshihiro Furukawa[20], Norbert Hertkorn[8], Alexander Ruf[21,22,23], Hisayoshi Yurimoto[24], Tomoki Nakamura[20], Takaaki Noguchi[25], Ryuji Okazaki[1], Hikaru Yabuta[26], Kanako Sakamoto[18], Shogo Tachibana[18,27], Harold C. Connolly, Jr.[28], Dante S. Lauretta[29], Masanao Abe[18,30], Toru Yada[18], Masahiro Nishimura[18], Kasumi Yogata[18], Aiko Nakato[18], Miwa Yoshitake[18], Ayako Suzuki[31], Akiko Miyazaki[18], Shizuho Furuya[27], Kentaro Hatakeda[31], Hiromichi Soejima[31], Yuya Hitomi[31], Kazuya Kumagai[31], Tomohiro Usui[18], Tasuku Hayashi[18], Daiki Yamamoto[18], Ryota Fukai[18], Kohei Kitazato[32], Seiji Sugita[16,27], Noriyuki Namiki[30,33], Masahiko Arakawa[34], Hitoshi Ikeda[18], Masateru Ishiguro[35], Naru Hirata[31], Koji Wada[16], Yoshiaki Ishihara[36], Rina Noguchi[37], Tomokatsu Morota[27], Naoya Sakatani[38], Koji Matsumoto[30,33], Hiroki Senshu[16], Rie Honda[39], Eri Tatsumi[40], Yasuhiro Yokota[18], Chikatoshi Honda[32], Tatsuhiro Michikami[41], Moe Matsuoka[18]§, Akira Miura[18], Hirotomo Noda[30,33], Tetsuya Yamada[18], Keisuke Yoshihara[18], Kosuke Kawahara[18], Masanobu Ozaki[18,30], Yu-ichi Iijima[18]‡, Hajime Yano[18,30], Masahiko Hayakawa[18], Takahiro Iwata[18], Ryudo Tsukizaki[18], Hirotaka Sawada[18], Satoshi Hosoda[18], Kazunori Ogawa[42], Chisato Okamoto[34]‡, Naoyuki Hirata[33], Kei Shirai[33], Yuri Shimaki[18], Manabu Yamada[16], Tatsuaki Okada[18,43], Yukio Yamamoto[18,30], Hiroshi Takeuchi[18,30], Atsushi Fujii[18], Yuto Takei[18], Kento Yoshikawa[36], Yuya Mimasu[18], Go Ono[36], Naoko Ogawa[18], Shota Kikuchi[16,33], Satoru Nakazawa[18], Fuyuto Terui[44], Satoshi Tanaka[18,30], Takanao Saiki[18], Makoto Yoshikawa[18,30], Sei-ichiro Watanabe[6], Yuichi Tsuda[18]

The Hayabusa2 spacecraft collected samples from the surface of the carbonaceous near-Earth asteroid (162173) Ryugu and brought them to Earth. The samples were expected to contain organic molecules, which record processes that occurred in the early Solar System. We analyzed organic molecules extracted from the Ryugu surface samples. We identified a variety of molecules containing the atoms CHNOS, formed by methylation, hydration, hydroxylation, and sulfurization reactions. Amino acids, aliphatic amines, carboxylic acids, polycyclic aromatic hydrocarbons, and nitrogen-heterocyclic compounds were detected, which had properties consistent with an abiotic origin. These compounds likely arose from an aqueous reaction on Ryugu's parent body and are similar to the organics in Ivuna-type meteorites. These molecules can survive on the surfaces of asteroids and be transported throughout the Solar System.

A variety of organic molecules have been identified in carbonaceous chondrite meteorites, especially the meteorite types that experienced aqueous alteration (reactions with liquid water). Prebiotic molecules, such as amino acids, have been found in meteorite soluble organic matter (SOM) (*1*), suggesting that they could have been delivered to the early Earth (*2*, *3*). It is unclear which Solar System objects are the parent bodies of carbonaceous chondrites (*4*). Carbonaceous (C-type) asteroids, common in the asteroid belt, have been hypothesized as possible parent bodies of carbonaceous chondrites on the basis of spectroscopic similarities (*5*).

The Hayabusa2 spacecraft investigated the near-Earth C-type asteroid (162173) Ryugu. Ryugu has a low-albedo surface consisting of hydrous minerals and carbonaceous materials (*6*). Hayabusa2 collected ~5 g of samples from Ryugu's surface and delivered them to Earth on 6 December 2020 (*7*). Unlike meteorites, these samples were collected from a specific spot on the surface of a well-characterized asteroid and were retrieved without contamination from the biosphere. We analyzed Ryugu samples to characterize their SOM contents with the goal of determining the evolutionary history of these organic compounds. Organics could have formed and/or been modified by chemical processes in the molecular cloud from which the Solar System formed, in the protosolar nebula during the process of planet formation or on the planetesimal that became the parent body of Ryugu. Because the surface of Ryugu is exposed to the vacuum of space, irradiation by energetic particles (cosmic rays), heating by sunlight, and micrometeoroid impacts all could have altered the SOM.

Ryugu samples investigated for SOM

All Ryugu samples are dominated by hydrous silicate minerals and contain organic matter similar to Ivuna-type carbonaceous (CI) chondrites (*8*). We investigated two samples, both collected during the first Hayabusa2 touchdown operation on 21 February 2019 (*7*, *9*).

Our main analysis was performed on an aggregate sample designated A0106 (fig. S1), consisting of grains <1 mm diameter with a total weight of 38.4 mg, which has elsewhere been investigated spectroscopically (*10*) and had its elemental and isotopic compositions analyzed (*11*). The A0106 sample has typical mineralogy for Ryugu consisting mainly of hydrous silicate minerals, including serpentine and saponite, with other associated minerals such as dolomite, pyrrhotite, and magnetite, indicating extensive aqueous alteration (*10*). We used solvent extracts to investigate the organic molecule content of A0106 following the analysis scheme shown in fig. S2. We also analyzed a single ~1-mm-sized grain (A0080) to determine the spatial distribution of organic compounds on its surface using in situ analysis methods (fig. S2).

Elemental and isotopic composition

Elemental and isotopic analyses were performed using mass spectrometry (*11*). The A0106 sample contained 3.76 ± 0.14 wt % of total carbon (C), 1.14 ± 0.09 wt % of total hydrogen (H), 0.16 ± 0.01 wt % of total nitrogen (N), and 3.3 ± 0.7 wt % of total sulfur (S). The concentration of pyrolyzed oxygen (O), liberated at 1400°C under a helium gas flow, was 12.9 ± 0.42 wt %. The total CHNOS content (~21.3 wt %) is likely to comprise hydrous minerals, carbonates, sulfides, and organics, including macromolecular insoluble organic matter and SOM, because these are detected in other Ryugu samples (*10*, *12*). The stable isotopic compositions were determined and are expressed in δ notations as offsets from international standards (*11*): $\delta^{13}C$ = −0.58 ± 2.0‰ relative to the Vienna Peedee Belemnite (VPDB) isotope reference, δD = +252 ± 13‰ relative to the Vienna Standard Mean Ocean Water (VSMOW) isotope reference, $\delta^{15}N$ = +43.0 ± 9.0‰ relative to Earth atmospheric nitrogen, $\delta^{34}S$ = −3.0 ± 2.3‰ relative to the Vienna Canyon Diablo Troilite (VCDT) isotope reference, and $\delta^{18}O$ = +12.6 ± 2.0‰ relative to VSMOW [all analyses were done in triplicate (*11*)]. Because we analyzed small aggregate grains from the first touchdown site, we consider these values representative of the average bulk composition of Ryugu. The corresponding elemental ratios (by weight) were: C/N ratio = 23.5 ± 0.4, O/H ratio = 11.4 ± 0.6, and C/S ratio = 1.15 for A0106 (table S1).

The C, N, and H abundances are at the top of the ranges previously measured for carbonaceous chondrites (Fig. 1, A to D, and table S2). Our measured abundances of C, H, and S are consistent with an independent bulk chemical analysis using ~25 mg of the Ryugu samples, which suggests that Ryugu has a composition more similar to CI chondrites than to other types of meteorite (*12*). The heavy isotope enrichments of H (δD ~+250‰) and N ($\delta^{15}N$ ~ +40‰) that we found in Ryugu are similar to previous analyses of the Ivuna and Orgueil CI chondrites (*13*) (Fig. 1, E and F). However, elemental and isotopic heterogeneities on small scales have been found in other Ryugu samples (*14*, *15*).

Diversity of organic molecules

We performed mass spectrometry on a methanol extract of the A0106 sample using electrospray ionization (ESI) and atmospheric pressure photoionization (APPI), coupled with Fourier transform–ion cyclotron resonance mass spectrometry (FT-ICR/MS) (*11*). These produced hundreds of thousands of ion signals with a mass to charge ratio (m/z) between 150 and 700 (Fig. 2, A, B, and F). The m/z signals obtained by negative charge ESI [ESI(−)], positive charge ESI [ESI(+)], and positive charge APPI [APPI(+)] were assigned to almost 20,000 elementary compositions consisting of C, H, N, O, and/or S (Fig. 2, C to F, and fig. S3). This diversity of compounds is consistent with previous results for carbonaceous chondrites (*16*). The chemical diversity of ionizable species (small molecules detectable with mass spectrometry) is much higher than terrestrial biological samples.

We identified a continuum of small molecules to macromolecules, with a range of carbon oxidation states from nonpolar or minimally polar (CH-containing, polycyclic aromatic hydrocarbons, and branched aliphatic molecules) to polar small molecules (CHO-containing) with various functional groups (CHN, CHS, CHNO, CHOS, or CHNOS) with different solubility. The most intense signals in the mass spectra were assigned to polythionates (Fig. 2A), indicating formation through a complex sulfur polymer chemistry governed by redox processes involving water-mineral interactions with metal sulfides. A homologous series of known molecular targets (CHN^+ or $CHNO^+$) has previously been observed in a solvent extract of the Murchison meteorite, a different type of carbonaceous chondrite (*17*). The Ryugu data contain an abundant series of signals with repetitive mass differences, which we interpret as evidence for a systematic reaction network including methylation, hydration, hydroxylation, and sulfurization. We did not detect magnesium-containing organic compounds such as CHOMg or CHOSMg, which have been observed in other chondritic meteorites including Murchison (*18*). The compound distribution indicates low-temperature (≲150°C) hydrothermal processing on Ryugu's parent body (*19*). The high diversity of N- and S-bearing molecules in Ryugu indicates that chemical processes occurred involving N and S chemistry (*20*, *21*).

Amino acids

We searched for amino acids in an acid-hydrolyzed hot water extract of the A0106 sample using a combination of three-dimensional high performance liquid chromatography with a high-sensitivity fluorescence detector (3D-HPLC/FD) at Kyushu University and ultrahigh performance liquid chromatography with fluorescence detection and high-resolution mass spectrometry (LC-FD/HRMS) at Goddard Space Flight Center (Fig. 3 and table S3). A total of 15 amino acids were both detected and quantified, and an additional five amino acids were tentatively identified but not quantified. These included proteinogenic (used by biology to form proteins) amino acids such as glycine ($C_2H_5NO_2$), D,L-alanine ($C_3H_7NO_2$), and D,L-valine ($C_5H_{11}NO_2$), as well as nonproteinogenic amino acids including β-alanine ($C_3H_7NO_2$); D,L-α-amino-*n*-butyric acid ($C_4H_9NO_2$); D,L-β-amino-*n*-butyric acid ($C_4H_9NO_2$); and several isomers of valine: D,L-norvaline, D,L-isovaline, and δ-amino-*n*-valeric acid (Fig. 3). The concentrations of each amino acid ranged from ~0.01 to 5.6 nmol g^{-1} (table S3).

Many of the nonproteinogenic amino acids identified in the Ryugu extract are rare or nonexistent in terrestrial biology. The chiral amino acids detected in Ryugu are in approximately racemic mixtures [the abundance of the D- and L-enantiomers are approximately equal (D/L ~ 1)], indicating nonbiological origins. The detection of approximately equal amounts of D- and L-alanine, a common proteinogenic amino acid, indicates that this Ryugu sample is pristine, with negligible biological L-amino acid contamination. However, there were excesses of L-serine and L-valine. There was a trace (picomole levels) of L-valine content in procedural solvent blanks, so contamination is likely the cause of the nonracemic valine in the A0106 extract.

There are differences in the amino acid concentrations measured using LC-FD/HRMS and 3D-HPLC/FD, which we attribute to different acid hydrolysis conditions and analytical techniques. Different sample preparation and analysis approaches are known to yield distinct results when investigating meteorite amino acids (*22*). The much lower glycine abundances measured by LC-FD/HRMS (~0.6 nmol g^{-1}) than by 3D-HPLC/FD (5.6 nmol g^{-1}) could have been the result of multiple evaporation steps implemented during sample preparation before LC-FD/HRMS analysis. These evaporation steps could have resulted in the additional loss of volatile species such as hydrogen cyanide (HCN) and formaldehyde. HCN, formaldehyde, and ammonia can synthesize glycine under

[1]Department of Earth and Planetary Sciences, Kyushu University, Fukuoka 819-0395, Japan. [2]Biogeochemistry Research Center, Japan Agency for Marine-Earth Science and Technology, Yokosuka 237-0061, Japan. [3]Solar System Exploration Division, NASA Goddard Space Flight Center, Greenbelt, MD 20771, USA. [4]Institute of Low Temperature Science, Hokkaido University, Sapporo 060-0189, Japan. [5]Graduate School of Pharmaceutical Sciences, Kyushu University, Fukuoka 812-8582, Japan. [6]Graduate School of Environmental Studies, Nagoya University, Nagoya 464-8601, Japan. [7]Graduate School of Bioagricultural Sciences, Nagoya University, Nagoya 464-8601, Japan. [8]Helmholtz Munich, Analytical BioGeoChemistry, 85764 Neuherberg, Germany. [9]Technische Universität München, Analytische Lebensmittel Chemie, 85354 Freising, Germany. [10]Max Planck Institute for Extraterrestrial Physics, 85748 Garching bei München, Germany. [11]Center for Research and Exploration in Space Science and Technology, NASA Goddard Space Flight Center, Greenbelt, MD 20771, USA. [12]Department of Physics, The Catholic University of America, Washington, DC 20064, USA. [13]Division of Geological and Planetary Sciences, California Institute of Technology, Pasadena, CA 91125, USA. [14]Université Grenoble Alpes, Centre National de la Recherche Scientifique (CNRS), Centre National d'Etudes Spatiales, L'Institut de Planétologie et d'Astrophysique de Grenoble, 38000 Grenoble, France. [15]Earth-Life Science Institute, Tokyo Institute of Technology, Tokyo 152-8550, Japan. [16]Planetary Exploration Research Center, Chiba Institute of Technology, Narashino 275-0016, Japan. [17]Université Paris-Saclay, CNRS, Institut de Chimie Physique, 91405 Orsay, France. [18]Institute of Space and Astronautical Science, Japan Aerospace Exploration Agency (JAXA), Sagamihara 252-5210, Japan. [19]Department of Life, Environment and Material Science, Fukuoka Institute of Technology, Fukuoka 811-0295, Japan. [20]Department of Earth Science, Tohoku University, Sendai 980-8578, Japan. [21]Université Aix-Marseille, CNRS, Laboratoire de Physique des Interactions Ioniques et Moléculaires, 13397 Marseille, France. [22]Department of Chemistry and Pharmacy, Ludwig-Maximilians-University, 81377 Munich, Germany. [23]Excellence Cluster ORIGINS, 85748 Garching, Germany. [24]Department of Earth and Planetary Sciences, Hokkaido University, Sapporo 060-0810, Japan. [25]Division of Earth and Planetary Sciences, Kyoto University, Kyoto 606-8502, Japan. [26]Department of Earth and Planetary Systems Science, Hiroshima University, Higashi-Hiroshima 739-8526, Japan. [27]Department of Earth and Planetary Science, University of Tokyo, Tokyo 113-0033, Japan. [28]Department of Geology, School of Earth and Environment, Rowan University, Glassboro, NJ 08028, USA. [29]Lunar and Planetary Laboratory, University of Arizona, Tucson, AZ 85721, USA. [30]School of Physical Sciences, The Graduate University for Advanced Studies, Hayama 240-0193, Japan. [31]Marine Works Japan Ltd., Yokosuka 237-0063, Japan. [32]Aizu Research Cluster for Space Science, University of Aizu, Aizu-Wakamatsu 965-8580, Japan. [33]Research of Interior Structure and Evolution of Solar System Bodies, National Astronomical Observatory of Japan, Mitaka 181-8588, Japan. [34]Department of Planetology, Kobe University, Kobe 657-8501, Japan. [35]Department of Physics and Astronomy, Seoul National University, Seoul 08826, Republic of Korea. [36]Research and Development Directorate, JAXA, Sagamihara 252-5210, Japan. [37]Faculty of Science, Niigata University, Niigata 950-2181, Japan. [38]Department of Physics, Rikkyo University, Tokyo 171-8501, Japan. [39]Center of Data Science, Ehime University, Matsuyama 790-8577, Japan. [40]Instituto de Astrofísica de Canarias, University of La Laguna, Tenerife E-38205, Spain. [41]Faculty of Engineering, Kindai University, Higashi-Hiroshima 739-2116, Japan. [42]JAXA Space Exploration Center, JAXA, Sagamihara 252-5210, Japan. [43]Department of Chemistry, University of Tokyo, Tokyo 113-0033, Japan. [44]Department of Mechanical Engineering, Kanagawa Institute of Technology, Atsugi 243-0292, Japan.

***Corresponding author. Email: naraoka@geo.kyushu-u.ac.jp** †Present address: School of Pharmaceutical Sciences, University of Shizuoka, Shizuoka 422-8526, Japan.
‡Deceased. §Present address: Geological Survey of Japan, National Institute of Advanced Industrial Science and Technology, Tsukuba 305-8567, Japan.

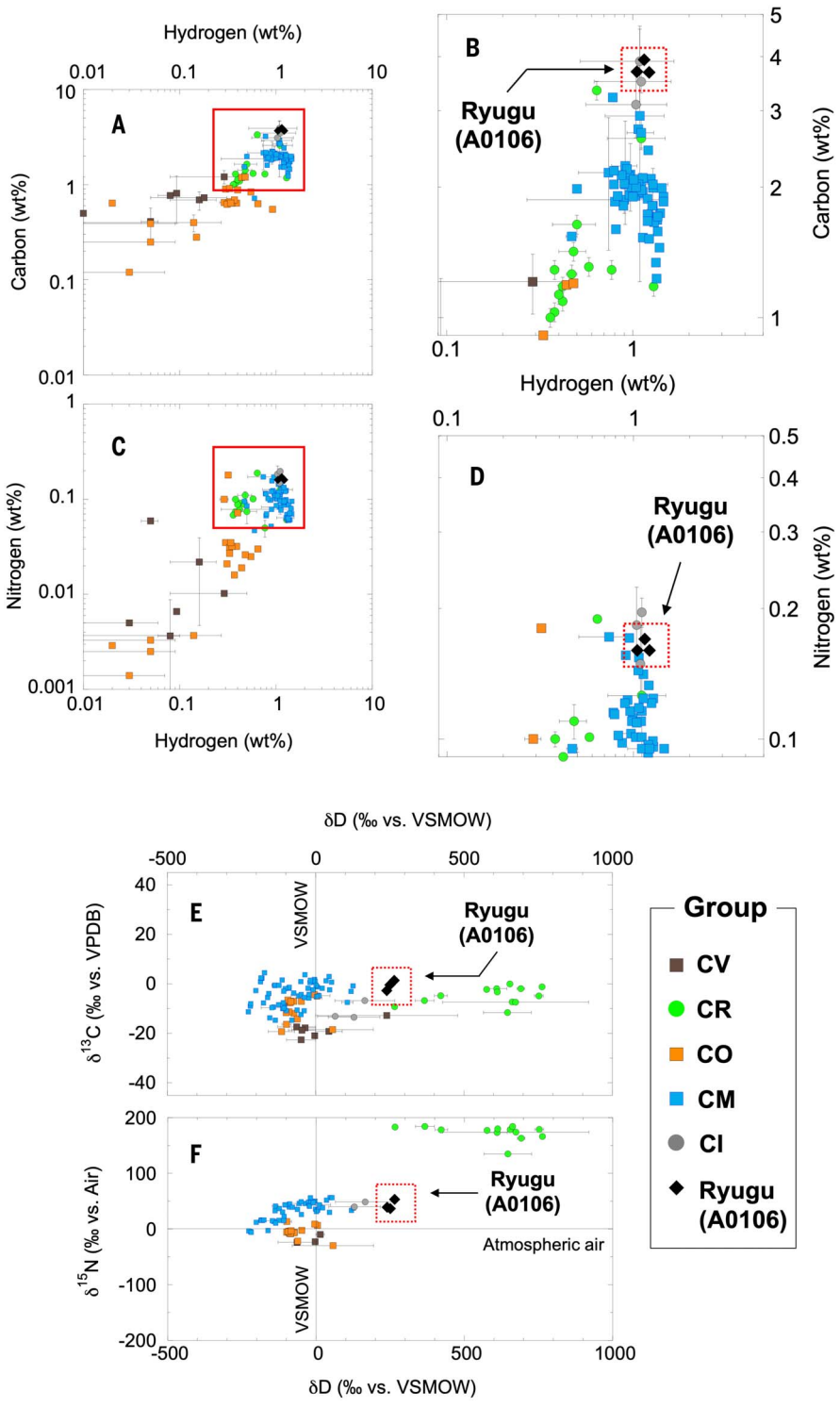

Fig. 1. Carbon, nitrogen, and hydrogen contents and stable isotopic compositions for the Ryugu sample A0106 compared with carbonaceous chondrites. Shown are: H-C (wt %) (**A**), enlarged H-C (wt %) (**B**), H-N (wt %) (**C**), enlarged H-N (wt %) (**D**), δD-δ^{13}C (‰) (**E**), and δD-δ^{15}N (‰) (**F**). Symbols shown in the legend indicate different groups of carbonaceous chondrite: Vigarano-type (CV), Renazzo-type (CR), Ornans-type (CO), Mighei-type (CM), and Ivuna-type (CI). Ryugu is most similar to the CI chondrites. Data sources for the carbonaceous chondrites are listed in table S2. Error bars are 1 SD for C, H and δD, and 2 SDs for N, δ^{13}C, and δ^{15}N.

alkaline conditions (Strecker synthesis) such as during sample preparation (*11*).

The overall amino acid distribution in the Ryugu extract is distinct from that in the CI meteorite Orgueil, with Ryugu also having lower amino acid abundances than Orgueil (*23*) (table S3). This could reflect different chemical formation environments or subsequent alteration conditions on their parent bodies. It is possible that Strecker synthesis could have been active during parent body aqueous alteration, producing glycine and other α-amino acids (those with an amino group one bond away from a carbonyl carbon) identified in the Ryugu extract. However, other amino acid formation and fractionation mechanisms must also have occurred on the Ryugu parent body, because β-, γ-, and δ-amino acids were also found (table S3). The straight-chain *n*-ω-amino acids, β-alanine, γ-amino-*n*-butyric acid, and δ-amino-*n*-valeric acid have higher abundances than other amino acids measured by LC-FD/HRMS in the Ryugu extract (table S3). This trend was similarly observed in previous measurements of thermally altered CO (Ornans-type) and CV (Vigarano-type) carbonaceous chondrites (*24*). These non–α-amino acids have been shown to be more resistant to thermal decomposition, surviving at temperatures up to ~300°C (*25*, *26*), which could explain their higher abundances (relative to α-amino acids) in the Ryugu sample.

Aliphatic amines and carboxylic acids

Hot water extracts of A0106 were measured using liquid chromatography with fluorescence detection and time-of-flight mass spectrometry (LC-FD/TOFMS) (*11*). Aliphatic amines were detected (Fig. 4); methylamine (CH_3NH_2) was the most abundant, followed by ethylamine ($C_2H_5NH_2$) and isopropylamine [$(CH_3)_2CHNH_2$], then *n*-propylamine ($C_3H_7NH_2$). These amines are likely present as salts in the grains, because the free amines are highly volatile and reactive (boiling point; ~267 K for free CH_3NH_2 at 1013 hPa compared with ~503 K for CH_3NH_2 hydrochloride at ~20 hPa). We applied the same technique to hexane and dichloromethane (DCM) extracts of A0106, but did not find other volatile compounds that have previously been detected in carbonaceous chondrites, such as methanol (CH_3OH), ethanol (C_2H_5OH), methyl formate ($HCOOCH_3$), acetone (CH_3COCH_3), diethyl ether ($C_2H_5OC_2H_5$), or acetonitrile (CH_3CN), which were all below the detection limits (fig. S4). This is consistent with our interpretation that the amines were retained as salts, not trapped volatiles in inclusions, insoluble organic material, or minerals. Ammonium salts (and amine salts) are known to be the major reservoir of nitrogen on the dwarf planet Ceres and in comets (*27*, *28*). A previous hyperspectral microscope study of Ryugu grains found evidence of amine or ammonium bonds (NH; ~3.1 μm) (*29*).

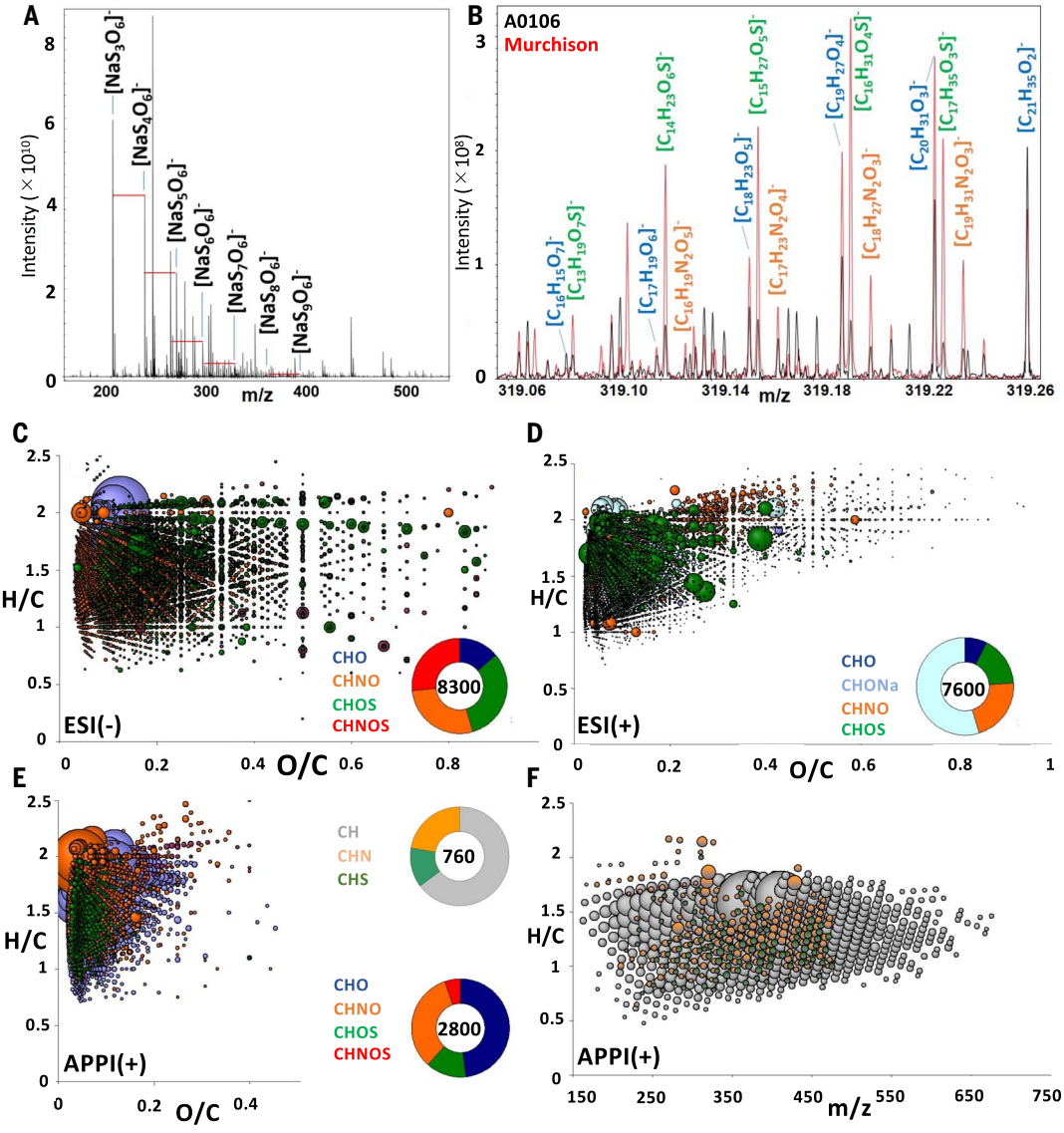

Fig. 2. Mass spectra of the Ryugu extract and derived elemental compositions. (**A**) Mass spectrum of negative ESI FT-ICR/MS with peaks assigned polythionates with three to nine sulfur atoms. (**B**) Detail around *m/z* = 319 with annotated elementary compositions, with Ryugu (black) compared with the Murchison meteorite (red) (*16*). (**C** to **E**) O/C-H/C atomic ratios of the compositional data as obtained with ESI(−) (C), ESI(+) (D), and APPI(+) (E). Colored annuli enclose the number of molecules assigned, with colors indicating the relative ratios of the chemical families (indicated in each legend). Data points use the same colors to indicate the family, and the size of each bubble indicates the intensity of the signal in the mass spectrum. (**F**) H/C atomic ratio as a function of *m/z*, measured using APPI(+), for nonoxygenated CH, CHN, and CHS compositions; colors are the same as used in (E). Figure S3 shows separate plots of each chemical family identified in (C) to (E).

Isopropyl amine, which has a branched chain, was more abundant than straight-chain propylamine. This is consistent with previous results for several carbonaceous chondrites (*30*, *31*). The predominance of branched chains could indicate that synthesis of these molecules occurred by a radical reaction. Alternatively, it might indicate a period of heating during aqueous alteration, because branched-chain carbon compounds are more thermodynamically stable than their straight-chain counterparts. The presence of methyl-, ethyl-, and propylamines in Ryugu is distinct from Orgueil, which contains butylamines ($C_4H_9NH_2$) at about half the abundance of *n*-propylamine (*32*). If this same ratio occurred in the Ryugu sample, butylamines would have been above the detection limits. The amines in Ryugu are also unlike the dust grains collected from the comet Wild 2 by the Stardust mission, for which only methyl- and ethylamine were detected (*33*).

Monocarboxylic acids (MCAs) were searched for using gas chromatography quadrupole mass spectrometry of the hot water extract of A0106. Formic acid (5.7 μmol g^{-1}) and acetic acid (9.5 μmol g^{-1}) were detected, and were the only MCAs above the detection limits (fig. S5 and table S4). MCAs are typically among the most abundant organic compounds in organic rich carbonaceous chondrites such as the CM (Mighei-type) meteorites Murchison and Murray and the CR (Renazzo-type) chondrites (*34*–*36*). We detected MCAs in A0106 with high concentrations and low molecular diversity, both consistent with low-temperature hydrothermal processing, as is thought to have occurred on Ryugu's parent body (*10*). The concentration of MCAs is known to decrease with increasing aqueous and/or thermal alteration experienced by meteorite samples (*36*, *37*). Although MCAs in A0106 have low molecular diversity, the concentrations of formic and acetic acids are high, similar to those observed in highly aqueously altered carbonaceous chondrites including ALH 83100 (a CM) and Orgueil and Ivuna (both CIs) (*38*, *39*). Aliphatic MCAs are substantially more abundant in the Ryugu sample than other structurally related organics such as aliphatic amino acids and amines. This is consistent with carbonaceous chondrites, for which the concentrations of MCAs (and most other meteoritic organic compounds) are known to decrease with increasing molecular weight (*1*, *36*). We found the same relationship between formic acid and acetic acid in A0106 (table S4).

Polycyclic aromatic hydrocarbons

We applied 2D gas chromatography with time-of-flight mass spectrometry (GC×GC-TOFMS) to the organic solvent extracts of the A0106 sample. We detected aromatic hydrocarbons at below parts per million abundances, including from alkylbenzenes

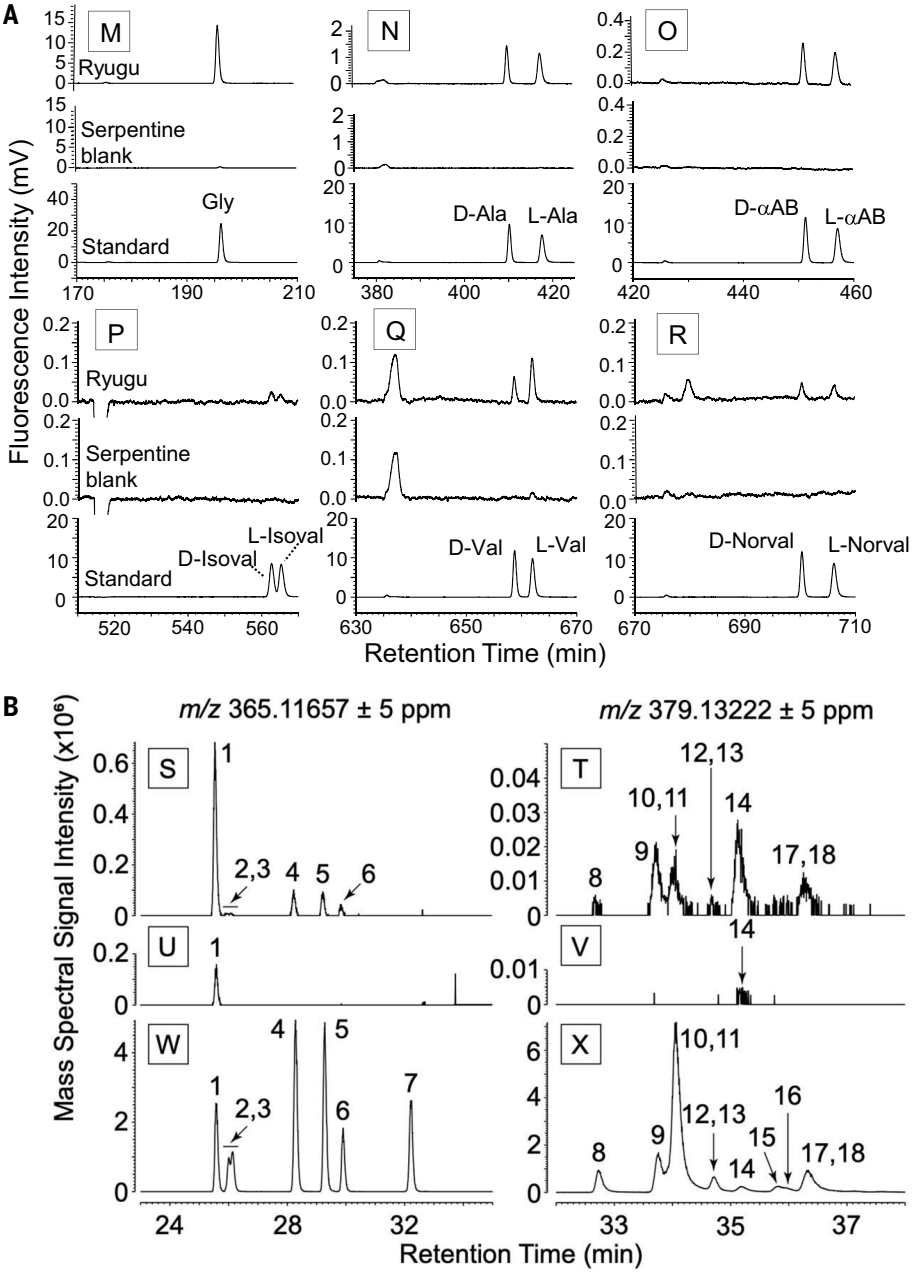

Fig. 3. Amino acids detected in the hydrolyzed hot water extract of the Ryugu sample. (**A**) Partial chromatograms obtained by 3D-HPLC/FD for glycine (Gly) (M), alanine (Ala) (N), α-amino-*n*-butyric acid (αAB) (O), isovaline (Isoval) (P), valine (Val) (Q), and norvaline (Norval) (R). In each panel, the Ryugu extract (top traces) is compared with baked serpentine blanks (middle traces) and terrestrial standards (lower traces). (**B**) Ion-extracted chromatograms from LC-FD/HRMS analysis of Ryugu sample (S and T), a serpentine blank (U and V), and mixed amino acid standards (W and X). Amino acids composed of four and five carbon atoms were detected in the Ryugu sample. Peak identifications are: (1) γ-amino-*n*-butyric acid, (2) D-β-amino-isobutyric acid, (3) L-β-amino-isobutyric acid, (4) D-β-amino-*n*-butyric acid, (5) L-β-amino-*n*-butyric acid, (6) α-amino-isobutyric acid, (7) D,L-α-amino-*n*-butyric acid, (8) 3-amino-2,2-dimethylbutyric acid, (9) γ-amino-*n*-valeric acid, (10) 3-amino-2-methylbutyric acid, (11) 4-amino-3-methylbutyric acid, (12) 3-amino-2-methylbutyric acid, (13) R-3-amino-2-ethylpropanoic acid, (14) δ-amino-*n*-valeric acid, (15) L-4-amino-2-methylbutyric acid, (16) D-4-amino-2-methylbutyric acid, (17) γ-amino-*n*-valeric acid, and (18) 3-amino-3-methylbutyric acid.

and polycyclic aromatic hydrocarbons (PAHs) (Fig. 5). Homologous series of large alkylated PAHs were identified using APPI FT-ICR/MS and assigned to methylation and hydration (Fig. 2C). The presence of alkylated PAHs (including alkylbenzenes) in the organic solvent extracts was confirmed using Fourier-transform infrared (FTIR) spectroscopy (*11*), which showed bands due to CH_2 or CH_3 bonds at 2850 to 2950 cm^{-1} (3.51 to 3.39 μm) (fig. S6A). The highest abundance PAHs were fluoranthene and pyrene (which contain four benzene rings) followed by chrysene/triphenylene (also four rings) and methylated fluoranthene and pyrene. Smaller PAHs containing two rings (naphthalene) and three rings (phenanthrene and anthracene) were detected at lower abundances.

Fluoranthene and pyrene are structural isomers (both have the formula $C_{16}H_{10}$) that are present in roughly equal amounts in CM chondrites (*40*–*42*). In the Ryugu sample, however, fluoranthene is substantially less abundant than pyrene (Fig. 5C). In the CI meteorite Ivuna, both fluoranthene and pyrene are below the detection limits, although phenanthrene and anthracene are abundant (*43*). Because selective synthesis is not expected to favor three- or four-ring PAHs, their variable relative abundances in meteorites could be due to aqueous fluid flow in their parent body. It has been proposed that three-ring and four-ring PAHs could be spatially separated during aqueous alteration of the Ivuna parent body because of their different aqueous solubilities (an effect known as asteroidal chromatography) (*44*). On Earth, hydrothermal petroleum often contains alkylbenzene and lower abundances of fluoranthene than of pyrene (*45*). Therefore, the difference in proportions of PAHs between Ryugu and carbonaceous chondrites could be due to different aqueous alteration effects on different parent bodies. However, we cannot rule out the possibility that the different proportions could be inherited from presolar syntheses in the interstellar medium, where PAHs are ubiquitous (*46*). PAHs with higher stability and lower volatility might have preferentially survived accretionary and hydrothermal processes on the parent body. For example, the higher thermal stability and lower volatility of pyrene over fluoranthene could have contributed to the unequal abundances of the two species in the Ryugu sample. Vaporization fractionation could be responsible for the lower abundance (compared with pyrene) of smaller PAHs such as naphthalene.

The FTIR spectrum of the fine suspended material in the water extract of the A0106 grain (fig. S6C) has its strongest absorption band at ~1000 cm^{-1} (~10 μm) due to silicates (Si-O bonds). Other bands are present at 750 to 1650 cm^{-1} (13.3 to 6.1 μm). Peaks at these wavelengths have often been observed in the interstellar medium (*47*) and have been assigned to large PAHs (*47*–*50*). The broad peaks at ~1400 cm^{-1} (7.14 μm) could also have a contribution from carbonates (*51*). The lack of the aromatic C–H stretching bands at ~3030 cm^{-1} (3.30 μm) suggests that the PAHs present in the Ryugu water extract are highly depleted in hydrogen, indicating large, unsaturated structures. Because small- to moderate-sized PAHs can be extracted with organic solvents such as DCM and methanol (MeOH), which we applied

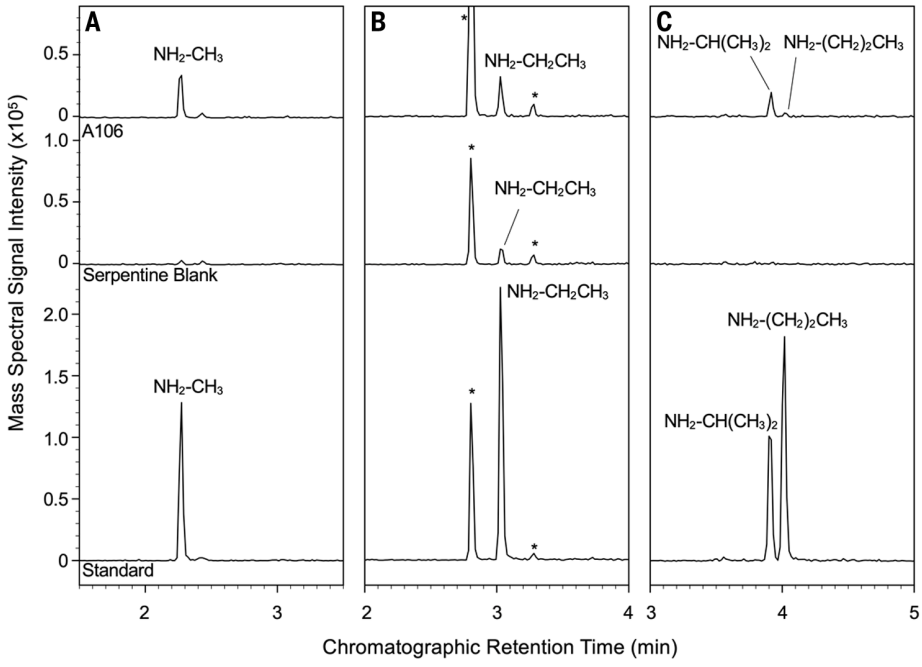

Fig. 4. Aliphatic amines in the hot water extract of Ryugu. Chromatograms were measured using LC-FD/TOFMS for methylamine (**A**), ethylamine (**B**), and n-propylamine and iso-propylamine (**C**). In each panel, the Ryugu sample (top trace) is compared with a baked serpentine blank (middle trace) and terrestrial standards (bottom trace). Asterisks indicate peaks introduced by the reagent used for derivatization.

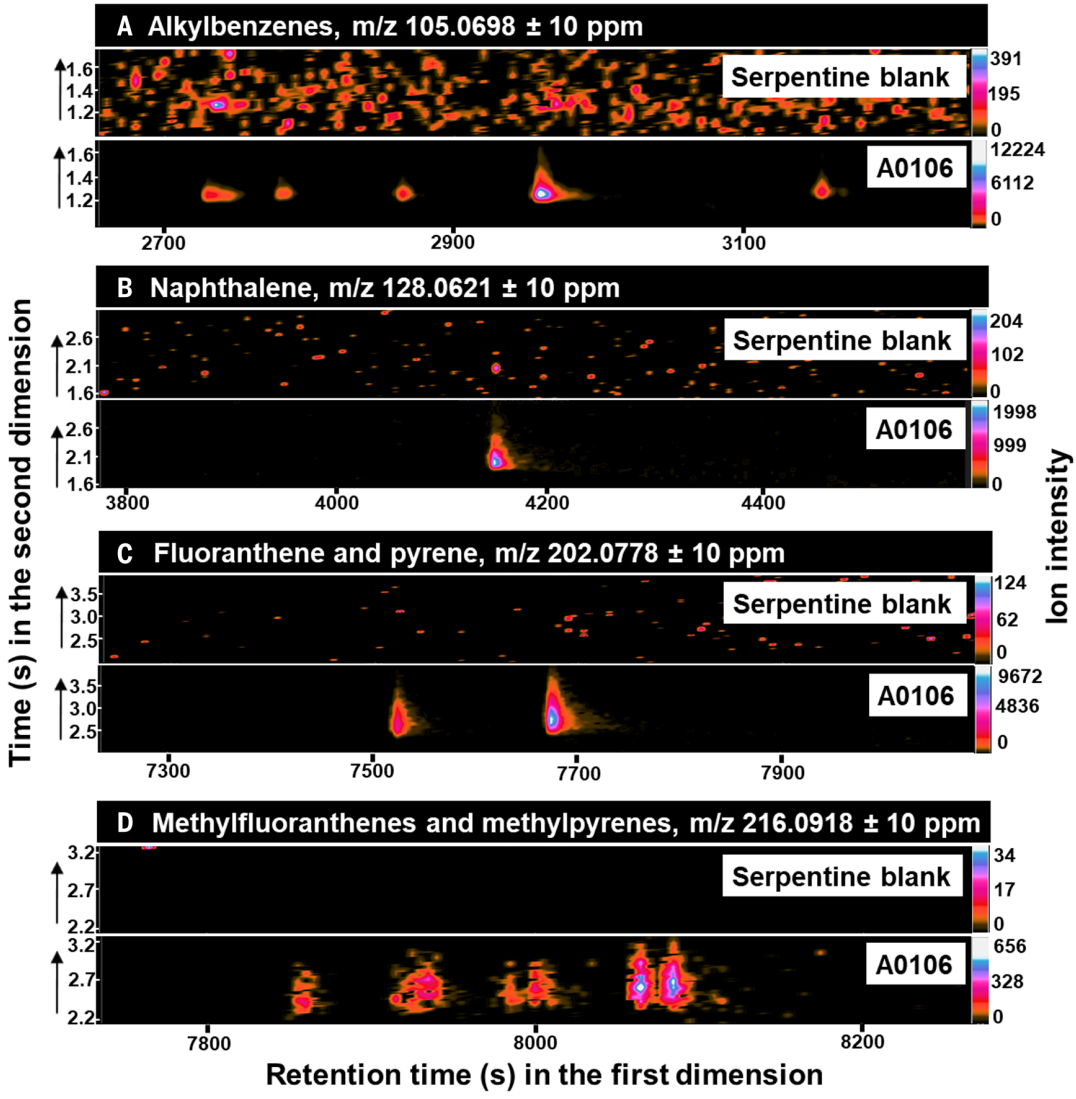
A Alkylbenzenes, m/z 105.0698 ± 10 ppm
B Naphthalene, m/z 128.0621 ± 10 ppm
C Fluoranthene and pyrene, m/z 202.0778 ± 10 ppm
D Methylfluoranthenes and methylpyrenes, m/z 216.0918 ± 10 ppm
Serpentine blank
A0106
Time (s) in the second dimension
Retention time (s) in the first dimension
Ion intensity

Fig. 5. Aromatic hydrocarbons in the Ryugu extract. Data were measured using GC×GC-TOFMS. (**A**) Alkylbenzenes in the hexane extract (*m/z* = 105.0698). (**B**) Naphthalene (*m/z* = 128.0621) in the DCM extract. (**C**) Fluoranthene (~7520 s) and pyrene (~7680 s) (*m/z* = 202.0778) in the DCM extract. (**D**) Methylfluoranthenes and methylpyrenes (*m/z* = 216.0918) in the DCM extract. In each panel, the Ryugu sample (lower) is compared with a fbaked serpentine blank (upper). Colors indicate concentration, as indicated on the color bar.

before extraction with water (fig. S2), we expect that the PAHs suspended in the water extract were dominated by very large and less soluble molecules that were not removed by the earlier analysis steps. The FTIR spectrum of the Ryugu sample is unlike those of other extraterrestrial materials, including carbonaceous chondrites. It is most similar to astronomical observations of interstellar PAHs (*50*), so it is possible that presolar PAHs (formed in the interstellar medium) were incorporated into Ryugu's parent body during its accretion, and then survived the subsequent aqueous alteration.

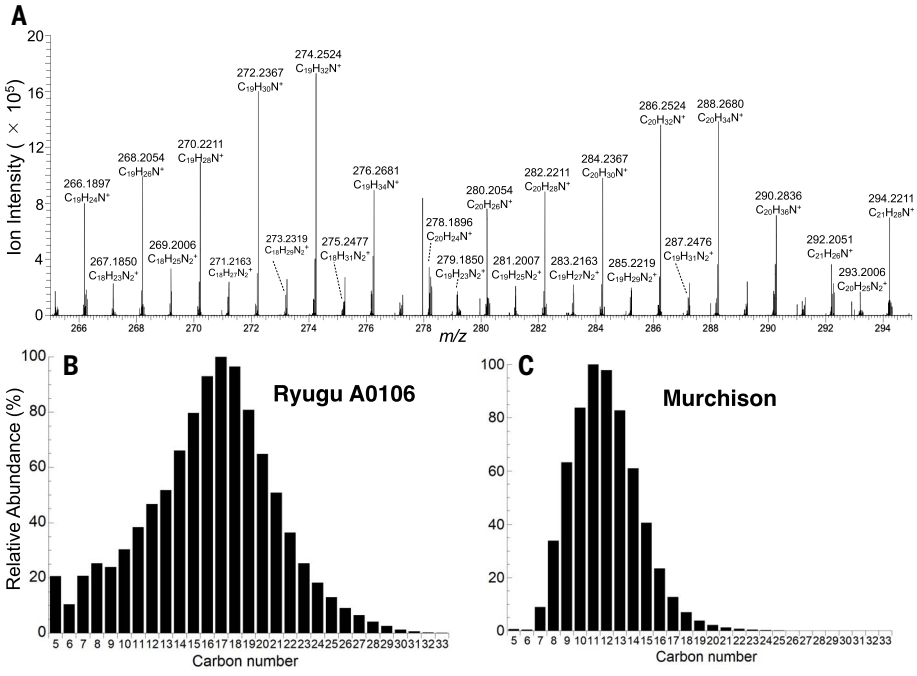

Fig. 6. CHN compounds in the methanol extract determined using nanoLC/high resolution mass spectrometry. (**A**) Example region of the mass spectrum of the A0106 sample (*73*), with peaks assigned to $C_nH_{2n-16}N^+$, $C_nH_{2n-14}N^+$, $C_nH_{2n-12}N^+$, $C_nH_{2n-10}N^+$, $C_nH_{2n-8}N^+$, $C_nH_{2n-6}N^+$, $C_nH_{2n-4}N^+$, $C_nH_{2n-15}N_2^+$, $C_nH_{2n-13}N_2^+$, $C_nH_{2n-11}N_2^+$, $C_nH_{2n-9}N_2^+$, and $C_nH_{2n-7}N_2^+$ (where C_n is the carbon number). (**B** and **C**) Histograms showing the relative abundances of $C_nH_{2n-4}N^+$ (alkylpyridines) as a function of carbon number, for Ryugu (B) and Murchison (*11*) (C). Abundances are normalized to a peak value of 100. The Ryugu distribution peaks at a higher carbon number than Murchison.

N-containing heterocyclic compounds

The methanol extract of A0106 was examined using nano-liquid chromatography/high-resolution mass spectrometry (nanoLC/HRMS) (*11*). Several classes of alkylated N-containing heterocyclic molecules were identified, and their presence was confirmed using ESI FT-ICR/MS (Fig. 2E). These alkylated N-heterocycles included pyridine, piperidine, pyrimidine, imidazole, or pyrrole rings with various amounts of alkylation (Fig. 6A). Alkylpyridines and alkylimidazoles (aromatic N-heterocycles) have previously been found in CM chondrites, whereas alkylpiperidines (aliphatic N-heterocycles) are more abundant in CR chondrites (*52*); the difference in relative abundances might reflect differing redox conditions on the meteorite parent bodies.

The alkylpyridine ($C_nH_{2n-4}N^+$) homologs that we identified in the Ryugu sample (Fig. 6B) have a different distribution pattern from those in CM chondrites (Fig. 6C). The number of C atoms in the Ryugu compounds was mostly between 11 and 22, with a maximum at 17, whereas the C number distribution for Murchison had a lower range, mostly from 8 to 16 with its maximum at 11. This difference could be caused by differences in the histories of hydrothermal activity (such as the water/rock ratio), solar radiation, and/or cosmic ray irradiation (*53*, *54*). Gas phase reactions at high temperature can produce polymeric series of N-containing heterocyclic compounds such as those found in meteorites (*55*). If the bell-shaped distributions

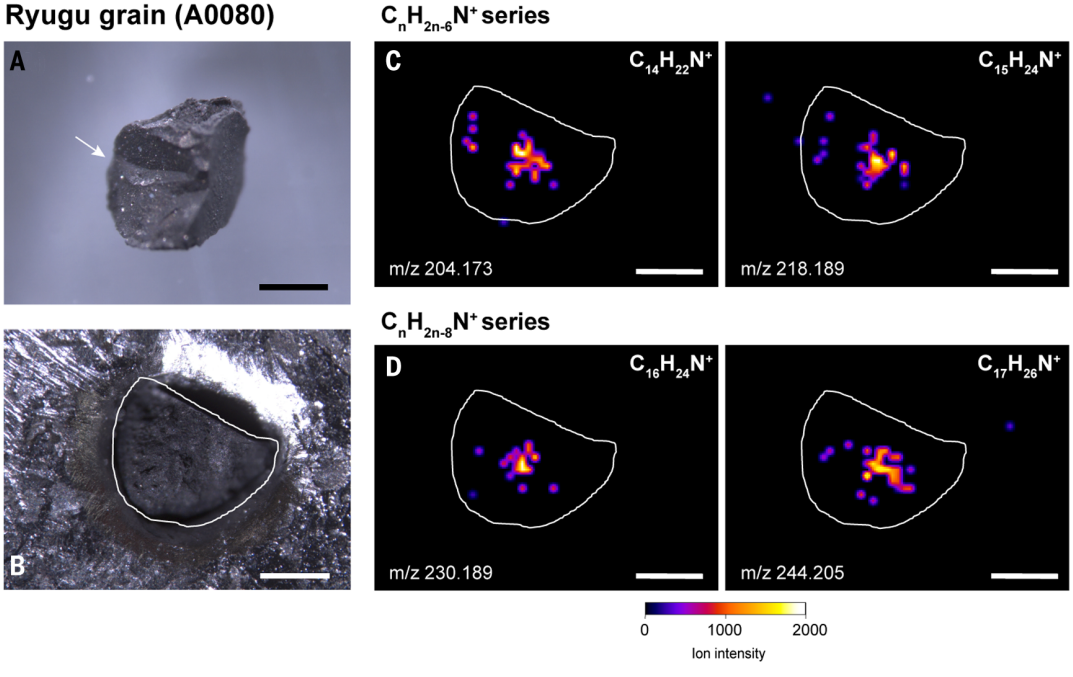

Fig. 7. Spatial distribution of CHN compounds on the surface of Ryugu grain A0080. (**A** and **B**) Optical images before sample preparation (A) and after embedding in an alloy (B). White arrow in (A) indicates the grain surface embedded in (B). Maps of organic molecule distribution were measured by DESI coupled with HRMS, for the $C_nH_{2n-6}N^+$ series (n =14, 15) (**C**) and $C_nH_{2n-8}N^+$ series (n =16, 17) (**D**) molecules. White outlines indicate the boundary between the A0080 grain and the surrounding metal. Scale bars, 500 μm.

for Ryugu and Murchison were caused by gas-phase synthesis, then the two bodies could have inherited their SOM from different regions of the solar nebula.

Alternatively, N-heterocyclic compounds can be synthesized through a reaction pathway using ammonia and simple aldehydes such as formaldehyde (*56*), which would require high abundances of aldehyde and ammonia in the Ryugu body in the past. Because formaldehyde and ammonia were abundant in the interstellar medium and the protosolar nebula (*57*, *58*), the Ryugu organic material might have inherited these characteristics from a molecular cloud environment. In interstellar-ice analog experiments at very low temperature, hexamethylenetetramine (HMT: $C_6H_{12}N_4$) is produced as a major compound from single-carbon compounds and ammonia (*59*). However, we did not detect HMT in any extracted fraction of our sample using FT-ICR/MS and nanoLC/HRMS. HMT has previously been detected in aqueous extracts of carbonaceous meteorites including Murchison (*60*). Under hydrothermal conditions, HMT is degraded to formaldehyde and ammonia at ~150°C, especially at alkaline pH, producing N-containing compounds such as amino acids and N-heterocycles (*61*, *62*). Because the aqueous fluid on Ryugu's parent body was probably alkaline (pH > 9) (*10*), we attribute the lack of HMT to the aqueous alteration history.

Sample surface distribution of organic molecules

We performed in situ analysis of the surface of the A0080 grain using electrically charged MeOH spraying by desorption electrospray ionization (DESI) coupled with HRMS (*11*). We detected >200 positive ion peaks ranging from m/z = 80 to 400, which we assigned to molecules containing the elements CHN, CHO, or CHNO and their alkylated homologs (Fig. 7 and fig. S7). These compounds were located on the uppermost layer of the intact grain surface; no treatment (e.g., cutting or polishing) was performed on A0080. Methanol spraying detached the molecules from the surface, implying weak interactions between the CHN compounds and the major minerals of the grain. The CHN compounds that we observed were mostly consistent with those detected in the methanol extract of the aggregate sample (A0106); however, the molecular distribution was not identical (Fig. 6A and fig. S7, B and C). We attribute the different molecular distributions to heterogeneous distribution of the SOM compounds between the Ryugu grains and/or differences in sensitivity between the two analytical methods.

Our molecular imaging shows spatial heterogeneity of the compounds across the surface of A0080 (Fig. 7). We expect the ion intensity to depend on the topography of the sample surface, which was not flattened. Although the region with highest SOM concentration is also the highest topographical area, the molecular imaging shows micrometer-scale differences in the spatial distribution of the CHN compounds depending on their molecular sizes and families (Fig. 7). Varying spatial distribution among different molecular sizes and compound classes were also observed among CHO and CHNO compounds. Previous studies have identified different spatial distributions of CHN compounds on CM chondrites, including Murray (*63*). The distinct distributions could be caused by interactions between organic molecules and minerals during aqueous alteration (*64*). Other synthesis routes could also explain these results, for example through SOM reactions with minerals and fluids in the Ryugu parent body (*65*).

Implications for asteroid organic chemistry

The molecular diversity of SOM in the Ryugu sample A0106 is as high as previously found for carbonaceous chondrites, and includes poly-sulfur-bearing species. By contrast, the molecular diversity of low-molecular-weight compounds, including aliphatic amines and carboxylic acids, was lower in the Ryugu sample than previously measured in the Murchison meteorite. The total SOM concentration in the A0106 sample was less than that of Murchison, closer to those of the unheated CI chondrites Ivuna and Orgueil.

The Ryugu organic matter seems to have been affected by aqueous alteration, which produced aromatic hydrocarbons similar to hydrothermal petroleum on Earth (*45*). However, the Ryugu samples have never experienced high temperatures (*12*). This is unlike the heated CI chondrites Yamato 980115 and Belgica 7904 [parent body temperatures ≲150°C (*66*, *67*)], which contain very low (or undetectable) abundances of amino acids and PAHs (*23*, *68*, *69*). Remote-sensing observations of Ryugu collected by the Hayabusa2 spacecraft showed evidence for thermal metamorphism at 300 to 400°C on Ryugu's parent body (*70*). However, we estimate that the effective heating temperature was ≲150°C for the Ryugu SOM (*11*). We ascribe this difference to protection of the organics by incorporation into hydrous minerals.

The SOM detected in the A0106 and A0080 samples indicates that Ryugu's surface materials host organic molecules despite the harsh environment caused by solar heating, ultraviolet irradiation, cosmic-ray irradiation, and high vacuum. The uppermost surface grains on Ryugu protect organic molecules, unlike meteorites, for which atmospheric ablation during Earth entry removes or modifies analogous near-surface material. Organic compounds on asteroids can be ejected from the surface by impacts or other causes (*71*, *72*), dispersing them through the Solar System (or beyond) as meteoroids or interplanetary dust particles. Therefore, SOM on C-type asteroids could be a source of organics delivered to other bodies.

REFERENCES AND NOTES

1. D. P. Glavin *et al.*, "The origin and evolution of organic matter in carbonaceous chondrites and links to their parent bodies," in *Primitive Meteorites and Asteroids*, N. Abreu, Ed. (Elsevier, 2018), pp. 205–271.
2. E. Anders, Pre-biotic organic matter from comets and asteroids. *Nature* **342**, 255–257 (1989). doi: 10.1038/342255a0; pmid: 11536617
3. C. Chyba, C. Sagan, Endogenous production, exogenous delivery and impact-shock synthesis of organic molecules: An inventory for the origins of life. *Nature* **355**, 125–132 (1992). doi: 10.1038/355125a0; pmid: 11538392
4. F. E. DeMeo, B. Carry, Solar System evolution from compositional mapping of the asteroid belt. *Nature* **505**, 629–634 (2014). doi: 10.1038/nature12908; pmid: 24476886
5. T. Hiroi, C. M. Pieters, M. E. Zolensky, M. E. Lipschutz, Evidence of thermal metamorphism on the C, g, B, and f asteroids. *Science* **261**, 1016–1018 (1993). doi: 10.1126/science.261.5124.1016; pmid: 17739619
6. K. Kitazato *et al.*, The surface composition of asteroid 162173 Ryugu from Hayabusa2 near-infrared spectroscopy. *Science* **364**, 272–275 (2019). doi: 10.1126/science.aav7432; pmid: 30890589
7. S. Tachibana *et al.*, Pebbles and sand on asteroid (162173) Ryugu: In situ observation and particles returned to Earth. *Science* **375**, 1011–1016 (2022). doi: 10.1126/science.abj8624; pmid: 35143255
8. T. Yada *et al.*, Preliminary analysis of the Hayabusa2 samples returned from C-type asteroid Ryugu. *Nat. Astron.* **6**, 214–220 (2022). doi: 10.1038/s41550-021-01550-6
9. T. Morota *et al.*, Sample collection from asteroid (162173) Ryugu by Hayabusa2: Implications for surface evolution. *Science* **368**, 654–659 (2020). doi: 10.1126/science.aaz6306; pmid: 32381723
10. T. Nakamura *et al.*, Formation and evolution of carbonaceous asteroid Ryugu: Direct evidence from returned samples. *Science* **379**, eabn8671 (2022). doi: 10.1126/science.abn8671; pmid: 36137011
11. Materials and methods are available as supplementary materials.
12. T. Yokoyama *et al.*, Samples returned from the asteroid Ryugu are similar to Ivuna-type carbonaceous meteorites. *Science* **379**, eabn7850 (2022). doi: 10.1126/science.abn7850; pmid: 35679354
13. J. F. Kerridge, Carbon, hydrogen and nitrogen in carbonaceous chondrites: Abundances and isotopic compositions in bulk samples. *Geochim. Cosmochim. Acta* **49**, 1707–1714 (1985). doi: 10.1016/0016-7037(85)90141-3; pmid: 11539652
14. R. Okazaki *et al.*, Noble gases and nitrogen in samples of asteroid Ryugu record its volatile sources and recent surface evolution. *Science* **379**, eabo0431 (2022). doi: 10.1126/science.abo0431; pmid: 36264828
15. H. Yabuta *et al.*, Macromolecular organic matter in samples of the asteroid (162173) Ryugu. *Science* **379**, eabn9057 (2023). doi: 10.1126/science.abn9057
16. P. Schmitt-Kopplin *et al.*, High molecular diversity of extraterrestrial organic matter in Murchison meteorite revealed 40 years after its fall. *Proc. Natl. Acad. Sci. U.S.A.* **107**, 2763–2768 (2010). doi: 10.1073/pnas.0912157107; pmid: 20160129
17. J. Hertzog, H. Naraoka, P. Schmitt-Kopplin, Profiling Murchison soluble organic matter for new organic compounds with APPI- and ESI-FT-ICR MS. *Life (Basel)* **9**, 48 (2019). doi: 10.3390/life9020048; pmid: 31174398
18. A. Ruf *et al.*, Previously unknown class of metalorganic compounds revealed in meteorites. *Proc. Natl. Acad. Sci. U.S.A.* **114**, 2819–2824 (2017). doi: 10.1073/pnas.1616019114; pmid: 28242686
19. M. Matzka *et al.*, Thermal history of asteroid parent bodies is reflected in their metalorganic chemistry. *Astrophys. J. Lett.* **915**, L7 (2021). doi: 10.3847/2041-8213/ac0727
20. G. Danger *et al.*, Exploring the link between molecular cloud ices and chondritic organic matter in laboratory. *Nat. Commun.* **12**, 3538 (2021). doi: 10.1038/s41467-021-23895-2; pmid: 34112800

21. A. Ruf *et al*., Sulfur ion irradiation experiments simulating space weathering of Solar System body surfaces. *Astron. Astrophys.* **655**, A74 (2021). doi: 10.1051/0004-6361/202141190
22. D. N. Simkus *et al*., Methodologies for analyzing soluble organic compounds in extraterrestrial samples: Amino acids, amines, monocarboxylic acids, aldehydes, and ketones. *Life (Basel)* **9**, 47 (2019). doi: 10.3390/life9020047; pmid: 31174308
23. A. Burton, S. Grunsfeld, J. Elsila, D. Glavin, J. Dworkin, The effects of parent-body hydrothermal heating on amino acid abundances in CI-like chondrites. *Polar Sci.* **8**, 255–263 (2014). doi: 10.1016/j.polar.2014.05.002
24. A. Burton *et al*., A propensity for *n*-ω-amino acids in thermally altered Antarctic meteorites. *Meteorit. Planet. Sci.* **47**, 374–386 (2012). doi: 10.1111/j.1945-5100.2012.01341.x
25. M. N. Islam, T. Kaneko, K. Kobayashi, Reaction of amino acids in a supercritical water-flow reactor simulating submarine hydrothermal systems. *Bull. Chem. Soc. Jpn.* **76**, 1171–1178 (2003). doi: 10.1246/bcsj.76.1171
26. J. Li, T. B. Brill, Spectroscopy of hydrothermal reactions, part 26: Kinetics of decarboxylation of aliphatic amino acids and comparison with the rates of racemization. *Int. J. Chem. Kinet.* **35**, 602–610 (2003). doi: 10.1002/kin.10160
27. M. C. De Sanctis *et al*., Ammoniated phyllosilicates with a likely outer Solar System origin on (1) Ceres. *Nature* **528**, 241–244 (2015). doi: 10.1038/nature16172; pmid: 26659184
28. O. Poch *et al*., Ammonium salts are a reservoir of nitrogen on a cometary nucleus and possibly on some asteroids. *Science* **367**, eaaw7462 (2020). doi: 10.1126/science.aaw7462; pmid: 32165559
29. C. Pilorget *et al*., First compositional analysis of Ryugu samples by MicrOmega hyperspectral microscope. *Nat. Astron.* **6**, 221–225 (2022). doi: 10.1038/s41550-021-01549-z
30. J. C. Aponte, J. P. Dworkin, J. E. Elsila, Assessing the origins of aliphatic amines in the Murchison meteorite from their compound-specific carbon isotopic ratios and enantiomeric composition. *Geochim. Cosmochim. Acta* **141**, 331–345 (2014). doi: 10.1016/j.gca.2014.06.035
31. J. C. Aponte, H. L. McLain, J. P. Dworkin, J. E. Elsila, Aliphatic amines in Antarctic CR2, CM2, and CM1/2 carbonaceous chondrites. *Geochim. Cosmochim. Acta* **189**, 296–311 (2015). doi: 10.1016/j.gca.2016.06.018
32. J. C. Aponte, J. P. Dworkin, J. E. Elsila, Indigenous aliphatic amines in the aqueously altered Orgueil meteorite. *Meteorit. Planet. Sci.* **50**, 1733–1749 (2015). doi: 10.1111/maps.12507
33. D. P. Glavin, J. P. Dworkin, S. A. Sandford, Detection of cometary amines in samples returned by Stardust. *Meteorit. Planet. Sci.* **43**, 399–413 (2008). doi: 10.1111/j.1945-5100.2008.tb00629.x
34. G. U. Yuen, K. A. Kvenvolden, Monocarboxylic acids in Murray and Murchison carbonaceous meteorites. *Nature* **246**, 301–303 (1973). doi: 10.1038/246301a0
35. Y. Huang *et al*., Molecular and compound-specific isotopic characterization of monocarboxylic acids in carbonaceous meteorite. *Geochim. Cosmochim. Acta* **69**, 1073–1084 (2005). doi: 10.1016/j.gca.2004.07.030
36. J. C. Aponte, H. K. Woodward, N. M. Abreu, J. E. Elsila, J. P. Dworkin, Molecular distribution, ^{13}C-isotope, and enantiomeric compositions of carbonaceous chondrite monocarboxylic acids. *Meteorit. Planet. Sci.* **54**, 415–430 (2019). doi: 10.1111/maps.13216; pmid: 32499671
37. H. Naraoka, A. Shimoyama, K. Harada, Molecular distribution of monocarboxylic acids in Asuka carbonaceous chondrites from Antarctica. *Orig. Life Evol. Biosph.* **29**, 187–201 (1999). doi: 10.1023/A:1006547127028; pmid: 10391772
38. J. C. Aponte, M. R. Alexandre, Y. A. J. Brearley, C. M. O'D. Alexander, Y. Huang, Effects of secondary alteration on the composition of free and IOM-derived monocarboxylic acids in carbonaceous chondrites. *Geochim. Cosmochim. Acta* **75**, 2309–2323 (2011). doi: 10.1016/j.gca.2011.01.040
39. J. C. Aponte, D. Whitaker, M. W. Powner, J. E. Elsila, J. P. Dworkin, Analyses of aliphatic aldehydes and ketones in carbonaceous chondrites. *ACS Earth Space Chem.* **3**, 463–472 (2019). doi: 10.1021/acsearthspacechem.9b00006; pmid: 32617450
40. B. P. Basile, B. S. Middleditch, J. Oró, Polycyclic aromatic hydrocarbons in the Murchison meteorite. *Org. Geochem.* **5**, 211–216 (1984). doi: 10.1016/0146-6380(84)90008-1
41. H. Naraoka, A. Shimoyama, M. Komiya, H. Yamamoto, K. Harada, Hydrocarbons in the Yamato-791198 carbonaceous chondrite from Antarctica. *Chem. Lett.* **17**, 831–834 (1988). doi: 10.1246/cl.1988.831
42. H. Naraoka, A. Shimoyama, K. Harada, Isotopic evidence from an Antarctic carbonaceous chondrite for two reaction pathways of extraterrestrial PAH formation. *Earth Planet. Sci. Lett.* **184**, 1–7 (2000). doi: 10.1016/S0012-821X(00)00316-2
43. M. R. Wing, J. L. Bada, The origin of the polycyclic aromatic hydrocarbons in meteorites. *Orig. Life Evol. Biosph.* **21**, 375–383 (1992). doi: 10.1007/BF01808308
44. M. R. Wing, J. L. Bada, Geochromatography on the parent body of the carbonaceous chondrite Ivuna. *Geochim. Cosmochim. Acta* **55**, 2937–2942 (1991). doi: 10.1016/0016-7037(91)90458-H
45. B. R. T. Simoneit, P. F. Lonsdale, Hydrothermal petroleum in mineralized mounds at the seabed of Guaymas Basin. *Nature* **295**, 198–202 (1982). doi: 10.1038/295198a0
46. A. Leger, J. L. Puget, Identification of the "unidentified IR emission features of interstellar dust? *Astron. Astrophys.* **137**, L5–L8 (1984).
47. E. Peeters *et al*., The rich 6 to 9 μm spectrum of interstellar PAHs. *Astron. Astrophys.* **390**, 1089–1113 (2002). doi: 10.1051/0004-6361:20020773
48. S. R. Langhoff, Theoretical infrared spectra for polycyclic aromatic hydrocarbon neutrals, cations, and anions. *J. Phys. Chem.* **100**, 2819–2841 (1996). doi: 10.1021/jp952074g
49. B. T. Draine, A. Li, Infrared emission from interstellar dust. IV. The silicate-graphite model in the post-*SPITZER* era. *Astrophys. J.* **657**, 810–837 (2007). doi: 10.1086/511055
50. A. G. G. M. Tielens, Interstellar polycyclic aromatic hydrocarbon molecules. *Annu. Rev. Astron. Astrophys.* **46**, 289–337 (2008). doi: 10.1146/annurev.astro.46.060407.145211
51. G. Matrajt *et al*., FTIR and Raman analyses of the Tagish Lake meteorite: Relationship with the aliphatic hydrocarbons observed in the Diffuse Interstellar Medium. *Astron. Astrophys.* **416**, 983–990 (2004). doi: 10.1051/0004-6361:20034526
52. H. Naraoka, M. Hashiguchi, Distinct distribution of soluble N-heterocyclic compounds between CM and CR chondrites. *Geochem. J.* **53**, 33–40 (2019). doi: 10.2343/geochemj.2.0546
53. F.-R. Orthous-Daunay *et al*., Ultraviolet-photon fingerprints on chondritic large organic molecules. *Geochem. J.* **53**, 21–32 (2019). doi: 10.2343/geochemj.2.0544
54. J. Isa *et al*., Aqueous alteration on asteroids simplifies soluble organic matter mixtures. *Astrophys. J. Lett.* **920**, L39 (2021). doi: 10.3847/2041-8213/ac2b34
55. D. V. Bekaert *et al*., High-temperature ionization-induced synthesis of biologically relevant molecules in the protosolar nebula. *Astrophys. J.* **859**, 142 (2018). doi: 10.3847/1538-4357/aabe7a
56. H. Naraoka, Y. Yamashita, M. Yamaguchi, F.-R. Orthous-Daunay, Molecular evolution of N-containing cyclic compounds in the parent body of the Murchison meteorite. *ACS Earth Space Chem.* **1**, 540–550 (2017). doi: 10.1021/acsearthspacechem.7b00058
57. P. Ehrenfreund, S. B. Charnley, Organic molecules in the interstellar medium, comets, and meteorites: A voyage from dark clouds to the early Earth. *Annu. Rev. Astron. Astrophys.* **38**, 427–483 (2000). doi: 10.1146/annurev.astro.38.1.427
58. J. Pegues *et al*., An ALMA survey of H_2CO in protoplanetary disks. *Astrophys. J.* **890**, 142 (2020). doi: 10.3847/1538-4357/ab64d9
59. M. P. Bernstein, S. A. Sandford, L. J. Allamandola, S. Chang, M. A. Scharberg, Organic compounds produced by photolysis of realistic interstellar and cometary ice analogs containing methanol. *Astrophys. J.* **454**, 327–344 (1995). doi: 10.1086/176485
60. Y. Oba *et al*., Extraterrestrial hexamethylenetetramine in meteorites-a precursor of prebiotic chemistry in the inner solar system. *Nat. Commun.* **11**, 6243 (2020). doi: 10.1038/s41467-020-20038-x; pmid: 33288754
61. Y. Wolman, S. L. Miller, J. Ibanez, J. Oró, Formaldehyde and ammonia as precursors to prebiotic amino acids. *Science* **174**, 1038–1041 (1971). doi: 10.1126/science.174.4013.1039; pmid: 5120091
62. V. Vinogradoff, S. Bernard, C. Le Guillou, L. Remusat, Evolution of interstellar organic compounds under asteroidal hydrothermal conditions. *Icarus* **305**, 358–370 (2018). doi: 10.1016/j.icarus.2017.12.019
63. H. Naraoka, M. Hashiguchi, In situ organic compound analysis on a meteorite surface by desorption electrospray ionization coupled with an Orbitrap mass spectrometer. *Rapid Commun. Mass Spectrom.* **32**, 959–964 (2018). doi: 10.1002/rcm.8121; pmid: 29569778
64. K. Muneishi, H. Naraoka, Interactions between organic compounds and olivine under aqueous conditions: A potential role for organic distribution in carbonaceous chondrites. *Meteorit. Planet. Sci.* **56**, 195–205 (2021). doi: 10.1111/maps.13614
65. M. Hashiguchi, H. Naraoka, High-mass resolution molecular imaging of organic compounds on the surface of Murchison meteorite. *Meteorit. Planet. Sci.* **54**, 452–468 (2019). doi: 10.1111/maps.13211
66. R. N. Clayton, T. K. Mayeda, Oxygen isotope studies of carbonaceous chondrites. *Geochim. Cosmochim. Acta* **63**, 2089–2104 (1999). doi: 10.1016/S0016-7037(99)00090-3
67. A. J. King *et al*., The Yamato-type (CY) carbonaceous chondrite group: Analogues for the surface of asteroid Ryugu? *Chem. Erde* **79**, 125531 (2019). doi: 10.1016/j.chemer.2019.08.003
68. A. Shimoyama, K. Harada, Amino acid depleted carbonaceous chondrites (C2) from Antarctica. *Geochem. J.* **18**, 281–286 (1984). doi: 10.2343/geochemj.18.281
69. Q. Chan, Y. Chikaraishi, Y. Takano, N. O. Ogawa, N. Ohkouchi, Amino acid compositions in heated carbonaceous chondrites and their compound-specific nitrogen isotopic ratios. *Earth Planets Space* **68**, 7 (2016). doi: 10.1186/s40623-016-0382-8
70. E. Tatsumi *et al*., Spectrally blue hydrated parent body of asteroid (162173) Ryugu. *Nat. Commun.* **12**, 5837 (2021). doi: 10.1038/s41467-021-26071-8; pmid: 34611167
71. M. Arakawa *et al*., An artificial impact on the asteroid (162173) Ryugu formed a crater in the gravity-dominated regime. *Science* **368**, 67–71 (2020). doi: 10.1126/science.aaz1701; pmid: 32193363
72. D. S. Lauretta *et al*., Episodes of particle ejection from the surface of the active asteroid (101955) Bennu. *Science* **366**, eaay3544 (2019). doi: 10.1126/science.aay3544; pmid: 31806784
73. H. Naraoka, Images and related data on the analysis of asteroid Ryugu samples used for: H. Naraoka *et al*., Soluble organic molecules in samples of the carbonaceous asteroid (162173) Ryugu, JAXA (2023); https://data.darts.isas.jaxa.jp/pub/hayabusa2/paper/sample/Naraoka_2022/.

ACKNOWLEDGMENTS

The Hayabusa2 project has been led by JAXA (the Japan Aerospace Exploration Agency) in collaboration with DLR (the German Space Center) and CNES (the French Space Center) and is supported by NASA and ASA (the Australian Space Agency). We thank all members of the Hayabusa2 project for their technical and scientific contributions. **Funding:** This work was supported by the Japan Society for the Promotion of Science (JSPS) under KAKENHI grants JP20H00202 (H.Na.), JP20H05846 (H.Na.), JP20K20485 (S.Sa.), JP20K14549 (H.Su.), JP21J00504 (T.K.), JP21H01203 (N.O.O.), JP21H04501 (Y.O.), and JP21KK0062 (Y.T.). J.P.D., J.C.A., E.T.P., D.P.G., H.L.M., J.E.E., and H.V.G. were supported by NASA under the Consortium for Hayabusa2 Analysis of Organic Solubles. F.-R.O.D. was supported by CNES (grant BC U53-6336-4500068838). J.M.E. was supported by NSF Graduate Research Fellowship "Emerging Worlds" (grant 18-EW18 2-0084). **Author contributions:** H.Na., Y.T., and J.P.D. designed the research. Y.T., N.O.O., P.S.-K., K.Ham., A.F., J.C.A., E.T.P., D.P.G., H.L.M., Y.O., T.K., M.Has, K.F., D.A., F.-R.O.-D., C.W., J.I., S.Sa., T.Yo., J.M.E., N.He., J.P.D., and H.Na. conducted experiments and analyzed data in cooperation with T.Yad., H.Yu., H.Yab., T.Nak., Y.C., N.Oh., H.Su., H.M., Y.F., A.R., V.V., R.T., H.C.C., and D.S.L. H.Na., Y.T., J.P.D., P.S.-K., H.V.G, J.E.E., K.Ham., A.F., Y.O., M.Has., F.-R.O.-D., J.I., and S.Tac. wrote the paper. M.Ab., T.Yad., M.N., K.Yog., A.N., M.Y., A.S., A.Miy., S.F., K.Hat., H.So., Y.H., K.Ku., T.U., T.H., D.Y., and R.F. curated samples. K.Ki., S.Su., N.N., M.Ar., H.I., M.I., Nar.H., K.W., Y.I., R.N., T.Mo., N.S., K.M., H.Su., R.H., E.T., Y.Y., C.H., T.Mi., M.M., A.Miu, H.No., T.Yam., K.Yos., K.K., M.O., Y.I., H.Yan, M.H., T.I., R.T., H.Sa., S.H., K.O., C.O., Nao.H., K.S., Y.S., M.Y., T.O., Y.Y., H.T., A.F., T.T., K.Yog., Y.M., G.O., N.Og., S.K., S.N., F.T., S.Tan., T.S., M.Y., S.W., and Y.T. contributed to the sample collection at Ryugu. All authors discussed the results and commented on the manuscript. **Competing interests:** The authors declare no competing interests. **Data and materials**

availability: The mass spectra and chromatographic data used in this study are available at the JAXA Data Archives and Transmission System (DARTS) at https://data.darts.isas.jaxa.jp/pub/hayabusa2/paper/sample/Naraoka_2022/ (*73*). Other data from the mission are available at the DARTS archive https://www.darts.isas.jaxa.jp/planet/project/hayabusa2/ and on the Small Bodies Node of the NASA Planetary Data System https://pds-smallbodies.astro.umd.edu/data_sb/missions/hayabusa2/. Material was allocated by the JAXA Astromaterials Science Research Group; the sample catalog is available at https://darts.isas.jaxa.jp/curation/hayabusa2/, and distribution for analysis is through an Announcement of Opportunity available at https://jaxa-ryugu-sample-ao.net. The samples of Ryugu used in this study were mostly consumed during the analysis, with the remaining materials returned to JAXA.

License information: Copyright © 2023 the authors, some rights reserved; exclusive licensee American Association for the Advancement of Science. No claim to original US government works. https://www.science.org/about/science-licenses-journal-article-reuse

SUPPLEMENTARY MATERIALS

science.org/doi/10.1126/science.abn9033
Materials and Methods
Supplementary Text
Figs. S1 to S8
Tables S1 to S5
References (*74*–*100*)

Submitted 29 December 2021; accepted 1 December 2022
10.1126/science.abn9033

RESEARCH ARTICLE SUMMARY

COSMOCHEMISTRY

Macromolecular organic matter in samples of the asteroid (162173) Ryugu

Hikaru Yabuta* *et al.*

INTRODUCTION: Organic compounds in asteroids and comets contain information about the early history of the Solar System. They could also have delivered organic material to early Earth. The Hayabusa2 spacecraft visited the carbonaceous asteroid Ryugu and collected samples of its surface materials, which were brought to Earth in December 2020.

RATIONALE: We investigated the macromolecular organic matter in the Ryugu samples, measuring its elemental, isotopic, and functional group compositions along with its small-scale structures and morphologies. Analytical methods used included spectro-microscopies, electron microscopy, and isotopic microscopy. We examined intact Ryugu grains and insoluble carbonaceous residues isolated by acid treatment of the Ryugu samples.

RESULTS: Organic matter is abundant in the Ryugu grains, distributed as submicrometer-sized organic grains and as organic matter dispersed in matrix. The Ryugu organic matter consists of aromatic carbons, aliphatic carbons, ketones, and carboxyls. The functional group compositions are consistent with those of insoluble organic matter (IOM) from primitive carbonaceous CI (Ivuna-type) and CM (Mighei-type) chondritic meteorites. Those meteorites experienced aqueous alteration (reactions with liquid water) on their parent bodies, which implies that the Ryugu organic material was also modified by aqueous alteration on the asteroid parent body.

The functional group distributions of the Ryugu organic matter vary on submicrometer scales in ways that relate to the morphologies: nanoparticulate and/or nanoglobular regions are aromatic-rich, whereas organic matter associated with Mg-rich phyllosilicate matrix and carbonates is IOM-like or occurs as diffuse carbon. The observed macromolecular diversity provides further evidence that the organics were modified by aqueous alteration on Ryugu's parent body. The diffuse carbon is similar to clay-bound organic matter that occurs in CI chondrites and the ungrouped C2-type meteorite Tagish Lake. No graphite-like material was found, which indicates that the Ryugu organic matter was not subjected to heating events on the parent body.

The bulk hydrogen and nitrogen isotopic ratios of the Ryugu grains are between the bulk values of CI chondrites and the IOM in CI chondrites. Some carbonaceous grains showed extreme deuterium (D) and/or nitrogen-15 (^{15}N) enrichments or depletions. These indicate an origin in the interstellar medium or presolar nebula. The bulk hydrogen isotopic ratios of insoluble carbonaceous residues from the Ryugu samples are lower than those in CI and CM chondrites. The range of D enrichments are consistent with the ranges of CI, CM, and Tagish Lake chondrites. The nitrogen isotopic ratios of the IOM from Ryugu samples were close to those in CI chondrites.

CONCLUSION: The organic matter in Ryugu probably consists of primordial materials that formed during (or before) the early stages of the Solar System's formation, which were later modified by heterogeneous aqueous alteration on Ryugu's parent body asteroid. Although the surface of Ryugu is exposed to solar wind, impacts, and heating by sunlight, the macromolecular organics in the surface grains of Ryugu are similar in their chemical, isotopic, and morphological compositions to those seen in primitive carbonaceous chondrites. The properties of Ryugu's organic matter could explain the low albedo of the asteroid's surface. ■

The complete list of authors and their affiliations is available in the full article online.
*Corresponding author. Email: hyabuta@hiroshima-u.ac.jp
Cite this article as H. Yabuta *et al.*, *Science* **379**, eabn9057 (2023). DOI: 10.1126/science.abn9057

READ THE FULL ARTICLE AT
https://doi.org/10.1126/science.abn9057

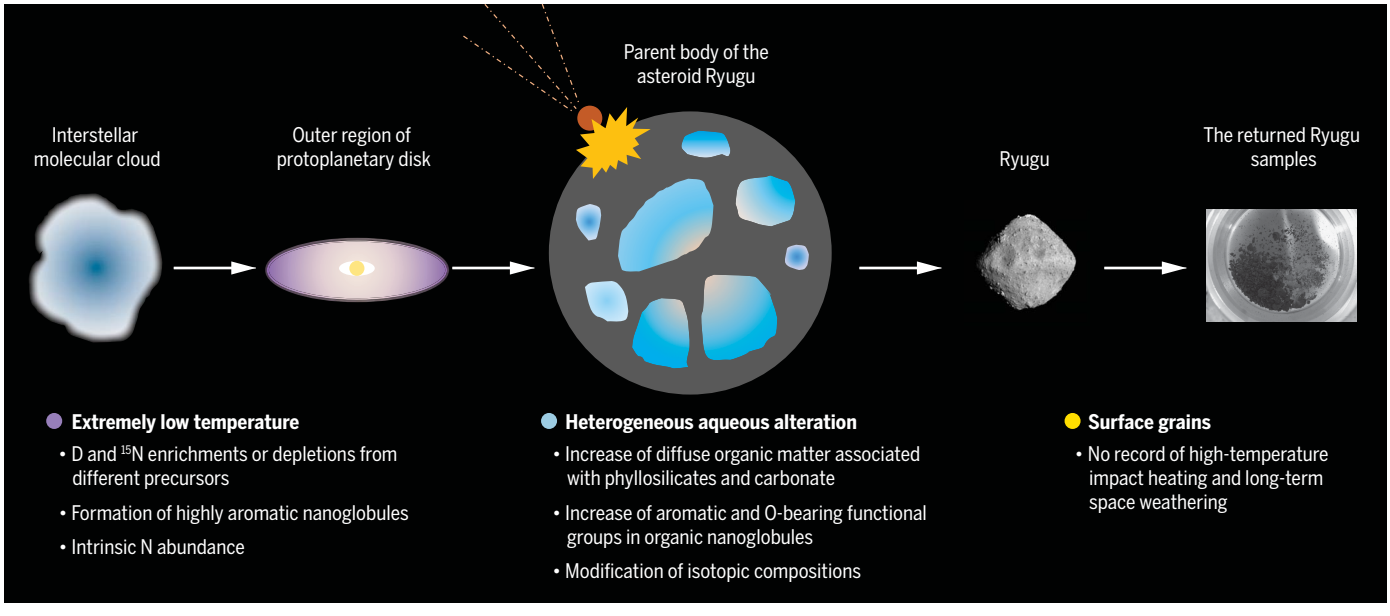
Interstellar molecular cloud
Outer region of protoplanetary disk
Parent body of the asteroid Ryugu
Ryugu
The returned Ryugu samples
Extremely low temperature
• D and 15N enrichments or depletions from different precursors
• Formation of highly aromatic nanoglobules
• Intrinsic N abundance
Heterogeneous aqueous alteration
• Increase of diffuse organic matter associated with phyllosilicates and carbonate
• Increase of aromatic and O-bearing functional groups in organic nanoglobules
• Modification of isotopic compositions
Surface grains
• No record of high-temperature impact heating and long-term space weathering

Chemical evolution of macromolecular organic matter in samples of asteroid Ryugu. Organic matter formed in the interstellar medium or in the outer region of the protoplanetary disk that formed the Solar System. It was then incorporated into a planetesimal—Ryugu's parent body—where it experienced varying degrees of reactions with liquid water. An impact ejected material from the parent body, which reassembled to form Ryugu. Samples were brought to Earth by Hayabusa2.

CREDIT: HIROSHIMA UNIVERSITY, JAXA, UNIVERSITY OF TOKYO, KOCHI UNIVERSITY, RIKKYO UNIVERSITY, NAGOYA UNIVERSITY, CHIBA INSTITUTE OF TECHNOLOGY, MEIJI UNIVERSITY, UNIVERSITY OF AIZU, AIST

RESEARCH ARTICLE

COSMOCHEMISTRY

Macromolecular organic matter in samples of the asteroid (162173) Ryugu

Hikaru Yabuta[1]*†, George D. Cody[2], Cécile Engrand[3], Yoko Kebukawa[4], Bradley De Gregorio[5], Lydie Bonal[6], Laurent Remusat[7], Rhonda Stroud[5]‡, Eric Quirico[6], Larry Nittler[2]§, Minako Hashiguchi[8], Mutsumi Komatsu[9,10], Taiga Okumura[11], Jérémie Mathurin[12], Emmanuel Dartois[13], Jean Duprat[7], Yoshio Takahashi[11,14], Yasuo Takeichi[14], David Kilcoyne[15]¶, Shohei Yamashita[14], Alexandre Dazzi[12], Ariane Deniset-Besseau[12], Scott Sandford[16], Zita Martins[17], Yusuke Tamenori[18], Takuji Ohigashi[19], Hiroki Suga[18], Daisuke Wakabayashi[14], Maximilien Verdier-Paoletti[7], Smail Mostefaoui[7], Gilles Montagnac[20], Jens Barosch[2], Kanami Kamide[1], Miho Shigenaka[1], Laure Bejach[3], Megumi Matsumoto[21], Yuma Enokido[21], Takaaki Noguchi[22], Hisayoshi Yurimoto[23], Tomoki Nakamura[21], Ryuji Okazaki[24], Hiroshi Naraoka[24], Kanako Sakamoto[25], Harold C. Connolly Jr.[26], Dante S. Lauretta[27], Masanao Abe[25,28], Tatsuaki Okada[25,29], Toru Yada[25], Masahiro Nishimura[25], Kasumi Yogata[25], Aiko Nakato[25], Miwa Yoshitake[25], Ayako Iwamae[30], Shizuho Furuya[11], Kentaro Hatakeda[30], Akiko Miyazaki[25], Hiromichi Soejima[30], Yuya Hitomi[30], Kazuya Kumagai[30], Tomohiro Usui[25], Tasuku Hayashi[25], Daiki Yamamoto[25], Ryota Fukai[25], Seiji Sugita[11,31], Kohei Kitazato[32], Naru Hirata[32], Rie Honda[33], Tomokatsu Morota[11], Eri Tatsumi[34], Naoya Sakatani[35], Noriyuki Namiki[28,36], Koji Matsumoto[28,36], Rina Noguchi[37], Koji Wada[31], Hiroki Senshu[31], Kazunori Ogawa[38], Yasuhiro Yokota[25], Yoshiaki Ishihara[38], Yuri Shimaki[25], Manabu Yamada[31], Chikatoshi Honda[32], Tatsuhiro Michikami[39], Moe Matsuoka[40], Naoyuki Hirata[41], Masahiko Arakawa[41], Chisato Okamoto[41]¶, Masateru Ishiguro[42], Ralf Jaumann[43], Jean-Pierre Bibring[44], Matthias Grott[45], Stefan Schröder[46], Katharina Otto[1,45], Cedric Pilorget[44,47], Nicole Schmitz[45], Jens Biele[48], Tra-Mi Ho[49], Aurélie Moussi-Soffys[50], Akira Miura[25], Hirotomo Noda[28,36], Tetsuya Yamada[25], Keisuke Yoshihara[25], Kosuke Kawahara[25], Hitoshi Ikeda[25], Yukio Yamamoto[25], Kei Shirai[41], Shota Kikuchi[31,36], Naoko Ogawa[25], Hiroshi Takeuchi[25,28], Go Ono[51], Yuya Mimasu[25], Kent Yoshikawa[51], Yuto Takei[25], Atsushi Fujii[25], Yu-ichi Iijima[25]¶, Satoru Nakazawa[25], Satoshi Hosoda[25], Takahiro Iwata[25,28], Masahiko Hayakawa[25], Hirotaka Sawada[38], Hajime Yano[25,28], Ryudo Tsukizaki[25], Masanobu Ozaki[25,28], Fuyuto Terui[52], Satoshi Tanaka[25,28], Masaki Fujimoto[25], Makoto Yoshikawa[25,28], Takanao Saiki[25], Shogo Tachibana[11,25], Sei-ichiro Watanabe[8], Yuichi Tsuda[25]

Samples of the carbonaceous asteroid (162173) Ryugu were collected and brought to Earth by the Hayabusa2 spacecraft. We investigated the macromolecular organic matter in Ryugu samples and found that it contains aromatic and aliphatic carbon, ketone, and carboxyl functional groups. The spectroscopic features of the organic matter are consistent with those in chemically primitive carbonaceous chondrite meteorites that experienced parent-body aqueous alteration (reactions with liquid water). The morphology of the organic carbon includes nanoglobules and diffuse carbon associated with phyllosilicate and carbonate minerals. Deuterium and/or nitrogen-15 enrichments indicate that the organic matter formed in a cold molecular cloud or the presolar nebula. The diversity of the organic matter indicates variable levels of aqueous alteration on Ryugu's parent body.

Organic compounds in asteroids and comets were produced and modified within the presolar molecular cloud, the protoplanetary disk, during the formation of planetesimals in the early Solar System and their subsequent evolution. Delivery of extraterrestrial organic compounds might have contributed to the habitability of terrestrial planets, including Earth. Analysis of pristine samples collected from primitive small bodies (asteroids and comets) could provide information on how organic compounds were formed and modified in space and which organic compounds were supplied to early Earth. Macromolecular organic matter, a dark, complex acid-insoluble organic matter (IOM), accounts for most carbon in primitive carbonaceous chondrite meteorites.

The Hayabusa2 asteroid sample return mission visited the carbonaceous (C-type) asteroid (162173) Ryugu. The mission goals included investigating the origin and evolution of organic compounds in the early Solar System (*1*). Remote sensing and lander observations showed that Ryugu is a dark, rubble-pile asteroid that contains hydrated minerals on its surface (*2*–*4*) and indicated a relationship between C-type asteroids and carbonaceous chondrites (*3*, *4*). The average albedo of Ryugu is consistent with the thermally metamorphosed subgroups of the CI1 and CM2 meteorites (*3*, *4*). CI1 meteorites are Ivuna-type carbonaceous chondrites of petrologic type 1 (extensively altered by aqueous fluids on the parent asteroid), and CM2 meteorites are Mighei-type carbonaceous chondrites of petrologic type 2 (moderately aqueously altered). Spectral and thermal inertia variations indicated that Ryugu consists of boulders that experienced different degrees of thermal and space weathering processes (*5*–*7*), derived from a much larger parent body and potentially additional materials from different asteroids (*8*).

The Hayabusa2 spacecraft collected the surface material from two touchdown sites on Ryugu and returned them to Earth on 6 December 2020. The Ryugu samples exhibit near-infrared absorption features as a result of OH and carbonate and/or organic C-H bonds, at 2.7 and 3.4 μm respectively (*9*, *10*), which indicates that the Ryugu samples are similar to CI carbonaceous chondrites (*9*).

We sought to determine the distributions and chemical characteristics of macromolecular organic matter in the Ryugu samples. We therefore measured the elemental, isotopic, and functional group compositions, structures, and textures of organic macromolecules from the Ryugu samples. The analytical procedures included micro–Fourier transform infrared (FTIR) spectroscopy, micro-Raman spectroscopy, synchrotron-based scanning transmission x-ray microscopy (STXM), x-ray absorption near-edge structure (XANES), scanning transmission electron microscopy (STEM) coupled with electron energy-loss spectroscopy (EELS) and energy-dispersive x-ray spectroscopy (EDS), atomic force microscope–based infrared (AFM-IR) spectroscopy, and nanometer-scale secondary ion mass spectrometry (NanoSIMS) (*11*). The analytical workflow (fig. S1) was designed to optimize the use of these complementary techniques.

The samples we used were selected aggregates stored in collection chamber A (from the first touchdown) and collection chamber C (from the second touchdown) of the spacecraft sample catcher (*12*) (table S1). We studied (i) intact grains (taken from aggregates designated A0108 and C0109), ranging from 200 to 900 μm in size per particle, and (ii) insoluble carbonaceous residues (fig. S2) isolated by acid treatment of Ryugu aggregates (designated A0106 and C0107). Each of these samples was split into several subsamples for analysis with different techniques (table S1).

Structural properties of macromolecular organic matter

To characterize the macromolecular structures of organic matter in Ryugu, we applied micro-Raman spectroscopy. Two peaks, identified as the D-band (~1350 cm^{-1}) and G-band (~1580 cm^{-1}) of polyaromatic molecular structures (*13*), are present in the Raman spectra of A0108 and C0109 (Fig. 1A and fig. S3A). The spectral features are broad, indicating lattice disorder in the organic macromolecules, and are superimposed on a fluorescence background. The numerical values of the derived

spectral parameters of the D- and G-bands, such as their full widths at half maximum (FWHM-$_D$ and FWHM-$_G$, respectively), peak positions (ω_D and ω_G), and intensity ratio (I_D/I_G), are similar for all grains examined from the two aggregates (Fig. 1, B to D, and fig. S3, B to D).

The macromolecular structures of organic matter in meteorites reflect the thermal histories of the meteorite parent bodies (*13*–*16*). To evaluate the thermal history of Ryugu, we compared the Raman parameters measured from the Ryugu samples with those measured from meteorites (Fig. 1, B to D, and fig. S3, B to D). The closest matches to Ryugu are the primitive CI1 and CM2 carbonaceous chondrites. The Ryugu samples are distinct from carbonaceous chondrites of petrologic type 3 (thermally metamorphosed) (Fig. 1B) and from the thermally metamorphosed subgroup of CM2, such as the Jbilet Winselwan meteorite (Fig. 1, C and D), and other ungrouped carbonaceous chondrites of petrologic type 2 (C2), such as the Wisconsin Range (WIS) 91600 and Pecora Escarpment (PCA) 02012 meteorites (Fig. 1, C and D). This indicates that the Ryugu samples A0108 and C0109 did not experience long-duration radiogenic thermal metamorphism on their parent bodies, as petrologic type 3 chondrites did (*17*), or impact-induced, short-duration heating, as experienced by some petrologic type 2 chondrites (*18*).

Functional group compositions

We used micro-FTIR spectroscopy to characterize the organic molecules and minerals. The FTIR spectra of the Ryugu grains show bands due to organic aliphatic C-H stretching (3000 to 2800 cm^{-1}, 3.33 to 3.57 μm), aromatic C=C stretching (~1600 cm^{-1}, ~6.25 μm), and carbonyl C=O stretching modes (~1700 cm^{-1}, ~5.88 μm), as well as bands due to mineral Si-O stretching (~1000 cm^{-1}, ~10.00 μm), structural OH stretching of phyllosilicates (~3680 cm^{-1}, ~2.72 μm), and the ν3 stretching mode of carbonates (~1435 cm^{-1}, ~6.97 μm) (Fig. 2A). The spectra also contain bands from interlayer water, of varying intensities, contributing at ~3300 cm^{-1} (~3.03 μm; stretching) and 1640 cm^{-1} (6.10 μm; bending). Part of this water is intrinsic to the Ryugu grains, and part can be attributed to water adsorbed on the grains under atmospheric conditions.

These absorption bands are commonly observed in unheated, aqueously altered carbonaceous chondrites (*19*, *20*), whereas organic features are weaker in thermally metamorphosed CM chondrites, such as the Jbilet Winselwan meteorite (Fig. 2A). The spectral shape of the OH band in the Ryugu samples is characteristic of Mg-rich phyllosilicates, which have been observed in CI chondrites as saponite and serpentine (*21*, *22*). There were large spectral heterogeneities among the Ryugu grains, but there is no obvious difference in the spectral variations observed between samples from chambers A and C. Compared with CI chondrites, the sulfate S=O stretching band (~1100 to 1200 cm^{-1}, ~9.09 to 8.33 μm) is absent from the spectra of Ryugu samples. The absence of sulfates is consistent with other elemental and mineralogical measurements of Ryugu samples (*23*, *24*). Sulfate can be produced by oxidation of sulfides during terrestrial weathering of the meteorites (*25*), so the lack of sulfate indicates that the Ryugu samples are pristine (*23*).

The shapes of the FTIR spectra of the grains are consistent with the reflectance spectra of Ryugu's surface acquired by the Hayabusa2 spacecraft (*4*). The OH band and aliphatic C-H band features in our absorption spectra are similar to reflectance spectra of other Ryugu samples (*9*), but we find lower intensities of aliphatic C-H peaks.

The FTIR spectra of insoluble carbonaceous residues obtained from our Ryugu samples show similar functional groups to those of the intact Ryugu grains (Fig. 2B). The aliphatic C-H stretching band (3000 to 2800 cm^{-1}, 3.33 to 3.57 μm) from the carbonaceous residue from Ryugu is more intense than those of IOM from meteorites (*26*, *27*). The peak intensity ratios of CH_2 to CH_3 (I_{CH2}/I_{CH3}) of the Ryugu residues are 1.9, whereas those of IOMs in Murchison and Ivuna meteorites are 1.2 and 1.3, respectively. Because I_{CH2}/I_{CH3} ratios are proportional to the molar ratios of CH_2 to CH_3 (CH_2/CH_3), we infer the CH_2/CH_3 ratios of the residue, which are higher than those of meteoritic IOMs. This could indicate that Ryugu's organic matter contains longer aliphatic chains, or aliphatic chains with a higher degree of cross-linking. The Ryugu carbonaceous residue also exhibits an absorption band of C=O (~1670 cm^{-1}, ~5.99 μm), which is not seen in meteoritic IOMs. We assign this C=O band to unsaturated ketones, aldehydes, or amides.

Chemical and morphological variations

Macromolecular diversity

We used synchrotron-based STXM, with spatial resolution of 30 to 50 nm, to produce

[1]Department of Earth and Planetary Systems Science, Hiroshima University, Hiroshima 739-8526, Japan. [2]Earth and Planets Laboratory, Carnegie Institution for Science, Washington, DC 20015, USA. [3]Laboratoire de Physique des 2 Infinis Irène Joliot-Curie, Université Paris-Saclay, Centre National de la Recherche Scientifique, 91405 Orsay, France. [4]Faculty of Engineering, Yokohama National University, Yokohama 240-8501, Japan. [5]Materials Science and Technology Division, US Naval Research Laboratory, Washington, DC 20375, USA. [6]Institut de Planétologie et d'Astrophysique, Université Grenoble Alpes, 38000 Grenoble, France. [7]Institut de Mineralogie, Physique des Materiaux et Cosmochimie, Museum National d'Histoire Naturelle, Centre National de la Recherche Scientifique, Sorbonne Université, 75231 Paris, France. [8]Graduate School of Environmental Studies, Nagoya University, Nagoya 464-8601, Japan. [9]Center for University-Wide Education, Saitama Prefectural University, Saitama 343-8540, Japan. [10]Department of Earth Sciences, Waseda University, Tokyo 169-8050, Japan. [11]Department of Earth and Planetary Science, The University of Tokyo, Tokyo 113-0033, Japan. [12]Institut Chimie Physique, Université Paris-Saclay, Centre National de la Recherche Scientifique, 91405 Orsay, France. [13]Institut des Sciences Moléculaires d'Orsay, Université Paris-Saclay, Centre National de la Recherche Scientifique, 91405 Orsay, France. [14]Institute of Materials Structure Science, High Energy Accelerator Research Organization, Tsukuba 305-0801, Japan. [15]Advanced Light Source, Lawrence Berkeley National Laboratory, Berkeley, CA 94720, USA. [16]NASA Ames Research Center, Moffett Field, CA 94035, USA. [17]Centro de Química Estrutural, Institute of Molecular Sciences and Department of Chemical Engineering, Instituto Superior Técnico, Universidade de Lisboa, Lisboa 1049-001, Portugal. [18]Japan Synchrotron Radiation Research Institute, Hyogo 679-5198, Japan. [19]Institute for Molecular Science, UVSOR Synchrotron Facility, Okazaki 444-8585, Japan. [20]École normale supérieure de Lyon, University Lyon 1, 69342 Lyon, France. [21]Department of Earth Science, Tohoku University, Sendai 980-8578, Japan. [22]Department of Earth and Planetary Sciences, Kyoto University, Kyoto 606-8502, Japan. [23]Department of Earth and Planetary Sciences, Hokkaido University, Sapporo 060-0810, Japan. [24]Department of Earth and Planetary Sciences, Kyushu University, Fukuoka 819-0395, Japan. [25]Institute of Space and Astronautical Science, Japan Aerospace Exploration Agency (JAXA), Sagamihara 252-5210, Japan. [26]Department of Geology, School of Earth and Environment, Rowan University, Glassboro, NJ 08028, USA. [27]Lunar and Planetary Laboratory, University of Arizona, Tucson, AZ 85721, USA. [28]School of Physical Sciences, The Graduate University for Advanced Studies, Hayama 240-0193, Japan. [29]Department of Chemistry, The University of Tokyo, Tokyo 113-0033, Japan. [30]Marine Works Japan Ltd., Yokosuka 237-0063, Japan. [31]Planetary Exploration Research Center, Chiba Institute of Technology, Narashino 275-0016, Japan. [32]Aizu Research Cluster for Space Science, University of Aizu, Aizu-Wakamatsu 965-8580, Japan. [33]Center of Data Science, Ehime University, Matsuyama 790-8577, Japan. [34]Instituto de Astrofísica de Canarias, University of La Laguna, Tenerife E-38205, Spain. [35]Department of Physics, Rikkyo University, Tokyo 171-8501, Japan. [36]Research of Interior Structure and Evolution of Solar System Bodies, National Astronomical Observatory of Japan, Mitaka 181-8588, Japan. [37]Faculty of Science, Niigata University, Niigata 950-2181, Japan. [38]JAXA Space Exploration Center, JAXA, Sagamihara 252-5210, Japan. [39]Faculty of Engineering, Kindai University, Higashi-Hiroshima 739-2116, Japan. [40]Geological Survey of Japan, National Institute of Advanced Industrial Science and Technology, Tsukuba 305-8567, Japan. [41]Department of Planetology, Kobe University, Kobe 657-8501, Japan. [42]Department of Physics and Astronomy, Seoul National University, Seoul 08826, Republic of Korea. [43]Freie Universität Berlin, Institute of Geological Sciences, Planetary Sciences and Remote Sensing, Berlin 12249, Germany. [44]Institut d'Astrophysique Spatiale, Université Paris-Saclay, Centre National de la Recherche Scientifique, 91405 Orsay, France. [45]Institute of Planetary Research, German Aerospace Center, Berlin 12489, Germany. [46]Department of Computer Science, Electrical and Space Engineering, Luleå University of Technology, 98128 Kiruna, Sweden. [47]Institut Universitaire de France, 75005 Paris, France. [48]Microgravity User Support Centre, German Aerospace Center, Cologne 53147, Germany. [49]Institute of Space Systems, German Aerospace Center, Bremen 28359, Germany. [50]Centre National d'Études Spatiales, 31401 Toulouse, France. [51]Research and Development Directorate, JAXA, Sagamihara 252-5210, Japan. [52]Department of Mechanical Engineering, Kanagawa Institute of Technology, Atsugi 243-0292, Japan.

***Corresponding author. Email: hyabuta@hiroshima-u.ac.jp**

†Present address: International Institute for Sustainability with Knotted Chiral Meta Matter, Hiroshima University, Hiroshima 739-8526, Japan.

‡Present address: Buseck Center for Meteorite Studies, Arizona State University, Tempe, AZ 85827, USA.

§Present address: School of Earth and Space Exploration, Arizona State University, Tempe, AZ 85827, USA. ¶Deceased.

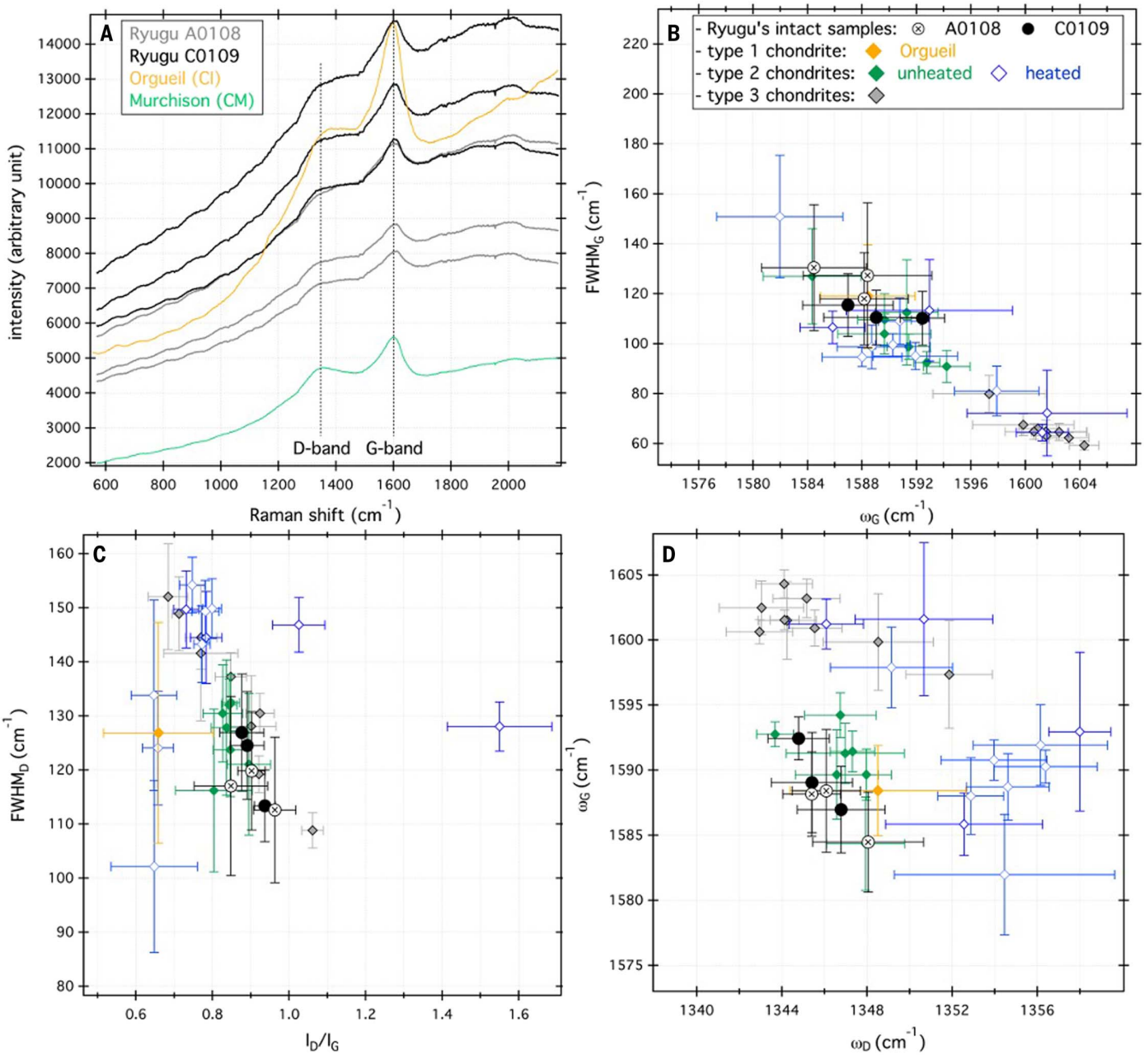

Fig. 1. Raman spectra and spectral parameters: Comparison between Ryugu samples and chondrites. (**A**) Average Raman spectra of Ryugu grains from chamber A (samples A0108-6, -10, and -18) (in gray) and chamber C (samples C0109-5, -9, and -12) (in black) compared with the meteorites Murchison (CM; green) and Orgueil (CI; yellow). All spectra were acquired in the same analytical conditions (*11*). (**B** to **D**) Average spectral parameters (error bars show standard deviations) determined from the Raman spectra: $FWHM_G$ as a function of ω_G (B); $FWHM_D$ as a function of I_D/I_G (C); and ω_G as a function of ω_D (D). Data are for individual grains from chamber A (open circles) and chamber C (black filled circles) compared with petrologic type 1 (Orgueil; orange diamond), unheated petrologic type 2 chondrites (green filled diamonds), heated petrologic type 2 chondrites (open blue diamonds), and petrologic type 3 chondrites (filled gray diamonds) (*11*). Petrologic type 2 chondrites were classified (*16*) as unheated (e.g., Murchison, Nogoya, and Tarda) or heated (e.g., Jbilet Winselwan and WIS 91600).

elemental x-ray maps and XANES spectra. Carbon x-ray maps (Fig. 3, A and B) show discrete grains of organic material with sizes of ~200 nm. X-ray absorption by carbon atoms is also present in the phyllosilicate matrix at low levels but nearly ubiquitously (Fig. 3B). Carbon-XANES spectra of the discrete grains show three major peaks, resulting from aromatic carbon (C=C, 285 eV), aromatic ketone (C=C-C=O, 286.7 eV), and carboxyl (COOH, 288.5 eV) functional groups (Fig. 3E), which have been observed in primitive extraterrestrial carbonaceous matter, such as carbonaceous chondrites (*28*, *29*) and their extracted IOMs (*30*), interplanetary dust particles (IDPs) (*31*), dust particles from Comet Wild 2 (*32*), and Antarctic micrometeorites (AMMs) (*33*). Some spectra of fine-grained matrices in the Ryugu samples contain an additional peak at 290.4 eV, which corresponds to a 1s-π^* transition of carbonate groups—e.g., in calcite and other carbonate minerals. However, our matrix XANES spectra containing this feature lack extended x-ray absorption fine structure

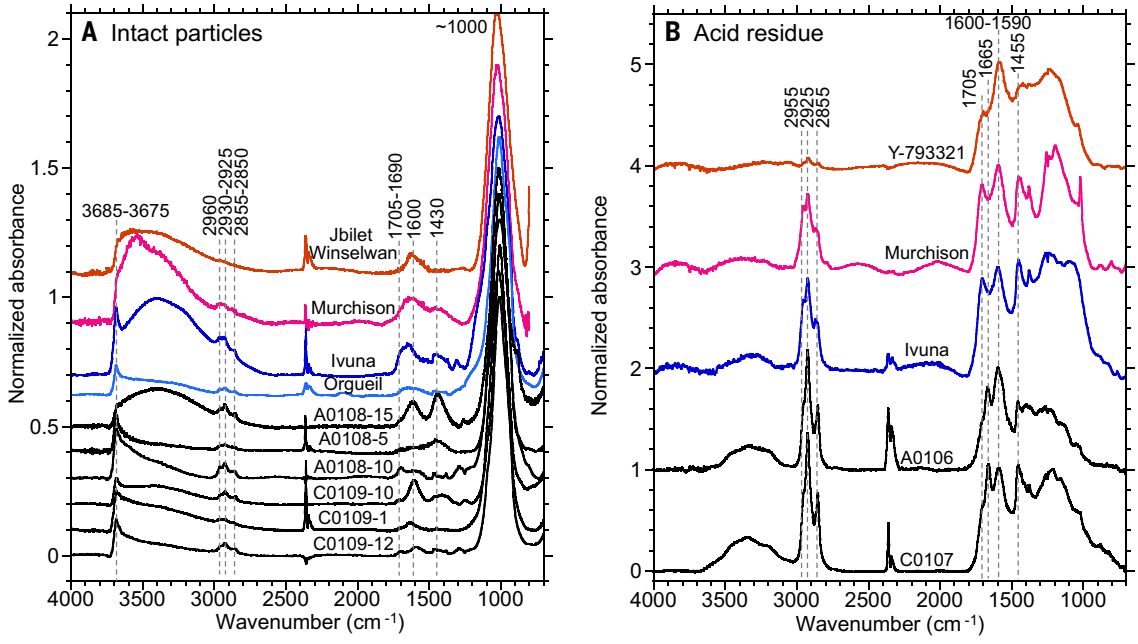

Fig. 2. Micro-FTIR spectra of Ryugu samples compared with chondrites. (**A**) Infrared transmission spectra (*11*) of six Ryugu grains from the aggregates A0108 and C0109 (black), heated CM chondrite (Jbilet Winselwan) (red), unheated CM Murchison (pink), and two CI chondrites Orgueil (light blue) and Ivuna (dark blue). All the spectra were baseline-corrected using spline curves and normalized by the peak height of the band at ~1000 cm^{-1} (~10.00 μm). Dashed lines indicate identified bands: silicate OH and SiO at 3685 to 3675 cm^{-1} (2.71 to 2.72 μm) and ~1000 cm^{-1} (~10.00 μm); aliphatic C-H bands at 2960 cm^{-1} (3.38 μm; CH_3 asymmetric stretching), 2930 to 2925 cm^{-1} (3.41 to 3.42 μm; CH_2 asymmetric stretching), 2855 to 2850 cm^{-1} (3.50 to 3.51 μm; CH_3 and CH_2 symmetric stretching), 1460 cm^{-1} (6.85 μm), and 1380 cm^{-1} (7.25 μm; bending); and other organic features at 1705 to 1690 cm^{-1} (5.87 to 5.92 μm; C=O) and ~1600 cm^{-1} (~6.25 μm; aromatic with some water bending mode contribution). Some spectra show a peak at ~1430 cm^{-1} (~6.99 μm) due to carbonates. A broad water stretching band at ~3400 cm^{-1} (~2.94 μm) is observed, which is weaker in samples that were measured at 60°C or higher temperatures. The peaks at 2360 cm^{-1} (4.24 μm) are due to atmospheric CO_2. The A0108-5 and C0109-1 Ryugu grains and the Murchison and Ivuna meteorites were measured at 60°C under N_2 flow. The Jbilet Winselwan meteorite was measured at 80°C under N_2 flow. The A0108-10 and C0109-12 Ryugu grains were measured at 80°C under vacuum. The Orgueil meteorite was measured at 130°C under vacuum. (**B**) Same as (A), but for insoluble carbonaceous residues from the Ryugu samples (A0106 and C0107) compared with IOM from the heated CM meteorite Y-793321 (*16*), the CM Murchison (*27*), and the CI meteorite Ivuna (*27*). The spectra were the averages of main fractions of A0106 and C0107, respectively, after baseline-correction using spline curves and normalization by the peak height of the aromatic C=C band at ~1600 cm^{-1} (~6.25 μm).

(EXAFS) features at higher energies (294 to 304 eV), indicating that the carbonate is not in a crystalline structure so is more likely to be molecular carbonate. A similar carbonate feature has previously been reported in clay-bound carbon from extensively hydrated carbonaceous chondrites, Ivuna (CI1), Orgueil (CI1), and Tagish Lake (C2) (*34*), and in diffuse carbon (organic matter) in the fine-grained matrices of Renazzo (CR2; a Renazzo-type carbonaceous chondrite of petrologic type 2), Murchison (CM2), and Orgueil (*28*).

We classify the STXM spectra of Ryugu organic matter on the basis of spectral shape similarities into four representative types: (i) highly aromatic (~25% of individual carbon grains), (ii) aromatic (~35% of individual grains), (iii) IOM-like (~40% of individual grains), and (iv) diffuse carbon associated with a molecular carbonate peak (Fig. 3E). Aromatic spectra show higher ratios of aromatic carbon to aromatic ketone compared with IOM-like spectra, whereas highly aromatic spectra show a broader peak for aromatic carbon, indicating increased diversity of aromatic structures. The frequency distributions of these classes were similar for both chamber A and C samples. We find a relationship between the morphology of organic matter and XANES spectral shape, with particulate and nanoglobular regions having more frequent aromatic or highly aromatic XANES spectra, whereas organic matter dispersed in the matrix more commonly has IOM-like or diffuse carbon spectra. These observations indicate that the molecular functional groups present are influenced by aqueous processing on the asteroid parent body. We did not find any evidence of long-duration thermal metamorphism, such as the 1s-σ* exciton (291.6 eV) peak of graphite or other graphitized carbon materials (*35*).

Similar characteristics are found for the insoluble carbonaceous residues from Ryugu. Average carbon-XANES spectra have IOM-like spectral shapes but with more prominent aromatic C=C, ketone, and carboxyl peaks compared with IOM from Orgueil and Murchison (Fig. 3E). Several hollow and solid organic nanoglobules are apparent in the x-ray absorption images (Fig. 3, C and D), which we confirmed using TEM imaging (Fig. 4, A and B). Their XANES spectra were either IOM-like, aromatic, or highly aromatic (Fig. 3E). The 290.4-eV carbonate feature was not observed in the insoluble carbonaceous residue, perhaps because this organic phase was incorporated into phyllosilicate interlayers and so was removed or destroyed during the acid-extraction process.

Nitrogen-XANES spectra (fig. S4A) of the Ryugu intact grains and insoluble residue did not show clear absorption peaks, indicating low abundances of N-rich Ryugu organics. This is consistent with carbonaceous chondrites, where N-rich particles are only occasionally observed (*32*). Oxygen-XANES spectra (fig. S4B) of Ryugu organic matter often contain a peak at ~531.3 eV, corresponding to carbonyl C=O bonds in the ketone and carboxyl functional groups (*36*). The peak intensity of the carbonyl absorption, relative to the main oxygen 1s-σ* peak in Ryugu, is similar to that of aqueously altered carbonaceous chondrites. We cannot determine whether these carbonyl functional groups are also present in the phyllosilicate-bound diffuse organic matter because its oxygen-XANES spectrum is dominated by the surrounding phyllosilicate.

Nanoscale morphologies

We performed TEM and STEM-EELS-EDS analysis (Fig. 4) on ultrathin sections of particles and carbonaceous residues, including from some of the same sections we analyzed

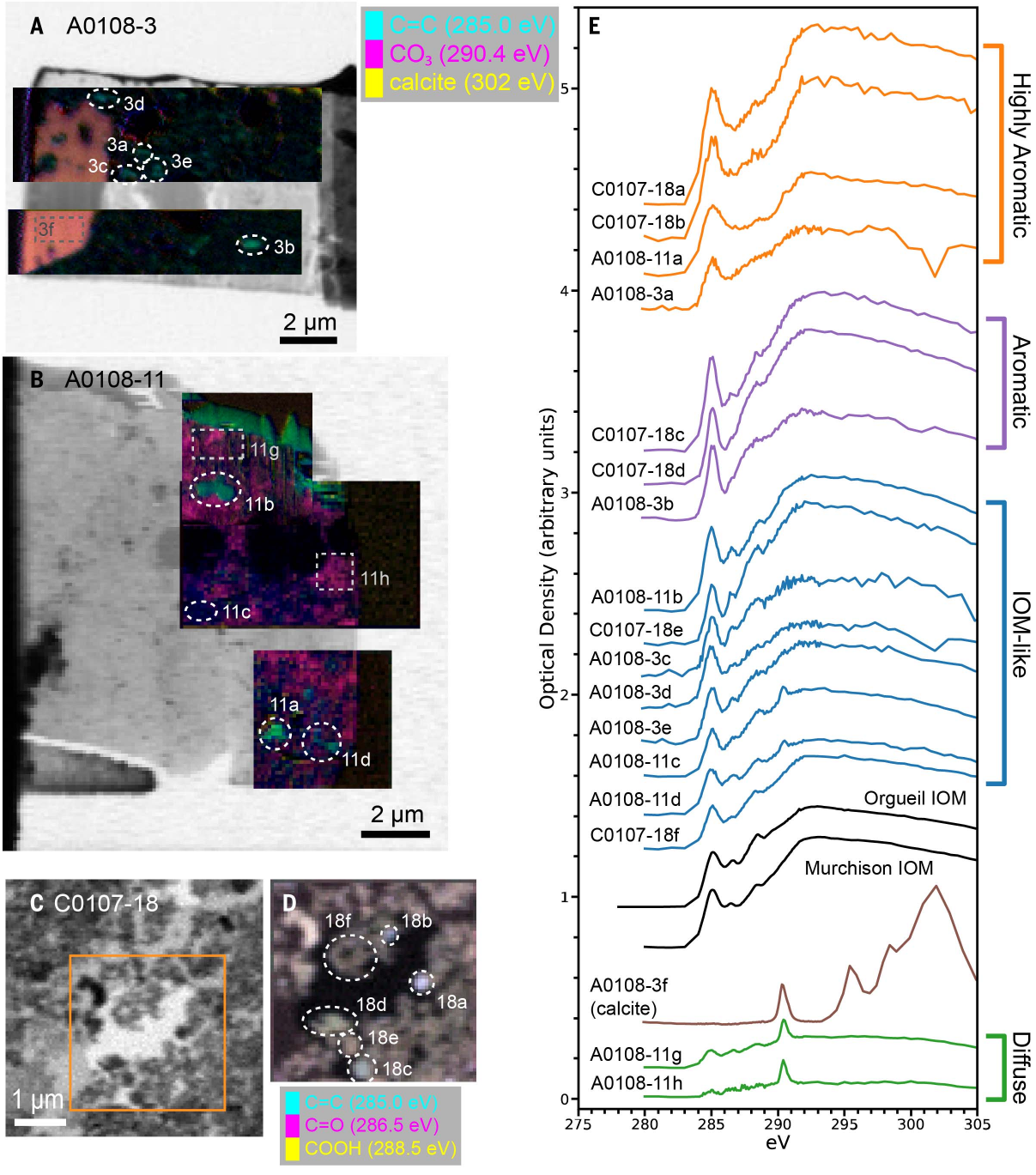

Fig. 3. STXM elemental maps and carbon-XANES spectra of Ryugu samples. (**A** and **B**) STXM grayscale images of FIB sections extracted from the Ryugu grains A0108-3, observed at 520 eV (A), and A0108-11, observed at 390 eV (B) (*11*). In both panels, color overlays on both FIB sections are false-color maps of x-ray absorptions due to aromatic C (cyan), carbonate functional groups (magenta), and calcite minerals (yellow). Dashed circles and boxes indicate regions measured for (E). (**C**) STXM image at 290 eV of insoluble carbonaceous residue from Ryugu sample C0107-18. The orange box shows the region in (D). (**D**) X-ray absorption map of aromatic carbon (cyan), ketones (magenta), and carboxyl (yellow) functional groups. Circled features are solid nanoglobules except for feature 18f, which is a cluster of typical Ryugu IOM. (**E**) Carbon-XANES spectra for carbonaceous grains and matrix regions identified in (A), (B), and (D). IOM from the meteorites Orgueil and Murchison (black) are shown for comparison (*11*).

previously with STXM. The two most abundant organic microstructures are nanoglobules (Fig. 4, A and B) and diffuse carbon mixed with phyllosilicates—i.e., clay-bound carbon (Fig. 4, C and E). Other microstructures include dense, irregularly shaped particles (Fig. 4B); diffuse organic matter trapped in vesicles in carbonate grains (Fig. 4, D and F); and organic matter coatings on sulfide grains. The presence of organic matter associated with Mg-rich phyllosilicates and carbonates, which likely formed through aqueous alteration (*24*), implies that much of the organic material was altered by low-temperature, aqueous processing on Ryugu's parent body. However, we also find nanodiamonds associated with amorphous organic carbon, which probably formed in the interstellar medium or the Solar System's protoplanetary

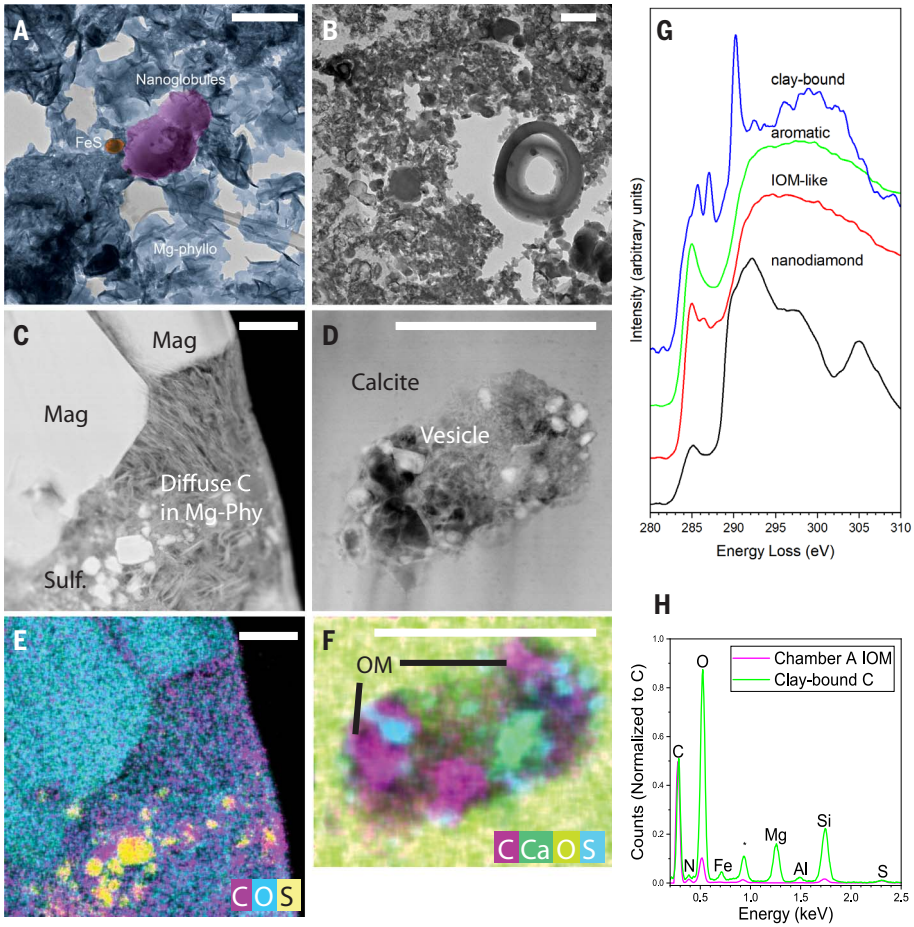

Fig. 4. STEM-EELS-EDS analysis of Ryugu samples. All scale bars are 500 nm. (**A**) False-color bright-field TEM image of the ultrathin section of C0109-11, indicating nanoglobules (magenta), Mg-phyllosilicates (blue), and FeS (orange). (**B**) Bright-field TEM image of insoluble organic residue from a microtome slice of sample C0107, showing hollow and solid nanoglobules and fluffy materials. (**C**) High-angle annular dark field (HAADF) STEM image of a FIB section of A0108-11 (region 11h in Fig. 3B) showing two magnetite grains (labeled Mag) adjacent to carbon-bearing Mg-rich phyllosilicates (Mg-phy) with Fe and Ni sulfide nanoparticles (Sulf). (**D**) HAADF STEM image of a vesicle in the large calcite grain from a FIB section of sample A0108-3 (region 3a in Fig. 3A). (**E**) EDS element map of carbon (magenta), oxygen (cyan), and sulfur (yellow) of the area shown in (C). (**F**) EDS element map of carbon (magenta), calcium (green), oxygen (yellow), and sulfur (cyan) of the vesicle shown in (D) showing diffuse organic matter, Fe,Ni-sulfides, and Ca-sulfate. (**G**) Carbon EEL spectra from molecular carbonate incorporated into phyllosilicates, i.e., clay-bound carbon (C0109-11), an aromatic nanoglobule (A0108-39), an IOM-like nanoglobule (C0109-11), and nanodiamonds (A0108-8). Spectra were acquired at 0.02 eV per channel, and are smoothed to 0.4-eV resolution, after power law background subtraction and arbitrary scaling. (**H**) EDS spectra from molecular carbonate clay-bound carbon (C0109-11; green) and an insoluble organic residue (A0106-9; magenta). The asterisk indicates a Cu background peak from the sample support and microscope.

nebula (*37*, *38*). The insoluble carbonaceous residues contain large nanoglobules and fluffy or porous material, comprising demineralized grain coatings, intergranular material, and small nanoglobules. These microstructures are present in samples from both chambers A and C, and they are consistent in size and shape with those in CI and CM chondrites (*28*, *34*).

Organic nanoglobules have previously been found in early Solar System materials, such as primitive carbonaceous chondrites (*39*–*42*), dust particles from Comet Wild 2 (*32*), IDPs (*43*), and AMMs (*33*, *44*). The nanoglobules in Ryugu grains occur in solid and hollow form, typically 50 to 500 nm in diameter, with a few reaching 2000 nm, consistent with nanoglobules in other extraterrestrial materials. The carbon EELS spectra of many of the Ryugu nanoglobules are dominated by an aromatic carbon peak at ~285 eV (Fig. 4G), corresponding to the aromatic-rich carbon-XANES spectra (Fig. 3E). Other prominent peaks are due to aromatic ketone (286.7 eV) and carboxyl (288.5 eV). The fluffy material in the insoluble carbonaceous residues shows these three peaks in varying intensities. The presence of both aromatic- and IOM-like nanoglobules of various sizes indicates that Ryugu experienced heterogeneous aqueous alteration on its parent body. Correlated STEM-NanoSIMS measurements of a 2000-nm nanoglobule (particle A0108-37; figs. S6 and S7) show high abundances of aromatic carbon and isotopically anomalous H and N, indicating preservation of material from the interstellar medium or protoplanetary nebula.

The widespread diffuse carbon mixed into phyllosilicates could have been formed from soluble molecules intercalated into clays through oxidation during aqueous alteration (*34*). Alternatively, the clay-bound diffuse carbon might have been released by hydrolysis of macromolecular organic material during the flow of aqueous fluids (*28*). The EELS spectra show peaks of either aromatic ketones or aliphatic carbon (287 eV) and carbonate (CO_3 at 290.4 eV) along with aromatic carbon (285 eV) (Fig. 4G). These EELS data are consistent with the carbon-XANES spectrum of the diffuse carbon (Fig. 3, B and E). The relative intensities of the 287-eV and 285-eV peaks vary compared with the 290.4-eV peak. This is consistent with clay-bound organics in CI chondrites (*34*) but sometimes is a better match to the ungrouped C2 chondrite Tagish Lake (*34*). In all cases, Mg is detected in the EDS spectra from the clay-bound organic matter (Fig. 4F); however, we cannot determine whether the Mg is associated with the carbonate. We find no evidence for crystalline Mg carbonate in the clay-bound organics, but the CO_3 feature could be associated with molecular CO_3, $MgCO_3$, or a combination of these.

Pockets of organic matter occur in vesicles inside carbonates (Fig. 4D). A STEM-EDS image (Fig. 4F) shows that this vesicle-bound, diffuse organic matter is associated with phyllosilicates and particles of sulfide and Fe-Ni with sizes of ~10 nm, embedded in a larger grain of calcite. This morphology could indicate carbonate formation from diffuse organic matter. The lack of distinct particle boundaries for the organic matter could indicate it is soluble and therefore potentially lost during our sample preparation, which used ultramicrotomy with a water bath.

We obtained AFM-IR maps of organic inclusions and nanoglobule-like matter at lateral resolutions of 25 and 50 nm. AFM-IR measurements map specific vibrational modes; we used the C=O and C=C modes. Samples from chambers A and C were analyzed using AFM-IR in both tapping and contact modes. Figure 5, A and H, shows combined maps of carbonyl C=O (1720 cm^{-1}, 5.81 μm), aromatic C=C (1600 cm^{-1}, 6.25 μm), and Si-O (1020 cm^{-1}, 9.80 μm) modes. The diffuse organic component within the phyllosilicate matrix is evident in both samples. The maps show small (up to ~100 nm) organic nanoglobule-like inclusions

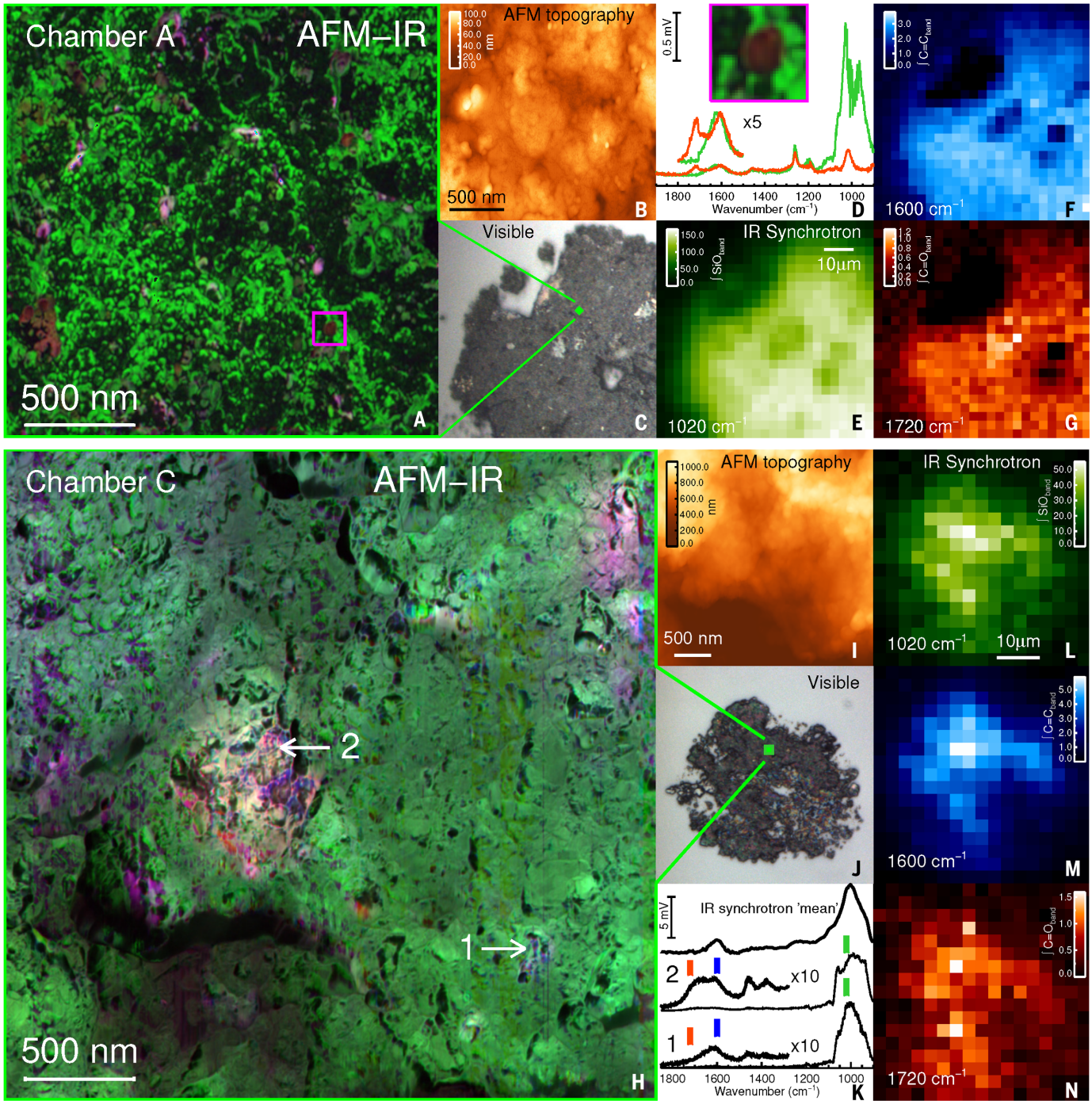

Fig. 5. AFM-IR analysis of intact Ryugu grains A0108 and C0109. (**A** and **H**) Composite AFM-IR images of the intact Ryugu grains A0108-15 in tapping mode, 2 μm by 2 μm (A), and C0109-4 in contact mode, 3 μm by 3 μm (H). Colors indicate the C=O (1720 cm^{-1}, 5.81 μm; red), C=C (1600 cm^{-1}, 6.25 μm; blue), and Si-O (1020 cm^{-1}, 9.80 μm; green) peaks. Each image has been normalized to its maximum peak value. Organic matter is widespread throughout each sample. In (A), small organic globules are visible (red-brown) surrounded by a dominant phyllosilicate. The magenta box indicates the inclusion used for (D). (**B**) AFM topographic map of the 2 μm–by–2 μm area in (A). (**C**) Visible light image (75 μm by 75 μm) showing the location of the AFM-IR map (green square). (**D**) AFM-IR spectrum (red) of the globule indicated in (A) and shown in the inset and background spectrum (green) taken in a region 100 nm away. The AFM-IR signal is shown in millivolts, which is proportional to optical depth (*11*). The C=C and C=O absorptions spectral region is also shown with a ×5 factor for better visibility. (**E** to **G**) Synchrotron FTIR maps of the same 75 μm–by–75 μm area as in (C) of the C=O (1720 cm^{-1}, 5.81 μm; red) (G), C=C (1600 cm^{-1}, 6.25 μm; blue) (F), and Si-O (1020 cm^{-1}, 9.80 μm; green) (E) peaks. Data were acquired with a 6 μm–by–6 μm beam size, sampled with 3-μm steps. Color bars show the integrated optical depths calculated for each band. (H) Organic matter in the Ryugu grain C0109-4 appears as red-purple inclusions standing out from the dominant phyllosilicate signal. Arrows indicate the positions used for the spectra in (K). (**I**) AFM topographic map of the 3 μm–by–3 μm area. (**J**) Visible image (51 μm by 51 μm) showing the location of the AFM-IR map (green square). (**K**) AFM-IR spectra of a C=O–poor region [labeled 1 in (H)] and organic inclusions (labeled 2) compared with the average synchrotron FTIR spectrum. Red, blue, and green tick marks indicate spectral positions corresponding to the AFM-IR images combined in (H). (**L** to **N**) Same as [(E) to (G)] but for the 51 μm–by–51 μm region shown in (J). To aid color-blind readers, another version of this figure with alternatives colors is provided as fig. S5.

in the chamber A sample (Fig. 5A) and organic inclusions in the chamber C samples (Fig. 5H). The abundances of carbonyl and C=C vary between the organic inclusions. These AFM-IR results are consistent with and complimentary to those from STEM-EELS-EDS and STXM-XANES discussed above.

Elemental abundances

The elemental abundances of macromolecular organic matter in meteorites are highly heterogeneous, both between meteorite groups and at the micrometer scale, reflecting the complex histories of these materials (*45*, *46*). We used NanoSIMS to map the H, C, N, O, and S elemental abundances of the Ryugu samples.

The ratios of O/C, N/C, and S/C in the acid-insoluble carbonaceous residues from Ryugu were estimated from NanoSIMS elemental maps of the major isotopes (^{16}O, $^{12}C^{14}N$, and ^{32}S) and were compared between samples taken from chambers A and C. The bulk O/C ratio (0.12 ± 0.03) in chamber A was consistent with those of CI (0.15 to 0.18), CM (0.11 to 0.23), and CR chondrites (0.11 to 0.22) (*45*). The bulk O/C ratio (0.04 ± 0.01) in chamber C was one-third of those values. We cannot determine whether this difference is the result of intrinsic differences between the two sampling sites or heterogeneity within the samples. There are smaller differences in the bulk ratios N/C [0.035 ± 0.006 (A0106); 0.021 ± 0.001 (C0107)] and S/C [0.032 ± 0.001 (A0106); 0.025 ± 0.001 (C0107)] between the two chambers, which are within the ranges of those for CI, CM, and CR chondrites ($0.026 < N/C < 0.039$ and $0.02 < S/C < 0.06$) (*45*).

We also used STEM-EDS to measure N, O, and S abundances, relative to C, at the nano- to micrometer scale. An EDS spectrum from an ~1-μm^2 region of an ultrathin section of carbonaceous residue from chamber A is shown in Fig. 4H. The average compositions measured for carbonaceous residues are $C_{100}N_1O_{10}S_{0.8}$ for chamber A and $C_{100}N_2O_{10}S_{0.8}$ for chamber C. The insoluble carbonaceous residues contain some nanoparticulate minerals, including chromite, with varying Al, Mg, and Fe and sulfides with variable Fe, Ni, and (more rarely) CuS. These particles were excluded from the STEM-EDS measurements when >4 nm in size. These nitrogen abundances are slightly lower than the bulk N/C ratio estimated using NanoSIMS and are consistent with the weak nitrogen-XANES absorption of the Ryugu grains.

Isotopic compositions

NanoSIMS was also used to measure the isotopic compositions of H, C, and N. The resulting maps (Fig. 6, A to C) show bulk enrichments of D (^2H) and/or ^{15}N in most analyzed Ryugu particles from aggregates A0108 and C0109, with a high degree of isotopic heterogeneity at the micrometer scale. The NanoSIMS H measurements are dominated by H from the organic matter but also include H in phyllosilicates and possible contamination by terrestrial water. The isotopic compositions are expressed in delta notation: $\delta R = [(R_{sample}/R_{standard}) - 1] \times 1000$, where R_{sample} is the isotopic ratio of the sample and $R_{standard}$ is the ratio of a terrestrial standard. The average measured H isotopic compositions (δD) of particles range from +254 ± 52 per mil (‰) to +490 ± 100‰ (table S3), consistent with the δD = +252 ± 13‰ measured in an analysis of other Ryugu grains with a different technique (*47*). There is no obvious difference between grains from chambers A and C. The bulk N isotopic compositions $\delta^{15}N$ = +39 ± 5 to +43 ± 4‰ are also within the range reported for other Ryugu grains, measured with different methods [$\delta^{15}N$ = +43.0 ± 9.0‰ (*47*) and $\delta^{15}N$ = 0 to +20‰ (*48*)]. Figure S8 shows that the bulk δD and $\delta^{15}N$ of the Ryugu grains are between the bulk values of CI chondrites [δD = +170 to +300‰ and $\delta^{15}N$ = +39 to +52‰ (*49*)] and IOM in CI chondrites [δD = ~+975‰ and $\delta^{15}N$ = +31‰ (*45*)].

Isotopic ratios determined for individual submicrometer- to micrometer-sized carbonaceous grains within the NanoSIMS maps are similar to those of carbonaceous chondrites and IDPs (*43*, *46*). Most grains are consistent with the bulk average, within the uncertainties, whereas a small fraction of outliers have D and/or ^{15}N enrichments or depletions (Fig. 6, D to F), which we term hotspots and coldspots, respectively. These have a similar range of compositions to those seen in CI (*46*) and CM (*50*) chondrites but smaller than that seen in CR chondrites (*29*). There is no correlation between δD and $\delta^{15}N$ for the hot- or coldspots, and a wide range of compositions occur over small spatial scales (Fig. 6, B and C). The origin(s) of the H and N isotopic anomalies in meteorites are debated; current consensus models propose that they reflect isotopic fractionation at low temperatures in interstellar clouds or the outer protoplanetary nebula (*51*–*54*).

The NanoSIMS measurements show that the bulk Ryugu particles, and almost all C-rich particles within them, have $\delta^{13}C$ values within the range of organic matter in carbonaceous chondrites [$\delta^{13}C$ = −35 to −5‰ (*45*)]. However, ~0.5% of the C-rich particles have ^{13}C enrichments or depletions (Fig. 6G) >2σ above or below the bulk values. These particles have a range of $\delta^{13}C$ and $\delta^{15}N$ values similar to those seen in organic grains with anomalous carbon isotopes in primitive CM chondrites. For the Ryugu samples, ^{13}C-rich particles have a wider range of $\delta^{15}N$ values compared with ^{13}C-poor ones, likely reflecting different origins. Two very small (≤150 nm) regions have much higher ^{13}C enrichments: $\delta^{13}C$ = 700 and 4800‰, which indicates that they are presolar grains that formed in the outflows of previous generations of stars (*55*).

The acid-insoluble carbonaceous residues from the Ryugu samples showed bulk D-enrichments [δD = +306 ± 42‰ (A0106) and +440 ± 52‰ (C0107)] (Fig. 7I) lower than the bulk hydrogen compositions of the IOM in CI chondrites (δD = +972‰ for Orgueil and +978‰ for Ivuna) and CM chondrites (+639‰ < δD < +893‰) (*45*). The distributions of D-rich hotspots [distribution modes δD = +1030‰ (A0106) and +1374‰ (C0107)] were consistent with CI and CM chondrites but not CR chondrites (*56*).

The bulk N isotopic compositions of the insoluble carbonaceous residues from Ryugu samples [$\delta^{15}N$ = +17.4 ± 1.9‰ (A0106) and +30 ± 4.3‰ (C0107)] (Fig. 7J) are consistent with those of IOM in CI chondrites ($\delta^{15}N$ = +30.7‰ for Orgueil and +31.9‰ for Ivuna) (*45*). $\delta^{15}N$ was more heterogeneous in the sample from chamber C than that from chamber A. The ^{15}N-rich hotspots [distribution modes $\delta^{15}N$ = +241‰ (A0106) and +348‰ (C0107)] were within the range of CI and CM carbonaceous chondrites (*57*). ^{15}N-depleted coldspots ($\delta^{15}N$ = −100 to −380‰) were detected. ^{15}N coldspots have previously been reported in the matrices of carbonaceous chondrites (*57*–*59*) and IDPs (*43*) and have been interpreted as indicating organic grains that have been partially equilibrated with protosolar or interstellar N_2 gas (*43*).

Comparison with D-type asteroids and comets

We compare the organic matter of Ryugu (a C-type asteroid) with other primitive small bodies in the early Solar System. Of the carbonaceous chondrites, the Tagish Lake meteorite is thought to be related to dark (D-type) asteroids, which are mainly located in the outer regions of the asteroid belt and among the trojan asteroids of Jupiter (*60*). Tagish Lake contains organic and mineralogical variations between different specimens that reflect variable degrees of alteration on the same parent body (*61*, *62*). The ratios D/H, H/C, and aliphatic carbon to aromatic carbon decrease systematically with increasing alteration of the Tagish Lake meteorite samples (*61*).

We infer that the organic matter in the Ryugu samples has not been heated to temperatures higher than 200°C based on the similarity of its chemical features with primitive carbonaceous CI and CM chondrites. Like the IOM from Orgueil (*63*) and Murchison (*64*), the organic macromolecules in the Ryugu samples likely contain polyaromatic structures that are composed of small numbers of aromatic rings with short, cross-linked aliphatic chains and various oxygen- and nitrogen-bearing functional groups. This macromolecular structure is distinct from graphitic or glassy carbon produced by heating: We did not find any evidence

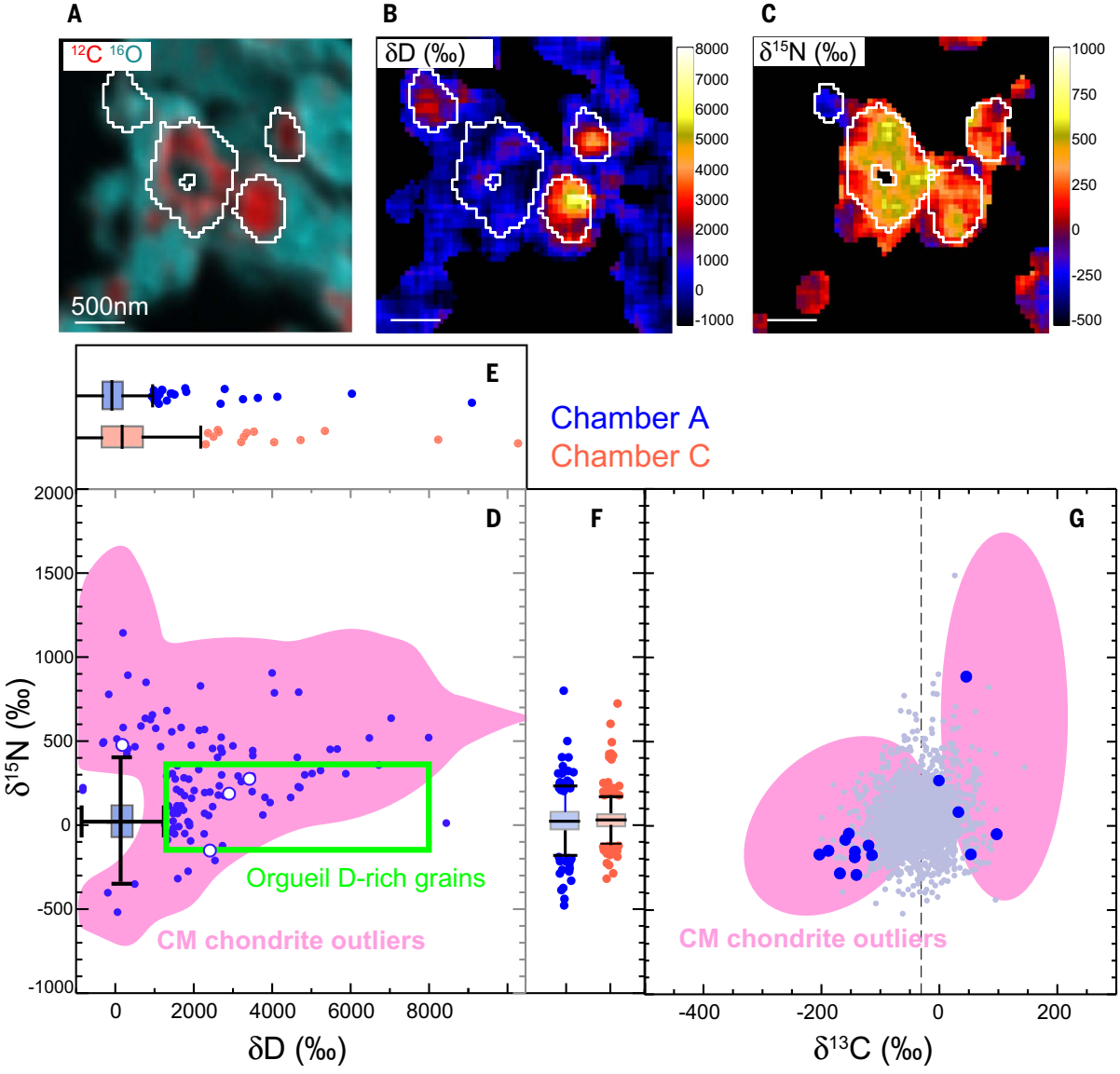

Fig. 6. NanoSIMS analysis of the intact Ryugu grains A0108 and C0109. (**A** to **C**) NanoSIMS images of an ~3 mm–by–3 mm area of a microtome slice from Ryugu grain A0108-11. (A) Map of ^{16}O (cyan) and ^{12}C (red). White outlines indicate four C-rich particles embedded in the silicate matrix. (B and C) Hydrogen (B) and nitrogen (C) isotope abundances of the same region. The ratios vary between the carbonaceous inclusions. (**D** to **F**) H and N isotopic ratios for individual C-rich particles [regions of interest (ROIs)] within Ryugu grains. Most ROIs are consistent (within the uncertainties) with the bulk averages; they are represented by box-and-whisker plots, where the box size represents the inner 50% of data around the median [interquartile range (IQR)] and the whiskers indicate the ±1.5 IQR range beyond that. Dots indicate outliers beyond those ranges (hotspots and coldspots) from A0108 (blue) and C0109 (orange). In (D), white dots indicate the grains shown in (A) to (C), and the error bar is 1σ. The distributions of H and N isotope ratios are consistent between (D) and those in (E) and (F) (acquired in different laboratories) and between the two Ryugu samples. The pink shaded region indicates the ranges of H and N hotspots and coldspots in primitive CM chondrite meteorites (*50*), and the green box indicates the ranges seen in CI chondrite Orgueil (*46*). The Ryugu outliers span a similar range to that of the CI and CM chondrites. (**G**) $\delta^{15}N$ as a function of $\delta^{13}C$ for the Ryugu grain A0109. The gray points indicate all C-rich ROIs, whereas blue circles are outliers (>2σ away from bulk average). The pink region is the same as in (D). The Ryugu outliers span a similar range to that seen in CM chondrites. The dashed vertical line indicates the bulk $\delta^{13}C$ of CI chondrite IOM.

of highly conjugated sp^2 carbon. Laboratory experiments have shown that aliphatic carbon in IOM from primitive carbonaceous chondrites is reduced after hydrous heating at 300°C for 6 days (*65*). Therefore, the higher abundance of aliphatic carbon in the organic residue of Ryugu—compared with that of primitive carbonaceous chondrites—indicates that the Ryugu grains did not experience short heating equivalent to the experimental conditions.

The distribution of organic functional groups present in the Ryugu samples is unlike aqueously altered carbonaceous chondrites, for which organic particles and nanoglobules show predominantly IOM-like XANES spectra with only occasional highly aromatic grains (*28*, *30*, *66*). Ryugu samples contain abundant aromatic-rich particles and nanoglobules, a high abundance of IOM-like diffuse carbon in matrix, and molecular carbonate associated with phyllosilicates. Progressive aqueous alteration in situ causes (i) an increase in the amount of diffuse organic matter associated with matrix phyllosilicates, (ii) an increase in the proportion of aromatic and oxygen-bearing functional groups in discrete organic particles and nanoglobules, and (iii) an increase in the variety of XANES spectral features. On the basis of these trends, much of the internal spectral variation in the Ryugu samples, including carbon grains with

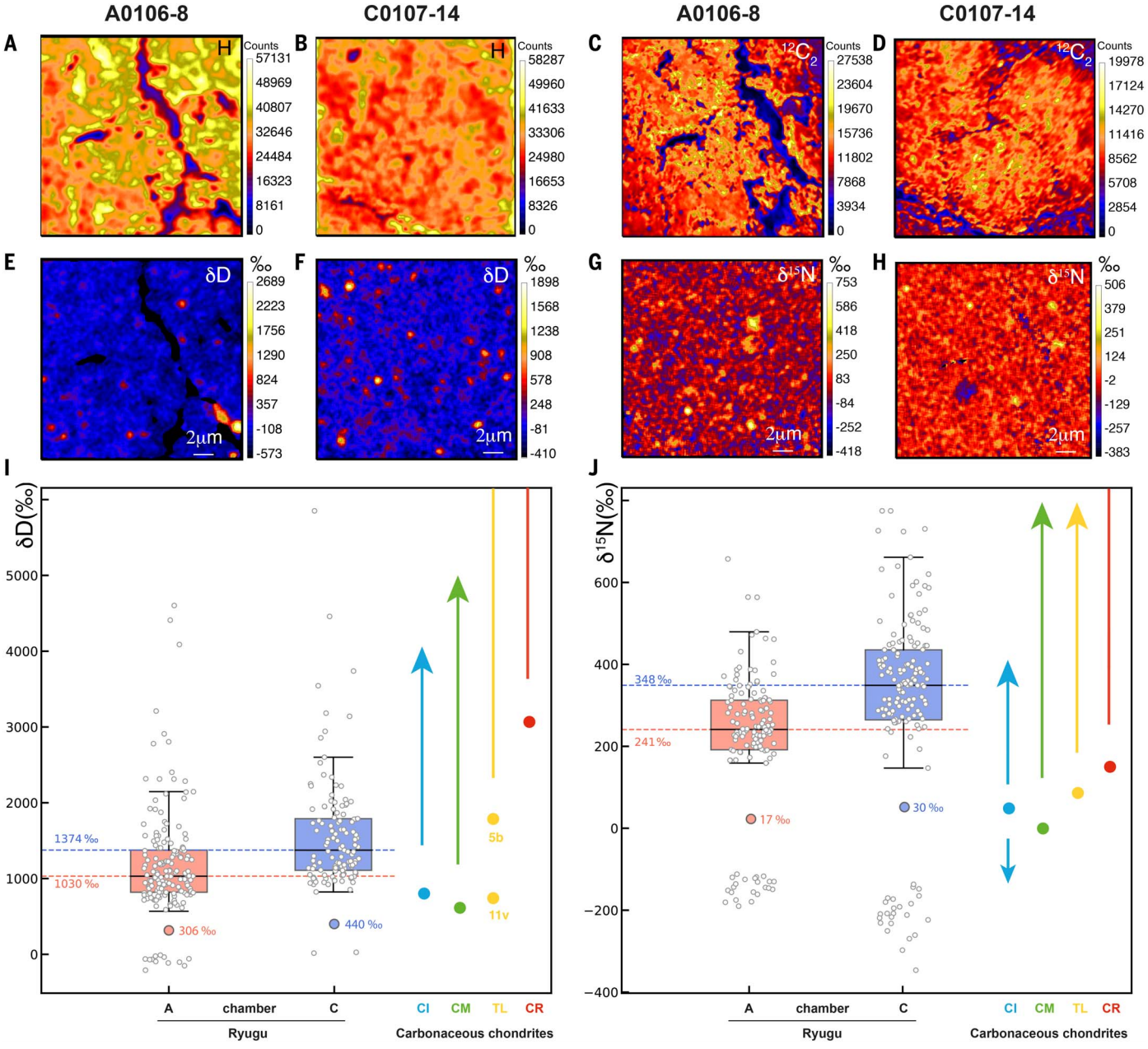

Fig. 7. NanoSIMS analysis of insoluble carbonaceous residues from Ryugu grains A0106 and C0107. (**A** to **D**) Hydrogen [(A) and (B)] and carbon [(C) and (D)] maps for insoluble carbonaceous residues of A0106 and C0107, respectively, acquired at the same locations. (**E** to **H**) The corresponding H [(E) and (F)] and N [(G) and (H)] isotope ratio maps show numerous micrometer-sized D-rich and ^{15}N-rich hotspots. The carbon and hydrogen images indicate that these hotspots consist of organic carbon. (**I** and **J**) Hydrogen (I) and nitrogen (J) box plot diagrams showing the distributions of isotope ratios in the insoluble carbonaceous residues A0106-8 (orange) and C0107-14 (blue). Open gray circles show hotspots (or coldspots), micrometer-sized areas with isotope ratios much higher (or lower) than the average composition. Large orange and blue circles indicate the bulk average value for each residue. Horizontal dashed lines indicate the mode of each distribution of hotspots. Data for the IOM of CI (light blue), CM (green), CR (red), and Tagish Lake (yellow) chondrites are shown for comparison. Filled circles are bulk values (*45*); for Tagish Lake, subsamples 5b (less altered) and 11v (altered) (*61*) are shown separately. Upward-pointing arrows (some extend beyond the plot) indicate the range of hotspots reported for those meteorites (*46*, *56*, *57*). For Orgueil, the downward arrow indicates the extent of ^{15}N-depleted coldspots.

an aromatic XANES spectral shape (Fig. 3E), likely developed through redistribution of organic matter and formation of additional organic molecules during aqueous alteration on the parent body rather than preaccretionary diversity inherited from the protosolar molecular cloud. Carbonaceous grains and nanoglobules with highly aromatic XANES spectra (not aromatic spectra; Fig. 3E) provide a possible exception to this proposal. These highly aromatic grains are more likely to represent original accreted materials because similar XANES spectra have been found in unaltered, petrologic type 3 carbonaceous chondrites (*30*) and in cometary dust particles (*32*). This is consistent with our observation of a large, highly aromatic nanoglobule containing D and ^{15}N isotopic anomalies (figs. S6 and S7).

The δD distributions of the C-rich particles in the Ryugu grains are consistent with those in the Tagish Lake meteorite (*56*) and CI and

CM chondrites (*46*, *57*). The δD distributions of the Ryugu insoluble carbonaceous residues from chambers A and C are within the ranges of IOMs in the most and least altered fragments of Tagish Lake, respectively (*61*). The hydrogen isotopic variations among the different lithologies of Tagish Lake have previously been explained by depletion of D through hydrogen isotopic exchange or hydrolysis of D-rich structures of IOM during various degrees of planetesimal hydrothermal alteration (*65*, *67*). By contrast, the δD distributions of our Ryugu samples are lower than those of less-altered CR chondrites (*56*), the most primitive class of IDPs (*68*), and comet-derived AMMs (*33*, *69*). We therefore propose that Ryugu organic matter is a product of heterogeneous aqueous processing, which occurred on both C- and D-type asteroids, of the common primordial materials formed at an earlier stage of the solar nebula. The $\delta^{15}N$ distributions of the intact grains and insoluble residues from our Ryugu samples were within the ranges of C-rich particles (*39*, *56*) and IOM (bulk) (*61*) in Tagish Lake and Comet Wild 2 (*32*) as well as CI and CM chondrites. However, they are lower than the $\delta^{15}N$ distributions of anhydrous IDPs (*43*, *68*) and the IOM from CR chondrites (*56*). Nitrogen isotopic compositions are less affected than hydrogen isotopes by modification through parent body processes (*45*, *57*, *61*, *66*), and their variations indicate mixing of different isotopic components from different precursors (*53*).

Nitrogen content can be an indicator of chemical evolution in the early Solar System. The measured N abundance (N/C = 0.01 to 0.035) of the insoluble carbonaceous residue in Ryugu samples is similar to that in primitive carbonaceous chondrites (*45*) and consistent with the total bulk N abundance (~0.15 wt %) (*47*). The N/C ratio of IOM from Tagish Lake (~0.042) is higher than those of the Ryugu samples. By contrast, some cometary materials, such as dust particles from Comet Wild 2, anhydrous AMMs, and ultracarbonaceous AMMs (UCAMMs), contain N-rich organics [N/C = 0.07 to 0.24 (*32*, *44*, *70*)]. Those are composed of a variety of nitrogen-bearing functional groups, such as imine, nitrile and/or heterocyclic N, or amide (*32*, *33*, *44*, *70*, *71*). The N contents of Comet 67P/Churyumov-Gerasimenko particles were heterogeneous (N/C = 0.018 to 0.06) (*72*) but lower than the N/C ratio of the Sun (0.3 ± 0.1) (*73*). The depletion of N in that comet might be because of the presence of ammonium salts (*74*, *75*). These variations in N/C between different Solar System objects could arise from partitioning between gas and solid phases in the cold interstellar cloud or outer solar nebula or from exposure to the warmer inner Solar System during perihelion passage (*74*) rather than from processing in the interiors of planetesimals. Experiments simulating parent-body aqueous alteration show the N/C ratios in meteoritic IOMs are not substantially modified (*65*, *76*). We therefore conclude that the N abundance in Ryugu macromolecular organic matter is intrinsic—not the product of extensive parent-body processing.

Conclusions

Our analysis of Ryugu samples indicates a direct link between macromolecular organic matter in C-type asteroids and that in primitive carbonaceous chondrites. The observed similarities and variations in molecular, isotopic, and morphological compositions between the Ryugu samples and other Solar System materials indicate a continuum of source material in the solar nebula, which was incorporated into C-type asteroids, D-type asteroids, and comets in the early Solar System. Macromolecular organic matter in the surface grains of asteroid Ryugu reflects various degrees of parent-body aqueous alteration and localized preservation of inherited nebular or molecular cloud history. The highly variable nature of the material indicates that the Ryugu organic matter is likely derived from material that was not subjected to long-term space weathering and was only recently exposed to the asteroid surface. The macromolecular organic matter shows no record of high-temperature impact heating of Ryugu, despite the asteroid being a rubble-pile body formed from impact debris and geomorphological evidence that it experienced subsequent impact cratering (*2*, *3*). This observation is consistent with the homogeneous reflectance spectra of Ryugu's surface (*3*).

Ryugu materials are much darker than those from primitive carbonaceous chondrites, despite having similar carbon contents (*23*, *47*), so some other factor (or factors) must determine the albedo. Possibilities include the macromolecular organic matter mixed with phyllosilicates (as discussed in this study) or nanophase sulfides (*24*), both of which have high light absorption efficiency owing to their small grain sizes. Such major, complex aromatic macromolecules in C- and/or D-type asteroids could have supplied the organic inventory and prebiotic molecules (*47*) that contributed to making Earth a habitable planet.

REFERENCES AND NOTES

1. S. Tachibana *et al*., Hayabusa2: Scientific importance of samples returned from C-type near-Earth asteroid (162173) 1999 JU_3. *Geochem. J.* **48**, 571–587 (2014). doi: 10.2343/geochemj.2.0350
2. S. Watanabe *et al*., Hayabusa2 arrives at the carbonaceous asteroid 162173 Ryugu—A spinning top–shaped rubble pile. *Science* **364**, 268–272 (2019). doi: 10.1126/science.aav8032; pmid: 30890588
3. S. Sugita *et al*., The geomorphology, color, and thermal properties of Ryugu: Implications for parent-body processes. *Science* **364**, eaaw0422 (2019). doi: 10.1126/science.aaw0422; pmid: 30890587
4. K. Kitazato *et al*., The surface composition of asteroid 162173 Ryugu from Hayabusa2 near-infrared spectroscopy. *Science* **364**, 272–275 (2019). doi: 10.1126/science.aav7432; pmid: 30890589
5. T. Morota *et al*., Sample collection from asteroid (162173) Ryugu by Hayabusa2: Implications for surface evolution. *Science* **368**, 654–659 (2020). doi: 10.1126/science.aaz6306; pmid: 32381723
6. N. Sakatani *et al*., Anomalously porous boulders on (162173) Ryugu as primordial materials from its parent body. *Nat. Astron.* **5**, 766–774 (2021). doi: 10.1038/s41550-021-01371-7
7. E. Tatsumi *et al*., Spectrally blue hydrated parent body of asteroid (162173) Ryugu. *Nat. Commun.* **12**, 5837 (2021). doi: 10.1038/s41467-021-26071-8; pmid: 34611167
8. E. Tatsumi *et al*., Collisional history of Ryugu's parent body from bright surface boulders. *Nat. Astron.* **5**, 39–45 (2021). doi: 10.1038/s41550-020-1179-z
9. T. Yada *et al*., Preliminary analysis of the Hayabusa2 samples returned from C-type asteroid Ryugu. *Nat. Astron.* **6**, 214–220 (2021). doi: 10.1038/s41550-021-01550-6
10. C. Pilorget *et al*., First compositional analysis of Ryugu samples by the MicrOmega hyperspectral microscope. *Nat. Astron.* **6**, 221–225 (2021). doi: 10.1038/s41550-021-01549-z
11. Materials and methods are available as supplementary materials.
12. S. Tachibana *et al*., Pebbles and sand on asteroid (162173) Ryugu: In situ observation and particles returned to Earth. *Science* **375**, 1011–1016 (2022). doi: 10.1126/science.abj8624; pmid: 35143255
13. L. Bonal, E. Quirico, M. Bourot-Denise, G. Montagnac, Determination of the petrologic type of CV3 chondrites by Raman spectroscopy of included organic matter. *Geochim. Cosmochim. Acta* **70**, 1849–1863 (2006). doi: 10.1016/j.gca.2005.12.004
14. H. Busemann, C. M. O'D. Alexander, L. R. Nittler, Characterization of insoluble organic matter in primitive meteorites by microRaman spectroscopy. *Meteorit. Planet. Sci.***42**, 1387–1416 (2007). doi: 10.1111/j.1945-5100.2007.tb00581.x
15. L. Bonal, E. Quirico, L. Flandinet, G. Montagnac, Thermal history of type 3 chondrites from the Antarctic meteorite collection determined by Raman spectroscopy of their polyaromatic carbonaceous matter. *Geochim. Cosmochim. Acta* **189**, 312–337 (2016). doi: 10.1016/j.gca.2016.06.017
16. E. Quirico *et al*., Prevalence and nature of heating processes in CM and C2-ungrouped chondrites as revealed by insoluble organic matter. *Geochim. Cosmochim. Acta* **241**, 17–37 (2018). doi: 10.1016/j.gca.2018.08.029
17. G. R. Huss, A. E. Rubin, J. N. Grossman, in *Meteorites and the Early Solar System II*, D. S. Lauretta, H. Y. McSween, Eds. (Univ. Arizona Press, 2006), pp. 567–586.
18. T. Nakamura, Yamato 793321 CM chondrite: Dehydrated regolith material of a hydrous asteroid. *Earth Planet. Sci. Lett.* **242**, 26–38 (2006). doi: 10.1016/j.epsl.2005.11.040
19. T. Osawa, H. Kagi, T. Nakamura, T. Noguchi, Infrared spectroscopic taxonomy for carbonaceous chondrites from speciation of hydrous components. *Meteorit. Planet. Sci.* **40**, 71–86 (2005). doi: 10.1111/j.1945-5100.2005.tb00365.x
20. Y. Kebukawa, C. M. O'D. Alexander, G. D. Cody, Comparison of FT-IR spectra of bulk and acid insoluble organic matter in chondritic meteorites: An implication for missing carbon during demineralization. *Meteorit. Planet. Sci.* **54**, 1632–1641 (2019). doi: 10.1111/maps.13302
21. P. Beck *et al*., Hydrous mineralogy of CM and CI chondrites from infrared spectroscopy and their relationship with low albedo asteroids. *Geochim. Cosmochim. Acta* **74**, 4881–4892 (2010). doi: 10.1016/j.gca.2010.05.020
22. D. Takir *et al*., Nature and degree of aqueous alteration in CM and CI carbonaceous chondrites. *Meteorit. Planet. Sci.* **48**, 1618–1637 (2013). doi: 10.1111/maps.12171
23. T. Yokoyama *et al*., Samples returned from the asteroid Ryugu are similar to Ivuna-type carbonaceous meteorites. *Science* **379**, eabn7850 (2023). doi: 10.1126/science.abn7850
24. T. Nakamura *et al*., Formation and evolution of carbonaceous asteroid Ryugu: Direct evidence from returned samples. *Science* **379**, eabn8671 (2023). doi: 10.1126/science.abn8671
25. M. Gounelle, M. E. Zolensky, The Orgueil meteorite: 150 years of history. *Meteorit. Planet. Sci.* **49**, 1769–1794 (2014). doi: 10.1111/maps.12351
26. Y. Kebukawa, C. M. O'D. Alexander, G. D. Cody, Compositional diversity in insoluble organic matter in type 1, 2 and 3 chondrites as detected by infrared spectroscopy. *Geochim. Cosmochim. Acta* **75**, 3530–3541 (2011). doi: 10.1016/j.gca.2011.03.037

27. F.-R. Orthous-Daunay *et al*., Mid-infrared study of the molecular structure variability of insoluble organic matter from primitive chondrites. *Icarus* **223**, 534–543 (2013). doi: 10.1016/j.icarus.2013.01.003
28. C. Le Guillou, S. Bernard, A. J. Brearley, L. Remusat, Evolution of organic matter in Orgueil, Murchison and Renazzo during parent body aqueous alteration: In situ investigations. *Geochim. Cosmochim. Acta* **131**, 368–392 (2014). doi: 10.1016/j.gca.2013.11.020
29. L. R. Nittler *et al*., A cometary building block in a primitive asteroidal meteorite. *Nat. Astron.* **3**, 659–666 (2019). doi: 10.1038/s41550-019-0737-8
30. B. T. De Gregorio *et al*., Isotopic and chemical variation of organic nanoglobules in primitive meteorites. *Meteorit. Planet. Sci.* **48**, 904–928 (2013). doi: 10.1111/maps.12109
31. L. P. Keller *et al*., The nature of molecular cloud material in interplanetary dust. *Geochim. Cosmochim. Acta* **68**, 2577–2589 (2004). doi: 10.1016/j.gca.2003.10.044
32. B. T. De Gregorio *et al*., Isotopic anomalies in organic nanoglobules from Comet 81P/Wild 2: Comparison to Murchison nanoglobules and isotopic anomalies induced in terrestrial organics by electron irradiation. *Geochim. Cosmochim. Acta* **74**, 4454–4470 (2010). doi: 10.1016/j.gca.2010.05.010
33. T. Noguchi *et al*., Variation of mineralogy and organic material during the early stages of aqueous activity recorded in Antarctic micrometeorites. *Geochim. Cosmochim. Acta* **208**, 119–144 (2017). doi: 10.1016/j.gca.2017.03.034
34. L. A. J. Garvie, P. R. Buseck, Prebiotic carbon in clays from Orgueil and Ivuna (CI), and Tagish Lake (C2 ungrouped) meteorites. *Meteorit. Planet. Sci.* **42**, 2111–2117 (2007). doi: 10.1111/j.1945-5100.2007.tb01011.x
35. G. D. Cody *et al*., Organic thermometry for chondritic parent bodies. *Earth Planet. Sci. Lett.* **272**, 446–455 (2008). doi: 10.1016/j.epsl.2008.05.008
36. C. M. O'D. Alexander, G. D. Cody, B. T. De Gregorio, L. R. Nittler, R. M. Stroud, The nature, origin and modification of insoluble organic matter in chondrites, the major source of Earth's C and N. *Chem. Erde* **77**, 227–256 (2017). doi: 10.1016/j.chemer.2017.01.007; pmid: 31007270
37. D. D. Clayton, Origin of heavy xenon in meteoritic diamonds. *Astrophys. J.* **340**, 613–619 (1989). doi: 10.1086/167422
38. Z. R. Dai *et al*., Possible in situ formation of meteoritic nanodiamonds in the early Solar System. *Nature* **418**, 157–159 (2002). doi: 10.1038/nature00897; pmid: 12110882
39. K. Nakamura-Messenger, S. Messenger, L. P. Keller, S. J. Clemett, M. E. Zolensky, Organic globules in the Tagish Lake meteorite: Remnants of the protosolar disk. *Science* **314**, 1439–1442 (2006). doi: 10.1126/science.1132175; pmid: 17138898
40. T. Matsumoto *et al*., Three-dimensional observation and morphological analysis of organic nanoglobules in a carbonaceous chondrite using X-ray micro-tomography. *Geochim. Cosmochim. Acta* **116**, 84–95 (2013). doi: 10.1016/j.gca.2012.05.007
41. M. Hashiguchi, S. Kobayashi, H. Yurimoto, In situ observation of D-rich carbonaceous globules embedded in NWA 801 CR2 chondrite. *Geochim. Cosmochim. Acta* **122**, 306–323 (2013). doi: 10.1016/j.gca.2013.08.007
42. C. Le Guillou, A. Brearley, Relationships between organics, water and early stages of aqueous alteration in the pristine CR3.0 chondrite MET 00426. *Geochim. Cosmochim. Acta* **131**, 344–367 (2014). doi: 10.1016/j.gca.2013.10.024
43. G. Matrajt, S. Messenger, D. Brownlee, D. Joswiak, Diverse forms of primordial organic matter identified in interplanetary dust particles. *Meteorit. Planet. Sci.* **47**, 525–549 (2012). doi: 10.1111/j.1945-5100.2011.01310.x
44. H. Yabuta *et al*., Formation of an ultracarbonaceous Antarctic micrometeorite through minimal aqueous alteration in a small porous icy body. *Geochim. Cosmochim. Acta* **214**, 172–190 (2017). doi: 10.1016/j.gca.2017.06.047
45. C. M. O'D. Alexander, M. Fogel, H. Yabuta, G. D. Cody, The origin and evolution of chondrites recorded in the elemental and isotopic compositions of their macromolecular organic matter. *Geochim. Cosmochim. Acta* **71**, 4380–4403 (2007). doi: 10.1016/j.gca.2007.06.052
46. L. Remusat, Y. Guan, Y. Wang, J. M. Eiler, Accretion and preservation of D-rich organic particles in carbonaceous chondrites: Evidence for important transport in the early Solar System nebula. *Astrophys. J.* **713**, 1048–1058 (2010). doi: 10.1088/0004-637X/713/2/1048
47. H. Naraoka *et al*., Soluble organic molecules in samples of the carbonaceous asteroid (162173) Ryugu. *Science* **379**, eabn9033 (2023). doi: 10.1126/science.abn9033
48. R. Okazaki *et al*., Noble gases and nitrogen in samples of asteroid Ryugu record its volatile sources and recent surface evolution. *Science* **379**, eabo0431 (2023). doi: 10.1126/science.abo0431
49. J. F. Kerridge, Carbon, hydrogen and nitrogen in carbonaceous chondrites: Abundances and isotopic compositions in bulk samples. *Geochim. Cosmochim. Acta* **49**, 1707–1714 (1985). doi: 10.1016/0016-7037(85)90141-3; pmid: 11539652
50. L. R. Nittler, C. M. O'D. Alexander, M. J. Verdier-Paoletti, paper presented at the 84th Annual Meeting of the Meteoritical Society, Chicago, IL, 15 to 21 August 2021.
51. Y. Aikawa, G. J. van Zadelhoff, E. F. van Dishoeck, E. Herbst, Warm molecular layers in protoplanetary disks. *Astron. Astrophys.* **386**, 622–632 (2002). doi: 10.1051/0004-6361:20020037
52. N. Watanabe, A. Kouchi, Ice surface reactions: A key to chemical evolution in space. *Prog. Surf. Sci.* **83**, 439–489 (2008). doi: 10.1016/j.progsurf.2008.10.001
53. J. Aléon, Multiple origins of nitrogen isotopic anomalies in meteorites and comets. *Astrophys. J.* **722**, 1342–1351 (2010). doi: 10.1088/0004-637X/722/2/1342
54. R. Terzieva, E. Herbst, The possibility of nitrogen isotopic fractionation in interstellar clouds. *Mon. Not. R. Astron. Soc.* **317**, 563–568 (2000). doi: 10.1046/j.1365-8711.2000.03618.x
55. E. K. Zinner, in *Meteorites, Comets, and Planets*, A. M. Davis, Ed. (Elsevier, 2005), pp. 17–39.
56. H. Busemann *et al*., Interstellar chemistry recorded in organic matter from primitive meteorites. *Science* **312**, 727–730 (2006). doi: 10.1126/science.1123878; pmid: 16675696
57. L. Remusat, J.-Y. Bonnet, S. Bernard, A. Buch, E. Quirico, Molecular and isotopic behavior of insoluble organic matter of the Orgueil meteorite upon heating. *Geochim. Cosmochim. Acta* **263**, 235–247 (2019). doi: 10.1016/j.gca.2019.07.013
58. C. Floss, F. Stadermann, Auger nanoprobe analysis of presolar ferromagnesian silicate grains from primitive CR chondrites QUE 99177 and MET 00426. *Geochim. Cosmochim. Acta* **73**, 2415–2440 (2009). doi: 10.1016/j.gca.2009.01.033
59. C. Vollmer *et al*., A primordial ^{15}N-depleted organic component detected within the carbonaceous chondrite Maribo. *Sci. Rep.* **10**, 20251 (2020). doi: 10.1038/s41598-020-77190-z; pmid: 33219224
60. T. Hiroi, M. E. Zolensky, C. M. Pieters, The Tagish Lake meteorite: A possible sample from a D-type asteroid. *Science* **293**, 2234–2236 (2001). doi: 10.1126/science.1063734; pmid: 11520950
61. C. D. K. Herd *et al*., Origin and evolution of prebiotic organic matter as inferred from the Tagish Lake meteorite. *Science* **332**, 1304–1307 (2011). doi: 10.1126/science.1203290; pmid: 21659601
62. C. M. Gilmour, C. D. K. Herd, P. Beck, Water abundance in the Tagish Lake meteorite from TGA and IR spectroscopy: Evaluation of aqueous alteration. *Meteorit. Planet. Sci.* **54**, 1951–1972 (2019). doi: 10.1111/maps.13362
63. A. Gardinier *et al*., Solid state CP/MAS ^{13}C NMR of the insoluble organic matter of the Orgueil and Murchison meteorites: Quantitative study. *Earth Planet. Sci. Lett.* **184**, 9–21 (2000). doi: 10.1016/S0012-821X(00)00300-9
64. G. D. Cody, C. M. O'D. Alexander, F. Tera, Solid-state (^{1}H and ^{13}C) nuclear magnetic resonance spectroscopy of insoluble organic residue in the Murchison meteorite: A self-consistent quantitative analysis. *Geochim. Cosmochim. Acta* **66**, 1851–1865 (2002). doi: 10.1016/S0016-7037(01)00888-2
65. H. Yabuta, L. B. Williams, G. D. Cody, C. M. O'D. Alexander, S. Pizzarello, The insoluble carbonaceous material of CM chondrites: A possible source of discrete organic compounds under hydrothermal conditions. *Meteorit. Planet. Sci.* **42**, 37–48 (2007). doi: 10.1111/j.1945-5100.2007.tb00216.x
66. V. Vinogradoff *et al*., Paris vs. Murchison: Impact of hydrothermal alteration on organic matter in CM chondrites. *Geochim. Cosmochim. Acta* **212**, 234–252 (2017). doi: 10.1016/j.gca.2017.06.009
67. Y. Oba, H. Naraoka, Elemental and isotope behavior of macromolecular organic matter from CM chondrites during hydrous pyrolysis. *Meteorit. Planet. Sci.* **44**, 943–953 (2009). doi: 10.1111/j.1945-5100.2009.tb00779.x
68. S. Messenger, Identification of molecular-cloud material in interplanetary dust particles. *Nature* **404**, 968–971 (2000). doi: 10.1038/35010053; pmid: 10801119
69. J. Duprat *et al*., Extreme deuterium excesses in ultracarbonaceous micrometeorites from central Antarctic snow. *Science* **328**, 742–745 (2010). doi: 10.1126/science.1184832; pmid: 20448182
70. G. D. Cody *et al*., Quantitative organic and light-element analysis of comet 81P/Wild 2 particles using C-, N-, and O-μ-XANES. *Meteorit. Planet. Sci.* **43**, 353–365 (2008). doi: 10.1111/j.1945-5100.2008.tb00627.x
71. E. Dartois *et al*., Ultracarbonaceous Antarctic micrometeorites, probing the Solar System beyond the nitrogen snow-line. *Icarus* **224**, 243–252 (2013). doi: 10.1016/j.icarus.2013.03.002
72. N. Fray *et al*., Nitrogen-to-carbon atomic ratio measured by COSIMA in the particles of comet 67P/Churyumov–Gerasimenko. *Mon. Not. R. Astron. Soc.* **469**, S506–S516 (2017). doi: 10.1093/mnras/stx2002
73. K. Lodders, in *Principles and Perspectives in Cosmochemistry*, A. Goswami, B. E. Reddy, Eds. (Springer, 2010), pp. 379–417.
74. O. Poch *et al*., Ammonium salts are a reservoir of nitrogen on a cometary nucleus and possibly on some asteroids. *Science* **367**, eaaw7462 (2020). doi: 10.1126/science.aaw7462; pmid: 32165559
75. K. Altwegg *et al*., Evidence of ammonium salts in comet 67P as explanation for the nitrogen depletion in cometary comae. *Nat. Astron.* **4**, 533–540 (2020). doi: 10.1038/s41550-019-0991-9
76. H. Naraoka *et al*., A chemical sequence of macromolecular organic matter in the CM chondrites. *Meteorit. Planet. Sci.* **39**, 401–406 (2004). doi: 10.1111/j.1945-5100.2004.tb00101.x

ACKNOWLEDGMENTS

We thank the anonymous reviewers for their helpful comments. The Hayabusa2 spacecraft was developed and built under the leadership of JAXA, with contributions from the German Aerospace Center (DLR) and the Centre National d'Études Spatiales (CNES) and in collaboration with NASA; Nagoya University; University of Tokyo; National Astronomical Observatory of Japan (NAOJ); University of Aizu; Kobe University; and other universities, institutes, and companies in Japan. We thank the many engineers, including N. Inaba at JAXA and T. Masuda, S. Yasuda, K. Matsushima, and T. Ohshima at NEC Corporation for their dedicated work on the Hayabusa2 mission. The STXM data were acquired at beam line 19A of the Photon Factory, High Energy Accelerator Research Organization, and at beam line 5.3.2.2 of the Advanced Light Source (ALS), Lawrence Berkeley National Laboratory. Use of the ALS was supported by the Department of Energy (contract no. DE-AC02-05CH11231). The synchrotron FTIR data were acquired at the SMIS beamline of SOLEIL. The NanoSIMS facility at Muséum National d'Histoire Naturelle (MNHN) in Paris was established by funds from the CNRS, Région Ile de France, Ministère délégué à l'Enseignement supérieur et à la Recherche, and the Muséum National d'Histoire Naturelle. The FIB facility at the University of Tokyo is supported by the Advanced Characterization Nanotechnology Platform in the Nanotechnology Platform Project sponsored by the Ministry of Education, Culture, Sports, Science and Technology (MEXT), Japan. We thank N. Sugimura at Waseda University, Y. Fujioka at Tohoku University, and C. Sandt and F. Borondics at SOLEIL for technical support. We thank S. Kawakami at Gifu Shotoku University, T. Fagan at Waseda University, M. E. Zolensky at NASA Johnson Space Center, MNHN, and B. Fectay and C. Bidaut for providing the meteorite samples used in this study. **Funding:** H.Yab. was supported by KAKENHI from the Japan Society for the Promotion of Science (JSPS) (grant nos. JP20H05846, 19H01954, 18H04461, and 20H04615) and the Astrobiology Center Program of the National Institutes of Natural Sciences (NINS) (grant nos. AB312007, AB022001, and AB032004). Y.Taka., Y.Takeic., Y.K., H.Su., S.Y., and D.W. were supported by KAKENHI from JSPS (grant no. JP17H06458). H.Yab., Y.K., M.Has., and H.Su. were supported by the JSPS Core-to-Core program "International Network of Planetary Sciences." L.Bo. and E.Q. acknowledge funding from the Centre National d'Etudes Spatiales (CNES-France). L.R. acknowledges funding from the European Research Council through the consolidator grant HYDROMA (grant agreement no. 819587). C.E., J.D., E.D., and J.M. acknowledge funding from CNES (MIAMI2), DIM-ACAV+ (C3E), LabEx P2IO, PCMI, and ANR (COMETOR ANR-18-CE31-0011). R.S. and B.D.G. acknowledge funding from NASA awards 80HQTR20T0014 and 80HQTR20T0050. L.N. acknowledges funding from NASA grants NNX16AK72G and 80NSSC20K0340. A.D., A.D.-B., and J.M. acknowledge funding from Paris Ile-de-France Region-DIM "Matériaux anciens et patrimoniaux." Centro de Química Estrutural (Z.M.) acknowledges the financial support of Fundação para a Ciência e Tecnologia (FCT) (grants UIDB/00100/2020, UIDP/00100/2020, and LA/P/0056/2020). **Author contributions:** H.Yab. led the research and wrote the paper with contributions from L.N., B.D.G., R.S., L.R., L.Bo., Y.K., and G.D.C. Sample preparation for the research: H.Yab., B.D.G., T.Oku., M.Has., C.E., L.Bo., M.Matsum., Y.E., K.Kam., and M.S.; Raman analyses: L.Bo., M.K., E.Q., G.M., and Y.K.; FTIR analyses: Y.K., E.Q., E.D., L.Bo., C.E., and J.D.; STXM analyses: B.D.G., H.Yab., Y.K., G.C., D.K., S.Sa.,

R.S., Y.Taka., T.Oh., H.Su., Y.Take., S.Y., D.W., and Y.Tam.; STEM-EELS-EDS analyses: R.S.; AFM-IR analyses: J.M., A.D., A.D.-B., E.D., C.E., J.D., and L.Be.; NanoSIMS analyses: L.R., L.N., M.V.-P., S.M., and J.Ba.; Interpretation and writing: H.Yab., L.N., R.S., B.D.G., R.L., L.B., Y.K., E.D., J.M., E.Q., M.K., G.D.C., C.E., S.Su., T.Oku., M.Has., and S.Tac.; Administration of the initial analysis: S.Tac., H.Yu., T.Na., T.No., R.O., H.Yab., H.Na., K.Sa., H.C.C., and D.S.L.; Sample curation: M.Ab., T.Oka., T.Yad., M.N., K.Yog., A.N., M.Yoshit., A.I., A.Miy., S.F., K.Hata., H.So., Y.H., K.Ku., T.U., T.H., D.Y., and R.F.; Sample collection at Ryugu: Y.Ts., T.S., F.T., S.Tan., M.O., R.T., H.Yan., H.Sa., M.Hay., T.I., S.H., Y.-i.I., A.F., Y.Takei., K.Yoshik., Y.M., G.O., H.T., N.O., S.K., K.S., Y.Ya., H.I., K.Ka., K.Yoshih., T.Yam., H.No., A.Miu., S.Su., K.Ki., Nao.H., R.H., T.Mo., E.T., T.O., N.Sa., N.N., K.M., R.N., K.W., H.Se., K.Ot., Y.Yo., Y.I., Y.S., M.Ya., C.H., T.Mi., M.Matsuo., Nar.H., M.Ar., C.O., M.I., H.Yan., S.Tac., R.O., S.W., T.Na., H.Yab., R.J., J.-P.B., M.G., S.Sc., K.Og., C.P., N.Sc., J.B., T.-M.H., and A.M.-S.; Project management: Y.Ts., S.W., M.Yoshik., M.F., and S.N. All authors discussed the results and commented on the manuscript. **Competing interests:** The authors declare that they have no competing interests. **Data and materials availability:** All images used in this study and machine-readable data files are available at the JAXA Data Archives and Transmission System (DARTS) at https://data.darts.isas.jaxa.jp/pub/hayabusa2/paper/sample/Yabuta_2022/. Data for all Hayabusa2 samples and other data from the mission are available at the DARTS archive at https://www.darts.isas.jaxa.jp/curation/hayabusa2 and https://www.darts.isas.jaxa.jp/planet/project/hayabusa2/, respectively. The samples of Ryugu are curated by the JAXA Astromaterials Science Research Group; distribution for analysis is through an Announcement of Opportunity available at https://jaxa-ryugu-sample-ao.net. The samples we used are listed in table S1.

License information: Copyright © 2023 the authors, some rights reserved; exclusive licensee American Association for the Advancement of Science. No claim to original US government works. https://www.science.org/about/science-licenses-journal-article-reuse

SUPPLEMENTARY MATERIALS

science.org/doi/10.1126/science.abn9057
Materials and Methods
Supplementary Text
Figs. S1 to S8
Tables S1 to S3
References (*77*–*85*)

Submitted 29 December 2021; accepted 21 December 2022
10.1126/science.abn9057

EDITORIAL

Science for humanity

This year marks the 175th anniversary of the American Association for the Advancement of Science (AAAS, the publisher of *Science*). In striving to advance its mission, the organization's theme for its annual meeting (2 to 5 March in Washington, DC), "Science for Humanity," reiterates its commitment to explore and make sense of the world through inquiry, evidence seeking, and discovery. The words of archbishop and Nobel laureate Desmond Tutu are a reminder that this pursuit must be shared by everyone if it is to serve all of society: "My humanity is bound up in yours, for we can only be human together." These words aptly capture the essence of the ties that bind us, which include our shared DNA, our need to bond with others, and our ability to collaborate. Science is intertwined with the human condition and stories of the human experience and is hence the great connector. The more we embrace our common humanity—and science as a unifier—the better we will understand what it means to be human and what it will take to sustain ourselves and our planet.

Science, disappointingly, has not always drawn people together. Research has revealed not only the magnificent complexity of humankind's genetic diversity but also our common ancestry from groups that lived in Africa 300,000 years ago, before the migrations that began about 60,000 years ago. However, different traits among humans that arose through evolution and environmental influences were used as the basis for rigid racial categories that were misused by some to question the humanity of certain members of society. The use of genetics research to falsely claim a scientific justification for the subjugation and oppression of groups deemed inferior fueled racist beliefs, with devastating consequences. Recently, the American Society for Human Genetics, the world's largest professional society for human geneticists, issued an apology for "its involvement in and silence on the misuse of human genetics research to justify and contribute to injustice in all forms." Likewise, AAAS is reflecting, and acting, on its own history. Among its founding members was Louis Agassiz, a noted advocate of polygenism (the theory of separate origins of human races) who promoted ideas of African inferiority that have since been debunked. AAAS, *Science*, and many in the scientific community once supported advocates of eugenics. Last year, AAAS released its Diversity, Equity, and Inclusion Report, laying out a plan to keep the organization accountable as it strives toward more inclusive and equitable representation in its membership, leadership, and partnerships.

Perhaps science for humanity can best be realized through a humanistic approach where science is seen, in part, as a social process that acknowledges the interconnectedness between scientists and the discovery of knowledge; as a collective endeavor for people to come together to solve societal problems; and as an equalizer capable of eliminating disparities, particularly those related to the question of who conducts science and who benefits from it.

"What will people in the future say about how science helped or harmed society on our watch?"

In their article, "Humanizing Science and Engineering for the Twenty-first Century," economist Kaye Husbands Fealing and her colleagues call for an integration of sciences, humanities, arts, and social sciences, reminding us to heed the warning voiced in 1945 by Vannevar Bush (who was then the director of the Office of Scientific Research and Development), "Science cannot live by and unto itself alone." Integrating humanities and science helps people understand what they have in common and build relationships that foster trust in one another and in science. Pushing beyond the discovery and advancement of knowledge, scientists bear social responsibilities that are critical if science is to be conducted for the benefit of all. Viewing and respecting humanity as a whole allows us all to move beyond self-interests and act on our humanitarian instincts.

What will people in the future say about how science helped or harmed society on our watch? How did we come together to collaboratively solve problems? How did we ensure that everyone who desired to pursue science had the opportunity to do so? Acting on these questions in earnest could help us ultimately answer the question of what it means to be human.

–Gilda A. Barabino

Gilda A. Barabino is president of the American Association for the Advancement of Science, Washington, DC, USA. She is also president of Olin College of Engineering, Needham, MA, USA. gbarabino@olin.edu

PHOTO: COURTESY LEISE JONES PHOTOGRAPHY

10.1126/science.adh2260

NEWS

> “FDA and HHS should clean up the industry to keep patients safe.”
>
> **U.S. Senator Elizabeth Warren (D–MA)** in *STAT*, about an audit report that found for-profit companies are increasingly running ethics boards that speedily review human subjects research.

IN BRIEF

Edited by **Jeffrey Brainard**

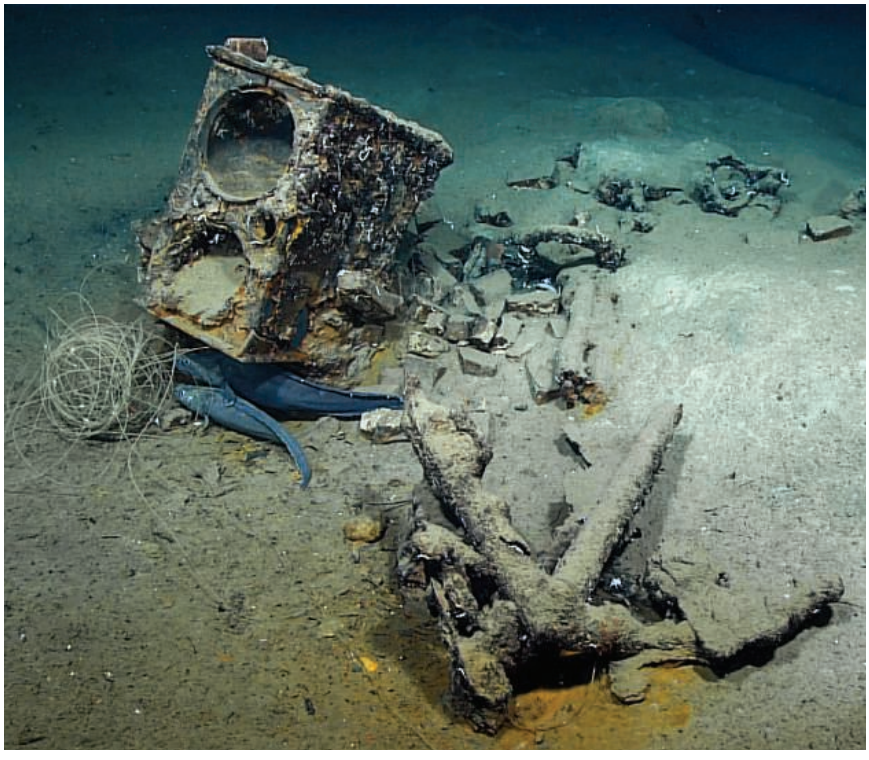

Expanded surveys for U.S. shipwrecks might turn up centuries-old artifacts like this cast iron stove (left), used to render blubber into oil, from the whaling ship *Industry*, whose wreckage was discovered last year.

PHOTO: NOAA OCEAN EXPLORATION

ARCHAEOLOGY

U.S. eyes wider surveys for shipwrecks

The United States wants to tighten rules for when oil and gas firms must look for marine archaeological sites before drilling offshore. A proposal released last week would require that the companies survey any area where they plan to disturb the sea floor, not just places where existing data or models suggest there is a shipwreck or other cultural site. The draft rule from the Bureau of Ocean Energy Management (BOEM) could have its greatest impact in the Gulf of Mexico. Energy companies and other explorers have found more than 600 shipwrecks or possible shipwrecks there—including, last year, a 207-year-old whaler, *Industry*, which was built in 1815 and sank in 1836. “We can increase the likelihood of identifying these important resources before they are inadvertently damaged” by an oil or gas company, says James Kendall, BOEM Gulf of Mexico regional director. The agency is accepting public comments through 17 April.

AGU restores protesters’ abstracts

CLIMATE POLICY | The American Geophysical Union (AGU) said last week it will restore the abstracts of conference presentations by two scientists it kicked out of its annual meeting for staging a climate change protest. The move reverses a previous decision by AGU, the largest U.S. professional organization for climate and earth scientists, and came after a report by its ethics committee. An AGU spokesperson declined to provide the report, citing confidentiality rules. According to an AGU summary, the ethics committee endorsed the society’s decision to remove Rose Abramoff and Peter Kalmus from the December 2022 conference after the two briefly mounted the stage before a session and unfurled a banner reading “Out Of The Lab & Into The Streets.” The incident led to Abramoff being fired from her job at Oak Ridge National Laboratory. AGU’s initial actions prompted objections from more than 2000 fellow scientists, who called on the society to reinstate the pair’s scientific contributions to the conference and close its professional misconduct investigation. An AGU statement last week invited Abramoff and Kalmus to work with the society to “expand existing methods of climate activism and engagement” through AGU. Abramoff wrote to *Science* in an email, “I hope that scientists will join me in taking up the offer.”

Experts think poison killed poet

FORENSICS | There has long been suspicion that an acclaimed Chilean poet who opposed dictator Augusto Pinochet was murdered in 1973—and last week, his family announced a recent toxicological investigation of his corpse revealed supporting evidence. Pablo Neruda’s teeth showed signs of *Clostridium botulinum*, a bacterium that produces a neurotoxin that paralyzes muscles and the nervous system and can eventually lead to death. Neruda died 2 weeks after Pinochet overthrew the Chilean government, from what was believed to be complications of prostate cancer. But those close to Neruda suspected foul play because of his closeness with deposed President Salvador Allende and accounts from Neruda’s driver stating the poet had been injected with something

the night he died, while in a hospital bed. The forensic investigators from four countries who inspected Neruda's corpse said he did not die from his cancer and ruled out postmortem contamination as a source of the deadly bacterium.

Long Covid IDs show racial skew

COVID-19 | Black and Hispanic people are more likely to develop Long Covid than white people, but they're less likely to be diagnosed, according to two studies published last week. One analyzed health records from some 62,000 adults in New York City. Within 6 months of infection, Black patients were up to twice as likely as white patients to develop Long Covid symptoms, and Hispanic people were as much as 1.6 times as likely, researchers report in the *Journal of General Internal Medicine*. But a review of 34,000 patients from across the United States, published in *BMC Medicine*, found most Long Covid patients were white women who lived in areas with low poverty. That suggests patients of color and those in poverty are not being diagnosed, the authors wrote.

Rail project threatens telescope

ASTRONOMY | Researchers are objecting to a plan, approved by India's government this month, to build a railway through the site of one of the world's largest meter-wave radio telescope arrays. The high-speed rail line will come as close as 1 kilometer to the 30 antennas, each 45 meters wide, that are part of the Giant Metrewave Radio Telescope (GMRT), in Narayangaon in Maharashtra state. Astronomers say radio interference created by the trains would harm data collection by the telescope array. Scientists from some 35 countries have used the GMRT to study a variety of phenomena. It was among the first in a generation of instruments initiated in the 1990s that focus on long wavelengths, in particular 21-centimeter waves from neutral hydrogen, which scientists hope to use to probe the universe's dark ages before the first stars were born.

Activist group slams NIH eviction

DISSENT | The animal rights group People for the Ethical Treatment of Animals last week demanded the U.S. National Institutes of Health provide a written assurance it won't again bar any PETA employees from the agency's public meetings, as it claims NIH did earlier this month. PETA said in a 15 February letter to acting NIH Director Lawrence Tabak that it will sue the biomedical research agency on First Amendment grounds if the assurance isn't forthcoming. A PETA vice president, Alka Chandna, was a confirmed public speaker at a 7 February National Institute of Mental Health council meeting at NIH's Bethesda, Maryland, headquarters. PETA says she was turned away by guards who cited her distribution there last fall of flyers protesting monkey experiments on the campus. In 2021, PETA sued NIH after the agency blocked potentially inflammatory Instagram and Facebook comments about animal research. NIH says it received the PETA letter and is "looking into" the matter; it will add Chandna's comments to the meeting minutes.

IN FOCUS Some types of sharks, such as catsharks and shysharks, hatch from egg cases, known as a "mermaid's purse." Each leathery pouch contains an embryo and yolk supply and is often deposited in a kelp forest, where the embryos of these oviparous sharks develop. This photo of egg cases, by student Tlhologello Sesana of South Africa, was one of the winners announced last month in the BioArt Awards annual photo competition sponsored by the Federation of American Societies for Experimental Biology.

PHOTO: TLHOLOGELLO SESANA/TSHWANE UNIVERSITY OF TECHNOLOGY

China plans asteroid hunter

ASTRONOMY | China is constructing the world's largest radar astronomy array, which will help track asteroids that could threaten Earth. The new observatory could help fill a void in the world's ability to detect such objects, created when the Arecibo Telescope in Puerto Rico collapsed in 2020. The following year, China completed a prototype of its planned array, the China Compound Eye, which included four dishes. The second phase, begun last week and to be completed by 2025, will add 25 dishes, each 30 meters across, in Yunyang county in Chongqing. A third phase, to expand the number of dishes to 100, is also planned. Normal radio astronomy is passive, and China has the world's largest dish of this type, the Five-hundred-meter Aperture Spherical Telescope. In contrast, radar-astronomy observatories that actively hunt asteroids transmit powerful radio signals and detect the echoes that bounce off objects. Their range is short—Saturn is about the limit—because the echoes are very faint. But the method provides information that normal telescopes can't, including the 3D shape, surface roughness, and movement of potential threats.

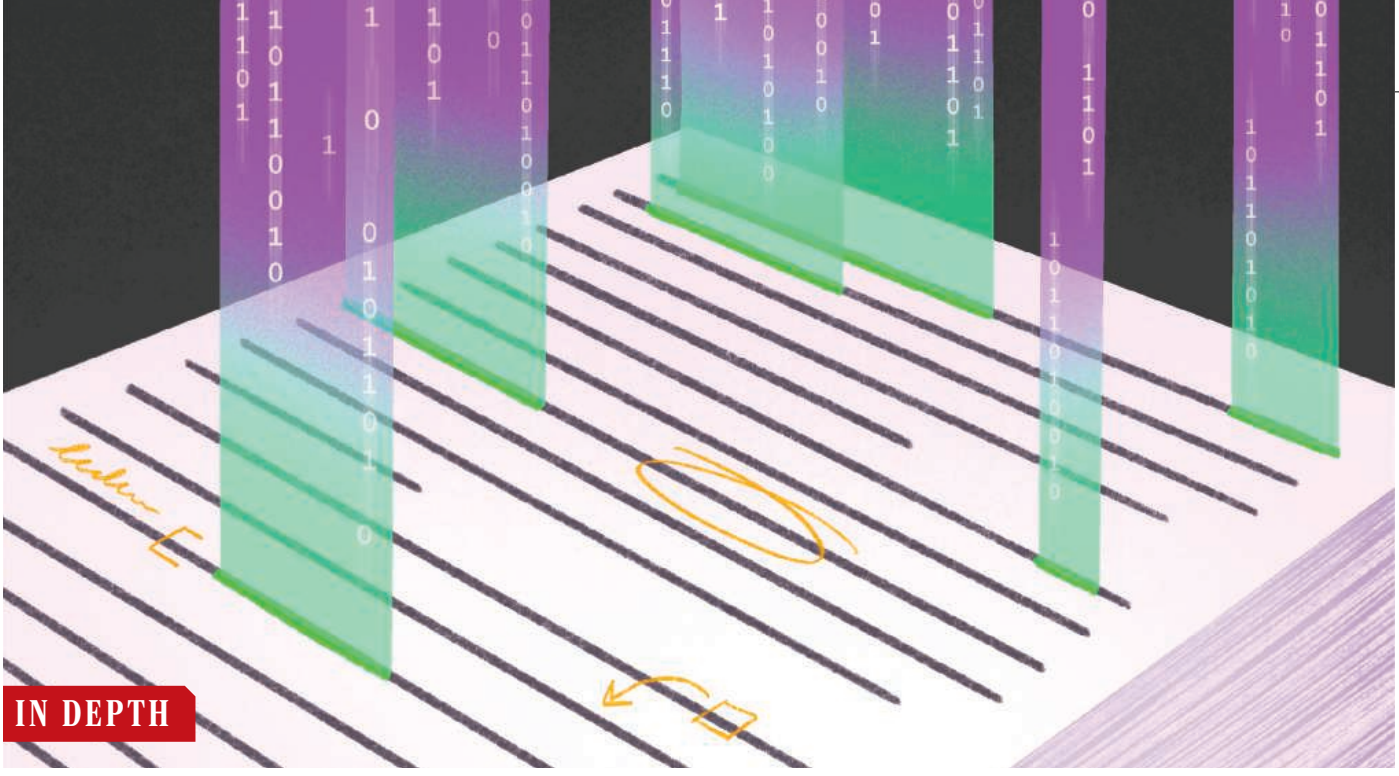

IN DEPTH

PUBLISHING

Journals take up arms against AI-written text

Many ask authors to disclose use of ChatGPT and other generative artificial intelligence

By **Jeffrey Brainard**

"It's all we've been talking about since November," says Patrick Franzen, publishing director for SPIE, the international society for optics and photonics. He's referring to ChatGPT, the artificial intelligence (AI)-powered chatbot unveiled that month. In response to a prompt, ChatGPT can spin out fluent and seemingly well-informed reports, essays—and scientific manuscripts. Worried about the ethics and accuracy of such content, Franzen and managers at other journals are scrambling to protect the scholarly literature from a potential flood of manuscripts written in whole or part by computer programs.

Some publishers have not yet formulated policies. Most of those that have avoid an outright ban on AI-generated text, but ask authors to disclose their use of the automated tools, as SPIE is likely to do. For now, editors and peer reviewers have few alternatives, as they lack enforcement tools. No software so far can consistently detect the synthetic text the majority of the time.

When the online tool ChatGPT was made available for free public use, scientists were among those who flocked to try it out. (ChatGPT's creator, the U.S.-based company OpenAI, has since limited access to subscribers.) Many reported its unprecedented and uncanny ability to create plausible-sounding text, dense with seemingly factual detail. ChatGPT and its brethren—including Google's Bard, unveiled earlier this month for select users, and Meta's Galactica, which was briefly available for public use in November 2022—are AI algorithms called large language models, trained on vast numbers of text samples pulled from the internet. The software identifies patterns and relationships among words, which allows the models to generate relevant responses to questions and prompts.

In some cases, the resulting text is indistinguishable from what people would write. For example, researchers who read medical journal abstracts generated by ChatGPT failed to identify one-third of them as written by machine, according to a December 2022 preprint. AI developers are expected to create even more powerful versions, including ones trained specifically on scientific literature—a prospect that has sent a shock wave through the scholarly publishing industry.

So far, scientists report playing around with ChatGPT to explore its capabilities, and a few have listed ChatGPT as a co-author on manuscripts. Publishing experts worry such limited use could morph into a spike of manuscripts containing substantial chunks of AI-written text.

One concern for journal managers is accuracy. If the software hasn't been exposed to enough training data to generate a correct response, it will often fabricate an answer, computer scientists have found. In November, Meta took down the public interface for Galactica, its scientist-specific large language model, just days after it was unveiled—users had identified myriad factual errors in the generated text. And a 2022 preprint study of Sparrow, an information-seeking chatbot developed by a Google subsidiary, found that up to 20% of its responses contained errors. AI text may also be biased toward established scientific ideas and hypotheses contained in the content on which the algorithms were trained. Journal editors also worry about ethics, suggesting authors who use text generators are sometimes presenting the outputs as if they wrote them—a transgression others have dubbed "aigiarism."

Many journals' new policies require that authors disclose use of text-generating tools and ban listing a large language model such as ChatGPT as a co-author, to underscore the human author's responsibility for ensuring the text's accuracy. That is the case for *Nature* and all Springer Nature journals, the JAMA Network, and groups that advise on best practices in publishing, such as the Committee on Publication Ethics and the World Association of Medical Editors. But at least one publisher has taken a tougher line:

ILLUSTRATION: A. MASTIN/*SCIENCE*

The *Science* family of journals announced a complete ban on generated text last month. The journals may loosen the policy in the future depending on what the scientific community decides is acceptable use of the text generators, Editor-in-Chief Holden Thorp says. "It's a lot easier to loosen our criteria than it is to tighten them."

Some publishing officials are still working out the details, such as when they might ask journal staff, editors, or reviewers to examine or fact check generated text disclosed by authors—tasks that would add to what is often already a heavy volunteer workload. Editors at the Taylor & Francis publishing group, whose forthcoming rule will likely require disclosure of such text, might sometimes ask authors to specify what parts of their manuscript were written by a computer, says Sabina Alam, director of publishing ethics and integrity. Searching for papers to include in a systematic review may be a legitimate use if the researcher follows proper methods in deciding which papers to include, for example, she says, whereas cutting and pasting it into a perspective or opinion piece "is not OK because it's not your perspective." The policy will likely evolve as the publishing industry gets more experience working with such manuscripts, she says. "We're seeing this as a phased approach. It's really early days."

Journal managers also say they are hoping to monitor the new technology using more technology: automated detectors that can flag synthetic text. But that isn't easy, says Domenic Rosati, a senior research scientist at scite.ai, a company that develops software to assist scientific publishers. "We're well past the time, in science in particular, of being able to say it's obvious [certain text came from] a machine because of its fluency or its lack of truthfulness."

Current detectors leave much to be desired. OpenAI unveiled its "classifier" last month, which categorizes submitted text on a scale from "likely" to have been written by a computer to "very unlikely." The classifier was training using paired samples of human writing and computer-generated text from 34 algorithms from five different companies, including OpenAI itself. But OpenAI concedes several limitations. The tool, still under development, correctly applies the "likely" label only 26% of the time. People can fool it by editing computer-generated text. And it may not consistently identify synthetic text on topics that were not included in the training data. Computer scientists say these limitations typically apply to other detectors as well.

Better solutions may be on the horizon. OpenAI said in December 2022 it is working on ways to "watermark" the generated text. It would program its models to insert words, spelling, and punctuation in a telltale order to create a secret code detectable by search engines. And last month, a team at Stanford University published a preprint describing DetectGPT, which, unlike other detectors, doesn't require training. This algorithm examines text by creating multiple, random variations and querying a text generator to rank which versions it prefers. The extent to which the generator the team studied—developed by OpenAI and similar to ChatGPT—prefers the original text versus the altered versions is consistently different for human-written versus AI-generated text, allowing DetectGPT to predict the likelihood that a sample came from a particular machine. But DetectGPT needs more development before journal editors can exclusively rely on its results to make decisions on manuscripts, for example, says Eric Williams, a doctoral student who led the Stanford team. The company TurnItIn, which markets a widely used plagiarism detector, said last week it plans to roll out a synthetic text detector as early as April. TurnItIn says the tool, trained on academic writing, can identify 97% of text generated by ChatGPT, with a false positive rate of one in 100.

> **"We're seeing this as a phased approach. It's really early days."**
> **Sabina Alam**, Taylor & Francis

A further computational challenge is rating the factual accuracy of robot-generated text and the quality of its summaries, Rosati says. His firm is working on an automated checker that would scour existing scientific literature to determine whether a particular citation in a manuscript actually presents the finding the manuscript claims it does, for example. That tool could turn up references fabricated by a machine as well as irrelevant or incorrect ones provided by humans, Rosati says.

Some editors see promise as well as peril in the emergence of ChatGPT and its relatives. Programmers are developing and refining software that creates hypotheses, writes computer code, and analyzes data, for example, to make researchers' work more efficient and productive. "I can see scenarios where there will be causes for concern, but then I also see a tremendous amount of opportunity with these types of tools," says Magdalena Skipper, editor-in-chief of *Nature*. "As with every tool, we have to understand the limitations. … It demands that we pay close attention to how these tools are developed, how they are used, and in what context." ■

MARINE SCIENCE

Iron stress threatens Southern Ocean phytoplankton

Lack of the nutrient limits the plants' productivity, key to climate and ecosystems

By **Warren Cornwall**

Off the icy shores of Antarctica each spring, an explosion of life unfolds that is so large it's visible from space. As iron-rich waters rise from below, the surface of the Southern Ocean swirls with psychedelic clouds of bright green phytoplankton—single-celled plants that suck up carbon from the atmosphere and form the base of the food chain by sustaining krill, which is in turn a major food source for fish, whales, and penguins.

Now, a group of scientists says that over the past quarter-century this seasonal bloom, a critical player in ecosystems and climate, might be at risk. Phytoplankton across the Southern Ocean are increasingly starved of iron—a building block for their photosynthetic machinery—and there are signs their productivity might be declining. The discovery, published this week in *Science* (p. 834), is a surprise, directly counter to the surge of productivity that many climate models predicted for the coming century.

The apparent speed of the change "is really alarming," says Adrian Marchetti, a biological oceanographer at the University of North Carolina, Chapel Hill, who studies phytoplankton but was not directly involved in the research. A big drop in phytoplankton "could really affect the global carbon cycle," adds Alison Gray, a University of Washington, Seattle, oceanographer who studies ocean carbon.

Ocean iron levels, although known to be an important factor limiting phytoplankton productivity in the Southern Ocean, are notoriously difficult to study. Neither robotic sensors nor research ships routinely look for the nutrient. So scientists have recently begun to infer its levels by looking for signals that phytoplankton are coping with an iron shortage.

The *Science* family of journals announced a complete ban on generated text last month. The journals may loosen the policy in the future depending on what the scientific community decides is acceptable use of the text generators, Editor-in-Chief Holden Thorp says. "It's a lot easier to loosen our criteria than it is to tighten them."

Some publishing officials are still working out the details, such as when they might ask journal staff, editors, or reviewers to examine or fact check generated text disclosed by authors—tasks that would add to what is often already a heavy volunteer workload. Editors at the Taylor & Francis publishing group, whose forthcoming rule will likely require disclosure of such text, might sometimes ask authors to specify what parts of their manuscript were written by a computer, says Sabina Alam, director of publishing ethics and integrity. Searching for papers to include in a systematic review may be a legitimate use if the researcher follows proper methods in deciding which papers to include, for example, she says, whereas cutting and pasting it into a perspective or opinion piece "is not OK because it's not your perspective." The policy will likely evolve as the publishing industry gets more experience working with such manuscripts, she says. "We're seeing this as a phased approach. It's really early days."

Journal managers also say they are hoping to monitor the new technology using more technology: automated detectors that can flag synthetic text. But that isn't easy, says Domenic Rosati, a senior research scientist at scite.ai, a company that develops software to assist scientific publishers. "We're well past the time, in science in particular, of being able to say it's obvious [certain text came from] a machine because of its fluency or its lack of truthfulness."

Current detectors leave much to be desired. OpenAI unveiled its "classifier" last month, which categorizes submitted text on a scale from "likely" to have been written by a computer to "very unlikely." The classifier was training using paired samples of human writing and computer-generated text from 34 algorithms from five different companies, including OpenAI itself. But OpenAI concedes several limitations. The tool, still under development, correctly applies the "likely" label only 26% of the time. People can fool it by editing computer-generated text. And it may not consistently identify synthetic text on topics that were not included in the training data. Computer scientists say these limitations typically apply to other detectors as well.

Better solutions may be on the horizon. OpenAI said in December 2022 it is working on ways to "watermark" the generated text. It would program its models to insert words, spelling, and punctuation in a telltale order to create a secret code detectable by search engines. And last month, a team at Stanford University published a preprint describing DetectGPT, which, unlike other detectors, doesn't require training. This algorithm examines text by creating multiple, random variations and querying a text generator to rank which versions it prefers. The extent to which the generator the team studied—developed by OpenAI and similar to ChatGPT—prefers the original text versus the altered versions is consistently different for human-written versus AI-generated text, allowing DetectGPT to predict the likelihood that a sample came from a particular machine. But DetectGPT needs more development before journal editors can exclusively rely on its results to make decisions on manuscripts, for example, says Eric Williams, a doctoral student who led the Stanford team. The company TurnItIn, which markets a widely used plagiarism detector, said last week it plans to roll out a synthetic text detector as early as April. TurnItIn says the tool, trained on academic writing, can identify 97% of text generated by ChatGPT, with a false positive rate of one in 100.

> **"We're seeing this as a phased approach. It's really early days."**
> **Sabina Alam**, Taylor & Francis

A further computational challenge is rating the factual accuracy of robot-generated text and the quality of its summaries, Rosati says. His firm is working on an automated checker that would scour existing scientific literature to determine whether a particular citation in a manuscript actually presents the finding the manuscript claims it does, for example. That tool could turn up references fabricated by a machine as well as irrelevant or incorrect ones provided by humans, Rosati says.

Some editors see promise as well as peril in the emergence of ChatGPT and its relatives. Programmers are developing and refining software that creates hypotheses, writes computer code, and analyzes data, for example, to make researchers' work more efficient and productive. "I can see scenarios where there will be causes for concern, but then I also see a tremendous amount of opportunity with these types of tools," says Magdalena Skipper, editor-in-chief of *Nature*. "As with every tool, we have to understand the limitations. … It demands that we pay close attention to how these tools are developed, how they are used, and in what context." ■

MARINE SCIENCE

Iron stress threatens Southern Ocean phytoplankton

Lack of the nutrient limits the plants' productivity, key to climate and ecosystems

By **Warren Cornwall**

Off the icy shores of Antarctica each spring, an explosion of life unfolds that is so large it's visible from space. As iron-rich waters rise from below, the surface of the Southern Ocean swirls with psychedelic clouds of bright green phytoplankton—single-celled plants that suck up carbon from the atmosphere and form the base of the food chain by sustaining krill, which is in turn a major food source for fish, whales, and penguins.

Now, a group of scientists says that over the past quarter-century this seasonal bloom, a critical player in ecosystems and climate, might be at risk. Phytoplankton across the Southern Ocean are increasingly starved of iron—a building block for their photosynthetic machinery—and there are signs their productivity might be declining. The discovery, published this week in *Science* (p. 834), is a surprise, directly counter to the surge of productivity that many climate models predicted for the coming century.

The apparent speed of the change "is really alarming," says Adrian Marchetti, a biological oceanographer at the University of North Carolina, Chapel Hill, who studies phytoplankton but was not directly involved in the research. A big drop in phytoplankton "could really affect the global carbon cycle," adds Alison Gray, a University of Washington, Seattle, oceanographer who studies ocean carbon.

Ocean iron levels, although known to be an important factor limiting phytoplankton productivity in the Southern Ocean, are notoriously difficult to study. Neither robotic sensors nor research ships routinely look for the nutrient. So scientists have recently begun to infer its levels by looking for signals that phytoplankton are coping with an iron shortage.

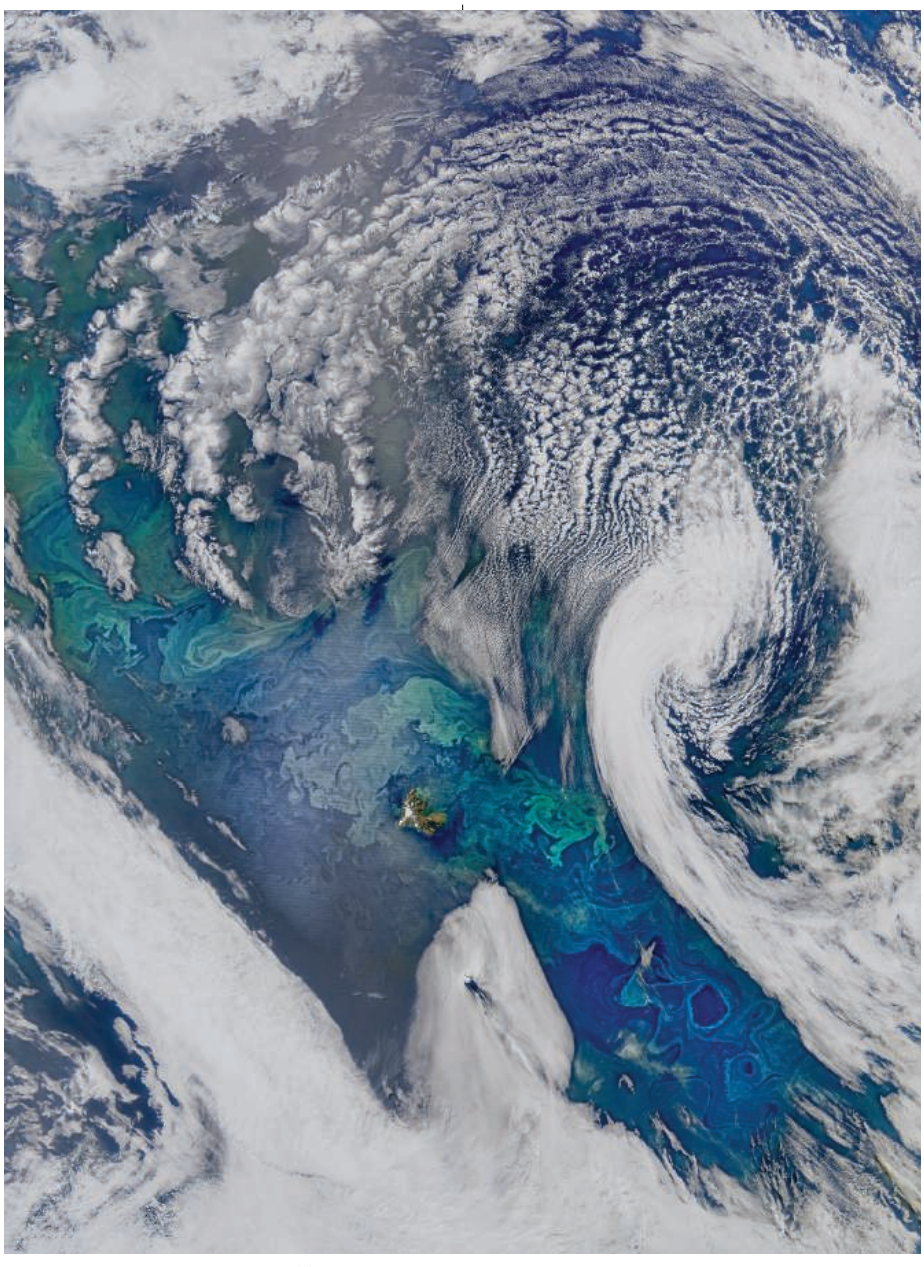

In a satellite image from November 2015, phytoplankton blooms swirl in the ocean around the Kerguelen Islands.

IMAGE: NASA

The new study analyzed light given off by phytoplankton for signs of a physiological process called nonphotochemical quenching—in which phytoplankton deal with an overload of sunlight by releasing heat. Quenching is an indicator of iron stress because phytoplankton deprived of the nutrient alter their physiology in ways that make them more susceptible to light exposure. In data from 194 trips by research vessels starting in 1996 and 47 sensor-laden floats set adrift starting in 2015, the researchers found quenching increased by nearly 5% per year, when adjusted for variations in light exposure. The trend suggests that over the past 2 decades, phytoplankton are struggling more and more to get enough iron, says Tommy Ryan-Keogh, a biogeochemist at the South African government's Southern Ocean Carbon and Climate Observatory and lead author of the *Science* paper.

Ryan-Keogh and his collaborators looked at phytoplankton productivity as well, using satellite imagery of the plankton blooms and measurements from ocean floats to track changes starting in 1998. They relied on models to convert the data into estimates of net phytoplankton productivity, finding a small but statistically significant decline in productivity in the Southern Ocean.

Even if the decline is real, it's not certain that iron is playing a role. Philip Boyd, a biogeochemist at the University of Tasmania who has studied iron dynamics in the Southern Ocean for decades, points to other potential factors. For example, marine animals could be eating more phytoplankton. "It's a long bow to directly connect iron stress with net primary production," he says.

It's also not clear why phytoplankton would face an iron shortage. Current climate and ocean models predict the opposite—that as climate changes, winds in the Southern Ocean will shift to the south, causing more upwelling that will bring iron from deep in the ocean toward the surface and fuel a burst of productivity. Ryan-Keogh proposes three possible reasons why the phytoplankton might be running short of iron: Ocean acidification due to rising carbon dioxide levels could be making it harder for them to absorb the nutrient, rising ocean temperatures might be speeding up their metabolism and increasing their iron demand, or changes in how different layers of the ocean mix might be limiting the movement of deeper, iron-rich water toward the surface. "Testing these will require quite a lot of lab work," Ryan-Keogh says.

Teasing apart what's happening will be important not only for understanding future ecosystem changes in the Southern Ocean, but also for predicting the fate of the global climate. The Southern Ocean is a significant carbon sink; half of all the carbon pollution that dissolves in the ocean does so there. Some of that dissolved carbon is taken up by phytoplankton and stored away as the plants—or the organisms that feed on them—die and sink to the bottom.

Alessandro Tagliabue, an oceanographer at the University of Liverpool who worked on the study, says the trend toward iron starvation might be temporary. But it's also possible the models that predict future abundance are misrepresenting something about the Southern Ocean and the organisms that live there. "We need to see why the models aren't reproducing the current trends," says Tagliabue, who specializes in modeling ocean biogeochemical processes.

Keith Moore, an oceanographer at the University of California, Irvine, who has worked on a number of widely used climate models, is confident the trend will be short lived. Although he says the paper makes a convincing case for a growing iron deficit in phytoplankton now, Moore expects that just as the models predict, the winds will eventually shift southward, and the phytoplankton bloom will be lusher than ever. "What's happening now may just be too subtle for those models to pick up," he says. ■

RESEARCH SECURITY

Canada bars funding for 'risky' foreign alliances

China is seen as main target in expanded reviews of projects with certain foreign entities

By **Jeffrey Mervis**

Canada's three major national research agencies will no longer fund proposals from scientists doing "sensitive" research that involves foreign collaborators deemed to pose a security risk to the country. Although the new policy, announced on 14 February, doesn't mention China, it parallels actions taken in recent years by the United States, Australia, and other countries to prevent their research investments from benefiting China's ruling party or military.

Under the new rules, defense and intelligence officers will do a second vetting of proposals that scientists have already flagged as potentially problematic. But some researchers fear those reviews could eliminate collaborations with China that now benefit Canada. They also want the government to spell out how it will decide which proposals pose too great a risk.

"Are we moving to a situation in which the intelligence community will be dictating what research will be funded?" asks Tamer Özsu, a computer scientist at the University of Waterloo. "If that happens, Canada could lose its reputation as a good partner in international collaborations."

François-Philippe Champagne, Canada's science minister, announced a new grant review policy last week.

PHOTO: BLAIR GABLE/REUTERS

Proponents of the expanded reviews say the new policy simply reflects the need for the government to be more careful in choosing those collaborations. "The intent is to make research as open as possible and as secure as necessary," says Chad Gaffield, head of U15, an organization representing the 15 largest Canadian research universities that has been working with government officials since 2018 on how to improve research security. Calling the new approach "a work in progress," Gaffield predicts that "we are going to get to a place where [the additional screening] will become routine and not a burden to researchers."

In July 2021, in the wake of growing political tensions with China, the Canadian government released new guidelines for research partnerships that were developed by a working group that Gaffield co-chairs. They ask grant applicants to judge whether their research "would be of interest to a foreign government … or have military applications" as well as whether their potential partners "are affiliated with" entities that pose a threat to Canada. Universities are supposed to address those concerns before submitting the grant application.

Those guidelines were first applied to a small program that funds collaborative projects, called Alliance Grants, run by the Natural Sciences and Engineering Research Council of Canada (NSERC). Last month, NSERC reported that 4% of the approximately 1000 applications it received were put through a second review by the Canadian Security Intelligence Service (CSIS). CSIS determined 32 of the 48 flagged proposals should not be funded. The new policy extends that pilot, which the government deemed a success, to all programs run by the three research councils.

Özsu is familiar with four of those rejected proposals. They would have supported work on cloud computing, software engineering, and data management done at a center he runs that is jointly funded by Huawei, a Chinese telecommunications giant. Each proposal earned high marks from NSERC's scientific reviewers, Özsu says, but was rejected for unspecified security reasons.

"The unwritten feedback to PIs [principal investigators] about their proposals was: 'Don't work with researchers and companies from China,'" he says. "And the attitude from intelligence agencies is one of condescension: 'You guys don't know what dangers are lurking and you need to trust us.'"

Last year, the government gave out $25 million to Canada's major research universities to hire research security officers who will work with faculty on meeting the new guidelines. The goal, Gaffield says, is to find ways to mitigate potential security risks so many of the collaborations can go forward. The new rules don't name particular countries, he notes, which allows the risks and benefits of each proposed collaboration to be judged on its own merits.

Even so, the new policy explicitly bans funding for any collaboration in a "sensitive research area" with someone "connected to military, national defense, or state security entities" seen as a threat to Canada. That broad scope could lead to regulatory overreach, worries Shawn Barber, a former Canadian diplomat who managed economic security for Public Safety Canada, one of the agencies that rolled out the new policy along with the health and science ministries.

"They've used a sledgehammer when a scalpel is what's needed," Barber says, noting the policy could bar collaborations on public health and other areas generally not seen as sensitive. "I wouldn't want to see a Canadian health researcher blocked from working with someone in China on preventing the next pandemic."

International collaborations have helped Canada grow its research enterprise beyond what the country is able to invest, Özsu says, pointing to his center as an example. "Canada punches above its weight because of our ability to partner with China and other countries," he says.

Gaffield agrees that continued collaboration with China is essential. "If you want to collaborate with the best, it's inevitable that there will be colleagues in China who you want to work with," he says. "So, we don't want this to have a chilling effect." ■

PHYSICS

Quantum computers take step toward reliability

Google's error-correction scheme works better as it gets bigger

By **Adrian Cho**

A scheme to reduce the errors that plague quantum computers is a step closer to reality, researchers at Google announced this week. Instead of ordinary bits that can be set to 0 or 1, a quantum computer uses qubits that can be set to 0 and 1 at the same time. But they are fragile. One tactic for protecting the information carried by one qubit is to spread it out over many others. Now, the Google team has shown it can reduce errors by spreading the information over more and more qubits. Such "scaling" marks a key step toward Google's goal of maintaining indefinitely one qubit's worth of information—a "logical" qubit—by encoding it on 1000 physical ones.

"This is a significant proof-of-concept demonstration," says Joschka Roffe, a theoretical physicist at the Free University of Berlin who was not involved in the experiment. Still, he notes, in spite of the scaling, Google's logical qubit isn't yet as reliable as the underlying physical ones.

A full-fledged quantum computer could perform certain tasks, such as cracking current internet encryption schemes, that overwhelm a conventional computer. Its qubits can be fashioned of many things, such as ions, photons, and atoms. Google's qubits are tiny circuits of superconducting metal that have a lower energy state denoting 0 and a higher one denoting 1. Microwaves can coax a circuit into either state—or into both at once. However, noise tends to destroy that two-way state in 20 microseconds, far too little time to run ambitious algorithms.

In an effort to fortify the qubits, Google engineers are following a tack taken in the 1940s for correcting errors in the first computers, in which noise sometimes flipped a bit from 0 to 1, or vice versa. Suppose you copy a bit's information onto two other bits. The probability that noise flips all three is far smaller. And if one flips, the computer can figure out which one it was by comparing pairs of bits.

The laws of quantum mechanics forbid using the exact same approach in quantum computers. It's impossible to copy the state of one qubit onto others. Moreover, measuring a qubit in a 0-and-1 state collapses it to either 0 or 1. Quantum error correction involves subtle workarounds, where a qubit's information is never measured directly, and, instead of being copied, the original qubit's state is expanded through a phenomenon called entanglement.

Take, for example, a single qubit in a 0-and-1 state. Using entanglement, two other qubits can be roped in to make a quantum state in which all three are 0 and simultaneously all three are 1. Call it 000-and-111. The information in that state is the same as in the original one and forms the logical qubit. Now, if, say, the second of these three data qubits flips, the state will become 010-and-101. To detect such a flip, researchers entangle additional qubits between the first and second and the second and third qubits. Measurements on those "ancillary" qubits reveal the flipped qubit in the original trio of qubits, which are never measured. In principle, researchers can ease the flipped qubit back to its original state.

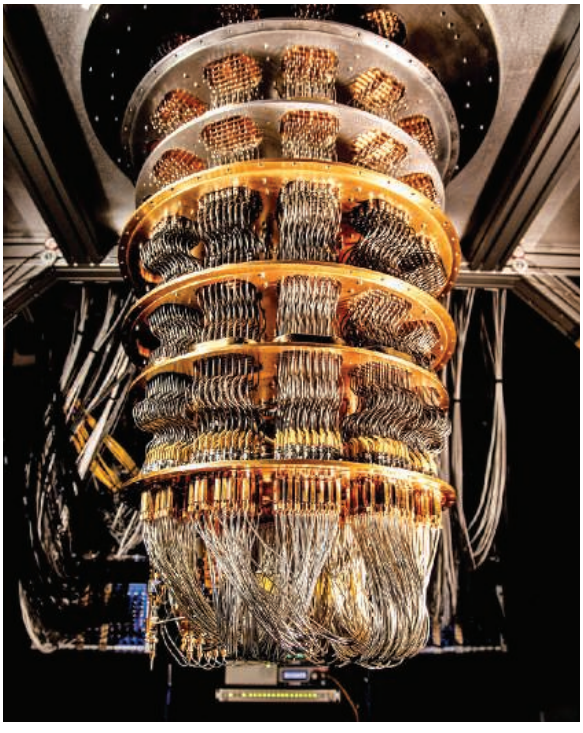

A refrigerator festooned with microwave cables cools Google's quantum chip nearly to absolute zero.

Now, the Google Quantum AI team has shown how the scheme improves when the information in the logical qubit is spread among more and more physical qubits. Using a 72-qubit chip, the team encoded a single logical qubit in two ways—in either a grid of 17 qubits (nine data and eight ancillary qubits) or 49 qubits (25 data and 24 ancillary qubits). Researchers put each grid through 25 cycles of measurements, looking for flipped qubits. Instead of correcting them, researchers just kept track of them, which sufficed for the experiment, says Julian Kelly, a physicist and director of quantum hardware at Google.

After the 25 cycles, they measured the data qubits directly to see whether the ancillary qubits tracked all the flips or more had sneaked in, meaning the machine lost track of the logical qubit. Over many trials, the probability per cycle of losing the logical qubit was 3.028% with the smaller grid and 2.914% with the bigger one, the team reported this week in *Nature*. Thus, the error rate shrank as the number of physical qubits increased—although just barely.

Those numbers may underwhelm, as even a single physical qubit has a lower error rate. But the scaling is more important than the actual reliability of the logical qubit, Kelly says. "The scalability is really the trick," he says. Still, to reach Google's goal of encoding a logical qubit on 1000 physical ones with an error rate of 0.0001%, the scaling must be 20 times better.

Google's experiment is not the only game in town, notes Greg Kuperberg, a mathematician at the University of California, Davis. A company called Quantinuum has performed an experiment in which the logical qubit is more robust than the underlying physical ones, using ion qubits, and physicists at Yale University have done the same in an experiment that mixes superconducting qubits and photons. However, ion systems may not scale as easily, and the Yale system is something of an "apples and oranges" comparison, Kuperberg notes.

Still, Kuperberg says, the results show physicists are on the threshold of using imperfect physical qubits to make much better logical ones. "I'm still going to call that the most important benchmark [in quantum computing] I can think of right now." ■

PHOTO: ERIK LUCERO/GOOGLE QUANTUM AI

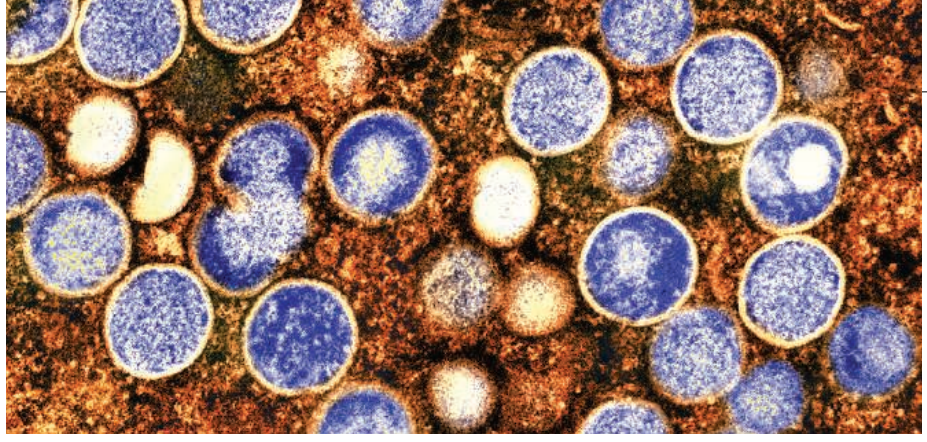

When HIV and the mpox virus (purple) infect the same person, the combination can be lethal.

IMAGE: NATIONAL INSTITUTE OF ALLERGY AND INFECTIOUS DISEASES/NATIONAL INSTITUTES OF HEALTH/SCIENCE SOURCE

MPOX

Deadly mpox risk in people with untreated HIV comes into view

Analysis of hundreds of patients suggests mpox is "a different disease" in immunocompromised patients

By **Kai Kupferschmidt**

In June 2022, a man in his 30s severely sick with mpox, the viral disease formerly known as monkeypox, was admitted to the Salvador Zubirán National Institute of Health Sciences and Nutrition hospital in Mexico City. Tests showed the patient was also HIV-positive, which he had not known, and that his blood had few CD4 cells, critical immune cells that HIV attacks. The man's immune system was so weak it could not keep mpox in check and painful lesions kept spreading across his body, eating away at, or necrotizing, the flesh, according to HIV researcher Brenda Crabtree Ramirez, who was on his care team. "He just kept getting worse and worse and worse," she says.

With no treatments available, his doctors got the hospital's ethics board to approve a desperate plan: They would transfer blood plasma from a colleague who had been vaccinated against mpox to the patient, in the hope that the antibodies from the donation might help fight his infection with the poxvirus. The experimental therapy failed—the man died 2 weeks later, one of the first deaths from the disease in Mexico.

Although mpox cases have plummeted globally since then, the outbreak still simmers in Latin America and other locations. The World Health Organization (WHO) last week reaffirmed that the disease remains a global emergency. And a grim report this week in *The Lancet*, which analyzes the death in Mexico and the cases of 381 other mpox patients who also had advanced HIV infections, makes clear the disease poses an enormous risk to those living with uncontrolled HIV. Of the 179 people with less than 200 CD4 cells per microliter—more than 500 is considered normal—27 died.

Mpox isn't just more severe in these immunocompromised patients, says Oriol Mitjà, an infectious disease researcher at the Germans Trias i Pujol University Hospital in Barcelona and one of the study authors. "It's like a different disease." In the cases where people had few CD4 cells, mpox's normally small skin lesions grew into large necrotizing patches and their infection sometimes spread to the lungs or caused severe secondary infections with bacteria.

Mitjà, Crabtree Ramirez, and their colleagues argue this disseminated form of mpox should be added to the list of AIDS-defining conditions, opportunistic secondary infections that are a typical sign of advanced HIV infection. That might alert physicians to test mpox patients for HIV to prioritize them for any possible treatments. Health authorities should also prioritize people living with HIV for vaccination, Mitjá says.

The data presented in the *Lancet* report are compelling and WHO plans to assemble a group to consider the research team's recommendation to make mpox an AIDS-defining condition, says Meg Doherty, who heads the program for HIV and other sexually transmitted infections at the agency.

In some ways the world may have been lucky with the strain of mpox virus that has been spreading globally. The two types previously known from cases in Africa were thought to kill 10% and 1% of patients, respectively. The current outbreak strain has infected more than 85,000 people globally, predominantly affecting gay men and their sexual networks, and caused fewer than 100 deaths, a mortality rate of about 0.1%. A paper published last week in the *Proceedings of the National Academy of Sciences* found that in a particular strain of laboratory mice, this virus, known as clade IIb, is far less deadly than its relatives. "We were unable to cause the mice to be sick even at 100 times the lethal dose [for the current strain]," says Bernard Moss, a poxvirus researcher at the U.S. National Institute of Allergy and Infectious Diseases and one of that study's authors.

But the *Lancet* paper, which covers more than one-quarter of all known mpox deaths for the clade IIb strain, shows the virus can still cause devastating disease in a particularly vulnerable group of people. Men who have sex with men are much more likely to acquire an HIV infection, but are also less likely in most parts of the world to have access to HIV testing and treatment, notes Gregg Gonsalves, a Yale School of Public Health epidemiologist and former HIV activist. "This creates a dangerous situation, in which our failures to address the AIDS epidemic among this population now may create new risks" for this group, he says.

The *Lancet* report also revealed an important dilemma for physicians caring for these coinfected people. When those with untreated HIV were started on antiretrovirals, one-quarter of them seemed to develop a condition in which the recovering immune system responds to the opportunistic infection—mpox in this case—with an overzealous inflammatory response. More than half the patients suspected to have this overreaction, known as immune reconstitution inflammatory syndrome, died. "We are grappling with these scenarios and clinicians do not know what the best approach is at this time," says Boghuma Titanji, an Emory University virologist not involved with the study.

There are now far fewer severely sick mpox patients in care than last year, Crabtree Ramirez says. But she worries conditions in Mexico may mean such cases will keep coming. On the one hand, there is little incentive for those with milder cases to be diagnosed because neither treatment nor a preventive vaccine is available. A diagnosis means mandatory isolation, "And for many people in Mexico, if they don't work, they don't eat," she says. But given the significant number of people at a high risk for deadly coinfection—almost half the people diagnosed with HIV in Mexico are at an advanced stage of the infection with a CD4 count of 200 or less—it is clear that mpox vaccines and drugs are needed, she says. "For me, it's unacceptable that people do not have access to what is needed to survive." ■

BIOLOGY

Stem cells hint at how bats live with viruses

Research team hits on formula to create stem cells from tissue of adult bats

By **Kai Kupferschmidt**

Compared with other mammals, bats are notorious for hosting more viruses that are dangerous to people but not themselves. It's an oddity that's drawn renewed attention since COVID-19 broke out in humans—many scientists suspect the coronavirus SARS-CoV-2 leaped from bats into people, directly or via an intermediate host. Seeking to create large quantities of bat tissue to help study why the flying animals are so virus-friendly, a research team now reports it has transformed adult bat cells into versatile stem cells that can be coaxed to form many kinds of tissue.

Scientists have coaxed cells from the greater horseshoe bat (*Rhinolophus ferrumequinum*) into a stem cell–like state that could make it easier to study how the animal harbors coronaviruses without apparent harm.

The advance, described this week in *Cell*, thrills many bat scientists. "If the work in this paper can be (easily) reproduced in other groups with different bat species, the impact will be huge!" says Linfa Wang, a bat coronavirus researcher at the Duke-NUS Medical School in Singapore. And early studies of the bat stem cells have already suggested the animals may not only tolerate viruses, but actually let them remain active, possibly because doing so has some advantage for the hosts.

The new work traces back to the spring of 2020. As the COVID-19 pandemic started, Thomas Zwaka, a stem cell researcher at the Icahn School of Medicine at Mount Sinai, became fascinated by the question of why bats carry so many viruses that can cause human disease. But researchers studying this question have been hampered by the fact that getting bat samples to study in the lab is difficult. "Even with a breeding colony [like our team has], it is still a challenge to get sufficient bat cells reliably and reproducibly for certain types of research," Wang says.

To sidestep that problem, Zwaka wanted to create bat stem cells that could be kept in the lab and be differentiated, as needed, into specific kinds of tissue. Some researchers had claimed years before to have done this, but the work had never been reproduced.

But with much of the world shut down by COVID-19, Zwaka first had to figure out how to get some bat tissue delivered to his laboratory. Javier Juste, an evolutionary biologist at the Spanish National Research Council, eventually agreed to send Zwaka some samples from a colony of greater horseshoe bats he was studying in Seville. To have fresh tissue that could survive the long flight, Juste prepared the bat samples at the airport in Madrid just before they were loaded on one of the few planes still crossing the Atlantic Ocean. In his New York City lab, Zwaka then tried to use a strategy developed in 2006 by Japanese researcher Shinya Yamanaka to force adult mammalian cells back into an earlier, stem cell–like state. But the recipe for creating these induced pluripotent stem (iPS) cells did not work on the bat samples.

After months of tweaking the formula, however, Zwaka and his colleagues finally found a combination of factors that worked. Several tests, including differentiating the transformed bat cells into multiple types of cells, suggested they were indeed pluripotent cells. The researchers then repeated the procedure with cells from a different bat species, the greater mouse-eared bat, with similar results. "The two bats are evolutionarily very distant," Zwaka says. "So this told us that our protocol probably works with many different bats."

In studying these cells, Zwaka's team noticed something interesting. Certain viruses can insert versions of their genes into the genomes of human or mouse cells, and these viral sequences sometimes reawaken in cells that are in a pluripotent state. And when Zwaka and colleagues looked for remnants of these viral sequences in the bat iPS cells, they found numerous active versions—as well as some proteins that these sequences produce.

"It's just striking how many of these virus sequences there are," says Zwaka, who proposes that bats don't restrain these active sequences because their replication may act as a defense strategy against other viruses or as a kind of self-vaccination.

That remains speculation for now, other bat researchers caution. Scientists have proposed before that viruses and bats have a symbiotic relationship, Wang says, but it is hard to prove.

Indeed, Kevin Olival, a bat researcher at the EcoHealth Alliance, a nonprofit research group based in New York City, says the data in the new *Cell* paper are too limited to conclude that bat stem cells are special in how they handle the integrated, or endogenous, viral sequences. But he thinks the new stem cell technique could help conduct similar sequence-hunting studies in a wide range of other mammals, "and see if bats really are above average in this sense."

Bat scientists, meanwhile, are enthusiastic about finally having a recipe for creating bat iPS cells. "We are already discussing in my team how to make use of these pluripotent cells," says Vincent Munster, a virologist at the U.S. National Institute of Allergy and Infectious Diseases. "This is a terrific paper," adds Jacob Hanna, a stem cell researcher at the Weizmann Institute of Science. "Undoubtedly this is going to become a widely used platform." ■

PHOTO: STEPHEN DALTON/SCIENCE SOURCE

FEATURES

Hyperfine's Swoop, the first U.S. FDA–approved low-field brain scanner, can be wheeled to a patient's bedside.

MRI FOR ALL

Portable low-field scanners could revolutionize medical imaging in nations rich and poor—if doctors embrace them

By **Adrian Cho**

The patient, a man in his 70s with a shock of silver hair, lies in the neuro intensive care unit (neuro ICU) at Yale New Haven Hospital. Looking at him, you'd never know that a few days earlier a tumor was removed from his pituitary gland. The operation didn't leave a mark because, as is standard, surgeons reached the tumor through his nose. He chats cheerfully with a pair of research associates who have come to check his progress with a new and potentially revolutionary device they are testing.

The cylindrical machine stands chest high and could be the brooding older brother of R2D2, the *Star Wars* robot. One of the researchers carefully guides the 630-kilogram self-propelled scanner up to the head of the bed, steering it with a joystick. Lifting the man by his bed sheet, the researchers help him ease his head into the Swoop—a portable magnetic resonance imaging (MRI) scanner made by a company called Hyperfine.

"Do you want ear plugs?" asks Vineetha Yadlapalli, the second researcher.

"Is it as loud as a regular MRI?"

"Not at all."

"Then I guess I don't need them."

After propping up the patient's legs to ease the strain on his back, Yadlapalli sets the machine to work, tapping in a few instructions from an iPad. The machine emits a low growl, then proceeds to beep and click. Within minutes, an image of the patient's brain appears on Yadlapalli's tablet.

PHOTO: DEREK DUDEK/HYPERFINE

For a half-hour, the man lies quietly, hands folded across his belly. He could be getting his hair set in an old-fashioned hair dryer. In a small way, he's a pioneer helping take MRI where it's never gone before.

In many cases, MRI sets the gold standard in medical imaging. The first useful MRI images emerged in the late 1970s. Within a decade, commercial scanners had spread through medicine, enabling physicians to image not just bone, but soft tissues. If doctors suspect you have had a stroke, developed a tumor, or torn cartilage in your knee, they'll likely prescribe an MRI.

If you're fortunate enough to be able to get one, that is. An MRI scanner employs a magnetic field to twirl atomic nuclei in living tissue—specifically the protons at the heart of hydrogen atoms—so that they emit radio waves. To generate the field, a standard scanner employs a large, powerful superconducting electromagnet that pushes a machine's cost to $1.5 million or more, pricing MRI out of reach of 70% of the world's population. Even in the United States, getting an MRI may require days of waiting and a midnight drive to some distant hospital. The patient must come to the scanner, not the other way around.

For years, some researchers have been striving to build scanners that use much smaller permanent magnets, made of the alloy often found in desk toys. They produce fields roughly 1/25th as strong as a standard MRI magnet, which once would have been far too weak to glean a usable image. But, thanks to better electronics, more efficient data collection, and new signal processing techniques, multiple groups have imaged the brain in such low fields—albeit with lower resolution than standard MRI. The result is scanners small enough to roll to a patient's bed and possibly cheap enough to make MRI accessible across the globe.

The machines mark a technological triumph. Kathryn Keenan, a biomedical engineer at the National Institute of Standards and Technology who is testing a Hyperfine scanner, says, "Everyone that comes through is superimpressed that it even works." Some say the scanners could also transform medical imaging. "We're potentially opening up a whole new field," says Kevin Sheth, a neurologist at the Yale School of Medicine who has worked extensively with the Swoop but has no financial interest in Hyperfine. "It's not a question of 'Is this going to happen?' It's going to be a thing."

In August 2020, the Swoop became the first low-field scanner to win U.S. Food and Drug Administration (FDA) approval to image the brain, and physicians are putting it through clinical studies at Yale New Haven and elsewhere. Other devices are close behind. But Andrew McDowell, a physicist and founder of the consulting firm NeuvoMR, LLC, cautions it's not clear there's a market for a low-field scanner, with its lower resolution. "The real challenge is going to be convincing doctors to start using it," he says. "That's very difficult because for good reasons they're very conservative."

AN MRI SCANNER WORKS nothing like a camera; it is actually a radio that tunes in to protons in living tissue. Like a tiny compass needle, each proton is magnetic, and ordinarily the protons point randomly in all directions (see graphic, above). However, an external magnetic field can align them. At that point, a pulse of radio waves of the right frequency and duration can tip them by 90°. The aligned protons then twirl like gyroscopes, emitting a radio signal of their own, whose frequency increases with the field's strength.

That fleeting monotone radio hum reveals little. To create an image, the scan-

Tuning in to the body

Although an MRI scanner makes images, it is a type of radio. To trace living tissues, it twirls the protons in hydrogen atoms (bottom) and deciphers the radio waves they emit. The radio signals from different tissues fade at different rates, enabling the machine to image internal structures. Conventional scanners are massive and expensive, but researchers are now shrinking the machines.

MRI on the go

Replacing the large superconducting magnet of a conventional MRI machine with a small permanent magnet (color) results in a scanner portable enough to use in a hospital room.

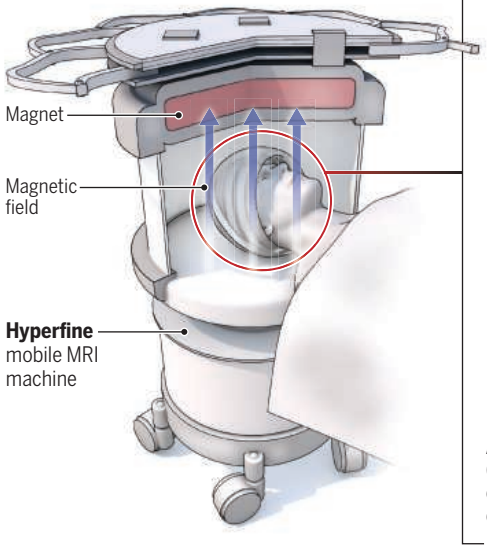

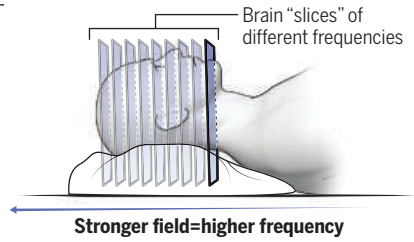

Singing different notes
Applied at the right moment, a magnetic gradient can make protons radiate at different frequencies that correspond to different slices through the head, enabling the machine to glean spatial information.

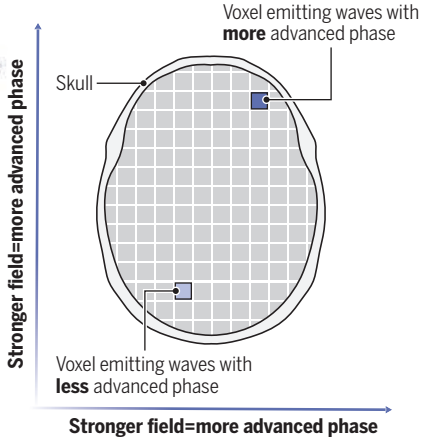
Voxel emitting waves with more advanced phase
Skull
Voxel emitting waves with less advanced phase
Stronger field=more advanced phase
Stronger field=more advanced phase

Ahead or behind the beat
Gradients in other directions set the waves from different spots ahead or behind in "phase"—which defines how far through their rotation the protons are.

Call and response

An MRI scanner uses a magnetic field and pulses of radio waves to set protons in tissue twirling. The protons then radiate radio waves of their own, which constitute the basic signal that the scanner tracks.

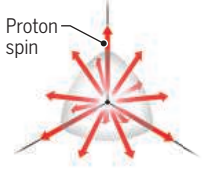

Lacking direction
Like compass needles, protons are magnetic. In the body, they usually point randomly in all directions.

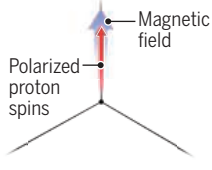

Straightening up
An external magnetic field makes the protons align so they point in the same direction along the field.

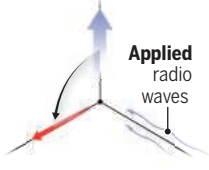

Tipping over
A pulse of radio waves of the right frequency and duration tips the protons perpendicular to the field.

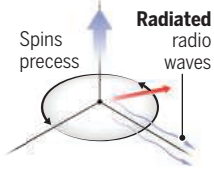

Taking a twirl
The protons then twirl together like gyroscopes and emit more radio waves—MRI's basic signal.

GRAPHIC: C. BICKEL/*SCIENCE*

ner must distinguish among waves coming from different points in the body. To do this, it sculpts the magnetic field, which makes protons at different locations sing at different frequencies and states of synchrony. The scanner must also distinguish one type of tissue from another, which it does by exploiting the fact that the radio signals fade at different rates in different tissues.

One reason the signal dies out is that the protons knock one another out of alignment through their own magnetic fields. The rate at which this happens differs between, say, fatty brain matter and watery cerebrospinal fluid. To measure the rate, the scanner applies pairs of pulses. The first pulse creates a signal that fades as the orientations of twirling protons fan out. The second reverses much of that evolution, eliciting an echo of the signal. The proton-proton interactions mute that echo, however. So the scanner can measure their rate by tracking how the echo shrinks as the delay between the two pulses increases.

While applying pair after pair of pulses, the scanner must simultaneously sort the echoes coming from different points in the brain. To do that, it relies on magnetic field gradients applied at key moments. For example, a gradient applied during the echo from chin to crown makes protons in different sideways slices through the head radiate at different frequencies. A gradient applied between pulses and across the head will set protons in vertical slices ahead or behind in their twirling, a "phase" difference that makes echoes from some slices reinforce one another and others cancel. By varying the gradient, the scanner can deduce the strength of the echo from each slice.

Over many repetitions, the scanner gathers a plethora of echoes in which intensity varies with delay, frequency, and phase. A standard mathematical algorithm decodes them to produce a map of how the proton-proton interactions vary throughout the brain, forming one type of MRI image. Other pulse sequences probe other tissue-specific processes—such as how fast protons diffuse, which can track fluid flow.

All that pulsing explains why MRI scans take time and why an MRI machine chirps, clicks, and buzzes. Those sounds emerge as mechanical stresses rattle the current-carrying coils that create the magnetic gradients. A technician can tell what kind of a scan a machine is doing just from those sounds, Yadlapalli says.

A stronger field makes all this easier by polarizing the protons more thoroughly and creating a bigger signal. A standard scanner's magnet produces a field of 1.5 tesla—30,000 times as strong as Earth's field—and some reach 3 or 7 tesla. Even so, the protons pointing along a 1.5-tesla field outnumber those pointing the other way by just 0.001%. Reduce the field strength by a factor of 25 and the polarization falls with it. The signal-to-noise ratio plummets even more, by a factor of nearly 300.

In principle, a low-field scanner could coax a signal from the noise by taking data over a longer time period—just as radio astronomers sift a weak signal from noise by training their dishes on a star for hours or days. That tack won't work with a human, who can hold still only so long. So, in developing low-field MRI, researchers had to find ways to extract data much faster.

One key element is better hardware, says Joshua Harper, a neural engineer at the German Paraguayan University. "We now have really fast, really cheap electronics," he says. "That's really why it works." Even so, doing low-field MRI in a hospital room is tricky. Metal in other machines and even the walls can distort the field, and static from other devices can disrupt the radio signal. So scanners employ countermeasures. For example, Hyperfine's Swoop uses antennas to measure radio noise and cancel it, similar to how noise-canceling headphones block sound.

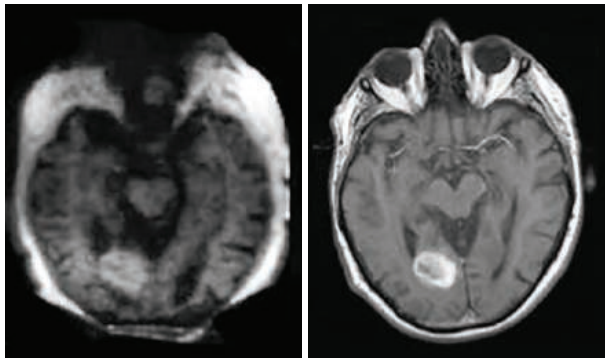

The resolution of a brain scan from a low-field machine (left) is coarser than conventional MRI (right), but both images clearly reveal a hemorrhage.

The new scanners also turn an aspect of the lower field to their advantage to run faster. To manipulate the protons, a high-field scanner must use higher frequency, higher energy radio waves, so it can pulse only so fast before it begins to heat the patient. Free of that speed limit, a low-field scanner can pulse faster and use more efficient pulse sequences, says Matthew Rosen of Massachusetts General Hospital, a physicist who co-founded Hyperfine. "We can interrogate very, very rapidly, doing things that you could never do at high field."

Even so, gathering data fast enough for standard image reconstruction remains a challenge. One solution is to employ novel signal processing techniques, including artificial intelligence. Hyperfine engineers use a set of training images to teach a program called a neural network to construct brain images from relatively sparse data, says Khan Siddiqui, Hyperfine's chief medical officer and chief strategy officer. "That's where our secret sauce comes in."

Compared with a standard scan, a low-field image looks blurrier. Still, physicists see its beauty. "It's this incredible physics success story," Rosen says. "It's not just we pointy headed physicists [goofing] off and doing stuff that nobody cares about." The technology vindicates those toiling in a forgotten corner of the field, McDowell says. "Who in their right mind would build a 65-millitesla machine when the glory is in building the 11-tesla one?"

HYPERFINE SAYS ITS SWOOP SCANNER is off to a pretty glorious start. It has sold more than 100 of the machines, mostly in the United States, at about $250,000 apiece. The goal is not to replace high-field scanners, but to expand how MRI is used, Siddiqui says. "Our portable scanner brings MRI closer to the patient, both in time and in distance." Hyperfine envisions using it in the neuro ICU to quickly assess patients too ill or unstable to wheel to a conventional MRI or a CT machine, which produces a type of 3D x-ray.

A Swoop's magnet consists of two disks and produces a field of 64 millitesla. A scan from it feels dramatically different from a standard scan. In a conventional scanner, an automated table glides you bodily into the cylindrical magnet. With the Swoop, an able patient can scooch into the magnet as if wriggling under a car's bumper. A helmetlike head piece containing the antennas cradles your head so snugly it may touch your nose, yet your arms and legs are free. The machine's chirping is soft, even soothing.

In late 2019 and early 2020, as the coronavirus pandemic took hold, Sheth and colleagues tested the Swoop's promise by scanning 50 ICU patients, including 20 with COVID-19. Because many were on ventilators and sedated, "we had no idea what their neurological status was and no way to take a look by any available imaging modality," Sheth recalls. "And this provided us a way to do that at the bedside." The scans revealed brain trauma in 37 cases, including eight COVID-19 patients, the researchers reported in January 2021 in *JAMA Neurology*.

The cheaper, smaller machines might also allow patients to get more frequent follow-up scans. That's a prospect that resonates

IMAGES: YALE SCHOOL OF MEDICINE

with Ronald Walsworth, a physicist at the University of Maryland, College Park, and co-founder of Hyperfine. In 2007, his then–2-year-old son developed a noncancerous brain tumor. He was treated successfully, says Walsworth, who serves on Hyperfine's advisory board. Still, he says, "There were signs that were not caught early and things that were not decided most efficiently because the MRIs only could happen once in a while."

The Swoop's advantages have won it fans. "Oh, my God, what a beautiful, beautiful piece of technology," says Steven Schiff, a pediatric neurosurgeon at Yale University who has no financial interest in Hyperfine. Still, the Swoop can miss details a high-field scanner would catch because its resolution of 1.5 millimeters is half that of a standard scanner. For example, Sheth's team used it to image the brains of 50 patients who had had an ischemic stroke, visible with standard MRI. The Swoop missed the five smallest, millimeter-size strokes, the researchers reported in April 2022 in *Science Advances*.

That finding shows physicians will have to exercise judgment in deciding when to use each type of scanner, Sheth says. "You shouldn't be too worried, but you should understand the context in which you might miss something," he says. Still, McDowell notes doctors may shy away from a low-field scanner if they think using it could leave them open to a malpractice suit.

IN MUCH OF THE WORLD, MRI is simply unavailable. A team in the Netherlands hopes its scanner will change that. Its magnet differs dramatically from the Swoop's. It consists of 4098 cubes of neodymium iron boron—an alloy developed in the 1980s by carmakers—embedded in a hollow plastic cylinder, and arranged in a configuration called a Halbach array to produce a uniform horizontal field. "Our system is intrinsically better and has fewer distortions," asserts Andrew Webb, an MRI physicist at Leiden University Medical Centre, so it requires less help from processing such as machine learning.

A private company, Multiwave Technologies in Switzerland, is trying to bring the scanner to market. It will apply for FDA approval this year and aims to rent its machines in a subscription model, says Tryfon Antonakakis, Multiwave's co-CEO. "Our goal is to make it as affordable as possible and not necessarily to be in the hospital," says Antonakakis, an engineer and applied mathematician. "We are looking to go into the mountains, into the medical deserts in developing countries."

Webb and his colleagues, including Martin van Gijzen, an applied mathematician at the Delft University of Technology, have another plan for spreading their technology: giving it away. "We made the decision—Martin, myself, all our team—that we were not going to patent things," Webb says. "Everything is going to be open source," so that anyone can download their design from the internet and build scanners. Webb and colleagues hope entrepreneurs in developing nations will manufacture them locally.

To seed the idea, they shipped a scanner, packaged as a kit, to Johnes Obungoloch, a biomedical engineer at Mbarara University of Science and Technology in Uganda, who was a graduate student at Pennsylvania State University, University Park, when Webb and Schiff were also there. In September 2022, Webb and others flew to Uganda to help Obungoloch and his team assemble the scanner in 11 days.

Johnes Obungoloch and Andrew Webb (second and third from right) with the magnet for a scanner that will guide surgeries at a pediatric hospital in Uganda.

Soon it will be put to use in a project to test the utility of low-field MRI in the developing world. The CURE Children's Hospital of Uganda, a 55-bed pediatric neurosurgical facility in Mbale run by an international nonprofit, plans to compare Obugoloch's scanner, a Swoop, and a CT scanner. Doctors will image children with hydrocephalus, in which cerebrospinal fluid collects in the brain and compresses it, potentially causing debilitating or fatal damage. Globally, hydrocephalus afflicts 400,000 children every year, and it accounts for 75% of the CURE hospital's patients. In Africa, an infection is the usual cause.

For years, Schiff and colleagues at the hospital have used CT scans to guide an innovative surgery that allows the fluid to drain into the brain's ventricles—an alternative to installing a shunt to the abdomen. However, a CT scan exposes children to considerable x-ray radiation, so CURE doctors will see whether low-field MRI images can guide surgeons. "If the MRI proves comparable to the CT scan, then there is no reason why we should be using the CT scan anymore," says Ronald Mulondo, a physician at CURE who directs the project.

The study is awaiting final governmental approval. If it's successful, Obungoloch envisions building more scanners, perhaps for Africa's six other CURE hospitals, and even sourcing some of the parts locally. Uganda has public health care, so that vision depends on government funding, he says.

Still, like their peers elsewhere, doctors in Uganda may have reservations about the technique's limited resolution, Obungoloch notes. "The radiologists see it and say, 'Well, this is a crappy image and we don't care how long it took you to acquire it.'" Government officials may also think Ugandans shouldn't have to settle for lower resolution imaging, no matter how useful, he says.

In truth, developers of low-field MRI are pushing for nothing less than a rethink of medical imaging. "Is the best technology the scanner that can provide the highest quality images, or is it the scanner that can lead to the most improved patient outcomes?" asks Harper, who collaborated on Webb's open-source rig and hopes to acquire a Swoop.

What will win over doctors, Sheth says, will be a "use case"—a killer app for the scanners. For example, they might be put into special ambulances for stroke care. He questions whether Hyperfine and others have found that use case, but predicts it will come.

Then there are patients to win over. After his time in the Hyperfine scanner, the pituitary tumor patient confides to Yadlapalli that it wasn't quite as comfortable as a regular MRI. Noting that he still can't breathe through his nose because of the surgery, he says the snug-fitting head basket bothered him. "I'd rather be scooted over to a real MRI." Call him a reluctant pioneer. ■

PHOTO: NO ATTRIBUTION

PERSPECTIVES

MICROBIOTA

A gut bacterial strain rescues stunted growth

Lactiplantibacillus plantarum promotes growth in undernourished mice

By **Jitender Yadav** and **Dana J. Philpott**

Undernutrition is a leading cause of infant and childhood mortality (*1*). Undernutrition not only has an impact on growth and development but also leads to impaired gut microbiota development. The transfer of gut microbiota from undernourished children to germ-free mice drives growth stunting and reduced weight, whereas mice on the identical diet but colonized with healthy children's microbiota grow normally (*2*). However, the mechanisms by which gut microbes contribute to postnatal growth are not clear. On page 826 of this issue, Schwarzer *et al.* (*3*) report that supplementation of undernourished mice with *Lactiplantibacillus plantarum* strain Lp^{WJL} improves systemic growth and weight gain. Notably, they find that the growth-promoting effect of Lp^{WJL} is mediated through bacterial peptidoglycan ligands that trigger the activation of nucleotide-binding oligomerization domain–containing protein 2 (NOD2)—an innate immune receptor that is usually associated with host defense and intestinal homeostasis—in intestinal epithelial cells.

Undernutrition has considerable short- and long-term impacts on health that include growth stunting, delayed physical and mental development, and increased susceptibility to infectious disease. Mechanistically, undernutrition results in low levels of growth hormones (GH) and insulin-like growth factor 1 (IGF-1), which together form what is known as the somatotropic axis. This axis plays a key role in controlling metabolism, physiological processes, and postnatal growth in mammals (*4*). Notably, gut microbes can affect the somatotropic axis by regulating GH and IGF-1 production (*5*), and impaired development of the gut microbiota may compound the effects of undernutrition by altering this axis (*6*). Specifically, the gut microbiota of undernourished children is associated with increases in the relative abundance of Proteobacteria (including pathogenic taxa), along with reduced relative abundances of several species of *Bifidobacterium* and *Lactobacillus* spp., as well as obligate anaerobic short-chain fatty acid–producing taxa (*7*).

By contrast, certain bacterial taxa positively correlate with healthy postnatal growth and development. One of these, Lp^{WJL}, was first described in a *Drosophila melanogaster* model to fully recapitulate the beneficial effects of a complex microbiota through its promotion of *D. melanogaster* juvenile growth and maturation (*8*). Furthermore, monocolonization of juvenile mice with Lp^{WJL} was shown to sustain the somatotropic axis and rescued the stunted growth effects of chronic undernutrition (*9*). However, mechanistically, how Lp^{WJL} positively affects the systemic growth of its mammalian host was not known.

Schwarzer *et al.* examined how Lp^{WJL} mechanistically protects against the adverse effects of undernutrition in mice. They show that Lp^{WJL} supplementation of malnourished mice of two different genetic backgrounds (C57BL/6 and BALB/c) reversed stunted postnatal growth and weight, which paralleled increases in circulating levels of insulin and IGF-1 (see the figure). A similar increase in systemic growth was also observed with heat-killed Lp^{WJL}, as well as with Lp^{WJL} isolated cell wall fractions. Cell wall fractions induced high activity of NOD2 in vitro. Specifically, NOD2 is an intracellular innate immune pattern recognition receptor for peptidoglycan ligands, including muramyl dipeptide (MDP), which is derived from bacterial cell walls. The authors found that the growth-promoting effects of Lp^{WJL} were no longer evident in malnourished *Nod2*-deficient mice, demonstrating that the growth-promoting effects of Lp^{WJL} are dependent on *Nod2*. Furthermore, they found that these effects were dependent on *Nod2* expression specifically in intestinal epithelial cells. NOD2 activation in intestinal epithelial cells with Lp^{WJL} led to induction of type 1 interferon (IFN), which can regulate intestinal epithelial homeostasis. Additionally, supplementation of malnourished mice with the NOD2-specific ligand MDP or the NOD2-activating adjuvant, mifamurtide (muramyl tripeptide phosphatidylethanolamine), increased IGF-1 in the circulation and promoted systemic growth in malnourished mice, further supporting the idea that the activation of NOD2 contributes to sustained

Improving growth in undernourished mice

Treatment of chronically undernourished mice with *Lactiplantibacillus plantarum* strain Lp^{WJL} leads to increased peptidoglycan and muramyl dipeptide (MDP) levels that activate nucleotide-binding oligomerization domain–containing protein 2 (NOD2) in intestinal epithelial cells to mediate cell proliferation. Lp^{WJL} supplementation also increases insulin-like growth factor 1 (IGF-1) levels in the circulation and improves systemic growth.

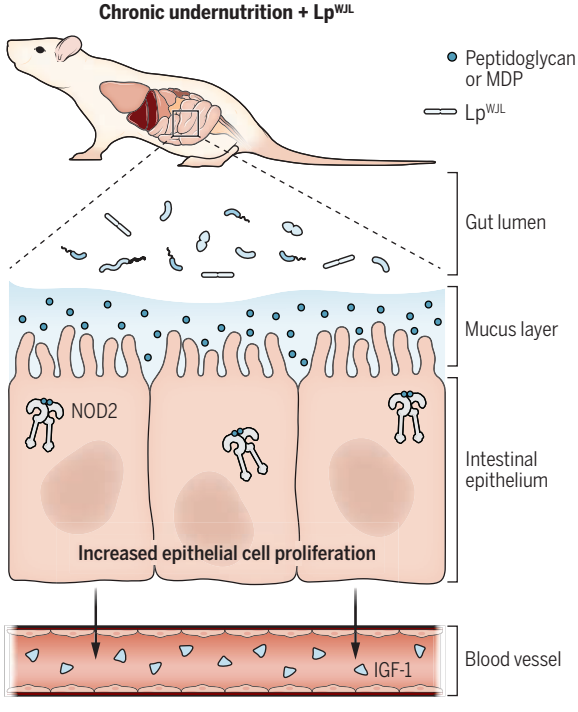

GRAPHIC: A. MASTIN/*SCIENCE*

Department of Immunology, Medical Sciences Building, University of Toronto, Toronto, ON, Canada. Email: dana.philpott@utoronto.ca

postnatal growth after undernutrition.

Loss-of-function mutation in the *NOD2* gene is the strongest genetic factor linked to the inflammatory bowel disease, Crohn's disease, in humans (*10*). NOD2 is expressed in intestinal stem cells, and its activation by MDP in intestinal organoid cultures leads to increased epithelial cell proliferation (*11*). The study of Schwarzer *et al.* also shows that supplementation of mice with Lp^{WJL} leads to NOD2-dependent increases in proliferation within the intestinal crypts, leading to the speculation that this increased epithelial cell proliferation and the consequent increase in the numbers of absorptive enterocytes might enhance nutrient absorption to promote systemic growth of malnourished mice. However, future studies are needed to understand this potential role of NOD2 in nutrient absorption and whether this is linked to the increases in circulating IGF-1 observed in the Lp^{WJL} supplemented animals.

Taken together, the study of Schwarzer *et al.* may have important implications for strategies to help combat the effects of undernutrition and potentially other chronic diseases. Although combating food insecurity is by far the most important and ethical way to prevent undernutrition, these findings suggest the possibility that supplementation of at-risk populations with NOD2 ligands or probiotic bacteria that release high levels of MDP may help to improve the dire consequences of undernutrition. Likewise, because NOD2 ligand deficiency is also observed in Crohn's disease, regardless of *NOD2* genotype (*12*), similar strategies may have adjuvant effects for the treatment of Crohn's disease and may specifically address the problem of stunting in children with this disease (*13*). ■

REFERENCES AND NOTES

1. R. E. Black *et al.*, *Lancet* **382**, 427 (2013).
2. L. V. Blanton *et al.*, *Science* **351**, aad3311 (2016).
3. M. Schwarzer *et al.*, *Science* **379**, 826 (2023).
4. V. Chesnokova, *Cells* **11**, 217 (2022).
5. F. De Vadder, A. Joly, F. Leulier, *J. Mol. Endocrinol.* **66**, R67 (2021).
6. F. Bäckhed, R. E. Ley, J. L. Sonnenburg, D. A. Peterson, J. I. Gordon, *Science* **307**, 1915 (2005).
7. M. Chawla, R. Gupta, B. Das, *Prog. Mol. Biol. Transl. Sci.* **192**, 205 (2022).
8. G. Storelli *et al.*, *Cell Metab.* **14**, 403 (2011).
9. M. Schwarzer *et al.*, *Science* **351**, 854 (2016).
10. A. Sazonovs *et al.*, *Nat. Genet.* **54**, 1275 (2022).
11. A. Levy *et al.*, *Proc. Natl. Acad. Sci. U.S.A.* **117**, 1994 (2020).
12. J. Gao *et al.*, *Cell Host Microbe* **30**, 1435 (2022).
13. M. Bouhuys, W. S. Lexmond, P. F. van Rheenen, *Pediatrics* **151**, e2022058037 (2023).

ACKNOWLEDGMENTS

D.J.P. is supported by grants from Canadian Institutes of Health Research.

10.1126/science.adg6247

GRAPHIC: K. HOLOSKI/*SCIENCE*

REGENERATION

Stem cells drive antler regeneration

Understanding the rapid growth of deer antlers could have applications in medicine

By **Datao Wang**[1] *and* **Tomas Landete-Castillejos**[2]

Understanding the biology underlying the regeneration of animal limbs, organs, and tissues could be a source of potential applications in medicine. Antlers of deer are a particularly good example because they show complete morphological, structural, and functional regeneration every year, unlike compensatory regeneration in response to injury, for example, as seen in the liver (*1*, *2*). An outstanding characteristic of the antler is the speed of regeneration: They can grow up to 2.75 cm per day and reach up to 15 kg in mass and 120 cm in length in ~3 months (*3*). How do deer antlers achieve such rapid and complete regeneration? On page 840 of this issue, Qin *et al.* (*4*) identify a population of antler blastema progenitor cells (ABPCs) that are responsible for the antler regenerative cycle. These findings add to the emerging idea that blastema progenitor cells are a common stem cell type in mammalian appendage regeneration.

After a limb or structure is lost, a population of undifferentiated cells called the blastema arises, which drives regeneration (*5*). Antler regeneration is driven by a reserve of undifferentiated cells that are located in the antlerogenic periosteum (the tissue in the pedicles where antlers form) (*6*). These cells constitute a growth center in the antler tip that grows upward; below this point, these cells differentiate into cartilage that later mineralizes into bone (*3*). Qin *et al.* developed a single-cell atlas of antler regeneration using tissue from antlerogenic periosteum, blastema, and the regenerating antler tip of sika deer (*Cervus nippon*). The results demonstrate the existence of a blastema-like structure that is similar to that involved in complete amphibian limb regeneration. Both contain

[1]Institute of Special Animal and Plant Sciences, Chinese Academy of Agricultural Sciences, Changchun, China. [2]Instituto de Investigación en Recursos Cinegéticos (IREC) e IDR, Universidad de Castilla–La Mancha (UCLM), Albacete, Spain. Email: tomas.landete@uclm.es

Blastema cells drive mammalian organ regeneration

A permanent population of paired mesoderm homeobox protein 1 (PRRX1)–expressing mesenchymal stem cells in the antler blastema generate antler blastema progenitor cells (ABPCs) that direct antler regeneration. ABPC-like cells also seem to exist in regenerative mammalian organs but not in regenerative tissues of axolotl or zebrafish.

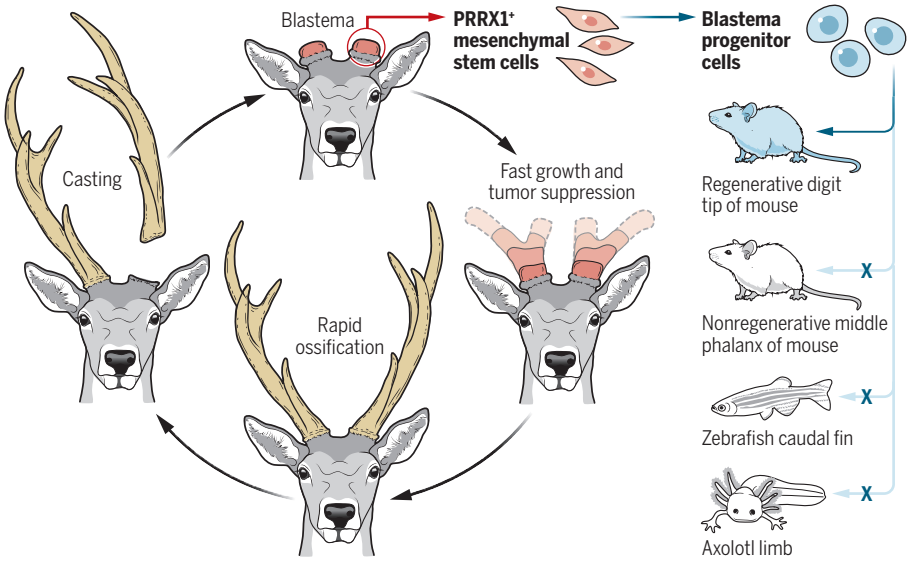

postnatal growth after undernutrition.

Loss-of-function mutation in the *NOD2* gene is the strongest genetic factor linked to the inflammatory bowel disease, Crohn's disease, in humans (*10*). NOD2 is expressed in intestinal stem cells, and its activation by MDP in intestinal organoid cultures leads to increased epithelial cell proliferation (*11*). The study of Schwarzer *et al.* also shows that supplementation of mice with Lp^{WJL} leads to NOD2-dependent increases in proliferation within the intestinal crypts, leading to the speculation that this increased epithelial cell proliferation and the consequent increase in the numbers of absorptive enterocytes might enhance nutrient absorption to promote systemic growth of malnourished mice. However, future studies are needed to understand this potential role of NOD2 in nutrient absorption and whether this is linked to the increases in circulating IGF-1 observed in the Lp^{WJL} supplemented animals.

Taken together, the study of Schwarzer *et al.* may have important implications for strategies to help combat the effects of undernutrition and potentially other chronic diseases. Although combating food insecurity is by far the most important and ethical way to prevent undernutrition, these findings suggest the possibility that supplementation of at-risk populations with NOD2 ligands or probiotic bacteria that release high levels of MDP may help to improve the dire consequences of undernutrition. Likewise, because NOD2 ligand deficiency is also observed in Crohn's disease, regardless of *NOD2* genotype (*12*), similar strategies may have adjuvant effects for the treatment of Crohn's disease and may specifically address the problem of stunting in children with this disease (*13*). ■

REFERENCES AND NOTES

1. R. E. Black *et al.*, *Lancet* **382**, 427 (2013).
2. L. V. Blanton *et al.*, *Science* **351**, aad3311 (2016).
3. M. Schwarzer *et al.*, *Science* **379**, 826 (2023).
4. V. Chesnokova, *Cells* **11**, 217 (2022).
5. F. De Vadder, A. Joly, F. Leulier, *J. Mol. Endocrinol.* **66**, R67 (2021).
6. F. Bäckhed, R. E. Ley, J. L. Sonnenburg, D. A. Peterson, J. I. Gordon, *Science* **307**, 1915 (2005).
7. M. Chawla, R. Gupta, B. Das, *Prog. Mol. Biol. Transl. Sci.* **192**, 205 (2022).
8. G. Storelli *et al.*, *Cell Metab.* **14**, 403 (2011).
9. M. Schwarzer *et al.*, *Science* **351**, 854 (2016).
10. A. Sazonovs *et al.*, *Nat. Genet.* **54**, 1275 (2022).
11. A. Levy *et al.*, *Proc. Natl. Acad. Sci. U.S.A.* **117**, 1994 (2020).
12. J. Gao *et al.*, *Cell Host Microbe* **30**, 1435 (2022).
13. M. Bouhuys, W. S. Lexmond, P. F. van Rheenen, *Pediatrics* **151**, e2022058037 (2023).

ACKNOWLEDGMENTS

D.J.P. is supported by grants from Canadian Institutes of Health Research.

10.1126/science.adg6247

GRAPHIC: K. HOLOSKI/*SCIENCE*

REGENERATION

Stem cells drive antler regeneration

Understanding the rapid growth of deer antlers could have applications in medicine

By **Datao Wang**[1] *and* **Tomas Landete-Castillejos**[2]

Understanding the biology underlying the regeneration of animal limbs, organs, and tissues could be a source of potential applications in medicine. Antlers of deer are a particularly good example because they show complete morphological, structural, and functional regeneration every year, unlike compensatory regeneration in response to injury, for example, as seen in the liver (*1*, *2*). An outstanding characteristic of the antler is the speed of regeneration: They can grow up to 2.75 cm per day and reach up to 15 kg in mass and 120 cm in length in ~3 months (*3*). How do deer antlers achieve such rapid and complete regeneration? On page 840 of this issue, Qin *et al.* (*4*) identify a population of antler blastema progenitor cells (ABPCs) that are responsible for the antler regenerative cycle. These findings add to the emerging idea that blastema progenitor cells are a common stem cell type in mammalian appendage regeneration.

After a limb or structure is lost, a population of undifferentiated cells called the blastema arises, which drives regeneration (*5*). Antler regeneration is driven by a reserve of undifferentiated cells that are located in the antlerogenic periosteum (the tissue in the pedicles where antlers form) (*6*). These cells constitute a growth center in the antler tip that grows upward; below this point, these cells differentiate into cartilage that later mineralizes into bone (*3*). Qin *et al.* developed a single-cell atlas of antler regeneration using tissue from antlerogenic periosteum, blastema, and the regenerating antler tip of sika deer (*Cervus nippon*). The results demonstrate the existence of a blastema-like structure that is similar to that involved in complete amphibian limb regeneration. Both contain

[1]Institute of Special Animal and Plant Sciences, Chinese Academy of Agricultural Sciences, Changchun, China. [2]Instituto de Investigación en Recursos Cinegéticos (IREC) e IDR, Universidad de Castilla–La Mancha (UCLM), Albacete, Spain. Email: tomas.landete@uclm.es

Blastema cells drive mammalian organ regeneration

A permanent population of paired mesoderm homeobox protein 1 (PRRX1)–expressing mesenchymal stem cells in the antler blastema generate antler blastema progenitor cells (ABPCs) that direct antler regeneration. ABPC-like cells also seem to exist in regenerative mammalian organs but not in regenerative tissues of axolotl or zebrafish.

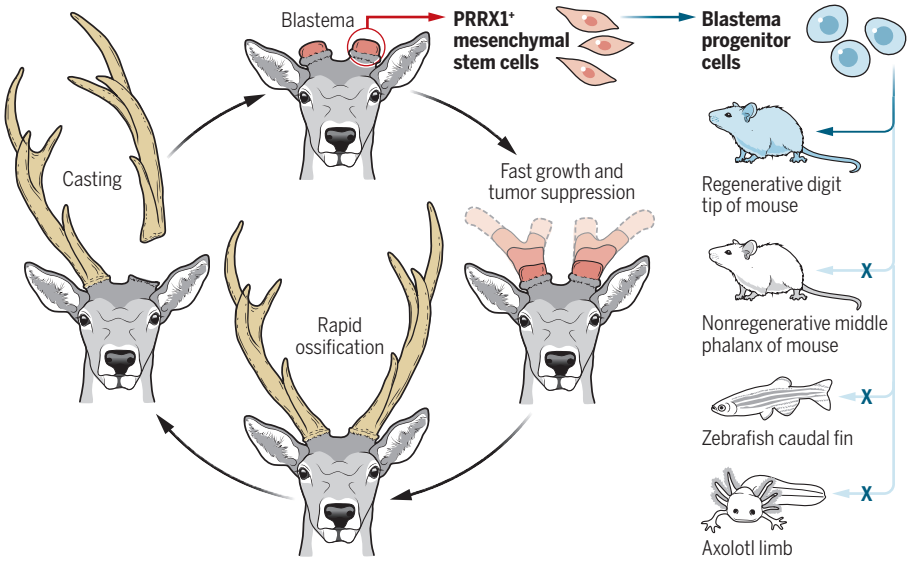

a population of paired mesoderm homeobox protein 1 (PRRX1)–expressing mesenchymal stem cells; however, the origin of PRRX1$^+$ mesenchymal stem cells is different: In salamanders, these cells originate from dedifferentiation (*7*) and no ABPC-like cells are present, whereas the blastema-like structure of antlers is derived directly from a preexisting PRRX1$^+$ mesenchymal stem cell population and differentiates into ABPCs (see the figure).

Does the ability to regenerate antlers arise simply because of the presence of PRRX1$^+$ mesenchymal stem cells? Findings from studies of digit regeneration in mice seem to confirm this suspicion: A specific cluster of PRRX1$^+$ cells with similar gene expression profiles to those of ABPCs was identified in the mouse digit-tip blastema but not in the nonregenerative middle phalanx (*8*). A comparison across species also reveals that ABPC-like cells do not occur in axolotl limbs and zebrafish caudal fins (lower animal models of complete regeneration). Therefore, ABPC-like cells appear to be essential and distinct for mammalian appendage regeneration compared with lower animals. The human fingertip also has a limited regenerative capacity, although this ability becomes weaker with age (*9*). An understanding of antler regeneration may inform ways to overcome the limited regeneration of human cells.

Qin *et al.* demonstrate that ABPCs maintain their self-renewal capability and have a higher colony-forming efficiency than other stem cell clusters in the antler, which supports fast growth for months. A population of stem cells in the antlerogenic periosteum, called antler stem cells (ASCs), appear to be progenitor cells derived from ABPCs and exhibit a much higher proliferation capacity than human bone marrow stem cells (hBMSCs), which are commonly used for stem cell research and clinical applications (*10*). In addition, exosomes secreted from ASCs prolong hBMSC proliferation, which attenuates cell senescence. This means that ASCs may confer regenerative potential to other cells through exosomes. Therefore, this strategy might be worth exploring to induce stem cell regenerative activity. In the future, ABPCs and ASCs should be compared using uniform markers to separate their roles in antler regeneration.

Despite the rapid growth of antlers, cancerous growth is avoided. The fast growth of antlers is driven by the high expression of proto-oncogenes in the regenerative tips of the antler, which in turn selects for the expression of tumor suppressor genes (*11*). Consequently, water-soluble extract from antler tips has shown possible anticancer effects when applied to human glioblastoma cells in vitro (by reducing cell proliferation or colony formation capacity and promoting apoptosis) (*12*) or to xenograft mouse models bearing human prostate cancer (by reducing tumor volume) (*13*). Considering the variety of tissues in the growing antler (skin, cartilage, bone, blood vessels, and nerves), this tumor-suppressive signaling may be a universal effect.

Because antlers are bone, the study of antler osteogenesis could have relevance for the study of bone damage repair and osteoporosis. The rapid growth of deer antlers requires amounts of calcium so large that dietary calcium intake cannot meet the demand, which thereby leads to the mobilization of skeletal calcium and temporary bone loss (called cyclic physiological osteoporosis) (*14*). Qin *et al.* demonstrate that ABPCs have a strong propensity for differentiation into osteoblasts and chondrocytes but cannot differentiate into adipocytes, which differs from the trilineage differentiation of BMSCs of the antler and thus indicates that ABPCs are skewed toward bone formation. Additionally, transplantation of ABPCs into rabbits with femoral condyle defects created more new cartilage and bone compared with the transplantation of rat BMSCs, revealing another potential avenue for anti-aging research.

Injection of ABPCs directly into humans, despite their efficiency in animal models, is not clinically acceptable, will likely induce immune rejection, and raises ethical concerns. Therefore, exosomes from ABPCs might be amenable to therapeutic development. Of note, the function and composition of exosomes need to be verified. Further research should also focus on how such fast growth rates are achieved, whether this sustained proliferation can delay aging or fight senescence in tissue repair, and what the mechanisms of achieving antitumor effects in antlers are. ■

REFERENCES AND NOTES

1. U. Kierdorf, C. Li, J. S. Price, *Semin. Cell Dev. Biol.* **20**, 535 (2009).
2. N. Fausto, J. S. Campbell, K. J. Riehle, *Hepatology* **43**, S45 (2006).
3. T. Landete-Castillejos *et al.*, *Bone* **128**, 115046 (2019).
4. T. Qin *et al.*, *Science* **379**, 840 (2023).
5. J. Simkin *et al.*, *Regeneration* **2**, 93 (2015).
6. D. Wang *et al.*, *Cell Death Dis.* **10**, 443 (2019).
7. T. Gerber *et al.*, *Science* **362**, eaaq0681 (2018).
8. M. A. Storer *et al.*, *Dev. Cell* **52**, 509 (2020).
9. S. Gupta, *Nature* **540**, S58 (2016).
10. J. Lei *et al.*, *Protein Cell* **13**, 220 (2022).
11. Y. Wang *et al.*, *Science* **364**, eaav6335 (2019).
12. L. Chonco *et al.*, *Sci. Rep.* **11**, 42 (2021).
13. Y. Tang *et al.*, *Biosci. Biotechnol. Biochem.* **83**, 348 (2019).
14. W. J. Banks Jr. *et al.*, *Anat. Rec.* **162**, 387 (1968).

ACKNOWLEDGMENTS

D.W. is supported by the National Natural Science Foundation of China (31901058) and the China Scholarship Council. T.L.-C. is supported by the Spanish National Cancer Association (AECC) (UCLM 2022-AYUDA-33655).

10.1126/science.adg9968

MATERIALS SCIENCE

Turning tissues into conducting matter

An electrically conducting soft polymer is synthesized within living tissue

By **Sahika Inal**

Electronic devices implanted into a tissue close to neurons of interest are meant to exchange signals with the nervous system. Such bioelectronic devices not only facilitate the study of neural communication, they can also hijack neural circuitry in a therapeutic approach known as bioelectronic medicine. The success of these applications relies on the robustness of the implanted devices and their compatibility with the body. Conventional bioelectronic devices have solid substrates that carry conducting films. Their rigidity can damage soft tissues and reduce an implant's long-term performance. On page 795 of this issue, Strakosas *et al.* (*1*) address the mechanical mismatch between soft and wet biological matter and solid-state electronics and describe an approach that generates electronics directly inside a tissue without a substrate, causing little damage to the tissue.

State-of-the-art implants are mostly made of stiff and hard materials, and insertion into human tissues can provoke inflammation. This creates a new tissue microenvironment that could harm the implant's electrical properties and disrupt its contact with target neurons (see the figure) (*2*).

The substrate of an implanted electronic device is a solid shuttle onto which electrodes are fabricated. It is the passive component of the device that carries the electronics and imparts mechanical rigidity. Flexible polymeric substrates, coatings such as elastomers, hydrogels with softness that matches that of the tissue, and materials that change stiffness upon implantation are means to overcome mechanical mismatches and improve device longevity (*3*). Electrode materials can also be more mechanically compliant. Semiconducting polymers such as poly(3,4-ethylenedioxythiophene) (PEDOT) are soft

Biological and Environmental Science and Engineering Division, King Abdullah University of Science and Technology (KAUST), Thuwal 23955-6900, Saudi Arabia. Email: sahika.inal@kaust.edu.sa

a population of paired mesoderm homeobox protein 1 (PRRX1)–expressing mesenchymal stem cells; however, the origin of PRRX1$^+$ mesenchymal stem cells is different: In salamanders, these cells originate from dedifferentiation (*7*) and no ABPC-like cells are present, whereas the blastema-like structure of antlers is derived directly from a preexisting PRRX1$^+$ mesenchymal stem cell population and differentiates into ABPCs (see the figure).

Does the ability to regenerate antlers arise simply because of the presence of PRRX1$^+$ mesenchymal stem cells? Findings from studies of digit regeneration in mice seem to confirm this suspicion: A specific cluster of PRRX1$^+$ cells with similar gene expression profiles to those of ABPCs was identified in the mouse digit-tip blastema but not in the nonregenerative middle phalanx (*8*). A comparison across species also reveals that ABPC-like cells do not occur in axolotl limbs and zebrafish caudal fins (lower animal models of complete regeneration). Therefore, ABPC-like cells appear to be essential and distinct for mammalian appendage regeneration compared with lower animals. The human fingertip also has a limited regenerative capacity, although this ability becomes weaker with age (*9*). An understanding of antler regeneration may inform ways to overcome the limited regeneration of human cells.

Qin *et al.* demonstrate that ABPCs maintain their self-renewal capability and have a higher colony-forming efficiency than other stem cell clusters in the antler, which supports fast growth for months. A population of stem cells in the antlerogenic periosteum, called antler stem cells (ASCs), appear to be progenitor cells derived from ABPCs and exhibit a much higher proliferation capacity than human bone marrow stem cells (hBMSCs), which are commonly used for stem cell research and clinical applications (*10*). In addition, exosomes secreted from ASCs prolong hBMSC proliferation, which attenuates cell senescence. This means that ASCs may confer regenerative potential to other cells through exosomes. Therefore, this strategy might be worth exploring to induce stem cell regenerative activity. In the future, ABPCs and ASCs should be compared using uniform markers to separate their roles in antler regeneration.

Despite the rapid growth of antlers, cancerous growth is avoided. The fast growth of antlers is driven by the high expression of proto-oncogenes in the regenerative tips of the antler, which in turn selects for the expression of tumor suppressor genes (*11*). Consequently, water-soluble extract from antler tips has shown possible anticancer effects when applied to human glioblastoma cells in vitro (by reducing cell proliferation or colony formation capacity and promoting apoptosis) (*12*) or to xenograft mouse models bearing human prostate cancer (by reducing tumor volume) (*13*). Considering the variety of tissues in the growing antler (skin, cartilage, bone, blood vessels, and nerves), this tumor-suppressive signaling may be a universal effect.

Because antlers are bone, the study of antler osteogenesis could have relevance for the study of bone damage repair and osteoporosis. The rapid growth of deer antlers requires amounts of calcium so large that dietary calcium intake cannot meet the demand, which thereby leads to the mobilization of skeletal calcium and temporary bone loss (called cyclic physiological osteoporosis) (*14*). Qin *et al.* demonstrate that ABPCs have a strong propensity for differentiation into osteoblasts and chondrocytes but cannot differentiate into adipocytes, which differs from the trilineage differentiation of BMSCs of the antler and thus indicates that ABPCs are skewed toward bone formation. Additionally, transplantation of ABPCs into rabbits with femoral condyle defects created more new cartilage and bone compared with the transplantation of rat BMSCs, revealing another potential avenue for anti-aging research.

Injection of ABPCs directly into humans, despite their efficiency in animal models, is not clinically acceptable, will likely induce immune rejection, and raises ethical concerns. Therefore, exosomes from ABPCs might be amenable to therapeutic development. Of note, the function and composition of exosomes need to be verified. Further research should also focus on how such fast growth rates are achieved, whether this sustained proliferation can delay aging or fight senescence in tissue repair, and what the mechanisms of achieving antitumor effects in antlers are. ■

REFERENCES AND NOTES

1. U. Kierdorf, C. Li, J. S. Price, *Semin. Cell Dev. Biol.* **20**, 535 (2009).
2. N. Fausto, J. S. Campbell, K. J. Riehle, *Hepatology* **43**, S45 (2006).
3. T. Landete-Castillejos *et al.*, *Bone* **128**, 115046 (2019).
4. T. Qin *et al.*, *Science* **379**, 840 (2023).
5. J. Simkin *et al.*, *Regeneration* **2**, 93 (2015).
6. D. Wang *et al.*, *Cell Death Dis.* **10**, 443 (2019).
7. T. Gerber *et al.*, *Science* **362**, eaaq0681 (2018).
8. M. A. Storer *et al.*, *Dev. Cell* **52**, 509 (2020).
9. S. Gupta, *Nature* **540**, S58 (2016).
10. J. Lei *et al.*, *Protein Cell* **13**, 220 (2022).
11. Y. Wang *et al.*, *Science* **364**, eaav6335 (2019).
12. L. Chonco *et al.*, *Sci. Rep.* **11**, 42 (2021).
13. Y. Tang *et al.*, *Biosci. Biotechnol. Biochem.* **83**, 348 (2019).
14. W. J. Banks Jr. *et al.*, *Anat. Rec.* **162**, 387 (1968).

ACKNOWLEDGMENTS

D.W. is supported by the National Natural Science Foundation of China (31901058) and the China Scholarship Council. T.L.-C. is supported by the Spanish National Cancer Association (AECC) (UCLM 2022-AYUDA-33655).

10.1126/science.adg9968

MATERIALS SCIENCE

Turning tissues into conducting matter

An electrically conducting soft polymer is synthesized within living tissue

By **Sahika Inal**

Electronic devices implanted into a tissue close to neurons of interest are meant to exchange signals with the nervous system. Such bioelectronic devices not only facilitate the study of neural communication, they can also hijack neural circuitry in a therapeutic approach known as bioelectronic medicine. The success of these applications relies on the robustness of the implanted devices and their compatibility with the body. Conventional bioelectronic devices have solid substrates that carry conducting films. Their rigidity can damage soft tissues and reduce an implant's long-term performance. On page 795 of this issue, Strakosas *et al.* (*1*) address the mechanical mismatch between soft and wet biological matter and solid-state electronics and describe an approach that generates electronics directly inside a tissue without a substrate, causing little damage to the tissue.

State-of-the-art implants are mostly made of stiff and hard materials, and insertion into human tissues can provoke inflammation. This creates a new tissue microenvironment that could harm the implant's electrical properties and disrupt its contact with target neurons (see the figure) (*2*).

The substrate of an implanted electronic device is a solid shuttle onto which electrodes are fabricated. It is the passive component of the device that carries the electronics and imparts mechanical rigidity. Flexible polymeric substrates, coatings such as elastomers, hydrogels with softness that matches that of the tissue, and materials that change stiffness upon implantation are means to overcome mechanical mismatches and improve device longevity (*3*). Electrode materials can also be more mechanically compliant. Semiconducting polymers such as poly(3,4-ethylenedioxythiophene) (PEDOT) are soft

Biological and Environmental Science and Engineering Division, King Abdullah University of Science and Technology (KAUST), Thuwal 23955-6900, Saudi Arabia. Email: sahika.inal@kaust.edu.sa

alternatives to inorganic counterparts. They have inherently low electrochemical impedance (resistance to current flow), which eases bidirectional communication with neurons. Electrodes made of soft conducting polymers can be patterned on ultrathin substrates (*4*) and even on substrates that dissolve in the body over time (*5*), although the former is primarily designed to conform horizontally on top of or to wrap around (rather than penetrate) a tissue.

Unfortunately, devices that are too tissue-compliant, with small dimensions and soft materials, are problematic because they can buckle at the tissue surface, making them hard to implant. One solution is to remove the substrate so that the mechanical property mismatch between the implant and tissue is no longer a design consideration. For example, a meshlike, porous construct that embeds the electronics has enough viscosity to be injected through a syringe and can also provide space for cells to invade the electronics after implantation (*6*). Removing substrates altogether may also help overcome a major device failure mode: the mechanical or chemical degradation of the physical device. A typical implant has at least two layers of deposited films, one of which is the patterned electrode on the substrate (the other is an insulating film). The layers can create degradation pathways through delamination, cracks, water ingress, and redox reactions. These can be mitigated if there are no substrates or solid film coatings.

Semiconducting polymers can be generated in an aqueous medium and in a living tissue if conditions are conducive for polymerization (*7*). Polymerization can be triggered by electrical fields applied through an electrode. PEDOT films, for example, have been generated on a gold electrode tip that was already implanted in a rat brain (*8*). However, this process of electropolymerization requires a substrate and application of a current. Electropolymerization can also cause scar tissue formation. One solution is enzymatic polymerization. This process has been demonstrated by using a peroxidase enzyme and hydrogen peroxide (H_2O_2), two agents found in living organisms. A mixture of a monomer, an acid, and H_2O_2 was injected into a living animal (the nematode *Caenorhabditis elegans*) that was genetically engineered to express peroxidase (*9*). When injected close to neurons that secrete the peroxidase, the mixture turned into a solid conducting film. Another method involved injecting a solution of an elastomer–metal particle composite into a target tissue where it solidified to form a conductive tissue interface (*10*).

Strakosas *et al.* built on these advances and demonstrate an implant fabrication method that integrates conducting polymer–based gels directly within genetically unmodified tissues. The innovation lies in the injected cocktail, which contains redox enzymes that break down metabolites already present in the target tissue (see the figure). This reaction generates H_2O_2, which then acts as the oxidant of an enzymatic polymerization that is catalyzed by horseradish peroxide (another agent in the mix). The authors selected a monomer that bears certain functional units so that as it polymerizes, it reacts with the primary amines of a biocompatible polymer, poly-L-lysine (also in the injected mixture). Cross-linking of these polymers results in a stable, soft conducting gel rather than a brittle conducting film. Using metabolites (lactate or glucose) present in the tissue, gel polymerization proceeded in the brain, fin, and heart of living zebrafish as well as in living leeches and isolated mammalian tissues, showing the universal applicability of the approach. In all cases, the volume of the conducting gel extended beyond that of conventional, two-dimensional implants and blended into the tissue. Three days after gel polymerization in the brain, fish behavior did not show abnormalities and the injection site had no signs of tissue damage.

Future work may address shortcomings and leverage opportunities. For example, Strakosas *et al.* implanted flexible metallic electrodes to contact the conducting gel. Making contact should instead involve a wireless method. It will also be a challenge to grow the gel precisely in a target area. This will require injecting known amounts and limiting diffusion of the mixture to off-target regions. The accessibility of human tissues to a syringe will differ from the animal models studied by Strakosas *et al.*, which may increase the invasiveness of the approach and cause implantation damage.

Another critical point concerns chronic use of the implant. During extended periods, the body's products can chemically alter the nature of the conducting gel, which could trigger decomposition and/or release cytotoxic by-products. Safety and stability analyses over long periods will be essential to determine whether such technology is useful for chronic implantations. However, the strategy of Strakosas *et al.* suggests that any living tissue can turn into electronic matter, and brings the field closer to generating seamless biotic-abiotic interfaces with a potentially long lifetime and minimum harm to tissues. ■

Bioelectronics in tissues

Implantation of a solid substrate carrying electrodes can trigger changes in cell type and density and cause tissue damage (left). By contrast, a substrate-free conducting gel (gray) can be synthesized from a liquid mixture (light blue) injected into tissue and is more biologically compatible (right).

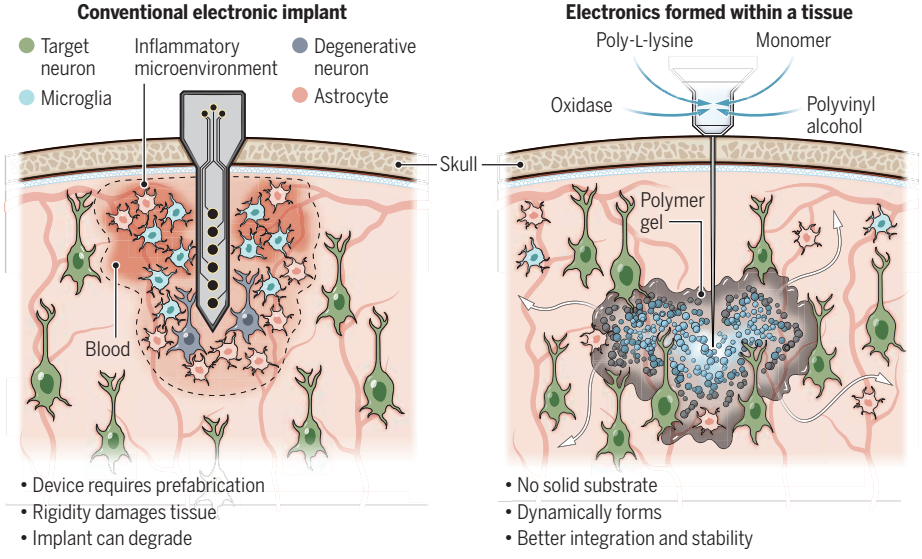

GRAPHIC: A. FISHER/*SCIENCE*

REFERENCES AND NOTES

1. X. Strakosas *et al.*, *Science* **379**, 795 (2022).
2. T. D. Y. Kozai, A. S. Jaquins-Gerstl, A. L. Vazquez, A. C. Michael, X. T. Cui, *ACS Chem. Neurosci.* **6**, 48 (2015).
3. M. Jorfi, J. L. Skousen, C. Weder, J. R. Capadona, *J. Neural Eng.* **12**, 011001 (2015).
4. W. Lee *et al.*, *Proc. Natl. Acad. Sci. U.S.A.* **114**, 10554 (2017).
5. K. J. Yu *et al.*, *Nat. Mater.* **15**, 782 (2016).
6. S. R. Patel, C. M. Lieber, *Nat. Biotechnol.* **37**, 1007 (2019).
7. Z. Zhou, K. Maxeiner, D. Y. W. Ng, T. Weil, *Acc. Chem. Res.* **55**, 2998 (2022).
8. L. Ouyang, C. L. Shaw, C. C. Kuo, A. L. Griffin, D. C. Martin, *J. Neural Eng.* **11**, 026005 (2014).
9. J. Liu *et al.*, *Science* **367**, 1372 (2020).
10. J. K. Trevathan *et al.*, *Adv. Healthc. Mater.* **8**, 1900892 (2019).

10.1126/science.adg4761

MEDICINE

Sweat as a diagnostic biofluid

Skin-interfaced microfluidic systems help assess health status and chemical exposure

By **Da Som Yang, Roozbeh Ghaffari, John A. Rogers**

Eccrine sweat glands in the skin are key components of an ingenious system for evaporative cooling. Their action is controlled by the sympathetic nervous system in an adaptive, closed-loop manner to help maintain thermal homeostasis during physical or mental exertion or exposure to high temperatures. Sweat not only removes heat but also helps excrete other chemicals and metabolites from the body. Recent advances in engineering have enabled eccrine sweat to be used for diagnostic purposes, in the form of soft microfluidic analysis systems (*1*, *2*) that gently adhere to the skin for in situ capture, storage, and biochemical evaluation of directly sourced microliter samples. These noninvasive technologies create a broad spectrum of possibilities for using sweat to assess health status and chemical balance, screen for disease conditions, monitor loss of essential chemical species, and detect trace toxins or exogenous agents without the need for external sample collection and analysis.

Eccrine glands appear across all regions of the body; in most circumstances, they are responsible for the largest total volume of sweat loss. The other two main types of sweat glands present in the dermis layer, the apocrine and apoeccrine glands, produce sweat with comparatively complex and variable chemical content. They also do so from specific anatomical regions that are not readily accessible given their location and hair coverage. These considerations motivate the choice of eccrine glands as a central focus for sweat analysis.

The historical standards for sweat assays rely on collection into absorbent pads or tubes followed by analysis with benchtop instrumentation. Quantitative measurements of the dynamics of sweating and the contents of sweat determined in this manner provide important insights into physiological health, psychological stress, nutritional balance, and exposure to foreign substances. Well-established examples include medical testing for cystic fibrosis (CF) based on chloride concentration (*3*), drug screening for banned substances through trace analysis (*4*), and hydration status for sports performance monitoring water and electrolyte loss (*5*).

Unlike blood and interstitial fluid sampling, sweat is collected noninvasively and also avoids issues in contamination, irritation, and inconveniences associated with other noninvasive biofluids such as saliva, tears, and urine. However, requirements for specialized equipment, skilled technicians, and strict protocols have limited the broad utility of sweat for routine diagnostics. Wearable microfluidic patches can perform analysis in real time—in a simple, cost-effective, and noninvasive manner—in nearly any setting, without the need for trained personnel. These devices are usually targeted at a single or specific set of compounds rather than the broad spectrum of sweat constituents. However, in situ analysis of sweat samples could be applied to a broad range of applications with medical relevance, including disease screening for CF, managing kidney disorders, tracking stress levels, monitoring of immune responses, and guiding the use of prescription drugs.

Skin-interfaced microfluidic devices leverage the natural pumping action of the eccrine glands, originating in secretory coils that connect through tubular lumen to ducts through the dermis and the epidermis, terminating at the surface of the skin (see the figure). Stimulation by cholinergic nerve endings that surround these coils drives an influx of Ca^{2+} ions into the surrounding cells and leads to transport of Cl^- and Na^+ ions into the lumen. A corresponding increase in the concentration of NaCl relative to that of the surrounding cells and interstitial spaces creates an osmotic pressure gradient that drives water into the lumen, ultimately manifesting as sweat that exits the skin pores (*2*, *6*).

The rates of flow and the volumes of sweat released from the skin depend on essential aspects of health and hydration status. In addition, active and passive transport mechanisms lead to diverse chemical content, spanning hundreds of constituents, including electrolytes, metabolites, hormones, proteins, pharmaceuticals, nutrients, organic pollutants, and heavy-metal toxins (*5*, *7*). Diagnostic insights based on concentrations of these species benefit from and frequently require precise knowledge of sweat rates; accumulated volumes of sweat loss; and often, body temperature, physical exertion, and cardiopulmonary activity.

Capabilities for these measurements follow from recently developed technologies. Soft, flexible microfluidic systems can establish robust, water-tight adhesive interfaces to the skin (*1*, *2*). These skin patches collect sweat directly as it emerges from the pores in the skin, passing through inlet ports on the base of the device into a network of microchannels and

Analyzing a chemically rich biofluid

Soft, skin-interfaced microfluidic sweat analysis systems enable assessments of health status, chemical balance, and environmental exposure.

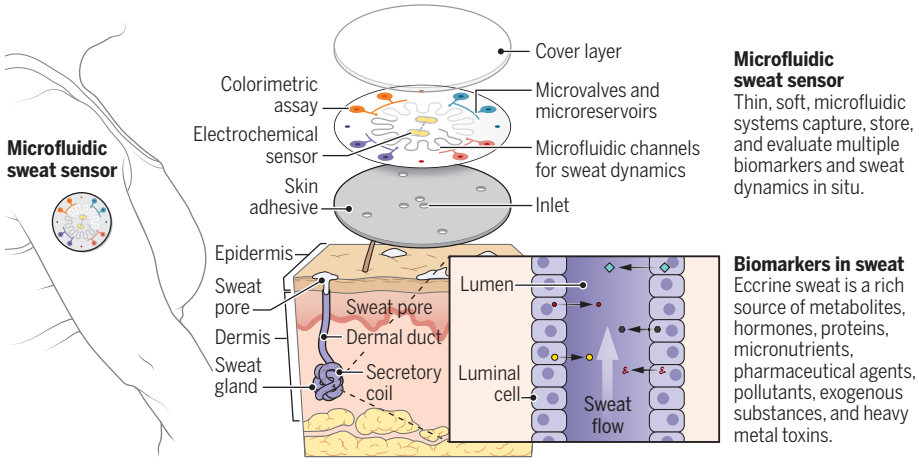

GRAPHIC: K. HOLOSKI/*SCIENCE*

Querrey Simpson Institute for Bioelectronics, Northwestern University, Evanston, IL 60208, USA. Email: ds.yang@northwestern.edu; rooz@northwestern.edu; jrogers@northwestern.edu

microvalves to microreservoirs for storage, sensing, or both. The devices allow measurements of the dynamics of sweat release. Monitoring regional sweat rate and accumulated sweat volume enable tracking of whole-body parameters for estimating loss of electrolytes and other chemical species through sweating. This sensing capability follows from devices that exploit microfluidic systems for capture, storage, and biomarker analysis of sweat. Integrated valves allow sequential routing into corresponding reservoirs, without mixing, as the basis for chronometric separation of consistent volumes of sweat samples over time. These sensors are validated against standard clinic assays for individual biomarkers such as gas chromatography–mass spectrometry or high-performance liquid chromatography. Microfluidic sweat devices used for capturing, manipulating, and analyzing minute volumes of sweat are essential to achieve sweat biomarker standardization and to mitigate the risks of environmental contamination or handling error in remote settings.

Colorimetric and fluorometric indicators and chemical assays can yield quantitative assessments of sweat dynamics, loss, and chemistry (*4*). Chemistries that respond to sweat biomarkers through changes in color or fluorescence intensity allow for quantitative measurements through analysis of digital images collected from transparent regions of the microfluidic structures (*4*). Examples of possible biomarkers include glucose, lactate, creatinine, ammonia, urea, chloride, sodium, zinc, iron, calcium, vitamin C, pH, xanthine, ketone, and alcohol (*4*, *8*).

Electrochemical sensors and associated wireless electronics can support additional options in chemical analysis (*9*). Electrochemical methods exist for glucose, lactate, ammonia, uric acid, potassium, sodium, chloride, calcium, zinc, copper, cadmium, lead, mercury, vitamin C, cortisol, caffeine, pH, levodopa, methylxanthine, tyrosine, dipyridamole, acetaminophen, nicotine, and alcohol (*9*, *10*). Electrochemical analysis allows continuous monitoring and applicability over a wide spectrum of analytes but increases device cost and creates limits on wearability that follow from requirements for power supply and data communication.

In all cases, device operation demands activation of the eccrine glands (*4*) through stimulation of thermoregulatory responses, applied most effectively to healthy adults exposed to warm, humid environments (such as a sauna, bath, or shower) or engaged in exercise. For infants, elderly patients, or other vulnerable populations, emerging alternatives include systems for induction of sweating through iontophoretic transport of pharmacological agents (*3*) through the skin and microfluidic device designs for capture of minute volumes of sweat that continuously emerge from the surface of the skin, known as insensible sweat (*7*, *11*).

Initial versions of these wearable technologies are in widespread commercial use for medical diagnostics and hydration monitoring. A prominent example of the former measures the concentration of chloride in sweat for CF screening, using a kit with regulatory certification for capturing sweat in coiled tubes and then analyzing extracted samples with a benchtop chloridometer. Advanced technologies exploit thin microfluidic "stickers" that support both collection and in situ colorimetric readout based on a chloride-based assay (*12*).

This form of analysis provides real-time, clinical-grade screening for CF without the need for trained personnel or benchtop chemical analyzers, at a price (~$10) that is a fraction of that of existing clinical grade sweat tests (~$250). Microfluidic stickers are simple, low-cost alternatives to clinical standards, with improved reliability and suitability for rapid, at-home tests and broad deployment. Investigational examples of wearable sweat-sensing platforms for medical applications appear in the literature but are not yet approved by the US Food and Drug Administration (FDA). This range of applications includes sensing of sweat urea for gout and kidney disease; monitoring of cortisol for physical and cognitive stress management; tracking of cytokines [such as interleukin-1α (IL-1α), IL-1β, IL-6, IL-8, tumor necrosis factor (TNF), and transforming growth factor–β (TGF-β)] for assessments of immune responses; and guiding the use of drugs relevant to neurological diseases, such as levodopa with Parkinson's patients (*4*, *11*).

A consumer version of this device concept is now available for applications in sports performance to determine whole-body loss of water and electrolytes through sweating. This system pairs with a smartphone application that provides quantitative, personalized feedback to guide rehydration and replenishment (*13*). Recent platforms both extend these capabilities in sweat monitoring and add sensors of complementary biophysical parameters (*14*). One such system monitors signs of heat exhaustion and dehydration for first responders and manual laborers. The technology integrates a single-use, skin-interfaced microfluidic system with a multiuse wireless electronic module for digital sensing, wireless communication, haptic alerts, data storage, and analytics (*4*). Large-scale validation studies with firefighters and workers in the oil and gas industry involve continuous measurements of sweat rate, sweat loss, electrolyte loss, skin temperature, and physical activity.

Other commercial devices integrate electrochemical sensors in wrist-worn bands to measure the concentration of ethanol in sweat, as a surrogate for blood alcohol. Assessments of additional biomarkers in sweat requires advanced analytical techniques to collect sweat samples by using absorbent pads, tubes, or microfluidic systems, each with FDA clearance and registration. Applications include screening for drugs (such as fentanyl, oxycodone, or hydromorphone) and measuring inflammatory cytokines such as IL-6. Ongoing efforts seek to establish lateral flow assays for these and other biomarkers (such as cortisol), with options for integration into microfluidic platforms that also support programmable modules to actively induce sweat for analysis or release components for transdermal delivery of drugs, vitamins, and chemical stimulants (*8*, *14*, *15*).

From the standpoint of human physiology, sweat is well established as a mechanism for loss of essential body substances and as a binary indicator for exposure to exogenous chemical species. By contrast, relationships between certain aspects of sweat chemistry and blood chemistry remain poorly understood. Research that addresses these uncertainties could apply across both known sweat biomarkers and newly discovered ones to further expand options in clinical application. With the addition of advanced electrochemical sensors, sweat collection strategies, closed-loop feedback systems, and transcutaneous drug and supplement delivery modules, future versions of soft microfluidic platforms may enable fully automated modes of operation that combine measurements of medical biomarkers, with clinical reporting and corresponding drug and nutrient delivery. ■

REFERENCES AND NOTES

1. A. Koh *et al.*, *Sci. Transl. Med.* **8**, 366ra165 (2016).
2. J. Choi *et al.*, *Sci. Adv.* **4**, eaar3921 (2018).
3. S. Emaminejad *et al.*, *Proc. Natl. Acad. Sci. U.S.A.* **114**, 4625 (2017).
4. R. Ghaffari *et al.*, *ACS Sens.* **6**, 2787 (2021).
5. L. B. Baker, A. S. Wolfe, *Eur. J. Appl. Physiol.* **120**, 719 (2020).
6. J. Heikenfeld *et al.*, *Nat. Biotechnol.* **37**, 407 (2019).
7. J. Brunmair *et al.*, *Nat. Commun.* **12**, 5993 (2021).
8. J. Kim *et al.*, *Adv. Sci.* **9**, 2103331 (2022).
9. W. Gao *et al.*, *Nature* **529**, 509 (2016).
10. J. Kim *et al.*, *Nat. Biotechnol.* **37**, 389 (2019).
11. H. Y. Y. Nyein *et al.*, *Nat. Commun.* **12**, 1823 (2021).
12. T. R. Ray *et al.*, *Sci. Transl. Med.* **13**, eabd8109 (2021).
13. L. B. Baker *et al.*, *Sci. Adv.* **6**, eabe3929 (2020).
14. R. Ghaffari *et al.*, *Adv. Funct. Mater.* **30**, 1907269 (2020).
15. S. Kim *et al.*, *Proc. Natl. Acad. Sci. U.S.A.* **117**, 27906 (2020).

ACKNOWLEDGMENTS

R.G. and J.A.R. are cofounders and R.G is an employee of Epicore Biosystems, a company that develops wearable microfluidic devices. D.S.Y. and R.G. contributed equally to this work.

10.1126/science.abq5916

RETROSPECTIVE

Christopher T. Walsh (1944–2023)

A luminous scholar and mentor at the interface of chemistry, biology, and medicine

By **Thomas V. O'Halloran**

Christopher Walsh, a pioneer committed to extending the frontiers of knowledge at the interfaces of chemistry, biology, and medicine, died on 10 January, a month before his 79th birthday. He was responsible for countless penetrating insights into complex catalytic chemistry in living systems. Our community has lost a creative force in drug discovery and a warm, inspiring mentor who opened doors for generations of diverse leaders.

After attending the Roxbury Latin School and then enrolling at Harvard University with the intention of pursuing a career as a physician, Chris started an undergraduate research project with E. O. Wilson on fire ant pheromones. This experience changed his trajectory. Upon publishing a first-author paper in *Nature*, Chris graduated in 1965 and decided to pursue a PhD with Leonard Spector in the lab of Nobel laureate Fritz Lipmann at the Rockefeller University in New York. He then returned to Boston for a postdoctoral fellowship at Brandeis University in 1970 with Robert Abeles. Work with Abeles and William Jencks inspired Chris's lifelong chemocentric approach to understanding the reactions of life. In 1972, the Massachusetts Institute of Technology (MIT) offered him an assistant professorship in chemistry. He negotiated a joint appointment in the chemistry and biology departments, and his successful navigation of both cultures lowered the hurdles for generations of interdisciplinary researchers.

Chris's research focused on the chemistry of enzymes and enzyme inhibitors, on antibiotic resistance mechanisms, inorganic and organic redox cofactors, and biosynthesis of biologically and medicinally active natural products. His opus includes more than 850 research papers and monographs. His first book, *Enzymatic Reaction Mechanisms* (1979), championed categorization of metabolism into a limited set of chemical reactions made possible by a wide array of organic and inorganic cofactors. His MIT students recount learning enzymatic mechanisms, one chapter draft at a time, and coming to see biology from a chemical perspective. Another of Chris's game-changing books, *Posttranslational Modification of Proteins: Expanding Nature's Inventory* (2005), took the community beyond the chemistry of the 20-some-odd amino acid chains into thousands of other types of functional groups and biological activities accessible in a systematic manner.

Chris uncovered a vast array of specific chemical modifications of proteins and natural products that control the biology of both hosts and pathogens. His group discovered mechanisms of enzymes that synthesize bacterial cell walls, break cyclopropane rings, or convert peptide bonds to heterocycles, as well as mechanisms of nickel- and iron-sulfur–dependent enzymes, flavin-dependent enzymes that detoxify mercury, and nonheme iron proteins that use O_2 to break unactivated C–H bonds before inserting a halogen. Some of his highest-impact work focused on natural product biosynthesis, nonribosomal peptide antibiotic assembly pathways, and the mechanisms of drug resistance to the antibiotic vancomycin, a frontline drug for treating patients with drug-resistant infections. This work greatly expanded our understanding of antibiotics such as penicillins, cephalosporins, and daptomycin, among others.

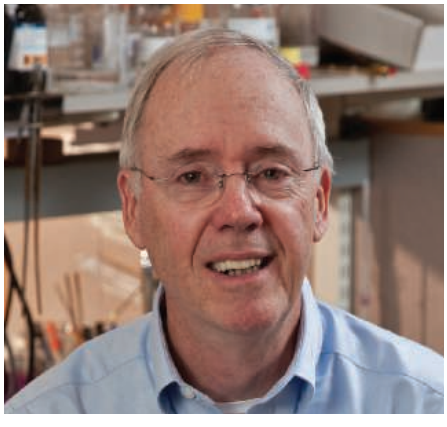

When he was not writing and mentoring more than 280 graduate students and postdocs, Chris made important contributions to both the basic and applied sides of the drug discovery ledger. After advising drug developers at Merck and Roche, Chris worked with biotech start-up companies. These efforts led to approval of several new therapeutics. Given his uncanny ability to recognize how breakthroughs in basic science could be translated into life-saving drugs, his counsel was widely sought. Chris was quick to note that people in his lab were not involved in commercial activities, and he rigorously held to the university limit of a single day of consulting per week. He was nonetheless generous with his time and mentored many former students in their own independent start-up companies.

Beginning with service as chair of MIT's Department of Chemistry (1982–1987), Chris focused his administrative and leadership energies on building bridges between the disciplines of chemistry, biology, and medicine. When the opportunity arose to extend his vision into the heart of the medical establishment, Walsh moved his lab to Harvard Medical School and served as founding chair of the Biological Chemistry and Molecular Pharmacology Department (1987–1995). He recruited a diverse cadre of investigators who brought together chemical and cell biology with biophysics to solve otherwise intractable problems in medicine. Many medical school departments around the country adopted this interdisciplinary model. Chris then took a leadership role in bench-to-bedside translational science as president and chief executive officer of the Dana-Farber Cancer Institute (1992–1995). There, Chris also continued to direct research and publish high-impact papers with his trainees. After 4 years leading the institute, he chose to go into "remission from academic administration" and stepped away from those responsibilities. He directed research at Harvard for another 18 years before closing the lab and moving west with his wife, Diana, president emerita of Wellesley College. He joined his daughter, Allison Kurian, on the Stanford University faculty, where he found new opportunities to write and work with another generation of eager students, including his grandson, Sean.

One of Chris's most important attributes was that of a mentor. As with many of the postdoctoral fellows in his lab, I found his photographic memory to be impressive and intimidating. He nonetheless had a light touch when it came to directing the lab. Chris taught us the finer arts of communication and delighted us with a rapier-like sense of humor that was sometimes deployed to let the air out of deserving colleagues. As a prolific scholar and a thoughtful teacher, Chris's legacy in the scientific community ripples forward in time, not just through his published work but also through the way he taught us how to lower barriers that once insulated chemistry from biology and medicine. ■

10.1126/science.adg9841

PHOTO: FRANK SITEMAN

Department of Chemistry and Department of Microbiology and Molecular Genetics, Michigan State University, East Lansing, MI 48824, USA. Email: ohallor8@msu.edu

CONFLICT AND ENVIRONMENT

Will war in Ukraine escalate the global land rush?

Land grabbing typically leads to social and environmental harms

By **Jampel Dell'Angelo[1], Maria Cristina Rulli[2], Paolo D'Odorico[3]**

The simultaneous occurrence in 2008 of interconnected shocks in climate, food production, and international finance underscored the emergence of a contemporary "global land rush." Since the turn of the century, a conservative estimate, limited to fully concluded deals, points to more than 45 million ha of land, approximately the size of Sweden or Morocco, having been acquired through transnational land deals for agricultural production (*1*). The unprecedented expansion of transnational land investments raised concerns about a neocolonial wave of land and water "grabbing" in the Global South (*2*, *3*). This has stimulated a heated debate in scholarly and policy arenas on the diverging trajectories of the contemporary global agrarian transition. We posit that impacts of the Russian invasion of Ukraine will fuel the resurgence of a new global rush for land, triggering transformations that will have cascading and long-lasting structural effects on multiple dimensions of rural development.

POST-2008 GLOBAL LAND RUSH

Large-scale land acquisitions (LSLAs) are defined as acquisitions of land of more than 200 ha, through concession, purchase, or lease, for agricultural production, forestry, energy needs, and other extractive and commercial purposes in low- and middle-income countries; they can be both transnational or domestic (*1*). Transnational LSLAs are generally commercial operations that target particularly extensive tracts of land, the median size being ~6500 ha (*1*). They tend to happen through governmental leases and concessions of exclusive land property and use rights to foreign investors, prevalently multinational companies with varying degrees of domestic actors' participation.

Promoters of LSLAs rhetorically describe the targeted land as marginal, unused, or

PHOTO: © ULET IFANSASTI/GREENPEACE

Rainforest in Central Kalimantan, an important orangutan habitat, is destroyed on this large-scale land concession exploited for oil palm export.

wasted. However, systematic literature and case study reviews have shown how LSLAs never happen on empty lands and are generally far from being consensual land sales. Rather, they tend to result in coercive, often violent, dynamics of dispossession of local inhabitants, traditional users, Indigenous people, small-scale farmers, and pastoralists (*4*).

Transnational LSLAs direct the contemporary agrarian transition toward intensive industrial agriculture, foreign control, and exclusive use of land, leading to dispossession, exclusion of traditional users, and concentration of land under the control of fewer holders. This specific model of production has been expanded in large parts of Africa, Asia, and Latin America and justified on the premise that it will lead to more efficient use of land and natural resources, yield improvements, and increased food production. LSLAs have been portrayed as bearers of more efficient agricultural production systems, reduced environmental impacts through intensification, and positive social impacts such as increased employment. Moreover, LSLAs are often promoted by governments in the Global South as ways to modernize their agricultural systems, improve access to markets and technology, and increase food production and security.

However, the narratives on which LSLAs are based and justified have been challenged, the positive impacts of LSLAs on food security have been questioned (*5*), and several ethical concerns have been raised (*6*). The literature reveals the structurally exploitative and socioenvironmentally unjust features of LSLAs (*4*, *7*). Their multidimensional detrimental impacts range from water appropriation (*3*), deforestation (*8*), increased fossil fuel consumption, food insecurity (*5*), and a variety of social and political effects such as reduced employment (*9*), dispossession of the commons, and the violent suppression of social mobilizations (*4*).

In the polarized scholarly and policy debate on the positive versus negative impacts of the post-2008 surge in transnational LSLAs, critical perspectives tend to define these acquisitions as "land grabs."

The International Land Coalition (ILC), a global alliance of civil society and intergovernmental organizations, defines land grabbing as LSLAs that violate human rights; are not transparent; do not seek free, prior, and informed consent; disregard social, economic, and environmental impacts; or are not based on democratic planning and participation.

However, scholars have pointed out the limits of technical or legalistic definitions and explained land grabbing in political terms as "[T]he capturing of control of relatively vast tracts of land and other natural resources through a variety of mechanisms and forms that involve large-scale capital that often shifts resource use orientation into extractive character…" [(*10*), page 609].

LSLAs and the associated global land rush can be seen as the symptom of a dominant agricultural model that is pushing large parts of the world from small-scale, often self-subsistence agricultural production, to commercial, commodified, and in many instances speculative systems of agricultural exploitation aiming to maximize shareholders' profits.

The primary purpose of LSLAs, especially when implemented by foreign companies, is to produce crops for export to satisfy global market demands and/or food security concerns of more powerful countries (*11*). This raises the ethical concern of transnational LSLAs being implemented in countries with high levels of malnourishment and water scarcity where much-needed local food demands are not met while the crops produced are being exported (*2*).

In addition to the appropriation of land, of its agricultural production, and of embedded water resources, transformations in land access rights and customs can lead to long-term and irreversible impacts, such as the risk that rural communities will not be able to return to their land or rebuild the socioeconomic relations that have historically underlain their use of commons, once they are forced to leave. There is evidence that resilient rural systems of common-pool resources traditionally governed by common property regimes (*12*), such as lands used by pastoralists and Indigenous groups, are preferential targets of LSLAs and increasingly vulnerable to the exogenous pressures of speculative agribusiness expansion (*4*).

IMPLICATIONS OF WAR IN UKRAINE

The extensive scientific literature on the post-2008 global land rush pointed out different drivers, remote and proximate causes, that underlined the surge in transnational LSLAs. This phenomenon has been explained by triggering factors such as crop failure, climate extremes, and increasing demands for agricultural products for food, feed, and biofuels, taking place in the context of rising national food security concerns and pressures for diversification in financial investments (*11*). While reviewing and disentangling these complex, multilevel, and interdependent causes is beyond the scope of our perspective, it is informative to note that there is a reemergence of similar challenges.

It has been pointed out that in recent years, the fast increase in transnational large-scale land investments and acquisitions slowed down (*7*); following the beginning of the war in Ukraine, signals and evidence for new emerging pressures on land are apparent, in particular in the Global South. Previous spikes in LSLAs were preceded by increasing prices of food, energy, and fertilizer associated with decreasing supply and/or rising demand. The onset of these trends has been a precursor of LSLAs (see the figure). Therefore,

[1]Department of Environmental Policy Analysis, Institute for Environmental Studies, IVM, Vrije Universiteit Amsterdam, Amsterdam, Netherlands. [2]Department of Civil and Environmental Engineering, Politecnico di Milano, Milano, Italy. [3]Department of Environmental Science, Policy and Management, University of California, Berkeley, CA, USA. Email: jampel.dellangelo@vu.nl; mariacristina.rulli@polimi.it; paolododo@berkeley.edu

although there are not expected to be major increases in the worldwide rates of LSLA 1 year after the beginning of the war, the ongoing escalating prices can be interpreted as an early warning sign of a forthcoming surge of LSLAs.

Social vulnerability, income inequality, and food insecurity are some of the most pressing contemporary global matters. Most of the key environmental and biophysical indicators for sustainable agricultural production have consistently worsened over the past decade. Geopolitical balances of power have shifted substantially since 2008. The world just experienced more than 2 years of a global pandemic, which led to major disruptions in trade and agricultural production. In this already deteriorated socioenvironmental global context, the war in Ukraine represents a shock with structural implications and cascading effects. Ukraine and Russia are central nodes in the global agricultural production web. Their exports of wheat and maize, two of the most important crops for global food security, have been interrupted.

In addition to the direct implications and destruction produced by the war, we argue that this conflict will lead to new controls on critical land resources. Production shocks, even of short duration, can have long-lasting structural implications for global development trajectories (*13*). This became clear during the 2008 global food crisis, when an 80% reduction in wheat exports from Ukraine induced food shortages in other regions of the world such as the Middle East, West Africa, and Pakistan.

Similarly, the war in Ukraine will have long-term effects that will expand well beyond the directly affected territories. Since the beginning of the war, decreasing crop supply, reduced fertilizer availability, increased oil costs, and rising production costs have affected global agricultural production. In this context, rising food prices and strategic concerns about food security will be followed by agribusiness development and financial investments to seek new opportunities for commercial agriculture. The long-term ramifications and escalating effects of the conflict will likely follow a logic of strong economic actors shifting costs onto more vulnerable people and/or the environment, while using the ongoing agricultural production and energy crisis as an opportunity to gain control over land and raw materials.

We anticipate that war in Ukraine will affect the global agrarian system through three main response mechanisms: expanding the domestic frontiers of agricultural cultivation over uncultivated land; intensifying agricultural production in previously acquired LSLAs; and provoking a new wave of LSLAs in the Global South.

The first mechanism relies on expanding cultivation into retired land under soil conservation programs and/or into protected areas. There are signals that different countries are resorting to this strategy to strengthen their domestic agricultural production. This happens because boosting production through intensification and crop yield increase is constrained by the ongoing fertilizer shortage. There is a strong risk that agriculture will be expanded over protected and conservation areas at the expense of natural ecosystems and biodiversity.

The second pathway will see large agribusiness companies exploit land that they have already acquired but not started to use for production. To date, about 44% of the agricultural land acquired by transnational corporations has yet to be put in production (*1*).

The third pathway will entail a new wave of LSLAs, both transnational and domestic, following patterns similar to what occurred in the post-2008 period and fundamentally exacerbating the global land rush. The new wave of large-scale land investments will take place in regions of the world where there is still potential for expanding the extent of cultivated land, to displace and replace smallholder farming with large-scale commercial agriculture. Similarly to the post-2008 period, countries in Sub-Saharan Africa, Southeast Asia, and South America will continue to be targeted.

Prime target countries for transnational land investments include those where governments report large fractions of their potential cropland areas as uncultivated—e.g., Myanmar, Cambodia, Ethiopia, Democratic Republic of Congo, Madagascar, Brazil, and Argentina. Historical evidence demonstrates that in moments of agricultural production crisis, financial speculation on agricultural commodities increases, and food prices soar even higher. Transnational large-scale agribusiness expansion responds to both national security concerns and financial interests. The 2008 food crisis showed that an increase in food export restrictions was followed by an increase in transnational land investments. In relation to the current rise in agricultural export restrictions, we expect the same pattern to emerge again.

Price trends as precursors of large-scale land acquisitions

Fluctuations in transnational large-scale land acquisitions (for agriculture, forestry, and forest concessions) and in the global prices of fertilizers, grains, and crude oil since 2000. Prices are expressed as monthly indices based on nominal US dollars, 2010 = 100. (See supplementary materials for details.)

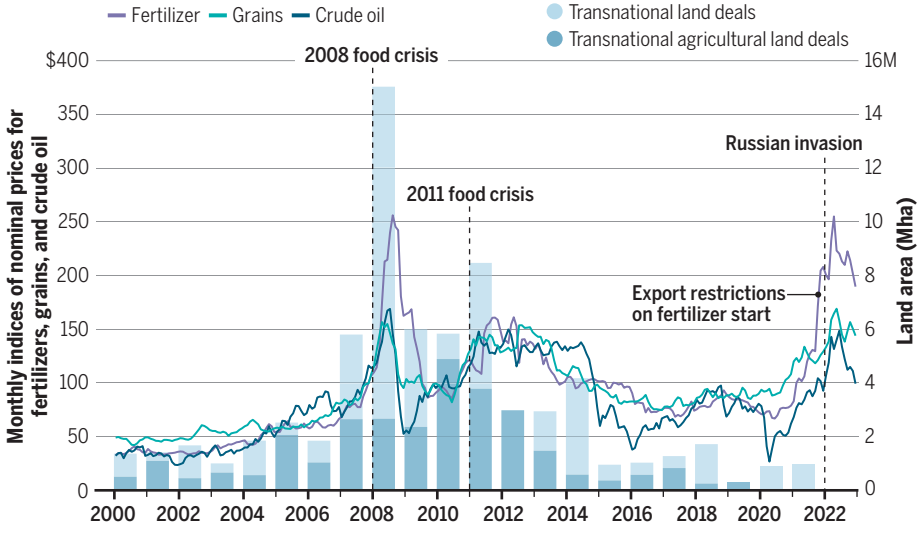

These three different pathways of agrarian transformation will produce substantial socioenvironmental impacts on rural systems in the Global South. The most pronounced long-term implications will arise from the new wave of transnational LSLAs. In general, this acceleration, both in terms of new investments and new exploitation of areas already under contract but not being used, will affect the Global South.

POLICY AND RESEARCH IMPLICATIONS

In addition to worries about the impacts produced by the war in the region, there are concerns about the cascading effects and irreversible long-term implications associated with the resurgence of a new rush for land in the Global South. The social repercussions of this agrarian transforma-

GRAPHIC: K. FRANKLIN/*SCIENCE*; (DATA) LAND MATRIX, WORLD BANK, AND U.S. BUREAU OF LABOR STATISTICS

tion will further exacerbate the negative impacts that have already been described in the post-2008 "land grabbing" literature. Dispossession, marginalization, violent repression, and loss of income and labor of local rural communities are among the most problematic aspects. The environmental impacts, in terms of water exploitation, deforestation, biodiversity loss, increased energy consumption, and CO_2 emissions, will likely increase, especially in new LSLAs. The scientific community plays a central role in continuing to expose the socioenvironmental trade-offs associated with the emergence of a new global land rush.

The connection between the current crises and the post-2008 phenomenon raises two fundamental governance questions. Were the governance and policy initiatives developed to address the post-2008 global land rush crisis effective? Will they be fit for governing the next wave of global land acquisitions triggered by the war?

In 2011, the Tirana Declaration of the ILC "Securing land access for the poor in times of intensified natural resource competition" provided a normative definition for land grabbing and urged national governments to implement more-stringent regulations. However, little progress has been made since then. Extensive policy and political economy analysis exposed the shortcomings and contradictions of land grabbing global governance (*14*)—for example, pointing to the ambiguous and often contradictory role that governmental and public organizations play in the global land rush (*10*).

Despite years of extensive discussions on land grabbing, the main regulations and safeguards related to agribusiness development in the Global South remain limited to aspirational recommendations such as the "Voluntary Guidelines on the Responsible Governance of Tenure of Land, Fisheries and Forests in the Context of National Food Security (VGGT)" or the "Responsible Investment in Agriculture and Food Systems (RAI)" principles. There is little evidence of these initiatives being successfully translated into effective and binding national policy frameworks and land reforms (*7, 10, 11*).

A new global rise in land grabbing reflects a complex, multiscale phenomenon, in response to which recommendations for discrete, narrow policy responses may seem a simplistic and reductionist panacea. That said, based on the lessons learnt from post-2008, it is increasingly apparent that the policies, institutional measures, and frameworks that are currently in place are ill-prepared for this new escalation.

There is a growing number of legislative initiatives that could play an important role in addressing land grabbing but are not doing so. Global food supply chains, deforestation, biodiversity, water, and climate change are all policy areas where attention to land grabbing should be "mainstreamed" and a coherent effort for policy integration and coordination should be supported. Similarly, main international trade agreements and investment treaties overlook land rights.

There is a strong need for policy development and the involvement of legal scholars. It is critical that the land tenure and human rights dimensions of land grabbing be addressed.

In this sense, a recent positive signal came in 2018 from the adoption by the United Nations General Assembly of the "Declaration on the Rights of Peasants and Other People Working in Rural Areas (UNDROP)," which represents a turning point in human rights law and provides an important legal and ethical foundation for the rights of peasants and a formal recognition of the "right to land." Social movements, civil society, and environmental organizations have been active in mobilizing and advocating for the right to land. But translating this putative right into legal frameworks and policies that determine control over land remains a challenge (*15*).

Moreover, during the last decade, the hydrological dimension of land grabbing, described as "global water grabbing" (*2, 3*), has attracted increasing scientific and societal attention. However, barely any concrete policy action has followed. This is an urgent, yet neglected, (water) governance priority that should be addressed at the national and international level.

When it comes to governance decisions related to LSLAs, a number of basic questions should be answered. Which values and priorities are being represented? Which private or public actors are involved? And what or whose interests do they represent (*10*)? Will human rights, the rights of nature, and the claims of unrepresented groups such as local communities, Indigenous groups, poor rural people, and future generations be sacrificed with the excuse of enhancing food security through increased agricultural production? In this moment, it is of utmost importance to prevent commercially speculative interests from exploiting narratives about food security and taking advantage of the emergency conditions the world is dealing with.

The shortcomings of global governance approaches to land grabbing demonstrate the limits of the neoliberal approach that liberalizes land markets while relegating social and environmental regulations to nonbinding measures.

We share the valid concerns about the actual feasibility of effective LSLAs regulations. The intrinsic problematic features of these acquisitions have been exposed by the scholarly community, and it is high time to support agricultural production alternatives that prioritize food sovereignty rather than commercial speculation (*6, 7, 11*).

The impacts of the Russian invasion of Ukraine go well beyond the territories involved in the conflict and raise concerns that require rethinking the current global food system. Serious consideration should be given to implementing alternatives that increase social inclusiveness and resilience in the face of agricultural production shocks, which will continue to happen in the future as a result of not only violent conflicts but also hydroclimatic change. It will be essential to empower local communities, support small-scale farmers, and develop effective and binding regulatory frameworks, institutions, and rigorous and strong land rights regimes. ■

REFERENCES AND NOTES

1. The Land Matrix [International Land Coalition (ILC), Centre de Coopération Internationale en Recherche Agronomique pour le Développement (CIRAD), Centre for Development and Environment (CDE), German Institute of Global and Area Studies (GIGA) and Deutsche Gesellschaft für Internationale Zusammenarbeit (GIZ)]; https://landmatrix.org/list/deals (accessed 20 January 2023).
2. J. Dell'Angelo, M. C. Rulli, P. D'Odorico, *Ecol. Econ.* **143**, 276 (2018).
3. M. C. Rulli, A. Saviori, P. D'Odorico, *Proc. Natl. Acad. Sci. U.S.A.* **110**, 892 (2013).
4. J. Dell'Angelo, P. D'odorico, M. C. Rulli, P. Marchand, *World Dev.* **92**, 1 (2017).
5. M. F. Müller *et al.*, *Proc. Natl. Acad. Sci. U.S.A.* **118**, e2020535118 (2021).
6. O. O. De Schutter, *J. Peasant Stud.* **38**, 249 (2011).
7. J. Lay *et al.*, "Taking stock of the global land rush: Few development benefits, many human and environmental risks," Analytical Report III (Centre for Development and Environment, University of Bern; Centre de coopération internationale en recherche agronomique pour le développement; German Institute for Global and Area Studies; Univ. of Pretoria; Bern Open Publishing; 2021).
8. K. F. Davis *et al.*, *Nat. Geosci.* **13**, 482 (2020).
9. K. Nolte, M. Ostermeier, *World Dev.* **98**, 430 (2017).
10. S. M. Borras Jr. *et al.*, *Globalizations* **17**, 608 (2020).
11. L. Cotula, "The international political economy of the global land rush: A critical appraisal of trends, scale, geography and drivers" in *The New Enclosures: Critical Perspectives on Corporate Land Deals* (Routledge, 2013), pp. 43–74.
12. T. Dietz, E. Ostrom, P. C. Stern, *Science* **302**, 1907 (2003).
13. D. Harvey, *A Brief History of Neoliberalism* (Oxford Univ. Press, 2007).
14. M. E. Margulis, N. McKeon, S. M. Borras Jr., *Globalizations* **10**, 1 (2013).
15. L. Cotula, "The right to land" in *The United Nations' Declaration on Peasants' Rights*, M. Albanese, A. Bessa, M. Brunori, P. F. Giuggioli, Eds. (Routledge, 2022).

ACKNOWLEDGMENTS

The authors received support from the European Union's Horizon 2020 research and innovation programme under the Marie Skłodowska-Curie Innovative Training Network NEWAVE, grant agreement no. 861509. We thank L. Cotula, A. Scheidel, A. Dell'Angelo, and anonymous reviewers for their valuable feedback.

SUPPLEMENTARY MATERIALS

science.org/doi/10.1126/science.adf9351

10.1126/science.adf9351

BOOKS *et al.*

Demonstrators gather at a women's rights march in Rome, Italy, on 26 November 2022.

PHOTO: MATTEO PLACUCCI/NURPHOTO VIA AP

ANTHROPOLOGY

Equality as a work in progress

History shows that neither patriarchy nor parity is inevitable

By **Sarah S. Richardson**

The future is female! Feminists are rallying in the streets in Iran. Thirty-one Nobel Prizes have been awarded to women in the past 20 years, more than in the previous century combined. The gender pay gap is closing. Or is it just the opposite? The success of right-wing movements around the world—from the defeat of *Roe* v. *Wade* in the United States to Vladimir Putin's chest-bearing gender traditionalism in Russia—suggests that the patriarchy is surging. And an old ogre is back: Pointing to plateauing progress toward gender parity in fields such as science and engineering, some claim renewed evidence that gender inequality is a biological inevitability that no social reforms can overcome.

In *The Patriarchs*, Angela Saini steps into this tumult, turning to archaeology, anthropology, and ancient history to warn readers that neither gender equality nor patriarchy is preordained. Touring the nonlinear, heterogeneous history of gender equality across the globe, Saini demonstrates that for the gender-fluid Neolithics and the gender-segregated ancient Athenians, as for today's post-#MeToo feminists and their detractors, patriarchy was and is neither inescapable nor permanently vanquished.

Although the book's title invokes the saturated term "patriarchy," this is no *Chalice and the Blade*–style revival of a vision of goddess-worshipping past utopias (*1*). Such feminist fantasies of ancient matriarchies shunted aside by violent male patriarchs, Saini argues, were as inflected with their authors' hopes for a feminist future as unrepentant biological determinists of the same era were committed to countering those hopes.

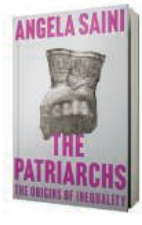

The Patriarchs
Angela Saini
Beacon Press, 2023.
256 pp.

The Patriarchs catches readers up to date on the scholarship, which in recent decades has considerably complexified our understanding of ancient and modern gender systems. According to Saini, this scholarship shows that human communities with high levels of gender equality have long coexisted with societies characterized by deeply patriarchal gender divisions and misogynist gender ideologies. Furthermore, within these diverse social systems, women and men experienced varying degrees of power, autonomy, and economic freedom.

Saini spotlights debates over the reigning gender system in the ancient city of Çatalhöyük, held up in the 1970s by archaeologists such as Marija Gimbutas as a fluid, gender-equal society. While the notion that Çatalhöyük was a goddess-worshipping matriarchy is now less certain, analyses of grave sites, nutritional status, and other markers of social roles do confirm remarkable gender similarities among its residents. Gimbutas hypothesized, much to the ridicule of her contemporaries, that a major shift in gender relations at Çatalhöyük occurred after the arrival of outsiders bringing a more patriarchal social structure. The broad outlines of this hypothesis have been confirmed with genetic evidence.

Although some archaeologists still tie themselves in knots trying to explain away findings such as evidence of female big-game hunters, decorated female warriors, or individuals with a mix of both masculine- and feminine-typical signifiers, today, more often than not, such findings are received with curiosity and even celebration. The variety of gender systems and of the experiences of individual men, women, and gender-diverse people in ancient history has been revealed in greater depth and detail by these archaeologists and ancient historians.

It is easy to think of the progress of the past half-century in linear terms, as a march toward gender equality and away from a grim patriarchal past. Saini dismantles this thinking. She points out, for example, that Western colonialism contributed to the destruction of diverse gender systems, which often granted greater freedom for women. As has been well documented in regions of the African continent, Native America, the Middle East, and South Asia, colonialism propagated Western ideologies of a gender binary. Enshrined in law and enforced by the state, Western colonialism displaced more gender-fluid and often matriarchal systems of relations. It also provoked traditionalist anti-colonial backlash, sometimes bringing stricter forms of gender segregation and oppression than had historically been the case.

Commentators frequently refer to the scourges of sex trafficking, forced marriage, and male domestic violence as relics of patriarchy and portray the oppressive regimes of the Taliban or Boko Haram as regressive traditionalism. Men's rights activists decry a crisis of masculinity, warning of the "decline of men." The feminist metaphor of "breaking the glass ceiling" figures women's upward mobility as a one-and-done event, the shards never to be reassembled.

But gender equality and inequality are constantly reinvented by humans. The interpretations we layer onto human history reflect our own hopes and dreams, situated interests, and assumptions and biases. The lesson? Neither biology nor history constrains the future of gender. It is up to us to envision, build, and sustain a world that enables the full flourishing of all. ■

The reviewer is at the Department of the History of Science, Harvard University, Cambridge, MA 02138, USA. Email: srichard@fas.harvard.edu

REFERENCES AND NOTES

1. R. Eisler, *The Chalice and the Blade: Our History, Our Future* (HarperCollins, 1987).

10.1126/science.adg2268

SCIENCE LIVES

The exceptional women of MIT

A 20th-century battle for equal treatment of female scientists resonates today

The Exceptions: Nancy Hopkins, MIT, and the Fight for Women in Science
Kate Zernike
Scribner, 2023. 432 pp.

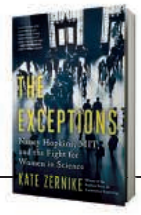

By **Meredith Wadman**

Nancy Hopkins was a college senior working in James Watson's lab at Harvard University when a visiting scientist, Francis Crick, introduced himself by grabbing her breasts. The 20-year-old Hopkins shrugged off the clumsy assault: In 1964, Hopkins thought that if she simply got on with doing outstanding science, she would earn the respect she deserved. Her slow and painful disillusionment during the following three decades unspools in distressing detail in the engrossing book *The Exceptions* by *New York Times* reporter Kate Zernike, with whom Hopkins shared her copious diaries, records, and correspondence.

The book's title derives from the thinking then current: that women in science were exceptional because it was unusual for a woman to be so bright. Zernike reclaims the term, making it clear that they were exceptional because of all they accomplished despite the formidable obstacles they confronted.

The put-downs, freeze-outs, and blatant disrespect from Hopkins's male colleagues escalated as she ascended the academic ranks at the Massachusetts Institute of Technology (MIT), where she was hired as an assistant professor in 1973 and is today an emeritus biologist. And yet the uber-tenacious Hopkins persisted, pioneering insertional mutagenesis in vertebrates by using zebrafish to identify hundreds of genes essential to embryonic development. In the process, she won herself election to the National Academy of Medicine and the National Academy of Sciences.

Almost all of Hopkins's male colleagues were either oblivious to her treatment as a second-class citizen or active participants in it. Immunologist Susumu Tonegawa relentlessly encroached on lab space that he and Hopkins were supposed to share. Molecular biologist David Baltimore pushed her top-ranked name down on a list of candidates the department was nominating for tenure. And department chair Phillip Sharp, a friend of Hopkins, acquiesced to the demands of geneticist Eric Lander, removing her from teaching a high-profile undergraduate biology course that she had developed and co-taught with Lander. Sharp swapped in molecular biologist Harvey Lodish in Hopkins's place. (Lodish and Lander had plans to monetize the course by writing a textbook.)

In the book's acknowledgments, Zernike thanks all of the previously named men for their interviews—except Tonegawa, who refused an interview request. But it is not clear whether or how much they pushed back on the above accounts, which are either not footnoted or are sourced to primary documents provided by Hopkins.

Zernike peoples her tale with similar stories from a supporting cast of outstanding female MIT scientists including cell biologist Mary-Lou Pardue and solid-state physicist Mildred Dresselhaus. Sixteen such women banded together in 1993 to protest MIT's treatment of its women science faculty.

With support from the dean of science and MIT's president, both men, Hopkins then led a committee that gathered data on metrics including women's salaries, lab space, teaching assignments, and grants relative to men. The resulting report found that the MIT faculty women often received less of everything compared with their equally accomplished male colleagues and that, in 1994, the percentage of women science faculty at MIT—8%—had not changed appreciably for 20 years (*1*).

By 2003, 4 years after the report was made public, the number of women in the MIT engineering faculty had nearly doubled; math, which had had not a single woman, had four tenured women; and female science faculty numbered 34, up from 22. The issue was also catapulted onto the agendas of major research universities across the country.

Zernike adds gripping daily life details that make Hopkins's story come deeply alive. The reader is with Hopkins as she sneaks into male colleagues' labs at night with her tape measure after the cancer center director baldly insists that she is not getting short shrift in lab space. One feels her chagrin when a woman on the cleaning staff, pointing to a common space that Tonegawa has filled with his glassware, asks: "Nancy, why do the others get everything and you get so little?" The cumulative weight of Hopkins's and her colleagues' experiences could make for disheartening reading, yet one puts down the book inspired by the women's grit, tenacity, and brilliance.

In 1999, Nancy Hopkins (center) and colleagues revealed that senior women faculty at MIT were marginalized.

PHOTO: ©1999 RICK FRIEDMAN

Women scientists today need those qualities just as much: Last month, I spoke with Hopkins for a *Science* news article describing dramatic laboratory and storage space discrimination faced by women scientists at the Scripps Institution of Oceanography, documented in a new report (*2*). "I looked at this thing and I thought, 'Oh my God, 30 years; I was doing this 30 years ago,'" she lamented. Being exceptional, it seems, remains a requirement for women in science. ■

The reviewer is a staff writer at *Science* magazine and the author of *The Vaccine Race: Science, Politics, and the Human Costs of Defeating Disease* (Viking, 2017).
Email: mwadman@aaas.org

REFERENCES AND NOTES

1. "A Study on the Status of Women Faculty in Science at MIT," The MIT Faculty Newsletter, vol. 11, no. 4 (1999); http://web.mit.edu/fnl/women/women.pdf.
2. M. Wadman, *Science* **379**, 317 (2023).

10.1126/science.adf4923

Better connected Asian elephant habitats would reduce the likelihood of harmful interactions between humans and wildlife.

PHOTO: AHIMSA CAMPOS-ARCEIZ

Edited by **Jennifer Sills**

Connect elephant habitats in Asia

The Aichi Biodiversity Target 11 called for 17% of terrestrial land and inland waters to be designated as connected protected areas by 2020. Some countries in Asia have made progress toward this goal (*1*). However, because the established protected areas are not well connected (*2*), the Endangered Asian elephant (*Elephas maximus L.*) remains at risk (*3*). To protect Asian elephants, South and Southeast Asian countries must protect and restore ecological connectivity between elephant habitats and accelerate transboundary conservation networks through international cooperation.

A keystone species with wide-reaching influence on ecosystem functions (*4*), Asian elephants reside in fragmented pockets with low levels of gene flow between them (*5*, *6*). Transboundary movement is increasingly difficult (*7*), and fences around elephant protected areas further impede gene flow within and outside reserves (*6*). Regionally, deforestation, linear infrastructure, and poor connectivity near protected areas create conditions that elevate the risk of negative interactions between humans and elephants (*8*).

The Kunming-Montreal Global Biodiversity Framework calls for protecting the "integrity, connectivity, and resilience" of 30% of land and inland waters by 2030 (*9*). The Convention on the Conservation of Migratory Species includes Asian elephants in Appendix 1, which promotes transboundary cooperation and protection of long-range movement (*7*). Protecting, restoring, and connecting elephant habitats locally, regionally, and continentally would facilitate elephant movement, increase the species' genetic diversity, and help Asian countries meet the 30% conservation target (*9*). Better habitat connectivity would also protect other species and preserve ecosystem functions and services under conditions of anthropogenic global warming. Protected natural habitats would benefit humans as well, given evidence that leaving 40% of land to nature would allow sustainable agricultural productivity (*10*).

Priya Davidar[1]*, Reeta Sharma[2], Shermin de Silva[3,4], Ahimsa Campos-Arceiz[5], Benoit Goossens[6,7], Jean-Philippe Puyravaud[1], Bilal Habib[2], Rahul De[2], Ee Phin Wong[8], Dinesh Neupane[5], Nurzhafarina Binti Othman[9], S. P. Goyal[2]

[1]Sigur Nature Trust, Mavinhalla PO, Nilgiris, TN 643223, India. [2]Wildlife Institute of India, Chandrabani, Dehradun, Uttarakhand 248001, India. [3]Department of Ecology, Behavior, and Evolution, University of California San Diego, La Jolla, CA, USA. [4]Trunks & Leaves Inc., Pittsfield, MA, USA. [5]Southeast Asia Biodiversity Research Institute, Chinese Academy of Sciences, and Center for Integrative Conservation, Xishuangbanna Tropical Botanical Garden, Chinese Academy of Sciences, Mengla, Yunnan 666303, China. [6]Danau Girang Field Centre, c/o Sabah Wildlife Department, Wisma Muis, Sabah, Malaysia. [7]Organisms and Environment Division, School of Biosciences, Cardiff University, Cardiff, UK. [8]Faculty of Science & Engineering, School of Environmental and Geographical Sciences, University of Nottingham Malaysia, 43500 Selangor, Malaysia. [9]Institute for Tropical Biology and Conservation, University Malaysia Sabah, 88400 Kota Kinabalu, Sabah, Malaysia.
*Corresponding author. Email: pdavidar@gmail.com

REFERENCES AND NOTES

1. Convention on Biological Diversity, "Aichi Target 11" (United Nations Environment Programme, Nairobi, Kenya, 2020); https://www.cbd.int/aichi-targets/target/11.
2. A. Brennan *et al.*, *Science* **376**, 1101 (2022).
3. C. Williams *et al.*, *Elephas maximus* (The IUCN Red List of Threatened Species, e.T7140A45818198, 2020).
4. A. Campos-Arceiz, S. Blake, *Acta Oecologica* **37**, 542 (2011).
5. R. De *et al.*, *Glob. Ecol. Conserv.* **32**, e01888 (2021).
6. J.-P. Puyravaud *et al.*, *Conservation* **2**, 709 (2022).
7. Convention on the Conservation of Migratory Species of Wild Animals Secretariat, "Convention on the Conservation of Migratory Species of Wild Animals (CMS)," Appendices 1 and II of CMS (United Nations Environment Programme, Bonn, Germany, 2020); https://www.cms.int/sites/default/files/basic_page_documents/appendices_cop13_e_0.pdf.
8. D. Vasudev, R. J. Fletcher, N. Srinivas, A. J. Marx, V. R. Goswami, *Proc. Natl. Acad. Sci. U.S.A.* **120**, e2211482119 (2023).
9. "Kunming-Montreal Global biodiversity framework," The Conference of the Parties to the Convention on Biological Diversity (Agenda Item 9A, United Nations Environment Programme, Montreal, Canada, 2022), p. 8; https://www.cbd.int/doc/c/e6d3/cd1d/daf663719a03902a9b116c34/cop-15-l-25-en.pdf.
10. K. Henderson, M. Loreau, *PLOS Comput. Biol.* **14**, e1006389 (2018).

10.1126/science.adg7470

Entanglement in fishing equipment threatens the North Atlantic right whale (*Eubalaena glacialis*) population.

US budget riders compromise conservation

In the story "Research gets a boost in final 2023 spending agreement" (23 December 2022, p. 1263), the *Science* News Staff describe the US omnibus budget bill's science investments, but they do not include the details of a last-minute rider that affects the Critically Endangered North Atlantic right whale (NARW) (*Eubalaena glacialis*) (*1*, *2*). Budget riders are additions to US federal budget bills. Because the bills are required to fund the US government, their eventual passage is guaranteed. If special interests can convince representatives to include a rider, they can bypass a full debate on policies that conflict with scientific evidence and established law. The use of appropriations riders as shortcuts to pass policies that circumvent existing environmental laws should not be tolerated.

With fewer than 350 individuals remaining, and their numbers in decline, NARWs are at risk of extinction (*3*). Entanglement in fishing gear is one of the primary drivers of their morbidity and mortality (*4*). In addition, because entanglement stunts the growth of individual NARWs and smaller females have fewer calves, entanglements reduce the species' calving rate for decades (*5*). Despite the threats posed by entanglements, the recent rider allows the government more time to finalize regulations that require fisheries to mitigate them (*2*).

The rider was introduced after a series of court cases established that according to US law, fisheries must consider the health of the NARW population. In July 2022, after the US National Marine Fisheries Service (NMFS) declared that fisheries affect but present "no jeopardy" to NARW's continued existence, a federal judge ruled that the agency had violated both the Endangered Species Act of 1973 (ESA) and Marine Mammal Protection Act of 1972 (*6*). The judge also ruled that NMFS's proposed management measures to mitigate fisheries' impacts on NARWs were insufficient, also in violation of the Marine Mammal Protection Act. In September 2022, groups associated with the fishing industry attempted to overturn the NMFS opinion of "no jeopardy," on the grounds that the decision's acknowledgment that fisheries affect NARWs overstated the risk. A judge rejected the proposed change given the evidence that the report understated rather than overstated the danger to NARWs (*7*). In November 2022, the court decided that new rules to reduce fisheries' impacts on NARWs should be in place by December 2024 (*8*). Yet the following month, the budget rider negated the court's ruling by extending the deadline to 2028.

Budget riders have been used to sidestep the ESA in the past. Previous riders, affecting gray wolves (*Canis lupus*) (*9*) and greater sage-grouse (*Centrocercus urophasianus*) (*10*), did not create the near-term risk of a species' extinction. However, they established a precedent in Congress for using riders to circumvent the ESA. Appropriations riders should not overrule established environmental legislation and decision-making that is based on science-based, peer-reviewed, wildlife conservation strategies.

Peter Corkeron[1]*, Kyla Bennett[2], Michael J. Moore[3]
[1]Falmouth, MA, USA. [2]Public Employees for Environmental Responsibility, Silver Spring, MD, USA. [3]Biology Department, Woods Hole Oceanographic Institution, Woods Hole, MA, USA.
*Corresponding author.
Email: peter.corkeron@icloud.com

The views and opinions expressed are those of the authors and do not necessarily reflect the views or positions of any entities they represent.

REFERENCES AND NOTES

1. J. G. Cooke, "*Eubalaena glacialis* (errata version published in 2020)" (The IUCN Red List of Threatened Species, 2020); https://www.iucnredlist.org/species/41712/178589687.
2. Consolidated Appropriations Act, 2023 (2022); https://www.congress.gov/bill/117th-congress/house-bill/2617/.
3. North Atlantic Right Whale Consortium, "North Atlantic right whales' downward trend continues as updated population numbers released," New England Aquarium (2022).
4. M. J. Moore *et al.*, *Dis. Aquat. Org.* **143**, 205 (2021).
5. M. J. Moore, *ICES J. Mar. Sci.* 10.1093/icesjms/fsac239 (2023).
6. J. Boasberg, "Memorandum Opinion on Civil Action No. 18-112" (2022); https://www.biologicaldiversity.org/species/mammals/North_Atlantic_right_whale/pdfs/218-2022-07-08-Decision-on-Summ-Judg-NARW-2-0.pdf.
7. J. Boasberg, "Memorandum Opinion on Civil Action No. 21-2509" (2022); https://www.biologicaldiversity.org/species/mammals/North_Atlantic_right_whale/pdfs/76-2022-09-08-MLA-SJ-Decision-North-Atlantic-Right-Whale.pdf.
8. C. Chase, "Judge grants US lobster fishery two-year reprieve from right whale-related restrictions," *Seafood Source* (2022); https://www.seafoodsource.com/news/supply-trade/us-lobster-fishery-gets-reprieve-from-court-in-ongoing-right-whale-lawsuit.
9. E. Byron, "Budget bill rider will delist wolves," *Helena Independent Record* (2011).
10. Consolidated Appropriations Act, 2018 (2018); https://www.congress.gov/bill/115th-congress/house-bill/1625/.

10.1126/science.adg6235

Federal journals need transparency policies

The US White House Office of Science and Technology Policy (OSTP) recently advised federal departments and agencies to promote free, immediate access to data that supports publications of federally funded research (*1*). However, the guidance did not address federal science journals' policies regarding access to data and computer code used in peer-reviewed articles. Federal journals should adopt the free, immediate data access policy of OSTP as well as the code access policies of top independent journals.

Three influential federally controlled health journals lack general policies regarding public access to data and code. *Emerging Infectious Diseases* (*2*) has no data access policy, except for requirements for public access to DNA data. *Environmental Health Perspectives* (*3*) also has no data access policy, except that genomic data "should be" posted. *Mortality and Morbidity Weekly Report* (*4*) has no policy on data access. In addition to falling short of OSTP's data access guidance, these journals do not meet the most modest data access policy identified by Oxford University Press (OUP), which encourages the release of all data where ethically possible (*5*). Finally, none of these journals requires or encourages public access to code.

PHOTO: FLORIDA FISH AND WILDLIFE CONSERVATION COMMISSION; TAKEN UNDER NOAA PERMIT 20556-01

Studies in various fields have long found that access to both data and code is essential for independent reproducibility of published research (*6*). Accordingly, many top journals require public access to both data and code as a condition of publication. Such journals include those associated with *Science* (*7*), *Nature* (*8*), the American Economic Association (*9*), and the *Proceedings of the National Academy of Sciences* (*10*). The federal *Journal of Fish and Wildlife Management* requires public disclosure of data (*11*), demonstrating that federal journals can adopt such policies. All federally controlled peer-reviewed journals should adopt strong transparency policies such as those used by top journals.

Randall Lutter
Manhattan Institute for Policy Research, New York, NY 10017, USA.
Email: rlutter@manhattan-institute.org

REFERENCES AND NOTES

1. US Office of Science and Technology Policy, "Ensuring free, immediate, and equitable access to federally funded research" (2022).
2. Centers for Disease Control and Prevention (CDC), "Author Resource Center," *Emerging Infectious Diseases* (2023); https://wwwnc.cdc.gov/eid/pdfs/Checklist.pdf.
3. National Institute of Environmental Health Sciences, "Author hub," *Environmental Health Perspectives* (2023); https://ehp.niehs.nih.gov/about-ehp/journal-information/policies.
4. CDC, "For authors," *Morbidity and Mortality Weekly Report* (2023); https://www.cdc.gov/mmwr/contributors/index.html.
5. Oxford Academic Press, "Research data" (2022).
6. National Academies of Sciences, Engineering, and Medicine, "Reproducibility and replicability in science" (2019).
7. "*Science* journals: Editorial policies," *Science* (2023).
8. "Nature research: Data availability statements and data citations policy: Guidance for authors," *Nature* (2023).
9. "Data and code availability policy," American Economic Association (2023).
10. "Editorial and journal policies: Editorial policies, materials and data availability," *Proceedings of the National Academies of Science USA* (2023).
11. U.S. Fish and Wildlife Service, "guide for authors, data archiving," *Journal of Fish and Wildlife Management* (2023).

10.1126/science.adg8152

TECHNICAL COMMENT ABSTRACTS

Comment on "Soybean photosynthesis and crop yield are improved by accelerating recovery from photoprotection"

Thomas Sinclair, James Specht, Kenneth Cassman, Larry Purcell, Thomas Rufty

De Souza *et al.* (Research Articles, 19 August 2022, eadc9831) recently claimed major soybean yield increases resulting from transformation of the nonphotochemical quenching mechanism of photosynthesis. However, there is little basis for the premise that such a transformation would result in yield increase. The field experiment was flawed and does not provide evidence for increases in crop yield.

Full text: dx.doi.org/10.1126/science.ade8506

Response to Comment on "Soybean photosynthesis and crop yield are improved by accelerating recovery from photoprotection"

Amanda P. De Souza *et al.*

We recently demonstrated that accelerating the relaxation of nonphotochemical quenching leads to higher soybean photosynthetic efficiency and yield. In response, Sinclair *et al*. assert that improved photosynthesis cannot improve crop yields and that there is only one valid experimental design for proving a genetic improvement in yield. We explain here why neither assertion is valid.

Full text: dx.doi.org/10.1126/science.adf2189

Share **Your Robotics Research** with the **World**.

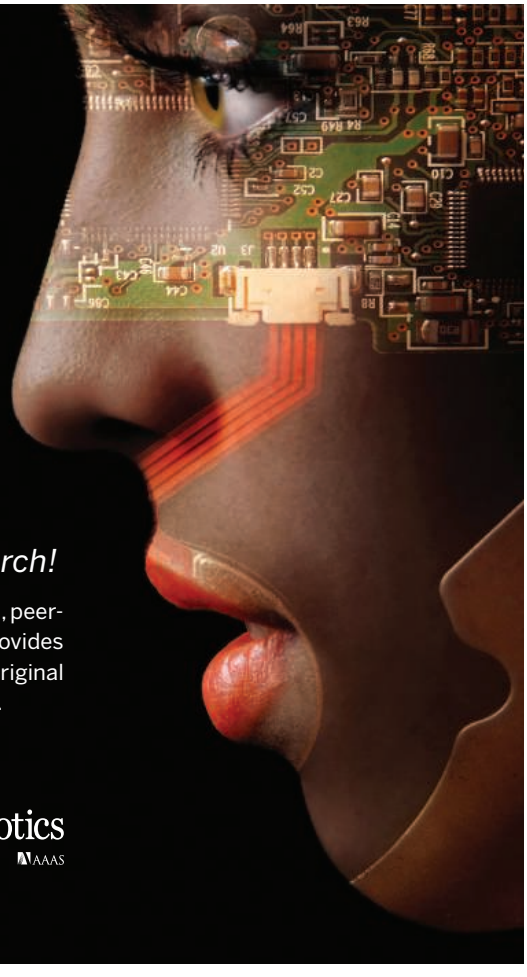

Shaping the future of robotics with high impact research!

As a multidisciplinary online-only journal, *Science Robotics* publishes original, peer-reviewed, research articles that advance the field of robotics. The journal provides a central forum for communication of new ideas, general principles, and original developments in research and applications of robotics for all environments.

Submit your research today. Learn more at: **science.org/journal/scirobotics**

Twitter: @SciRobotics
Facebook: @ScienceRobotics

Science Robotics
AAAS

RESEARCH

IN *SCIENCE* JOURNALS

Edited by
Michael Funk

PHOTO: WIM VAN EGMOND/SCIENCE SOURCE

PRIMARY PRODUCTIVITY

Stress effects

The Southern Ocean is a major sink for atmospheric carbon dioxide, and this is mediated by net primary productivity there. Primary productivity in turn is affected by seasonal changes in light and iron availability. Ryan-Keogh *et al*. present a 25-year-long record of irradiance-normalized nonphotochemical quenching by Southern Ocean phytoplankton, which they used to infer iron stress. They found that iron stress increased between 1996 and 2021, and that net primary production decreased as a result. These results are evidence of important ongoing changes to the Southern Ocean carbon cycle that have implications for climate change. —HJS *Science*, abl5237, this issue p. 834

Microscopy image of *Chaetoceros debilis*, a marine diatom that contributes to the primary productivity of nutrient-rich waters in the Southern Ocean.

NEUROSCIENCE

Encoding lasting motivations in the brain

After mating successfully, male and female mice typically lose interest in sexual behavior, and then interest gradually returns over several days to weeks. Little is known about how such experience-dependent changes are represented in neural circuits. Zhou *et al*. found that estrogen receptor 2–expressing neurons in a brain region called the bed nucleus of the stria terminalis encoded the experience of ejaculation. In both sexes, activation of these neurons suppressed subsequent appetite for sexual activity, whereas inactivation of the neurons restored this motivation. Hyperexcitability of these neurons closely corresponded to a change in ionic conductance mediated by HCN (hyperpolarization-activated cyclic nucleotide–gated) channels, which are highly expressed in males. —PRS

Science, abl4038, this issue p. 820

B CELLS

An IL-21 reservoir for B cells

B cells undergo antigen-driven selection in germinal centers (GCs), enabling some of these cells to exit and differentiate into antibody-secreting cells (ASCs). Positive selection of GC B cells depends on the successful integration of signals from the B cell receptor, as well as CD40 ligand and interleukin-21 (IL-21) signals originating from follicular helper T cells. Chen *et al*. discovered that IL-21 bioavailability is dynamically regulated by heparan sulfate on B cells. Enzymatic N-sulfation of heparan sulfate is suppressed in GC B cells to ensure selection stringency, but is subsequently up-regulated in ASC precursors, establishing a reservoir of bound IL-21 that increases IL-21 signaling and ASC differentiation. These findings provide fresh insights into how IL-21 availability and signal strength influence the fate of GC B cells. —IRW

Sci. Immunol. **8**, eadd1728 (2023).

HIV

Realizing TACK for HIV-1

Antiretroviral drugs are essential components of the HIV-1 treatment toolbox. Although these drugs are effective at controlling viral load in individuals living with HIV-1, they do not represent a curative strategy. Interestingly, some non-nucleoside reverse transcriptase inhibitors also kill HIV-1–infected cells, but they require a high drug concentration to do so. With this secondary activity in mind, Balibar *et al*. discovered reverse transcriptase inhibitors that in addition to retaining conventional antiviral function, also promote selective cytotoxicity of HIV-1–infected cells at clinically meaningful concentrations. These targeted activator of cell kill (TACK) molecules were able to kill HIV-1–infected $CD4^+$ T cells isolated from people with HIV-1, supporting further clinical development of this strategy. —CSM

Sci. Transl. Med. **15**, eabn2038 (2023).

PALEOECOLOGY

A major marine shift

We know that the end-Cretaceous extinction event drove ecological change and species turnover in terrestrial systems, but we know less about how this event may have altered marine systems. Guinot and Condamine looked at a large database of elasmobranch (sharks, skates, and rays) fossils to test for changes that may have occurred in marine ecosystems at the end

of the Cretaceous. They found substantial loss of species, especially those that fed on shelled prey and those on the ocean bottom. Pelagic species and those at higher latitudes had higher survival, showing that differential species survival shaped marine systems across the Cretaceous–Paleogene boundary. —SNV

Science, abn2080, this issue p. 802

PALEONTOLOGY

How to get big

Over evolutionary history, many different taxa have evolved very large body sizes. The general consensus has been that an animal grows to a large size based on an increase in growth rate. However, very few studies have explored this question across many species within a comparative phylogenetic framework. D'Emic *et al*. looked across a large dataset of non-avialan theropod dinosaurs, which had an array of body sizes. They found evidence supporting changes in growth rate contributing to body size change, but also found that changes in the duration of growth played a large role. —SNV

Science, adc8714, this issue p. 811

PLASTIC UPCYCLING

Plastics to fuels in ionic liquids

Polyethylene and polypropylene have many useful properties, but their resistance to chemical degradation makes processing their waste a challenge. In particular, heating to high temperatures to crack the underlying carbon–carbon bonds can be energy intensive. Zhang *et al*. report that an aluminum chloride–based ionic liquid medium can promote the breakdown of these polyolefin plastics into liquid fuels at temperatures below 100°C. The method compensates for the energy directed toward bond scission with energy released from alkylation reactions among the resulting intermediates. —JSY

Science, ade7485, this issue p. 807

STRATOSPHERE

Fired up

Large wildfires can generate pyrocumulonimbus clouds that transport smoke into the stratosphere and have major impacts on the stratospheric aerosol budget and climate. Katich *et al*. analyzed 13 years of airborne observations to determine the chemical and physical compositions of pyrocumulonimbus smoke and to quantify its effects on stratospheric aerosols. These clouds are responsible for as much as 25% of the black carbon and organic aerosols now in the lower stratosphere and may become an even more important influence on future climate as the frequency and severity of extreme fires increase. —HJS

Science, add3101, this issue p. 815

A new solvent-catalyst system enables conversion of waste hydrocarbon plastic, pictured above, into components of liquid fuel.

IN OTHER JOURNALS

Edited by **Caroline Ash** *and* **Jesse Smith**

ATHEROSCLEROSIS

Autoimmune features of atherosclerosis

Atherosclerosis, the formation of plaque in the arteries, is a key pathology contributing to myocardial infarction, stroke, and other disorders causing large numbers of deaths in humans. Atherosclerosis had been traditionally viewed as a lipid disorder, and inflammation is known to play a major role as well, but now Depuydt *et al*. have identified a potential autoimmune aspect to it. Through detailed analysis of T cells and their interactions with macrophages in the atherosclerotic plaques and blood of human patients, the authors identified T cells with an autoimmune phenotype, which may indicate additional directions for future treatment approaches. —YN

Nat. Cardiovasc. Res. 10.1038/s44161-022-00208-4 (2023).

SCIENCE EDUCATION

Rubric-based holistic review

To increase the diversity of admitted students, graduate programs need to evaluate the structures in place to evaluate potential applicants. Young *et al.* implemented a rubric-based holistic review process for all applicants to a graduate physics program, assessing 18 metrics including grade point average, test scores, research experience, noncognitive competencies, and fit with the program. Over a 3-year evaluation period, faculty ratings of applicant's grades, research experience, and noncognitive competencies did not differ based on the applicant's sex or undergraduate background. Differences that were observed reflected known systematic inequities such as scoring lower on the GRE and women performing more volunteer work. Collectively,

PHOTOS (LEFT TO RIGHT): RENÉ NOTENBOMER/ALAMY STOCK PHOTO; THIERRY MONASSE/GETTY IMAGES

ALSO IN *SCIENCE* JOURNALS

Edited by **Michael Funk**

CONSERVATION BIOLOGY

Managing species on the brink

As we face a global extinction crisis, international commitments promise to prevent extinctions of threatened species. However, some of the most threatened species are often overlooked: those that now exist only in zoos, aquaria, gardens, or seed banks, which are classified as "extinct in the wild." Smith *et al*. synthesized data on extinct-in-the-wild plant and animal species to assess their state of risk and what actions are being taken to recover them. Most ex situ populations are small (less than 1000 individuals) and were founded by few individuals, likely with low genetic diversity. Reestablishment of species in the wild has been successful in some cases, but it has only been attempted for about one-fourth of current extinct-in-the-wild species. —BEL

Science, add2889, this issue p. 794

BIOELECTRONICS

A recipe for in situ bioelectronic materials

There are challenges in making materials that are soft enough to be interfaced with living tissue but firm enough to be inserted into the body. Strakosas *et al*. bypassed this challenge by developing a route to the polymer in vivo (see the Perspective by Inal). They introduced a complex precursor system including an oxidase to generate hydrogen peroxide in situ, a peroxidase to catalyze oxidative polymerization, a water-soluble conjugated monomer, a polyelectrolyte with counterions for covalent cross linking, and a surfactant for stabilization. With this cocktail, the authors were able to induce polymerization and subsequent gelation in different tissue environments. Demonstrations include the ex situ fabrication of this conducting gel in zebrafish (brain, fin, and heart), in food samples (beef, pork, chicken, and tofu), and a proof of concept of in vivo stimulation of a leech nerve. —MSL

Science, adc9998, this issue p. 795; see also adg4761, p. 758

MICROBIOTA

Bacterial cell walls stimulate mice growth

Malnutrition in infancy results in skeletal stunting and disrupts the establishment of the gut microbiota. Schwarzer *et al*. built on their earlier findings in the bacterium *Lactiplantibacillus plantarum* (Lp^{WJL}) in fruit flies to show that this strain of bacterium alone elevates circulating levels of insulin growth factor–1 (IGF-1) in malnourished mice (see the Perspective by Yadav and Philpot). Lp^{WJL} did not need to be alive to have this effect, because a cell wall extract was sufficient to increase femur length and stimulate IGF-1. This effect was mediated through an innate immune receptor in the gut called NOD2, which recognizes bacterial muramyl dipeptide structures. The authors suggest that Lp^{WJL} stimulates malnutrition-suppressed NOD2 signaling in the crypt. Increased NOD2 signaling increases intestinal cell proliferation and improves nutrient absorption, which then stimulates activity of the nutrient-sensitive growth hormone/IGF-1/insulin axis, prompting postnatal growth. —CA

Science, ade9767, this issue p. 826; see also adg6247, p. 756

ORGAN REGENERATION

A tale of antler regeneration

Mammals have largely lost the capacity to regenerate appendages or organs. One exception is the annual regeneration of antlers in deer, which provides a valuable model for studying organ regeneration in mammals. Qin *et al*. constructed a comprehensive cell atlas of antler regeneration using single-cell transcriptomics (see the Perspective by Wang and Landete-Castillejos). Antler regeneration involves a stem cell–based regenerative process. A key population of antler blastema progenitor cells (ABPCs) displays self-renewal, osteogenic-chondrogenic differentiation, and bone tissue repair potential. Cross-species comparison revealed that the mouse has a similar type of ABPC (in the regenerative digit tip), but nonmammalian species do not, suggesting that mammals may have a distinctive regeneration mechanism. —SMH

Science, add0488, this issue p. 840; see also adg6018, p. 757

INFLAMMATION

Inflammation-inducing traffic jams

The NLRP3 inflammasome is activated by diverse cellular stresses to produce proinflammatory cytokines. Lee *et al*. revealed that this inflammasome is activated by disruptions in endosomal trafficking in various cell types, including bone marrow–derived macrophages. Chemical interference with endosomal trafficking potentiated NLRP3 activation, although it was insufficient to activate NLRP3 by itself. Activated NLRP3 was recruited to endolysosomal vesicles, where it colocalized with a key signaling lipid, which the authors speculate may be the additional stimulus required for NLRP3 activation. —WW

Sci. Signal. **16**, eabm7134 (2023).

of the Cretaceous. They found substantial loss of species, especially those that fed on shelled prey and those on the ocean bottom. Pelagic species and those at higher latitudes had higher survival, showing that differential species survival shaped marine systems across the Cretaceous–Paleogene boundary. —SNV

Science, abn2080, this issue p. 802

PALEONTOLOGY

How to get big

Over evolutionary history, many different taxa have evolved very large body sizes. The general consensus has been that an animal grows to a large size based on an increase in growth rate. However, very few studies have explored this question across many species within a comparative phylogenetic framework. D'Emic *et al*. looked across a large dataset of non-avialan theropod dinosaurs, which had an array of body sizes. They found evidence supporting changes in growth rate contributing to body size change, but also found that changes in the duration of growth played a large role. —SNV

Science, adc8714, this issue p. 811

PLASTIC UPCYCLING

Plastics to fuels in ionic liquids

Polyethylene and polypropylene have many useful properties, but their resistance to chemical degradation makes processing their waste a challenge. In particular, heating to high temperatures to crack the underlying carbon–carbon bonds can be energy intensive. Zhang *et al*. report that an aluminum chloride–based ionic liquid medium can promote the breakdown of these polyolefin plastics into liquid fuels at temperatures below 100°C. The method compensates for the energy directed toward bond scission with energy released from alkylation reactions among the resulting intermediates. —JSY

Science, ade7485, this issue p. 807

STRATOSPHERE

Fired up

Large wildfires can generate pyrocumulonimbus clouds that transport smoke into the stratosphere and have major impacts on the stratospheric aerosol budget and climate. Katich *et al*. analyzed 13 years of airborne observations to determine the chemical and physical compositions of pyrocumulonimbus smoke and to quantify its effects on stratospheric aerosols. These clouds are responsible for as much as 25% of the black carbon and organic aerosols now in the lower stratosphere and may become an even more important influence on future climate as the frequency and severity of extreme fires increase. —HJS

Science, add3101, this issue p. 815

A new solvent-catalyst system enables conversion of waste hydrocarbon plastic, pictured above, into components of liquid fuel.

IN OTHER JOURNALS

Edited by **Caroline Ash** *and* **Jesse Smith**

ATHEROSCLEROSIS

Autoimmune features of atherosclerosis

Atherosclerosis, the formation of plaque in the arteries, is a key pathology contributing to myocardial infarction, stroke, and other disorders causing large numbers of deaths in humans. Atherosclerosis had been traditionally viewed as a lipid disorder, and inflammation is known to play a major role as well, but now Depuydt *et al*. have identified a potential autoimmune aspect to it. Through detailed analysis of T cells and their interactions with macrophages in the atherosclerotic plaques and blood of human patients, the authors identified T cells with an autoimmune phenotype, which may indicate additional directions for future treatment approaches. —YN

Nat. Cardiovasc. Res. 10.1038/s44161-022-00208-4 (2023).

SCIENCE EDUCATION

Rubric-based holistic review

To increase the diversity of admitted students, graduate programs need to evaluate the structures in place to evaluate potential applicants. Young *et al.* implemented a rubric-based holistic review process for all applicants to a graduate physics program, assessing 18 metrics including grade point average, test scores, research experience, noncognitive competencies, and fit with the program. Over a 3-year evaluation period, faculty ratings of applicant's grades, research experience, and noncognitive competencies did not differ based on the applicant's sex or undergraduate background. Differences that were observed reflected known systematic inequities such as scoring lower on the GRE and women performing more volunteer work. Collectively,

PHOTOS (LEFT TO RIGHT): RENÉ NOTENBOMER/ALAMY STOCK PHOTO; THIERRY MONASSE/GETTY IMAGES

Cornfield weeds, such as *Papaver rhoeas* shown here, may offer wheat monocultures some benefit by supplementing root mycobiota.

AGROECOLOGY

Friendly neighborhood weeds

Intensive agriculture is damaging to soil microbe communities, including plant beneficial organisms. Although many crops are grown in monocultures, exposure to weeds is not always problematic because weeds can recruit microbial partners from the surrounding soil and from other plants. Hu *et al*. observed these "neighbor effects" between weeds and wheat plants in field and laboratory experiments. Although weeds did not change the soil microbial community, the authors found that wheat plants grown with weed species had more fungi associated with their roots, indicating local-scale dispersal between plants. However, the contribution of weeds to the wheat microbiota, and any associated increases in wheat performance, depended on the species of weed involved. —BEL

J. Ecol. 10.1111/1365-2745.14073 (2023).

these results suggest rubric-based holistic review as a method with strong potential for making graduate admissions in physics, and across STEM, more equitable. —MMc

Phys. Rev. Phys. Educ. Res. **18**, 020140 (2022).

PLASMONIC CHEMISTRY

Surface-tuned energy flows

The pathway of light-driven reactions on plasmonic silver nanoparticles has been shown to depend on surface-adsorbed anions that control the adsorption state of the reactants. Stefancu *et al*. investigated the reaction of methylene blue co-adsorbed with halide anions on silver nanoparticles when this molecule underwent plasmon-assisted resonant laser excitation at a 632.8-nanometer wavelength. Methylene blue adsorbed as dimers when surface chloride was present, and excitation led to N-demethylation that produced thionine. When iodide was on the surface, only the monomer adsorbed. This molecular conformation could not undergo demethylation, and instead, a triplet state formed that was deactivated through the formation of singlet oxygen. —PDS

ACS Nano. 10.1021/acsnano.2c12116 (2023).

ROBOTICS

Legless super-jumping robots

Insects such as click beetles can jump without using appendages to heights 10 to 30 times their body length. This is accomplished by storing elastic energy in their skeletal muscle that is released with the triggering of their thoracic hinge. Wang *et al.* used this as inspiration for robots that can jump up to 40 times their body length. A series of different designs were explored to maximize jumping height and fracture resistance while minimizing size and weight. A combination of a coiled muscle and buckled actuation beam was shown to enable rapid spontaneous activation once a triggering threshold was reached. —MSL

Proc. Natl. Acad. Sci. U.S.A. **120**, e2210651120 (2023).

COVID-19 THERAPY

Lambda shows potential

Type III interferon (IFN-γ) is a cytokine mostly restricted to mucosal surfaces that can confer antiviral protection without fueling damaging proinflammatory responses. Therefore, it has shown promise as a therapeutic for viral infections. Two phase 2 clinical trials previously reported that a pegylated form of recombinant IFN-γ that was originally developed as a treatment for chronic viral hepatitis reduced the duration and severity of severe acute respiratory syndrome coronavirus 2 (SARS-CoV-2) infection when administered early. Reis *et al.* conducted a large phase 3 clinical trial in which individuals received a single dose of either pegylated IFN-γ or a placebo within 7 days after the onset of COVID-19 symptoms. Regardless of vaccination status or the variant of concern with which they were infected, subjects receiving the IFN-γ showed an approximately 50% reduction in symptoms compared with controls. Pegylated IFN-γ may therefore be a useful addition to the anti–COVID-19 armamentarium, especially as a prophylactic for certain at-risk groups. —STS

N. Engl. J. Med. **388**, 518 (2023).

CELL BIOLOGY

Small molecule boosts mitochondria

Mitochondria are in a constant state of division and fusion to maintain their integrity and to promote metabolic homeostasis. Mitofusin 1 (MFN1) and MFN2 are dynamin-like GTPases that mediate outer mitochondrial membrane fusion. The neuromuscular disorder Charcot-Marie-Tooth disease type 2A (CMT2A) is linked to defects in MFN2. Guo *et al*. describe a small molecule, S89, which directly targets MFN1 and promotes GTP hydrolysis and mitochondrial fusion by MFN1 but not MFN2. The S89 molecule works by relieving MFN1 autoinhibition and boosts the activity of endogenous MFN1 when MFN2 is defective, thereby restoring mitochondrial function in CMT2A patient–derived cells. S89 also protected mouse heart tissue from ischemia/reperfusion injury by preventing mitochondrial damage. Elevated mitochondrial fusion may thus also prove beneficial across a range of metabolic regulation, immune responses, and neurological conditions. —SMH

Nat. Chem. Biol. 10.1038/s41589-022-01224-y (2023).

RESEARCH ARTICLE

BIOELECTRONICS

Metabolite-induced in vivo fabrication of substrate-free organic bioelectronics

Xenofon Strakosas[1,2]*†, Hanne Biesmans[1]†, Tobias Abrahamsson[1], Karin Hellman[2], Malin Silverå Ejneby[1], Mary J. Donahue[1], Peter Ekström[2], Fredrik Ek[2], Marios Savvakis[1], Martin Hjort[2], David Bliman[3,4], Mathieu Linares[1,5], Caroline Lindholm[1], Eleni Stavrinidou[1], Jennifer Y. Gerasimov[1], Daniel T. Simon[1], Roger Olsson[2,3], Magnus Berggren[1]*

Interfacing electronics with neural tissue is crucial for understanding complex biological functions, but conventional bioelectronics consist of rigid electrodes fundamentally incompatible with living systems. The difference between static solid-state electronics and dynamic biological matter makes seamless integration of the two challenging. To address this incompatibility, we developed a method to dynamically create soft substrate-free conducting materials within the biological environment. We demonstrate in vivo electrode formation in zebrafish and leech models, using endogenous metabolites to trigger enzymatic polymerization of organic precursors within an injectable gel, thereby forming conducting polymer gels with long-range conductivity. This approach can be used to target specific biological substructures and is suitable for nerve stimulation, paving the way for fully integrated, in vivo–fabricated electronics within the nervous system.

Interfacing neural tissues with advanced digital and electronic instrumentation is one approach to probing the complex signaling characteristics of the nervous system. Even though several functional bioelectronic implants have been demonstrated, the rapid formation of scar tissue around the implantation site affects the lifetime, precision, and overall fidelity of the biological–electronic interface (*1*). Most of these technologies are based on thin films, requiring a planar [or in some cases three-dimensional (3D)–structured] substrate of varying stiffness. The material interfaces that such technologies necessitate—e.g., substrate-active material, active material-encapsulation, etc.—introduce complexity and lead to the common failure mode of delamination of one or more layers. Successful long-term integration of neural stimulation and recording technologies thus relies on matching the electrical and viscoelastic characteristics of the device to those of the nervous system in a seamless manner.

When designing a system complementary to the characteristics of the nervous system, bioelectronic electrode technology should extend far beyond the 2D arrangements of lines and pads organized along hard, planar substrates that form the basis of classic electronic design. Various strategies have been undertaken to design electrodes that seamlessly connect to the structures of the nervous system. With the rise of flexible and soft electronics based on intrinsically electroactive conducting polymers capable of mixed ion–electron conduction, bioelectronic electrodes with matched impedance characteristics have been implemented on ultraflexible and ultrasoft substrates (*2*). Electrodes based on conductive polymers (i.e., organic electronics) (*3*, *4*) conformally integrate with the surface of the brain in animal models and have been demonstrated for electrocorticography (*5*, *6*). Even though soft and flexible electrodes allow for conformal contact with the brain and nerves, the substrate represents a major limitation for reaching structures deep within the sensitive neural tissue in a minimally invasive way (*7*). To circumvent this limitation, conducting polymers have been formed within the target biological system, introduced as monomers from a solution and polymerized in vivo to derive "impregnated" (*8*) electrodes and even bicontinuous amalgamations with neural tissue (*9*). However, polymerization requires chemical (*10*) and/or electrical (*10*) energy, which can potentially be harmful to sensitive neural tissue. To further advance the concept of in vivo polymerization, genetic engineering of an animal was carried out to express enzymes that promote local polymerization in specific cells in close proximity to the target tissue in vivo in the nematode *Caenorhabditis elegans* (*11*). Owing to its reliance on genetic engineering, however, this technique cannot be ethically extended to humans to provide an advanced interface with the brain.

Progress has been made on using endogenous enzymatic activity to catalyze the oxidative polymerization of precursors to produce mixed ion–electron conduction polymers in vivo. The biocompatible precursors are based on an organic trithiophene-based monomer with a 2,5-bis(2,3-dihydrothieno[3,4-b][1,4]dioxin-5-yl)thiophene (ETE) backbone, which is monofunctionalized on the central thiophene with a 4-ethoxybutane-1-sulfonic acid salt side chain (ETE-S). The water-soluble trithiophene monomer has a low oxidation potential (~0.3 V versus Ag/AgCl), allowing for enzymatic polymerization in vivo (*12*). Endogenous peroxidase enzymes polymerize ETE-S in plants (*13*) and in the small freshwater animal *Hydra vulgaris* (*14*). The peroxidases utilize local H_2O_2 as a catalyst to produce radical monomers, which further polymerize and aggregate to form conducting polymers integrated with the tissue.

There is a remaining leap that must be taken to produce a truly versatile mixed ion–electron conduction electrode system that would fulfill all the requirements for a self-organized in vivo neural interface system that is high-performing, minimally invasive, and stable. We propose that such electrode technology would exhibit the following characteristics: (a) dispensed as a fluid (*15*) that is compatible with the environment of the target neural tissue and can diffuse within a desired distance of the injection site; (b) consists of, and generates, only nontoxic components to drive polymerization and cross-linking; forms an electrode that is (c) homogeneous, (d) long-term stable, and (e) gelled (soft) with (f) high conductivity and high volumetric capacitance while (g) conformally interfacing with neural structures at different length scales.

We report an approach to producing self-organized, high-performing electrode structures within the peripheral nervous system (PNS) and central nervous system (CNS), which is applicable to a wide range of tissue and animal models. Our approach relies on the injection of a multicomponent mixture that has been designed to fulfill all the criteria, (a) to (g), listed above. The mixture includes an ETE derivative with a 2-ethoxyacetic acid sodium salt side chain [ETE-COONa: addressing (a), (b), (d), (f)], poly(vinyl alcohol) (*16*, *17*) [(PVA): (c), (e)], poly-L-lysine (*18*) [(PLL: (d), (e), (g)], horseradish peroxidase [HRP: (b)], oxidase enzymes [ROx: (b)] (*12*, *19*), and 1-ethyl-3-[3-dimethylaminopropyl]carbodiimide/*N*-hydroxysulfosuccinimide [EDC/sulfo-NHS: (d)]. The polymerization of ETE-COONa is mediated by the ROx–HRP enzyme cascade whereby the ROx consumes endogenous metabolites within the physiological target to produce H_2O_2 locally, which then serves as an electron acceptor

[1]Laboratory of Organic Electronics, Department of Science and Technology, Linköping University, 601 74 Norrköping, Sweden. [2]Chemical Biology and Therapeutics, Department of Experimental Medical Science, Lund University, SE-221 84 Lund, Sweden. [3]Department of Chemistry and Molecular Biology, University of Gothenburg, SE-405 30 Gothenburg, Sweden. [4]IRLAB Therapeutics AB, Arvid Wallgrens Backe 20, 413 46 Gothenburg, Sweden. [5]Scientific Visualization Group, Department of Science and Technology, Linköping University, 601 74 Norrköping, Sweden.
*Corresponding author. Email: magnus.berggren@liu.se (M.B.); xenofon.strakosas@liu.se (X.S.)
†These authors contributed equally to this work.

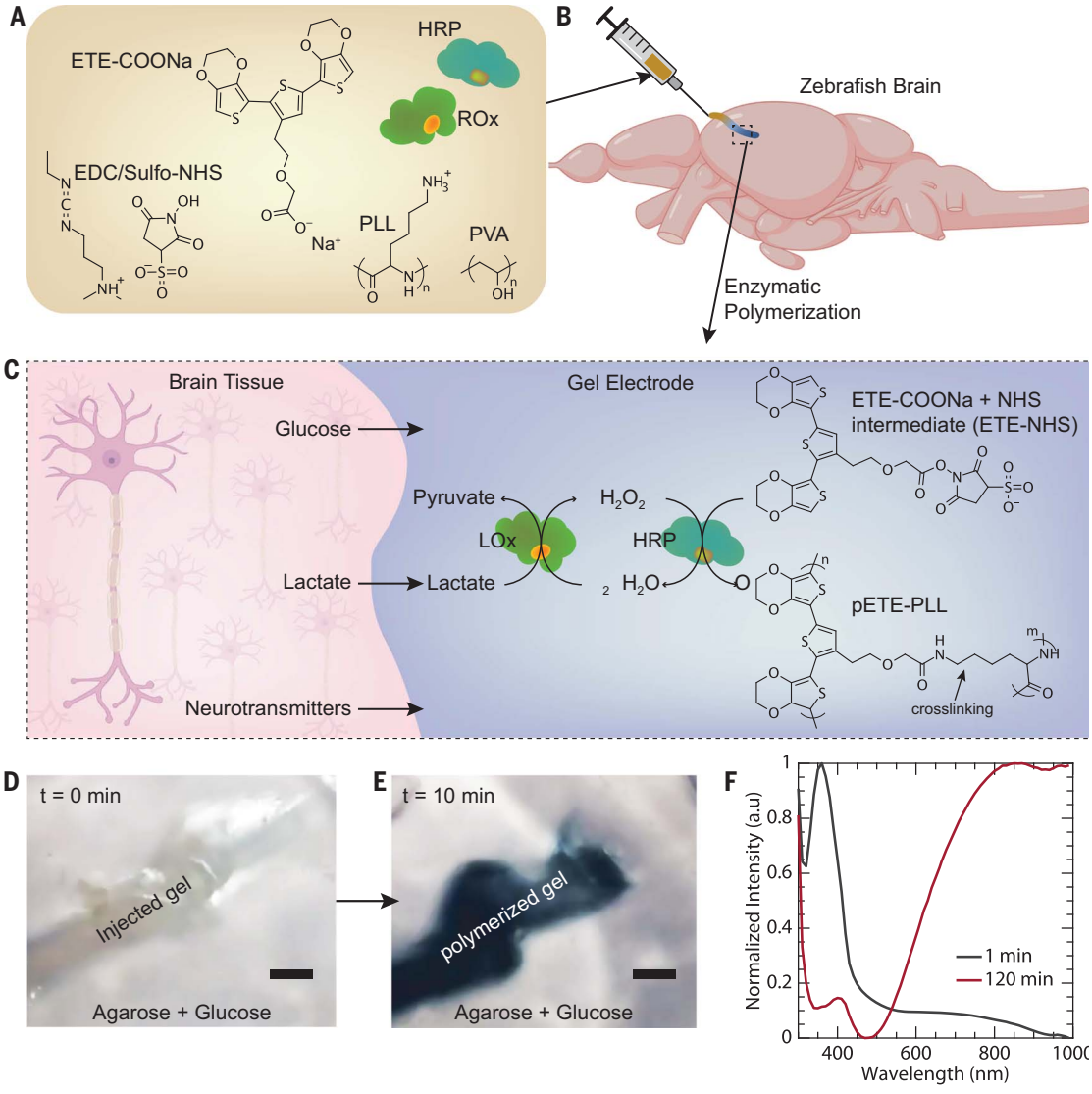

Fig. 1. In vivo polymerization of conducting polymer gels induced by endogenous metabolites. (**A**) Schematic representation showing the gel components. Each component contributes to the process of polymerization or cross-linking. (**B**) Polymerization occurs dynamically in the CNS after the introduction of the gel. (**C**) Schematic of the in vivo polymerization mechanism. (**D**) Cocktail gel (yellow-brown color) injected in agarose gel containing 5 mM glucose and (**E**) subsequently polymerized (turning dark blue) after 10 min. Scale bars, 1 mm. (**F**) UV-vis spectra from cocktail gels injected into agarose 1 min after injection (black line) and 120 min after injection (red line) (n = 1 representative UV-vis measurement).

in the oxidation of ETE-COONa by HRP. We show that by taking advantage of the enzymatic polymerization and cross-linking around nervous tissue, it is possible to fabricate soft electrodes in vivo in a broad variety of model organisms.

Design, operating principle, and polymerization of gel electrodes.

Unlike in plants (*13*) and hydra (*14*), where the endogenous environment promotes spontaneous ETE-S polymerization, the native environment in zebrafish brains does not efficiently polymerize ETE-S. We introduced neat ETE-S solution (2 mg ml^{-1} ETE-S in water) in extracted brains of zebrafish (*Danio rerio*) and allowed the polymerization to proceed over 3 hours. Fluorescence microscopy images from zebrafish brain slices showed that the injected ETE-S can be excited with blue light (excitation: 485 nm; emission: 525 nm) (fig. S1A). This fluorescence is attributed to aggregated but nonpolymerized ETE-S (fig. S1B). Because ETE-S is enzymatically polymerized by peroxidases in the presence of H_2O_2, in vivo polymerization in nerve tissue is limited either by the absence of peroxidases or H_2O_2, or both.

To overcome this limitation, we devised a strategy to polymerize ETE analogs in various tissues and animal models. The concept allows for local production of H_2O_2 by oxidase enzymes and subsequent polymerization of ETE-derivatives by peroxidase enzymes (*12*). The enzymes are introduced in the tissue, in which endogenous metabolites that are ubiquitous in nervous tissue fuel the enzymatic polymerization cascade. To improve the stability of the conducting polymer, we used a cocktail gel containing ETE-COONa (rather than ETE-S), oxidase enzymes [ROx: glucose oxidase (GOx) or lactate oxidase (LOx)], and HRP embedded in a PVA:PLL polymer matrix (Fig. 1A). EDC/sulfo-NHS was added in the gel to activate the carboxylic acid toward amide bond formation. Specifically, EDC/sulfo-NHS reacts with the carboxyl groups of ETE-COONa to generate an intermediate ester (ETE-NHS; Fig. 1C, upper right) that reacts with the primary amine groups of PLL, hydroxyl groups of PVA, as well as other amine and alcohol groups that may exist in tissue (*20*). The gels are then introduced into the tissue to polymerize in situ and form soft electronic conductors (Fig. 1B). Metabolites from the tissue diffuse into the injected gels and ROx enzymes catalyze their oxidation, producing H_2O_2 as a byproduct in the presence of O_2. Then HRP locally converts H_2O_2 to H_2O and in the process, ETE monomers are converted into radicals that undergo further polymerization. The polymerized ETE-NHS intermediates cross-link with the PLL to form a stable pETE-PLL–conducting polymer gel electrode (Fig. 1C). The resulting electrode reaches a shape and configuration dictated by the diffusion and chemical kinetics of the

components introduced into the target biological system, as well as the native microenvironment within that system.

The polymerization of ETE can be visualized optically or by fluorescence imaging. Cocktail gels with glucose oxidase (GOx) were injected in 0.6% agarose gels containing 5 mM glucose. Agarose has been widely used to mimic the mechanical properties of the brain, and the GOx gel polymerizes fully at glucose concentrations >100 μM within a time span of 45 min (fig. S2). The color of the injected solution transitioned from yellow to dark blue within seconds (Fig. 1, D and E, and movie S1). The dark blue color is distinctive for p-type semiconducting and conducting polymers. Ultraviolet-visible (UV-vis) absorption spectroscopy further validated the formation of a doped conducting polymer. In solution, ETE monomers absorb light with a peak at 350 nm. At higher concentrations, the monomer will aggregate and shift the peak to 400 to 450 nm. Undoped polymer exhibits absorption between 500 and 600 nm, and absorbances >600 nm correspond to doped polymer. UV-vis spectra of the injected gels in agarose showed that the absorption peak at 350 nm decreased over time, and a broad absorption band with a maximum at 850 nm (and extending beyond 1000 nm) increased over time. This broad peak is in part composed of polaron transition bands (*13*, *21*), indicating the formation of a doped conducting polymer (Fig. 1F). Rheology measurements of the gels before and after polymerization were performed and show that the gels have low viscosity. After polymerization, the increase in viscosity implies the formation of a soft polymer network (fig. S3).

We additionally injected gels into agarose using an Au-coated microcapillary and monitored the ETE monomer fluorescence (excitation: 350 nm; emission: 450 nm) over time (fig. S4, A and B). Time lapse imaging in fluorescence mode showed a depletion of nonpolymerized monomer at the injection site. During injection of the gel into the agarose with 5 mM glucose, fluorescence increased rapidly, followed by a 99% decay in intensity within 1 min indicating initial diffusion and subsequent polymerization of ETE (fig. S4, C and D, and movie S2). In agarose without glucose, the fluorescence intensity dropped by 20% after injection of the gel, likely owing to diffusion and subsequent dilution of the monomer (fig. S4, E and F, and movie S3). In glucose-containing agarose, the impedance measured using the Au-coated capillary dropped significantly after injection of the polymer (fig. S4, G and H), indicating effective in situ formation of conducting material.

Electrical properties of gels

All cocktail gels were prepared by mixing the individual components in MES buffer at pH 6.9. During mixing, however, strong electrostatic interactions between the negatively charged ETE-COONa or ETE-NHS, the medium, and the positively charged lysines of PLL, HRP, or both resulted in the formation of particulates, which produced a cloudy suspension (fig. S5, G and H). The effect was more pronounced with increased concentrations of ETE and PLL. Density functional theory and molecular dynamics calculations (fig. S5) confirm the aggregation. In the absence of PLL, ETE-NHS molecules aggregate through π-π stacking (fig. S5, A and B). In the presence of PLL, however, the sulfonate group of ETE-NHS intermediate interacts mainly Coulombically with the charged group of the lysine, resulting in aggregation between a PLL chain and a manifold of ETE-NHS monomers (fig. S5, B to D). Aggregation between ETE-NHS molecules still occurs to some extent in the absence of PLL, but to a lesser degree (fig. S5, E and F). To reduce the aggregation and improve the

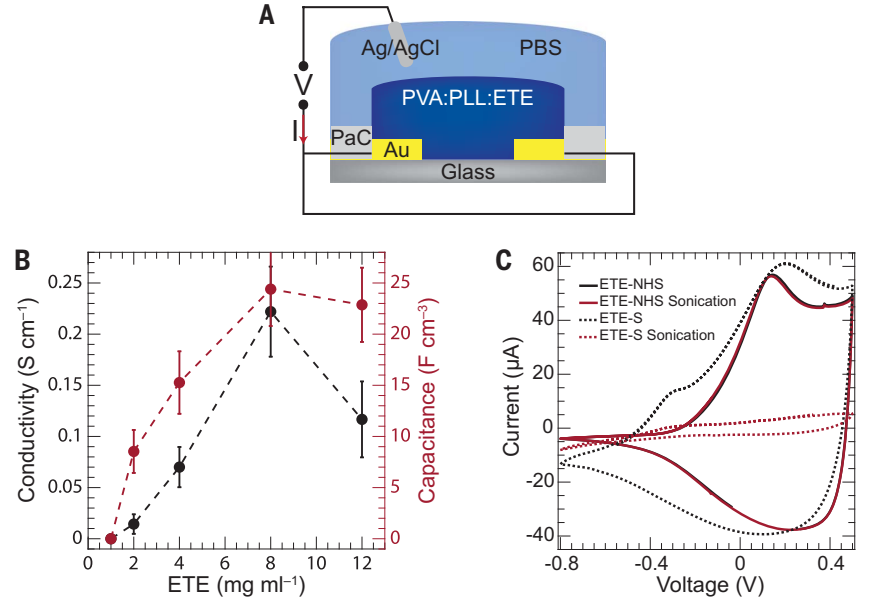

Fig. 2. Electrical and electrochemical stability. (**A**) Schematic of the electrochemical platform used to characterize the electrical, electrochemical, and stability properties of the polymerized gels. (**B**) Conductivity and specific capacitance as a function of monomer concentration (n = 3 independent measurements). Datapoints represent the mean ±SD. (**C**) Cyclic voltammetry of ETE-COONa with sulfo-NHS (ETE-NHS) versus ETE-S gel films before and after the platforms were sonicated for 10 min in deionized water (n = 3 independent current-voltage measurements).

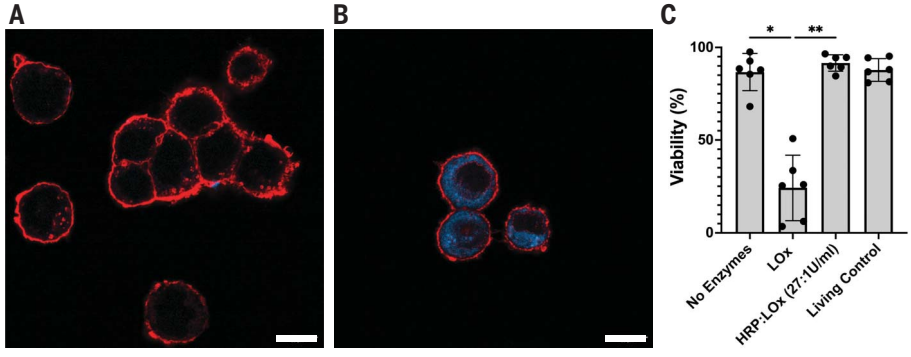

Fig. 3. Cell biocompatibility. (**A**) Confocal fluorescent images of cultured PC12 cells in control media without ETE or enzymes. WGA (red) was used to stain the cell membranes. Scale bar, 20 μm. (**B**) Confocal fluorescent images of cultured PC12 cells in media incubated with cocktail gels containing ETE-COONa with NHS (ETE-NHS) and LOx for 24 hours, showing unpolymerized monomer uptake by the cells. Red structures are cell membranes, and blue structures represent ETE-monomers. Scale bar, 20 μm. (**C**) Live/Dead assay of cells incubated with media preconditioned with gels containing ETE and various combinations of cocktail enzymes. Data are presented as means ± SD. Kruskas-Wallis was used to test significance. *P = 0.0332, **P = 0.0021 after comparison of all means (n = 6 replicates for every group).

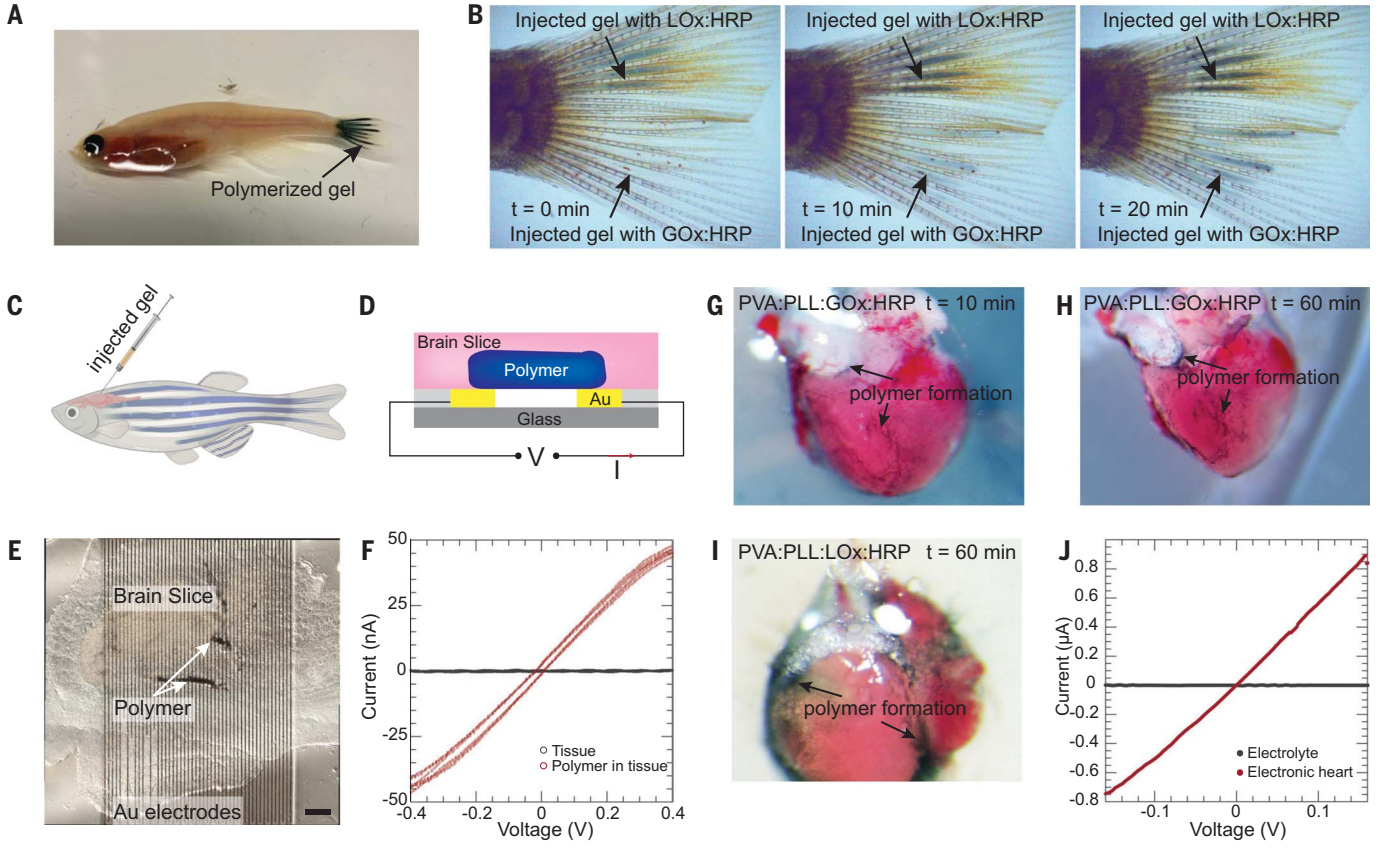

Fig. 4. In vivo polymerization in zebrafish. (**A**) Photograph of an anesthetized albino zebrafish with gel polymerized in the fin. (**B**) Time-lapse microscope images from a zebrafish fin during polymerization of gels. (**C**) Schematic showing injection of gel into zebrafish brain. (**D**) Schematic of a zebrafish brain slice integrated with Au metal electrodes for electrical measurements. (**E**) Microscope image of brain slice integrated with metal electrodes for electrical measurements. Scale bar, 200 μm. (**F**) Current–voltage characteristics from brain slice samples on Au electrodes (electrode spacing, 15 μm) (n = 3 independent current-voltage measurements). (**G** and **H**) Microscope images of extracted zebrafish heart immersed in cocktail gels with GOx as oxidase enzyme. (**I**) Microscope image of a heart that is immersed in cocktail gels with LOx as the oxidase enzyme. (**J**) Electrical measurements from a zebrafish heart on Au electrodes (20-μm spacing) compared to phosphate-buffered saline electrolyte control. The heart was previously immersed in gels with LOx for 120 min (n = 3 independent current-voltage measurements).

homogeneity of the suspension, we added PVA with the intent of balancing the charge on the PLL (*17*) (fig. S5, G and H). The addition of PVA notably enhanced the solubility of the ETE and PLL mixture (*17*), resulting in a solution that was visibly clear for concentrations of ETE-NHS up to 8 mg ml^{-1} (fig. S5, G and H).

The electrical characteristics of the conducting gels are highly dependent on gel formulation. We studied the electrical characteristics of the gels for different ETE-NHS concentrations using Au microelectrode arrays (MEAs) patterned with a double layer of parylene C (PaC) (*22*, *23*) (Fig. 2A). Gel cocktails were drop-cast on top of the MEAs and allowed to dehydrate for 10 min. Upon the addition of 5 mM glucose, the gels polymerized (fig. S6A). For further characterization steps, the area of the formed conducting polymer gel was defined through PaC peel-off (of the top PaC layer) (*22*) after the gels were polymerized and dried (fig. S6B). During polymerization, a small voltage of 0.1 V, which does not induce polymerization, was applied between two adjacent Au electrodes (fig. S6C). An increase in current exhibiting sigmoidal behavior was measured with a delayed onset of typically 500 s after addition of glucose (fig. S6D). The time at which current onset occurred depended on the concentrations of enzymes, metabolites, and supporting biopolymers. However, the maximum current level was primarily dependent on the concentration of ETE-monomer.

Both conductivity and capacitance increased while increasing ETE-NHS concentration up to 8 mg ml^{-1}, and peak values of conductivity σ = 0.25 S cm^{-1} and specific capacitance C_v = 25 F cm^{-3} (Fig. 2B) were measured. The measured conductivity values, however, did not represent the maximum conductivity of the gels, as they could be further doped electrochemically. To illustrate this concept, we used the gels as channel materials in organic electrochemical transistors (OECTs) (fig. S6E). We found that the drain current (I_d) at zero gate voltage was low, and that I_d increased for negative gate voltages. The increase in the current indicates that the gels were not intrinsically fully doped (fig. S6F). We believe that this was the case because after polymerization, the carboxyl/sulfo-NHS groups of ETE-NHS were bound to the amine groups of PLL and thus could not self-dope the polymer.

Stability and biocompatiblity

Apart from the electrical properties, long-term structural stability is an important feature of the formed gels when interfacing with biological structures. We designed the gels such that the formed polymer would be cross-linked. To test the stability, glucose-induced gels were polymerized on top of MEAs. After the formation and characterization of the conducting gels, the coated MEAs were sonicated in DI water for 10 min to induce harsh mechanical stresses. Cyclic voltammetry before and after sonication showed that ETE-NHS–based gel films did not lose electrical or electrochemical characteristics after this treatment (Fig. 2C, solid lines). By contrast, when ETE-S was used as the monomer in the gels, the ETE-S–based films lost most of their capacitance after

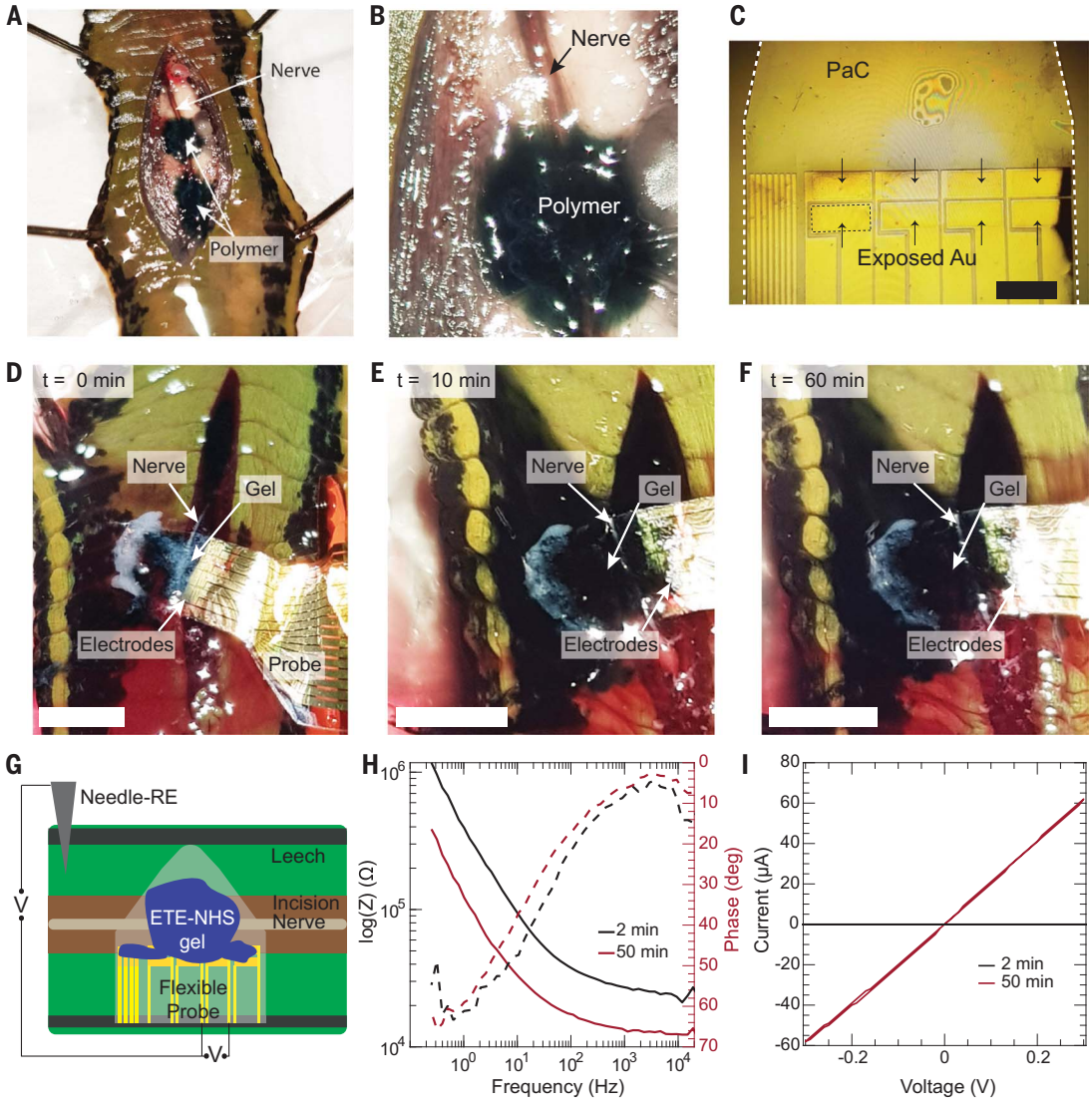

Fig. 5. In vivo polymerization around the nervous system of medicinal leeches and the dynamic change of electrochemical properties on flexible probes. (**A**) Leech with polymerized gels, induced by lactate, around its central nerve. (**B**) Close-up of the polymerized gel from (A). (**C**) Microscope image depicting the flexible PaC-based probe with eight patterned electrodes. The Au line interconnects are insulated with PaC. Dashed white lines show the edges of the probe. The PaC substrate is extended beyond the Au electrodes. Scale bar, 500 μm. (**D** to **F**) Change in the color of the conducting gel from clear to dark blue on top of the flexible probes over 1 hour. Scale bars, 2.5 mm. (**G**), Schematic of circuit connections on the Au electrodes for measurement of EIS and current between Au electrodes (after connection via the polymerized gel). (**H**) EIS measurements of all Au electrodes 2 min (black) and 50 min (red) after gel deposition (Z is solid line, phase is dashed line; n = 1 representative impedance measurement). (**I**) Current–voltage characteristics between two adjacent electrodes after 2 min (black) and 50 min (red) of gel deposition (n = 1 representative current-voltage measurement).

sonication (Fig. 2C, dotted lines). The stability of the ETE-NHS–based films and degradation of ETE-S–based films could also be visually observed before and after sonication (fig. S7, A to D). In addition to these mechanical fatigue tests, the devices were imposed to repeated voltage cycling (1000 cycles) without significant loss of capacitance (fig. S7E). Lastly, ETE-NHS patterned polymer gels were incubated with PC-12 cells for 72 hours without loss of electrical performance (fig. S7F). These complementary findings indicate that ETE-NHS does indeed covalently bind to PLL and cross-link the bulk of the gel films, allowing for long-term stability.

Finally, gel formulations were optimized for biocompatibility. The gel electrode system can potentially induce toxicity in sensitive tissues either through exposure to individual reactants or as a result of the chemistry associated with the actual polymerization mechanism. Although we expect most activated ETE-NHS monomers to bind to PLL, unbound monomers may diffuse away from the gel to the surrounding tissue with potentially toxic effects. Moreover, ROx enzymes can continuously turn over metabolites and produce high amounts of H_2O_2 that can be cytotoxic (*24*). We prepared three different gel formulations: (i) ETE-NHS without enzymes, (ii) ETE-NHS + LOx, and (iii) ETE-NHS + LOx + HRP. Organic electrochemical transistor-based H_2O_2 sensors (with gates modified with platinum nanoparticles to catalyze H_2O_2) (*24*, *25*) were used to verify and compare levels of H_2O_2 production with and without HRP (fig. S8, A to D). Conditioned media incubated with gels showed increasing H_2O_2 with increasing incubation time until all present metabolites were consumed. We saw that a ratio of 27:1 units of HRP:LOx produced an optimal amount of H_2O_2 (i.e., less than 100 μM) for this specific system, so this ratio was used for further cell experiments. Fluorescent images and UV-vis spectra show that only the gels with a combination of ETE-NHS + LOx + HRP were nonfluorescent, indicating that the ETE polymerized in conditioned cell media (fig. S9, A to C). For nonpolymerized gels, ETE monomers diffused through the media and subsequently attached to, or passed through, the cell membrane when the conditioned medium was used to incubate PC-12 cells (Fig. 3, A and B). The diffused monomers were found to be nontoxic to cells (Fig. 3C, first bin). The LOx activity, however, was toxic to cells owing to the excessive production of H_2O_2 (Fig. 3C, second bin). The gels with optimized HRP:LOx ratios activities were shown to be significantly better for cell viability survival than the gels without HRP (Fig. 3C, second and third bins).

In vivo polymerization in zebrafish brain, fin, and heart

Gels were injected in live zebrafish to validate the enzyme-triggered in vivo polymerization.

Anesthetized albino zebrafish were used as a model to visualize polymerization owing to their versatility and general transparency. Cocktail gels (~100 nl) injected into the tailfins polymerized in vivo, resulting in a distinct dark color along the whole length of the fin cavities (Fig. 4A). Glucose and lactate were both shown to act as catalysts for polymerization, with lactate inducing a relatively faster polymerization, presumably because of its higher concentrations in zebrafish tissues (Fig. 4B and movie S4) (*26*).

The versatility of this approach is highlighted in gels injected into the zebrafish brain. Cocktail gels with LOx (HRP:LOx, 27:1 U/ml; ~10 nl total volume) as the oxidase enzyme were injected into the brains of anesthetized zebrafish (Fig. 4C). After injection, zebrafish were left to swim for 3 hours. The brains were then extracted and dissected, and brain slices were prepared. The dark blue polymer could also be seen optically on fixed brain slices (fig. S10A). By contrast, a yellow color was observed on brain slices where only neat ETE-S solution was injected (fig. S10B). UV-vis spectra from brain slices that optically exhibited signs of polymerization showed an absorption spectrum with a peak at 600 nm and no peak at 350 to 400 nm (Fig. 1F and fig. S10C), indicating depletion of the trimers and polymer formation with semiconducting behavior. The brain slices were then placed on top of MEAs to characterize their electrical behavior (Fig. 4D). Measurements were performed in regions where dark spots were observed along the brain slices (Fig. 4E). In dehydrated brain slices, a linear (ohmic) current was observed when a small voltage between −0.5 and 0.5 V was applied (n = 3 brains). The magnitude of the current was higher than in control tissue samples (Fig. 4F). When cocktail gels with GOx as the oxidative enzyme were injected into the brains of zebrafish, however, no polymerization occurred. Optical inspection of the brain slices showed no sign of a dark blue region. The poor performance of GOx-containing gels was expected as zebrafish brains, much like their human counterparts, are known to have low glucose and high lactate concentrations (*26*, *27*). UV-vis spectra from brain slices that optically exhibited signs of polymerization showed a wide absorption spectrum from 550 to 950 nm with a peak at 600 nm. These gels do not have peaks at 350 to 400 nm, in contrast to an injected ETE-S solution (Fig. 1F and fig. S10C).

To better visualize the in vivo polymerization induced by lactate versus glucose, we extracted whole brains, dissected them in half, and immersed the brains in cocktail gels (fig. S10D). In gels with LOx, the interface between the solution and the dissected part of the brain turned dark blue (fig. S10E). In gels with GOx, no change in color was observed (fig. S10F). The brains were subsequently placed on top of patterned metal electrodes to examine the electrical behavior of the dark-colored regions. The brains were placed with the dissected part, corresponding to the interior of the brain, facing the electrodes (fig. S10, G and H). In brains that were soaked in LOx gels, a linear current was observed when a voltage sweep was applied (fig. S10I, red line). The magnitude of the current could reach microamperes with linear behavior for both wet and dry samples. No current was observed in brains that were immersed in GOx cocktail gels (fig. S10I, black line).

Moreover, LOx-based gels appeared to be nontoxic. Gels based on LOx were injected into the brains of anesthetized zebrafish. After anesthesia, the zebrafish were left to swim for 72 hours with the injected gels (n = 9 fish). The fish suffered no mortalities, and we did not observe any changes to the zebrafish swimming behavior or general appearance (see materials and methods). To investigate the impact of the gels on the brain tissue, we extracted the brains after 48 hours and serially sectioned them (14-μm thickness). Alternate sections were stained with methylene blue/thionine (MB&T) or hematoxylin and Eosin (H&E). Polymer was observed in the granular cell layer of the cerebellum (corpus cerebelli) without any signs of structural tissue damage due to the injection or the formed polymer (fig. S11).

Zebrafish hearts were also extracted and immersed in cocktail gels. In gels with either GOx or LOx, dark blue lines were observed on the surface of the hearts, indicating that both glucose and lactate induced polymerization in the zebrafish heart. The glucose-induced polymerization was overall slower compared to lactate. The polymerization in the heart did not occur everywhere, but rather threaded structures along the surface of the heart were observed, with the structures' size increasing over time (Fig. 4,G and H). We speculate that the cocktail gel polymerizes in regions in which exchange of glucose or lactate between the heart tissue and the surrounding electrolyte occurs, e.g., around coronary arteries. This is expected, as local tissue glucose levels often covary with local blood flow (*28*). The polymerization and formation of the threaded structures were more prominent in heart samples that were incubated in gels with LOx (Fig. 4I). The hearts were removed from the LOx gels and then integrated with MEAs. A linear current response to the application of a linear voltage sweep, following Ohm's law, was apparent for hearts incubated in LOx gels but not evident for the electrolyte-only controls (Fig. 4J). In addition to electrical functionalization, the selective polymerization, in combination with local coloration from monomer to polymer transition, may be of utility for local staining in regions of interest.

These findings highlight that the formation of electronic conductors fueled by endogenous metabolites can develop soft electronics in various biological tissues and environments. Indeed, we injected gels with GOx and LOx in tenderized beef, pork, and freshly killed chicken muscle, observing polymerization in all tissues explored (fig. S12 and movie S5). In a plant-based tofu sample, polymerization is inefficient or does not occur owing to the lack or low concentration of specific metabolites (fig. S12). Owing to the abundance of metabolites and neurotransmitters in animal models and their corresponding enzymes, in vivo polymerization and formation of conductors are not limited to a specific tissue or model, and large local variations in metabolite concentrations between and within animal tissues (e.g., glucose levels have been reported to vary from 0.4 mM in the lower respiratory tract (*29*) to up to 500 mM in the lumen of the small intestine (*30*)) should allow for structure-specific polymerization as long as a suitable oxidase can be used.

Ex vivo polymerization around the nervous system of medicinal leeches as an in situ electrode area extension

For neuroscience applications, conducting polymers have been extensively used as coatings on implantable metal electrodes to improve recordings and stimulation in the CNS or PNS because they reduce the electrochemical impedance of metal electrodes by increasing their electroactive surface area. This benefit is more prominent for micrometer-sized electrodes, for which impedance becomes a limiting factor. Moreover, conducting polymers are softer than conventional electrode materials and are thus less prone to triggering an immune response in the tissue.

As a proof of concept, we first attempted to induce ex vivo polymerization of gels at the interface between nervous tissue and Au electrodes to reduce their impedance. We used medicinal leeches (*Hirudo medicinalis*) as models owing to their simple, easily accessible, and well-characterized nervous system. Drop-cast gels with LOx as the primary enzyme polymerized around the connecting nerve of the leech (Fig. 5, A and B), and in the leech muscles, in the span of 5 to 15 min (fig. S13), whereas gels with GOx did not polymerize (fig. S13). As in zebrafish brains, lactate concentrations in leeches are higher than those of glucose (*31*).

Patterned Au electrodes on a flexible PaC-based probe were used to interface with the leech nerve via gels polymerized around the nerve. A printed circuit board was applied as an interface between the electrode probe and the recording system (fig. S14E). Each probe comprised eight electrodes in total, each electrode having an area of 450 by 200 μm^2 and with 50-μm spacing between adjacent electrodes (Fig. 5C). The Au electrodes were placed

1 to 2 mm away from the nerve (with the probe substrate placed under the nerve), and 2 μl of Lox-based ETE cocktail gel was drop-cast on top of the electrodes and around the nerve. The color of the dropcast solution changed from white to dark blue over time, and the polymerized gel surrounded the nerve while also covering the Au electrodes (Fig. 5, D to F). When the presence of the probe prevented metabolites from reaching the gel, blood was manually transferred on top of the gel. During polymerization, the impedance of the Au electrodes was monitored by using electrochemical impedance spectroscopy (EIS) versus a reference metal electrode in the leech muscle (Fig. 5G). This impedance decreased significantly with a phase shift toward lower frequencies (Fig. 5H), indicating increased capacitance of the electrode. In this case, the reduction in impedance was caused by the presence of the conducting polymer itself along with the contribution of multiple metal electrodes (of the eight in total on the probe) being interconnected through the in situ–formed conducting polymer. The connection between Au electrodes was also verified by applying a voltage sweep between two adjacent electrodes, which resulted in a linear current 50 min after deposition of the cocktail gel (Fig. 5I, red line). No current was observed 2 min after deposition of the gels (Fig. 5I, black line). To verify that the polymer itself can reduce the impedance of individual electrodes, we also patterned gels on top of individual Au electrodes on the flexible probe by using a parylene peel-off technique (fig. S14, A and B) and induced polymerization with a lactate-containing solution (fig. S14C), which decreased the impedance of the gel patterned Au electrode at low frequencies (fig. S14D). These impedance measurements agree with studies in which conducting polymers increase the capacitance of Au electrodes (*22*).

The patterned polymer electrodes were then used to investigate whether the polymerized gel could act as an extended electrode to stimulate the connecting nerve and induce muscle contractions in the semi-intact leech model (fig S14E). When a control Au electrode on the flexible probe was placed 1 to 2 mm away from the nerve, stimulation with 250 cathodic current pulses (100 to 300 μA, 1-ms duration, 30 Hz) resulted in clear muscle movements, with a response frequency of 50 to 60% (table S1). Equivalent movement response occurred with the polymerized patterned gel electrodes (movie S6). There was no obvious difference in the stimulation threshold when the polymerized patterned gel was in contact with the nerve from underneath (fig. S14E and table S1). To test more precisely if it is possible to stimulate the nerve with the patterned gel as an extended electrode, a nerve model suitable for more fine and robust electrophysiological measurements would be preferable. However, although, the current threshold did not change, the voltage output for patterned gels was ~0.5 V and capacitive in nature (fig. S14E), whereas the required voltage for the Au electrode alone was ~2 V. Capacitive charge injection is in general preferable to faradaic charge injection because it prevents redox reactions that can create or deplete chemical species in the biological environment (*32*). Overall, in the leech experiments, we demonstrated that the concept of in vivo–polymerized gels is still under exploration and needs optimization before stimulating nerves (e.g., gel area, speed of polymerization, nerve model, etc.). However, we demonstrate that polymerized gels can indeed improve the properties and performance of current electrodes by, for example, lowering the electrode impedance and minimizing or eliminating faradaic charge injection during stimulation. Because the relatively large Au electrodes and gels were not suitable for low-amplitude and high-frequency recording, it was not possible to use them for electrophysiological recordings in the leech system.

A strategy for enzymatic polymerization fueled by endogenous metabolites for in vivo formation of substrate-free organic electronics, in both vertebrate and invertebrate models, was reported. Gels containing enzymes and small electroactive monomers were injected into the biological tissue, and endogenous metabolites induced polymerization of the monomers. This resulted in organic electronic gels without the requirement of a rigid—and thus inherently biologically and rheologically incompatible—substrate material. Such in vivo–manufactured gel electrodes were demonstrated in agarose gels, cell culture, zebrafish and leech model systems, and mammalian muscle tissue, and as the channel material in OECTs, demonstrating the broad versatility of the endogenously fueled polymerization method. From spectroscopic, electrical, mechanical, and neurophysiological investigations, we conclude that the developed electrode technology forms a biological-electronic amalgamation with precisely the performance and compatibility characteristics required for seamless integration with living systems, going far beyond the current state of the art in thin-film and/or substrate-based bioelectronics. The gel formulation was optimized for conducting polymer gels with high stability and biocompatibility. Owing to the plethora of metabolites, our method is not limited to specific biological models but is rather universal and could be tailored to match local fluxes of endogenous substances matched to their corresponding oxidase enzymes (metabolites, neurotransmitters, other biomarkers). Furthermore, the endogenous compound–fueled polymerization method does not necessitate genetic manipulation of target cells or tissue, making it more easily translatable. In addition, selective polymerization combined with the color change ensuing from monomer to polymer transition may be of utility for local staining in regions of interest. We believe that these locally and in vivo–formed organic electronic systems promise a paradigm shift in the development and interface of electronics with biology, seamlessly blurring the distinction between the biological and technological or electronic materials and systems.

REFERENCES AND NOTES

1. J. W. Salatino, K. A. Ludwig, T. D. Y. Kozai, E. K. Purcell, *Nat. Biomed. Eng.* **1**, 862–877 (2017).
2. M. Aizawa, *Proc. Annu. Int. Conf. IEE Eng. Med. Biol. Soc.* **13**, 1792–1793 (1991).
3. C. Boehler, S. Carli, L. Fadiga, T. Stieglitz, M. Asplund, *Nat. Protoc.* **15**, 3557–3578 (2020).
4. Y. Liu, V. R. Feig, Z. Bao, *Adv. Healthc. Mater.* **10**, e2001916 (2021).
5. D. Khodagholy *et al.*, *Adv. Mater.* **23**, H268–H272 (2011).
6. E. Castagnola *et al.*, *IEEE Trans. Neural Syst. Rehabil. Eng.* **23**, 342–350 (2015).
7. E. Lopez-Sola, R. Sanchez-Todo, È. Lleal, *J. Neural Eng.* **17**, 041002 (2020).
8. E. Khor, H. C. Li, A. Wee, *Biomaterials* **16**, 657–661 (1995).
9. S. M. Richardson-Burns *et al.*, *Biomaterials* **28**, 1539–1552 (2007).
10. L. Ouyang, C. L. Shaw, C. C. Kuo, A. L. Griffin, D. C. Martin, *J. Neural Eng.* **11**, 026005 (2014).
11. J. Liu *et al.*, *Science* **367**, 1372–1376 (2020).
12. G. Dufil *et al.*, *J. Mater. Chem. B Mater. Biol. Med.* **8**, 4221–4227 (2020).
13. E. Stavrinidou *et al.*, *Proc. Natl. Acad. Sci. U.S.A.* **114**, 2807–2812 (2017).
14. G. Tommasini *et al.*, *Bioact. Mater.* **10**, 107–116 (2021).
15. S. Spieth *et al.*, *Biomed. Microdevices* **14**, 799–809 (2012).
16. B. E. B. Jensen *et al.*, *Nanoscale* **5**, 6758–6766 (2013).
17. C. Brough *et al.*, *AAPS PharmSciTech* **17**, 167–179 (2016).
18. L. Richert *et al.*, *Biomacromolecules* **5**, 284–294 (2004).
19. K. E. Hammel *et al.*, *J. Biol. Chem.* **268**, 12274–12281 (1993).
20. J. Deng *et al.*, *Nat. Mater.* **20**, 229–236 (2021).
21. A. V. Volkov *et al.*, *Adv. Electron. Mater.* **3**, 1700096 (2017).
22. M. Sessolo *et al.*, *Adv. Mater.* **25**, 2135–2139 (2013).
23. M. J. Donahue *et al.*, *Adv. Mater.* **30**, 1705031 (2018).
24. X. Strakosas *et al.*, *Adv. Sci. (Weinh.)* **9**, e2101711 (2022).
25. X. Strakosas *et al.*, *J. Appl. Polym. Sci.* **134**, 44483 (2017).
26. Y. C. Tseng *et al.*, *Front. Zool.* **11**, 53 (2014).
27. W. M. Abi-Saab *et al.*, *J. Cereb. Blood Flow Metab.* **22**, 271–279 (2002).
28. K. Takeuchi *et al.*, *Circulation* **98** (Suppl), II234–II239, discussion II240–II241 (1998).
29. J. P. Garnett, E. H. Baker, D. L. Baines, *Eur. Respir. J.* **40**, 1269–1276 (2012).
30. R. P. Ferraris, S. Yasharpour, K. C. K. Lloyd, R. Mirzayan, J. M. Diamond, *Am. J. Physiol.* **259**, G822–G837 (1990).
31. U. Hoeger, A. Wenning, U. Greisinger, *J. Exp. Biol.* **147**, 43–51 (1989).
32. S. F. Cogan, *Annu. Rev. Biomed. Eng.* **10**, 275–309 (2008).
33. X. Strakosas *et al.*, Metabolite-induced in vivo fabrication of substrate-free organic bioelectronics, Zenodo (2022); https://doi.org/10.5281/zenodo.7078627.

ACKNOWLEDGMENTS

We thank T.-P. Ruoko, E. Głowacki, C. Musumeci, T. Arbring Sjöström, S. Rossi, C. Li, D. Priyadarshini, and A. Halder for invaluable insight and guidance, and R. Henriksen for donating fresh chicken tissue. This work was carried out within the "e-NeuroPharma" projects supported by the European Research Council (AdG 2018 Magnus Berggren, 834677), the Swedish Research Council (2018-06197), and the Swedish Foundation for Strategic Research (RMX18-0083). Additional funding was provided by the Knut and Alice Wallenberg Foundation and the Önnesjö Foundation. M.L. thanks the Swedish National Infrastructure for Computing (SNIC) for providing computer resources. Part of the study was

accomplished within MultiPark and NanoLund Strategic Research Areas at Lund University. Funding for M.H. was provided by the Swedish Research Council (2021-05231). **Funding:** European Research Council (AdG 2018 Magnus Berggren, 834677), Swedish Research Council (2018-06197), Swedish Foundation for Strategic Research (RMX18-0083), and Swedish Research Council (2021-05231). Additional funding was provided by the Knut and Alice Wallenberg Foundation and the Önnesjö Foundation. **Author contributions:** Conceptualization: X.S., H.B., T.A., D.T.S., R.O., M.B. Methodology: X.S., H.B., T.A., E.S., D.T.S., R.O., M.B. Monomer synthesis: T.A., D.B. Zebrafish experiments: X.S., K.H., P.E., M.H., F.E. Leech experiments: X.S., M.J.D., M.S.E., H.B. Cell work: H.B., X.S., C.L. Electrical characterization: X.S., M.J.D., M.S., M.J. Simulations: M.L. Funding acquisition: R.O., M.B. Supervision: J.G., C.L., D.T.S., R.O., M.B. Writing – original draft: X.S., H.B., M.B. Writing – review and editing: All authors reviewed and edited the draft. **Competing interests:** The authors declare that they have no competing interests. **Data and materials availability:** The data and codes that support the findings of this study are available at Zenodo (*33*). **License information:** Copyright © 2023 the authors, some rights reserved; exclusive licensee American Association for the Advancement of Science. No claim to original US government works. https://www.sciencemag.org/about/science-licenses-journal-article-reuse

SUPPLEMENTARY MATERIALS

science.org/doi/10.1126/science.adc9998
Materials and Methods
Supplementary Text
Figs. S1 to S20
Table S1
References (*34–45*)
MDAR Reproducibility Checklist
Movies S1 to S6

Submitted 13 May 2022; accepted 22 December 2022
10.1126/science.adc9998

PALEONTOLOGY

Global impact and selectivity of the Cretaceous-Paleogene mass extinction among sharks, skates, and rays

Guillaume Guinot* and Fabien L. Condamine

The Cretaceous-Paleogene event was the last mass extinction event, yet its impact and long-term effects on species-level marine vertebrate diversity remain largely uncharacterized. We quantified elasmobranch (sharks, skates, and rays) speciation, extinction, and ecological change resulting from the end-Cretaceous event using >3200 fossil occurrences and 675 species spanning the Late Cretaceous–Paleocene interval at global scale. Elasmobranchs declined by >62% at the Cretaceous-Paleogene boundary and did not fully recover in the Paleocene. The end-Cretaceous event triggered a heterogeneous pattern of extinction, with rays and durophagous species reaching the highest levels of extinction (>72%) and sharks and nondurophagous species being less affected. Taxa with large geographic ranges and/or those restricted to high-latitude settings show higher survival. The Cretaceous-Paleogene event drastically altered the evolutionary history of marine ecosystems.

The most recent biological mass extinction occurred ~66 million years ago (Ma), marking the Cretaceous-Paleogene (K-Pg) boundary. This event caused mass worldwide extinctions among a large range of clades and eliminated large metazoan vertebrate groups (*1*). Although the causes of this mass extinction are intensely debated (*2*, *3*), previous estimates suggest that the K-Pg extinction removed >40% of genera and 55 to 76% of species (*4*–*6*). There is also increasing evidence pointing to a variable degree of severity of this event between clades (*1*), ecologies (*7*), and geographical areas (*8*, *9*). However, global estimates of diversity loss are primarily extrapolated from genus- or family-level data on marine invertebrate clades that may not reflect the complexity of extinction patterns at the K-Pg boundary. Global species-level analyses of K-Pg extinction patterns among marine vertebrates, using bias-corrected approaches, are comparatively rare (*10*). Yet, marine vertebrate clades could provide different tales of extinction and postextinction recovery because of their higher trophic position. Only a few speciose vertebrate groups crossed the K-Pg boundary. Elasmobranchs (sharks, skates, and rays) represent an important component of marine ecosystems since the Mesozoic (*11*, *12*), are further characterized by a dense fossil record matching that of marine invertebrates (*12*), and have developed a wide range of ecologies (*13*).

To assess the impact of the K-Pg extinction event, we compiled global species-level fossil occurrence data for elasmobranchs covering a time interval between 93.9 and 56 Ma (most of the Late Cretaceous and Paleocene). This dataset represents 2582 occurrences for 675 species (3218 occurrences for 258 genera; table S1 and data S1). We estimated speciation and extinction rates, their temporal shifts, and the magnitude of rate change using Bayesian process–based birth-death models that incorporated the temporal and taxon-specific variation of the preservation processes and uncertainties associated with the age of fossil occurrences (*14*).

Magnitude of the K-Pg extinction and clade-specific patterns

We identified the K-Pg event in elasmobranch species diversity with an increase in extinction rate that started in the latest Maastrichtian (Fig. 1) [66.6 Ma, log Bayes factors (BF) > 6 with a 95% credibility interval (CI) of 66.72 to 66.27 Ma, fig. S1]. The K-Pg extinction rate significantly exceeds background extinction in the Maastrichtian and Paleocene with a mean of 1.763 events per lineage per million years (Myr) (95% CI 0.528 to 2.762; peaking at 1.949 events per lineage per Myr with 95% CI 0.976 to 2.993, at 66.01 Ma with 95% CI 66.26 to 65.91) during the K-Pg compared with 0.170 events per lineage per Myr (95% CI 0.115 to 0.284) in the Maastrichtian (t = −27.923, df = 15.001, $P = 2.391 \times 10^{-14}$), and 0.156 events per lineage per Myr (95% CI 0.078 to 0.295) during the Paleocene (t = −28.179, df = 15.016, $P = 2.043 \times 10^{-14}$). The K-Pg extinction diminished elasmobranch diversity by 62.6% (Table 1) as measured by the number of extinct species between 66.6 and 65.8 Ma, at which time extinction rate significantly decreased (log BF > 6, 95% CI 65.82 to 65.37 Ma). Analyzing the fossil record at the genus level indicates a 44.94% diversity drop across the K-Pg boundary (Table 1 and fig. S2) (*15*). According to our data, the K-Pg event was brief at geological scale and lasted for ~800,000 years. The diversity drop at the K-Pg cannot be attributed to a bias in preservation rates (q) because the expected number of species occurrences per lineage per Myr is similar throughout the K-Pg (Maastrichtian: mean q = 0.890, 95% CI 0.787 to 0.980; and Danian: mean q = 0.697, 95% CI 0.583 to 0.838) (fig. S3). We also evaluated the impact of singletons by excluding taxa represented by a single occurrence. We found very similar extinction intensities for species- (63.97%) and genus-level estimates (42.65%) once singletons were excluded (fig. S4 and S5) (*15*), confirming the robustness of the mass extinction pattern identified. Previous work on K-Pg elasmobranch extinction intensity provided equivocal estimates (species, 84% ± 5% to 45% ± 9%; genera, 56% ± 10% to 34% ± 11%), depending on the inclusion or exclusion of singletons, respectively (*11*). Such uncertainty in previous extinction percentages may be explained by the absence of correction for paleontological biases. Our estimations take into account fossil record biases and are based on revised and greatly expanded datasets from the last two decades (*12*, *13*), which further refine estimates of elasmobranch extinction intensity at the K-Pg.

Previous analyses have pointed out heterogeneous extinction within elasmobranchs (*11*, *12*, *16*). We analyzed the extinction patterns of the two main elasmobranch clades (sharks and batomorphs) separately and found stronger extinction rates and percentages for batomorphs than sharks (Table 1 and figs. S6 and S7) (t = −7.603, df = 7.20, P = 0.0001), suggesting phylogenetic selectivity in the extinction pattern. This selectivity during the K-Pg is further exemplified within sharks and batomorphs, with some orders being strongly affected (Lamniformes and Orectolobiformes) and even coming close to complete extinction (Rajiformes and Rhinopristiformes), and others (Carcharhiniformes, Hexanchiformes, and Squaliformes) showing no marked shifts in extinction rates (figs. S8 to S16). We found similar patterns of extinction heterogeneity with analyses at the genus level (figs. S17 to S25) (*15*). Furthermore, some clades (lamniforms and hexanchiforms) appear to experience a declining phase (negative net diversification) before the K-Pg event, whereas others (rajiforms and orectolobiforms) show a sudden increase in extinction rates although they were previously in a diversification phase. Comparisons of global-scale extinction patterns with regional data are hampered by the rarity of fine-scale samplings from geological sections including the K-Pg boundary. Our results

Institut des Sciences de l'Évolution de Montpellier, Université de Montpellier, CNRS, IRD, EPHE, Place Eugène Bataillon, 34095 Montpellier, France.
*Corresponding author. Email: guillaume.guinot@umontpellier.fr

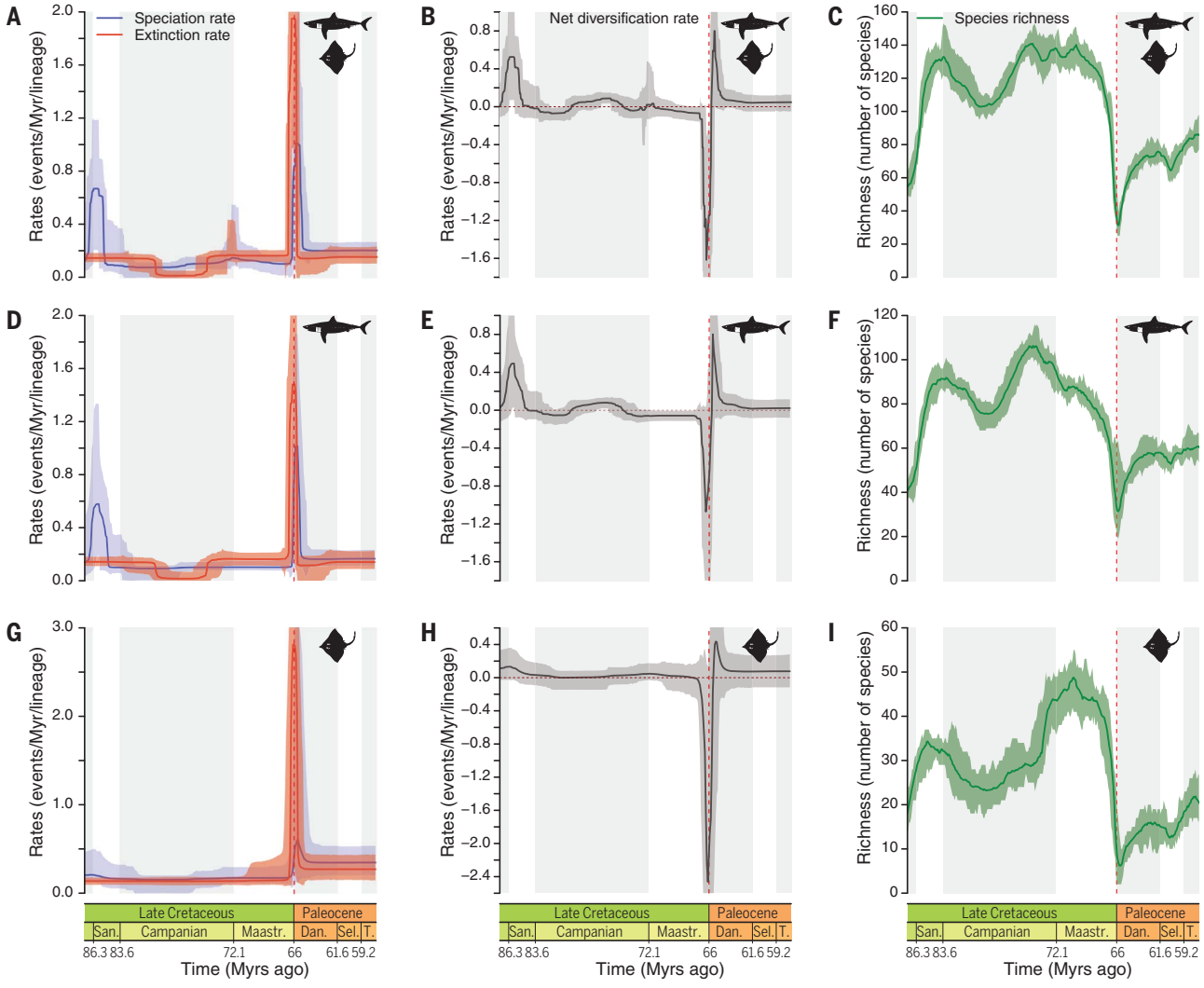

Fig. 1. Diversification and diversity dynamics of elasmobranchs (sharks, rays, and skates) across the K-Pg mass extinction. Bayesian inferences of temporal variations of speciation and extinction rates, net diversification rates (speciation minus extinction), and number of species for all elasmobranchs (**A** to **C**), sharks (**D** to **F**), and rays and skates (**G** to **I**). Extinction rates [(A), (D), and (G)] increase sharply at the K-Pg boundary (red dashed vertical line), with significant rate shifts determined by log BF > 6 (figs. S1, S6, and S7). Net diversification rates [(B), (E), and (H)] become strongly negative during the K-Pg event, reaching 1.95 extinction events per lineage per million years for all elasmobranchs (Table 1, details). The number of species through time [(C), (F), and (I)] quickly drops at the K-Pg boundary, particularly for rays and skates, and we did not find evidence for a postextinction recovery until the end of the Paleocene. Similar trends are found at the genus level (figs. S23 to S25). San., Santonian; Maastr., Maastrichtian; Dan., Danian; Sel., Selandian; T., Thanetian.

are congruent with the only such analysis of elasmobranch faunas in Denmark (*17*), in which squaliforms and carcharhiniforms are less affected than other clades, whereas neither of the two recorded batomorph species cross the boundary.

Ecological selectivity at the K-Pg extinction

Taxonomic-level analyses of extinctions provide partial insights into the aftermath of past extinction events over the functioning of paleoecosystems, especially in the case of clades including taxa with a large array of ecologies. The ecological patterns of diversification and extinction events can be decoupled from the associated increase or loss of taxa (*18*). We therefore complemented our estimates of paleodiversity with an approach that used phenotypic traits linked with broad feeding preferences to test for the ecological selectivity of the K-Pg extinction. The elasmobranch fossil record is mainly represented by teeth, which are the main elements involved in the processing of food items (*13*). We separated our dataset into two dental categories (*15*), termed ecomorphotypes: durophagous and nondurophagous. The durophagous group includes all taxa whose teeth display a crushing or grinding component in their morphology and encompasses taxa capable of consuming prey with hard exoskeletons such as shelled molluscs and crustaceans (for example, many skates and rays, heterodontiforms, the extinct ptychodontiforms, some orectolobiforms, and few carcharhiniforms). This group was further divided into two more ecomorphotypes to differentiate the degree of specialization to durophagy from generalist durophagous (crushing type) to specialized durophagous (crinding type). The nondurophagous group includes taxa with cuspidate teeth that display a wide range of tooth sizes and likely encompasses species with different ecologies (*15*). We categorized nondurophagous

Table 1. Impact of the K-Pg event on the diversity of sharks and rays. We identified when the extinction rate upshifted before and downshifted after the K-Pg extinction based on log Bayes factors > 6 (*15*). Times of upshift and downshift determine the duration of the extinction event. We obtained the mean diversity (species or genus) at the upshift and calculated the number of victims (species or genus) between upshift and downshift times (no taxa originate in this time interval), which both allow computing the percentage of extinction (number of victims over mean diversity). The estimations of extinction rates during the K-Pg event show the magnitude of the event and its heterogeneity among elasmobranchs.

Clade	Taxonomic level	Mean diversity before extinction	Number of victims during extinction time	Percentage of extinction	Extinction rate (events/Myr/lineage)
All elasmobranchs	Species	92.6	58	62.63	1.95 (0.98–2.97)
	Genus	89	40	44.94	1.14 (0.53–1.85)
All sharks	Species	59.4	35	58.92	1.48 (0.16–2.26)
	Genus	58.5	17	29.06	0.05 (0.02–0.76)
All rays	Species	30.3	22	72.61	2.80 (0.31–5.812)
	Genus	24.5	21	85.71	1.13 (0.11–2.75)
All durophagous	Species	43.6	32	73.39	3.55 (1.33–5.93)
	Genus	42.7	26	60.89	1.17 (0.245–2.43)
All nondurophagous	Species	43.5	26	59.77	1.25 (0.16–2.19)
	Genus	49.4	13	26.32	0.05 (0.021–0.31)

species into three classes (small, medium, and large) based on measurement of tooth crown height (data S1) (*15*) on the basis of previous work (*19*).

Our results suggest strong ecological selectivity, with durophagous species being much more affected than nondurophagous species ($t = 10.663$, df = 5.23, $P = 9.566 \times 10^{-5}$) (Fig. 2, Table 1, and figs. S26 to S32), and this contrast is even more marked based on genus-level data (Table 1 and figs. S33 to S39). Extinction rates for durophagous species exceed those of batomorphs, indicating that durophagous sharks and batomorphs responded similarly to extinction (Table 1). Conversely, nondurophagous species show a less sharp diversity loss at the K-Pg boundary. Our results suggest an increase in species extinction during the end Campanian–Paleocene interval for small- and medium-sized species, with a weak peak around 66 Ma, and relatively stable extinction for large species. Furthermore, our results support ecological selectivity of the K-Pg event against species that relied on lower parts of the food web. Growing evidence points to high levels of extinction at the bottom of marine food webs linked with strong upheavals in the biogeochemical cycling of the oceans (*20*–*22*). The high extinction rates of durophagous elasmobranchs indicate that the huge diversity loss of primary producers and consumers directly affected elasmobranchs that relied on hard-shelled invertebrates. More generalist shark clades seem less affected, whether they are adapted to deep or cool environments (squaliforms) or not (carcharhiniforms), and large sharks taken together do not show marked extinction. This suggests decreasing extinction intensity toward mesopredators. Lamniformes are probably the only strictly nondurophagous clade that show an increase in extinction rates at the K-Pg boundary. The lamniform extinction pattern is not recovered in our ecomorphological datasets (especially the medium and large categories), which suggests a distinct response of this clade to the K-Pg extinction. Nevertheless, lamniforms represent 90% of large and 83% of medium species that went extinct at the K-Pg. Late Cretaceous lamniforms are meso- to top predators that display a wide range of strong ecological specializations (*19*), which likely makes them more prone to extinction (*23*). Lamniforms were probably strongly hit by the K-Pg event because of a high trophic position and dietary specialization, which is consistent with the pattern found for marine actinopterygians (*12*, *24*). We therefore highlight the bottom-up trophic dynamics of the K-Pg extinction in elasmobranchs, but with lower extinction among generalist mesopredators.

Heterogeneous age-dependent extinction between sharks and rays

During a mass extinction, the law of constant extinction can be broken (*25*). Studying marine invertebrate groups generally points to age-dependent extinction (*26*), such that recently originated species turn over faster than old species, indicating evidence of taxon selectivity for survival. We fitted a Bayesian age-dependent extinction model to estimate the probability of extinction to be dependent on taxon age (*15*). Analyzing all elasmobranchs, we found higher extinction rates in old species than in young species in the Maastrichtian ($\phi = 3.5092$, 95% CI 1.5442 to 6.7414), whereas there is no effect in pre- and post-Maastrichtian times (table S2). Separating sharks and rays, we found higher extinction rates in old shark species than in young shark species in the Maastrichtian ($\phi = 4.6602$, 95% CI 1.2691 to 14.3273) and no effect in pre-Maastrichtian and Paleocene, whereas batomorph species show no age-dependent extinction in all time intervals (table S2). Shark species with long temporal ranges show higher extinction,

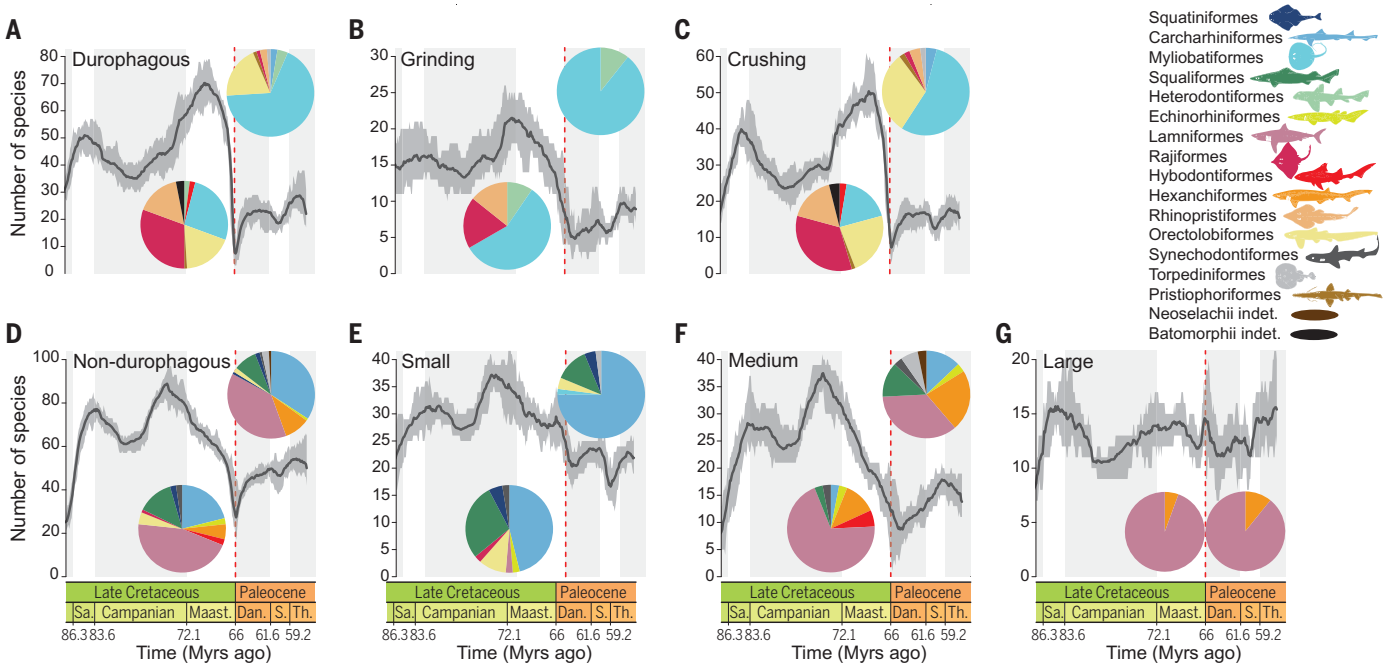

Fig. 2. Evolution of species richness among dental ecomorphotypes across the K-Pg boundary. Estimated paleodiversity variations are represented by the gray curves (mean richness) and associated gray shadings (95% CI) for all durophagous (**A**), Grinding (**B**), Crushing (**C**), all nondurophagous (**D**), small nondurophagous (**E**), medium nondurophagous (**F**), and large nondurophagous (**G**) ecomorphotypes. Pie charts represent clade contribution to the species diversity of each ecomorphotype before (Maastrichtian) and after (Paleocene) the K-Pg event (figs. S43 to S45 and tables S13 and S14) (*15*), which is represented by the red dashed vertical lines. Sa., Santonian; Maastr., Maastrichtian; Dan., Danian; S., Selandian; Th., Thanetian.

suggesting a lack of evolutionary novelty or poor fitness to a rapidly changing environment, which is consistent with the results that some shark clades were in decline before the K-Pg event (for example, lamniformes and hexanchiformes).

Geographic selectivity at the K-Pg extinction

One of the characteristics of mass extinctions is that they are geographically widespread (*27*), as opposed to background extinctions (*28*), although they do not require that high extinction be uniform at global scale (*4*). We compiled the latest (mostly Maastrichtian) geographic occurrences before the K-Pg extinction for genera that survived the K-Pg event and for those that went extinct (data S1 and S2). We performed paleogeographic coordinate reconstructions (*29*) for each of the 822 genus-level occurrences fitting these criteria in our dataset and computed three geographic range measures using standardized numbers of geographic occurrences per genus (*15*). We found significantly larger mean paleogeographic ranges for surviving genera than for extinct genera (table S3) (*15*), which supports a positive relationship between large geographic range and survival for elasmobranchs during the K-Pg event. Furthermore, we found that genera restricted to lower paleolatitude settings show much lower survival than their high-paleolatitude congeners, regardless of the splitting value between high and low latitudes (Fig. 3A). This biogeographic selectivity is also recovered when singletons are excluded from the analysis and held after various sensitivity tests (tables S4 to S6) (*15*). Although this pattern is also found for durophagous and nondurophagous genera separately (tables S7 to S10), the high proportion of durophagous taxa in lower-latitude settings provides clues to the higher extinction of durophagous species recovered in our analyses (Fig. 3B). This result suggests either that high-latitude settings were more resistant to extinction or that the intensity of the K-Pg upheavals decreased from low to high latitudes. Such a biogeographic selectivity toward the higher survival of high-latitude taxa has rarely been reported for the K-Pg event (*30*). This extinction pattern was reported for bivalves (*8*) and other benthic invertebrates (*31*), which likely represented main prey items of durophagous elasmobranchs. We therefore tested for a potential link between diversification of durophagous elasmobranchs and bivalve diversity along with six abiotic proxies across the 83.6- to 57-Ma time interval. We used a multivariate birth-death model to simultaneously evaluate correlations with explanatory variables and diversification processes of durophagous species (*15*). Among seven

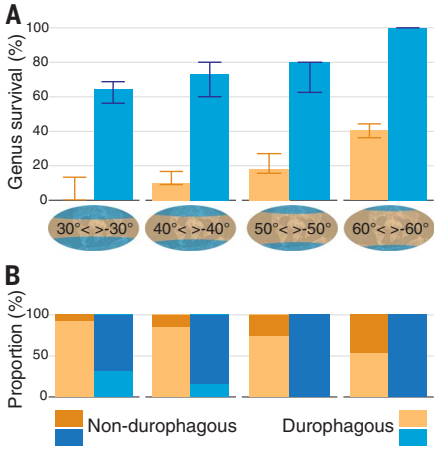

Fig. 3. The paleolatitudinal pattern of elasmobranch genus extinction and survival at the K-Pg event. (**A**) Histograms represent the proportion (median) of survival for genera occurring exclusively in low (orange) and high latitudes (blue) according to four values splitting high- and low-latitude settings (table S4) (*15*) as represented on paleomaps. Orange and blue bars indicate range between minimum and maximum values. (**B**) Proportion of nondurophagous (dark orange and blue) and durophagous (light orange and blue) genera in higher- and lower-latitude settings (table S9). Paleomaps shows K/Pg paleogeography (used with permission, 2020 Colorado Plateau Geosystems Inc.).

tested variables, we found that extinction rates of durophagous species are mainly explained by the diversity dynamics of bivalves (figs. S40 to S42 and table S11) (*15*), such that drops in bivalve diversity led to higher extinction in durophagous species. Comparing the contribution of elasmobranch orders with the ecomorphotypes (Fig. 2, figs. S43 to S45, and tables S12 and S13) further highlights the effects of the K-Pg extinction over the evolution of the ecological structure of global elasmobranch communities. We show that this event produced a major shift in the proportion of elasmobranch clades within the durophagous ecomorphotype. Our data indicate high proportions of durophagous rajiforms (especially the extinct Sclerorhynchoidei) and rhinopristiforms in the Maastrichtian, whereas the contribution of these clades to the durophagous ecomorphotype is inconspicuous in the Paleocene. Conversely, the proportion of durophagous myliobatiforms strongly increases in the post–K-Pg. This suggests that the strong extinction suffered by rajiforms and rhinopristiforms freed ecological niches, which were subsequently filled by the myliobatiforms (especially dasyatoids) in the Paleocene. The K-Pg extinction also affected the ecological equilibrium in nondurophagous elasmobranchs, most notably through an increase in the proportion of small carcharhiniforms in the postextinction fauna. The dominance of small carcharhiniforms in the Paleocene occurred mainly at the expense of squaliforms, whose diversity shifted toward medium-sized nondurophagous in the Paleocene. Similarly, the hexanchiforms, another clade that adapted to cool or deep environments, also increased in proportion among medium-sized and, to a lesser extent, large nondurophagous categories.

Postextinction recovery

Post–K-Pg recovery was more rapid for sharks and particularly for nondurophagous taxa (table S14). However, our analyses point to a delayed recovery of durophagous elasmobranchs, which did not reach pre–K-Pg diversity during the Paleocene and account for a lower proportion of the total Paleocene fauna (tables S12 and S13 and fig. S43) than in the Maastrichtian (40 versus 52%). Previous works showed a slow post–K-Pg recovery in marine bivalves (*32*), and results of our multivariate birth-death analyses indicate that the pattern for durophagous elasmobranchs is probably due to a lagged recovery in primary consumers. Conversely, although lamniforms suffered high extinction, they account for a large proportion of nondurophagous postextinction elasmobranchs, which supports the rapid turnover for this clade (*19*). Taken together, our results point to a role of the K-Pg event in reshaping the taxonomic composition of the main elasmobranch ecologies along with a long-term lag in recovery for hard-shell prey consumers.

Profile for extinction risks

Extant elasmobranchs are facing strong human-driven pressures leading to high extinction risk for most species (*33*). Understanding how this clade responded to past mass extinctions helps identify the features of extinction victims and survivors. Our analyses provide a profiling of extinction victims during the K-Pg event in which batomorphs, durophagous, and strictly low-latitude species with restricted geographic ranges, as well as old shark species, show higher extinction rates than other elasmobranch species. We further report a lagged recovery of durophagous species associated with a deep restructuring of clade contributions within this ecomorphotype. Causal hypotheses for the K-Pg mass extinction are still debated. Whereas some data suggest a primary role of bolide impact (*2*), others support a combined effect of the latter with longer-term climatic upheavals and massive volcanism (*3*). The elasmobranch extinction pattern reported here cannot reject any of these hypotheses, but it provides important clues on the putative causal mechanisms of the K-Pg extinction.

REFERENCES AND NOTES

1. N. MacLeod *et al.*, *J. Geol. Soc. London* **154**, 265–292 (1997).
2. P. Schulte *et al.*, *Science* **327**, 1214–1218 (2010).
3. J. D. Archibald *et al.*, *Science* **328**, 973–973 (2010).
4. R. H. Bambach, *Annu. Rev. Earth Planet. Sci.* **34**, 127–155 (2006).
5. S. M. Stanley, *Proc. Natl. Acad. Sci. U.S.A.* **113**, E6325–E6334 (2016).
6. J. F. Hoyal Cuthill, N. Guttenberg, G. E. Budd, *Nature* **588**, 636–641 (2020).
7. P. Bown, *Geology* **33**, 653–656 (2005).
8. D. A. Vilhena *et al.*, *Sci. Rep.* **3**, 1790 (2013).
9. S. Jiang, T. J. Bralower, M. E. Patzkowsky, L. R. Kump, J. D. Schueth, *Nat. Geosci.* **3**, 280–285 (2010).
10. R. B. J. Benson, R. J. Butler, J. Lindgren, A. S. Smith, *Proc. Biol. Sci.* **277**, 829–834 (2010).
11. J. Kriwet, M. J. Benton, *Palaeogeogr. Palaeoclimatol. Palaeoecol.* **214**, 181–194 (2004).
12. G. Guinot, L. Cavin, *Biol. Rev. Camb. Philos. Soc.* **91**, 950–981 (2016).
13. H. Cappetta, *Chondrichthyes - Mesozoic and Cenozoic Elasmobranchii: Teeth*, vol. 3E of *Handbook of Paleoichthyology* (Verlag F. Pfeil, 2012).
14. D. Silvestro, N. Salamin, A. Antonelli, X. Meyer, *Paleobiology* **45**, 546–570 (2019).
15. Materials and methods available as supplementary materials.
16. M. Friedman, L. C. Sallan, *Palaeontology* **55**, 707–742 (2012).
17. J. S. Adolfssen, D. J. Ward, *Palaeontology* **57**, 591–629 (2014).
18. G. R. McGhee Jr., M. E. Clapham, P. M. Sheehan, D. J. Bottjer, M. L. Droser, *Palaeogeogr. Palaeoclimatol. Palaeoecol.* **370**, 260–270 (2013).
19. F. L. Condamine, J. Romieu, G. Guinot, *Proc. Natl. Acad. Sci. U.S.A.* **116**, 20584–20590 (2019).
20. S. D'Hondt, *Annu. Rev. Ecol. Evol. Syst.* **36**, 295–317 (2005).
21. H. K. Coxall, S. D'Hondt, J. C. Zachos, *Geology* **34**, 297–300 (2006).
22. S. A. Alvarez *et al.*, *Nature* **574**, 242–245 (2019).
23. A. Purvis, J. L. Gittleman, G. Cowlishaw, G. M. Mace, *Proc. Biol. Sci.* **267**, 1947–1952 (2000).
24. M. Friedman, *Proc. Natl. Acad. Sci. U.S.A.* **106**, 5218–5223 (2009).
25. L. Van Valen, *Evol. Theory* **1**, 1–30 (1973).
26. D. Silvestro *et al.*, *Ecol. Lett.* **23**, 439–446 (2020).
27. J. J. Sepkoski, in *Patterns and Processes in the History of Life*, D. M. Raup, D. Jablonski, Eds. (Springer Berlin Heidelberg, 1986), *Dahlem Workshop Reports*, pp. 277–295.
28. J. L. Payne, S. Finnegan, *Proc. Natl. Acad. Sci. U.S.A.* **104**, 10506–10511 (2007).
29. R. D. Müller *et al.*, *Geochem. Geophys. Geosyst.* **19**, 2243–2261 (2018).
30. N. MacLeod, G. Keller, *Paleobiology* **20**, 143–177 (1994).
31. Á. T. Kocsis, C. J. Reddin, W. Kiessling, *Proc. Biol. Sci.* **285**, 20180232 (2018).
32. D. Jablonski, K. Roy, J. W. Valentine, R. M. Price, P. S. Anderson, *Science* **300**, 1133–1135 (2003).
33. N. K. Dulvy *et al.*, *Curr. Biol.* **31**, 5118–5119 (2021).

ACKNOWLEDGMENTS

This project benefited from the Montpellier Bioinformatics Biodiversity platform for the analyses. We thank P. Ricard and J. Lagavulin for their support during this work and thank three anonymous reviewers for their helpful comments. **Funding:** No fundings supported this work. **Author contributions:** G.G. and F.L.C. designed and coordinated the research program; G.G. and F.L.C. set up the methodology; G.G. acquired the fossil data; G.G. and F.L.C. performed the analyses; and G.G. and F.L.C. wrote the original draft and reviewed and edited the text. **Competing interests:** The authors declare no competing interests. **Data and materials availability:** All data are available in the manuscript or in the supplementary materials.

License information: Copyright © 2023 the authors, some rights reserved; exclusive licensee American Association for the Advancement of Science. No claim to original US government works. https://www.science.org/about/science-licenses-journal-article-reuse

SUPPLEMENTARY MATERIALS

science.org/doi/10.1126/science.abn2080
Materials and Methods
Supplementary Text
Figs. S1 to S50
Tables S1 to S14
References (*34–113*)
MDAR Reproducibility Checklist
Data S1 to S3

Submitted 18 November 2021; resubmitted 7 September 2022
Accepted 26 January 2023
10.1126/science.abn2080

PLASTIC UPCYCLING

Low-temperature upcycling of polyolefins into liquid alkanes via tandem cracking-alkylation

Wei Zhang[1]*, Sungmin Kim[2], Lennart Wahl[1], Rachit Khare[1], Lillian Hale[2], Jianzhi Hu[2], Donald M. Camaioni[2], Oliver Y. Gutiérrez[2], Yue Liu[1,3]*, Johannes A. Lercher[1,2]*

Selective upcycling of polyolefin waste has been hampered by the relatively high temperatures that are required to cleave the carbon-carbon (C–C) bonds at reasonably high rates. We present a distinctive approach that uses a highly ionic reaction environment to increase the polymer reactivity and lower the energy of ionic transition states. Combining endothermic cleavage of the polymer C–C bonds with exothermic alkylation reactions of the cracking products enables full conversion of polyethylene and polypropylene to liquid isoalkanes (C_6 to C_{10}) at temperatures below 100°C. Both reactions are catalyzed by a Lewis acidic species that is generated in a chloroaluminate ionic liquid. The alkylate product forms a separate phase and is easily separated from the reactant catalyst mixture. The process can convert unprocessed postconsumer items to high-quality liquid alkanes with high yields.

Plastic is ubiquitous in products that range from packaging and textiles to medical equipment and vehicle components (*1*). More than 360 million tonnes per year (estimated 3 to 4% of the total carbon processed per year) of plastic is produced globally, and most of the disposed plastic accumulates in landfills or is dispersed into water bodies (*2*, *3*). The chemically inert polyolefins, which amount to more than half of all plastics, are challenging to convert below their melting or softening point (*4*). At the present time, recycling technologies are still dominated by mechanical recycling and thermal conversion (incineration and pyrolysis) (*5*, *6*). As a consequence, catalytic upgrading of polyolefin waste into fuels and value-added chemicals has seen substantial research attention, and exciting solutions based on multifunctional catalysts have been emerging (*7*).

Conversion of waste polyolefins is particularly challenging because of the $C(sp^3)$–$C(sp^3)$ bonds, which are more stable than the C-heteroatom bonds of functionalized polymers such as polyesters and polyamides (*8*). Additionally, the endothermic cleavage of the C–C bonds renders processes thermodynamically unfavorable at low temperatures. As a result, converting polyolefins typically requires severe reaction conditions to overcome the kinetic and thermodynamic constraints (*9*). This has been addressed in recent pioneering contributions through the integration of the endothermic C–C cleavage with exothermic reactions—including hydrogenolysis (*10*–*13*), cross-metathesis (*14*, *15*), and aromatization (*16*)—which achieves conversions beyond the equilibria for cracking (fig. S1).

Thermodynamically balancing the exothermic and endothermic kinetically coupled reactions, however, is insufficient to allow for industrially compatible rates below 100°C. The stability of C–C bonds and steric and diffusional barriers that limit the contact of polymer strands with catalytically active sites lead to very slow rates (*17*). As a consequence, most tandem processes require moderate to high reaction temperatures (typically 200° to 250°C) and diverse catalyst functions for relevant conversion rates; these processes lack precise spatiotemporal control over reactive intermediates among catalytic sites (*18*) and complicate product separation and catalyst recovery (*19*). Approaches that would allow selective conversions at substantially lower temperatures would facilitate reactive polymer recycling and open possibilities for decentralized catalytic upgrading.

To achieve this, we turn to coupling cracking of the polymer with alkylation of the formed alkenes by light isoparaffins [isobutane and isopentane (iC_5)]. At present, the refining process is used to produce triple-branched alkanes with a high octane number, which are used in high-octane gasoline (*20*). Conceptually, linking the endothermic

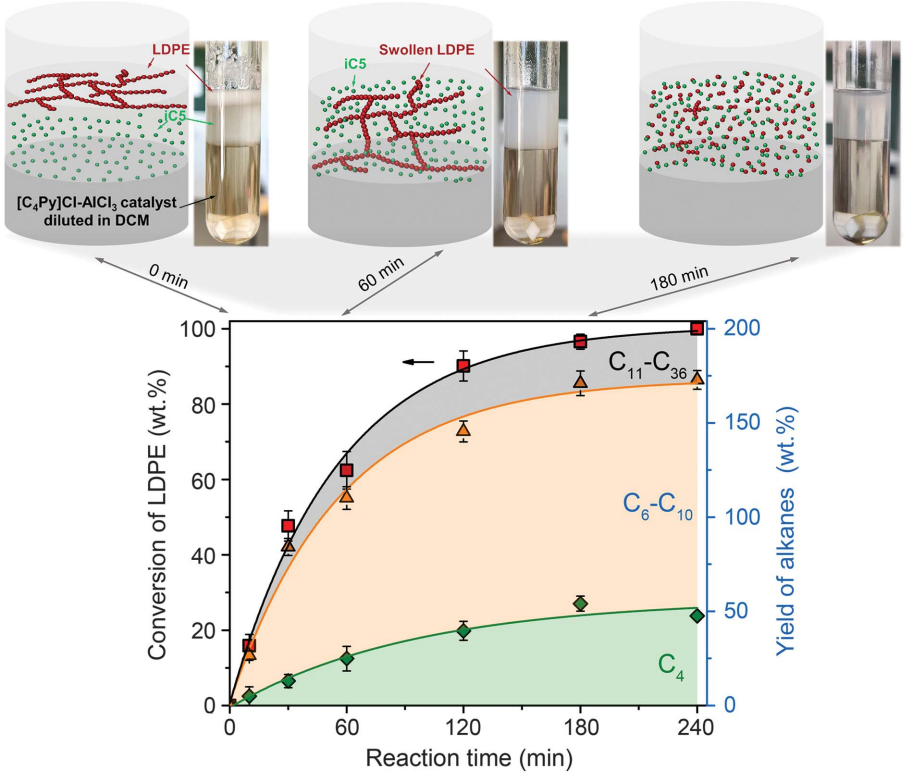

Fig. 1. One-pot catalytic LDPE and iC_5 upcycling into liquid alkanes over Lewis acidic chloroaluminate ionic liquid at 70°C. The time-resolved conversion profile of LDPE and cumulative yield of alkanes (C_4, green diamonds; C_6 to C_{10}, orange triangles; C_{11} to C_{36}, red squares) (bottom). Reaction conditions were as follows: LDPE, 200 mg; iC_5, 800 mg; $[C_4Py]Cl\text{-}AlCl_3$ ($[C_4Py]Cl:AlCl_3$ molar ratio of 1: 2), 3 mmol; TBC as an additive, 0.05 mmol (5 mg); DCM, 3 ml; and temperature, 70°C. The snapshots of the LDPE conversion (top) are at 0, 60, and 180 min from left to right. Curves represent the optimal fit to the data, and all data were repeated at least five times and are shown as mean data points with error bars.

[1]Department of Chemistry and Catalysis Research Center, Technische Universität München, Lichtenbergstr. 4, 85747 Garching, Germany. [2]Institute for Integrated Catalysis, Pacific Northwest National Laboratory, PO Box 999, Richland, WA 99352, USA. [3]Shanghai Key Laboratory of Green Chemistry and Chemical Processes, School of Chemistry and Molecular Engineering, East China Normal University, Shanghai 200062, PR China.
*Corresponding author. Email: w.zhang@tum.de (W.Z.); liuyue@chem.ecnu.edu.cn (Y.L.); johannes.lercher@ch.tum.de (J.A.L.)

cleavage of the polymer C–C bonds to the exothermic alkylation of isoparaffins (i.e., alkylation of the primary alkenes formed from the C–C cleavage by using paraffins whose carbon atoms are retained in the products) couples the two reactions kinetically and, hence, thermodynamically allows full conversion of the polymer below 100°C. All of these reactions are posited to share carbenium ions as intermediates (*21*), which means that they can operate simultaneously within the same medium and with the same catalyst. We showed recently that a highly polar reaction environment strongly increases the standard chemical potential and reactivity of a nonionic reactant (the polymer in this case) and stabilizes the carbenium ion transition states, thereby lowering the overall free-energy barrier of the coupled reactions and notably enhancing reactivity (*22*, *23*).

Combining the concurrent tandem catalysis of cracking-alkylation and polarity-tailored reactant environments, we report here a strategy for the catalytic upgrading of discarded polyolefins and isoparaffins (recycled from the light end of products formed in the process) into gasoline-range alkanes in a single stage. The process enables the upcycling of waste polyethylene with full conversion at 70°C to a narrow distribution of branched liquid alkanes (C_6 to C_{10}) on Lewis acidic chloroaluminate ionic liquid [which is being used as the source of the alkylation catalyst species (*24*)]. Besides its function in generating the active sites, the presence of the high concentration of ions in the ionic liquid is critical for the high conversion rate of the polyolefin at such low temperatures; it not only stabilizes carbenium ions as intermediates, thereby determining the overall reaction rate in the cracking-alkylation reaction, but also allows for easy separation of nonpolar alkane products from the reaction medium.

To visualize the conversion, experiments in glass-tube reactors using commercial low-density polyethylene (LDPE; weight-averaged molecular weight of ~4000, number-averaged molecular weight of ~1700) and iC_5 as substrates (the latter would be replaced by low–molecular weight, branched product alkanes in translation to a semicontinuous process) are shown as examples in Fig. 1. The Lewis acidic chloroaluminate ionic liquid consists of *N*-butylpyridinium chloride and anhydrous $AlCl_3$ in a 1:2 molar ratio and is diluted in the present experiments in dichloromethane (denoted as $[C_4Py]Cl\text{-}AlCl_3$; see the materials and methods for details). The liquid catalyst, together with iC_5, led to complete LDPE conversion at 70°C after 3 hours in the presence of small amounts of *tert*-butyl chloride (TBC) to provide an initial concentration of carbenium ions to start the chain process. The yield of alkane products (C_4 to C_{36}) was twice as high as the amount of LDPE converted, reaching ~200 wt % (this suggests that, on average, an alkene with five C atoms is added relative to initial LDPE, and the stoichiometric mass ratio of LDPE/iC_5 was 1:1; see details in fig. S2); these products were present in the organic phase at the top, which was separated from the inorganic ionic liquid phase at the bottom. The main products were highly branched C_6 to C_{10} liquid alkanes (identified by gas chromatography–mass spectrometry in fig. S3), which accounted for ~126 wt % yield. Other products were gaseous isobutane (iC_4, ~48 wt %) and large alkanes (C_{11} to C_{36}, ~27 wt %). We found only traces of propane and propene (<0.1 wt %) in the headspace (fig. S4). The absence of methane and ethane allows us

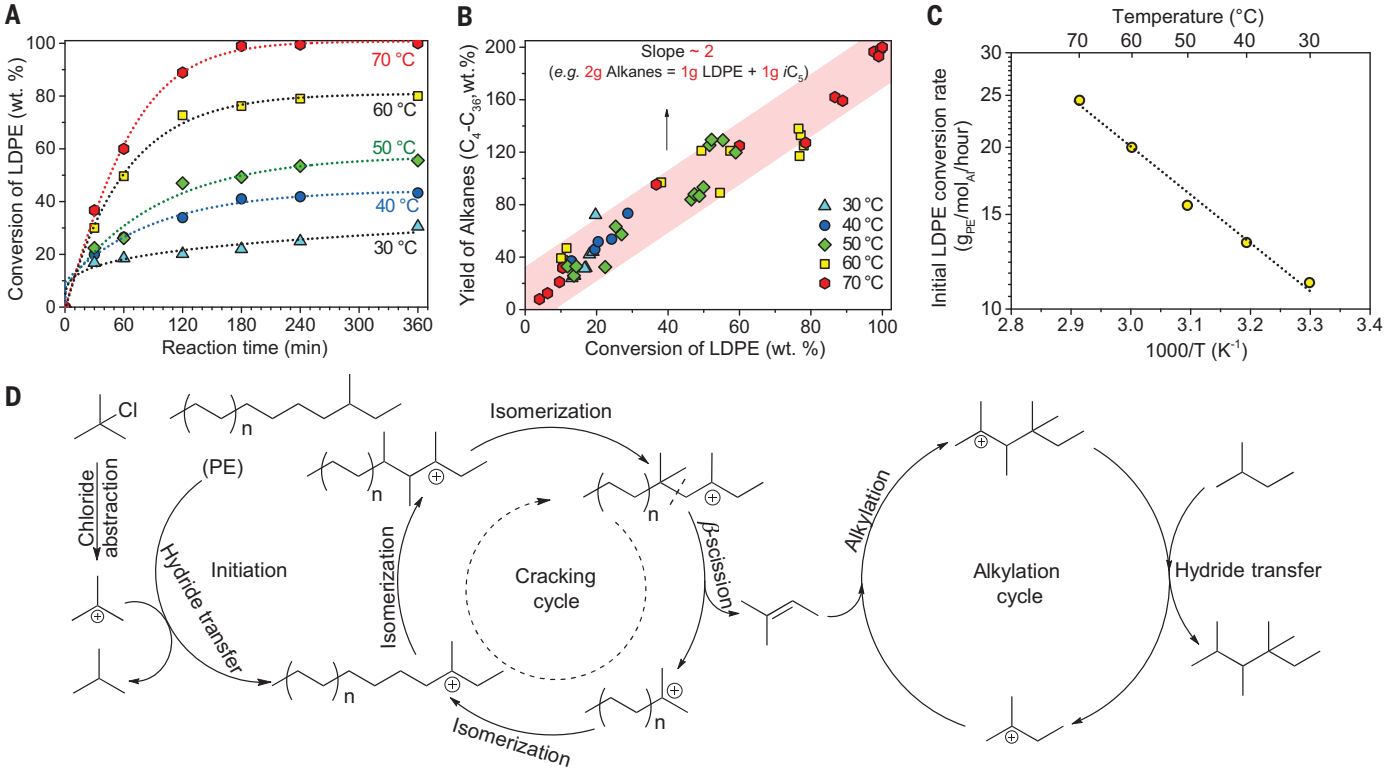

Fig. 2. Low-temperature catalytic performance for LDPE to alkanes and proposed reaction mechanism. (**A**) Time-resolved conversion profile of LDPE in the presence of TBC at different temperatures. Curves represent the optimal fit to the data, and all data were repeated at least five times and are shown as mean data points. (**B**) The corresponding mass yield to alkanes (C_4 to C_{36}) plotted against LDPE conversion. Reaction conditions were as follows: LDPE, 200 mg; iC_5, 800 mg; $[C_4Py]Cl\text{-}AlCl_3$, 3 mmol; TBC, 0.05 mmol; DCM, 3 ml; and temperature, 30° to 70°C. The red-shaded region represents a general linear fit to the data and is used to guide the eye. (**C**) Arrhenius plot for LDPE conversion with initial rates normalized to the aluminum content. (**D**) Proposed reaction mechanism for the tandem cracking-alkylation process of a polyolefin with iC_5. The 2-methyl-butene formed in the cracking cycle is depicted as an example that is based on the ratio of the molecular weight of the carbon products, which suggests that the ratio of converted LDPE and iC_5 is about 1:1 in the reaction, as deduced from Fig. 2B. PE, polyethylene.

to conclude that the reaction occurs overwhelmingly via carbenium ions and does not involve C–C cleavage via carbonium ions (figs. S5 and S6).

The control experiment with LDPE in the absence of iC_5 resulted in only 28 wt % LDPE conversion and produced a red-orange liquid with gaseous products that dominated the product distribution (~39 wt % isobutane and ~26 wt % pentane; see fig. S7). The yield of liquid alkanes in the range of C_6 to C_{10} was only 15 wt % (i.e., lower than the 61 wt % that was observed in the presence of iC_5), whereas the yield of large hydrocarbons (C_{11} to C_{36}) was as high as 20 wt %. In the absence of iC_5, olefinic hydrocarbons likely interact with the chloroaluminate anions, which deactivates the catalyst and yields adamantanes and acid-soluble conjunct polymers (so-called "red oil") (fig. S8) (*25*). In the presence of iC_5, alkanes were preferentially formed and accumulated in the iC_5-containing phase, separated in this way from the polar [ionic liquid with dichloromethane (DCM)] phase. Thus, iC_5 acts as an alkylating agent to form an alkane mixture, which resembles that of an isobutane or *n*-butene alkylation in the refining industry (*24*).

Because $[C_4Py]Cl\text{-}AlCl_3$ ionic liquid contains both Lewis and Brønsted acid sites (fig. S9A), the question arises whether the catalysis follows a reaction pathway that combines carbenium ion formation and sequential reactions catalyzed solely by Lewis acid sites or a reaction pathway that combines the carbonium ions formed by Brønsted acids with sequential reactions of carbenium ions (*26*). Carbenium ions are formed from alkanes at Lewis acid sites via hydride abstraction, whereas strong Brønsted acid sites form carbonium ions on the polymer strands that may crack or eliminate H_2 to form carbenium ions (*27*).

To discern the potential reaction pathways, we added co-reagents, including protic compounds [H_2O and CF_3COOH to generate carbonium ions (*28*)] and TBC [to generate carbenium ions (*29*)]. Adding protic co-reagents did not change the reaction rates or the product distribution compared with the reaction in their absence (see fig. S9B). Although traces of H_2 evolved, other products of protolytic cracking such as methane or ethane were completely absent. Thus, we rule out Brønsted acids and carbonium ions as the pathway to form carbenium ions. By contrast, adding TBC substantially enhanced the initial reaction rate by at least one order of magnitude and led to a nearly full conversion after 180 min, whereas only 20% was converted in its absence (fig. S9, B and C). The nature of the initiator did not markedly influence the rate of reaction (fig. S10, A and B). Control experiments using *n*-hexadecane as a model for LDPE reacting with iC_5 led to an identical enhancement (fig. S10, C and D). Thus, we conclude that most of the carbenium ions are initiated via hydride abstraction from polymer strands by *tert*-butyl carbenium ions formed from TBC, with the reaction propagating via a carbenium ion chain mechanism (*29*). The high reaction rate is determined by the rate of polymer cracking via a carbenium ion chain mechanism, and the faster alkylation of intermediately formed alkenes with an isoalkane (eventually from the light fraction of the products) shifts the equilibrium such that full conversion is possible.

Temperature-dependent experiments (Fig. 2A) showed that the LDPE conversion increased from 20 to 90% after a 2-hour reaction time, when the reaction temperature was raised from 30° to 70°C. The yield of alkanes points to an overall single alkylation step, which leads to a yield of products that is approximately twice the mass of LDPE converted (Fig. 2B). In return, such an average product yield indicates that the average size of the intermediately formed alkene is close to pentene, followed by alkylation with iC_5 to yield decane isomers (fig. S11A). Actually, the main products are branched alkanes, with an average carbon number of ~8.4, which is lower than the theoretical value of 10. The lower carbon production represents higher H/C ratios, which means that the competing cyclization occurs and produces some polycyclic alkanes and acid-soluble oil with decreased H/C ratios. Evidently, the detected cyclohexanes and adamantanes as by-products (fig. S11B) agree well with this trend.

Figure 2C shows the logarithmic dependence of the initial rate of LDPE conversion on the inverse temperature; from this, the apparent activation energy of the overall reaction was 17 ± 2 kJ/mol, which is much lower than the reported apparent activation barriers (163 to 303 kJ/mol) for the depolymerization of polyethylene so far (*19*). We also studied different isoalkanes using iC_4 and iC_6 as alkylating components for LDPE upcycling, which reached nearly 100 wt % of LDPE conversion and yielded branched alkanes (linear alkanes are negligible) under optimal conditions (fig. S12). This result demonstrates the practicability of recycling the lighter alkane product, that is, using iC_4 and iC_5 as the alkylation agents (details of recycling of light isoparaffins are given below).

To account for the tandem reaction proceeding with a constant rate, we posit two (independent) linked catalytic cycles based on carbenium ions, with cracking-derived alkenes serving as the linking intermediates (Fig. 2D). The fundamental differences in the reactivity dictate that in the initial stage of the reaction, hydride transfer from both the isoalkanes and the polyolefin dominates. As the reaction progresses, cracking of the polymer strands becomes predominantly associated with the cooperative action of alkylation. Thus, overall, the observed rates and product distributions are well explained by the two catalytic cycles depicted in Fig. 2D. The reaction is initiated by chloride abstraction from TBC. The formed carbenium ions abstract a hydride, preferentially from tertiary carbon atoms, both at branches in the polymer and in the more abundant iC_5. The carbenium ions formed in the polymer strands tend to undergo skeletal isomerization

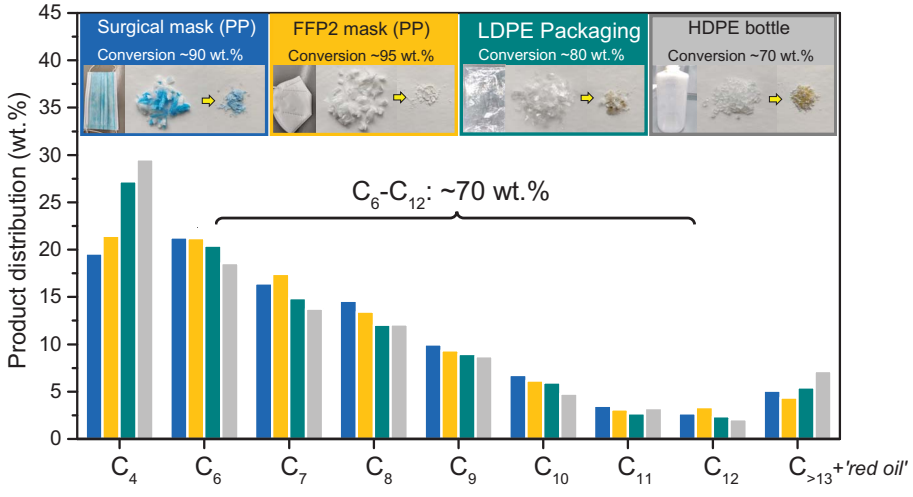

Fig. 3. Selective deconstruction of postconsumer polyolefin waste into liquid alkanes. Product distribution of tandem cracking-alkylation of postconsumer polyolefin waste with iC_5 with $[C_4Py]Cl\text{-}AlCl_3$. No methane, ethane, or propane was detected; all products were branched alkanes. Reaction conditions were as follows: polyolefin waste, 200 mg; iC_5, 800 mg; $[C_4Py]Cl\text{-}AlCl_3$, 3 mmol; TBC, 0.05 mmol; and DCM, 3 ml. Reaction temperatures and times were as follows: disposable surgical mask, 70°C for 6 hours; FFP2 mask, 70°C for 6 hours; food packaging, 70°C for 48 hours; and HDPE bottle, 100°C for 48 hours. PP, polypropylene; FFP, filtering face piece.

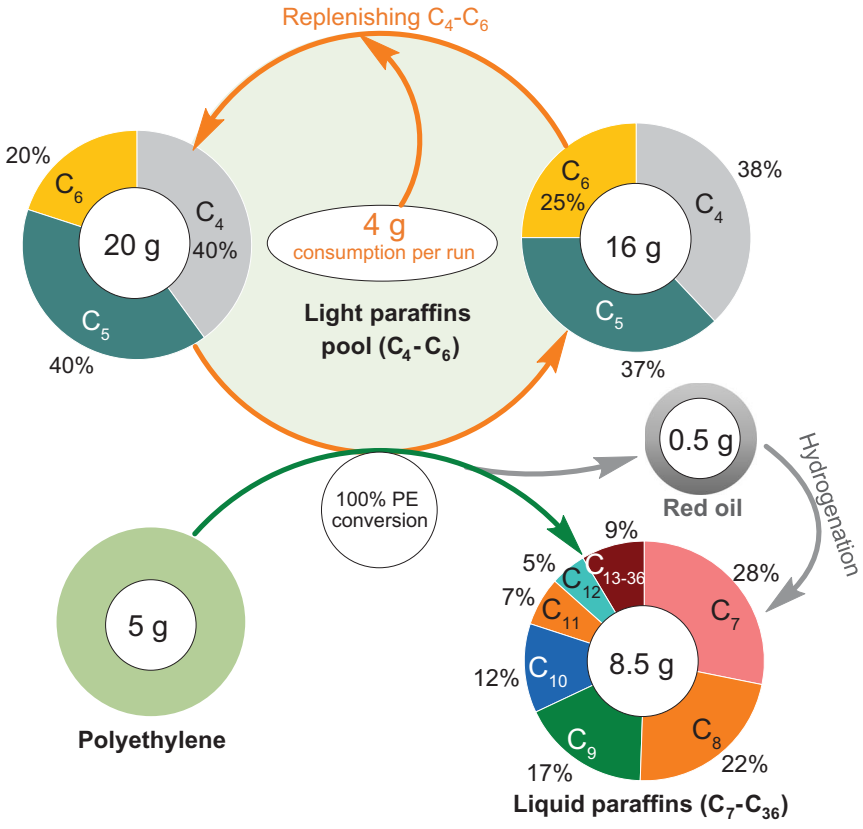

Fig. 4. Full conversion of polyethylene and isoparaffins that are recycled from the light products formed in the process. Cracking-alkylation of LDPE with light paraffin mixture (C_4 to C_6) as recycled light products from polyolefin deconstruction, which gives full LDPE conversion and branched C_{7+} alkanes. Each run only consumed 4 g of light paraffins from the pool, yielding 8.5 g of liquid isoparaffins (C_7 to C_{36}) and a minor amount of red oil as side products (0.5 g) that can easily hydrogenate to saturated hydrocarbons (fig. S20). Reaction conditions were as follows: LDPE, 5 g; initial light paraffin pool, 20 g (C_4, 40 wt %; C_5, 40 wt %; C_6, 20 wt %); [C_4Py]Cl-$AlCl_3$, 30 mmol; TBC, 100 mg; DCM, 75 ml; 2 MPa (N_2); temperature, 70°C; and reaction time, 2 hours.

and cracking via β-scission. Alkenes formed in this process (cracking cycle) react with carbenium ions formed from isoalkanes in the alkylation cycle. The detailed pathways using *n*-hexadecane as a model for LDPE are shown in figs. S13 and S14. The chemistry observed in this latter cycle is identical to that of the alkylation of isobutane with *n*-butene on such ionic liquid-based catalysts (*30*). Unless terminated by hydrogen transfer, these two cycles operate independently from each other, with their relative rates determining the product distribution. The rate of cracking in these coupled processes allows the use of an unusually low concentration of isoalkanes in the overall pool of reactive substrates compared with conventional isobutane and *n*-butene alkylation.

The final question to be addressed is the nature of the active sites that initiate and stabilize the chain propagation and catalysis that was observed. The speciation of [C_4Py]Cl-$AlCl_3$ ionic liquid depends closely on the initial ratio between *N*-butylpyridinium chloride and anhydrous aluminum chloride, in which monomeric $AlCl_4^-$ and dimeric $Al_2Cl_7^-$ dominate at equilibrium (fig. S15). In situ ^{27}Al magic-angle spinning nuclear magnetic resonance spectroscopy (^{27}Al MAS NMR) and Raman spectroscopy showed that increasing the initial fraction of anhydrous aluminum chloride promotes the transformation from $AlCl_4^-$ to $Al_2Cl_7^-$, which in turn results in improved reaction rates (fig. S16). The observed catalytic behavior seems to be determined by the Lewis acidic $Al_2Cl_7^-$ anions (fig. S17), which were generally proposed as the catalytically active sites for catalysis over past decades (*31*). Intriguingly, further kinetic analysis uncovered that the reaction rate was not proportional to the concentration of $Al_2Cl_7^-$ (fig. S18) but rather to the transient aluminum trichloride ($AlCl_3$*) derived from the dissociation of $Al_2Cl_7^-$ (fig. S19). Unlike anhydrous aluminum chloride that features dimeric Al_2Cl_6, $AlCl_3$* species were undetectable and typically ignored because of the extremely small value of the equilibrium dissociation constant (*26*). To substantiate this inference, we plotted, in fig. S19, the turnover frequencies of [C_4Py]Cl-$AlCl_3$ against the concentration of $AlCl_3$*, which showed a linear correlation. Thus, we conclude that increasing the molar ratio of $AlCl_3$ to [C_4Py]Cl increases the concentration of dimeric $Al_2Cl_7^-$ species, which in turn results in an increased concentration of $AlCl_3$* active species.

The strategy described can near-quantitatively convert a wide selection of polymer consumer products with selectivity to C_6 to C_{12} products totaling more than 70 wt %, as exemplified by the results of reactions run using face masks, food packaging, and a high-density polyethylene (HDPE) bottle (Fig. 3). Depolymerization of HDPE bottles is less straightforward because of their compact structure, which lowers the contact surface or site between catalyst and granules, and will require further practical measures to increase dispersion. In practical implementation, the formed light isoalkanes (C_4 to C_6) can be recycled back as alkylating agents, which will ideally enable full conversion (because we hardly produce other light alkanes, including methane, ethane, and propane). To test this, we used the light isoparaffins mixture (C_4 to C_6) as the alkylating component for LDPE upcycling to simulate the recycling experiments, which reached full LDPE conversion and yielded branched alkanes (linear alkanes are negligible) (Fig. 4). Repeated batch experiments showed that the [C_4Py]Cl-$AlCl_3$ catalyst retained its activity and can be used at least five times without regeneration, thereby constantly reaching full LDPE conversion (fig. S20A). Some minor by-products, including red oil complexed with chloroaluminate anions, can be easily converted into saturated hydrocarbons via hydrogenation (fig. S20, B and C), which regenerates the [C_4Py]Cl-$AlCl_3$ ionic liquid. These results demonstrate the practicability of recycling the lighter alkane product as the alkylation agent. Although practical challenges will exist, scaling these results to a quasi-continuous process (conceptualized in fig. S21) is concluded to be highly promising and will integrate recycling of all light hydrocarbons or polymer swelling components.

Acidic chloroaluminate-based ionic liquids as emerging alkylation catalysts have already been industrially used in the paraffin alkylation process at Chevron's Salt Lake City refinery and China National Petroleum Corporation (CNPC), which demonstrates the stability of such catalysts (*32*). We thus envision that this upcycling strategy can be rapidly implemented not only in newly designed plants but also in existing refining technology. The synchronous release of alkenes via polyolefin cracking in the presented cascade cracking-alkylation conceptually allows for better control of product distribution and minimization of the formation of red oil waste (*27*), making polyolefins a

potential feed for refining alkylation. This work opens a transformative scalable approach to convert polyolefins and enables a critical contribution to a circular carbon economy.

REFERENCES AND NOTES

1. R. Geyer, J. R. Jambeck, K. L. Law, *Sci. Adv.* **3**, e1700782 (2017).
2. J. M. Garcia, M. L. Robertson, *Science* **358**, 870–872 (2017).
3. G. W. Coates, Y. D. Y. L. Getzler, *Nat. Rev. Mater.* **5**, 501–516 (2020).
4. S. C. Kosloski-Oh, Z. A. Wood, Y. Manjarrez, J. P. de Los Rios, M. E. Fieser, *Mater. Horiz.* **8**, 1084–1129 (2021).
5. Z. O. G. Schyns, M. P. Shaver, *Macromol. Rapid Commun.* **42**, e2000415 (2021).
6. S. M. Al-Salem, A. Antelava, A. Constantinou, G. Manos, A. Dutta, *J. Environ. Manage.* **197**, 177–198 (2017).
7. A. J. Martín, C. Mondelli, S. D. Jaydev, J. Pérez-Ramírez, *Chem* **7**, 1487–1533 (2021).
8. I. Vollmer *et al*., *Angew. Chem. Int. Ed.* **59**, 15402–15423 (2020).
9. L. O. Mark, M. C. Cendejas, I. Hermans, *ChemSusChem* **13**, 5808–5836 (2020).
10. G. Celik *et al*., *ACS Cent. Sci.* **5**, 1795–1803 (2019).
11. J. E. Rorrer, G. T. Beckham, Y. Román-Leshkov, *JACS Au* **1**, 8–12 (2020).
12. A. Tennakoon *et al*., *Nat. Catal.* **3**, 893–901 (2020).
13. S. Liu, P. A. Kots, B. C. Vance, A. Danielson, D. G. Vlachos, *Sci. Adv.* **7**, eabf8283 (2021).
14. X. Jia, C. Qin, T. Friedberger, Z. Guan, Z. Huang, *Sci. Adv.* **2**, e1501591 (2016).
15. N. Morlanés, S. G. Kavitake, D. C. Rosenfeld, J.-M. Basset, *ACS Catal.* **9**, 1274–1282 (2019).
16. F. Zhang *et al*., *Science* **370**, 437–441 (2020).
17. D. P. Serrano, J. Aguado, J. M. Escola, *ACS Catal.* **2**, 1924–1941 (2012).
18. H. Yan *et al*., *Science* **371**, 1257–1260 (2021).
19. L. D. Ellis *et al*., *Nat. Catal.* **4**, 539–556 (2021).
20. GlobalData, "Refinery alkylation units market installed capacity and capital expenditure (CapEx) forecast by region and countries including details of all active plants, planned and announced projects, 2022-2026," Report code GDGE1353ICR (2021).
21. A. Feller, I. Zuazo, A. Guzman, J. O. Barth, J. A. Lercher, *J. Catal.* **216**, 313–323 (2003).
22. N. Pfriem *et al*., *Science* **372**, 952–957 (2021).
23. L. Milaković, P. H. Hintermeier, Y. Liu, E. Baráth, J. A. Lercher, *Angew. Chem. Int. Ed.* **60**, 24806–24810 (2021).
24. H. K. C. Timken, S. Elomari, S. Trumbull, R. Cleverdon, "Integrated alkylation process using ionic liquid catalysts," US Patent 7,432,408 (2008).
25. C. J. Adams, M. J. Earle, K. R. Seddon, *Green Chem.* **2**, 21–24 (2000).
26. J. Estager, J. D. Holbrey, M. Swadźba-Kwaśny, *Chem. Soc. Rev.* **43**, 847–886 (2014).
27. A. Feller, J. A. Lercher, in *Advances in Catalysis*, H. Knüpffer, Ed. (Academic Press, 2004), vol. 48, pp. 229–295.
28. A. S. Amarasekara, *Chem. Rev.* **116**, 6133–6183 (2016).
29. S. Aschauer, L. Schilder, W. Korth, S. Fritschi, A. Jess, *Catal. Lett.* **141**, 1405–1419 (2011).
30. Y. Chauvin, A. Hirschauer, H. Olivier, *J. Mol. Catal.* **92**, 155–165 (1994).
31. R. Kore *et al*., *ACS Catal.* **7**, 7014–7028 (2017).
32. H. K. Timken, H. Luo, B.-K. Chang, E. Carter, M. Cole, in *Commercial Applications of Ionic Liquids*, M. B. Shiflett, Ed. (Springer, 2020), pp. 33–47.

ACKNOWLEDGMENTS

We thank A. Wellmann, H. Xu, B. Yang, and J. Mai from the Technische Universität München for their assistance in experiment setup and data collection. We thank W. Hu from Pacific Northwest National Laboratory for support with in situ NMR measurements. We also thank G. L. Haller (Yale University) for his careful reading of the manuscript and helpful suggestions. **Funding:** This work was supported by the US Department of Energy, Office of Science, Office of Basic Energy Sciences, Division of Chemical Sciences, Geosciences and Biosciences (Toward a polyolefin-based refinery: Understanding and controlling the critical reaction steps, FWP 78459) (J.A.L., O.Y.G., J.H., S.K., D.M.C., and L.H.). **Author contributions:** W.Z., Y.L., and J.A.L. conceived the research; W.Z. carried out the reactions and performed the characterizations for selected materials. J.H., S.K., and L.W. provided data on the in situ NMR measurements. R.K., L.H., D.M.C., and O.Y.G. contributed to the discussion and helped to revise the manuscript. All authors contributed to the writing of the manuscript. **Competing interests:** The authors declare that they have no competing interests. **Data and materials availability:** All data are available in the main text or the supplementary materials. **License information:** Copyright © 2023 the authors, some rights reserved; exclusive licensee American Association for the Advancement of Science. No claim to original US government works. https://www.science.org/about/science-licenses-journal-article-reuse

SUPPLEMENTARY MATERIALS

science.org/doi/10.1126/science.ade7485
Materials and Methods
Figs. S1 to S21
References (*33*–*49*)

Submitted 5 September 2022; accepted 30 January 2023
10.1126/science.ade7485

PALEONTOLOGY

Developmental strategies underlying gigantism and miniaturization in non-avialan theropod dinosaurs

Michael D. D'Emic[1,2]*, Patrick M. O'Connor[3,4], Riley S. Sombathy[1,4,5], Ignacio Cerda[6,7], Thomas R. Pascucci[1], David Varricchio[8], Diego Pol[9], Anjali Dave[1], Rodolfo A. Coria[10], Kristina A. Curry Rogers[11]

In amniotes, the predominant developmental strategy underlying body size evolution is thought to be adjustments to the rate of growth rather than its duration. However, most theoretical and experimental studies supporting this axiom focus on pairwise comparisons and/or lack an explicit phylogenetic framework. We present the first large-scale phylogenetic comparative analysis examining developmental strategies underlying the evolution of body size, focusing on non-avialan theropod dinosaurs. We reconstruct ancestral states of growth rate and body mass in a taxonomically rich dataset, finding that contrary to expectations, changes in the rate and duration of growth played nearly equal roles in the evolution of the vast body size disparity present in non-avialan theropods—and perhaps that of amniotes in general.

The concept of heterochrony—changes in the relative rate and/or timing of developmental events—was formalized by Alberch *et al.* (*1*) and has been used to explain the evolution of morphology and body size disparity in a variety of vertebrate clades for more than a century. Heterochrony is often invoked in studies of body size evolution, but most hypotheses rest on pairwise comparisons of sister taxa (implied or assumed to be ancestor-descendent pairs) or very few species of a given clade (*2*–*18*), most often examined outside of an explicit phylogenetic context. Vertebrate postnatal or post-hatching growth can generally be divided into three phases bounded by the onset and offset of a period of rapid growth (*1*, *3*). Over the past two decades, acceleration or deceleration of the rapid growth phase has been inferred to be the predominant mechanism influencing body size evolution in most amniotes, including several clades of non-avialan dinosaurs (*2*, *3*, *5*–*10*) and mammals (*12*–*17*). Much less commonly inferred mechanisms include changes in the duration of the rapid growth phase (prolongation or truncation through a change in the onset and/or offset timepoint of the phase of rapid growth), which have been used to explain body size change in a limited few groups [e.g., some lizards (*18*), crocodilelline archosaurs (*19*), and synapsids (*17*, *20*)]. Evidence for changes in rate versus timing is mixed or wanting in birds (*2*, *21*–*23*). Metabolic theory predicts that changes in growth rates are the predominant mechanism underlying body size evolution; most somatic cells are body size–invariant (*24*) indicating that the evolution of body size largely involves changes in the number of cells rather than their size. A larger number of cells translates to higher metabolic and mitotic activity per unit body mass and thus accelerated growth (*25*). The overwhelming inference of changes in developmental rate over duration leading to body size evolution is axiomatic in review articles (*26*), broad comparative studies of extant taxa (*27*, *28*), and the popular scientific literature (*29*).

However, no study to date has analyzed the evolution of developmental rate and duration in an explicit phylogenetic comparative framework, in part because there are few abundantly sampled, long-lived clades containing a diversity of body sizes with which to test the frequency of distinct heterochronic mechanisms. We assembled a comprehensive dataset of body size and growth data for non-avialan theropod dinosaurs, established reliable protocols and proxies for estimating missing data in osteohistological cross sections, and developed a novel, standardized framework for analyzing the relative contribution of changes to growth rate and duration over the evolutionary span of a clade. Femora and tibiae were used to infer individual ages and body masses over ontogeny for each specimen in our dataset, because these elements scale tightly with one another and have a strongly predictive relationship with body mass (fig. S1). Dorsal ribs and fibulae, which often undergo less of the dense remodeling that obscures the cortical growth record, were used to ensure that the rapid (i.e., maximum annual) phase of growth was recorded in a given individual (i.e., the phase of growth preserving the most widely spaced cortical growth marks). Some specimens were unavailable for thin sectioning, but histological features could be sufficiently resolved in computed tomographic data.

Our dataset includes measurements of ~500 annually deposited cortical growth marks (CGM) from more than 80 skeletal elements of 42 non-avialan theropod dinosaur species of disparate body sizes (<0.5 m to >12 m body length) and ecologies (data S1). This dataset is derived from a cosmopolitan taxon sample and ranges from some of the geologically oldest non-avialan theropods (e.g., *Herrerasaurus*, ca. 230 Ma) to those immediately preceding the K–Pg extinction event (e.g., *Tyrannosaurus*, *Majungasaurus*, ca. 66–68 Ma). We estimate maximum annual growth rates for 36 of these 42 taxa, plot them on a time-calibrated phylogeny (Fig. 1), and provide novel detailed histological descriptions for 10 previously unsampled taxa. We performed ancestral state reconstructions of body mass and annual growth rate using maximum likelihood to estimate the relative contribution of acceleration or prolongation for lineage-specific body size increases, and deceleration or truncation for lineage-specific body size decreases, in the evolution of dinosaurs on the line to birds.

This greatly expanded histological dataset reveals a wide range of growth records and tissue types indicative of a diversity of growth strategies, broader than the range found in smaller theropod datasets (e.g., *2, 30*). Even small derived clades within Theropoda exhibit cortical bone histology corresponding to a high diversity of growth rates. For example, *Ceratosaurus* grew rapidly with plexiform neurovascular canal organization densely permeating a cortex of woven to parallel-fibered bone that is interspersed with few growth marks. By contrast, the similarly sized ceratosaurian *Majungasaurus* grew much more slowly (slower than extant *Alligator*; data S1), with longitudinal to circumferential neurovascular canal organization surrounding parallel-fibered to lamellar tissue that is interrupted by many closely spaced lines of arrested growth.

Although developmental plasticity has been inferred for several early dinosaurs and their relatives (*4*), about three-quarters of the species in our dataset belong to the clade Avetheropoda, a group inferred to have relatively low intraspecific variation in growth (*31*), an inference further confirmed by our expanded sampling. We find low intraspecific variation in several of the avetheropods in our dataset (when excluding data from young juveniles or old adults whose bones do not preserve the explosive phase of growth), including: *Acrocanthosaurus* (maximum annual growth rate 46 to 60%), *Aniksosaurus* (103 to 113%), *Gorgosaurus* (40 to 75%), *Sinornithomimus* (182 to 214%), and *Troodon* (77 to 79%). A notable exception in our dataset is *Allosaurus*, a

[1]Department of Biology, Adelphi University, Garden City, NY, USA. [2]Department of Anatomical Sciences, Stony Brook University, Stony Brook, NY, USA. [3]Department of Biomedical Sciences, Ohio University Heritage College of Osteopathic Medicine, Athens, OH, USA. [4]Ohio Center for Ecological and Evolutionary Studies, Ohio University, Athens, OH, USA. [5]Department of Biological Sciences, Ohio University, Athens, OH, USA. [6]Consejo Nacional de Investigaciones Científicas y Técnicas (CONICET), Ciudad Autónoma de Buenos Aires, República Argentina. [7]Instituto de Investigación en Paleobiología y Geología, Universidad Nacional de Río Negro, Museo Carlos Ameghino, Cipolletti, Río Negro, Argentina. [8]Department of Earth Sciences, Montana State University, Bozeman, MT, USA. [9]CONICET-Museo Paleontológico Egidio Feruglio, Trelew, Chubut, Argentina. [10]Museo Carmen Funes, Plaza Huincul, Neuquén, Argentina. [11]Biology and Geology Departments, Macalester College, St. Paul, MN, USA.
*Corresponding author. Email: mdemic@adelphi.edu

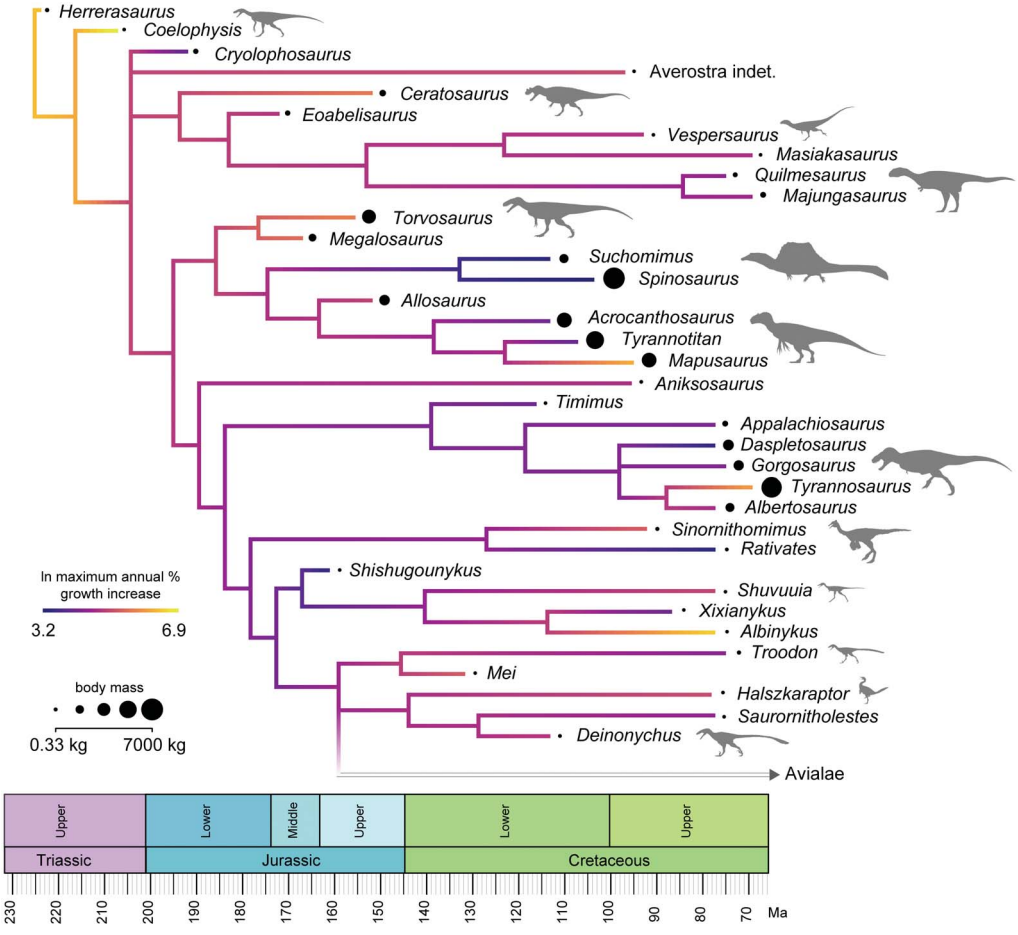

Fig. 1. Evolution of maximum annual growth rate and body mass in non-avialan theropods. Ancestral states reconstructed through maximum likelihood are shown as colors on lineages that are scaled to geologic time, whereas black circle size indicates estimated adult body mass. Yellow and/or orange colors and larger circles indicate faster-growing and larger individuals, respectively. Silhouettes from PhyloPic (see acknowledgments and data S1).

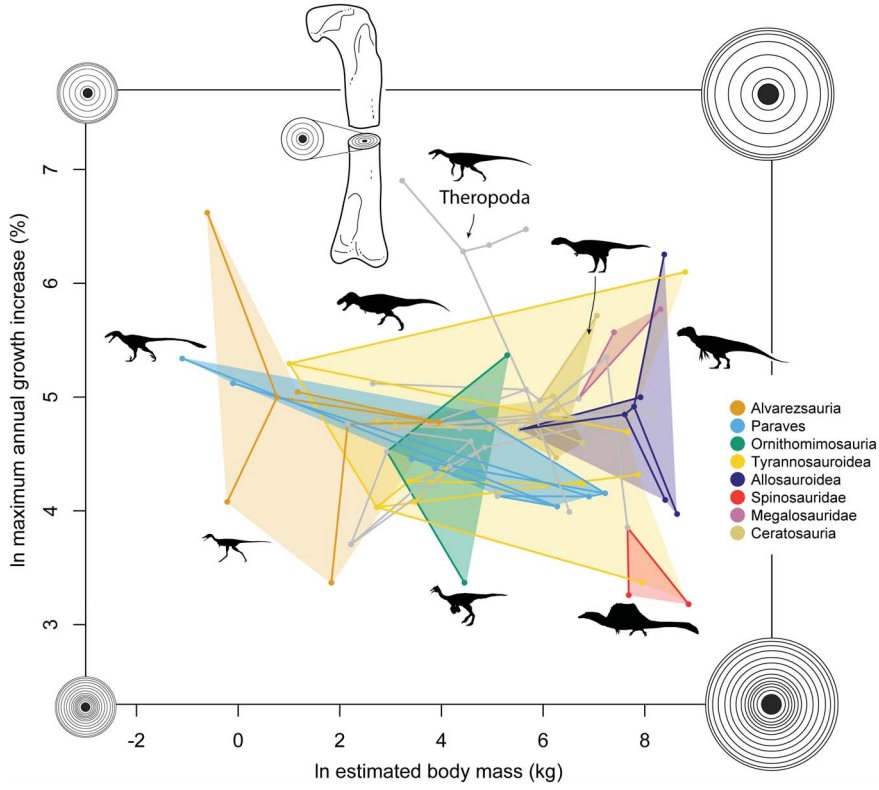

Fig. 2. Phylomorphospace plot of non-avialan theropod maximum annual growth rate and body mass evolution. Concentric circles at each corner of the morphospace schematically represent cortical growth marks within diaphyseal cross sections as shown in the illustrated theropod femur; these indicate idealized "end members" in growth and body size. The branches represent evolutionary paths in body size and growth rate. Silhouettes from PhyloPic (see acknowledgments and data S1).

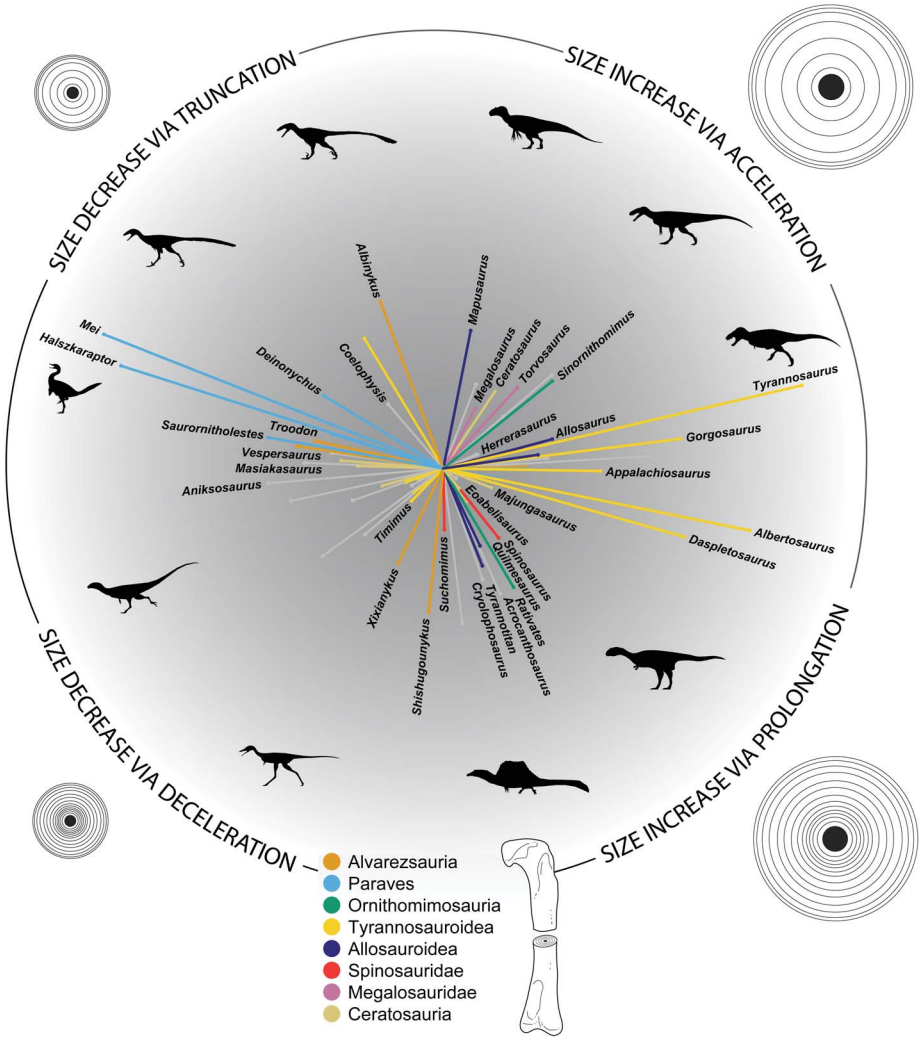

Fig. 3. Evolutionary mechanisms underlying body size evolution in non-avialan theropods. Each vector represents a reconstructed ancestor-descendent transition, with the length indicating the magnitude of change on that branch (on a natural log scale as in Fig. 2). The direction of each vector indicates the predominant mechanism underlying the evolution of body size in that lineage. Line colors pertain to members of the eight highlighted clades listed at the bottom of the figure. Concentric circles at each corner of the plot indicate schematic bone cross sections showing cortical growth marks as in Fig. 2. Silhouettes from PhyloPic (see acknowledgments and data S1).

taxon that is inferred to have sex-based or cryptic taxonomic differences that require a larger dataset to untangle.

We reconstruct the ancestral theropod condition as having high maximum annual growth rates (Fig. 1), consistent with both independently derived estimates of ancestrally high daily growth rates (*2*, *32*) and the inference of endothermy in early dinosaurs and their relatives (*33*). The distribution of non-avialan theropod maximum annual growth rates is strongly positively skewed (median maximum growth rate per year = 114%; Shapiro-Wilk test $W \sim 0.71$; $P \sim 1\ e^{-7}$; fig. S2). Non-avialan theropods exhibit no significant trend in maximum annual growth rate through their evolution ($r = 0.3$; $P = 0.07$; fig. S3). However, there is a consistent decrease in maximum annual growth rate along the stem of the phylogeny on the line toward birds (Fig. 1), wherein the ancestral averostran, coelurosaurian, and maniraptoriform maximum annual growth rate fell from ~150 to ~110 to ~75%, respectively. This steady decrease parallels the trend of sustained miniaturization along the stem to birds (*34*). However, paravians decouple these trends, growing more quickly at even smaller body sizes (maximum annual growth rate increase ~100%). Substantial decreases in maximum annual growth rate evolved independently in spinosaurids, tyrannosauroids, and early maniraptorans, whereas increases evolved independently in derived allosauroids, alvarezsauroids, and paravians (Fig. 1). There is no relationship between body mass and maximum annual growth rate (fig. S4; $r = 0.02$; $P = 0.38$). This pattern is underscored by the marked range of variation in the growth rates of the largest theropods, such as some derived allosauroids and spinosaurids, groups that increased body mass by at most ~60% per year. By contrast, derived megalosaurids, ceratosaurians, some tyrannosaurids, and some allosauroids increased their mass more than 200% per year (Figs. 1 and 2). Similar disparity is exhibited by the smallest theropods, with ornithomimosaurs, alvarezsaurids, and smaller tyrannosauroids exhibiting a wide range of rates (Figs. 1 and 2).

Plotting each lineage as a vector in a phylomorphospace of body mass versus maximum annual growth rate, with the absolute value of its ancestral state at the center of a circle, reveals both the relative frequency of body size changes and the mechanisms underlying them (Fig. 3). Within our sample, ~60% of branches record an increase in size, compared with ~40% that record a decrease. Changes in the rate of the rapid growth phase occur on 50.7% of branches, whereas changes in its duration occur on 49.3%. The most common evolutionary change is size increase through acceleration of the explosive growth phase (31.3% of branches), followed closely by size increase through its prolongation (28.4%), size decrease through its truncation (20.9%; Fig. 3), and size decrease through its deceleration (19.4%). Analyzing theropod growth evolution as a percentage increase per year (i.e., relative growth rather than the typically compared absolute growth) (e.g., *2*, *3*), and analyzing it in a phylogenetic framework (i.e., comparing explicitly hypothesized ancestor-descendent values) contradicts the results of some previous studies. For example, we find that gigantism in allosauroids evolved through a range of growth strategies, not just

prolongation (*30*) or acceleration (*5*). We find support for some previous evolutionary hypotheses, including truncation of rapid growth characterizing the close relatives of birds (*2*, *21*), and exceptionally high variability in alvarezsauroid growth rates (*35*). Our results generally align with clade-specific morphological studies of heterochrony in several theropod clades, including peramorphosis in carcharodontosaurids with prolonged, slow development (*36*) and paedomorphosis in paravians with truncated, rapid development (*37*). We find that many non-avialan theropods grew proportionally slower than extant crocodylians (data S1), and changes in developmental duration were found to be similar in frequency to changes in developmental rate. Once quantified and analyzed in a phylogenetic framework, we predict that diverse growth strategies will be recognized in other clades, such as those currently thought to evolve in body size primarily through changes in developmental duration [e.g., crocodile-line archosaurs and lizards (*18*, *19*)]. Just as broad, phylogenetic comparative studies have repeatedly failed to find support for directional evolution in body size [i.e., Cope's Rule (*38*)], with increased scrutiny the developmental mechanisms underlying body size evolution may be found to be equally prevalent across Amniota as a whole.

REFERENCES AND NOTES

1. P. Alberch, S. J. Gould, G. F. Oster, D. B. Wake, *Paleobiology* **5**, 296–317 (1979).
2. K. Padian, A. J. de Ricqlès, J. R. Horner, *Nature* **412**, 405–408 (2001).
3. G. M. Erickson *et al*., *Nature* **430**, 772–775 (2004).
4. K. E. J. Chapelle, J. Botha, J. N. Choiniere, *Biol. Lett.* **17**, 20200843 (2021).
5. M. D. D'Emic, K. M. Melstrom, D. R. Eddy, *Palaeogeogr. Palaeoclimatol. Palaeoecol.* **333–334**, 13–23 (2012).
6. G. M. Erickson, K. C. Rogers, S. A. Yerby, *Nature* **412**, 429–433 (2001).
7. K. Padian, J. R. Horner, A. de Ricqlès, *J. Vertebr. Paleontol.* **24**, 555–571 (2004).
8. R. Redelstorff, P. M. Sander, *J. Vertebr. Paleontol.* **29**, 1087–1099 (2009).
9. P. Sander *et al*., *Org. Divers. Evol.* **4**, 165–173 (2004).
10. K. Stein *et al*., *Proc. Natl. Acad. Sci. U.S.A.* **107**, 9258–9263 (2010).
11. T. M. Lehman, H. N. Woodward, *Paleobiology* **34**, 264–281 (2008).
12. M. Köhler, S. Moyà-Solà, *Proc. Natl. Acad. Sci. U.S.A.* **106**, 20354–20358 (2009).
13. S. Herrera-Álvarez, E. Karlsson, O. A. Ryder, K. Lindblad-Toh, A. J. Crawford, *Mol. Biol. Evol.* **38**, 1715–1730 (2021).
14. E. S. Long, K. L. Courtney, J. C. Lippert, C. M. Wall-Scheffler, *Oecologia* **189**, 675–685 (2019).
15. M. Köhler *et al*., *Sci. Rep.* **11**, 22862 (2021).
16. A. Ozgul *et al*., *Science* **325**, 464–467 (2009).
17. G. Orlandi-Oliveras, C. Nacarino-Meneses, G. D. Koufos, M. Köhler, *Sci. Rep.* **8**, 17203 (2018).
18. G. M. Erickson, A. J. de Ricqlès, V. de Buffrénil, R. E. Molnar, M. K. Bayless, *J. Vertebr. Paleontol.* **23**, 966–970 (2003).
19. G. M. Erickson, C. A. Brochu, *Nature* **398**, 205–206 (1999).
20. A. K. Huttenlocker, J. Botha-Brink, *PeerJ* **2**, e325 (2014).
21. A. Chinsamy, A. Elzanowski, *Nature* **412**, 402–403 (2001).
22. S. T. Turvey, O. R. Green, R. N. Holdaway, *Nature* **435**, 940–943 (2005).
23. G. M. Erickson *et al*., *PLOS ONE* **4**, e7390 (2009).
24. V. M. Savage *et al*., *Proc. Natl. Acad. Sci. U.S.A.* **104**, 4718–4723 (2007).
25. M. D. D'Emic, R. B. J. Benson, *Bone* **57**, 300–310 (2013).
26. G. M. Erickson, *Annu. Rev. Earth Planet. Sci.* **42**, 675–697 (2014).
27. T. J. Case, *Q. Rev. Biol.* **53**, 243–282 (1978).
28. J. M. Starck, R. E. Ricklefs, in *Avian Growth and Development: Evolution Within the Altricial Precocial Spectrum*, J. M. Starck, R. E. Ricklefs, Eds. (Oxford Univ. Press, 1998), ch. 1.
29. J. R. Horner, K. Padian, A. de Ricqlès, *Sci. Am.* **293**, 56–63 (2005).
30. T. M. Cullen *et al*., *Proc. Biol. Sci.* **287**, 20202258 (2020).
31. C. T. Griffin, S. J. Nesbitt, *Proc. Natl. Acad. Sci. U.S.A.* **113**, 14757–14762 (2016).
32. J. Cubo, N. Le Roy, C. Martinez-Maza, L. Montes, *Paleobiology* **38**, 335–349 (2012).
33. G. Grigg *et al*., *Biol. Rev.* (2021).
34. M. S. Y. Lee, A. Cau, D. Naish, G. J. Dyke, *Syst. Biol.* **63**, 442–449 (2014).
35. Z. Qin *et al*., *Curr. Biol.* **31**, 3687–3693.e5 (2021).
36. J. I. Canale, F. E. Novas, L. Salgado, R. A. Coria, *Palaontol. Z.* **89**, 983–993 (2015).
37. B. A. S. Bhullar *et al*., *Nature* **487**, 223–226 (2012).
38. R. J. Butler, A. Goswami, *J. Evol. Biol.* **21**, 1673–1682 (2008).

ACKNOWLEDGMENTS

Thanks to B. Britt, M. Brown, R. Cifelli, K. Davies, J. Ebersole, J. Foster, G. Erickson, E. Howlett, R. Irmis, D. Krause, J. Larsen, J. McHugh, K. Melstrom, M. Norell, C. Sagebiel, J. Scanella, V. Schneider, P. Sereno, B. Strilisky, S. Werning, and J. Whitlock for loans, discussion, and/or permission to study thin sections, and E-T. Lamm and J. Groenke for sampling assistance. Silhouettes from PhyloPic are gratefully acknowledged from the following (licenses in data S1): T. Dixon, A. Farke, S. Hartmann, T. M. Keesey, S. Reid, J. Sertich, and N. Tamura. We thank the three anonymous reviewers whose comments significantly improved the original version of this manuscript. **Funding:** This work was funded by the following: US National Science Foundation (EAR1525915) to P.M.O. Adelphi University Horace McDonell Awards to R.S.S. and T.R.P. **Author contributions:** Conceptualization: M.D.D., P.M.O., and K.C.R. Methodology: M.D.D. and P.M.O. Investigation: M.D.D., P.M.O., R.S.S., I.C., T.R.P., A.D., D.V., D.P., R.A.C., and K.C.R. Visualization: M.D.D., P.M.O., R.S.S., I.C., T.R.P., A.D., and D.V. Funding acquisition: P.M.O. and K.C.R. Project administration: M.D.D. Supervision: M.D.D. Writing – original draft: M.D.D., P.M.O., and R.S.S. Writing – review and editing: M.D.D., P.M.O., R.S.S., I.C., T.R.P., A.D., D.V., D.P., R.A.C., and K.C.R. **Competing interests:** Authors declare that they have no competing interests. **Data and materials availability:** All data are available in the main text, the supplementary materials, or on figshare (see data S1 for links). **License information:** Copyright © 2023 the authors, some rights reserved; exclusive licensee American Association for the Advancement of Science. No claim to original US government works. https://www.sciencemag.org/about/science-licenses-journal-article-reuse

SUPPLEMENTARY MATERIALS

science.org/doi/10.1126/science.adc8714
Materials and Methods
Histological Descriptions
Figs. S1 to S5
Data S1 and S2
References (*39*–*105*)
MDAR Reproducibility Checklist

Submitted 5 May 2022; resubmitted 14 October 2022
Accepted 1 February 2023
10.1126/science.adc8714

STRATOSPHERE

Pyrocumulonimbus affect average stratospheric aerosol composition

J. M. Katich[1,2]†, E. C. Apel[3], I. Bourgeois[1,2], C. A. Brock[1], T. P. Bui[4], P. Campuzano-Jost[2,5], R. Commane[6], B. Daube[7], M. Dollner[8], M. Fromm[9], K. D. Froyd[1,2], A. J. Hills[3], R. S. Hornbrook[3], J. L. Jimenez[2,5], A. Kupc[1,2,8], K. D. Lamb[1,2]‡, K. McKain[10], F. Moore[2,10], D. M. Murphy[1], B. A. Nault[2,5,11], J. Peischl[1,2], A. E. Perring[12], D. A. Peterson[13], E. A. Ray[1,2], K. H. Rosenlof[1], T. Ryerson[1]§, G. P. Schill[1,2], J. C. Schroder[2,5,14], B. Weinzierl[7], C. Thompson[1,2], C. J. Williamson[1,2]¶#, S. C. Wofsy[7], P. Yu[15], J. P. Schwarz[1]*

Pyrocumulonimbus (pyroCb) are wildfire-generated convective clouds that can inject smoke directly into the stratosphere. PyroCb have been tracked for years, yet their apparent rarity and episodic nature lead to highly uncertain climate impacts. In situ measurements of pyroCb smoke reveal its distinctive and exceptionally stable aerosol properties and define the long-term influence of pyroCb activity on the stratospheric aerosol budget. Analysis of 13 years of airborne observations shows that pyroCb are responsible for 10 to 25% of the black carbon and organic aerosols in the "present-day" lower stratosphere, with similar impacts in both the North and South Hemispheres. These results suggest that, should pyroCb increase in frequency and/or magnitude in future climates, they could generate dominant trends in stratospheric aerosol.

Pyrocumulonimbus (pyroCb) clouds, which are triggered by intense wildfires, have the potential to efficiently transport large quantities of smoke into the upper troposphere and lower stratosphere (UT/LS) (*1*–*3*). The largest of these events rival moderate volcanic eruptions in their disruption of the global radiative balance (*4*, *5*). However, the temporal (especially long-term) and geographical extent to which these rare events affect the atmosphere are poorly known, and thus their impacts on climate and stratospheric aerosol and chemistry (including the ozone layer) remain highly uncertain (*6*–*8*). Climate change has increased the occurrence of extreme wildfires (*9*–*11*), and pyroCb events are therefore expected to also increase in frequency in the coming decades (*12*, *13*). To date, critical in situ measurements of pyroCb injections remain extremely limited (*14*–*22*) owing to the highly episodic nature of pyroCb and the logistical difficulties of fielding extensive airborne scientific instrument payloads on short notice. In situ measurements provide the specifics of pyroCb smoke composition (gas and aerosol phase) as well as aerosol microphysical properties that are necessary to understand the full impacts of pyroCb activity on the stratosphere.

Major pyroCb events that inject huge amounts of smoke into the stratosphere are rare; prior to 2017, only a handful of pyroCb had been observed to have perturbed the atmosphere over hemispheric spatial scales. In 2017, the largest pyroCb event observed to date in the satellite era formed in the Pacific Northwest of North America [dubbed the Pacific Northwest Event, or PNE (*4*)]. The ensuing smoke plume, which girdled the northern polar LS region within weeks of injection (*4*, *5*), is estimated to have generated 0.9 K per day additional heating in the Arctic UT/LS for a month (*20*). The PNE smoke injection was so large that it was monitored for more than 8 months with remote-sensing techniques (*21*, *23*) and dominated contributions to the LS from several additional pyroCb events that occurred across the Northern Hemisphere (NH) during that particularly active year of pyroCb. However, as we find here, the influence of the pyroCb smoke plume in the LS lasts over much longer time scales than merely their intense initial periods, and indeed longer than is possible to track with remote measurements.

Here we present detailed composition and aerosol microphysical information obtained from direct observations of pyroCb smoke in 2017. Findings drawn from their analysis are assessed in the context of in situ LS observations dating back to 2006 and are used to quantify the smoke's average impact on LS composition. The NASA Atmospheric Tomography (ATom) mission (*24*), using the world's largest atmospheric research aircraft fully outfitted with state-of-the-art instrumentation (measuring gases, particles, and meteorology), intercepted 2017 pyroCb smoke from the Pacific Northwest in the arctic LS. The aircraft conducted a series of repeated global-scale measurements that allowed direct LS sampling of the affected region approximately a year before, the year of, and the year after the injections, without intentionally targeting any air masses (Fig. 1, left). We have used these observations to advance knowledge about (i) the chemical and physical properties of pyroCb smoke, (ii) the rates of transformation of these properties, (iii) the utility of aerosol microphysical measurements to detect and track pyroCb in the LS, and (iv) the extent that pyroCb activity contributes to average LS aerosol loadings.

The first extended sampling of the 2017 smoke occurred between 7 and 11 weeks after the initial pyroCb injection. Data from this initial sampling was used to assess the chemical and physical properties of pyroCb smoke, which are needed for modeling of pyroCb plumes, their climate impacts, and their potential chemical impacts on the stratosphere. Seven months passed before a second set of observations in the same region were obtained. We used these latter measurements, in conjunction with the earlier results, to constrain the rates of transformation of key properties of the smoke aerosols, and we discovered exceptionally stable features of pyroCb smoke that can be used to "fingerprint" a fraction of pyroCb-sourced particles in the LS. No other dataset tracks pyroCb smoke over such a long period of time. Finally, using these fingerprints, we expanded consideration of stratospheric pyroCb influences to a total of 12 airborne mission datasets going back to 2006 in both the North and South Hemispheres to estimate long-term pyroCb influences on the LS in our recent climate. We found that, considering their size and frequency relative to typical fires, pyroCb are responsible for a disproportionate amount of stratospheric aerosol. These sequential findings are presented below.

The chemical composition and physical properties of stratospheric pyroCb smoke

On the first sampling of the 2017 pyroCb smoke from the tropopause up to an altitude of 12.5 km

[1]National Oceanic and Atmospheric Administration (NOAA) Chemical Sciences Laboratory (CSL), Boulder, CO, USA. [2]Cooperative Institute for Research in Environmental Sciences, University of Colorado, Boulder, CO, USA. [3]Atmospheric Chemistry Observations and Modeling Laboratory, National Center for Atmospheric Research, Boulder, CO, USA. [4]NASA Ames Research Center, Moffett Field, CA, USA. [5]Department of Chemistry, University of Colorado, Boulder, CO, USA. [6]Department of Earth and Environmental Sciences and School of Engineering and Applied Sciences, Lamont-Doherty Earth Observatory, Columbia University, Palisades, NY, USA. [7]Department of Earth and Planetary Sciences, Harvard University, Cambridge, MA, USA. [8]Aerosol Physics and Environmental Physics, Faculty of Physics, University of Vienna, Vienna, Austria. [9]Naval Research Laboratory, Washington, DC, USA. [10]NOAA Global Monitoring Laboratory, Boulder, CO, USA. [11]Center for Aerosol and Cloud Chemistry, Aerodyne Research Inc., Billerica, MA, USA. [12]Department of Chemistry, Colgate University, Hamilton, NY, USA. [13]Naval Research Laboratory, Monterey, CA, USA. [14]Colorado Department of Public Health and Environment, Denver, CO, USA. [15]Institute of Environmental and Climate Research, Jinan University, Guangzhou, People's Republic of China.
*Corresponding author. Email: joshua.p.schwarz@noaa.gov
†Present address: Ball Aerospace, Boulder, CO, USA.
‡Present address: Department of Earth and Environmental Engineering, Columbia University, New York, NY, USA.
§Present address: Scientific Aviation, Boulder, CO, USA.
¶Present address: Atmospheric Composition Research, Climate Research Programme, Finnish Meteorological Institute, Helsinki, Finland.
#Present address: Institute for Atmospheric and Earth System Research, Department of Physics, Faculty of Science, University of Helsinki, Helsinki, Finland.

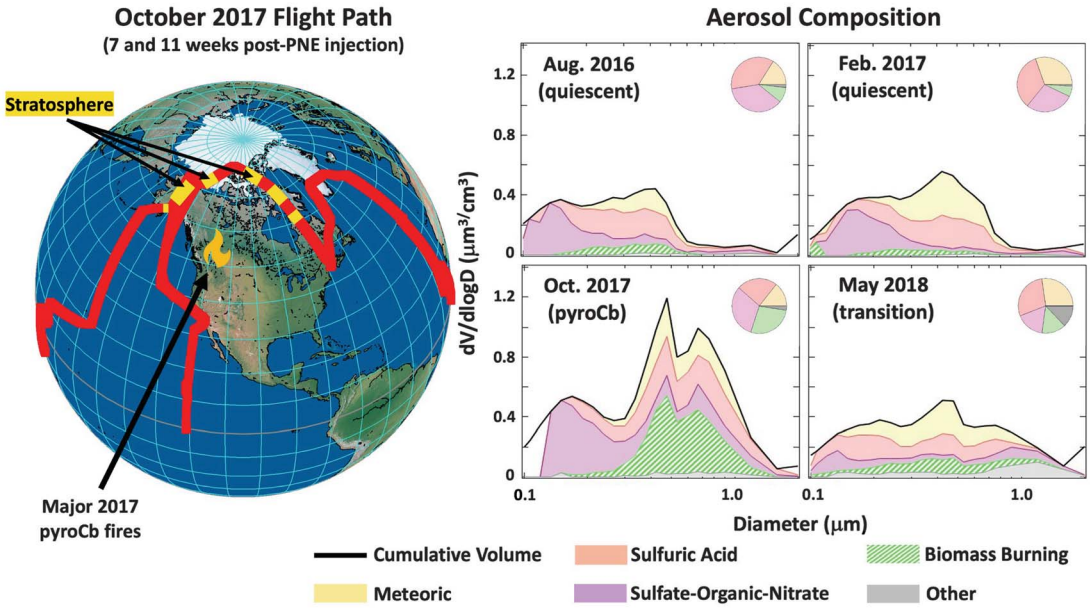

Fig. 1. Overview of in situ PNE Sampling. (**Left**) Relevant portions of the October 2017 flight path in the troposphere (red) and stratosphere in this paper (yellow) with British Columbia indicated by a flame symbol. (**Right**) Size-resolved aerosol particle–type in the Northern Hemisphere LS between August 2016 and May 2018 for particles between 0.1 and 1.5 μm (inset pie charts provide fractional comparison over all sizes). Aerosol sources from biomass burning (green) are significantly enhanced October 2017, particularly between 0.3 and 1 μm, compared with quiescent times. Note that the particle typing does not indicate mixing state.

in the stratosphere north of 55°N, concentration enhancements relative to stratospheric backgrounds were high (summarized with uncertainties in table S1). Refractory black carbon (rBC), an efficiently light-absorbing and thus climate-active species that is uniquely associated with combustion, was enhanced by a factor of 3.5, whereas organic aerosol (OA), another by-product of combustion (among other sources), was enhanced by a factor of three. Other aerosol-phase materials such as nitrate and ammonium also increased, but not by enough to allow calculation of meaningful enhancement factors. Sulfate aerosol was not enhanced in the pyroCb smoke.

Unlike the aerosol-phase materials, gas-phase biomass burning (BB) tracers [including carbon monoxide (CO), acetonitrile (CH_3CN), and others] could not be differentiated from background values in the air. When gas-phase species are scaled to the absolute rBC enhancement (~10 parts per thousand by mass) and their respective expected BB emissions factors (*25*, *26*), it is clear that the related gas-phase enhancements were small relative to background variability, and in most cases on the order of instrument limits of detection. Further, the lifetimes of gaseous species such as CO and ethane (C_2H_6) in the LS are much shorter than that of rBC. Therefore, the chemical impacts of the gas-phase species from pyroCb can be expected to lose significance more quickly than those associated with aerosol-phase materials that remain distinct from backgrounds over longer times and/or at higher dilution.

The enhanced concentrations of the various species reflect the amount of injected material and its subsequent dilution at the points of sampling. However, the relative concentration of different species is of greater fundamental importance. Specifically, the concentration ratio of rBC to light-scattering aerosol (predominantly OA in BB smoke) is a critical parameter for relating pyroCb plume light absorption to remote measurements (*23*) and is needed for modeling plume radiative impacts and self-lofting. This ratio is not directly available from remote-sensing techniques. The rBC/OA ratio specific to the 2017 pyroCb sampling was determined after subtraction of typical LS concentrations for those species (details in supplementary materials). For this earliest 2017 pyroCb interception, which provides the first in situ determination of the rBC/OA ratio for a global-scale pyroCb event, the ratio was constrained to an upper bound of 0.016 ± 0.008. This is consistent with the value (0.02) that Yu *et al.* (*23*) inferred from remote-sensing observations of plume loft for the PNE. We observed very similar ratios in stratospheric quiescent conditions (~0.016) and in fresh, non-pyroCb processed emissions from a major 2019 Washington, USA, fire (the Williams Flats Fire) that was extensively sampled (ratios of 0.012 to 0.019). It is notable that these ratios, measured over such a wide range of altitude, temperature, and age, reveal no large-scale changes in rBC/OA attributable to secondary chemistry, aerosol microphysical mechanisms, or unrelated sources and sinks large enough to drive stratospheric aerosol loads. The estimates from pyroCb measured in different ways and different stages (young, aged, diffuse, etc.) indicate the potential for reasonable uniformity in this ratio for pyroCb emissions ejected from their convective cells.

The microphysical properties of aerosols, including their size and the ways that mixtures of different species are found within individual particles (i.e., internally mixed), are critical to determining aerosol physical and chemical behavior and are directly quantifiable with in situ sampling. PyroCb-sourced particles have a specific feature that differs from that found both in most background LS aerosols and those associated with typical non-pyroCb wildfire emissions: PyroCb aerosols are larger than the typical accumulation mode size (yet still predominantly in the fine mode) (fig. S2). Figure 1, right, presents the very strong aerosol-volume enhancement observed in the October 2017 sampling that is solely due to BB-sourced particles in the 0.3- to 1.0-μm-diameter size range. This is larger than the bulk enhancement noted above; in this size range, BB aerosol concentration was enhanced by a factor of four over the quiescent LS conditions. Individual-particle composition measurements showed that pyroCb aerosol was predominantly organic in nature, as expected from BB (Fig. 1). This reflects the tropospheric origin of these particles and contrasts sharply with the composition expected were the aerosol material slowly formed in the stratosphere by the oxidation of sulfur-containing gases into aerosol sulfate. Further, compositional measurements of individual LS meteoric–sulfuric acid particles observed in the same air masses as the pyroCb smoke exhibited little or no organic material—a strong indication that secondary aerosol formation by the organic gases associated with the fire emissions, for example, by condensation or photochemistry, was also not strongly active in the smoke-influenced air over the time scale since injection.

We find that the most sensitive tool for collecting mixing-state information relevant to

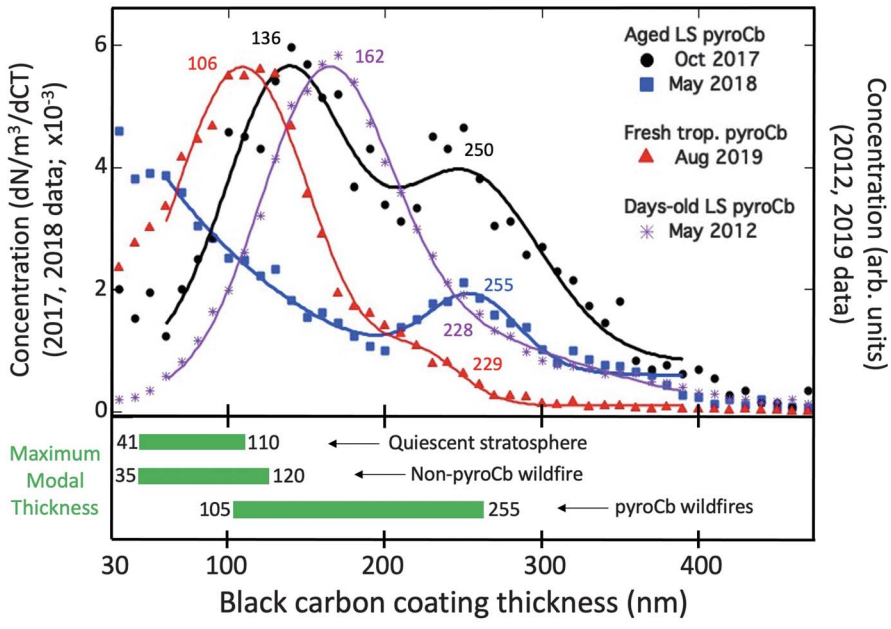

Fig. 2. The microphysical fingerprint of pyroCb. (**Top**) PyroCb-influenced stratospheric rBC coating thicknesses observed in October 2017 (black) and May 2018 (blue), alongside rBC coatings from fresh pyroCb smoke in the troposphere (red) and days-old LS pyroCb smoke (purple). Individual points represent in situ data; solid curves are double-Gaussian fits to those data. Inset numbers indicate the modes of the corresponding color-matched double-Gaussian curve. (**Bottom**) CTs in quiescent stratosphere, tropospheric wildfires, and UT/LS pyroCb smoke. Green bands represent the range of modes of observed CTs.

pyroCb activity is specific to rBC-containing particles. The large size of bulk aerosol from pyroCb translates to much larger amounts of additional aerosol material (within individual particles) associated with rBC than has been reported in past literature (*18*, *19*, *26*–*29*). We present this information through a quantity that scales with the amount of additional material associated with rBC: a coating thickness (CT) quantified by interpreting measured optical sizes of individual particles with consideration of their rBC mass content in a convenient (Mie shell-and-core) theoretical framework (*26*, *30*). Figure 2 includes a histogram of CT for the LS sampling of the global-scale pyroCb smoke measured in October 2017 (black circles). The largest mode of the 2017 sampling, at ~250 nm, is larger than modes previously observed in typical ("quiescent") stratospheric measurements (*26*), or direct samplings of fresh non-pyroCb wildfires plumes (*27*–*29*), where modes top out at 110 and 120 nm, respectively. Further, the tail of CT in the 2017 sampling extends beyond 400 nm, far larger than CTs reported in past observations. Larger CTs are associated with increased light absorption by rBC; here, the 250-nm-thick coating of the largest mode of the pyroCb-rBC causes ~40% more light absorption than the most thickly coated mode from non-pyroCb wildfires (at ~100-nm thickness). Averaged over the entire distribution of rBC coating thicknesses, this value is reduced to 15% higher efficiency in absorbing light. Hence, these microphysical properties of rBC-containing aerosol, quite distinct from those produced by other sources, have complex implications for pyroCb radiative and physical impacts in the atmosphere and on climate in general.

Constraining the rates of chemical and physical transformations in stratospheric pyroCb smoke

The second sampling of the pyroCb smoke that originated in 2017 occurred 7 months after the first, after remote-sensing techniques could no longer clearly detect the smoke in the sampled airmasses. However, these measurements did not occur in otherwise unperturbed conditions. Rather, a separate influence of large-scale dust and pollution transport also contributed to bulk enhancements of aerosol. Hence, the bulk composition and chemical makeup of the aerosol could not be meaningfully used to track changes specifically in the pyroCb-sourced material. However, although the bulk enhancement of rBC changed (and may have also been influenced by the additional input to the air), the rBC-specific microphysical characteristics of the pyroCb-aerosol remained distinct.

Figure 2 shows that the most heavily coated rBC mode (blue squares) was present with virtually unchanged size, meaning that no appreciable further accumulation or degradation of the internally mixed material had occurred. The consistency between this mode observed in October 2017 and May 2018 is notable. Considering that just a small fraction, roughly 2%, of aerosol particles that we sampled in the stratosphere during October 2017 were found to contain rBC, at first look this finding does not appear to be relevant to the bulk of the pyroCb smoke. However, because the material internally mixed with the rBC can reasonably be expected to act as a chemical proxy for the bulk aerosol from pyroCb, the implications of this finding are broad. The stability of the measured CT points to the chemical and physical stability of all pyroCb smoke in the LS. This finding, that the pyroCb smoke properties are so stable in the LS, coupled with the consistently smaller range of CT from non-pyroCb wildfires, hints that strong convective lifting is the dominant mechanism determining the properties of the smoke injected into the LS via pyroCb activity. We speculate that a combination of aqueous and/or ice phase processes and coagulation and enhanced condensation of low-volatility gases within the convective column of the pyroCb drive fast transformations of aerosol to the near-stable state existing after injection into the LS. The formation of heavily coated rBC appears to be a general accumulation-mode aerosol characteristic of pyroCb smoke in the stratosphere. Interestingly, the 2017 distribution is consistent with the aerosol size distribution from a known pyroCb smoke plume interception that occurred in 2002 (*15*, *25*), which also presents an atypically large total-aerosol particle distribution (fig. S2).

Our observation of the exceptional long-term physical stability of pyroCb-sourced aerosol in the LS contradicts contemporary expectations that UT/LS OAs undergo destructive photochemical reactions on timelines of 5 months and could imply wider and longer-term impacts from pyroCb (and potentially biomass burning more generally) in this region than previously anticipated. Specifically, Yu *et al.* (*23*) achieved a 150-day model lifetime for pyroCb organics in the LS by modeling photochemical destruction to match decay in remote-sensing observations, and a 250-day lifetime in the absence of such chemistry (via transport and/or dilution). Tropospheric studies by Hodzic *et al.* (*31*) and Lou *et al.* (*32*) inferred from tropospheric simulations that relatively strong chemical or photolytic removal was needed to reproduce UT secondary organic aerosols. Those lifetimes imply changes in rBC coating thickness of 30 and 20% over 7 months, respectively, inconsistent with the observed stability demonstrated by the ~250-nm CT mode measured in 2017 and 2018. Rather, our observations are consistent with older conclusions from in situ measurements (*33*) that carbonaceous particles larger than 300 nm can persist in the stratosphere for many months without undergoing mass depletion. If chemistry only negligibly destroys pyroCb aerosol in the LS,

then the main sinks in this region will be limited to those associated with large-scale transport and stratospheric-tropospheric exchange and sedimentation mechanisms. If this is also true for the upper troposphere, then previous studies may have incorrectly ascribed other loss processes such as wet deposition to photochemical loss. The lifetimes obtained from remote measurements of high-altitude plumes may instead reflect dilution and mixing into the larger stratosphere. In fact, our estimate of the *e*-folding time for such mixing, derived from the observed concentration change of the large-coating rBC mode, is ~5 months, consistent with the observations on the dissolution of the larger pyroCb plume at higher altitudes (*23*).

Fingerprints of pyroCb persist in LS aerosol microphysical properties

The distinctive and persistent aerosol microphysical features introduced above remained discernible in the LS longer than any other feature of the injection measured either remotely or by in situ techniques. In fact, because of both their persistence and the contrast they provide to rBC emitted by non-pyroCb sources, we find that measurements of thickly coated rBC concentrations can be used to assess the long-term influence of pyroCb activity in the LS. First we explore the contrast, then we test its utility for identifying pyroCb aerosol contributions in LS data obtained since 2006. Figure 2 shows that pyroCb events can generate larger coating thickness modes (modes up to 255 nm) than non-pyroCb fires (modes up to 120 nm). Further, we find a contrast in the percentage of rBC-containing particles with CTs greater than 200 nm ($P_{>200}$) from different sources. In both the published literature (*26*–*29*) and an expansive set of previously unpublished open-burning smoke data (African smoke encountered during the NASA ATom and North American wildfires sampled during the 2019 NASA/NOAA FIREX-AQ mission), we find that non-pyroCb BB sources generate $P_{>200}$ on average of just 2% with a standard deviation of 1%. PyroCbs generate $P_{>200}$ at least as high as 37% (tables S2 and S3). Two unpublished pyroCb CT distributions shown in Fig. 1 provide further support for the occurrence of these pyroCb smoke characteristics over a wider altitude range. On 14 May 2012, days-old smoke transported through the stratosphere from a pyroCb event in Russia was sampled at 12 km over the continental US. The rBC within that plume was heavily coated (Fig. 1, purple curve), with a primary mode at 162 nm, a secondary mode at 228 nm, and a tail extending beyond 300 nm. More recently, we obtained direct sampling of a small-scale pyroCb in the troposphere at 8- to 9-km altitude within hours of emission from the August 2019 Williams Flats Fire in Washington, USA (*34*). CTs from that dataset (Fig. 2, red triangles) again exhibit heavily coated rBC populations enhanced over those of a typical wildfire with a secondary CT mode centered at 229 nm. The CT distributions from both these events showed $P_{>200}$ well beyond 3%.

Examination of two published UT/LS pyroCb smoke samplings using the same rBC-measurement technique used here provide additional case studies fully consistent with our findings. Dahlkötter *et al.* (*18*) sampled days-old pyroCb smoke in the UT/LS and reported evidence for a CT mode at 160 nm, with a shoulder extending at least to 250 nm. Ditas *et al.* (*19*) sampled wildfire smoke in the LS and reported large CTs with the tail of the distribution extending beyond 300 nm. We have revisited the back-trajectory analysis of that sampling (fig. S4) and now associate it unequivocally with a pyroCb event in Siberia (details in supplementary materials). Although individual modes are less evident in that dataset than here, Ditas *et al.* inferred large CT modes by decomposing the distribution into multiple Gaussians; their pyroCb-affected coating thickness distribution shows a mode at ~220 nm. These publications did not include $P_{>200}$ values. Note that we also observed stratospheric air with low $P_{>200}$. These observations rule out the possibility of widespread generation of CTs larger than 200 nm by interactions of convective columns with non-pyroCb smoke; such an effect would be expected to provide a much more regular signal on a seasonal basis. In total, we are not aware of any noteworthy nonlaboratory sources of rBC that produce coatings in the larger pyroCb range (fossil fuel sources generate $P_{>200} \sim 0$). Our observations and the associated literature search indicate that $P_{>200}$ of >2% are unequivocally produced by pyroCb, that only pyroCb generate CT modes of >120 nm, and large non-pyroCb sources typically only generate $P_{>200}$ of ≤3%.

To test the utility of these features, we identified evidence of convincing pyroCb influence in an extensive collection of airborne campaigns spanning the past 13 years, limited to data in the LS over a wide latitude range (table S4). We examined these large datasets of stratospheric air for observations of CT distributions with at least one mode at thicknesses larger than those seen from non-pyroCb wildfires (i.e., >120 nm), while simultaneously having $P_{>200}$ of five standard deviations above that of non-pyroCb sources (table S3). The published literature provides information on independently documented pyroCb activity.

Most of the datasets did not indicate strong pyroCb influence, consistent with a lack of known pyroCb activity affecting their sampled regions or time windows. However, clear instances of pyroCb influence were indeed found ("flagged"). The earliest example of obvious pyroCb contributions being flagged occurred in the LS at roughly 30°N latitude in July 2007 (TC4 mission; see supplementary materials). In this case, the influence was traced back to the Milford Flat pyroCb in Utah, USA, which occurred 1 week prior. The CT distribution is bimodal, with the larger mode at 169 nm. Southern Hemisphere LS air was flagged in March 2010 during research flights south of New Zealand (HIPPO mission; see supplementary materials). We attribute this to a February 2010 pyroCb formation in western Australia, from which long-range transport of aerosol layers were clearly visible at ~12 km by remote sensing (*35*). Earlier sampling in this region, in 2009, was also flagged, with a clear CT mode at 179 nm and $P_{>200} \sim 27\%$. A case can be made to link the flagging to the major Australian Black Saturday fires ~9 months prior, although satellite imagery indicated that LS conditions were consistent with quiescent periods by June 2009 (*36*). On the basis of our findings here, that the CT signatures of 2017 injections were the longest-lived discernible features of the pyroCb smoke in the LS, and that ~10 months after injection we observed $P_{>200} \sim 22\%$, this association is reasonable. Finally, a flagging occurred at about the same time in the NH, with $P_{>200} \sim 12\%$. We do not find an associated documented pyroCb event but consider this case a good illustration of the value of these measurements used for identifying potential pyroCb injections in the LS, especially in the historical record prior to the recent proliferation in pyroCb research.

Constraining pyroCb influence in the lower stratosphere

The long-term persistence of thickly coated rBC in the LS, together with the associations we found between such features and documented pyroCb events, supports the use of this microphysical fingerprint to infer pyroCb influence in the LS even when it is not generating a five–standard deviation enhancement in $P_{>200}$, as above. In this case, the fractional contributions of pyroCb to the entire LS rBC population are estimated on the basis of observed $P_{>200}$ coupled with assumptions about different source characteristic and some simple algebra (tables S3 to S5 and supplementary text). In brief, we assume different fixed-source values for $P_{>200}$ produced by pyroCb and non-pyroCb (i.e., all other rBC sources) and calculate the relative contributions of each on the basis of the observed number fraction. Having attributed the rBC sourced by pyroCb in this way, we have a powerful proxy for all the pyroCb-sourced aerosol in the air mass. This attribution provides no information on LS aerosols arising from different sources (e.g., mineral dust, sulfate, etc.).

Our reexamination of the 13 years of in situ stratospheric data collected in both the Northern and Southern Hemispheres has produced statistically significant estimates of long-term pyroCb influence in each hemisphere. These are the first such estimates based on in situ sampling of pyroCb smoke in the stratosphere and are not obtainable from remote-sensing or other bulk-aerosol techniques. These data were assembled from both localized (i.e., collected with research aircraft operating from a fixed base) and global-scale campaigns (i.e., with aircraft transiting across wide latitude ranges from near one pole to the other). None of the campaigns targeted pyroCb influence, so all the sampling was unbiased. Each set of measurements typically extended over ~1 month. We have 12 independent measurements for the NH and 9 for the Southern Hemisphere (SH). For much of these data (all the SH data and >80% of the NH data), concurrent sulfur hexafluoride (SF_6) concentration measurements were available and were evaluated. SF_6, a long-lived tracer of anthropogenic origin, follows the large-scale movement of air in the stratosphere as driven by the Brewer-Dobson circulation, with entry of rising air in the tropics that then arches over a range of altitudes to descend at the poles. Depending on the path taken by a particular air parcel, its age after entry into the stratosphere can vary widely before finally reaching the poles, with faster transport occurring at lower altitudes (see supplementary materials for the surface trends, observed SF_6 histograms, and mean age of air related to altitude in the LS). SF_6 measurements enabled analysis of pyroCb as a function of mean age of air or mean altitude in the stratosphere and provide context to how representative our findings are in the LS.

We find that pyroCb activity has an impact on stratospheric rBC much larger than expected given their relative frequency and size compared with non-pyroCb fires and other sources of rBC. Over the entire 13-year dataset, pyroCb activity increased rBC in the NH LS by 10 to 25%, and by 10 to 22% in the SH LS. These ranges reflect uncertainties arising from the assumptions on source-dependent microphysical characteristics for rBC, statistical uncertainty, and variations depending on inclusion or exclusion of the strong pyroCb late-2017 NH observations in the calculations. This attribution for rBC can be approximately associated with OA on the basis of the reasonable stability of rBC/OA ratios explored above in fresh wildfire plumes, UT/LS pyroCb smoke, and in the quiescent LS (supplementary materials). On average, these results were obtained for air of 1-year mean age in the NH, and 1.5 years in the SH. Analysis of the subset of LS air that spent on average 3 years since surface interactions (corresponding to a range of 5 to 10 km above the tropopause in the stratosphere) produces a very similar pyroCb influence estimate with poorer statistics. This strengthens the relevance of these attribution fractions to larger volumes of stratospheric air, over longer times. The supplementary materials include a mass-balance check based on the measurements made 10 months after the PNE, when the smoke can be assumed to be well mixed in the background, and show that these results are not unphysical.

Implications

PyroCb efficiently inject aerosols with distinctive features into the UT/LS, and those aerosols survive without significant photochemical or chemical degradation for time scales of at least 1 year and make up ~1/5 of all lower stratospheric rBC and OA over decadal time scales.

The aerosol fingerprints of pyroCb can be used to detect pyroCb compositional contributions over a wide range of magnitudes and air mass age in the LS, even as their local concentrations decrease to levels below the detection threshold of remote-sensing or in situ gas-phase measurements, and without any need for a priori knowledge of specific pyroCb events. Using them to constrain pyroCb influence in the LS informs mechanisms of stratospheric dynamics and chemistry from other potentially important perturbations of the LS. These include volcanoes, rocket emissions, climate interventions, nuclear winter, and supersonic transport emissions. Hence these finding are very broadly relevant.

The direct transport of pyroCb aerosols to the stratosphere explains the heightened influence of pyroCb activity on the region compared with typical wildfires. For example, the PNE represents only a small fraction of the 2017 NH burned area and only ~5% of the CO emissions (*37*, *38*). Yet nearly 1 year later, it was still responsible for ~40% of the black carbon aerosol well mixed into the NH LS and observed in untargeted sampling (table S5). This result was so unexpected that we performed a simple mass balance test to confirm that it is physical. Clearly, representation of large pyroCb events in models is necessary to capture both year-to-year stratospheric variability at this level and shorter-term larger radiative impacts. The radiative effects of the PNE were recently estimated through modeling (*39*) to manifest a net negative top of the atmosphere forcing. This result was strongly dependent on rapid atmospheric adjustments in the stratosphere driven by localized heating by the smoke. By extension, the long-term pyroCb influence found here would also provide a net-negative influence, approximately one-fifth that of the typical LS.

Although the fractional importance of pyroCb activity to total LS aerosol varies with the strength of non-pyroCb sources to this background (for example, oxidation of sulfur species to sulfate), it is such an efficient transport pathway of aerosol that it may well have a dominant impact on either future trends of stratospheric aerosol or their uncertainties. This speculation springs from expectations for increases in both atmospheric instability and wildfire frequency, size, and geographic distribution, which could have strong synergistic impacts on pyroCb frequency and strength (*12*, *13*, *40*, *41*). Indeed, some of these expectations are already being met: The pyroCb "super" outbreak in Australia during 2019 and 2020 injected three times more smoke into the stratosphere than the PNE (*42*). Clearly, the significance of pyroCb activity to stratospheric aerosol highlights the importance of robust predictions of pyroCb development, frequency, and size both currently and in future climates, because these events have tremendous potential to shift global stratospheric aerosol composition and chemistry, as well as dynamics (*7*, *8*, *39*).

REFERENCES AND NOTES

1. M. Fromm *et al.*, *Geophys. Res. Lett.* **27**, 1407–1410 (2000).
2. M. D. Fromm, R. Servranckx, *Geophys. Res. Lett.* **30**, 1542 (2003).
3. M. Fromm *et al.*, *Bull. Am. Meteorol. Soc.* **91**, 1193–1210 (2010).
4. D. A. Peterson *et al.*, *NPJ Clim. Atmos. Sci.* **1**, 30 (2018).
5. S. M. Khaykin *et al.*, *Geophys. Res. Lett.* **45**, 1639–1646 (2018).
6. D. A. Peterson *et al.*, *J. Appl. Meteorol. Climatol.* **56**, 471–493 (2017).
7. S. Solomon *et al.*, *Proc. Natl. Acad. Sci. U.S.A.* **119**, e2117325119 (2022).
8. P. Bernath, C. Boone, J. Crouse, *Science* **375**, 1292–1295 (2022).
9. E. S. Kasischke, M. R. Turetsky, *Geophys. Res. Lett.* **33**, L09703 (2006).
10. J. T. Abatzoglou, A. P. Williams, *Proc. Natl. Acad. Sci. U.S.A.* **113**, 11770–11775 (2016).
11. A. L. Westerling, *Philos. Trans. R. Soc. London Ser. B* **371**, 20150178 (2016).
12. D. A. Peterson, E. J. Hyer, J. R. Campbell, J. E. Solbrig, M. D. Fromm, *Mon. Weather Rev.* **145**, 2235–2255 (2017).
13. G. Di Virgilio *et al.*, *Geophys. Res. Lett.* **46**, 8517–8526 (2019).
14. A. E. Waibel *et al.*, *Chemosphere, Glob. Chang. Sci.* **1**, 233–248 (1999).
15. H. J. Jost *et al.*, *Geophys. Res. Lett.* **31**, 1–5 (2004).
16. P. K. Hudson *et al.*, *J. Geophys. Res.* **109**, D23S27 (2004).
17. E. A. Ray, *J. Geophys. Res.* **109**, D18304 (2004).
18. F. Dahlkötter *et al.*, *Atmos. Chem. Phys.* **14**, 6111–6137 (2014).
19. J. Ditas *et al.*, *Proc. Natl. Acad. Sci. U.S.A.* **115**, E11595–E11603 (2018).
20. K. Christian *et al.*, *Geophys. Res. Lett.* **46**, 10061–10071 (2019).
21. O. Torres *et al.*, *J. Geophys. Res. Atmos.* **125**, e2020JD032579 (2020).
22. J. J. D. Hooghiem *et al.*, *Atmos. Chem. Phys.* **20**, 13985–14003 (2020).
23. P. Yu *et al.*, *Science* **365**, 587–590 (2019).
24. C. R. Thompson *et al.*, *Bull. Am. Meteorol. Soc.* **103**, E761–E790 (2022).
25. M. Fromm, D. Peterson, L. Di Girolamo, *J. Geophys. Res. Atmos.* **124**, 13254–13272 (2019).
26. J. P. Schwarz *et al.*, *J. Geophys. Res.* **113**, D03203 (2008).
27. J. W. Taylor *et al.*, *Atmos. Chem. Phys.* **14**, 13755–13771 (2014).
28. A. E. Perring *et al.*, *J. Geophys. Res. Atmos.* **122**, 1086–1097 (2017).

29. J. Ko, T. Krasowsky, G. Ban-Weiss, . *Atmos. Chem. Phys.* **20**, 15635–15664 (2020).
30. J. P. Schwarz *et al*., *Geophys. Res. Lett.* **35**, L13810 (2008).
31. A. Hodzic *et al*., *Atmos. Chem. Phys.* **16**, 7917–7941 (2016).
32. S. Lou *et al*., *J. Adv. Model. Earth Syst.* **12**, e2020MS002266 (2020).
33. D. M. Murphy, D. J. Cziczo, P. K. Hudson, D. S. Thomson, *J. Geophys. Res.* **112**, D04203 (2007).
34. D. A. Peterson *et al*., *Bull. Am. Meteorol. Soc.* **103**, E2140–E2167 (2022).
35. A. Foth *et al*., *Atmos. Chem. Phys.* **19**, 6217–6233 (2019).
36. J. M. Siddaway, S. V. Petelina, *J. Geophys. Res.* **116**, D06203 (2011).
37. H. C. Pumphrey *et al*., *Atmos. Chem. Phys.* **21**, 16645–16659 (2021).
38. C. Wiedinmyer *et al*., *Geosci. Model Dev.* **4**, 625–641 (2011).
39. C. C. Liu *et al*., *Geophys. Res. Lett.* **49**, (2022).
40. J. Chen, A. Dai, Y. Zhang, K. L. Rasmussen, *J. Clim.* **33**, 2025–2050 (2020).
41. M. Taszarek, J. T. Allen, M. Marchio, H. E. Brooks, *NPJ Clim. Atmos. Sci.* **4**, 35 (2021).
42. D. A. Peterson *et al*., *NPJ Clim. Atmos. Sci.* **4**, 38 (2021).
43. S. C. Wofsy *et al*., ATom: Merged Atmospheric Chemistry, Trace Gases, and Aerosols, version 2, ORNL DAAC (2021); https://doi.org/10.3334/ORNLDAAC/1925.

ACKNOWLEDGMENTS

We thank the ATom science team and leadership, the DC-8 pilots and crew for their outstanding commitment to the mission, and K. Aikin of NOAA CSL for assistance with creating the figures. **Funding:** This work was supported by the ATom investigation under NASA's Earth Venture program (grant NNX15AJ23G). Elements of the manuscript were supported by the National Center for Atmospheric Research, which is a major facility sponsored by the National Science Foundation under cooperative agreement 1852977. A.K. was supported by the Austrian Science Fund's Erwin Schrodinger Fellowship J-3613. B.A.N., J.C.S., P.C.-J., and J.L.J. were supported by NASA grants NNX15AH33A and 80NSSC21K1451. D.A.P. was supported by the Navel Research Laboratory Base Program and NASA Modeling, Analysis, and Prediction (MAP) Program (80HQTR21T0099). J.M.K., I.B., P.C.-J., K.D.F., J.L.J., A.K., K.D.L., K.M., F.M., B.A.N., J.P., E.A.R., G.P.S., J.C.S., C.T., and C.J.W. were fully or partly supported by NOAA cooperative agreement NA17OAR4320101. B.W. and M.D. have received funding from the European Research Council (ERC) under the European Union's Horizon 2020 research and innovation program under grant agreement 640458 (A-LIFE). Additional support was provided by the University of Vienna. **Author contributions:** Data collection and curation: E.C.A., A.E.P., F.M., I.B., C.A.B., K.M., T.P.B., P.C.-J., R.C., B.D., M.D., K.D.F., A.J.H., R.S.H., J.L.J., A.K., K.D.L., D.M.M., B.A.N., J.P., E.A.R., T.R., G.P.S., J.C.S., B.W., C.T., C.J.W., S.C.W., and J.P.S. Analysis: E.C.A., I.B., C.A.B., T.P.B., P.C.-J., R.C., B.D., M.D., K.D.F., A.J.H., R.S.H., J.L.J., A.K., D.M.M., B.A.N., J.P., T.R., G.P.S., J.C.S., B.W., C.T., C.J.W., S.C.W., and J.P.S. Funding acquisition: S.C.W., T.R., and J.P.S. Methodology: J.M.K., P.C.-J., M.F., K.D.F., J.L.J., D.M.M., D.A.P., G.P.S., P.Y., and J.P.S. Writing, review, and editing: All authors. **Competing interests:** The authors declare that they have no competing interests. **Data and materials availability:** rBC microphysical property data from past field campaigns and ATom used here are available at https://csl.noaa.gov/groups/csl6/measurements/data/2022-Katich-etal/. All other data are from ATom and have been deposited with the Oak Ridge National Laboratory Distributed Active Archive Center (ORNL DAAC) (*43*). **License information:** Copyright © 2023 the authors, some rights reserved; exclusive licensee American Association for the Advancement of Science. No claim to original US government works. https://www.science.org/about/science-licenses-journal-article-reuse

SUPPLEMENTARY MATERIALS

science.org/doi/10.1126/science.add3101
Materials and Methods
Supplementary Text
Figs. S1 to S5
Tables S1 to S4
References (*44*–*54*)

Submitted 3 June 2022; accepted 31 January 2023
10.1126/science.add3101

NEUROSCIENCE

Hyperexcited limbic neurons represent sexual satiety and reduce mating motivation

Xiaojuan Zhou[1]†, Ang Li[1,2]†, Xue Mi[1]†, Yixuan Li[1,2], Zhaoyi Ding[1], Min An[1], Yalan Chen[1], Wei Li[1], Xianming Tao[1], Xinfeng Chen[1,2], Ying Li[1]*

Transient sexual experiences can have long-lasting effects on behavioral decisions, but the neural coding that accounts for this change is unclear. We found that the ejaculation experience selectively activated estrogen receptor 2 (*Esr2*)–expressing neurons in the bed nucleus of the stria terminalis (BNST)—BNST^{Esr2}—and led to persistent decreases in firing threshold for days, during which time the mice displayed sexual satiety. Inhibition of hyperexcited BNST^{Esr2} elicited fast mating recovery in satiated mice of both sexes. In males, such hyperexcitability reduced mating motivation and was partially mediated by larger HCN (hyperpolarization-activated cyclic nucleotide-gated) currents. Thus, BNST^{Esr2} not only encode a specific mating action but also represent a persistent state of sexual satiety, and alterations in a neuronal ion channel contribute to sexual experience–dependent long-term changes to mating drive.

Transient social experiences (such as a sexual experience) can lead to long-lasting changes in internal states and affect social behaviors, such as mating, aggression, and parental care (*1*–*3*). For example, after successful mating with ejaculation, many species quickly display an inhibition of the tendency to mate for hours, days, or longer, an effect known as sexual satiety (*4*). This inhibition is essential not only for avoiding excessive risk-taking or the energy-consuming search for new sexual partners but also for increasing the fertilization rate (*5*). Yet relatively little is known about how such experience-dependent changes are represented in neural circuits and result in long-lasting effects on behavioral decisions.

Experiencing ejaculation drives sexual satiety in both sexes

When we presented a male mouse with a female mouse in estrus, the male typically began to investigate the female and attempted to mount her within minutes, during which time the female played an active role by either showing receptive behavior (lordosis) or rejecting the male (by sitting down or fleeing) (Fig. 1A and movie S1). After mating successfully, males and females typically lose interest in sexual behavior (*6*, *7*), with substantial effects on both the readiness to transition from copulatory-seeking behavior to mating and the execution of different mating actions, which gradually returns over several days to weeks (Fig. 1, B to D, and fig. S1). In female mice, experiencing ejaculation by vasectomized male mice (referred to as the ejaculatory reflex) can suppress sexual receptiveness soon after mating (Fig. 1, C and D) and induce luteal activity for ~2 weeks (fig. S1, E to H) (*7*). However, no such change was observed in mice that experienced multiple intromissions but were separated from their partner before ejaculation (Fig. 1, B to D).

Ejaculation selectively activates *Esr2*-expressing BNSTpr neurons

In rats and gerbils, ejaculation-induced expression of c-Fos is present in different brain regions corresponding to successive stages of the vomeronasal pathway, including the posterior bed nucleus of the stria terminalis (BNSTp), posterodorsal medial amygdala (MeApd), and medial subparafascicular thalamic nucleus (mSPF), but not the median preoptic nucleus (MPN) (*8*, *9*). These have been identified to play key roles in transforming neural representation of external social cues into behavioral decisions that drive sex-specific mating actions (*10*–*19*). Using fluorescence in situ hybridization (FISH), we examined which brain regions were preferentially active in ejaculated male mice as compared with those that experienced multiple intromissions without ejaculation (fig. S2A). We observed the highest fold-change in the number of *Fos*$^+$ neurons in the BNSTp and, to a lesser extent, in the MeApd, but there were no significant changes in the mSPF or MPN (fig. S2, B and C). At the anatomical level, BNSTp neurons send major projections to the MeA and hypothalamic areas (*20*), both of which show stable changes in representing conspecific social cues after a sexual experience (*21*, *22*). Therefore, we sought to examine the genetic identity of the ejaculation-activated neurons in the BNSTp and whether they encode sexual experience–dependent changes and regulate behavioral decisions in the long term.

According to recent single-nuclei RNA sequencing (snRNA-seq), the principal nucleus of the BNST (BNSTpr) contains two sexually dimorphic neuronal clusters that express either estrogen receptor 2 (*Esr2*) or suppression of tumorigenicity 18 (*St18*) (*23*). Using multiplex FISH, we determined that BNSTpr neurons expressing *Esr2* (BNST^{Esr2}) located in both the dorsal and ventral compartments were activated after ejaculation, whereas *St18*-expressing neurons (BNST^{St18}) were preferentially activated during male-female interactions before ejaculation (fig. S3). To directly monitor BNST^{Esr2} or BNST^{St18} activity during mating, we performed single cell–resolution Ca^{2+} imaging using head-mounted microendoscopes in freely behaving *Esr2-Cre* or *St18-Cre* mice (Fig. 1E and fig. S5A; evaluation of both mouse lines is provided in fig. S4). In both sexes, a majority of BNST^{Esr2} were activated by social sniffing and ejaculation but not by other mating actions (Fig. 1G and fig. S5B). This response contrasts with that in BNST^{St18}, most of which were activated by social sniffing and intromission but not by ejaculation (Fig. 1I and fig. S5E). Moreover, distinct BNSTpr neuronal subsets that were activated by either ejaculation or other mating actions, although spatially intermingled (fig. S5, C and F), were for the most part distinct from neurons activated during early social sniffing, with the relative activity of each neuron during sexual behaviors and during sniffing being negatively correlated (fig. S5, D and G).

Ejaculation-induced BNST^{Esr2} activation dramatically decreased in both sexes after males and females were separated, but the postejaculatory spontaneous activity in individual neurons differed. As compared with the baseline before an intruder was introduced, some BNST^{Esr2} were transiently activated during ejaculation, whereas others displayed higher spontaneous activities for 1 to 2 min after ejaculation (fig. S6, A to C). Such persistent activation typically lasted throughout the rest of the recording period (5 to 30 min) during a single day and was gradually reduced over time, although the time constant after which this activation was no longer significantly different from the baseline was unclear (Fig. 1F and fig. S6, D and E). These results suggested that a subset of ejaculation-activated BNST^{Esr2} may encode persistent changes in internal states after successful mating. By contrast, nearby nonoverlapping BNST^{St18} consisted of neurons that were selectively activated during sniffing an opposite-sex intruder (fig. S5, E to G) or during mating actions other than ejaculation (Fig. 1H).

Hyperactivated BNST^{Esr2} encode sexual satiety

Male BNSTpr neurons that express *Aromatase* (BNST^{Arom}) respond differently to the two sexes (*17*). Using FISH, we found that 37% of

[1]Chinese Institute for Brain Research, Beijing 102206, China. [2]Academy for Advanced Interdisciplinary Studies, Peking University, Beijing 102206, China.
*Corresponding author. Email: liying@cibr.ac.cn
†These authors contributed equally to this work.

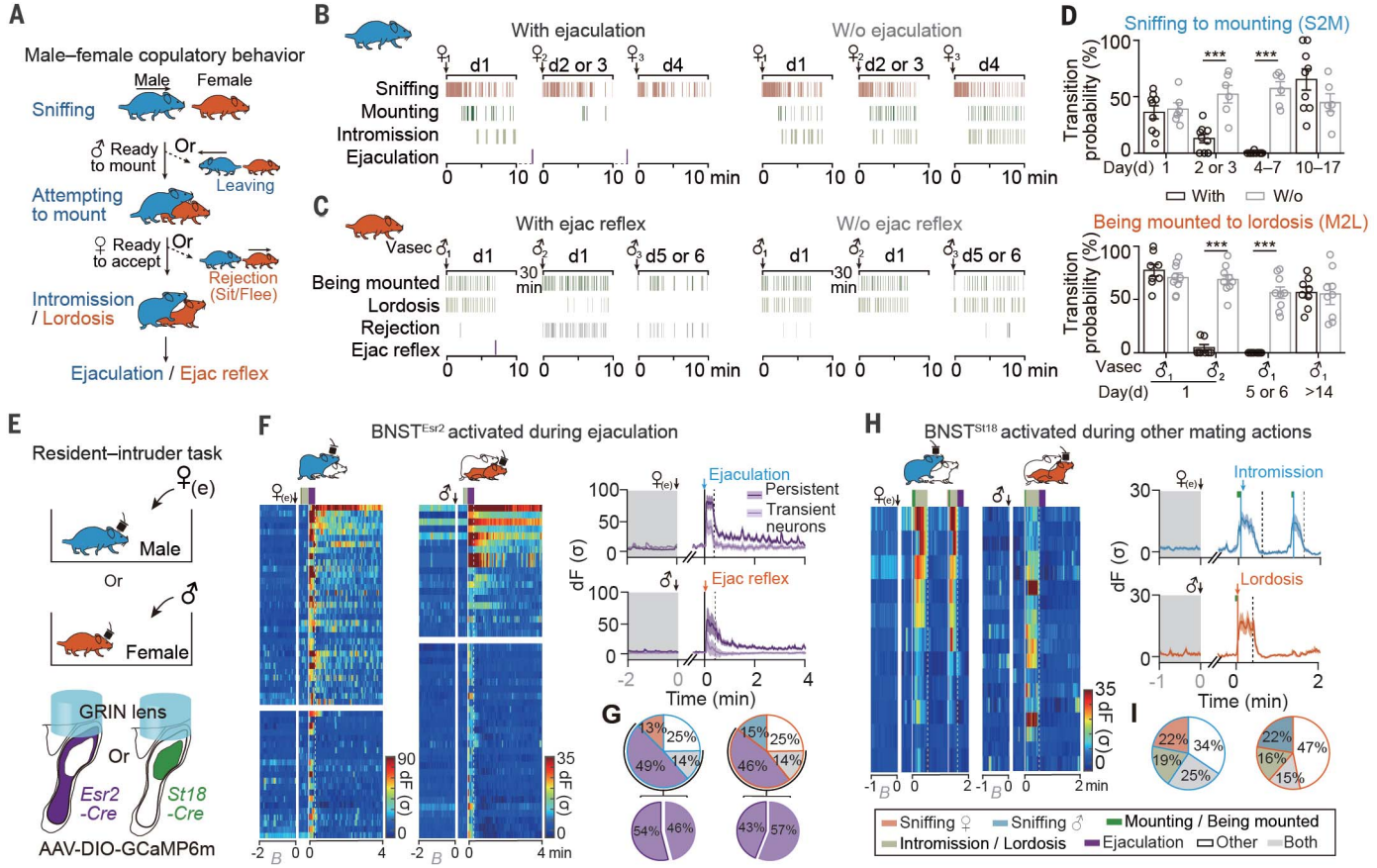

Fig. 1. Ejaculation drives sexual satiety and selectively activates *Esr2* neurons in the BNSTpr of both sexes. (**A**) Typical male and female mating behaviors in mice. (**B** and **C**) Behavioral events of (B) male or (C) female virgin mice 10 min after the initial sniffing of female intruders on consecutive days or being mounted by two different vasectomized (vasec) male mice on day 1 (d1) and by a new male on d5 or d6 (theoretically in another estrous cycle). Males either (left) were allowed to ejaculate during mating or (right) were separated from the female before ejaculation. (**D**) The probability of transitioning from copulatory-seeking behavior to mating in (top) male and (bottom) female mice during the period shown in (B) and (C). Data are shown as the mean ± SEM. Mann-Whitney *U*-test was used; ***$P < 0.001$. (**E**) (Top) Experimental design and (bottom) schematic of microendoscopic Ca^{2+} imaging. e, in estrus; GRIN, gradient index. (**F** and **H**) Heatmaps of representative Ca^{2+} activity of (F) $BNST^{Esr2}$ or (H) $BNST^{St18}$ before intruder introduction (spontaneous baseline, *B*) and corresponding to the experience of (F) ejaculation or (H) other mating actions in (left) males and (right) females. Colored bars at the top indicate mating behaviors as defined in (H). Line charts show averaged Ca^{2+} activity of neurons in each subpopulation; shading indicates SEM. Solid and dashed vertical lines indicate onset and offset of different mating actions, respectively. (**G** and **I**) Fractions of (G) $BNST^{Esr2}$ or (I) $BNST^{St18}$ activated during different behavioral events. Bottom pie charts in (G) show fractions of ejaculation-responsive neurons displaying either persistent or transient activation. In (G), data are from 323 neurons from four males and 197 neurons from four females. In (I), data are from 64 neurons from two males and 184 neurons from three females.

$BNST^{Arom}$ express *Esr2*, whereas 35% express *St18* (fig. S7). The activities of male $BNST^{Esr2}$ and $BNST^{St18}$ were greater upon introduction of a female intruder as compared with a male intruder (fig. S8, A and B). However, such responses subsided significantly in $BNST^{Esr2}$, but not in $BNST^{St18}$, during later investigations (fig. S8C), particularly after the first mount (fig. S8D).

To further examine whether $BNST^{Esr2}$ activity encoded sexual satiety, socially isolated (for at least 1 day) male mice were allowed to interact with a female intruder in either estrus or diestrus and then were tested again with a different estrous female 24 hours later (Fig. 2A). Four out of five of the examined male mice were able to perform another mating 24 hours after ejaculation (Fig. 2B), suggesting that they were not fully satiated before mating on day 2. As compared with the baseline activity on day 1, only behaviorally satiated mice displayed spontaneous Ca^{2+} transients that had larger amplitudes and occurred more frequently (Fig. 2C, group 3). Such an increase could last throughout the sexual refractory period for days and returned to the baseline level associated with virgin mice once the mice were ready to mate again; the increase quickly occurred again after another ejaculation-induced sexual satiety (fig. S9, A to C). By contrast, in the unmated (group 1) or recently mated but unsatiated (group 2) males, spontaneous Ca^{2+} transients of $BNST^{Esr2}$ remained stable 24 hours after the social experience (Fig. 2C). As another indicator of encoding sexual satiety in $BNST^{Esr2}$, the spontaneous Ca^{2+} transients (Fig. 2D) and the activity of $BNST^{Esr2}$ upon the introduction of a female intruder (fig. S8E) negatively correlated with the readiness to transition from sniffing to mounting.

Similarly, in sexually satiated females, the amplitude and frequency of spontaneous Ca^{2+} transients were also increased regardless of fertilization state (Fig. 2, E and F). Such increases typically lasted throughout pseudopregnancy or pregnancy and the period of lactation and decreased to baseline levels associated with virgin females after behavioral recovery (fig. S9, D to F). However, the spontaneous Ca^{2+} transients in $BNST^{Esr2}$ from virgin females in estrus versus diestrus were similar

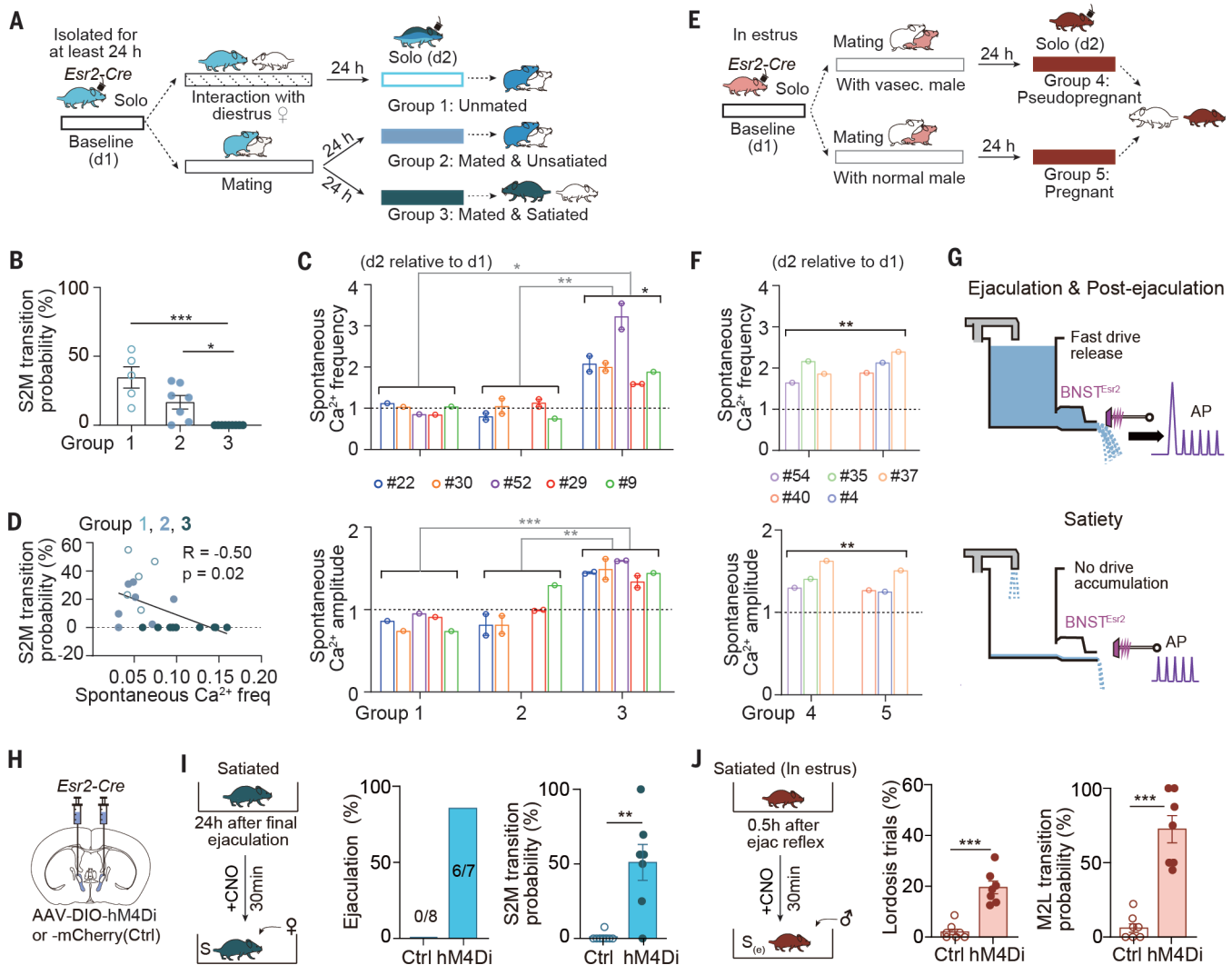

Fig. 2. Hyperactivated BNST^{Esr2} encode persistent sexual satiety in both sexes. (**A** and **E**) Examining the spontaneous Ca^{2+} activity of BNST^{Esr2} in individually isolated (A) male and (E) female mice before day 1 (d1) and 24 hours after d2 exposure to an opposite-sex intruder. (**B**) Probability of transitioning from sniffing to mounting (S2M; 10 min after initial sniffing) in unmated (group 1; five trials from five mice), mated and unsatiated (group 2; seven trials from four mice), and mated and satiated (group 3; nine trials from five mice) males on day 2. (**C** and **F**) Averaged (top) frequency and (bottom) amplitude of spontaneous Ca^{2+} transients of BNST^{Esr2} in (C) male and (F) female mice on day 2. The data point from each mouse was normalized to its baseline value on day 1. Comparison was done for each group with the baseline unless otherwise specified. The #37 female was first exposed to a vasectomized male and then was exposed to an intact male after behavioral recovery. (**D**) Correlation between the probability of transitioning from sniffing to mounting and the averaged spontaneous Ca^{2+} frequency of BNST^{Esr2} in each mouse. (**G**) A hydraulic model to reconcile the responses of BNST^{Esr2} during ejaculation, soon after ejaculation, and during sexual satiety. (**H**) Strategy to bilaterally express hM4Di or mCherry (control) in BNST^{Esr2}. (**I** and **J**) Behaviors of sexually satiated (I) male and (J) female mice exposed to an opposite-sex intruder, 30 min after CNO injection. M2L, transitioning from being mounted to lordosis. In (B) and (C), Kruskal-Wallis test with Dunn's multiple comparisons correction was used. In (F), (I), and (J), Mann-Whitney *U*-test was used; $^*P < 0.05$, $^{**}P < 0.01$, $^{***}P < 0.001$. For all relevant panels, data are shown as the mean ± SEM.

but were lower than those in virgin males (fig. S9, G to I).

To investigate whether persistent activation of BNST^{Esr2} is necessary to maintain sexual satiety, we expressed G_i-coupled DREADD (designer receptor exclusively activated by designer drugs) hM4Di bilaterally in the BNST of *Esr2-Cre* mice (Fig. 2H). In six of seven satiated males, inhibition of BNST^{Esr2} by means of intraperitoneal injection of clozapine-*N*-oxide (CNO) restored their mating behavior in 30 min and led to ejaculation (Fig. 2I), with the readiness to transition from sniffing to mounting comparable with that in virgin males (fig. S10, A to C). The same manipulation largely restored sexual receptiveness in recently mated females (Fig. 2J and fig. S10, D and E), who typically show a reduced interest in males (*24*). Similar deficits in achieving sexual satiety were also observed in BNST^{Esr2}-ablated mice of both sexes after consecutive ejaculation experiences (fig. S11).

Activation of male BNST^{Esr2} reduces mating motivation

In virgin males, both chemogenetic silencing and ablation of BNST^{Esr2} induced more frequent mounting behaviors toward male intruders, whereas chemogenetic silencing additionally increased their readiness to transition from sniffing to mounting toward female intruders and delayed the ejaculation latency by almost twofold (figs. S11D and S12, A to C). However, chemogenetic inhibition of BNST^{Esr2}

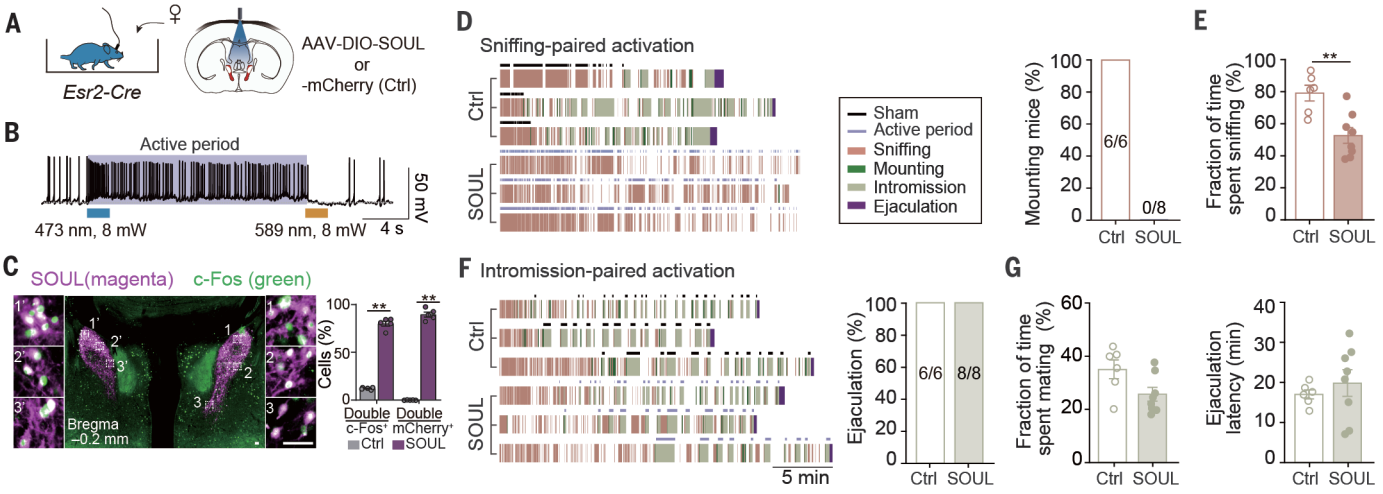

Fig. 3. Optogenetic activation of BNST^{Esr2} during early sniffing selectively inhibits male intention to mate. (**A**) Transcranial optical stimulation through the intact skull of virgin male mice. (**B**) Current-clamp traces illustrating activation of a SOUL-expressing BNST^{Esr2} in acute brain slices upon blue-light activation (blue bar) and orange-light deactivation (orange bar). (**C**) Colabeling of SOUL (magenta) and c-Fos (green) in a coronal BNST section, with boxed regions magnified after photostimulation. Scale bar, 50 μm. (Right) Overlap between mCherry and c-Fos expression. (**D** to **G**) Behaviors of males associated with [(D) and (E)] sniffing-paired or [(F) and (G)] intromission-paired photostimulation of BNST^{Esr2}. Shown in (D) and (F) (left) are behavior raster plots and the active period as in (B), and (right) are fraction of males that either (D) initiated mounting within 15 min or (F) ejaculated. Mann-Whitney *U*-test was used; $^{**}P < 0.01$, $^{***}P < 0.001$. For (A) to (G), data are shown as the mean ± SEM.

in virgin females did not overcome the effect of cycling hormones that increased their sexual receptiveness (fig. S12, D and E). Because female BNST^{Esr2} displayed less frequent firing rates than that of male ones during baseline before an intruder was introduced (fig. S9I), further inactivation may be less effective in up-regulating mating performance in female mice.

Consistently, chemogenetic activation of BNST^{Esr2} strongly suppressed sexual behavior in male mice (fig. S13, A to C), which is contrary to the effect of activating BNST^{Arom} (*13*), *Esr1*-expressing neurons in the BNSTpr (BNST^{Esr1}) (*18*), or nearby nonoverlapping BNST^{St18} (fig. S13, E to G). However, such an effect was not observed in estrous female mice (fig. S13D). Chemogenetic activation of male BNST^{Esr2} could possibly suppress mounting actions and/or motivational states to carry out sexual behaviors. To distinguish between these possibilities, we expressed a step-function opsin with ultrahigh light sensitivity (SOUL) (*25*) and performed transcranial optical stimulation to noninvasively activate BNST^{Esr2} during different mating phases (Fig. 3A). Transient application of blue light resulted in persistent activation of SOUL-expressing neurons, which were largely suppressed by transient application of orange light, as verified with ex vivo recordings (Fig. 3B). Using this approach, we induced robust expression of c-Fos protein bilaterally in SOUL-expressing BNST^{Esr2} in behaving mice (Fig. 3C). Sniffing-paired activation of BNST^{Esr2} (occurred with the first sniffing of an intruder) was effective in suppressing the initiation of an attempted mount (Fig. 3D). This manipulation also reduced the fraction of time spent sniffing a female intruder during the premounting period in early investigation (within 10 min after the initial sniffing) (Fig. 3E), which largely mimicked the behaviors in sexually satiated male mice (fig. S1D). However, intromission-paired optogenetic activation (Fig. 3F) or inhibition (fig. S14) of BNST^{Esr2} (occurred with the first intromission) did not interrupt ongoing mating actions. These males spent a similar amount of time in mating (including both mounting and intromission) without affecting ejaculation latency from the first mount (Fig. 3G and fig. S14D).

Elevated expression of HCN in male BNST^{Esr2} mediates sexual satiety

To determine how transient mating experience may lead to persistent changes in BNST^{Esr2} activity that lasts for days, we recorded from fluorescently labeled BNST^{Esr2} with whole-cell patch clamp recording in brain slices from virgin, sexually satiated, and behaviorally recovered Esr2-Cre:histone 2b (H2B)–green fluorescent protein (GFP) mice of both sexes (fig. S15A). A higher fraction of BNST^{Esr2} exhibited spontaneous firing in satiated mice as compared with virgin or recovered mice and also displayed more frequent firing rates (fig. S15B). Despite comparable input resistance and membrane capacitance, the resting membrane potentials (RMPs) were highest and the rheobases (the most negative step current required to elicit all-or-none firing) were lowest in BNST^{Esr2} from satiated mice (fig. S15, C and D), which were thus primed to fire action potentials after smaller depolarization. Such changes were largely restored in behaviorally recovered mice.

The hyperexcitability of satiated BNST^{Esr2} suggested a change in ion channels that influences the firing pattern and spike threshold (*26*). Negative current injection in BNST^{Esr2} revealed a depolarizing voltage "sag," which is mainly mediated by hyperpolarization-activated cyclic nucleotide-gated (HCN) cation channels (Fig. 4A). In BNST^{Esr2} with substantial voltage sag (>10% of peak voltage), perfusion of a selective HCN blocker, ZD-7288 (20 μM), significantly reduced the size of the voltage sag and firing rates (Fig. 4B). In male (but not female) mice, the size of this voltage sag was larger in satiated versus virgin or recovered BNST^{Esr2} (Fig. 4C). However, such an increase was not observed in males at 30 min after ejaculation, during which time BNST^{Esr2} hyperexcitability was already presented (fig. S15E). Moreover, the fraction of BNST^{Esr2} that displayed substantial voltage sag in males was higher than that in females (Fig. 4D). To examine the functional relevance of HCN channels in regulating sexual satiety, we administered (intracranially) either ZD-7288 (1 mM) or artificial cerebrospinal fluid (ACSF; vehicle control) into both sides of the BNSTpr (250 nl each) of sexually satiated mice (fig. S16, A and B). Application of ZD-7288 significantly restored sexual behavior (including ejaculation) after

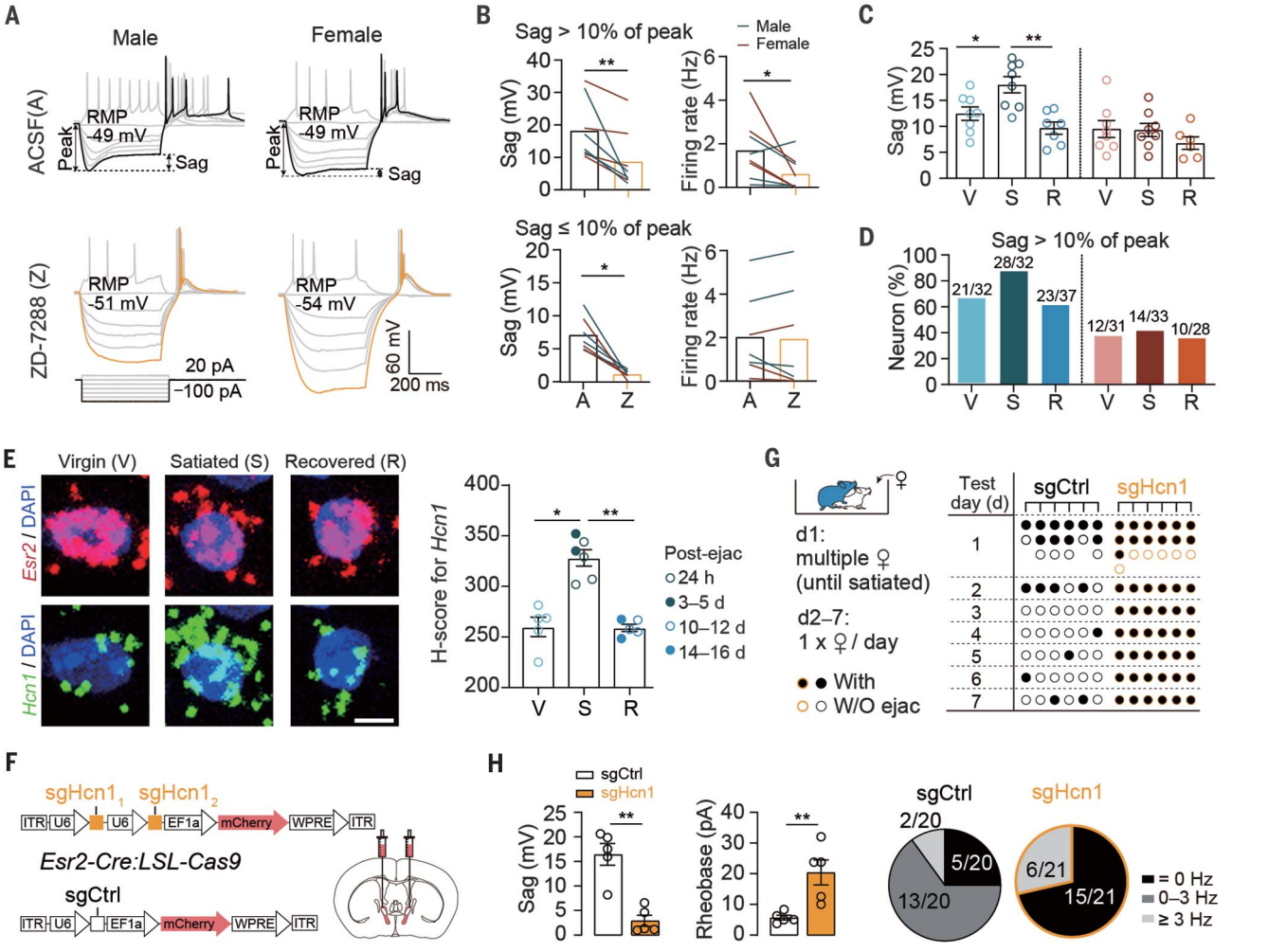

Fig. 4. Increased HCN currents (I_h) contribute to hyperexcitability of BNST^{Esr2} in sexually satiated male mice. (**A**) Current clamp recordings from BNST^{Esr2} in satiated (left) male or (right) female mice in response to 500-ms current steps (−100 to 20 pA, 20-pA step) (top) in the presence of ACSF or (bottom) 10 min after the perfusion of ZD-7288 (20 μM). The I_h-associated voltage sag was measured as the voltage deflection in response to a −100-pA step current. (**B**) The (left) size of voltage sag and (right) firing rates in BNST^{Esr2} (top) with or (bottom) without substantial voltage sag. Wilcoxon matched-pairs signed-rank test was used. (**C** and **D**) The (C) size of voltage sag in BNST^{Esr2} and (D) fraction of BNST^{Esr2} with substantial voltage sag in brain slices from virgin, satiated, and recovered (blue) male and (orange) female mice. In (C), one-way analysis of variance with Tukey's multiple comparisons test was used. In (D), the number of recorded neurons (three to six neurons per mouse) in each group is shown above each bar. (**E**) The expression of *Hcn1* mRNA in BNST^{Esr2} from virgin (12 sections from five mice), satiated (15 sections from six mice), or recovered males (10 sections from five mice). Scale bar, 5 μm. Kruskal-Wallis test with Dunn's multiple comparisons correction was used. (**F**) Schematic showing AAV sgControl and AAV sgHcn1 vector design and bilateral viral infection in the BNST. (**G**) Consecutive mating tests in males across 7 days at 2 to 3 weeks after virus injection (left). (**H**) Comparison of the (left) voltage sag and (middle) rheobase between sgControl (20 neurons from five satiated mice) and sgHcn1 (21 neurons from five mice with multiple ejaculations) group. Pie plots show fractions of neurons with different firing rates. Mann-Whitney *U*-test was used; $^*P < 0.05$, $^{**}P < 0.01$. For (B) to (D) and (H), data are shown as the mean ± SEM.

~1 hour in five of six satiated males but did not restore sexual receptiveness in recently mated females (fig. S16, C to G).

There are four mammalian subunits, referred to as HCN1 to HCN4, that constitute the molecular substrate of a persistent sodium current (also known as I_h) (*27*, *28*). On the basis of a systematic reanalysis of a published snRNA-seq dataset for the BNST (*23*), we found that *Hcn1*, but not the other subunits, was highly enriched in BNST^{Esr2} (fig. S17). To examine the levels of *Hcn1* before and at multiple times after ejaculation, we performed single-cell quantification of *Hcn1* mRNA in the BNSTpr using FISH. In male mice, the expression level of *Hcn1* [calculated as H-score (*29*)] in satiated BNST^{Esr2} was significantly higher than that in BNST^{Esr2} from virgin and recovered males (Fig. 4E). To further examine the self-autonomous function of *Hcn1* on BNST^{Esr2}, we crossed *Esr2-Cre* mice with mice in which Cre-dependent Cas9–enhanced GFP (EGFP) was inserted (*30*) and applied adeno-associated virus (AAV)–mediated expression of a single-guide RNA (sgRNA) (sgControl or sgHcn1) bilaterally to the BNST (Fig. 4F). CRISPR-Cas9–mediated disruption of *Hcn1* was sufficient to reduce sexual satiety after consecutive ejaculations across days without changing mating performance in male mice (Fig. 4G and fig. S18A). In whole-cell recordings, individual Cas9-expressing BNST^{Esr2} with *Hcn1* disruption showed a reduced voltage sag, increased firing threshold (rheobase), and silent spontaneous firing in a higher proportion (Fig. 4H). However, the same disruption of *Hcn1* in female BNST^{Esr2} did not restore their sexual receptiveness at 0.5 to 1 hour after mating (fig. S18B).

Discussion

The finding that BNST^{Esr2} represent sexual satiety is notable, given the lack of knowledge about where and how lasting motivational states might be encoded in the brain. Whether activated during ejaculation, soon after ejaculation (their off-dynamics remain unclear), or during sexual satiety period, BNST^{Esr2} in both sexes may commonly represent a sexual satiety state and play a particular role in reducing internal mating motivation after successful mating (Fig. 2G). A similar model (also known as the hydraulic model) was proposed by Lorenz more than 70 years ago to explain how flexible behavioral decisions are made in concert with dynamic internal motivational states (*31*). However, stimulating BNST^{Esr2} was ineffective in suppressing mating actions in virgin females but not males. How can these findings be reconciled with the common role of BNST^{Esr2} in encoding sexual satiety in both sexes? One possibility is that the activity of BNST^{Esr2} may not be sufficient to drive sexual satiety in female mice and might need other cofactors such as hormonal state. In virgin male mice, inhibition of BNST^{Esr2} also leads to indiscriminate mating behaviors, suggesting potential roles of BNST^{Esr2} in behaviors not directly related to sexual satiety.

Our findings also indicated that the post-ejaculation activation of BNST^{Esr2} in both sexes can result in long-lasting modifications of their excitability and firing threshold, which are mediated partially by HCN channels selectively in male but not female mice. This finding may be extended to the understanding of persistent changes in other forms of social behaviors as well as cognitive functions (*32*–*36*). Together, our findings revealed that experience-dependent changes in ion channels, which are effective in regulating cellular firing patterns and/or excitability, may serve as a general mechanism that contributes to long-lasting modifications in internal states.

REFERENCES AND NOTES

1. D. J. Anderson, *Nat. Rev. Neurosci.* **17**, 692–704 (2016).
2. P. Chen, W. Hong, *Neuron* **98**, 16–30 (2018).
3. D. Wei, V. Talwar, D. Lin, *Neuron* **109**, 1600–1620 (2021).
4. E. M. Hull, R. I. Wood, K. E. McKenna, in *Neurobiology of Male Sexual Behavior*, D. N. Jimmy Ed. (Academic Press, 2006), chap. 33.
5. B. V. Phillips-Farfán, A. Fernández-Guasti, *Neurosci. Biobehav. Rev.* **33**, 442–455 (2009).
6. T. E. McGill, *J. Genet. Psychol.* **103**, 53–57 (1963).
7. T. E. McGill, R. C. Coughlin, *J. Reprod. Fertil.* **21**, 215–220 (1970).
8. L. M. Coolen, H. J. Peters, J. G. Veening, *Brain Res.* **738**, 67–82 (1996).
9. M. M. Heeb, P. Yahr, *Neuroscience* **72**, 1049–1071 (1996).
10. K. K. Ishii *et al*., *Neuron* **95**, 123–137.e8 (2017).
11. T. Yamaguchi *et al*., *Nat. Neurosci.* **23**, 1111–1124 (2020).
12. C. F. Yang *et al*., *Cell* **153**, 896–909 (2013).
13. Y. C. Wei *et al*., *Nat. Commun.* **9**, 279 (2018).
14. S. Inoue *et al*., *Cell* **179**, 1393–1408.e16 (2019).
15. T. Karigo *et al*., *Nature* **589**, 258–263 (2021).
16. M. Liu, D. W. Kim, H. Zeng, D. J. Anderson, *Neuron* **110**, 841–856.e6 (2022).
17. D. W. Bayless *et al*., *Cell* **176**, 1190–1205.e20 (2019).
18. B. Yang, T. Karigo, D. J. Anderson, *Nature* **608**, 741–749 (2022).
19. S. X. Zhang *et al*., *Nature* **597**, 245–249 (2021).
20. H. W. Dong, L. W. Swanson, *J. Comp. Neurol.* **471**, 396–433 (2004).
21. Y. Li *et al*., *Cell* **171**, 1176–1190.e17 (2017).
22. R. Remedios *et al*., *Nature* **550**, 388–392 (2017).
23. J. D. Welch *et al*., *Cell* **177**, 1873–1887.e17 (2019).
24. L. Yin *et al*., *Neuron* **110**, 3000–3017.e8 (2022).
25. X. Gong *et al*., *Neuron* **107**, 38–51.e8 (2020).
26. B. P. Bean, *Nat. Rev. Neurosci.* **8**, 451–465 (2007).
27. R. B. Robinson, S. A. Siegelbaum, *Annu. Rev. Physiol.* **65**, 453–480 (2003).
28. R. Hazra *et al*., *Mol. Cell. Neurosci.* **46**, 699–709 (2011).
29. S. Jolly *et al*., *Sci. Rep.* **9**, 12353 (2019).
30. R. J. Platt *et al*., *Cell* **159**, 440–455 (2014).
31. K. Lorenz, *Symp. Soc. Exp. Biol.* **4**, 221–268 (1950).
32. S. J. Thuault *et al*., *J. Neurosci.* **33**, 13583–13599 (2013).
33. S. Stagkourakis *et al*., *Nat. Neurosci.* **21**, 834–842 (2018).
34. T. Notomi, R. Shigemoto, *J. Comp. Neurol.* **471**, 241–276 (2004).
35. D. Tsay, J. T. Dudman, S. A. Siegelbaum, *Neuron* **56**, 1076–1089 (2007).
36. M. F. Nolan *et al*., *Cell* **115**, 551–564 (2003).
37. X. Zhou *et al*., Source data of Hyperexcited limbic neurons represent sexual satiety and reduce mating motivation. Zenodo (2022); doi:10.5281/zenodo.7482944.

ACKNOWLEDGMENTS

The authors thank Q. Yang, Y. R. Yang, P. X. Wu, Y. Q. Zhang, and X. Zhao for technical help; CIBR LARC staff for animal care; the CIBR Imaging Core, Instrumentation Core, Vector Core, Genetic Manipulation Core, Oxford Instruments, and Inscopix for technical support; C. Dulac, M. M. Luo, Y. Xiang, and M. Jing for constructive comments on the manuscript; and members of the Li laboratory for helpful comments on this project. **Funding:** This work was supported by STI2030–Major Project 2021ZD0203900 (Yin.L.); Human Frontier Science Program CDA00005 (Yin.L.); The National Natural Science Foundation of China 32071012 (Yin.L.); Beijing Nova Program Z191100001119084 (Yin.L.); and China Postdoctoral Science Foundation award 2021M700454 (X.T.). **Author contributions:** Conceptualization: X.Z., A.L., X.M., and Yin.L. Methodology: X.Z., A.L., and X.M. Investigation: X.Z., A.L., X.M., Z.D., M.A., Yix.L., Y.C., W.L., X.T., and X.C. Formal analysis: X.Z., A.L., X.M., and Z.D. Funding acquisition: Yin.L., X.Z., and X.T. Supervision: Yin.L. Writing – original draft: Yin.L. Writing – review and editing: Yin.L., X.Z., A.L., and X.M. **Competing interests:** The authors declare no competing interests. **Data and materials availability:** The processed data used to generate the figures can be found at Zenodo (*37*). The custom analysis code in this paper is publicly available on GitHub (https://github.com/LiLab-CIBR/sexual-satiety). **License information:** Copyright © 2023 the authors, some rights reserved; exclusive licensee American Association for the Advancement of Science. No claim to original US government works. https://www.science.org/about/science-licenses-journal-article-reuse

SUPPLEMENTARY MATERIALS

science.org/doi/10.1126/science.abl4038
Materials and Methods
Supplementary Text
Figs. S1 to S18
Table S1
References (*38*–*43*)
Movie S1
MDAR Reproducibility Checklist

View/request a protocol for this paper from *Bio-protocol*.

Submitted 20 June 2022; resubmitted 28 November 2022
Accepted 27 January 2023
Published online 9 February 2023
10.1126/science.abl4038

RESEARCH ARTICLE SUMMARY

MICROBIOTA

Microbe-mediated intestinal NOD2 stimulation improves linear growth of undernourished infant mice

Martin Schwarzer*, Umesh Kumar Gautam, Kassem Makki, Anne Lambert, Tomáš Brabec, Amélie Joly, Dagmar Šrůtková, Pierre Poinsot, Tereza Novotná, Stéphanie Geoffroy, Pascal Courtin, Petra Petr Hermanová, Renata C. Matos, Jonathan J. M. Landry, Céline Gérard, Anne-Laure Bulteau, Tomáš Hudcovic, Hana Kozáková, Dominik Filipp, Marie-Pierre Chapot-Chartier, Marek Šinkora, Noël Peretti, Ivo Gomperts Boneca, Mathias Chamaillard, Hubert Vidal, Filipe De Vadder, François Leulier*

INTRODUCTION: Growth in size and weight is an intrinsic process in each individual's ontogeny. The highest rate of growth takes place after birth and in mammals is governed by the somatotropic axis, where growth hormone (GH) instructs the liver and peripheral tissues to produce insulin-like growth factor–1 (IGF-1) to promote organ and systemic growth. Nutrition is paramount to growth, and chronic undernutrition triggers a state of GH resistance manifested by low circulating IGF-1, leading to stunting. Recent studies have shown that not only nutrients but also components of the intestinal microbiota can be critical in shaping host growth dynamics. Previously, we established that the intestinal microbiota is necessary to buffer the deleterious effect of chronic undernutrition on mouse systemic postnatal growth. We showed that microbial stimulation supports the activity of the somatotropic axis in juveniles by improving the GH sensitivity of peripheral tissues and increasing the circulating levels of IGF-1. Furthermore, using monoxenic mice, we showed that a strain of *Lactiplantibacillus plantarum* (strain Lp^{WJL}), which was selected because of its ability to promote growth in a *Drosophila* model of diet-induced stunting, recapitulates the beneficial effects of a complex microbiota on the somatotropic axis and juvenile growth of malnourished mice in a strictly strain-dependent manner.

RATIONALE: Here, we studied the effect Lp^{WJL} on mouse postnatal growth in a new preclinical model of diet-induced stunting in conventional animals. We investigated both the bacterial cues and host mechanisms underpinning the complex local and whole-body adaptations triggered by such intestinal bacterium leading to improved systemic growth despite chronic undernutrition.

RESULTS: We report a new preclinical mouse model of diet-induced stunting in conventional mice without small intestinal inflammation but associated with altered crypt cell proliferation. Using this model, we show that Lp^{WJL} sustains the postnatal growth of malnourished conventional animals by orchestrating metabolic and hormonal changes in the juvenile host manifested as improved circulating levels and activity of IGF-1 and insulin. We identified cell walls isolated from Lp^{WJL}, as well as ligands of the pattern recognition receptor NOD2, as being sufficient bacterial cues stimulating animal growth. Further, we found that NOD2 is necessary in intestinal epithelial cells for Lp^{WJL}-mediated improvement of intestinal crypt cell proliferation, type I interferon–regulated gene induction, IGF-1 production, and postnatal growth promotion in malnourished conventional animals.

CONCLUSION: Our results demonstrate that bacterial cell walls or purified NOD2 ligands are sensed by the pattern recognition receptor NOD2 in the intestinal epithelial cells and sustain postnatal juvenile growth despite chronic undernutrition. We posit that one of the mechanisms by which Lp^{WJL} and its cell wall exert its postnatal growth–promoting properties is the buffering of the deleterious effect of undernutrition on small intestinal crypt cell proliferation through NOD2-dependent bacterial cell walls sensing. Our results suggest that, coupled with renutrition strategies, supplementation of evidence-based probiotics such as Lp^{WJL} or defined bacteria-derived postbiotics such as Lp^{WJL} cell walls and/or NOD2 agonists have the potential to alleviate persistent stunting, one of the long-term sequelae of undernutrition that still affects >149 million children under 5 years of age in low- and middle-income countries. ■

The list of author affiliations is available in the full article.
*Corresponding author. Email: schwarzer@biomed.cas.cz (M.S.); francois.leulier@ens-lyon.fr (F.L.)

READ THE FULL ARTICLE AT
https://doi.org/10.1126/science.ade9767

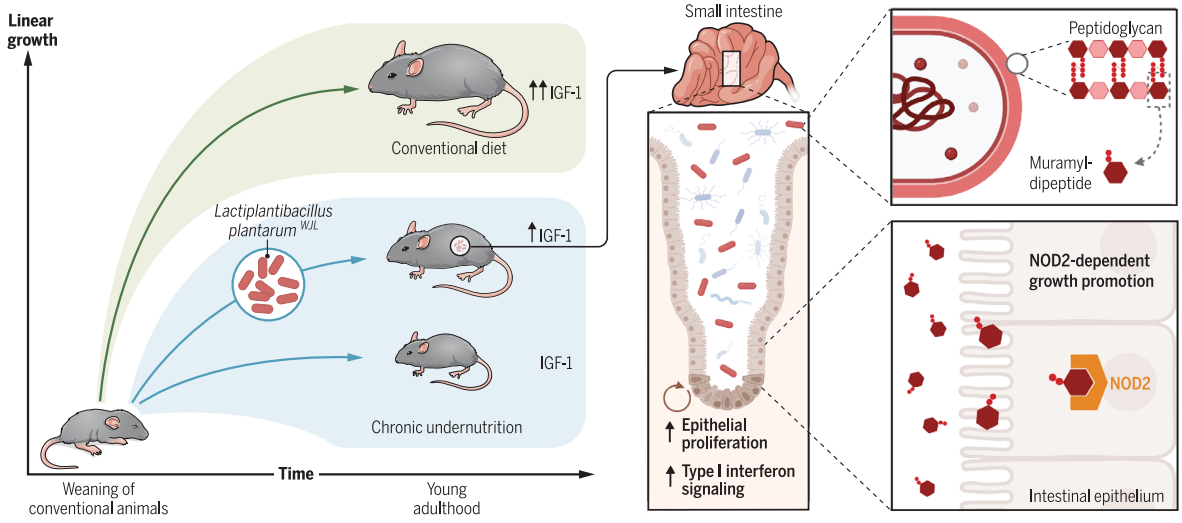

Lp^{WJL} or its purified cell wall improves the growth of undernourished infant mice through intestinal NOD2 signaling. Chronic undernutrition after weaning leads to stunting, which is alleviated by Lp^{WJL}. Lp^{WJL} peptidoglycans engage NOD2 in the intestinal epithelium, which increases the proliferation of small intestinal stem cells, type I interferon signaling, IGF-1 production, and postnatal growth despite undernutrition.

MICROBIOTA

Microbe-mediated intestinal NOD2 stimulation improves linear growth of undernourished infant mice

Martin Schwarzer[1,2]*, Umesh Kumar Gautam[1], Kassem Makki[2,3]†, Anne Lambert[2], Tomáš Brabec[4], Amélie Joly[2], Dagmar Šrůtková[1], Pierre Poinsot[2,3,5], Tereza Novotná[1], Stéphanie Geoffroy[2]‡, Pascal Courtin[6], Petra Petr Hermanová[1], Renata C. Matos[2], Jonathan J. M. Landry[7], Céline Gérard[3], Anne-Laure Bulteau[2]§, Tomáš Hudcovic[1], Hana Kozáková[1], Dominik Filipp[4], Marie-Pierre Chapot-Chartier[6], Marek Šinkora[1], Noël Peretti[3,5], Ivo Gomperts Boneca[8], Mathias Chamaillard[9], Hubert Vidal[3], Filipe De Vadder[2], François Leulier[2]*

The intestinal microbiota is known to influence postnatal growth. We previously found that a strain of *Lactiplantibacillus plantarum* (strain Lp^{WJL}) buffers the adverse effects of chronic undernutrition on the growth of juvenile germ-free mice. Here, we report that Lp^{WJL} sustains the postnatal growth of malnourished conventional animals and supports both insulin-like growth factor–1 (IGF-1) and insulin production and activity. We have identified cell walls isolated from Lp^{WJL}, as well as muramyl dipeptide and mifamurtide, as sufficient cues to stimulate animal growth despite undernutrition. Further, we found that NOD2 is necessary in intestinal epithelial cells for Lp^{WJL}-mediated IGF-1 production and for postnatal growth promotion in malnourished conventional animals. These findings indicate that, coupled with renutrition, bacteria cell walls or purified NOD2 ligands have the potential to alleviate stunting.

Linear and ponderal growth is an inherent capacity of all juvenile multicellular organisms. In mammals, postnatal growth is controlled by the somatotropic axis, where growth hormone (GH) instructs the liver and peripheral tissues to produce insulin-like growth factor–1 (IGF-1) to promote organ and systemic growth (*1*). Next to IGF-1, insulin is the main anabolic hormone of the body, regulating carbohydrate, lipid, and protein metabolism (*2*). Although the somatotropic axis is of key importance during growth, a coordinated regulation of metabolism is required to provide substrates and fuels to the growing tissues. As a consequence, insulin also influences animal development and growth (*3*).

[1]Laboratory of Gnotobiology, Institute of Microbiology of the Czech Academy of Sciences, 54922 Novy Hradek, Czech Republic. [2]Institut de Génomique Fonctionnelle de Lyon, Ecole Normale Supérieure de Lyon, CNRS UMR5242, UCBL Lyon-1, F-69007 Lyon, France. [3]CarMeN Laboratory, INSERM, INRAE, Université Claude Bernard Lyon 1, 69310 Pierre-Bénite, France. [4]Laboratory of Immunobiology, Institute of Molecular Genetics of the Czech Academy of Sciences, 14220 Prague, Czech Republic. [5]Univ Lyon, Hospices Civil de Lyon, Gastro-enterology and Pediatric Nutrition, Hôpital Femme Mere Enfant, F-69500 Bron, France. [6]Université Paris-Saclay, INRAE, AgroParisTech, Micalis Institute, 78350 Jouy-en-Josas, France. [7]Genomics Core Facility, European Molecular Biology Laboratory, 69117 Heidelberg, Germany. [8]Institut Pasteur, Université Paris Cité, CNRS UMR6047, INSERM U1306, Biology and Genetics of the Bacterial Cell Wall Unit, F-75015 Paris, France. [9]University of Lille, Inserm, U1003, F-59000 Lille, France.
***Corresponding author. Email: schwarzer@biomed.cas.cz (M.Sc.); francois.leulier@ens-lyon.fr (F.L.)**
†Present address: Department of Molecular and Clinical Medicine/Wallenberg Laboratory, Institute of Medicine, University of Gothenburg and Sahlgrenska University Hospital, 40530 Gothenburg, Sweden.
‡Present address: Bioaster, Institut de Recherche Technologique, 69007 Lyon, France.
§Present address: LVMH Research 185, 45804 Saint Jean de Braye Cedex, France.

Nutrition is paramount to growth, and chronic undernutrition triggers a state of GH resistance manifested by low circulating IGF-1, leading to stunting (*4*, *5*). In addition to its influence on nutrition, the microbial environment also shapes systemic growth (*6*, *7*). Acute malnutrition triggers an altered maturation of the intestinal microbiota in malnourished children, which contributes to stunting and wasting (*8*, *9*), and the absence of microbial stimulation has negative impacts on the circulating levels of IGF-1 (*10*, *11*) and insulin (*12*) in germ-free mice.

Previously, we established that the intestinal microbiota is necessary to maximize mouse systemic postnatal growth under normal nutritional conditions and during chronic undernutrition (*10*). We showed that microbial stimulation supports the activity of the somatotropic axis in juveniles by improving the GH sensitivity of peripheral tissues and increasing the circulating levels of IGF-1 (*10*). Furthermore, using monoxenic mice, we showed that a strain of *Lactiplantibacillus plantarum* (strain Lp^{WJL}), which was selected because of its ability to promote growth in a *Drosophila* model of diet-induced stunting (*13*), recapitulates the beneficial effects of the complex microbiota on the somatotropic axis and on the juvenile growth of well-fed or malnourished mice in a strictly strain-dependent manner (*10*).

Here, we build on these results and study the effect of Lp^{WJL} on the postnatal growth in a new preclinical model of diet-induced stunting in conventional animals and investigate the mechanisms by which this specific intestinal bacterium triggers a complex, whole-body adaptation leading to enhanced systemic growth.

Results

Diet-induced stunting in conventional mice

On the basis of our previous findings (*10*), we aimed to model chronic undernutrition in conventional mice. To this end, we designed an AIN93G-based modified isocaloric diet low in fat and protein [malnourished (MAL)] (table S1 and Fig. 1B). The macroscopic growth parameters (weight and size gains) of C57Bl/6J male mice weaned on MAL diet were severely altered compared with mice weaned on an AIN93G diet [conventional (CON)] (table S1 and Fig. 1, A to K). At postnatal day 56, MAL mice were stunted and had shorter body size (Fig. 1, A and C to E) and femur bone length (Fig. 1, F and G) compared with CON mice. The diminished length gain was accompanied by lower global weight gain, as well as a lower final weight of individual organs (Fig. 1, H to K). The stunted phenotype of MAL-fed animals was not the result of an alteration of the food intake compared with the CON-fed group; the relative food intake was even increased on the MAL diet during the last week of the protocol (fig. S1). Feeding the MAL diet to male mice of another genetic background (BALB/c) resulted in a similar phenotype (fig. S2).

Recently, Brown *et al.* (*14*) reported a mouse model of environmental enteropathy (EE) resulting in a moderately stunted phenotype. EE is a poorly understood disorder of the small intestine marked by chronic intestinal inflammation, villous blunting, and increased intestinal permeability (*15*). To test for putative EE in our model, we assessed the expression of several markers of small intestine integrity and inflammation and found no difference between CON and MAL animals (fig. S3A). Moreover, we detected no difference in intestinal integrity as assessed by the functional test of fluorescein isothiocyanate–dextran uptake (fig. S3B). In addition, the levels of proinflammatory markers in sera were similar between the experimental groups, except for the levels of granulocyte colony–stimulating factor and interleukin-6, which were both significantly decreased in MAL-fed mice (fig. S3C). Jejunal histology showed that MAL-fed mice had slightly shorter villi and lower crypt depth (fig. S3D), but we did not observe signs of severe villus blunting or tissue destruction, which are common signs of EE (*16*). Previously, Ueno *et al.* (*17*) reported a lower number of proliferating cells in the small intestine of stunted mice fed with a low-protein, low-fat diet. Consistent with this, the MAL-fed mice had a lower number of Ki67^{+} cells in ileal crypts compared with CON-fed animals, suggesting a lower renewal rate of the intestinal epithelium during chronic undernutrition (fig. S3E).

The growth factor IGF-1 is the main endocrine determinant of postnatal growth (*18*, *19*), and its production and activity is reduced upon poor nutrition (*20*). As expected, we

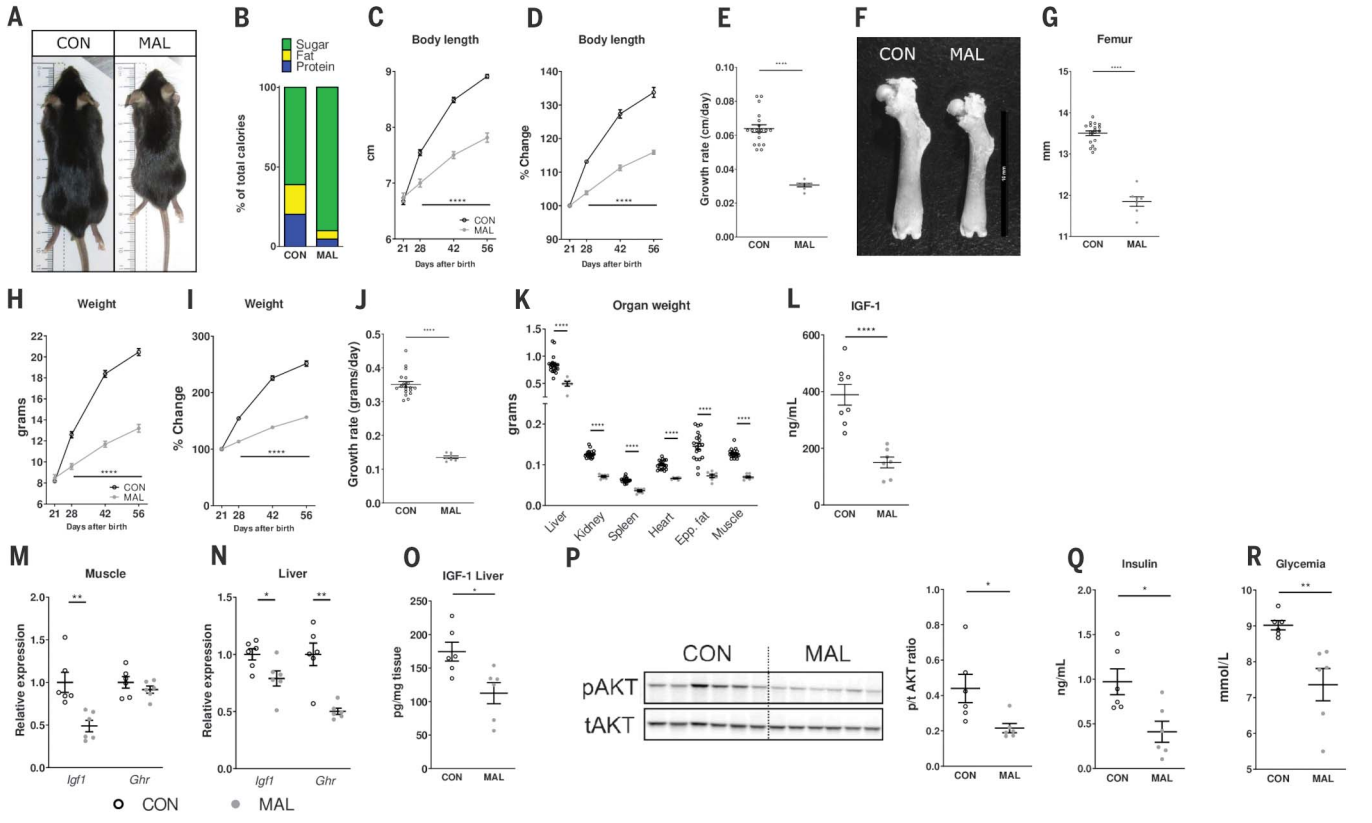

Fig. 1. Feeding a low-protein and low-fat diet induces stunting in C57Bl/6J juvenile male mice. (**A**) Representative images of C57Bl/6J male mice fed for 35 days after weaning a control diet (CON) or a low-protein, low-fat isocaloric diet (MAL). (**B**) Schematic of the components of each diet, expressed as a percentage of total calories. (**C** to **G**) Body length growth curves (C), relative body length growth curves (D), body length growth rate (E), representative picture of femur bones (F), and quantification of femur bone length (G) at day 56 after birth of mice fed CON (black open circles, n = 19) and MAL (gray circles, n = 7) diets. (**H** to **K**) Weight growth curves (H), relative weight growth curves (I), weight growth rate (J), and organ weight (K) at day 56 after birth of mice fed CON (black open circles, n = 19) and MAL (gray circles, n = 7) diets. (**L**) IGF-1 levels in sera of CON (black open circles, n = 8) and MAL (gray circles, n = 7) mice at day 56 after birth. (**M** and **N**) Expression levels of *Igf1* and *Ghr* depicted as fold change relative to the CON-fed mice in muscle (M) and liver (N) at day 56 after birth. (**O**) IGF-1 levels in liver tissues. (**P**) Western blots and quantification of phospho-S473-Akt in liver of CON- and MAL-fed mice. (**Q** and **R**) Insulin levels in sera of CON- and MAL-fed mice (Q) and glycemia (R) at day 56 after birth. CON, n = 6; MAL, n = 6. Data are presented as mean ± SEM and dot plots with mean ± SEM. Unpaired Student's t test, $^{*}P < 0.05$, $^{**}P < 0.01$, $^{****}P < 0.0001$.

found lower levels of circulating IGF-1 in the sera of MAL-fed animals (Fig. 1L). Concomitantly, *Igf1* expression was reduced both in the muscle and liver of MAL-fed animals (Fig. 1, M and N). The production of IGF-1 in peripheral tissues is activated by GH signaling (*1*). We found that GH receptor expression was significantly lower in the liver of stunted mice (Fig. 1N). The liver is the main source of circulating IGF-1 (*21*). Consistent with the increased *Igf1* expression, the IGF-1 content per milligram of liver tissue was higher in CON-fed animals (Fig. 1O). This result, together with the higher weight of liver tissues in CON animals (Fig. 1K), indicates that the liver of CON mice produced a significantly higher total amount of IGF-1. Next, we assessed the signaling activity of the insulin receptors (InRs) and IGF-1 receptors (IGF-1Rs) in the liver. The phosphorylation of Akt at Ser^{473} (phospho-S473-Akt), a marker of both InR and IGF-1R signaling (*22*), was reduced in the liver of MAL-fed animals compared with the CON group (Fig. 1P). Insulin is another potent anabolic hormone with growth-promoting properties (*23*). Insulin levels are decreased during protein malnutrition in humans (*24*) and in animal models (*25*). We found that MAL animals had significantly lower circulating levels of both insulin and glucose after fasting compared with the CON group (Fig. 1, Q to R). Taken together, our results establish a new preclinical model of mouse chronic undernutrition resulting in severe stunting associated with low levels of IGF-1 and insulin and low signaling activity of the somatotropic axis with no signs of EE.

Lp^{WJL} treatment improves systemic growth

Previously, we have shown that the Lp^{WJL} strain sustains the growth and development of *Drosophila* juveniles upon nutrient scarcity (*13*). This strain-specific growth-promoting property is also observed in a monoxenic mouse models during chronic undernutrition (*10*). We now wanted to test whether the Lp^{WJL} strain retains its beneficial effects on juvenile growth in the context of a malnourished conventional mouse model. To this end, male mice were weaned on the MAL diet and regularly administered 2×10^8 colony-forming units (CFU) of live Lp^{WJL} or a placebo for 5 weeks (Fig. 2A). Administration of Lp^{WJL} alone without improved nutrition supported body and femur length (Fig. 2, B to E) and weight gains (Fig. 2, G and H), resulting in animals that were 3.5% longer and 10% heavier at 8 weeks of age compared with the placebo group (Fig. 2, F and J). Lp^{WJL} administration resulted in longer femur bones (Fig. 2E) and increased mass of kidney, epididymal fat, and muscle

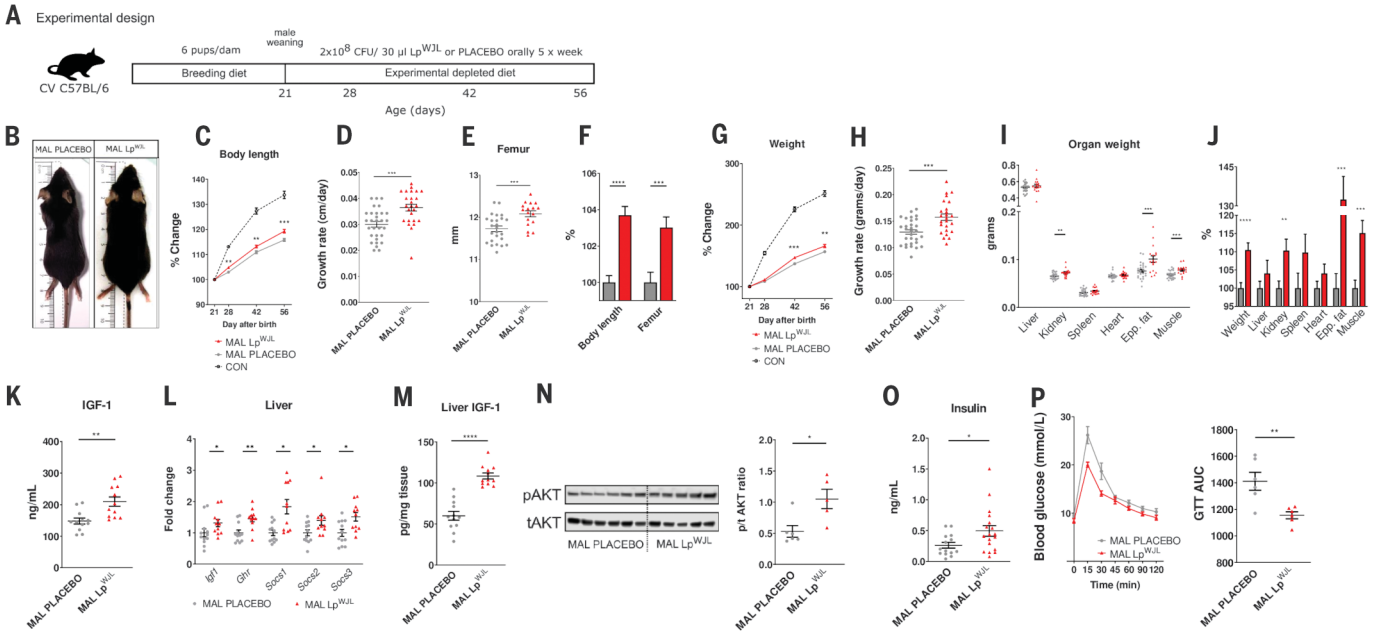

Fig. 2. Lp^{WJL} treatment improves postweaning growth, increases IGF-1/insulin levels, and improves glucose metabolism in undernourished C57Bl/6J juvenile male mice. (**A**) Experimental design. (**B**) Representative images of 56-day-old MAL-fed C57Bl/6J male mice treated either with placebo (MAL PLACEBO) or with Lp^{WJL} (MAL Lp^{WJL}). (**C** and **D**) Relative body length growth curves (C) and body length growth rate (D) of MAL-fed mice treated with placebo (gray circles, *n* = 30) and Lp^{WJL} (red triangles, *n* = 26). (**E**) Quantification of femur bone length at day 56 after birth after treatment with placebo (gray circles, *n* = 27) and Lp^{WJL} (red triangles, *n* = 17). (**F**) Percentage body and femur bone length gain after Lp^{WJL} treatment compared with placebo. (**G** and **H**) Relative weight growth curves (G) and weight growth rate (H) of MAL-fed mice treated with placebo (gray circles, *n* = 30) and Lp^{WJL} (red triangles, *n* = 26). Black open circles, dotted line in (C) and (G) are CON males from Fig. 1 for comparison, *n* = 19. (**I**) Organ weight at day 56 after birth of MAL-fed mice treated with placebo (gray) (*n* = 27) and Lp^{WJL} (red) (*n* = 17). (**J**) Percentage weight and organ weight gain after Lp^{WJL} treatment compared with placebo. (**K**) IGF-1 levels in sera of placebo (gray) and Lp^{WJL} (red) MAL-fed mice. (**L**) Expression levels of *Igf1*, *Ghr*, and *Socs* genes depicted as fold change relative to the placebo-treated mice in liver. (**M**) IGF-1 levels in liver tissues at day 56 after birth. MAL PLACEBO, *n* = 12; MAL Lp^{WJL}, *n* = 12. (**N**) Representative Western blots and quantification of phospho-S473-Akt in liver of MAL placebo–treated (*n* = 6) and MAL Lp^{WJL}–treated (*n* = 5) mice. (**O**) Insulin levels in sera of MAL placebo–treated (*n* = 14) and MAL Lp^{WJL}–treated (*n* = 18) mice at day 56 after birth. (**P**) Intraperitoneal glucose tolerance test (2 g/kg) of MAL placebo–treated (*n* = 6) and MAL Lp^{WJL}–treated (*n* = 6) mice at day 50 after birth. Data are presented as mean ± SEM and dot plots with mean ± SEM. Unpaired Student's *t* test, **P* < 0.05, ***P* < 0.01, ****P* < 0.001, *****P* < 0.0001.

tissues after 5 weeks of treatment at postnatal day 56 (Fig. 2I). These observed postweaning growth differences were not a result of an alteration in the food intake or relative food intake between Lp^{WJL} and placebo groups (fig. S4, A to E). Similar results were obtained in BALB/c male mice, suggesting that improved growth was not specific to the C57Bl/6J mouse genetic background (fig. S5, A to D). To test the possibility that the placebo-treated mice were only delayed in growth and would catch up later in life, we extended the treatment for 4 more weeks. At postnatal day 84, we still observed significant differences in body and femur length between placebo- and Lp^{WJL}-treated male mice on the MAL diet (fig. S6, A to C). We next sought to determine the changes induced by Lp^{WJL} treatment on the IGF-1 and insulin circulating levels and related signaling pathways in MAL-fed mice. We found significantly increased levels of IGF-1 in the sera of Lp^{WJL}-treated mice compared with the placebo group (Fig. 2K). The relative expressions of *Igf1* and *Ghr* were also increased in the liver, suggesting a higher GH sensitivity (Fig. 2L). This was further supported by increased expression of the GH signaling pathway transcriptional target genes *Socs1*, *Socs2*, and *Socs3* (Fig. 2L) and the higher IGF-1 content per milligram of liver tissue in the Lp^{WJL}-treated animals (Fig. 2M). In Lp^{WJL}-treated mice, we detected significantly increased phosphorylation of Akt at Ser^{473} in the liver (Fig. 2N), which was accompanied by increased levels of fasting insulin in the sera, suggesting higher activity of the InR/IGF-1R pathway in these animals (Fig. 2O). Accordingly, blood glucose control was improved by Lp^{WJL} treatment, as reflected by a faster glucose clearance after intraperitoneal glucose injection (Fig. 2P). These data align with a recent clinical study in which the authors reported a significant increase in the levels of both IGF-1 and insulin in severe acute malnourished Bangladeshi children who received microbiota-directed therapeutic food treatment (*8*).

Exploring whether the effects of Lp^{WJL} treatment are sex specific, we found that both male and female Lp^{WJL}-treated mice on the MAL diet had significantly improved body and femur length compared with placebo-treated animals (fig. S7, A to C and H to J). We found no differences in fed or fasted glycemia, and the levels of fed and fasted IGF-1 were significantly increased in Lp^{WJL}-treated animals of both sexes (fig. S7, D, E, K, and L). There were no differences in fed insulin levels for either sex (fig. S7, F and M). Consistent with our previous results, Lp^{WJL}-treated male mice had increased fasted insulin levels compared with placebo controls (fig. S7F). Conversely, Lp^{WJL}-treated females had decreased fasted insulin levels (fig. S7M), suggesting that IGF-1 is the main endocrine driver of growth in both sexes. Both male and female Lp^{WJL}-treated mice had improved blood glucose control with significantly lower area under the curve values after glucose injection (fig. S7, G and N). Collectively, our results show that Lp^{WJL} treatment

sensitizes the somatotropic axis and supports IGF-1 and insulin signaling, which together improved the metabolic status of the malnourished juvenile mice and consequently improved systemic growth and promoted weight gain.

The growth-promoting effects of Lp^{WJL} are strain specific

Using *Drosophila* and mouse monoxenic models, we previously showed that the growth-promoting properties of *L. plantarum* are strain specific. Despite similar intestinal tract colonization abilities, Lp^{WJL} is a marked growth promoter, whereas other *L. plantarum* strains, including NIZO2877 ($Lp^{NIZO2877}$), show a milder effect (*10*). To determine whether this strain specificity also holds true in conventional mice, we administered 2×10^8 CFU of either live Lp^{WJL} or live $Lp^{NIZO2877}$ to male mice weaned on the MAL diet and monitored their juvenile growth. Similar to the placebo treatment, and in contrast to Lp^{WJL}, the administration of the $Lp^{NIZO2877}$ had no impact on length and femur growth (Fig. 3, A to C), confirming that the growth benefit depends on the *L. plantarum* strain used. We also observed that Lp^{WJL} and $Lp^{NIZO2877}$ differed in their ability to sustain IGF-1 and insulin levels in sera. Levels in $Lp^{NIZO2877}$-treated animals resembled those of placebo-treated animals (Fig. 3, D and E). $Lp^{NIZO2877}$ treatment had no impact on the blood glucose control of mice on the MAL diet, as reflected by glucose clearance during a glucose tolerance test (Fig. 3F). These data establish that the growth-promoting property of *L. plantarum* in malnourished conventional animals is strain specific. This strain specificity indicates that a biological interaction occurs between Lp^{WJL} and host cells to establish a molecular dialogue supporting systemic growth.

Lp^{WJL} isolated cell walls are sufficient to promote growth

Bacterial cell walls (CW) are a major source of molecular determinants shaping the host-microbe interaction (*26*–*28*). Previously, we found in a *Drosophila* model that sensing of *L. plantarum* CW fragments by the host plays an important role in *L. plantarum*–mediated growth promotion under nutrient scarcity (*29*, *30*). This prompted us to test the hypothesis that host sensing of bacterial CW underscores the Lp^{WJL} growth-promoting capability in mice. First, we treated the MAL-fed male mice with 2×10^8 CFU of heat-killed (HK) Lp^{WJL}. HK Lp^{WJL} administration significantly improved the length growth rate of the mice (Fig. 3, G and H), and their femur length was also significantly longer compared with the placebo-treated group (Fig. 3I). Similar to live Lp^{WJL} treatment, the treatment with HK bacteria led to an increase of IGF-1 and insulin levels in sera (Fig. 3, J and K) and lower blood glucose during a glucose tolerance test (Fig. 3L).

Encouraged by these results and to further explore the role of the bacteria CW, we isolated the CW from Lp^{WJL} or $Lp^{NIZO2877}$ and treated the MAL-fed male mice with CW amounts corresponding to the CW amounts purified from 2×10^8 CFU cells. Lp^{WJL} CW treatments significantly improved the length growth rates of the juvenile mice (Fig. 3, G and H) and increased their femur length compared with the placebo-treated group (Fig. 3I). In stark contrast, treatment with $Lp^{NIZO2877}$ CW had no significant effect on the length growth rates (Fig. 3, G and H), and the mice resembled the placebo-treated group in physical traits. Treatment with Lp^{WJL} CW led to an increase of IGF-1 and insulin levels in sera, whereas treatment with $Lp^{NIZO2877}$ CW had no effect on these parameters (Fig. 3, J and K). Similar to when mice were treated with live Lp^{WJL} cells, the Lp^{WJL} CW treatment led to lower blood glucose during a glucose tolerance test (Fig. 3L). Feeding with $Lp^{NIZO2877}$ CW failed to significantly decrease the area under the curve after the glucose challenge (Fig. 3L). These data demonstrate that HK Lp^{WJL} and, more specifically, Lp^{WJL} isolated CW, are sufficient to support improved growth and glucose metabolism during chronic undernutrition.

NOD2 is necessary for Lp^{WJL}-mediated growth promotion

Our results suggest that HK Lp^{WJL} and isolated CW from Lp^{WJL} can be sensed by the host and induce metabolic and hormonal changes, leading to improved growth kinetics during chronic undernutrition. To identify such host-sensing and signaling mechanism(s), we tested the signaling potential of HK strains and their CW in human embryonic kidney (HEK) cells stably transfected with a set of innate immune receptors previously reported to sense molecular determinants from bacteria CW (NOD1, NOD2, TLR2, and TLR4) (*31*, *32*). We observed that HK Lp^{WJL} signaling through the NOD2 receptor was increased compared with HK $Lp^{NIZO2877}$. Signaling of both HK strains through the TLR2 receptor was comparable (fig. S8A). Similarly to HK bacterial strains, Lp^{WJL} CW signaling through the NOD2 receptor was significantly increased compared with the $Lp^{NIZO2877}$ CW. By contrast, $Lp^{NIZO2877}$ CW signaling through the TLR2 receptor was

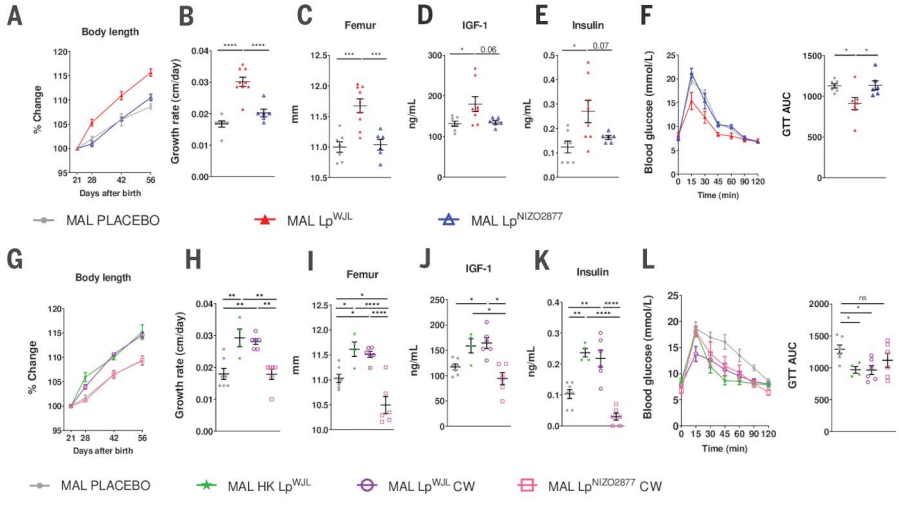

Fig. 3. The growth-promoting and metabolic effects of Lp^{WJL} are strain specific and can be replicated by HK Lp^{WJL} or Lp^{WJL} isolated CW. (**A** to **C**) Relative body length growth curves (A), body length growth rate (B), and femur length (C) at day 56 after birth of placebo-treated (MAL PLACEBO, gray circles, $n = 7$), Lp^{WJL}-treated (MAL Lp^{WJL}, red triangles, $n = 9$), and $Lp^{NIZO2877}$-treated (MAL $Lp^{NIZO2877}$, blue open triangles, $n = 6$) MAL-fed mice. (**D** and **E**) IGF-1 (D) and insulin (E) levels in sera of placebo-treated (gray circles, $n = 7$), Lp^{WJL}-treated (red triangles, $n = 8$), and $Lp^{NIZO2877}$-treated (blue open triangles, $n = 6$) MAL-fed mice at day 56 after birth. (**F**) Intraperitoneal glucose tolerance test (2 g/kg) of placebo-treated (gray circles, $n = 7$), Lp^{WJL}-treated (red triangles, $n = 7$), and $Lp^{NIZO2877}$-treated (blue open triangles, $n = 6$) MAL-fed mice at day 50 after birth. (**G** to **K**) Relative body length growth curves (G), body length growth rate (H), femur length (I), IGF-1 (J), and insulin levels (K) in sera at day 56 after birth. (**L**) Intraperitoneal glucose tolerance test (2 g/kg) at day 50 after birth in placebo-treated (gray circles, $n = 7$), HK Lp^{WJL}–treated (MAL HK Lp^{WJL}, green stars, $n = 4$), Lp^{WJL} CW–treated (MAL Lp^{WJL} CW, purple open circles, $n = 6$), and $Lp^{NIZO2877}$-treated (MAL $Lp^{NIZO2877}$ CW, pink open squares, $n = 6$) MAL-fed mice. Data are presented as mean ± SEM and dot plots with mean ± SEM. ANOVA with Tukey's multiple-comparisons test, $^*P < 0.05$, $^{**}P < 0.01$, $^{***}P < 0.001$, $^{****}P < 0.0001$.

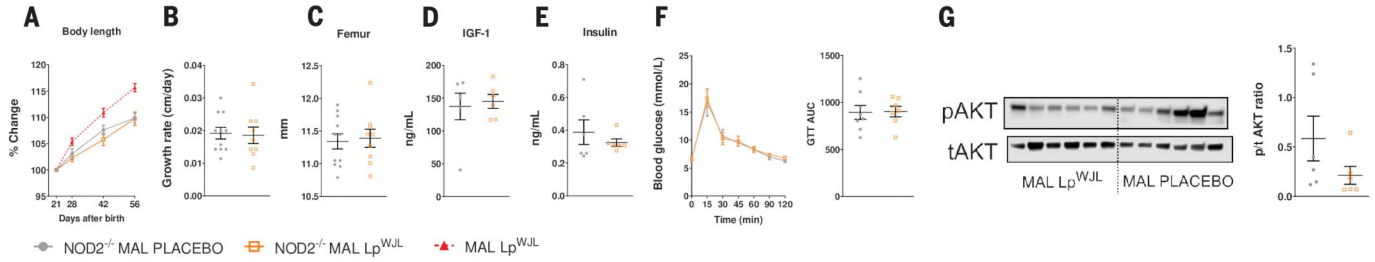

Fig. 4. NOD2 sensing is necessary for Lp^{WJL}-mediated growth-promoting and metabolic effects. (**A** to **C**) Relative body length growth curves (A), body length growth rate (B), and femur length (C) of placebo-treated (gray circles, n = 11) and Lp^{WJL}-treated (orange open squares, n = 9) MAL-fed NOD2 KO mice. Red triangles, dotted line in (A) are MAL Lp^{WJL} males from Fig. 3 for comparison, n = 9. (**D** and **E**) IGF-1 (D) and insulin (E) levels in sera of placebo-treated (gray circles, n = 6) and Lp^{WJL}-treated (orange open squares, n = 6) MAL-fed NOD2 KO mice at day 56 after birth. (**F**) Intraperitoneal glucose tolerance test (2 g/kg) of placebo-treated (gray circles, n = 8) and Lp^{WJL}-treated (orange open squares, n = 7) MAL-fed NOD KO mice at day 50 after birth. (**G**) Representative Western blots and quantification of phospho-S473-Akt in liver of NOD2 KO MAL placebo–treated (gray circles, n = 6) and MAL Lp^{WJL}–treated (orange open squares, n = 6) mice. Data are presented as mean ± SEM and dot plots with mean ± SEM, unpaired Student's t test.

increased compared with Lp^{WJL} CW (fig. S8A). Neither HK bacteria nor the isolated CW were able to signal through the NOD1 or TLR4 receptor in this assay (fig. S8A). Peptidoglycans (PGs) are the major CW component of Gram-positive bacteria (*26*). We therefore extracted and analyzed the composition of the PGs from the two strains. We found no differences in muropeptide composition and only subtle differences in meso-diaminopimelic acid amidation and sugar acetylation of specific muropeptides (fig. S8B and table S2). When tested in the NOD2 HEK cell system, the isolated PGs from each strain or their mutanolysin digests did not elicit any differences in NOD2 signaling (fig. S8C). Therefore, these results indicate that the observed strain specificity does not stem from variation in PG structure but rather from physiological attributes of the individual strains. This could be the differential ability of shedding CW fragments in the intestine or additional strain-specific molecular determinants in the bacterial cell envelope, such as D-alanylation of teichoic acids, which we have shown to be an important Lp CW feature shaping *Drosophila* growth (*30*).

To test the possible importance of NOD2-mediated Lp^{WJL} recognition in the growth promotion and improvement of the metabolic status of undernourished mice in vivo, we used Nod2-deficient (Nod2$^{-/-}$) mice and, as a control, mice deficient in the MyD88 cytoplasmic adapter molecule (MyD88$^{-/-}$) essential for the signaling of several TLRs (*33*). First, we confirmed that these two knockout (KO) mice models responded to the MAL diet similarly to C57Bl/6J mice in terms of growth phenotypes. In both genetic contexts, male mice were stunted and showed low levels of IGF-1 in sera when weaned on the MAL diet compared with the CON-fed animals (fig. S9, A and B). Next, we assessed the impact of Lp^{WJL} treatment in these genetic contexts. We found that Nod2$^{-/-}$ male mice failed to benefit from the Lp^{WJL} treatment, as shown by the absence of length gains (Fig. 4, A and B) and the lack of femur size gain compared with the placebo-treated group (Fig. 4C). Concomitantly, Lp^{WJL}-treated Nod2$^{-/-}$ mice had similar fasted levels of IGF-1 and insulin in sera (Fig. 4, D and E), and their glucose tolerance was unchanged compared with placebo-treated MAL-fed mice (Fig. 4F). Finally, there was no difference in phosphorylation of Akt at Ser^{473} in liver (Fig. 4G). In contrast to Nod2$^{-/-}$ mice, undernourished MyD88$^{-/-}$ male mice still benefited from Lp^{WJL} administration, as demonstrated by significantly higher length growth rates (fig. S10, A and B), significantly increased fasted IGF-1 in sera (fig. S10C), and faster glucose clearance compared with the MyD88$^{-/-}$ placebo-treated mice (fig. S10D).

Having established that NOD2 is necessary for the Lp^{WJL}-mediated growth-promoting and metabolic effects, we wondered whether treatment of mice with synthetic NOD2-activating derivatives, such as bacterial CW–derived muramyldipeptide (MDP) or synthetic NOD2-activating adjuvant mifamurtide (muramyltripeptide phosphatidylethanolamine) (*34*), would be able to improve juvenile growth during undernutrition. We treated male mice orally with 25 μg of MDP dissolved in placebo or an isomolar amount of 62.5 μg of mifamurtide dissolved in dimethyl sulfoxide (DMSO)/placebo. We observed that the length gains and final femur length of MDP-treated mice was improved compared with placebo, but not to the extent of Lp^{WJL}-treated mice (fig. S11, A to C). MDP treatment increased the levels of IGF-1 compared with placebo (fig. S11D), but failed to increase the insulin levels or the glucose clearance after glucose injection (fig. S11, E and F). We observed a similar growth-promoting effect after mifamurtide treatment, with increases in both IGF-1 and insulin (fig. S11, G to K). Again, there was no difference in glucose clearance after glucose injection compared with the DMSO/placebo–treated controls (fig. S11L). These results establish that NOD2 sensing and signaling is necessary for the Lp^{WJL}-mediated growth-promoting and metabolic effects, and that synthetic NOD2 ligands can partially mimic the Lp^{WJL} effects.

NOD2 is necessary for the Lp^{WJL}-mediated increase in Ki67^{+} cell numbers in the small intestine

We initially observed that the MAL-fed mice had lower number of Ki67^{+} cells in small intestinal crypts compared with CON-fed animals (fig. S3E), which suggested a lower renewal rate of the intestinal epithelium and altered function of intestinal stem cells (ISCs) during chronic undernutrition (*35*). It was previously reported that NOD2 stimulation in the small intestine crypt contributes to ISC survival and function (*36*). In the light of our results establishing that NOD2 is a key sensor supporting the increased growth after Lp^{WJL} treatment, we analyzed the jejunum of Lp^{WJL}- and placebo-treated mice and observed increased numbers of Ki67^{+} cells per intestinal crypt in Lp^{WJL}-treated mice compared with the placebo group (Fig. 5A). This phenomenon was reminiscent of *Lacticaseibacillus rhamnosus*–mediated cell proliferation in the small intestine crypts previously reported by Jones *et al.* (*37*). Further, we performed a transcriptome analysis by RNA sequencing of the whole jejunal tissue of Lp^{WJL}- and placebo-treated mice, and found that many up-regulated genes in Lp^{WJL}-treated animals were genes responding to type I interferon (IFN) (Fig. 5, B and C). A positive correlation between fecal IFN-β and the rate of weight gain has been recently reported after treatment of severely acutely malnourished Bangladeshi children

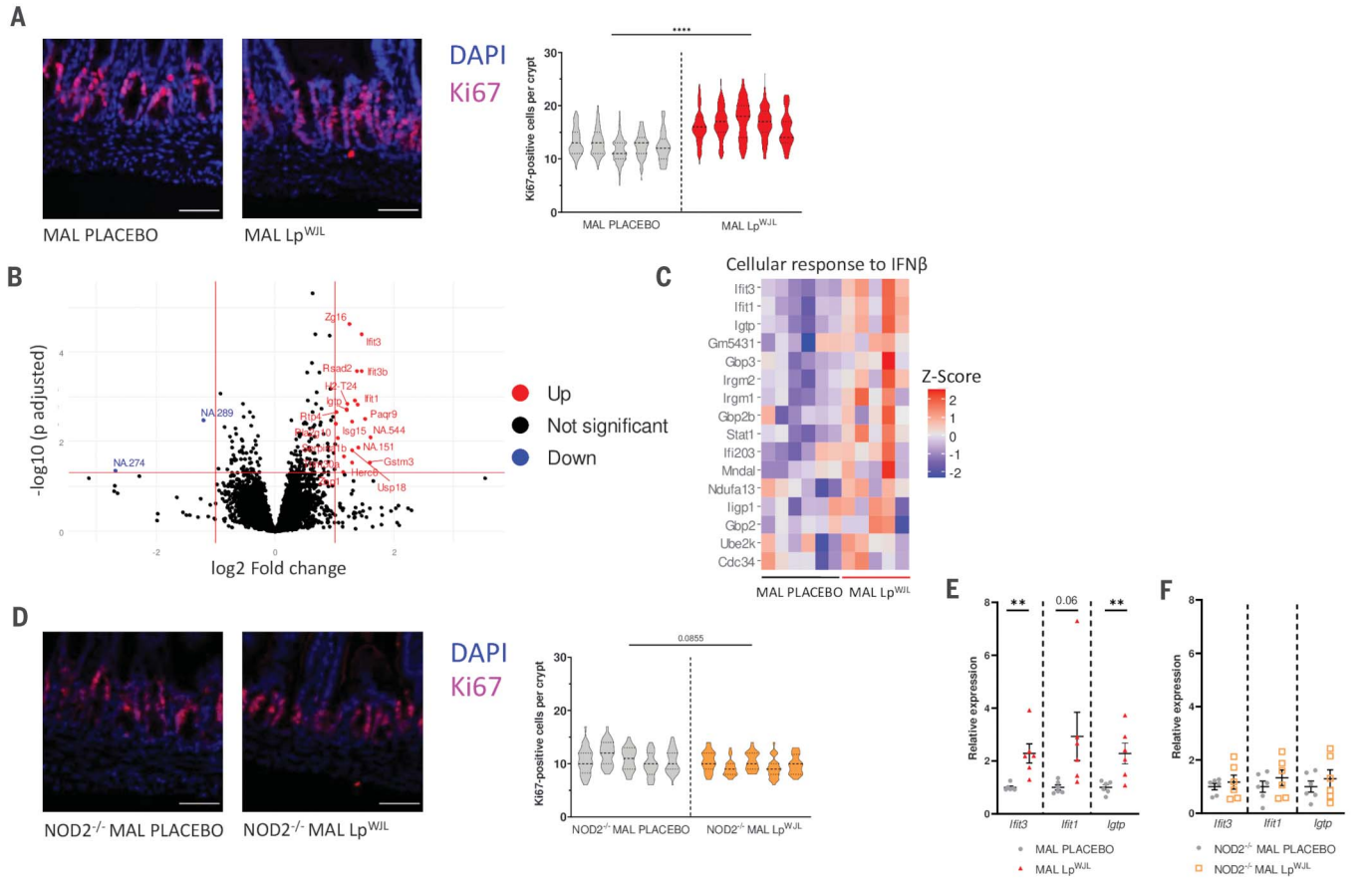

Fig. 5. NOD2-dependent Lp^{WJL} sensing increases the number of Ki67^{+} cells and expression of type I IFN response genes in the small intestine. (**A**) Representative images of Ki67 staining in the jejunum of MAL-fed C57Bl/6J male mice and quantification of Ki67^{+} cells/crypt (n = 5 mice/group). Scale bar, 50 μm. Each violin plot represents a single mouse with minimum of 24 crypts/mouse counted. (**B**) RNA-sequencing analysis of pathways changed in jejunum of Lp^{WJL}-treated (n = 5) MAL-fed C57Bl/6J male mice compared with placebo (n = 6). DESeq2 calculated log fold changes were used as input and analyzed for enrichment of pathways using the Gene Ontology (GO) resource. (**C**) Heatmap of the most changed genes from the cellular response to IFNβ gene set showing values of individual samples. (**D**) Representative images of Ki67 staining in the jejunum of MAL-fed NOD2 KO male mice and quantification of Ki67^{+} cells/crypt (n = 5 mice/group). Scale bar, 50 μm. Each violin plot represents a single mouse with 20 to 34 crypts/mouse counted. (**E**) Expression levels of *Ifit3*, *Ifit1*, and *Igtp* genes in the jejunum of MAL-fed C57Bl/6J male mice depicted as fold change relative to the placebo-treated (gray circles, n = 6) and Lp^{WJL}-treated (red triangles, n = 6) mice. (**F**) Expression levels of *Ifit3*, *Ifit1*, and *Igtp* genes in the jejunum of MAL-fed NOD2 KO male mice depicted as fold change relative to the placebo-treated (gray circles, n = 6) and Lp^{WJL}-treated (orange open squares, n = 6) mice. Data are presented as violin plots and dot plots with mean ± SEM. Data in (A) and (D) were analyzed by nested t test. Data in (E) and (F) were analyzed by unpaired Student's t test, $^{**}P < 0.01$, $^{****}P < 0.0001$.

with a Gram-positive *B. infantis* probiotic strain (*38*). Stimulation of NOD2 has been shown to induce the type I IFN response (*39*), and concomitantly, type I IFNs play an important role in the stimulation of intestinal epithelial homeostasis (*40*). These results prompted us to investigate the expression of the Ki67^{+} marker in the intestinal crypt of NOD2$^{-/-}$ mice. We found no significant difference in the number of Ki67^{+} cells between the jejunal crypts of Lp^{WJL}- and placebo-treated mice (Fig. 5D). Furthermore, we examined the expression of three genes, *Ifit3*, *Ifit1*, and *Igtp*, that were up-regulated by Lp^{WJL} treatment in wild-type MAL-fed animals (Fig. 5E) and found no difference between the Lp^{WJL}- and placebo-treated groups of NOD2$^{-/-}$ mice (Fig. 5F). These data further confirm the key role of NOD2 in the recognition and signaling of orally administered Lp^{WJL}.

Intestinal NOD2 is necessary for Lp^{WJL}-mediated growth promotion

The observed changes in the small intestine after Lp^{WJL} treatment in WT and NOD2$^{-/-}$ mice suggested that sensing by NOD2 in the intestinal crypt might be the key for the Lp^{WJL}-induced improved growth kinetics during chronic undernutrition. Conversely, given the central role of the GH/IGF-1 axis activity in the liver during the systemic response triggered by Lp^{WJL}, we could not exclude the possibility that, as previously reported in the context of obesity and fatty liver disease (*34*, *41*), NOD2 is required within hepatocytes to regulate endocrine signals in response to infiltrating PG fragments. To test these hypotheses, we used tissue-specific NOD2 KO strategies. First, we used a transgenic mouse model with an intestinal epithelial cell (IEC)–specific Cre driver Vil1-iCre construct encoding a tamoxifen-inducible Cre recombinase (*42*) (fig. S12A). We crossed Vil1-iCre mice to a Rosa26-fl-STOP-fl-TdTomato reporter mouse strain and analyzed the intestinal compartment by flow cytometry (fig. S12 B) and fluorescence microscopy (fig. S12C). We confirmed that Vil1-iCre is expressed and recombined in the IEC compartment [including the ISC compartment, as previously reported (*42*)]. Next, we crossed the Vil1-iCre to the NOD2$^{fl/fl}$ (fig. S12A) strain, which led to

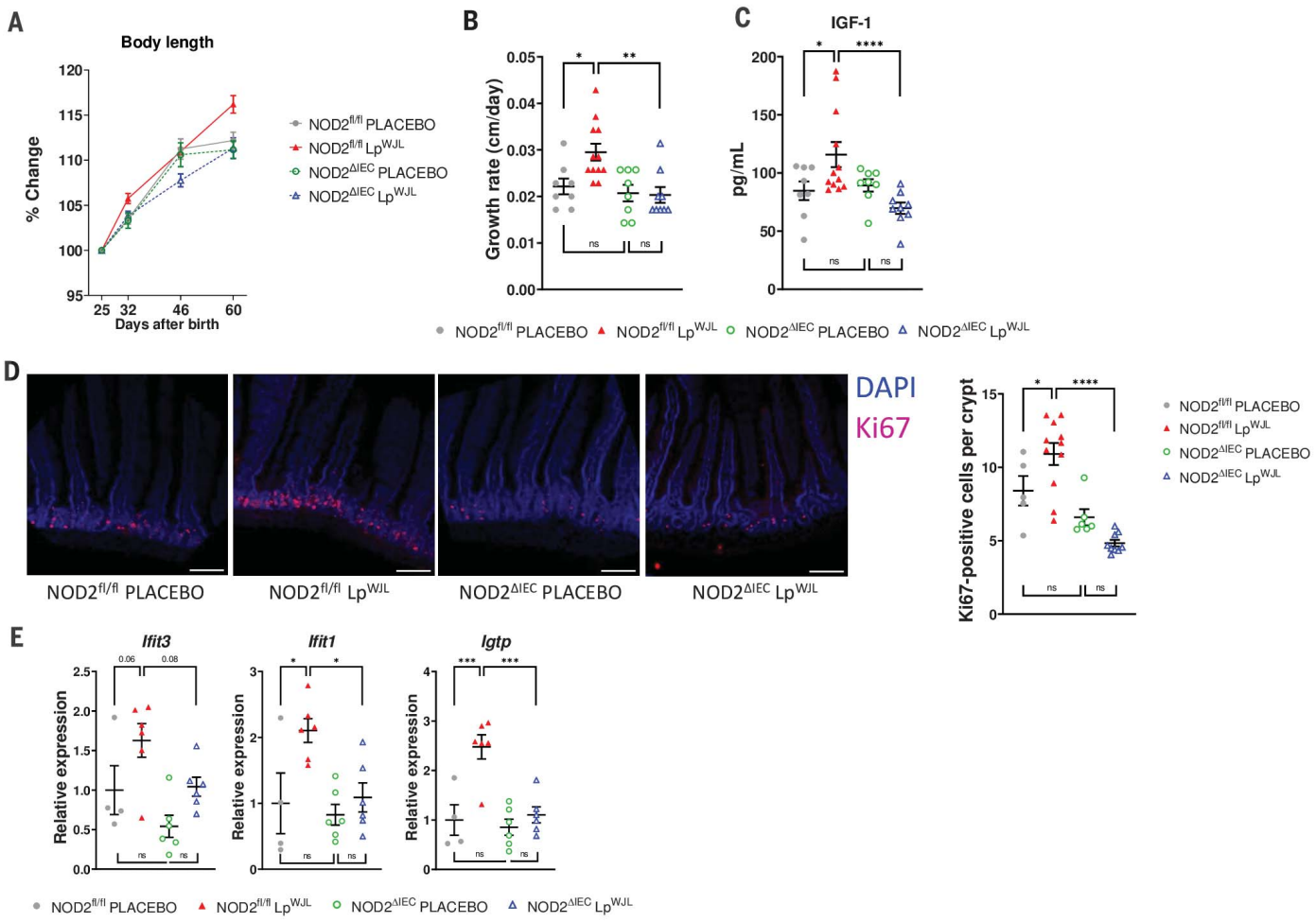

Fig. 6. NOD2-dependent sensing of Lp^{WJL} in the intestinal epithelial compartment is necessary to support juvenile growth during chronic undernutrition. (**A** to **C**) Relative body length growth curves (A), body length growth rate (B), and IGF-1 levels (C) in sera at day 60 after birth of $NOD2^{fl/fl}$ placebo–treated (gray circles, n = 8), $NOD2^{\Delta IEC}$ placebo–treated (green open circles, n = 8), $NOD2^{fl/fl}$ Lp^{WJL}–treated (red triangles, n = 12), and $NOD2^{\Delta IEC}$ Lp^{WJL}–treated (blue open triangles, n = 9) MAL-fed mice. (**D**) Representative images of Ki67 staining in the jejunum of $NOD2^{fl/fl}$ placebo–treated (gray circles, n = 5), $NOD2^{\Delta IEC}$ placebo–treated (green open circles, n = 6), $NOD2^{fl/fl}$ Lp^{WJL}–treated (red triangles, n = 11), and $NOD2^{\Delta IEC}$ Lp^{WJL}–treated (blue open triangles, n = 9) MAL-fed mice. Scale bar, 100 μm. Each dot represents a mean of 33 to 57 crypts/mouse counted. (**E**) Expression levels of *Ifit3*, *Ifit1*, and *Igtp* genes in the jejunum of $NOD2^{fl/fl}$ placebo–treated (gray circles, n = 4), $NOD2^{\Delta IEC}$ placebo–treated (green open circles, n = 6), $NOD2^{fl/fl}$ Lp^{WJL}–treated (red triangles, n = 6), and $NOD2^{\Delta IEC}$ Lp^{WJL}–treated (blue open triangles, n = 6) MAL-fed mice. Data are depicted as fold change relative to the $NOD2^{fl/fl}$ placebo–treated mice. Data are presented as dot plots with mean ± SEM. Data were tested by two-way ANOVA to compare between genotypes and treatments, *P < 0.05, **P < 0.01, ***P < 0.001, ****P < 0.0001.

the IEC-specific Cre-driven genetic depletion of NOD2 ($NOD2^{\Delta IEC}$) (fig. S12B). We weaned the male $NOD2^{\Delta IEC}$ and their $NOD2^{fl/fl}$ male littermates on a MAL diet and treated them with Lp^{WJL} or placebo for 5 weeks. Lp^{WJL}-treated $NOD2^{fl/fl}$ mice showed improved length growth rate compared with Lp^{WJL}-treated $NOD2^{\Delta IEC}$ mice and the $NOD2^{fl/fl}$ placebo–treated group (Fig. 6, A and B). Concomitantly, there was no length growth difference between the placebo- and Lp^{WJL}-treated $NOD2^{\Delta IEC}$ groups (Fig. 6, A and B). The increased growth was accompanied by increased IGF-1 in Lp^{WJL}-treated $NOD2^{fl/fl}$ mice compared with Lp^{WJL} $NOD2^{\Delta IEC}$ and $NOD2^{fl/fl}$ placebo-treated animals (Fig. 6C). Lp^{WJL}-treated $NOD2^{fl/fl}$ mice had also significantly higher numbers of $Ki67^{+}$ cells in the intestinal crypts and increased expression of type I IFN response genes compared with all other groups (Fig. 6, D and E). These results establish that NOD2 is required in the intestinal epithelium compartment to support Lp^{WJL}-mediated intestinal response and growth promotion.

To explore the possible role of NOD2 within hepatocytes, we used a transgenic hepatocyte-specific constitutive Cre driver [Alb-Cre (*21*)] to selectively knock out the *Nod2* gene in hepatocytes (fig. S12A). We first verified the specificity of the driver with the Rosa26-fl-STOP-fl-TdTomato reporter mouse strain (fig. S12H) and crossed the Alb-Cre to $NOD2^{fl/fl}$ strain ($NOD2^{\Delta Hep}$), which led to the hepatocyte-specific Cre-driven genetic depletion of NOD2 (fig. S12A). We weaned the male $NOD2^{\Delta Hep}$ mice and their $NOD2^{fl/fl}$ male littermates on a MAL diet and treated them with Lp^{WJL} for 5 weeks. We did not detect any significant differences between length growth rate or in the levels of IGF-1 between the Lp^{WJL}-treated $NOD2^{fl/fl}$ and the $NOD2^{\Delta Hep}$ groups (fig. S13, A to C). Therefore, these results indicate that NOD2 is not required in hepatocytes to support the growth of Lp^{WJL}-treated mice. These results reinforce the crucial role of the NOD2 in the intestinal epithelial compartment to support Lp^{WJL}-mediated juvenile growth promotion during chronic undernutrition.

Conclusion

Our results establish that treatment with the bacterial strain Lp^{WJL} or its CW supports the postnatal growth of chronically undernourished juvenile mice by orchestrating metabolic and

hormonal changes in the juvenile host, which are manifested as improved circulating levels of IGF-1 and insulin. The ability of purified CW to support growth, together with the strain specificity of the bacteria-mediated growth promotion phenotypes, point to an important role of the host machinery involved in the sensing of bacterial CW to alleviate stunting upon chronic undernutrition. Consistent with this hypothesis, we demonstrate that NOD2, a key host sensor of bacterial CW, is necessary for Lp^{WJL}-mediated growth promotion, and that NOD2 ligands are sufficient to support improved growth. Specifically, we show that Lp^{WJL} NOD2 sensing and signaling supporting growth occur solely in the intestinal epithelium.

NOD2 is an intracellular innate immune sensor expressed in epithelial and immune cells of the intestine, which ensures the maintenance of intestinal inflammatory and immune homeostasis (*43*–*45*). NOD2 is also strongly expressed in stem cells of the intestinal crypts (*46*), where it controls their proliferation and survival in response to bacterial PGs, the main components of Gram-positive bacteria CW (*36*). This NOD2-dependent ISC phenotype is reminiscent of the increased number of proliferating cells in the small intestinal crypts upon Lp^{WJL} treatment, a feature lost in $NOD2^{-/-}$ mice. Stem cell proliferation in the crypt is the major biological process ensuring homeostasis of the intestinal epithelium, a prerequisite for its absorptive and protective functions (*47*). Chronic undernutrition diminishes the number of proliferative ISCs (*17*, *48*), resulting in shorter villi and reduced absorptive epithelial cell numbers, which overall results in a decrease of the small intestinal absorptive area and decreased nutrient absorption (*17*, *48*). We therefore posit that one of the mechanisms by which Lp^{WJL} and its CW exert their postnatal growth–promoting properties is by buffering of the deleterious effect of undernutrition on small intestinal crypt cell proliferation through NOD2-dependent bacterial PG sensing. Lp^{WJL}-mediated NOD2 signaling in the crypt improves intestinal cell proliferation and epithelium maturation, and thus nutrient absorption, which would translate into increased activity of the nutrient-sensitive GH/IGF-1/insulin axis and ultimately improve postnatal growth in a systemic manner. However, this presumption requires further experimental testing.

Collectively, our findings establish that NOD2-dependent sensing in the intestinal epithelial compartment of bacterial CW contributes to sustained postnatal growth upon undernutrition. Our results suggest that, coupled with renutrition strategies, supplementation of evidence-based probiotics such as Lp^{WJL} or defined bacteria-derived postbiotics such as Lp^{WJL} CW and/or NOD2 agonists have the potential to alleviate persistent stunting, one of the long-term sequelae of undernutrition that still affects >149 million children under the age of 5 years in low- and middle-income countries (*49*).

Materials and Methods

Animals

Institute of Functional Genomics (IGFL), Lyon, France: Specific pathogen free C57Bl/6J and BALB/c breeders (8 to 9 weeks old) were purchased from Envigo (France). After 1 week of acclimatization at the conventional animal room at IGFL, mice were mated and offspring were used for experiments. Mice were kept in Innorack IVC Mouse 3.5 disposable cages (Inovive, USA), exposed to 12:12 hours light-dark cycles, supplied with tap water and fed *ad libitum* RM3 diet (SDS Diets). All experiments were performed in accordance with the European Community Council Directive of September 22, 2010 (2010/63/EU) regarding the protection of animals used for experimental and other scientific purposes. The research project was approved by a local animal care and user committee (C2EA015) and subsequently authorized by the French Ministry of Research (APAFIS#3147-2015112516275348 v6 and APAFIS#11985-2017100609104032 v7). Results depicted in Figs. 1 and 2 and related supplementary figures were generated at IGFL by using 13% cellulose AIN93G diet (CON, Envigo, containing 17.7% of crude protein and 7.2% of fat; table S1) or the experimental diet low in proteins and fats (MAL, Envigo; table S1).

Institute of Microbiology of the Czech Academy of Sciences, Novy Hradek, Czech Republic: Conventional C57Bl/6J were bred in Laboratory of Gnotobiology for more than 10 generations. C57Bl/6J MyD88 KO and Rosa26TdTOMATO (B6;129S6-Gt(ROSA)26Sortm14(CAG-tdTomato) Hze/J) (*50*) mice were provided by Dr. Dominik Filipp (Institute of Molecular Genetics, Prague, Czech Republic) and C57Bl/6J NOD2 KO mice were a kind gift from Dr. Tomas Hrncir (Laboratory of Gnotobiology, Novy Hradek, Czech Republic). $NOD2^{fl/fl}$ C57Bl/6J mice (originaly from Dr. P. Rosenstiel, Institute for Clinical Molecular Biology, Christian-Albrechts-University, Kiel, Germany) and Alb-CRE (129S.Cg-Speer6-ps1Tg(Alb-cre)21Mgn/MdfJ) (*51*) backcrossed four times with the $NOD2^{fl/fl}$ C57Bl/6J strain creating Alb-CRE $NOD2^{fl/fl}$ were provided by Dr. Ivo Gompers-Boneca (Institute Pasteur, Paris, France). Vil1-CreERT (B6.Cg-Tg(Vil1-cre/ERT2)23Syr/J) (*42*) $NOD2^{fl/fl}$ mice were provided by Dr. Mathias Chamaillard (University of Lille, Lille, France).

Mice were kept in IVC cages (Tecniplast, Italy), exposed to 12:12 hours light-dark cycles, supplied with tap water, and fed *ad libitum* mouse breeding diet V1124-300 (Ssniff Spezialdiäten GmbH) sterile diet (irradiated ~25 kGy, Bioster, Czech Republic). Animal experiments in Laboratory of Gnotobiology were approved by the Committee for Protection and Use of Experimental Animals of the Institute of Microbiology of the Czech Academy of Science (approval ID: 22/2018, 24/2018 and 56/2021). Results depicted in Figs. 3 to 6 and related supplementary figures were generated at Laboratory of Gnotobiology by using sterile 13% cellulose AIN93G diet (CON, Envigo; table S1) and sterile experimental diet low in proteins and fats (MAL, Envigo; table S1), both irradiated ~45 kGy (Bioster, Czech Republic).

Experimental design

Conventional BALB/c, C57Bl/6J, C57Bl/6J NOD2 KO and C57Bl/6J MyD88 KO mice (10-11 weeks old) were mated. After the delivery the litter size was reduced to six offspring per dam and at day 21 male or female mice were weaned either on the 13% cellulose AIN93G diet (CON, Envigo, containing 17.7% of crude protein and 7.2% of fat; table S1) or the experimental diet low in proteins and fats (MAL, Envigo; table S1) and followed regularly until 42, 56, or 84 days after birth.

For intestinal epithelium-specific KO, $NOD2^{fl/fl}$ mice were crossed to a Vil1-CreERT $NOD2^{fl/fl}$ line, which allows gene deletion in all epithelial cells of the intestine upon tamoxifen administration. The Cre enzyme was induced by three i.p. injection of 0.1 (0.3 mg total/mice) mg tamoxifen (Merck # 85256 Supelco) dissolved in sunflower oil (2 mg/ml) on days 10, 11 and 12 after birth. Male mice were weaned at day 25 after birth on MAL diet and followed until day 60. For hepatocyte-specific KO, $NOD2^{fl/fl}$ mice were crossed to an Alb-CRE $NOD2^{fl/fl}$. Male mice were weaned at day 21 after birth on MAL diet and followed until day 56. The tissue specificity of Vil1-CreERT and Alb-Cre were verified by crossing them to Rosa26TdTOMATO mice.

Mice weaned on the MAL diet were followed without treatment or treated 5x/week by the placebo or Lp^{WJL} or $Lp^{NIZO2877}$ or heat-killed Lp^{WJL} or Lp^{WJL} purified cell-wall or $Lp^{NIZO2877}$ purified cell-wall. The daily treatment dose corresponded to 2×10^8 CFU/30 µl of solution. Muramyldipeptide (InvivoGen, USA, # tlrl-mdp) was dissolved in placebo and mice were treated with 25 µg/30 µl 5x/week. Mifamurtide (CliniSciences, France) was dissolved in DMSO (Merck) to obtain 50 µg/µl stock solution. DMSO stock solution was used to create 62.5 µg mifamurtide (equimolar to 25 µg of MDP)/30 µl of placebo and this was administered to mice 5x/week. Control group received DMSO/placebo mixture. All solutions were administered by a pipette onto the tongue of the mouse. Mouse was held until the solution was swallowed.

For the measurement of body length mice were briefly anesthetized by isoflurane (Piramal

Healthcare, UK). Weight was measured twice and the scales (Acculab mini PP201, Sartorius, Germany) were tared between the measurements. Food intake was measured by subtracting the amount of remaining and spilled food pellets from the amount of food provided during the experiment. Food and bedding were removed at 8 a.m. Fed and fasted glucose levels were measured by tail-tip bleeding with glucometer FreeStyle Lite (Abbott, Canada). Mice were sacrificed after 5 hours fasting by isoflurane inhalation and cervical dislocation. All animals were sacrificed within one hour between 1:00 and 2:00 p.m. Heart, spleen, liver, kidney, epididymal adipose tissue, and gastrocnemius muscle were removed and weighed. Liver, gastrocnemius muscle, and sections of small intestine were snap-frozen and stored at −80°C until processing.

Genotyping of NOD2$^{fl/fl}$, Vil1-Cre, and Alb-Cre mice

Mouse tail tip was cut off and DNA was extracted using the KAPA Mouse Genotyping Kit (Merck, MGKITKB) following the manufacturer's manual. After the quick centrifugation extracted DNA was diluted 10x with 10 mM Tris-HCl (pH 8.0–8.5). Each PCR reaction (20 μl) consisted of 10 μl 2X KAPA2G Fast (HotStart) Genotyping Mix with dye, 2 μl template DNA (10X diluted), 0.5 μM of each forward and reverse primers (table S3). The PCR product was separated on 1.2% agarose (TopBio, P045) gel in 1x ultrapure TAE buffer (Invitrogen, 15558042), stained in ethidium bromide solution and visualized with fluorescent image analyzer (FLA-7000, Fujifilm).

Flow cytometry analysis

Small intestine was dissected, cleaned from mesenteric fat and Peyer's patches were removed. Duodenum, and 6 cm of jejunum and ileum were separated and cut open longitudinally. Tissues were cut to 2 cm long pieces and washed by vigorous shaking in ice-cold PBS to remove luminal contents. Cleaned tissue pieces were incubated twice in HBSS buffer (Merck, H6648) supplemented with 3% FBS and 2mM EDTA for 20 min at 37°C. Remaining tissue was discarded and the buffer containing epithelial cells was collected. Single cell suspension of epithelial cells was obtained by digestion in TrypLE enzyme (Gibco, 12604013) for 1 min at 37°C. Cells were washed with HBSS buffer supplemented with 3% FBS and 2mM EDTA and used for flow cytometry analysis. For the isolation of liver cells, 2-cm portion of liver was dissected and cut to ~2mm pieces. These pieces were incubated in RMPI (Gibco, 21875034) medium supplemented with collagenase D (1 mg/ml, Roche), DNAse I (40 U/ml, Roche) and 3% FBS for 1 hour at 37°C. Every 20 min, cell suspension was dislodged from tissue pieces by serial pipetting using cut tip. Cell suspension was then passed through 100μm filter, washed with HBSS buffer supplemented with 3% FBS and 2 mM EDTA and used for flow cytometry analysis. Staining was performed in HBSS buffer supplemented with 3% FBS and 2 mM EDTA on ice for 20 min. Intestinal epithelial cells were stained with CD45-FITC (BioLegend, clone 30-F11) and EpCAM-APC (BioLegend, clone G8.8). Liver cells were stained with CD45-FITC (BioLegend, clone 30-F11) and CD31-APC (BioLegend, clone 390). Hoechst 33258 was added directly prior to the analysis to determine cell viability. Samples were analyzed using LSRII or Symphony FACS flow cytometers (both BD Biosciences). Flow cytometry data were analyzed using FlowJO software (v10.8.1, BD Biosciences).

Bacterial strains preparation for mouse treatment

Lp^{WJL}, formally *Lactobacillus,* reclassified based on (*52*), originally isolated from posterior midgut of adult *Drosophila* (kind gift from Prof. Won Jae Lee, South Korea) was cultured overnight in Man, Rogosa and Sharpe (MRS) medium (Biokar Diagnostics, France) at 37°C without agitation. After centrifugation (20,000*g* for 60 min, RT) the pellet was dissolved in cryoprotectant containing 20% maltodextrin and 2% dextrose (Neobiosys, France), lyophilized and the powder was stored at −20°C until use. The viability was checked regularly by plating appropriate serial dilution on the MRS agar plates and counting the colonies after incubation at 37°C for 48 hours. *Lactiplantibacillus plantarum*^{NIZO2877} (Lp^{NIZO2877}, formally *Lactobacillus*, reclassified based on (*52*), originally isolated from a sausage in Vietnam (kind gift from Prof. Michiel Kleerebezem, NIZO food research BV, Netherlands) were cultured overnight in MRS medium (Oxoid, Thermo Scientific, CM0359) at 37°C without agitation. Aliquots were centrifuged and after discarding the supernatant, the pellet was snap-frozen in liquid nitrogen and stored at −80°C. Lp^{NIZO2877} remained viable and no decrease in viability was observed during the experiment. For the mouse treatment, the lyophilized Lp^{WJL} was each day freshly dissolved in sterile PBS to the concentration 2×10^8 CFU/30 μl which corresponded to one treatment dose. Placebo for mouse treatment was created by dissolving lyophilized control cryoprotectant (non-inoculated controll culture batch of the Lp^{WJL} lyophilized culture batch) in sterile PBS. Heat-killed bacteria were prepared as described for Lp^{WJL} and kept at 65°C for 30 min. Successful bacterial inactivation was verified by plating on the MRS agar plates and incubating at 37°C for 48 hours. Frozen pellet of Lp^{NIZO2877} cultures were dissolved in placebo to the concentration 2×10^8 CFU/30 μl. Lp^{WJL} and Lp^{NIZO2877} isolated cell wall was dissolved in placebo to correspond to the 2×10^8 CFU/30 μl per treatment dose.

Purification of L. plantarum cell wall and preparation for mouse treatment

Purification of Lp^{WJL} and Lp^{NIZO2877} cell wall was performed as previously described (*30*). Briefly, *L. plantarum* cells were grown in MRS medium and harvested at mid-exponential phase. After washing with MilliQ water, the cells were boiled for 10 min and centrifuged at 5000*g* at 4°C. CFUs (3.75×10^{10}) were resuspended in 1 ml of SDS 5% in 50 mM of MES (Sigma-M8250) pH 5.5, pre-heated at 60°C and boiled for 25 min. After centrifugation at 20,000*g*, the pellets were resuspended in 1 ml of SDS 5% in 50 mM of MES pH 5.5, pre-heated at 60°C and boiled for 15 min and then washed with MilliQ water to remove SDS traces. Next, the pellets were sequentially enzymatically treated with 2 mg/ml of Pronase (Roche 165921) in 50 mM of MES (Sigma-M8250) at pH 6.0 for 90 min at 60°C; 200 μg/ml of trypsin (Sigma T-0303) in 50 mM of MES (Sigma-M8250) at pH 6.0 for 2 hours at 37°C with shaking; DNase (Sigma-D-4527) and RNase (Sigma-R-5503) (50 μg/ml) in 50 mM of MES (Sigma-M8250) at pH 6.0 for 1 hour at 37°C. After boiling for 15 min with SDS 2% in 50 mM of MES (Sigma-M8250) at pH 5.5 and centrifugation at 20,000*g* for 10 min, the pellets were washed with MilliQ water to remove SDS traces. Purified cell walls were lyophilized and stored at −80°C until use. Lp^{WJL} and Lp^{NIZO2877} isolated cell wall was dissolved in placebo to correspond to the 2×10^8 CFU/30 μl per treatment dose.

Extraction and analysis of peptidoglycan

L. plantarum strains were grown in MRS medium up to an $OD_{600\ nm}$ of 1. Cells were boiled in SDS, then treated with proteases, DNase and RNase as described above to prepare cell walls. The lyophilized material was then sheared with glass beads. The cell walls were resuspended in Milli-Q H_2O and the suspension was added to lysing matrix tubes containing 0.1 mm silica beads (MP Biomedicals). Tubes were homogenized with a MP Biomedicals FastPrep 24 Homogeniser (4.5 m/s intensity for 30 s). After centrifugation of the suspension at 200*g* for 1 min to remove glass beads, insoluble material containing cell walls was recovered by centrifugation 20,000*g* for 15 min. The pellet was resuspended in 4% SDS in 10 mM MES pH 5.5 for 15 min and boiled for 15 min. The final pellet was washed four times with 10 mM MES pH 5.5 and twice with MilliQ H_2O to remove SDS traces. The purified cell walls were lyophilized and treated with hydrofluoric acid (48%) for 19h at 0°C to remove covalently bound secondary cell wall polymers. The remaining insoluble purified peptidoglycan was washed twice with 250 mM Tris-HCl pH 8.0 and four times with MilliQ H_2O and

lyophilized. Peptidoglycan was digested with mutanolysin (Sigma Aldrich) and the resulting soluble muropeptides were reduced by $NaBH_4$ as described previously (*53*). The reduced muropeptides were separated by reverse phase ultra-high-pressure liquid chromatography (RP-UHPLC) with a 1290 chromatography system (Agilent Technologies) and a Zorbax RRHD Eclipse Plus C18 column (100 by 2.1 mm; particle size, 1.8 μm; Agilent Technologies) at 50°C using ammonium phosphate buffer and methanol linear gradient. The eluted muropeptides were detected by UV absorbance at 202 nm. Muropeptides were identified by LC-MS using an UHPLC instrument (Vanquish Flex, Thermo Scientific) connected to a Q-Exactive Focus mass spectrometer (Thermo Fisher Scientific). Muropeptides were quantified by integration of the peak areas of the UV profiles.

Intraperitoneal glucose tolerance test

At Day 50 after birth, animals were fasted for 5 hours (starting at 8 a.m.) before being intraperitoneally injected with D-glucose in sterile PBS (2 g/kg body weight; Merck, G7021). Glucose levels were measured by tail-tip bleeding with glucometer FreeStyle Lite (Abbott, Canada) before injection and 15, 30, 45, 60, 90, and 120 min after glucose administration.

FITC–dextran uptake assay

The intestinal permeability in vivo was measured by determination of the amount of FITC-dextran in blood after oral administration as described previously (*54*). Mice were fasted for 4 hours and then received 360 mg/kg b. w. of FITC-dextran (molecular weight 4.0 kDa; Merck, 46944) by intragastric gavage. Blood samples were obtained after 4 hours and serum was collected. The concentration of FITC-dextran was determined by spectrophotofluorometry (Safire2, Tecan Group Ltd., Switzerland) with an excitation wavelength of 483 nm and an emission wavelength of 525 nm using serially diluted FITC-dextran as standard.

Histology and morphometric analysis

Five cm long sections of mouse jejunum were collected, flushed with cold PBS, fixed in 4% paraformaldehyde-PBS at 4°C and processed by the Swiss-rolling technique (*55*). Subsequently, samples were processed by the Leica TP1020 tissue processor (Leica) and embedded into paraffin. Paraffin-embedded tissues were cut into 5-μm sections, dewaxed in a xylene bath and rehydrated in solutions of decreasing alcohol content before staining with hematoxylin and eosin (H&E) using standard techniques. H&E-stained tissues were visualized under a light microscope Leica DM6000 (Leica) and pictures were taken using LAS X software (Leica). Villous length and crypt depth were measured using Fiji 2.0.0 software. Segments of the jejunum and ileum were embedded in TissueTec (Takara, Tissue-Tek® O.C.T. Compound) or fixed in 4% paraformaldehyde-PBS, swiss-rolled and embedded in tissue freezing medium (Leica) and subsequently frozen in vapors of liquid nitrogen and stored at −80°C until used. Cryosections (10 μm thick for the segments, 100 μm thick for the swiss rolls) were obtained on CM3050S Cryostat (Leica). Sections from the segments of jejunum and ileum were incubated with rabbit anti-Ki67 (1:100, AbCam, ab15580) and corresponding secondary antibody (1:400, Alexa Fluor 488, Life Technologies). The sections were mounted with VECTASHIELD® Antifade Mounting Medium with DAPI H-1200 (Thermo Scientific). Images were acquired using a Carl Zeiss LSM 780 inverted confocal microscope at a 20x magnification. Sections from the swiss rolls were incubated with rat anti-Ki67 (1:100, eBiosciences™, SolA15) and/or rabbit anti-villin (1:500, AbCam, ab130751) and with corresponding secondary antibody (1:400, Alexa Fluor 488 or Alexa Fluor 555, Invitrogen). Samples were mounted in ROTI Mount FluorCare DAPI (Roth) and image acquisition was performed using a Leica SP8 upright confocal microscope. Post-acquisition image analysis was performed with Fiji 2.0.0 software (*56*). Adjacent imaged fields were stitched together using the stitching tool available with the Fiji 2.0.0 software (*57*).

Stimulation of human embryonic kidney 293 cells stably transfected with TLRs and NODs

Human embryonic kidney (HEK) 293 cells stably transfected with plasmid carrying human (h)TLR2/CD14 gene were kindly provided by Prof. M. Yazdanbakhsh (Leiden, Netherlands), hTLR4/MD2/CD14 were a gift of Prof. B. Bohle (Vienna, Austria) and hNOD2 and hNOD1 expressing cells were purchased from InvivoGen (USA). Cells were stimulated for 20 hours in 96-well plates with Pam3CSK4 (5 μg/ml, InvivoGen, tlrl-pms), ultrapure LPS from *E. coli* 0111:B4 (5 μg/ml, InvivoGen, tlrl-3pelps), muramyl dipeptide (MDP, 5 μg /ml, InvivoGen, tlrl-mdp) and L-Ala-γ-D-Glu-mDAP (Tri-DAP, 10 μg /ml, InvivoGen, tlrl-tdap) as positive or negative controls, respectively. Heat-killed Lp^{WJL} and $Lp^{NIZO2877}$ and purified Lp^{WJL} and $Lp^{NIZO2877}$ cell-wall dissolved in sterile PBS were used at concentrations corresponding to 10^8 CFU/ml. Lp^{WJL} and $Lp^{NIZO2877}$ purified PG and PG digested with mutanolysin (PGD) were tested at concentrations 100 μg/ml and 10 μg/ml, respectively. Concentrations of IL-8 were analyzed in cell supernatants by ELISA (Thermo Scientific) according to the manufacturer's instructions.

Serum factors measurement

At the end of experiment, blood was collected and left to clot at RT for 2 hours. Sera were separated by centrifugation (2000*g* for 5 min, 4°C) and stored at −80°C until used. Levels of Insulin-like Growth Factor 1 (IGF-1) were measured by Mouse/Rat IGF-1 Quantikine ELISA (R&D systems) and insulin was measured by Ultrasensitive Mouse Insulin ELISA (Alpco, Salem, USA) according to manufacturer's instructions. G-CSF, IL-6, TNF-α, IL-1β and MCP-1 levels were determined by the custom multiplex Millipore Mouse Milliplex MAP Kit (Millipore Corp.) using the Bio-Plex System (Bio-Rad Laboratories, USA).

Liver IGF-1 measurement

Liver tissues were weighed and homogenized in lysis buffer containing PBS, 1% Triton X100 and a protease inhibitor mixture (Roche, cOmplete, EDTA-free Protease Inhibitor Cocktail). After centrifugation (12,000*g* for 10 min, 4°C) supernatants were collected and used at dilution 1:10 to determine the IGF-1 levels by Mouse/Rat IGF-1 Quantikine ELISA (R&D systems) according to manufacturer's instructions. Results are expressed as pg/mg of tissue.

Bone length measurement

Femur and tibia bones were removed at sacrifice, fixed in 4% of paraformaldehyde-PBS overnight at 4°C, washed with PBS and stored in 70% ethanol. Bone length was measured by digital caliper (Festa) and photographs of the bones were taken with Leica stereomicroscope M205FA.

RNA extraction and quantitative RT-PCR

Total RNA from liver, muscle and jejunum was isolated and purified using NucleoSpin RNA kit (Macherey-Nagel, iBioTech, 740984.250). Total RNA was quantified and assessed for purity using a NanoDrop ND-1000 Spectrophotometer (Thermo Scientific). Reverse transcription of 1 μg of RNA was performed using Superscript II enzyme (Invitrogen, 18064014) and random primers (Invitrogen, 48190011). Quantitative PCR was performed on a Biorad CFX96 apparatus (Biorad) using SYBRGreenER qPCR Supermix (Invitrogen, 11762500) for liver and muscle samples and Takyon™ No ROX SYBR Mastermix blue dTTP (Eurogentec, UF-NSMT-B0701) for jejunum samples, cDNA (1/100 dilution of the reverse transcription products) and gene specific primer sets (Supplementary Table 3). Melting curves of the detected amplicons were analyzed to ensure specific and unique amplification. PCR efficiency for each primer set was calculated using serial dilution of cDNA. For liver and muscle samples, *Tbp (A)* was used as an internal control to normalize gene expression using the $2^{-\Delta Ct}$ method (*58*). For jejunum samples, *Tbp (B)* and *Rpl32* were used as control genes to normalize target genes expression using the CFX Manager™ software (Biorad).

RNA sequencing

Total RNA from 1 cm piece of proximal jejunum was isolated and purified using NucleoSpin RNA kit (Macherey-Nagel, iBioTech, 740984.250). RNAs were quantified and assessed for purity using a NanoDrop ND-1000 Spectrophotometer (Thermo Scientific). Individually barcoded stranded mRNA-seq libraries were prepared from high quality total RNA samples (~500 ng/sample) using the New England Biolabs NEBNext RNA Ultra II Kit implemented on the liquid handling robot Beckman Coulter hybrid i7. Obtained libraries that passed the QC step were pooled in equimolar amounts; 2 pM solution of this pool was loaded on the Illumina sequencer NextSeq 500 and sequenced unidirectionally, generating ~500 million reads, each 85 bases long. Read quality was assessed by FastqQC (*59*). STAR aligner (*60*) (version STAR_2.6.0a) was used to align the reads back to the GRCm38 reference genome. The gene count tables were generated during the alignment step using the GRCm38.99 annotation in gtf format. Raw read counts were used as an input for deferential expression analysis. This analysis was carried out using DESeq2 Bioconductor package (v 1.34.0) in R (v 4.1.1), using mouse genotype as the main effect. During the data exploration with Principle Component Analysis, one of the Lp^{WJL} MAL replicates showed a discordant gene expression pattern compare to its sample group. The sample was therefore removed for the downstream analysis. Log2-fold change values calculated by DESeq2 were used for gene set enrichment analysis (GSEA) using clusterProfiler R Bioconductor package (v 3.14.3) using Gene ontology resource as gene set input.

Western blot analysis

Frozen liver samples were homogenized in RIPA Plus lysis buffer (50 mmol/L Tris-HCl pH7.4, 1% NP-40, 0.5% Na deoxycholate, 0.1% SDS, 150 mmol/L NaCl, 2 mmol/L EDTA and 50 mmol/L NaF) supplemented with 1× of protease inhibitors (Complete Protease Inhibitor Cocktail, Roche). After centrifugation of the lysates, protein concentration was estimated in the supernatant using a PierceTM BCA Protein Assay Kit (Thermo Scientific, 23227). Total proteins (30 µg) were separated on 10% SDS-polyacrylamide gel (Euromedex, TO-A053-500G) or Mini-PROTEAN® TGX Precast Gels (Bio-Rad, #4561096) and then transferred to Immobilon-P Polyvinylidene fluoride membranes 0.22 µm (Merck Millipore, IPVH00010). Membranes were blocked with 5% BSA in TBS 1× Tween 0.1% for one hour before being probed overnight at 4°C with the following specific primary antibodies: rabbit monoclonal anti-total Akt (C67E7) (#4691) and rabbit monoclonal anti-phospho S473 Akt (D9E) (#4060) from Cell Signaling. After washing, Ab binding was revealed by incubation with horseradish peroxidase (HRP)-conjugated secondary antibodies (one-hour incubation at room temperature, anti-Rabbit IgG HRP-linked antibody, 1:10000, #172-1019, Bio-RAD) and ECL (Luminata Forte Western HRP Substrate, Millipore, WBLUF0100). Signals were recorded by the ChemiDoc XRS+ (Bio-Rad) or C-DiGit® Blot Scanner (Li-Cor) and quantified using Fiji 2.0.0 software (*56*).

Data treatment and statistics

Statistical analysis was performed with GraphPad Prism software version 8.4.2 for Windows (GraphPad Software, San Diego, California USA, www.graphpad.com) using one-way ANOVA with Tukey's post-test for multiple group comparison and two-tailed *t* test for comparison between two groups. Analysis of intestinal morphology and $Ki67^+$ cell numbers was performed by the nested *t* test. Data in Fig. 6 were tested by two-way ANOVA to compare between genotypes and treatments. Values of $P < 0.05$ were considered statistically different. Data are expressed as the mean ± standard error of the mean (SEM) or dot plots with mean ± SEM.

REFERENCES AND NOTES

1. A. A. Butler, D. LeRoith, *Endocrinology* **142**, 1685–1688 (2001).
2. V. L. Tokarz, P. E. MacDonald, A. Klip, *J. Cell Biol.* **217**, 2273–2289 (2018).
3. C. J. Kenyon, *Nature* **464**, 504–512 (2010).
4. P. K. Fazeli, A. Klibanski, *J. Endocrinol.* **220**, R57–R65 (2014).
5. J. P. Thissen, J. M. Ketelslegers, L. E. Underwood, *Endocr. Rev.* **15**, 80–101 (1994).
6. L. V. Blanton, M. J. Barratt, M. R. Charbonneau, T. Ahmed, J. I. Gordon, *Science* **352**, 1533 (2016).
7. F. Leulier *et al*., *Cell Metab.* **25**, 522–534 (2017).
8. J. L. Gehrig *et al*., *Science* **365**, eaau4732 (2019).
9. M. I. Smith *et al*., *Science* **339**, 548–554 (2013).
10. M. Schwarzer *et al*., *Science* **351**, 854–857 (2016).
11. J. Yan *et al*., *Proc. Natl. Acad. Sci. U.S.A.* **113**, E7554–E7563 (2016).
12. A. Molinaro *et al*., *Mol. Metab.* **6**, 1371–1380 (2017).
13. G. Storelli *et al*., *Cell Metab.* **14**, 403–414 (2011).
14. E. M. Brown *et al*., *Nat. Commun.* **6**, 7806 (2015).
15. M. Kosek *et al*., *Clin. Infect. Dis.* **59**, S239–S247 (2014).
16. V. Owino *et al*., *Pediatrics* **138**, e20160641 (2016).
17. P. M. Ueno *et al*., *Am. J. Physiol. Gastrointest. Liver Physiol.* **301**, G612–G622 (2011).
18. J. L. Liu, D. LeRoith, *Endocrinology* **140**, 5178–5184 (1999).
19. E. Stratikopoulos, M. Szabolcs, I. Dragatsis, A. Klinakis, A. Efstratiadis, *Proc. Natl. Acad. Sci. U.S.A.* **105**, 19378–19383 (2008).
20. C. P. Hawkes, A. Grimberg, *Pediatr. Endocrinol. Rev.* **13**, 499–511 (2015).
21. S. Yakar *et al*., *Proc. Natl. Acad. Sci. U.S.A.* **96**, 7324–7329 (1999).
22. H. Werner, D. Weinstein, I. Bentov, *Arch. Physiol. Biochem.* **114**, 17–22 (2008).
23. R. K. Menon, M. A. Sperling, *Endocrinol. Metab. Clin. North Am.* **25**, 633–647 (1996).
24. B. K. Das, J. Ramesh, J. K. Agarwal, O. P. Mishra, R. P. Bhatt, *J. Trop. Pediatr.* **44**, 139–141 (1998).
25. W. Okitolonda, S. M. Brichard, J. C. Henquin, *Diabetologia* **30**, 946–951 (1987).
26. M. P. Chapot-Chartier, S. Kulakauskas, *Microb. Cell Fact.* **13** (Suppl 1), S9 (2014).
27. R. Sengupta *et al*., *Mediators Inflamm.* **2013**, 237921 (2013).
28. M. T. Sorbara, D. J. Philpott, *Immunol. Rev.* **243**, 40–60 (2011).
29. B. Erkosar *et al*., *Cell Host Microbe* **18**, 445–455 (2015).
30. R. C. Matos *et al*., *Nat. Microbiol.* **2**, 1635–1647 (2017).
31. H. Kozakova *et al*., *Cell. Mol. Immunol.* **13**, 251–262 (2016).
32. D. M. Underhill, *Immunol. Rev.* **219**, 75–87 (2007).
33. T. Kawai, S. Akira, *Cell Death Differ.* **13**, 816–825 (2006).
34. J. F. Cavallari *et al*., *Cell Metab.* **25**, 1063–1074.e3 (2017).
35. Y. G. Cao *et al*., *Cell Host Microbe* **30**, 1295–1310.e8 (2022).
36. A. Levy *et al*., *Proc. Natl. Acad. Sci. U.S.A.* **117**, 1994–2003 (2020).
37. R. M. Jones *et al*., *EMBO J.* **32**, 3017–3028 (2013).
38. M. J. Barratt *et al*., *Sci. Transl. Med.* **14**, eabk1107 (2022).
39. A. K. Pandey *et al*., *PLOS Pathog.* **5**, e1000500 (2009).
40. K. P. Kotredes, B. Thomas, A. M. Gamero, *Front. Immunol.* **8**, 410 (2017).
41. J. F. Cavallari *et al*., *Am. J. Physiol. Endocrinol. Metab.* **319**, E305–E314 (2020).
42. F. El Marjou *et al*., *Genesis* **39**, 186–193 (2004).
43. Z. Al Nabhani, G. Dietrich, J. P. Hugot, F. Barreau, *PLOS Pathog.* **13**, e1006177 (2017).
44. R. Caruso, N. Warner, N. Inohara, G. Núñez, *Immunity* **41**, 898–908 (2014).
45. D. J. Philpott, M. T. Sorbara, S. J. Robertson, K. Croitoru, S. E. Girardin, *Nat. Rev. Immunol.* **14**, 9–23 (2014).
46. G. Nigro, R. Rossi, P. H. Commere, P. Jay, P. J. Sansonetti, *Cell Host Microbe* **15**, 792–798 (2014).
47. S. Umar, *Curr. Gastroenterol. Rep.* **12**, 340–348 (2010).
48. R. P. Ferraris, H. V. Carey, *Annu. Rev. Nutr.* **20**, 195–219 (2000).
49. V. Mannar, R. Micha, "Global Nutrition Report 2020: Action on equity to end malnutrition" (Development Initiatives Poverty Research, 2020); https://resourcecentre.savethechildren.net/document/global-nutrition-report-2020-action-equity-end-malnutrition/.
50. L. Madisen *et al*., *Nat. Neurosci.* **13**, 133–140 (2010).
51. C. Postic *et al*., *J. Biol. Chem.* **274**, 305–315 (1999).
52. J. Zheng *et al*., *Int. J. Syst. Evol. Microbiol.* **70**, 2782–2858 (2020).
53. E. Bernard *et al*., *J. Biol. Chem.* **286**, 23950–23958 (2011).
54. D. Srutkova *et al*., *PLOS ONE* **10**, e0134050 (2015).
55. C. Moolenbeek, E. J. Ruitenberg, *Lab. Anim.* **15**, 57–59 (1981).
56. J. Schindelin *et al*., *Nat. Methods* **9**, 676–682 (2012).
57. S. Preibisch, S. Saalfeld, P. Tomancak, *Bioinformatics* **25**, 1463–1465 (2009).
58. K. J. Livak, T. D. Schmittgen, *Methods* **25**, 402–408 (2001).
59. S. Andrews, "FastQC: A quality control tool for high throughput sequence data" (Babraham Bioinformatics, 2010); https://www.bioinformatics.babraham.ac.uk/projects/fastqc/.
60. A. Dobin *et al*., *Bioinformatics* **29**, 15–21 (2013).
61. B. Glauner, *Anal. Biochem.* **172**, 451–464 (1988).

ACKNOWLEDGMENTS

We thank the anonymous reviewers for their insightful comments and suggestions; the EMBL GeneCore facilities for expert technical assistance with mRNA sequencing; and J. Valterová, S. Meisnerová, J. Jarkovská, B. Draboňová, M. Salomon-Mallet, and S. Palussière for excellent technical assistance. **Funding:** The work in F.L.'s laboratory was supported by the FINOVI Foundation, the Fondation pour la Recherche Médicale (Equipe FRM DEq.Q grant 20180339196), and the Agence Nationale de la Recherche (grant ANR-18-CE15-0011). Work in M.Sc.'s laboratory was supported by a Neuron Impuls grant from Neuron Fund, grants 18-07015Y and 21-19640M from the Czech Science Foundation, and by the Ministry of Education, Youth and Sports of the Czech Republic (EMBO installation grant 4139). M.Sc. was supported by a J. E. Purkyne Fellowship from the Czech Academy of Sciences. The work in the laboratories of H.V., I.B., and M.C. is supported by the INSERM National Program "Microbiota." F.D.V. was supported by a grant from Fondation des Treilles. The work in I.G.B.'s laboratory was supported by the Agence Nationale de la Recherche (grant ANR-16-CE15-0021). D.F. was supported by the Czech Science Foundation (grant 20-30350S). **Data and materials**

availability: All data are provided in the main manuscript. Sequencing data are available at the European Nucleotide Archive (https://www.ebi.ac.uk/ena) as project PRJEB56002. **Author contributions:** F.L. and M.Sc. conceived the project and designed the experiments with inputs from H.V., N.P., H.K., M.Ši., I.G.B., and M.C. M.Sc., A.J., P.P., F.D.V., K.M., A.L., S.G., R.C.M., C.G., and A.-L.B. performed the mouse experiments at IGFL. M.Sc., U.K.G., D.S., T.N., P.P.H., and T.H. performed the mouse experiments in Laboratory of Gnotobiology. T.B., J.J.M.L., A.J., and D.F. analyzed the RNAseq data, T.B. and M.Sc. performed the Cre x TdTomato mouse experiments. P.C. and M.-P.C.-C. isolated and analyzed the bacterial peptidoglycan. M.Sc., F.L., U.K.G., P.P., F.D.V., K.M., A.J., A.L., D.S., S.G., P.P.H., R.C.M., C.G., A.-L.B., and T.H. analyzed the data. M.Sc. and F.L. wrote the manuscript with assistance by the remaining authors. **Competing interests:** F.L. and M.Sc. disclose that they are inventors of licensed patents (WO2015173386A1, WO2017137547A1, and WO2019034826A1) covering the use of specific probiotic strains for improving the juvenile growth of animals and humans. The remaining authors declare no competing interests. **License information:** Copyright © 2023 the authors, some rights reserved; exclusive licensee American Association for the Advancement of Science. No claim to original US government works. https://www.science.org/about/science-licenses-journal-article-reuse

SUPPLEMENTARY MATERIALS

science.org/doi/10.1126/science.ade9767
Figs. S1 to S13
Tables S1 to S3
Reference (*61*)
MDAR Reproducibility Checklist

View/request a protocol for this paper from *Bio-protocol*.

Submitted 20 September 2022; accepted 4 January 2023
10.1126/science.ade9767

PRIMARY PRODUCTIVITY

Multidecadal trend of increasing iron stress in Southern Ocean phytoplankton

Thomas J. Ryan-Keogh[1]*†, Sandy J. Thomalla[1,2]†, Pedro M. S. Monteiro[1,3], Alessandro Tagliabue[4]

Southern Ocean primary productivity is principally controlled by adjustments in light and iron limitation, but the spatial and temporal determinants of iron availability, accessibility, and demand are poorly constrained, which hinders accurate long-term projections. We present a multidecadal record of phytoplankton photophysiology between 1996 and 2022 from historical in situ datasets collected by Biogeochemical Argo (BGC-Argo) floats and ship-based platforms. We find a significant multidecadal trend in irradiance-normalized nonphotochemical quenching due to increasing iron stress, with concomitant declines in regional net primary production. The observed trend of increasing iron stress results from changing Southern Ocean mixed-layer physics as well as complex biological and chemical feedback that is indicative of important ongoing changes to the Southern Ocean carbon cycle.

The Southern Ocean acts as the climate flywheel of the planet; it buffers the impacts of climate change by accounting for half of the total oceanic uptake of anthropogenic CO_2 and absorbing three-quarters of the excess heat generated by anthropogenic CO_2 (*1*, *2*) while also regulating the supply of nutrients in support of low-latitude productivity (*3*). Net primary production (NPP) is a major contributor to biological carbon export, ~2 Pg of C per year (*4*), in the Southern Ocean and supports rich marine ecosystems (*5*), driven in part by high macronutrient availability and summertime light levels but ultimately constrained by seasonal changes in light and a scarce supply of the essential micronutrient iron (Fe) (*6*, *7*). Substantial progress has been made in understanding the range of Southern Ocean Fe supply mechanisms and biogeochemical cycling processes that act to govern contemporary NPP (*8*, *9*). Fe availability in the surface ocean is a complex mix of concurrent biotic and abiotic processes that rapidly consume and recycle Fe, as well as removing it from solution by particle scavenging and colloidal pumping (*9*). A central role is played by the mixed-layer depth, which influences seasonal and subseasonal Fe supply (*8*, *10*) by simultaneously altering light availability, which affects phytoplankton growth and Fe demand (*11*, *12*). It is likely that anthropogenic forcing will affect all of these supply and removal terms (*13*) in a complex manner by influencing Fe availability, NPP, ecosystem function, and the transfer of carbon, energy, and nutrients through pelagic and benthic food webs (*5*). Observational constraints on how climate variability affects Fe availability for phytoplankton is, therefore, a crucial component of Southern Ocean environmental change.

The Southern Ocean experiences climate variability associated with the Southern Annular Mode (SAM) (*14*–*16*), with the recent increase in the positive phase of the SAM due to ozone depletion and greenhouse gases driving an intensification and poleward shift of the westerly winds (*15*). This is considered the clearest and most persistent change in Southern Hemisphere climate in the past half century (*17*). Changes in Southern Ocean winds that are associated with the SAM elicit widespread alterations of ocean vertical stratification and mixed-layer depth (*18*–*20*), which affects nutrient supply and the light environment, which interact seasonally to influence phytoplankton growth (*5*). The poleward shift of the westerly winds may also influence atmospheric dust deposition and further alter Fe supply to the surface ocean (*21*). Any observable climate adjustments will integrate changes associated with the SAM such as altered ocean stratification, mixing, and atmospheric deposition, with stronger projected changes in warming, carbonate chemistry, and ocean transport (*22*). Crucial to both contemporary and future trends in NPP is the response of Fe supply, availability, and demand, which will be a key driver. However, there are presently poor constraints on changing Fe supply and demand and little consensus on the impact of ocean warming and altered carbonate chemistry on Fe bioavailability in the Southern Ocean (*5*, *13*). Earth system models tend to predict increased Southern Ocean NPP by the end of the 21st century but are typified by marked intermodel disagreement (*23*). These uncertainties in NPP trends are amplified by poor constraints on the Fe cycle components of Earth system models themselves (*24*), especially regarding projected changes in Fe stress (*25*), for which there are no observation-based datasets presently available.

It is not possible to directly infer Fe stress from observed ambient concentrations because standing stocks are severely depleted by biological uptake (*26*) that is being maintained by recycling (*10*), and there is substantial plasticity of phytoplankton cellular contents and requirements (*11*, *12*), which necessitates experimental approaches (*27*). Manipulation experiments of natural or cultured communities incubated in bottles (*6*) or through in situ open ocean fertilization (*28*, *29*) provide insight regarding the role of Fe addition, whereas proteomic techniques quantify cellular responses to in situ resource stresses of specific organisms (*30*). Results from decades of research have identified various responses in the probability of energy allocation of photons from a net balance perspective in response to varying Fe and light conditions that stem from the central role that Fe plays in photosynthesis (Fig. 1). For example, under optimal light and Fe-replete conditions (Fig. 1A), phytoplankton photochemistry is at maximum capacity, with any remaining energy being dissipated as either fluorescence or nonphotochemical quenching [(NPQ) the dissipation of excess energy in the form of heat] (*31*). Under nutrient-replete conditions with high light stress (Fig. 1B), there is a reduction in photochemistry to prevent photodamage to photosystem II and a reduction in fluorescence (i.e., the common scenario of suppressed fluorescence measured during daylight hours), with the dominant sink of excess energy being NPQ. Phytoplankton can adjust to low average light levels by synthesizing additional photosynthetic reaction centers for increased light absorption (*32*). However, because of the high Fe requirement of reaction centers, Southern Ocean phytoplankton have evolved a photoacclimation strategy in response to their typically low-light and Fe environment (*7*, *27*) that economizes their Fe use by enhancing light absorption through increased light-harvesting antennae size (with additional pigment complexes) rather than the number of reaction centers (*12*). Selective pressure for this strategy, however, reduces the efficiency of excitation energy transfer (from light-harvesting pigments to reaction centers) and can result in a bottleneck and buildup of protons under low-Fe conditions (*33*). The result of this scenario (under optimal light- and Fe-depleted conditions) (Fig. 1C) is an equal allocation of energy to photochemistry (as in an optimal light and Fe scenario) (Fig. 1A) but with a greater proportion of energy being dissipated as fluorescence. This drives the universal and readily observed increase in fluorescence to chlorophyll (Chl) ratios under low-Fe conditions (*34*, *35*). If we consider an Fe-limited but high-light environment (Fig. 1D), phytoplankton avoid overexcitation and

[1]Southern Ocean Carbon-Climate Observatory, CSIR, Cape Town 7700, South Africa. [2]Marine and Antarctic Research for Innovation and Sustainability, University of Cape Town, Cape Town 7700, South Africa. [3]School for Climate Studies, Stellenbosch University, Stellenbosch 7602, South Africa. [4]Department of Earth, Ocean and Ecological Sciences, School of Environmental Sciences, University of Liverpool, Liverpool L69 3GP, UK.
*Corresponding author. Email: tryankeogh@csir.co.za
†These authors contributed equally to this work.

damage to their photosystems by reducing photochemistry and fluorescence, with the dominant energy sink being NPQ. This is further supported by an increase in the synthesis of photoprotective pigments involved in the xanthophyll cycle under Fe-limiting conditions (*36*). An observed increase in NPQ (in surface sunlit waters) is thus expected to reflect an increase in Fe stress under high-light conditions. Although this photophysiological plasticity may not be common to all Southern Ocean phytoplankton, with a few exceptions that exhibit limited NPQ capacity to the same stressors (table S1), experiments that expressed a measurable increase in NPQ from excess energy diversion were always in response to Fe-limiting conditions (table S1). These photophysiological responses to Fe and light have a well-founded mechanistic basis and the potential to provide a diagnostic appraisal of environmental conditions (*37*).

Changing photophysiology in the Southern Ocean

An in vivo approach developed by Ryan-Keogh and Thomalla (*38*) quantifies the degree of NPQ (which manifests as a measurable decrease in the ratio of photons emitted as fluorescence to those absorbed by pigments) as a function of available light [irradiance-normalized NPQ, referred to as α_{NPQ} in Ryan-Keogh and Thomalla (*38*)]. Because the dominant influence of "instantaneous" environmental light conditions on the degree of quenching are accounted for in the determination of irradiance-normalized NPQ (as the slope of NPQ against in situ irradiance; see materials and methods), this approach fingerprints the photophysiological response of phytoplankton to their environment, independent of current light conditions and inclusive of pigment configuration. A particular strength of this approach is that it can be applied to any ocean profile with coincident measurements of fluorescence, photosynthetically active radiation, and backscatter or beam attenuation [e.g., ship-based, Biogeochemical Argo (BGC-Argo) profiling floats, or autonomous gliders], which provides an opportunity to deliver a long-term time series by taking advantage of historical measurements (materials and methods). Here, we quantify irradiance-normalized NPQ from a dataset of 47 BGC-Argo floats and 194 cruises that make up a total of 5795 profiles and span 26 years (Fig. 2 and materials and methods) to produce the first multidecadal (1996 to 2022) in situ assessment of irradiance-normalized NPQ in the Southern Ocean biome (defined here as the spatial extent of the subpolar and ice biomes) (*39*). We find a significant (F-statistic = 260.50, $P < 0.001$, correlation coefficient $r^2 = 0.92$) (Table 1) positive linear trend in irradiance-normalized NPQ (Fig. 2) in the Southern Ocean (4.69% year^{-1}) that is robust ($P < 0.001$ to <0.05) across different seasons (fig. S1, A to D), ocean basins (fig. S1, E to G), and frontal zones (fig. S1, H to J). Moreover, this trend is not affected by an unequal distribution of observations by year, with no change in trend when the sample size is

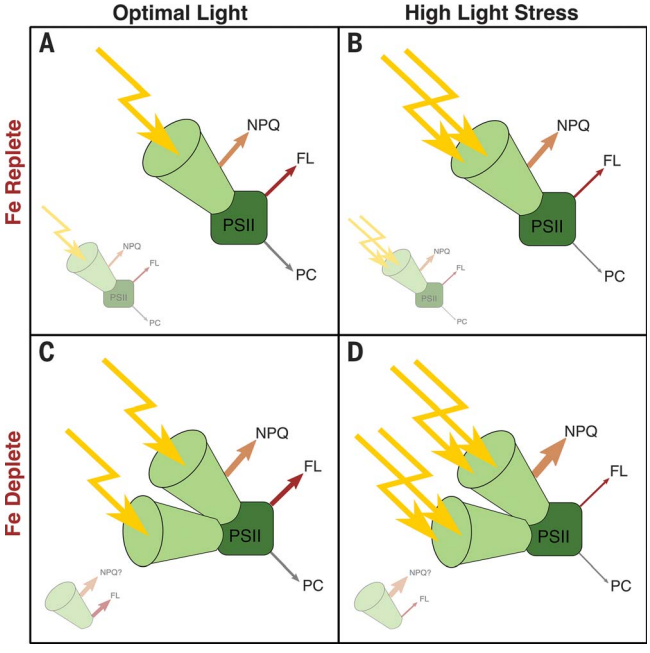

Fig. 1. Schematic of the proportional energy allocation at photosystem II (PSII) under different Fe and light scenarios that phytoplankton may encounter. (**A**) Optimal light and iron scenario in which photochemistry (PC) is at its maximum with any remaining energy dissipated as fluorescence (FL) or NPQ. (**B**) High-light stress scenario in which there is a reduction in PC to prevent damage to PSII and a reduction in FL, with NPQ acting as the dominant energy sink. (**C**) Fe-limiting scenario with an increased light-harvesting antenna size to maintain PC as in (A), but with an increase in FL. (**D**) Both a high-light stress and Fe-limiting scenario, in which both PC and FL will be reduced with NPQ again acting as the dominant energy sink. The opaque background units in (A) and (B) represent complete reaction centers with light-harvesting antennae, whereas the opaque background units in (C) and (D) represent the synthesis of energetically decoupled light-harvesting antennae, which may absorb light with only FL and potentially NPQ acting as energy sinks.

Table 1. Trends of irradiance-normalized NPQ and NPP. Normalized ordinary least-squares regression results of irradiance-normalized NPQ (1996 to 2022), NPP from two production models applied to BGC-Argo data (2014 to 2021), NPP from four production models applied to remote sensing data (1998 to 2021), and NPP from CMIP6 outputs (1996 to 2021). CbPM1 refers to the Behrenfeld *et al*. (*49*) model, and CbPM2 refers to the Westberry *et al*. (*50*) model.

Platform	Date range	Parameter	Slope	Intercept	r^2	F-statistic	P value
In situ	1996 to 2022	Irradiance-normalized NPQ	4.69×10^{-2}	−93.18	0.92	260.49	2.18×10^{-14}
	2014 to 2021	VGPM	−0.08	172.29	0.43	4.45	0.08
		CbPM1	−0.10	197.73	0.81	25.60	2.31×10^{-3}
Remote sensing	1998 to 2021	VGPM	0.01	−15.79	0.55	26.97	3.30×10^{-5}
		CbPM1	−0.02	32.85	0.61	34.13	7.05×10^{-6}
		CbPM2	−0.01	25.80	0.57	29.08	2.05×10^{-5}
		CAFE	−0.01	19.47	0.46	18.75	2.69×10^{-4}
Earth system models	1996 to 2021	CMIP6 median	7.96×10^{-4}	−0.60	0.10	2.83	0.15
		CMIP6 range	-2.25×10^{-3} to 2.19×10^{-3}	−0.38 to 5.51	1.54×10^{-3} to 0.42	0.04 to 17.53	7.92×10^{-3} to 0.98

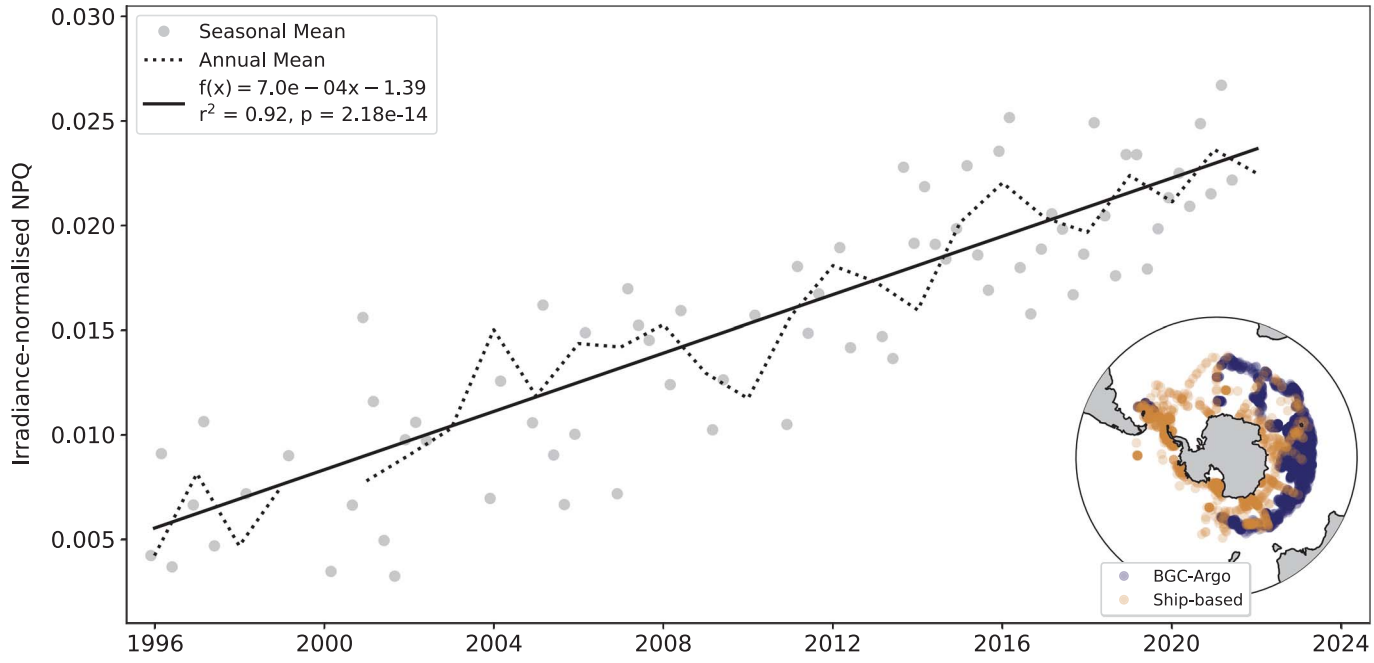

Fig. 2. Distribution and trend of irradiance-normalized NPQ. Seasonal and annual means, with an ordinary least-squares regression on the annual mean, of irradiance-normalized NPQ determined from the combined BGC-Argo and ship-based dataset. (Inset) A map showing distribution of BGC-Argo and ship-based profiles (1996 to 2022).

retained at a minimum (n = 3) over time (fig. S2A) or by using a Monte Carlo experiment in which the years were randomly sampled (i.e., a jackknife resampling of 75% of the 1996 to 2022 range) (fig. S2B). These additional tests are indicative of the robustness of the detected trend in irradiance-normalized NPQ that is not notably affected by seasonal, spatial, or temporal bias in data coverage. The link between Southern Ocean contemporary climate variability and the trend in annual mean irradiance-normalized NPQ is highlighted by its significant correlation with the decadal rolling mean of the SAM index (r^2 = 0.62, P < 0.001) (fig. S3), which implies that Southern Ocean phytoplankton are experiencing a multidecadal photophysiological adjustment, through their irradiance-normalized NPQ, to changes in nutrient and light availability from altered stratification, mixed-layer dynamics, and dust deposition. If this trend were driven primarily by increasing Fe stress, it would suggest notable implications for adjustments in regional NPP and the effectiveness of the biological carbon pump.

The likelihood that variability in irradiance-normalized NPQ is primarily reflecting Fe stress is supported by the fact that this proxy was markedly higher in control versus Fe-addition incubation experiments in the sub-Antarctic Southern Ocean (*38*), that it is well correlated with elevated fluorescence to Chl ratios in Fe-limited regions of the Southern Ocean (*35*), and that it reproduces known gradients in Southern Ocean Fe limitation from both natural and artificial Fe fertilization experiments. For example, BGC-Argo profiles upstream and downstream of the Kerguelen Plateau (Fig. 3A), a region with a well-characterized island mass Fe fertilization effect (*40*), show significantly lower irradiance-normalized NPQ values [t-statistic = −12.74, P < 0.001, degrees of freedom (df) = 1011] in Fe-fertilized downstream waters (mean 16.6×10^{-3}, SE = 0.41×10^{-3}, n = 525) compared with Fe-limited upstream locations (mean 23.3×10^{-3}, SE = 0.44×10^{-3}, n = 470). Similarly, ship-based profiles in and out of Fe-addition patches during the Southern Ocean Iron Release Experiment (SOIREE) (*28*) and Southern Ocean Iron Experiment (SOFEx) (*29*) mesoscale Fe fertilization experiments (Fig. 3A) are typified by irradiance-normalized NPQ values that are significantly lower (t-statistic = 2.95 and 2.66, P < 0.05, df = 12 and 18, respectively) in patch (mean 3.0×10^{-3}, SE = 1.24×10^{-3}, and mean 3.3×10^{-3}, SE = 0.97×10^{-3}, n = 6 and 8, respectively) compared with out of patch (mean 9.1×10^{-3}, SE = 1.72×10^{-3}, and mean 21.6×10^{-3}, SE = 4.79×10^{-3}, n = 4 and 16, respectively). Lastly, across all available Southern Ocean data, irradiance-normalized NPQ values in spring (Fig. 3B) and summer (Fig. 3C) are significantly higher than those from autumn (spring: t-statistic = 2.10, P < 0.05, df = 2392; summer: t-statistic = 3.29, P < 0.001, df = 3555) (fig. S4A) and winter (spring: t-statistic = 3.92, P < 0.001, df = 2236; summer: t-statistic = 4.89, P < 0.001, df = 3399) (fig. S4B), in accordance with expected spring- and summertime Fe depletion from biological utilization (*7*, *10*). Because a photoacclimation response to seasonal variability in light would drive the opposite relationship, this further supports the role of Fe stress in driving irradiance-normalized NPQ.

Although the effect of instantaneous light is accounted for when deriving irradiance-normalized NPQ, longer-term photoacclimation strategies may also affect the trend (and seasonal characteristics) that is observed in irradiance-normalized NPQ. These photophysiological adjustments can also be detected through changes in cellular Chl to carbon (Chl:C) ratios; however, it is important to note that these reflect phytoplankton's combined photoacclimation and nutrient allocation response. Chl:C ratios are expected to increase in response to low light (*41*), but photoacclimation occurs more effectively during Fe-replete conditions (*42*), such that the degree of response in Chl:C is primarily dependent on Fe availability. Particulate backscatter (b_{bp}) (from both satellite and in situ sensors) can act as proxies for phytoplankton carbon (*43*–*45*), and their proportion relative to Chl can be used to infer cellular Chl:C ratios. The positive trend observed in Chl:C from satellite remote sensing (r^2 = 0.62, 0.81% year^{-1}, P < 0.001) (fig. S5) for the coincident period (1998 to 2021) suggests that phytoplankton are responding to a reduction in available light by increasing cellular packaging of Chl. This is supported by a spatially coherent trend of a marked decrease in mixed-layer light across the Southern Ocean (fig. S6). As such, photoacclimation or

photoadaptation to low-light conditions may contribute to the observed trend in irradiance-normalized NPQ. That said, any reduction in available light in the typically Fe-stressed Southern Ocean (*7*, *27*) would increase Fe demand (*12*, *46*) and increase Fe stress in the absence of sufficient increases in Fe supply. When the trend in Chl:C is investigated in situ (2015 to 2021) (restricted to BGC-Argo because, unlike irradiance-normalized NPQ, fluorescence-derived estimates of Chl and optical proxies for carbon cannot be merged across different sensors from the ship-based dataset because of differences in sensors and manufacturer calibration coefficients), the integrated mixed-layer trend (although insignificant) is instead negative (r^2 = 0.50, −3.59% year^{-1}, P = 0.07), which reflects a more typical response to Fe stress (i.e., a decrease in Chl:C with a decrease in growth rates under Fe-limiting conditions), with no evidence of photoacclimation or photoadaptation. Moreover, a significant negative relationship is observed between in situ increasing irradiance-normalized NPQ and decreasing Chl:C (2015 to 2021) (r^2 = 0.51 to 0.54, P < 0.001) (fig. S7, A to C), which strongly suggests that the photophysiological trend in irradiance-normalized NPQ is in response to Fe stress (rather than low light). Similarly, when the seasonal characteristics are investigated, Chl:C ratios are significantly higher in winter than in summer (t-statistic = 18.7 to 21.9, P < 0.001, df = 2019 to 2113) (fig. S8), which reflects typical photoacclimation in response to low-light conditions (*41*). Were photoacclimation the dominant driver of seasonal variability in NPQ, it would elicit an increase in irradiance-normalized NPQ in winter. The opposite response, however (Fig. 3, B and C), suggests that Fe stress is instead most likely to be the dominant driver of seasonal variability in irradiance-normalized NPQ.

Trends in primary productivity

Any trend of increasing Fe stress should reflect in concurrent reductions in photosynthetic capacity and a decline in overall productivity, with large implications for biogeochemical cycling and carbon drawdown (*47*). We note, however, that a decline in NPP, although expected in response to an increase in Fe stress, is not a certainty (or a necessary requirement to verify Fe stress), as indeed an increase in standing stocks (from increasing NPP) could drive an increase in Fe stress. Similarly, trends in NPP may also reflect top-down controls of grazing that are independent of Fe stress. Nonetheless, when we apply two models of NPP (*48*, *49*) to the Southern Ocean BGC-Argo dataset (restricted to this platform for the same reason as described above, 2014 to 2021; see materials and methods), we observe a decrease in NPP for both models (Fig. 4). Although the decline in NPP from the carbon-based productivity model (CbPM) is significant (10% year^{-1}, r^2 = 0.81, P < 0.01) (Fig. 4A and Table 1), the decreasing trend from the vertically generalized productivity model (VGPM) is insignificant (8% year^{-1}, r^2 = 0.43, P = 0.08) (Fig. 4A), but both are on a similar order of magnitude as the increase in irradiance-normalized NPQ for the same time period (4.72% year^{-1}, r^2 = 0.56, P < 0.05). When we apply the same two NPP models in combination with an additional two NPP models (*50*, *51*) to a concomitant 24-year time series (1998 to 2021) from the Ocean Color Climate Change Initiative product (*52*) (materials and methods), we see dominant declines in NPP for the subpolar and ice biomes (*39*) from the carbon-based CbPMs and absorption-based carbon, absorption, and fluorescence euphotic-resolving (CAFE) model (with 61 to 80% of the trends being negative and 10 to 29% positive) (Fig. 4, B to D). Although the VGPM shows an increase in NPP (77% positive and 13% negative) (Fig. 4C), this can be explained by its strong dependence on trends in Chl that are augmented by Southern Ocean warming (*5*, *53*). Similar results were observed in a recent study by Pinkerton *et al.* (*54*) (with different satellite data and trend detection methods), but with all trends in NPP from the CbPM being negative with an overall negative but insignificant trend of −0.15% year^{-1} (P = 0.17), whereas NPP trends from the VGPM were positive and significant (0.8% year^{-1}, P < 0.001). However, when we investigate trends in NPP for the same period (1996 to 2021) from Earth system models of the Coupled Model Intercomparison Project phase 6 (CMIP6), we see very little multidecadal variability, with trends in NPP that range from −0.22 to 0.21% year^{-1} (r^2 = 1.5×10^{-3} to 0.42) (Fig. 4F and Table 1). Although most Earth system models show insignificant trends in NPP, three display significant positive trends (0.10 to 0.15% year^{-1}, P < 0.05) (Table 1), whereas two others depict significant negative trends (−0.01 and −0.22% year^{-1}, P < 0.05) (Table 1). Once projected to the end of the century, however, most CMIP6 models (>80%) agree on an increasing trend in NPP (*23*) at odds with trends currently observed to be ongoing.

Sensitivity of Fe limitation to climate drivers

The progressive trend of increasing in situ irradiance-normalized NPQ observed here over the past 26 years reflects the impact of a suite of concurrent physical, chemical, and biological processes on the Southern Ocean Fe

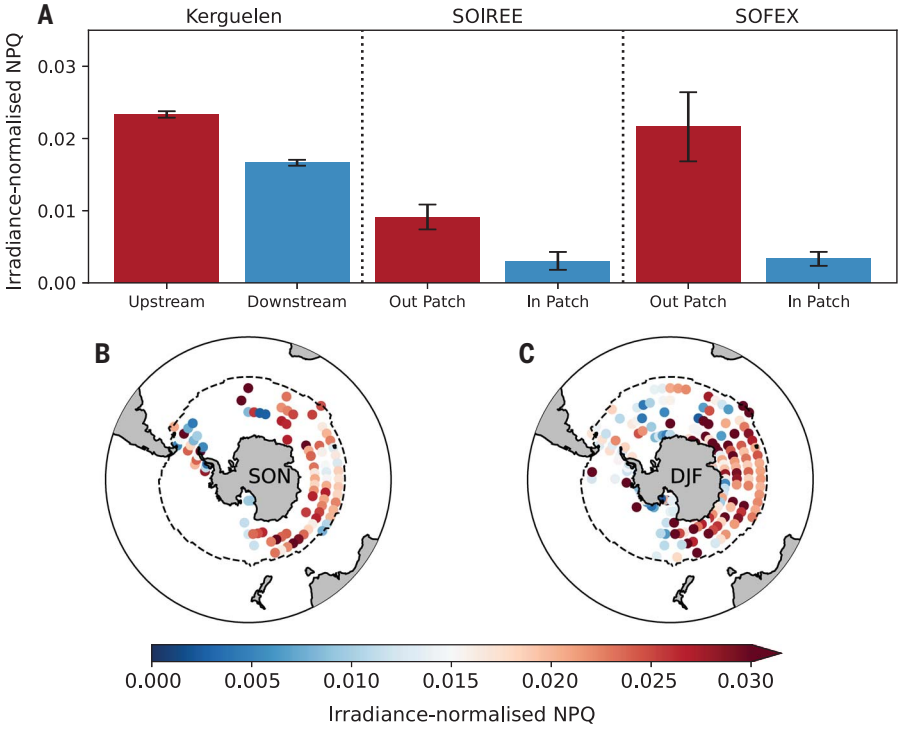

Fig. 3. Robustness of irradiance-normalized NPQ as a proxy for Fe stress demonstrated through natural and artificial Fe gradients and seasonal Fe depletion. (**A**) Mean irradiance-normalized NPQ ± SEs from BGC-Argo profiles upstream and downstream of the Kerguelen plateau and from ship-based profiles in and out of Fe-fertilized patches during SOIREE and SOFEX. (**B** and **C**) Maps of irradiance-normalized NPQ based on combined BGC-Argo and ship-based profiles (1996 to 2021) for spring (SON: September, October, and November) (B) and summer (DJF: December, January, and February) (C) gridded to 5° × 5°. The dashed lines represent the spatial extent of the Southern Ocean defined as the subpolar and ice biomes from Fay and McKinley (*39*). See fig. S4 for winter and autumn.

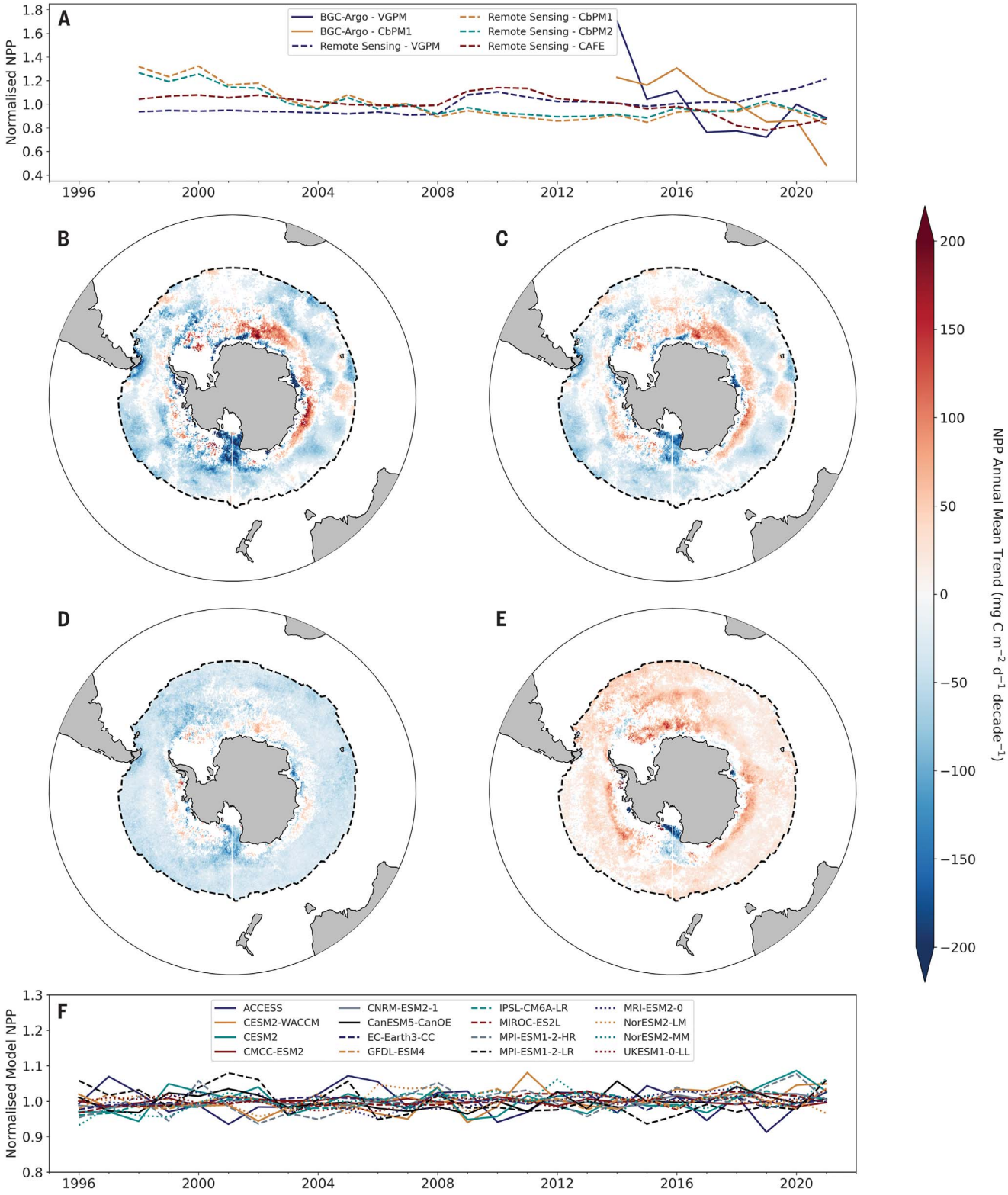

Fig. 4. Comparing NPP for the Southern Ocean from BGC-Argo, remote sensing, and Earth system models. (**A** to **F**) Normalized annual means of NPP derived from BGC-Argo by using two different NPP models (2014 to 2021) and derived from remote sensing by using four different NPP models (1998 to 2021) averaged across the subpolar and ice biomes from Fay and McKinley (*39*); decadal trends (1998 to 2021) from remote sensing by using CbPM1 (B), CbPM2 (C), CAFE (D), and VGPM (E); and normalized annual means of NPP from CMIP6 model outputs (1996 to 2021) (F). Statistics of the normalized annual trends of NPP models from (A) and (F) can be found in Table 1. Normalization was performed by dividing the data by the mean value. CbPM1 refers to the Behrenfeld *et al.* (*49*) model, and CbPM2 refers to the Westberry *et al.* (*50*) model. The dashed lines in (B), (C), (D), and (E) represent the spatial extent of the Southern Ocean defined as the subpolar and ice biomes from Fay and McKinley (*39*). Please refer to the supplementary materials for details of the CMIP6 models.

cycle and the response of phytoplankton production (inclusive of physiological plasticity and adaptability), ranging from changing Fe supply, speciation, and recycling to adjustments in phytoplankton Fe demands and interactions with other microbes (*9*, *55*). The key challenge is that large scale in situ datasets are largely concerned with ocean physics at spatiotemporal scales that are not matched by biological and chemical process experiments (*9*). Overall, the trend in irradiance-normalized NPQ showed moderate correlations with the dominant climate trends of reduced pH and surface warming (r^2 = 0.42 and 0.36, respectively; $P < 0.001$) (fig. S9, A and B, and table S2). This relationship with pH would agree with previous studies that exhibit reduced Fe uptake under ocean acidification scenarios (*56*) due to potential inhibition of the Fe uptake mechanisms (*57*). Moreover, ocean acidification is likely to affect the availability of Fe bound to organic ligands because a lower pH will affect both Fe adsorption and complexation (*58*, *59*). Direct impacts of a reduced pH on NPQ are also likely because this mechanism relies upon a trans–thylakoid membrane pH gradient (*60*), which would be impacted by a buildup of intracellular hydrogen ions (*61*). The relationship with surface warming more likely reflects independent changes to Fe delivery (*14*) or poorly constrained impacts on Fe speciation, bioavailability, and demand (*13*). Relating the trend in irradiance-normalized NPQ to the dominant SAM-driven response of altered wind (namely vertical mixing and stratification) showed some linkages, with a significant correlation between deeper summer mixed-layer depths (r^2 = 0.39, $P < 0.05$) (fig. S9C), but no correlation with autumn, winter, or spring mixed-layer depths ($P > 0.05$) (fig. S9, D to F). Recent evidence (*24*) has shown that in the Southern Ocean summer, there is a deepening of the mixed layer ($-3.4 \pm 1.5\%$ decade^{-1}), which could increase Fe demand (by decreasing light availability), and a notable increase in stratification ($8.1 \pm 4.1\%$ decade^{-1}), which could negatively affect subseasonal Fe supply (e.g., from storm-driven entrainment) (*8*). Furthermore, it is also likely that for some key regions of the Southern Ocean, local signals linked to changing Fe supply from dust, margins, glaciers, or sea ice may be important (*5*).

Adjustments in irradiance-normalized NPQ are fingerprinted by the well-understood response of phytoplankton photophysiology to Fe limitation. If the trend in irradiance-normalized NPQ observed here is indeed reflecting a long-term increase in Fe stress, with an amplitude adjustment in time (Fig. 2) similar to that observed from natural Fe fertilization (Fig. 3A), alongside a concomitant decrease in NPP (from in situ BGC-Argo floats, 2014 to 2021, and CbPM satellite derived) (Fig. 4, A and B), the implications are that Earth system models may be underestimating ongoing change in the Southern Ocean. Both CMIP5 and CMIP6 Earth system models tend to project a trend of increasing NPP and reducing Fe stress in the Southern Ocean by the end of the 21st century in response to climate change (*23*), which is the opposite of the observed trend that is emerging across the region in this study. Improved knowledge of how Fe stress interacts with other limiting factors and the role of parallel changes in phytoplankton species composition and top-down control by grazers would enable us to link changing climate drivers, growing Fe stress, and altered NPP more robustly in the Southern Ocean and improve confidence in projections. A major strength of irradiance-normalized NPQ is that it is a photophysiological in situ measurement that can be applied retrospectively to appropriately equipped platforms to span timeframes that reflect an integrated response to climate change and may help provide emergent constraints for Earth system models for improved climate projections.

REFERENCES AND NOTES

1. T. L. Frölicher *et al*., *J. Clim.* **28**, 862–886 (2015).
2. N. Gruber, P. Landschützer, N. S. Lovenduski, *Annu. Rev. Mar. Sci.* **11**, 159–186 (2019).
3. J. L. Sarmiento, N. Gruber, M. A. Brzezinski, J. P. Dunne, *Nature* **427**, 56–60 (2004).
4. R. Schlitzer, *Deep Sea Res. Part II Top. Stud. Oceanogr.* **49**, 1623–1644 (2002).
5. S. F. Henley *et al*., *Front. Mar. Sci.* **7**, 581 (2020).
6. J. H. Martin, R. M. Gordon, S. E. Fitzwater, *Nature* **345**, 156–158 (1990).
7. P. W. Boyd, *J. Phycol.* **38**, 844–861 (2002).
8. S.-A. Nicholson *et al*., *Geophys. Res. Lett.* **46**, 14567–14575 (2019).
9. A. Tagliabue *et al*., *Nature* **543**, 51–59 (2017).
10. A. Tagliabue *et al*., *Nat. Geosci.* **7**, 314–320 (2014).
11. W. G. Sunda, S. A. Huntsman, *Mar. Chem.* **50**, 189–206 (1995).
12. R. F. Strzepek, P. W. Boyd, W. G. Sunda, *Proc. Natl. Acad. Sci. U.S.A.* **116**, 4388–4393 (2019).
13. D. A. Hutchins, P. W. Boyd, *Nat. Clim. Chang.* **6**, 1072–1079 (2016).
14. S. A. Henson *et al*., *Biogeosciences* **7**, 621–640 (2010).
15. N. C. Swart, J. C. Fyfe, O. A. Saenko, M. Eby, *Biogeosciences* **11**, 6107–6117 (2014).
16. A. G. Marshall, M. A. Hemer, H. H. Hendon, K. L. McInnes, *Ocean Model.* **129**, 58–74 (2018).
17. L. M. Polvani, D. W. Waugh, G. J. P. Correa, S.-W. Son, *J. Clim.* **24**, 795–812 (2011).
18. N. S. Lovenduski, N. Gruber, *Geophys. Res. Lett.* **32**, L11603 (2005).
19. J. B. Sallée, K. G. Speer, S. R. Rintoul, *Nat. Geosci.* **3**, 273–279 (2010).
20. J.-B. Sallée *et al*., *Nature* **591**, 592–598 (2021).
21. C. M. Laluraj, M. Thamban, K. Satheesan, *Atmos. Environ.* **90**, 23–32 (2014).
22. M. Meredith *et al*., in *IPCC Special Report on the Ocean and Cryosphere in a Changing Climate*, H.-O. Pörtner *et al*., Eds. (2019).
23. A. Tagliabue *et al*., *Front. Clim.* **3**, 738224 (2021).
24. A. Tagliabue *et al*., *Global Biogeochem. Cycles* **30**, 149–174 (2016).
25. A. Tagliabue *et al*., *Glob. Change Biol.* **26**, 6168–6179 (2020).
26. T. J. Ryan-Keogh *et al*., *J. Mar. Syst.* **166**, 87–96 (2017).
27. C. M. Moore *et al*., *Nat. Geosci.* **6**, 701–710 (2013).
28. P. W. Boyd *et al*., *Nature* **407**, 695–702 (2000).
29. K. H. Coale *et al*., *Science* **304**, 408–414 (2004).
30. M. A. Saito *et al*., *Science* **345**, 1173–1177 (2014).
31. M. A. van Leeuwe, J. Stefels, *Biogeochemistry* **83**, 61–70 (2007).
32. P. G. Falkowski, J. La Roche, *J. Phycol.* **27**, 8–14 (1991).
33. J. A. Raven, *New Phytol.* **116**, 1–18 (1990).
34. P. S. Schrader, A. J. Milligan, M. J. Behrenfeld, *PLOS ONE* **6**, e18753 (2011).
35. C. Schallenberg, R. F. Strzepek, S. Bestley, B. Wojtasiewicz, T. W. Trull, *Geophys. Res. Lett.* **49**, e2021GL097616 (2022).
36. R. J. Geider, J. La Roche, R. M. Greene, M. Olaizola, *J. Phycol.* **29**, 755–766 (1993).
37. M. J. Behrenfeld, A. J. Milligan, *Annu. Rev. Mar. Sci.* **5**, 217–246 (2013).
38. T. J. Ryan-Keogh, S. J. Thomalla, *Front. Mar. Sci.* **7**, 275 (2020).
39. A. R. Fay, G. A. McKinley, *Earth Syst. Sci. Data* **6**, 273–284 (2014).
40. S. Blain, B. Queguiner, T. Trull, *Deep Sea Res. Part II Top. Stud. Oceanogr.* **55**, 559–565 (2008).
41. K. H. Halsey, B. M. Jones, *Annu. Rev. Mar. Sci.* **7**, 265–297 (2015).
42. C. M. Moore *et al*., *Deep Sea Res. Part II Top. Stud. Oceanogr.* **54**, 2045–2065 (2007).
43. G. Dall'Olmo, T. K. Westberry, M. J. Behrenfeld, E. Boss, W. H. Slade, *Biogeosciences* **6**, 947–967 (2009).
44. V. Martinez-Vicente, G. Dall'Olmo, G. Tarran, E. Boss, S. Sathyendranath, *Geophys. Res. Lett.* **40**, 1154–1158 (2013).
45. J. R. Graff *et al*., *Deep Sea Res. Part I Oceanogr. Res. Pap.* **102**, 16–25 (2015).
46. R. F. Strzepek, K. A. Hunter, R. D. Frew, P. J. Harrison, P. W. Boyd, *Limnol. Oceanogr.* **57**, 1182–1200 (2012).
47. K. Petrou, M. A. Doblin, P. J. Ralph, *Mar. Biol.* **158**, 1029–1041 (2011).
48. M. J. Behrenfeld, P. G. Falkowski, *Limnol. Oceanogr.* **42**, 1–20 (1997).
49. M. J. Behrenfeld, E. Boss, D. A. Siegel, D. M. Shea, *Global Biogeochem. Cycles* **19**, GB1006 (2005).
50. T. Westberry, M. J. Behrenfeld, D. A. Siegel, E. Boss, *Global Biogeochem. Cycles* **22**, GB2024 (2008).
51. G. M. Silsbe, M. J. Behrenfeld, K. H. Halsey, A. J. Milligan, T. K. Westberry, *Global Biogeochem. Cycles* **30**, 1756–1777 (2016).
52. S. Sathyendranath *et al*., *Sensors* **19**, 4285 (2019).
53. M. Auger, R. Morrow, E. Kestenare, J.-B. Sallée, R. Cowley, *Nat. Commun.* **12**, 514 (2021).
54. M. H. Pinkerton *et al*., *Front. Ecol. Evol.* **9**, 592027 (2021).
55. P. W. Boyd, M. J. Ellwood, A. Tagliabue, B. S. Twining, *Nat. Geosci.* **10**, 167–173 (2017).
56. D. Shi, Y. Xu, B. M. Hopkinson, F. M. M. Morel, *Science* **327**, 676–679 (2010).
57. J. B. McQuaid *et al*., *Nature* **555**, 534–537 (2018).
58. X. Liu, F. J. Millero, *Mar. Chem.* **77**, 43–54 (2002).
59. K. L. Wilde, J. L. Stauber, S. J. Markich, N. M. Franklin, P. L. Brown, *Arch. Environ. Contam. Toxicol.* **51**, 174–185 (2006).
60. P. Müller, X.-P. Li, K. K. Niyogi, *Plant Physiol.* **125**, 1558–1566 (2001).
61. L. T. Bach *et al*., *New Phytol.* **199**, 121–134 (2013).

ACKNOWLEDGMENTS

The BGC-Argo data were collected and made freely available by the International Argo Program and the national programs that contribute to it (http://www.argo.ucsd.edu, http://argo.jcommops.org). The Argo Program is part of the Global Ocean Observing System. We acknowledge the World Climate Research Programme's Working Group on Coupled Modeling, which is responsible for CMIP, and we thank the climate modeling groups (listed in the materials and methods of this work) for producing and making available their model output. **Funding:** T.J.R.K., S.J.T., and P.M.S.M. were supported through the CSIR's Southern Ocean and Carbon Climate Observatory (SOCCO) Programme (http://socco.org.za/) funded by the Department of Science and Innovation (DST/CON 0182/2017) and the CSIR's Parliamentary Grant. A.T. received funding from the European Research Council (ERC) under the European Union's Horizon 2020 research and innovation program (grant agreement no. 724289). **Author contributions:** Conceptualization: T.J.R.K. and S.J.T.; Formal analysis: T.J.R.K. and A.T.; Investigation: T.J.R.K.; Methodology: T.J.R.K., S.J.T., and A.T.; Funding acquisition: T.J.R.K., S.J.T., and P.M.S.M.; Visualization: T.J.R.K.; Writing – original draft: S.J.T.; Writing – review & editing: T.J.R.K., P.M.S.M., and A.T. **Competing interests:** The authors declare that they have no competing interests. **Data and materials availability:** BGC-Argo data were made available through the biogeochemical argo database

(table S3; https://biogeochemical-argo.org/). Ship-based data were downloaded from various online repositories (table S4). Southern Annular Mode data were retrieved from https://climatedataguide.ucar.edu/climate-data/. Core Argo mixed-layer depth data were retrieved from http://mixedlayer.ucsd.edu/. GLODAPv2.2021 data were retrieved from https://www.glodap.info/index.php/merged-and-adjusted-data-product/. Ocean color climate change initiative data were retrieved from https://esa-oceancolour-cci.org/, with ocean color PAR data retrieved from https://www.globcolour.info/. Hadley EN4.2.2 temperature and salinity data were retrieved from https://www.metoffice.gov.uk/hadobs/en4/download-en4-2-2.html. Sea surface temperatures were retrieved from https://www.ghrsst.org/. CMIP6 data were obtained from https://esgf.llnl.gov/. **License information:** Copyright © 2023 the authors, some rights reserved; exclusive licensee American Association for the Advancement of Science. No claim to original US government works. https://www.science.org/about/science-licenses-journal-article-reuse

SUPPLEMENTARY MATERIALS

science.org/doi/10.1126/science.abl5237
Materials and Methods
Figs. S1 to S11
Tables S1 to S4
References (*62*–*86*)

Submitted 19 July 2021; accepted 26 January 2023
10.1126/science.abl5237

ORGAN REGENERATION

A population of stem cells with strong regenerative potential discovered in deer antlers

Tao Qin[1]†, Guokun Zhang[2]†, Yi Zheng[3]†, Shengyou Li[3]†, Yuan Yuan[1]†, Qingjie Li[4]†, Mingliang Hu[1], Huazhe Si[5], Guanning Wei[6], Xueli Gao[1], Xinxin Cui[1], Bing Xia[3], Jing Ren[2], Kun Wang[1], Hengxing Ba[2], Zhen Liu[2], Rasmus Heller[7], Zhipeng Li[5]*, Wen Wang[1,8]*, Jinghui Huang[3]*, Chunyi Li[2,9]*, Qiang Qiu[1]*

The annual regrowth of deer antlers provides a valuable model for studying organ regeneration in mammals. We describe a single-cell atlas of antler regrowth. The earliest-stage antler initiators were mesenchymal cells that express the paired related homeobox 1 gene (*PRRX1*$^+$ mesenchymal cells). We also identified a population of "antler blastema progenitor cells" (ABPCs) that developed from the *PRRX1*$^+$ mesenchymal cells and directed the antler regeneration process. Cross-species comparisons identified ABPCs in several mammalian blastema. In vivo and in vitro ABPCs displayed strong self-renewal ability and could generate osteochondral lineage cells. Last, we observed a spatially well-structured pattern of cellular and gene expression in antler growth center during the peak growth stage, revealing the cellular mechanisms involved in rapid antler elongation.

Lower vertebrates have a remarkable capacity to heal in a scar-free manner and regenerate lost appendages, even at the adult stage (*1*–*5*). By contrast, mammals have largely lost the capacity for appendage or organ regeneration (*6*). However, deer antler offers a singular model to study spontaneous regeneration in mammals because its regeneration is similar and clinically relevant to mammalian long-bone development (*7*–*9*). Every year in early spring, hard antlers are cast from their pedicles, then both antler bone and cartilage are regenerated from the pedicle periosteum located in the pedicle stumps. In late spring and early summer, antlers grow and calcify in about 3 to 4 months with a growth rate of 2.75 cm/day and a mineral apposition rate of 3.2 μm/day, the highest among medium- to large-sized mammals (*10*, *11*). At the end of the summer, the antlers lose their velvet skin cover, leaving dead bone ready for fighting during the rut. Antlers are cast in the next spring, and then a new round of their regeneration starts. Studies on antler regeneration have mainly focused on histological (*12*) and morphological (*13*) aspects of the regeneration process. Previous findings identified some positively selected genes, regulatory elements, and highly expressed genes associated with rapid antler growth (*14*), but the detailed cellular and molecular mechanisms involved in antler regeneration remain unclear.

To address this fundamental question, we set out to investigate in detail the cellular composition and gene expression dynamics of antler tissue throughout its regeneration cycle using single-cell transcriptome sequencing (scRNA-seq), then used in vivo and in vitro experiments to assess the potency and functionality of key populations of stem cells.

Single-cell transcriptomic atlas of antler regeneration

During antler regeneration, cartilage and bone are fully regenerated annually at a rapid rate (*11*). To comprehensively assess the gene transcription dynamics and cell type changes that occur during antler regeneration, we applied scRNA-seq of sika deer (*Cervus nippon*) antlers at various stages of the regeneration process (10 days before casting, and 0, 2, 5, 10, 45, 60, and 90 days after casting) (Fig. 1A and fig. S1, A and B) (*15*). To ensure the accuracy and reliability of the subsequent analysis, we generated a chromosome-level genome assembly of a male sika deer (fig. S2 and tables S1 and S2), providing a solid foundation for the scRNA-seq analysis.

In total, we analyzed 74,730 cells covering the critical stages of antler regeneration (Fig. 1B and table S2). Cells from all samples were pooled and visualized so that the cells could be assigned to eight putative cell populations (Fig. 1B). These populations (associated markers in parentheses) are *PRRX1*$^+$ mesenchymal cells (PMCs; *PRRX1*, *POSTN*, and *LUM*), *SOX9*$^+$ chondroblasts (*SOX9* and *SOX6*), *PHEX*$^+$ osteoblasts (*PHEX*), *COL3A1*$^+$ fibroblasts (*COL3A1* and *COL12A1*), *CHAD*$^+$ chondrocytes (*CHAD*, *SCRG1*), *ACTA2*$^+$ pericytes (*ACTA2* and *MYLK*), *PECAM1*$^+$ endothelial cells (*PECAM1* and *VWF*), and *PTPRC*$^+$ immune cells (*PTPRC* and *LCP1*) (Fig. 1D and table S3). Of these, PMCs were particularly abundant in the samples (fig. S1, C and D). Cells of this type are reportedly crucial during limb regeneration in frog (*16*) and axolotl (*2*), as well as digit tip regeneration in mouse (*17*), supporting a key role in antler regeneration.

Next, we explored the lineage relationships among cell subtypes (Fig. 1C and fig. S1E) (*15*). This regeneration trajectory was dominated by PMCs, chondroblasts, and chondrocytes, with a general trend of progressive change from PMCs to chondroblasts and chondrocytes (Fig. 1C). Concomitantly, genes highly expressed in PMCs (such as *POSTN* and *PRRX1*) were gradually down-regulated, whereas characteristic genes in chondroblasts (such as *SOX6*) and chondrocytes (for example, *CHAD*, *ACAN*, and *COL2A1*) were up-regulated upon terminal differentiation (Fig. 1C). The samples from 10 days before casting and 0 days after casting had a highly similar cell composition, and PMCs were already present in the periosteum at the preregeneration time point (10 days before casting), suggesting that PMCs are permanently present in the antler-generating tissues and are not formed by dedifferentiation (fig. S1B). This is in sharp contrast to the process observed in axolotl limb regeneration (*2*), in which the *PRRX1*$^+$ cell population first undergoes dedifferentiation to form progenitor cells and subsequently redifferentiates to form a *PRRX1*$^+$ cell population. The reconstructed regeneration trajectory suggests that the annual cycle of antler regeneration is based on PMCs, in accordance with the notion that organ regeneration is a stem cell–based process in mammals (*6*, *18*).

Cell population dynamics during antler regeneration

To analyze the osteochondral regeneration process in detail, we performed a subclassification analysis of the annotated cell types (Fig. 2A, fig. S3A, and table S3). As described above, in the pedicle periosteum at 10 days before casting (preregeneration) and 0 days after casting, the PMCs were abundant and represented a major periosteal cell population (Fig. 2B and fig. S3B), appearing to be the key cells for antler osteochondral regeneration. We thus analyzed the cellular composition of PMCs and found three subtypes: periosteal stromal cells (*SFRP2*$^+$ cell population; PMC1), periosteal mesenchymal progenitor cells (*PMF1*$^+$ cell population; PMC2), and chemotactic periosteal cells (*CXCL14*$^+$ cell population; PMC3) (Fig. 2A). These cells were immunohistochemically confirmed to reside simultaneously in the pedicle periosteum (fig. S3C).

[1]School of Ecology and Environment, Northwestern Polytechnical University, Xi'an 710072, China. [2]Institute of Antler Science and Product Technology, Changchun Sci-Tech University, Changchun, China. [3]Department of Orthopaedics, Xijing Hospital, Fourth Military Medical University, Xi'an 710032, China. [4]Research Center of Traditional Chinese Medicine, The Affiliated Hospital to Changchun University of Chinese Medicine, Changchun 130021, China. [5]College of Animal Science and Technology, Jilin Agricultural University, Changchun, China. [6]School of Life Sciences, Jilin University, Changchun 130012, Jilin, China. [7]Section for Computational and RNA Biology, Department of Biology, University of Copenhagen, N 2200 Copenhagen, Denmark. [8]Center for Excellence in Animal Evolution and Genetics, Chinese Academy of Sciences, Kunming 650223, China. [9]College of Traditional Chinese Medicine, Jilin Agricultural University, Changchun, China.
*Corresponding author. Email: qiuqiang@lzu.edu.cn (Q.Q.); lichunyi1959@163.com (C.L.); huangjh@fmmu.edu.cn (J.H.); wenwang@nwpu.edu.cn (W.W.); zhipengli@jlau.edu.cn (Z.L.)
†These authors contributed equally to this work.

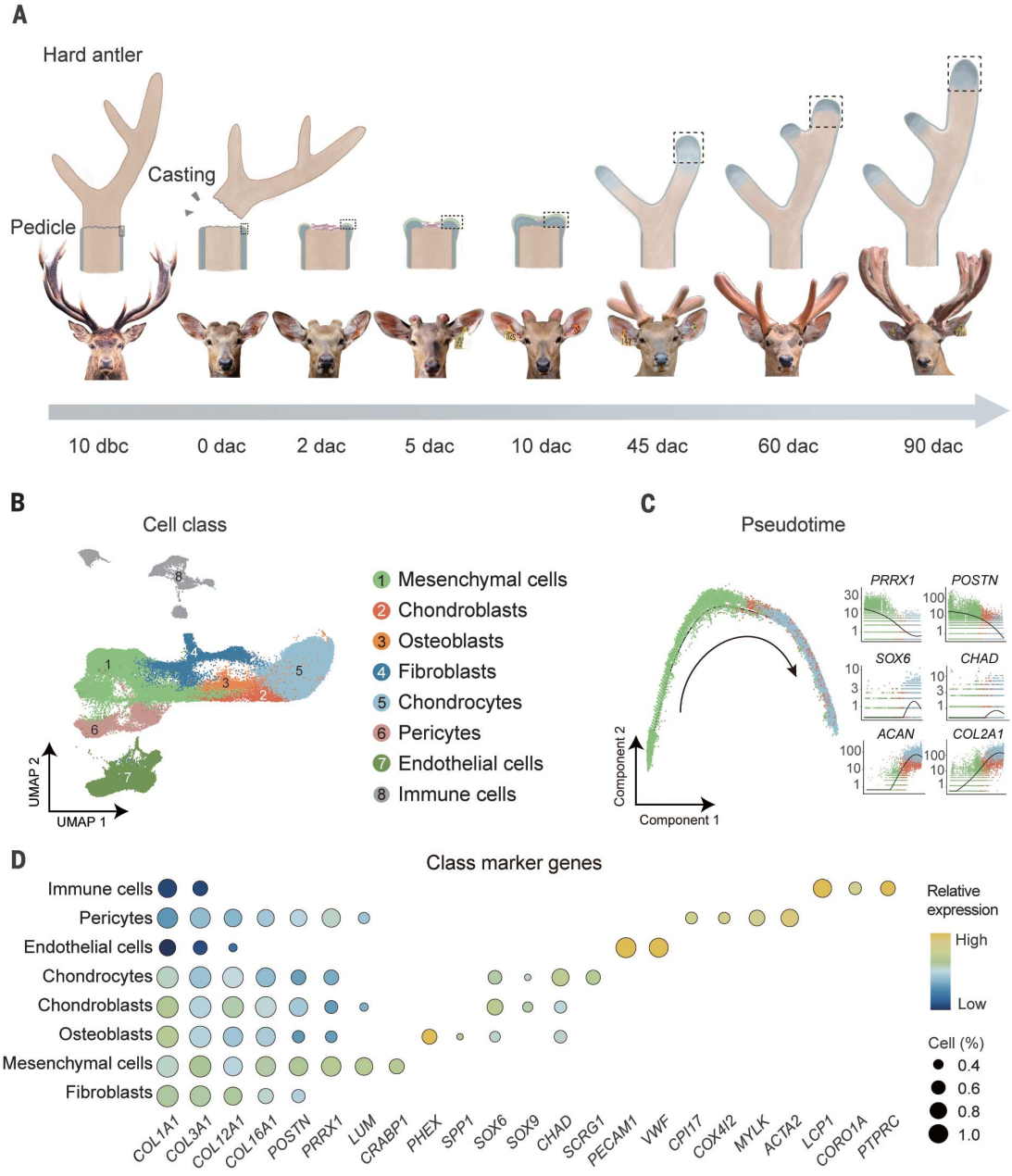

Fig. 1. An integrated developing cell atlas of regenerating antlers. (**A**) Schematic of the workflow of scRNA-seq–based antler regeneration analysis, using samples collected from sites (outlined with black dotted lines) during indicated phases of the process. dbc, days before casting; dac, days after casting. (**B**) Uniform manifold approximation and projection (UMAP) atlas of color-coded cell classes involved in antler regeneration based on the scRNA-seq data. (**C**) (Left) Developmental trajectory of *PRRX1*$^{+}$ mesenchymal cells (PMCs) to chondroblasts and chondrocytes inferred by Monocle 2 and colored by cell clusters (left panel). (Right) Plots showing the relative expression of differentially expressed genes in pseudotime order. Each dot indicates a single cell, with color coding showing cell clusters. (**D**) Dot plot showing cell class–level marker gene expression.

In addition to the three mesenchymal subtypes detected at 10 days before casting and 0 days after casting, another type of PMC (denoted PMC4, expressing *TNN*), as well as small proportions of chondrogenic cells, were observed at 5 days after casting (Fig. 2B), indicating that cellular heterogeneity had increased and chondrogenic differentiation had begun by 5 days after casting. Because PMCs were abundant at both 0 and 5 days after casting (Fig. 2B), we compared the ability of cell masses at these two points to generate antlers ectopically in nude mice (*15*). In contrast to cell masses at 0 days after casting, which generated fibrous connective tissue, cell masses at 5 days after casting successfully differentiated into an antler-like structure (with cartilage and bone) by 45 days after transplantation (Fig. 2C and fig. S4A), confirming their ectopic antler generation capacity. We further transplanted cell masses at 5 days after casting into the heads of *tdTOMATO* (red fluorescent protein)-labeled nude mice. No red fluorescence was visualized in the regenerated cartilage and chondrocytes (fig. S5A), and the single-cell atlas showed that the chondrocytes did not express the *tdTOMATO* (fig. S5, B and C), confirming that the regenerated cartilage was derived from the tissue transplanted 5 days after casting and not from the host cells. The PMC4 cells at 5 days after casting highly expressed multiple genes that support regeneration, including *PTN*, *TNC*, *TNN*, and *DLX5*, which are associated mainly with chondrogenesis and limb development (Fig. 2, D and E, and fig. S4). A pseudotime analysis showed that regenerating cartilage in both antlers and nude mouse heads was formed by differentiation of PMC4 (fig. S4E and fig. S5, D and E) (*15*), corroborating that they are the key cell population for antler regeneration.

We further delineated the origin of the PMC4 cell population. Because PMC1, PMC2, and PMC3 were present at earlier time points (10 days before casting and 0 days after casting) than PMC4 (5 days after casting), we initially compared the transcriptomic similarities of PMC4 to other PMCs. The gene expression

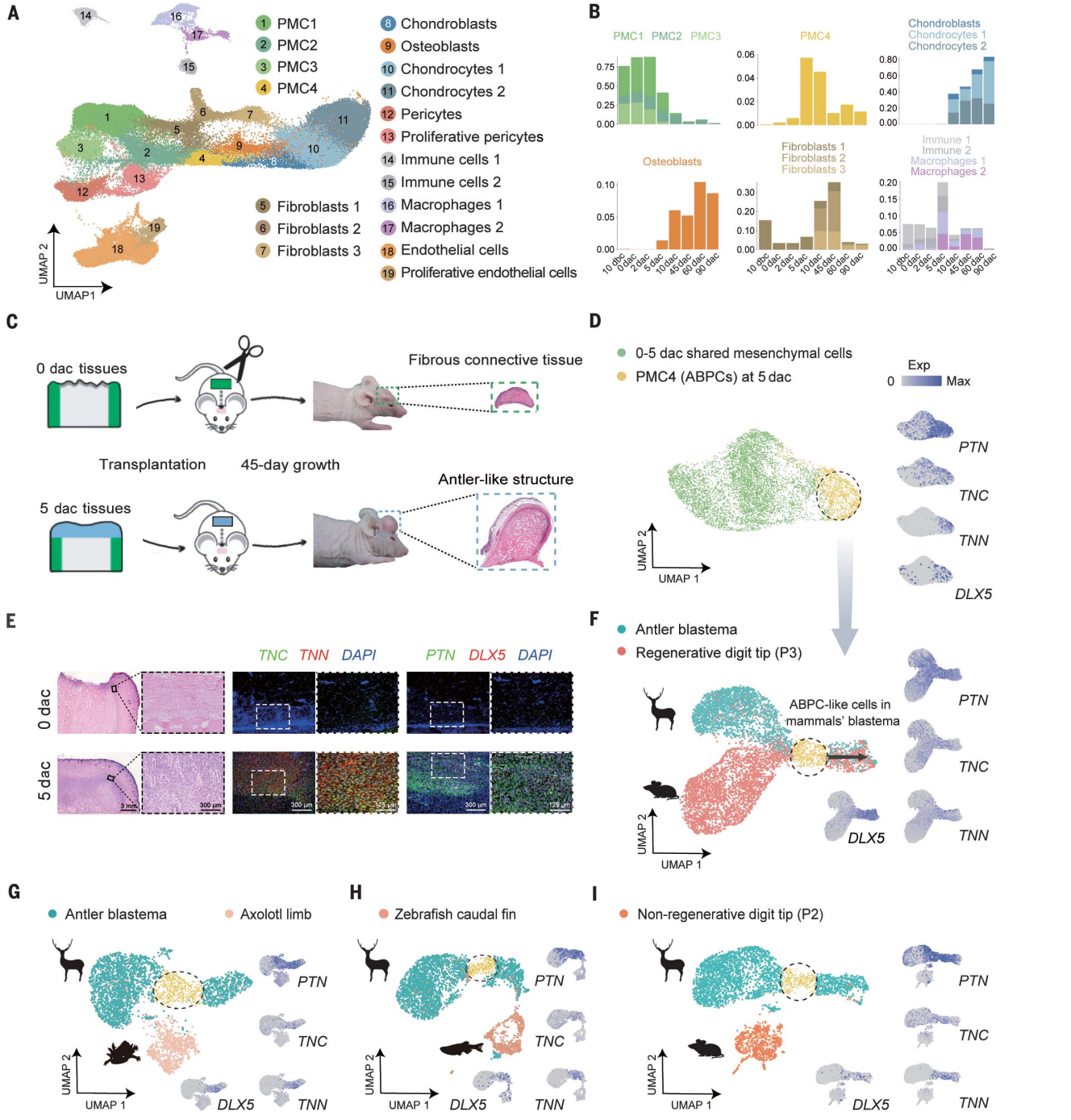

Fig. 2. Cellular dynamic atlas of antler regeneration and identification of critical regenerative progenitor cells. (**A**) UMAP atlas of antler regeneration with color-coded cell types, annotated by means of scRNA-seq analysis of cell-lineage specific markers. (**B**) Proportions of cell types at indicated time points. (**C**) Schematic illustration of ectopic antler-generation assays. Cell masses collected at 0 and 5 days after casting were transplanted onto heads of nude mice. The former remained fibrous connective tissue, but the latter had differentiated into an antler-like structure by 45 days after transplantation. (**D**) UMAP atlas based on scRNA-seq data of mesenchymal cells present in tissues sampled at 0 to 5 days after casting (green) and PMC4 [defined as antler blastema progenitor cells (ABPCs)] specifically expressed in tissues sampled at 5 days after casting (yellow). Feature plots to the right (blue) visualize expression of PMC4 marker genes (*PTN*, *TNC*, *TNN*, and *DLX5*). (**E**) Longitudinal sections of (top) pedicle periosteum at 0 days after casting and (bottom) regenerating antler tissues at 5 days after casting, stained with hematoxylin and eosin and selective marker genes. The boxed areas correspond to the higher-magnification views. (**F**) UMAP atlas based on integrated single-cell analysis of antler blastema (blue) and mouse regenerative digit tip (P3) (red). ABPC-like cells are circled with a dashed line. The arrow indicates the differentiation direction of ABPC-like cells toward osteochondral cells. Feature plots to the right visualize expression of ABPC marker genes (*PTN*, *TNC*, *TNN*, and *DLX5*). (**G** to **I**) UMAP atlas based on (G) integrated single-cell analysis of antler blastema (blue) and axolotl limb (orange), (H) zebrafish caudal fin (orange), and (I) mouse nonregenerative digit tip (P2) (orange). ABPCs are circled with a dashed line. Feature plots to the right visualize expression of ABPC marker genes (*PTN*, *TNC*, *TNN*, and *DLX5*).

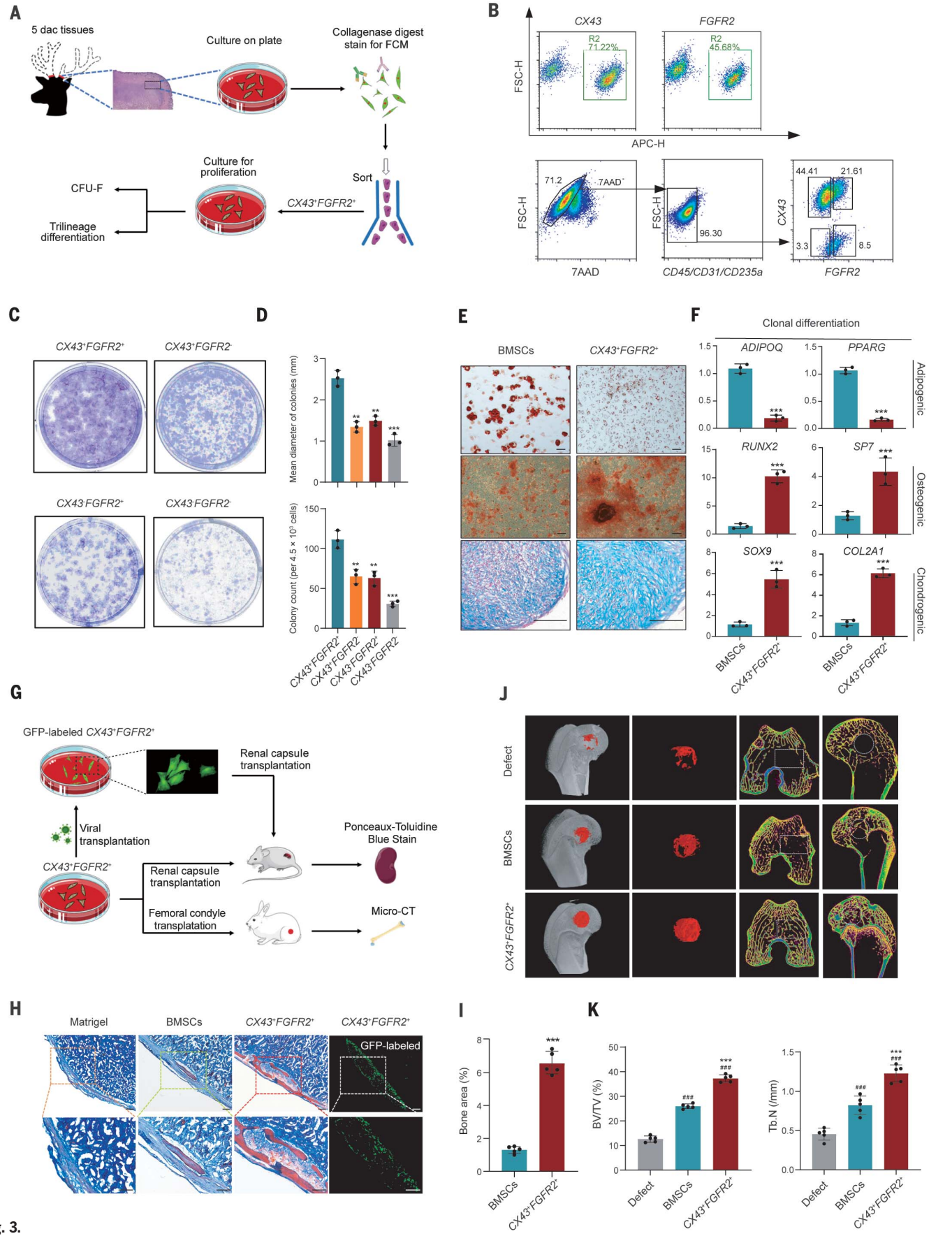
A
5 dac tissues
Culture on plate
Collagenase digest stain for FCM
Sort
Culture for proliferation
CFU-F
Trilineage differentiation
CX43+FGFR2+
B
CX43
FGFR2
R2 71.22%
R2 45.68%
FSC-H
APC-H
71.2
7AAD-
7AAD
96.30
CD45/CD31/CD235a
44.41
21.61
3.3
8.5
C
D
CX43+FGFR2+
CX43+FGFR2-
CX43-FGFR2+
CX43-FGFR2-
Mean diameter of colonies (mm)
Colony count (per 4.5 × 10^5 cells)
E
BMSCs
CX43+FGFR2+
F
Clonal differentiation
ADIPOQ
PPARG
RUNX2
SP7
SOX9
COL2A1
Adipogenic
Osteogenic
Chondrogenic
G
GFP-labeled CX43+FGFR2+
Viral transplantation
Renal capsule transplantation
Ponceaux-Toluidine Blue Stain
Femoral condyle transplatation
Micro-CT
J
Defect
BMSCs
CX43+FGFR2+
H
Matrigel
BMSCs
CX43+FGFR2+
CX43+FGFR2+
GFP-labeled
I
Bone area (%)
K
BV/TV (%)
Tb.N (/mm)

Fig. 3.

Fig. 3. Phenotypic and functional characterization of ABPCs (*CX43*$^+$*FGFR2*$^+$ cells). (**A**) Experimental scheme of *CX43*$^+$*FGFR2*$^+$ cells isolation and characterization in vitro. (**B**) (Top) Flow cytometric analysis detected expression of *CX43* and *FGFR2* in ABPCs. (Bottom) Flow cytometry gating strategies for sorting *CX43*$^+$*FGFR2*$^+$ cells at 5 days after casting. (**C**) Representative crystal violet staining of fibroblast colony-forming unit (CFU-F) colonies from populations sorted with flow cytometry. (**D**) Numbers and mean diameters of the CFU-F colonies. $^{**}P < 0.01$; $^{***}P < 0.001$ versus *CX43*$^+$*FGFR2*$^+$ cells. (**E**) Representative (top) oil red O, (middle) alizarin red, and (bottom) alcian blue stainings after adipogenic, osteogenic, and chondrogenic differentiation of clonally expanded *CX43*$^+$*FGFR2*$^+$ cells and BMSCs. Scale bar, 100 μm. (**F**) Results of reverse transcription polymerase chain reaction analyses of adipogenic, osteogenic, and chondrogenic marker genes in clonally expanded *CX43*$^+$*FGFR2*$^+$ cells and BMSCs before and after in vitro differentiation. $^{***}P < 0.001$ versus BMSCs. (**G**) Experimental scheme of *CX43*$^+$*FGFR2*$^+$ cells characterization in vivo. (**H**) Results of histological analysis of subcapsular xenografts 8 weeks after implantation of Matrigel, BMSCs, *CX43*$^+$*FGFR2*$^+$ cells, and GFP-labeled *CX43*$^+$*FGFR2*$^+$ cells in immunodeficient mice. Scale bar, 100 μm. (**I**) Bone areas formed in renal subcapsular layers 8 weeks after implantation of *CX43*$^+$*FGFR2*$^+$ cells and BMSCs. $^{***}P < 0.001$ versus BMSCs. (**J**) Results of micro–computed tomography analysis of femoral condyle defects repair by means of local transplantation of *CX43*$^+$*FGFR2*$^+$ cells and BMSCs in rabbits. (**K**) *CX43*$^+$*FGFR2*$^+$ cells achieved higher bone-volume fractions [bone volume/total volume (BV/TV)] and trabecular numbers (Tb.N) than that of BMSCs in repairs of femoral condyle defects in rabbit. $^{\#\#\#}P < 0.001$ versus Defect; $^{***}P < 0.001$ versus BMSCs.

profile of PMC4 showed higher correlation to PMC2 than to PMC1 and PMC3 (fig. S6A). The Gene Ontology functional enrichment results indicated that the highly expressed genes in PMC2 were involved mainly in skeletal system development (fig. S6B and table S4). The pseudotime analysis further identified a major trajectory from PMC2 to PMC4 (fig. S6) (*15*). In vivo lineage tracing of cell differentiation would provide further insights into this process, but carrying out such controlled experiments in a large wild animal is not possible. Overall, our data suggests that PMC2 might be a population of resting stem cells residing in the periosteum before regeneration, which becomes activated and starts to form PMC4 by 5 days after casting, when the antler regeneration process starts. Concomitantly, expression of the suppressor genes (*SFRP1*, *SFRP2*, and *SFRP4*) of the Wnt pathway declined, whereas expression of *WNT5B*, *TGFBI*, and *TGFB1* genes increased (fig. S6E), suggesting that the Wnt and TGFβ pathways might be involved in PMC4 formation.

In addition, proliferating pericytes and endothelial cells (*TOP2A* and *MKI67*) were also found at 5 days after casting (fig. S3D), which could be related to formation of the vascular network involved in antler growth (*19*). We also observed a increase in macrophages (*CD86*), which are required for wound healing or epimorphic regeneration in mammals and amphibians, at 5 days after casting (Fig. 2B). This indicates that the immune system also plays an important role in antler regeneration, similar to its reported involvement in amphibian appendage regeneration (*20*).

The cell populations at 5 days after casting meet the definition of a blastema. This is a cell mass that, through migration and proliferation, transiently forms at an injury plane and is endowed with the morphogenetic information required to regenerate an organ (*21*). Because PMC4 was identified as the key cell population for antler regeneration, we refer to these cells as "antler blastema progenitor cells" (ABPCs). We further compared the cellular composition in the blastema across species [deer antler, mouse regenerative digit tip (distal phalanx, P3), axolotl limb, and zebrafish caudal fin] using data from this and previous studies (fig. S7) (*3*, *22*, *23*). Although the blastema cell composition varies greatly among species, *PRRX1*$^+$ cells were the most abundant cell type across species. We identified several conserved marker genes, such as *POSTN* and *DCN*, which suggests a conserved core mechanism in the process of appendage regeneration (fig. S7G). We identified a specific subtype of *PRRX1*$^+$ cells in the mouse digit tip (P3) blastema with gene expression profiles similar to those of ABPCs but not to those of nonregenerative digit tip (middle phalanx, P2), axolotl limb, and zebrafish caudal fin blastema (Fig. 2, F to I; figs. S7 and S8; and tables S5 and S6). These findings indicate the potential existence of a cell population across mammals that is essential and specific for mammalian appendage regeneration.

We observed greater heterogeneity of cellular populations at 10 days after casting than at the earlier time points, with large proportions of ABPCs (4.53%), chondroblasts (6.75%), chondrocytes (30.78%), and osteoblasts (8.16%) (Fig. 2B). We also observed increases in the expression of chondrogenic genes such as *SOX6*, *ACAN*, and *CHAD* (fig. S3E), indicating that cartilage had developed rapidly by 10 days after casting. At 45, 60, and 90 days after casting, the proportion of chondrocytes and osteoblasts had increased further (Fig. 2B). Furthermore, expression of genes involved in ossification (*PAPSS2*, *PHOSPHO1*, and *IBSP*) had increased (fig. S3E), indicating that the endochondral ossification processes of antler development had started at this stage.

At this stage, we have focused mostly on the bone regeneration process in antler regrowth. However, antler regrowth also requires the proliferation of other cell types, such as the extracellular matrix of cartilage. Concordantly, we identified three fibroblastic cell clusters, denoted fibroblast 1, fibroblast 2, and fibroblast 3 (Fig. 2A and fig. S9A). During antler regeneration, we found that fibroblast 1 together with PMC2 were already present in periosteum before regeneration (10 days before casting) (Fig. 2B). Fibroblast 2 and 3 cells started to appear at 10 days after casting, were maintained at high levels during mid-regeneration stages (10 to 45 days after casting), and substantially declined during the antler ossification period (60 to 90 days after casting) (Fig. 2B). The pseudotime analysis showed a differentiation trajectory from fibroblast 1 to fibroblasts 2 and 3 (fig. S9B), which potentially secrete the large amounts of collagen needed to form the extracellular matrix of cartilage during antler regeneration.

Phenotypic and functional characterization of ABPCs at 5 days after casting

ABPCs in the blastema at 5 days after casting play a crucial role in antler regeneration. We isolated ABPCs for further phenotypic and functional characterization (Fig. 3A). We identified a cluster of genes enriched in ABPCs (fig. S10A and table S7). Two cell surface markers (*CX43* and *FGFR2*) were highly and differentially expressed in ABPCs (Fig. 3B and fig. S10B). Subsequently, *CX43*$^+$*FGFR2*$^+$ ABPCs were sorted with flow cytometry for functional analysis (Fig. 3B).

The colonies formed by *CX43*$^+$*FGFR2*$^+$ cells could clonally expand and be serially passaged, generating secondary and tertiary colonies that maintained the immunophenotypes, indicating their self-renewal ability. Moreover, these cells had a much higher colony-formation efficiency and generated much larger colonies than did *CX43*$^+$*FGFR2*$^-$, *CX43*$^-$*FGFR2*$^+$, and *CX43*$^-$*FGFR2*$^-$ cells (Fig. 3, C and D). Next, we subjected clonal cultures to in vitro differentiation assays. The *CX43*$^+$*FGFR2*$^+$ cells showed strong osteogenic and chondrogenic, but not adipogenic, differentiation capability (Fig. 3E and fig. S10C). This differs markedly from the trilineage differentiation of bone marrow stromal cells (BMSCs), currently the most widely used stem cells in bone regenerative medicine (*24*). In addition, under the same conditions, the *CX43*$^+$*FGFR2*$^+$ cells showed stronger osteochondrogenic differentiation ability than did BMSCs, manifested by higher expression levels of osteogenesis markers (*RUNX2* and *SP7*) and chondrogenesis markers (*SOX9* and *COL2A1*) but not adipogenesis markers (*ADIPOQ* and *PPARG*) (Fig. 3F). Thus, deer antler *CX43*$^+$*FGFR2*$^+$ cells maintain self-renewal capability and have strong potency

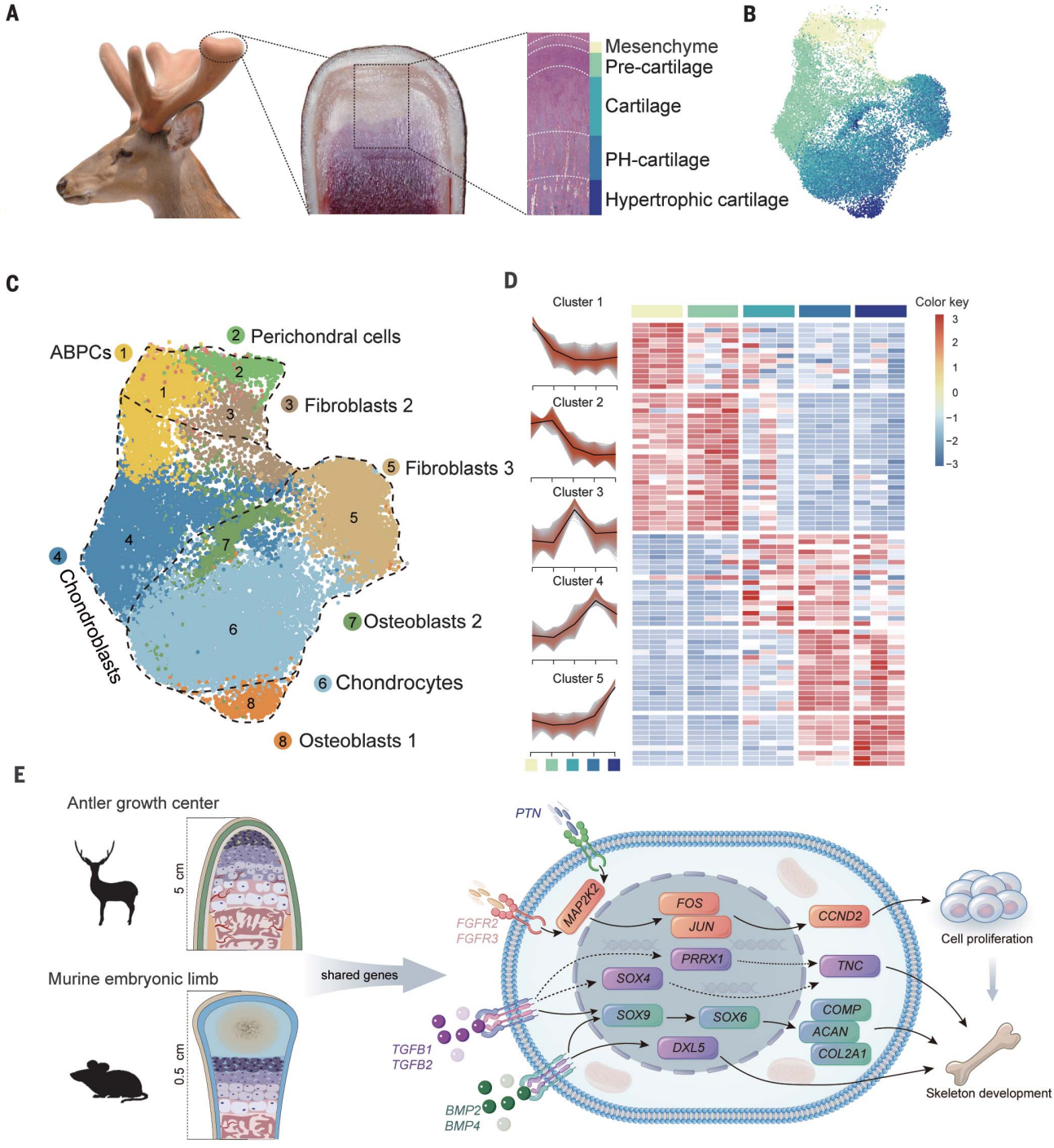

Fig. 4. Spatial cellular and genetic heterogeneity in rapid antler growth. (**A**) (Left) Antler in the rapid growth period, with an antler growth center (AGC) circled by a dashed line. (Middle) The distinct AGC morphology. (Right) Histological section of AGC. (**B**) UMAP atlas of merged scRNA-seq data from mesenchyme layers, precartilage layers, cartilage layers, prehypertrophic cartilage layers (PH cartilage layers), and hypertrophic cartilage layers (n = 30,045 cells). Each dot indicates a single cell and is colored according to its layers. (**C**) UMAP atlas of the AGC with color-coded cell-types identified with scRNA-seq analysis. (**D**) (Left) Fuzzy c-means clustering identifying general patterns of gene expression across the five tissue layers in AGC. (Right) Heatmap of gene expression levels from distal to proximal AGC cell layers. The gene details are shown in table S9. (**E**) Schematic diagram of shared highly expressed genes in AGC and mouse embryonic limb.

toward osteochondrogenic differentiation, highlighting their potential utility in cell-based therapy for bone and cartilage regeneration.

To further assess the in vivo differentiation potential of *CX43*$^{+}$*FGFR2*$^{+}$ cells, we transplanted cell cultures into renal capsules of immunodeficient mice (Fig. 3G). Eight weeks after transplantation, the *CX43*$^{+}$*FGFR2*$^{+}$ cells showed a strong osteochondral differentiation capacity (Fig. 3H). They formed significantly greater areas of new cartilage and bone than did BMSCs (Fig. 3I). Furthermore, the regenerated cartilage and bone were derived from the *CX43*$^{+}$*FGFR2*$^{+}$ cells labeled with green fluorescence (Fig. 3H). To further assess their potential

therapeutic value in regenerative medicine and bone remodeling, *CX43*$^+$*FGFR2*$^+$ cells were used to repair femoral condyle defects in rabbit, with BMSCs as controls. After 8 weeks, both BMSCs and *CX43*$^+$*FGFR2*$^+$ cells had filled the cavities with newly formed bone, but the *CX43*$^+$*FGFR2*$^+$ cells generated higher numbers of new trabecular bone (Fig. 3, J and K, and fig. S10). Thus, *CX43*$^+$*FGFR2*$^+$ cells have a strong capacity to promote bone formation in vivo, with potential for cell-based therapies to promote bone regeneration (for example, for bone or cartilage injuries, nonunion fractures, and osteoporosis). In contrast to other stem cell types, *CX43*$^+$*FGFR2*$^+$ cells have advantages including superior proliferative and osteochondral differentiation ability and ex vivo expansion. Nevertheless, we stress that many concerns about the use of deer *CX43*$^+$*FGFR2*$^+$ cells in the clinic remain to be addressed in future studies, including their detailed molecular regulation mechanisms and the safety hazards involved in their use, as well as ethical and legal concerns.

Spatial cellular and genetic heterogeneity during rapid antler growth

The rate of bone growth in deer antler is the highest recorded for any animal (*10*). The antler growth process is spatially well organized, with an antler growth center (AGC) forming at the antler tip (*12*) (Fig. 4A). The AGC becomes the primary growth center for rapid antler elongation and recapitulates the growth center of the embryonic long bone histologically (*10*). To characterize its spatial heterogeneity at cellular and gene expression levels, we applied scRNA-seq and bulk RNA-seq analyses to AGC tissue layers at 60 days after casting, around the time point when antlers grow most rapidly in sika deer (Fig. 4A and table S2).

The single-cell mapping matched the histological spatial location distribution (Fig. 4B, fig. S11A, and table S8). The mesenchyme layer at the most distal part of the antler tip was composed mainly of perichondral cells (29.68%) and ABPCs (49.96%) (Fig. 4, B and C, and fig. S11), suggesting that the ABPCs that formed by 5 days after casting persist at the tip as a stem cell pool for antler growth. The precartilage layer was dominated by chondroblasts (51.90%), which are key cells for chondrogenesis, and a smaller proportion of ABPCs (20.52%) (Fig. 4, B and C, and fig. S11). The cartilage and prehypertrophic cartilage (PH cartilage) layers were dominated by chondrocytes (61.47%) (Fig. 4, B and C, and fig. S11). The hypertrophic cartilage layers consisted mainly of osteoblasts (63.87%) (Fig. 4, B and C, and fig. S11), which is in line with the histological findings that hypertrophic cartilage is being replaced by spongy bone (*10*). The spatial heterogeneity of cell composition in the AGC was confirmed with histology (fig. S11). We reconstructed the spatial cellular atlas of the AGC from distal to proximal layers, expanding our understanding of the spatial locations of major cell populations during the rapid elongation of deer antler.

Next, we assessed the global variation in gene expression across the AGC tissue layers, using the bulk RNA-seq data (table S2). Principal components analysis (PCA) revealed a gradient of layer samples that matched their positions along a proximal–distal axis of the AGC (fig. S11E), suggesting that the gene expression variation trajectory follows a pattern similar to that found in the AGC tissue layers. Highly expressed genes in mesenchyme layers were found to be involved in cell proliferation (for example, *IGF1*, *IGFBP2*, and *IGFBP4*) and stem cell maintenance (such as *SFRP1* and *SFRP2*) (Fig. 4D and table S9). This is expected because the rapid cell proliferation in antlers presumably requires factors that not only stimulate rapid cell proliferation but also maintain the stemness of ABPCs and control the cell cycle. Genes highly expressed specifically in the precartilage layers (for example, *WNT10B*, *WNT10A*, and *WNT6*) were associated with the Wnt pathway (Fig. 4D and table S9), suggesting that this signaling pathway could be involved in early differentiation of stem cells toward chondrogenesis. The highly expressed genes in the cartilage layers and PH cartilage layers were related to cartilage development (such as *SOX6* and *SOX9*) and extracellular matrix organization (such as *COL2A1*) (Fig. 4D and table S9). The highly expressed genes in the hypertrophic cartilage layers were related to chondrocyte mineralization (such as *MMP9* and *MMP12*) (Fig. 4D and table S9).

The histology of deer AGCs resembles the growth plates of developing long bone in mammals (*10*), suggesting that they may share similar growth mechanisms. To test this hypothesis, we reanalyzed the scRNA-seq profiles of mouse embryonic limbs and compared them with AGCs (*25*). We found that they shared 151 highly expressed genes (table S10) primarily related to extracellular matrix organization, skeletal system development, cartilage development, and cell proliferation (table S10). Several core genes of the mitogen-activated protein kinase (MAPK) signal pathway (*FGFR2*, *FGFR3*, *MAP2K2*, *FOS*, and *JUN*), bone morphogenetic protein (BMP) signal pathway (*BMP2* and *BMP4*), and transforming growth factor–β (TGFβ) signal pathway (*TGFB1* and *TGFB2*) were highly expressed in both AGCs and mouse neonatal growth plates (*26*, *27*). The marker genes (*PRRX1*, *TNC*, *DLX5*, *PTN*, and *SOX4*) for ABPCs were also identified during rapid limb development in mice, suggesting potential roles of those genes for rapid skeleton development in mammals (Fig. 4E, fig. S11, and table S10). Moreover, we detected multiple angiogenesis-related genes (*VAV3*, *ANGPTL2*, *MYH9*, and *ACTG1*) in AGC (table S10), most likely related to the highly vascularized cartilage in deer antlers (*19*). This is a distinctive feature of antler growth, which differs sharply from the avascular chondrogenesis in mice and human tissues and serves the high metabolic demands of rapidly growing antler tissue (*14*).

Conclusion

We present a spatiotemporal cellular atlas of antler regeneration, which provides a useful genetic and histological resource for mammalian organ regeneration. Our results show that antler regeneration is consistent with a conceptual stem cell–based regenerative process. We provide evidence for the existence of a blastema-like structure that is present during antler regeneration and is similar to the structure involved in amphibian limb regeneration, suggesting that the blastema is a conserved biological feature in vertebrate tissue regeneration. We further identified a population of regenerative progenitor cells, ABPCs, in the antler blastema, with impressive capacities for self-renewal, osteogenic–chondrogenic differentiation, and bone-tissue repair. This provides a cellular basis for understanding antler regeneration and extends the catalog of known mammalian stem cell systems. Cross-species comparison showed that a cell type similar to ABPCs is present in mouse regenerative digit tip (P3) but not in mouse nonregenerative digit tip (P2), axolotl limb, or zebrafish caudal fin. This suggests the existence of relatively conserved cellular and molecular mechanisms for the only two known cases of regenerative capacity in mammalian appendage organs.

Our in vitro and in vivo results suggest that deer ABPCs may have an application in clinical bone repair. Beyond this, induction of regular human mesenchymal or other cells into ABPC-like cells through activation of key characteristic genes could potentially be used in regenerative medicine for skeletal injuries or limb regeneration.

REFERENCES AND NOTES

1. J. A. Goldman, K. D. Poss, *Nat. Rev. Genet.* **21**, 511–525 (2020).
2. T. Gerber *et al.*, *Science* **362**, eaaq0681 (2018).
3. Y. Hou *et al.*, *Sci. Adv.* **6**, eaba2084 (2020).
4. J. Godwin, *BioEssays* **36**, 861–871 (2014).
5. J. P. Brockes, A. Kumar, *Nat. Rev. Mol. Cell Biol.* **3**, 566–574 (2002).
6. S. E. Iismaa *et al.*, *NPJ Regen. Med.* **3**, 6 (2018).
7. R. J. Goss, *Anat. Rec.* **241**, 291–302 (1995).
8. C. Li, H. Zhao, Z. Liu, C. McMahon, *Int. J. Biochem. Cell Biol.* **56**, 111–122 (2014).
9. U. Kierdorf, H. Kierdorf, T. Szuwart, *J. Morphol.* **268**, 726–738 (2007).
10. J. S. Price, S. Allen, C. Faucheux, T. Althnaian, J. G. Mount, *J. Anat.* **207**, 603–618 (2005).
11. T. Landete-Castillejos *et al.*, *Bone* **128**, 115046 (2019).
12. C. Li, J. M. Suttie, D. E. Clark, *Anat. Rec. A Discov. Mol. Cell. Evol. Biol.* **282A**, 163–174 (2005).
13. C. Li, J. M. Suttie, D. E. Clark, *J. Morphol.* **262**, 731–740 (2004).
14. Y. Wang *et al.*, *Science* **364**, eaav6335 (2019).
15. Materials and methods are available as supplementary materials.

16. T.-Y. Lin *et al*., *Dev. Cell* **56**, 1541–1551.e6 (2021).
17. G. L. Johnson, E. J. Masias, J. A. Lehoczky, *Dev. Cell* **52**, 525–540.e5 (2020).
18. C. Li, *Birth Defects Res. C Embryo Today* **96**, 51–62 (2012).
19. D. E. Clark, C. Li, W. Wang, S. K. Martin, J. M. Suttie, *Anat. Rec. A Discov. Mol. Cell. Evol. Biol.* **288A**, 973–981 (2006).
20. J. W. Godwin, A. R. Pinto, N. A. Rosenthal, *Proc. Natl. Acad. Sci. U.S.A.* **110**, 9415–9420 (2013).
21. A. W. Seifert, K. Muneoka, *Dev. Biol.* **433**, 190–199 (2018).
22. M. A. Storer *et al*., *Dev. Cell* **52**, 509–524.e9 (2020).
23. H. Li *et al*., *Protein Cell* **12**, 57–66 (2021).
24. A. Arthur, S. Gronthos, *Int. J. Mol. Sci.* **21**, 9759 (2020).
25. N. H. Kelly, N. P. T. Huynh, F. Guilak, *Matrix Biol.* **89**, 1–10 (2020).
26. L.-A. Stanton, T. M. Underhill, F. Beier, *Dev. Biol.* **263**, 165–175 (2003).
27. E. Kozhemyakina, A. B. Lassar, E. Zelzer, *Development* **142**, 817–831 (2015).

ACKNOWLEDGMENTS

We thank P. Fennessy for critical reading of the manuscript and Jilin Dong Ao Deer Industry Group Co. for providing deer antler samples. We also thank Z. Wang, Q. Guan, J. Li, S. Wang, and D. Wang from the Institute of Antler Science and Product Technology for their help in single-cell separation. **Funding:** This study was supported by the National Key Research and Development Program of China (grant 2021YFA0805000), the National Natural Science Foundation of China (grants 32225009, 31970392, 82122043, 32030016, 32122083, and U20A20403), the Strategic Priority Research Program of the Chinese Academy of Sciences (grant ref. XDA16010105), the Talents Team Construction Fund of Northwestern Polytechnical University, the Research Funds for Interdisciplinary Subject (grant NWPU 19SH030408), and the 1000 Talents Project of Shaanxi Province. **Author contributions:** Q.Q., C.L., J.H., and W.W. designed this project and research aspects. Z. Li, Q.L., H.S., T.Q., Z. Liu, and G.Z. performed sample collection and sequencing library construction. M.H. and Y.Y. performed data analysis including genome assembly and annotation. S.L. and Y.Z. performed flow cytometry. Y.Z., S.L., G.W., G.Z., X.C., J.R., B.X., H.B., and X.G. performed functional experiments. T.Q. and Y.Y. performed scRNA-seq analysis. K.W., G.W., and T.Q. contributed to figure design. T.Q., Q.Q., W.W., Z. Li, and J.H. wrote the manuscript. W.W. and R.H. amended it. **Competing interests:** Q.Q., J.H., T.Q., Y.Z., and W.W. are inventors on a patent application related to this work filed by Northwestern Polytechnical University and Fourth Military Medical University (patent application no. CN202211737365.3). **Data and materials availability:** All sequencing data and genome assemblies have been deposited in the NCBI database (accession ID: PRJNA831044). All other data needed to evaluate conclusions in the paper are present in the paper and/or supplementary materials. Additional data related to this paper may be requested from the authors. **License information:** Copyright © 2023 the authors, some rights reserved; exclusive licensee American Association for the Advancement of Science. No claim to original US government works. https://www.science.org/about/science-licenses-journal-article-reuse

SUPPLEMENTARY MATERIALS

science.org/doi/10.1126/science.add0488
Materials and Methods
Figs. S1 to S11
Tables S1 to S11
References (*28*–*54*)
MDAR Reproducibility Checklist

Submitted 17 May 2022; resubmitted 16 November 2022
Accepted 10 January 2023
10.1126/science.add0488

REVIEW SUMMARY

CONSERVATION BIOLOGY

Extinct in the wild: The precarious state of Earth's most threatened group of species

Donal Smith*, Thomas Abeli, Emily Beckman Bruns, Sarah E. Dalrymple, Jeremy Foster, Tania C. Gilbert, Carolyn J. Hogg, Natasha A. Lloyd, Abby Meyer, Axel Moehrenschlager, Olivia Murrell, Jon Paul Rodriguez, Paul P. Smith, Andrew Terry, John G. Ewen

BACKGROUND: As international commitments to prevent extinction and improve the status of threatened species go unmet, a crisis of species loss unprecedented in human history intensifies. The field of conservation biology has, however, begun to demonstrate that species can be recovered, and extinctions in the wild prevented and even reversed. These successes suggest that the post-2020 global biodiversity draft targets of arresting the increase in extinction rates and reducing the proportion of threatened species are within our capacity. A nexus of responsibility, vulnerability, and opportunity lies in those species that—having been entirely extirpated in the wild—exist solely in zoos, aquariums, botanical gardens, or seed banks—i.e., those that qualify for the International Union for Conservation of Nature (IUCN) Red List of Threatened Species (Red List) category of extinct in the wild (EW). This is a considerably overlooked category; despite being considered most at risk, the populations of EW species are not assessed under the Red List process. Consequently, we have largely ignored the extent of, and variation in, extinction risk of the very group of species for which humans are most responsible, and whose futures are among the least assured.

ADVANCES: We reveal the dynamic and perilous state occupied by EW species. We provide an overview of the fates of the 95 species that, since 1950, are known to have persisted in ex situ care despite extirpation in the wild and characterize the present statuses of the 84 species currently assessed as EW. We found considerable variation and alarming deficiencies in factors critical to their long-term recovery potential. Where known, most EW species, already compromised by their small number of founders, are maintained at levels at which the risks to demographic security and loss of genetic diversity are considered intolerably high. Further, most depend on maintenance at a small number of institutions. Even when individuals are spread across institutions, metapopulation management is often lacking, especially in plants. By pausing generational turnover, seed storage may offer protection from many ex situ processes, but we find that most EW plant species are not represented in seed storage institutions. Underscored by the finding that we have lost 11 species entirely under our care to extinction since 1950, we highlight the need to drive recovery and return EW species to the wild. We know this to be possible as we report on 12 species that have recovered wild status having once been restricted to ex situ care. Although most EW animal species have been subject to translocations back to wild conditions, most EW plant species have not. Overall, 41 extant EW species have never been subject to such actions.

OUTLOOK: The cases we examined chart more than 70 years of attempts to use ex situ conservation to prevent extinction and facilitate the recovery of species on the very brink, highlighting both the fragility of this space and the potential for success despite that fragility. Ensuring that the fortunes of EW species continue to bend away from extinction requires a redoubling of effort and a collective realization—in the minds of the conservation community, legislators, and the public—of their existence and plight. In response, the IUCN World Conservation Congress 2020 called for the reestablishment of EW species in the wild by 2030. We urge a forward-looking approach to rescue, revitalize, release, and reinforce populations: responsibly rescue suitable species close to extinction into ex situ care, revitalize and strengthen current ex situ populations to ensure continued viability, engage in ambitious and innovative release programs to return species to the wild, and drive recovery of released populations through continued reinforcement and management. Though we recognize that the challenges decision makers face are considerable, we argue that real opportunities to prevent extinction and return previously lost species to the wild abound and we must take them. ■

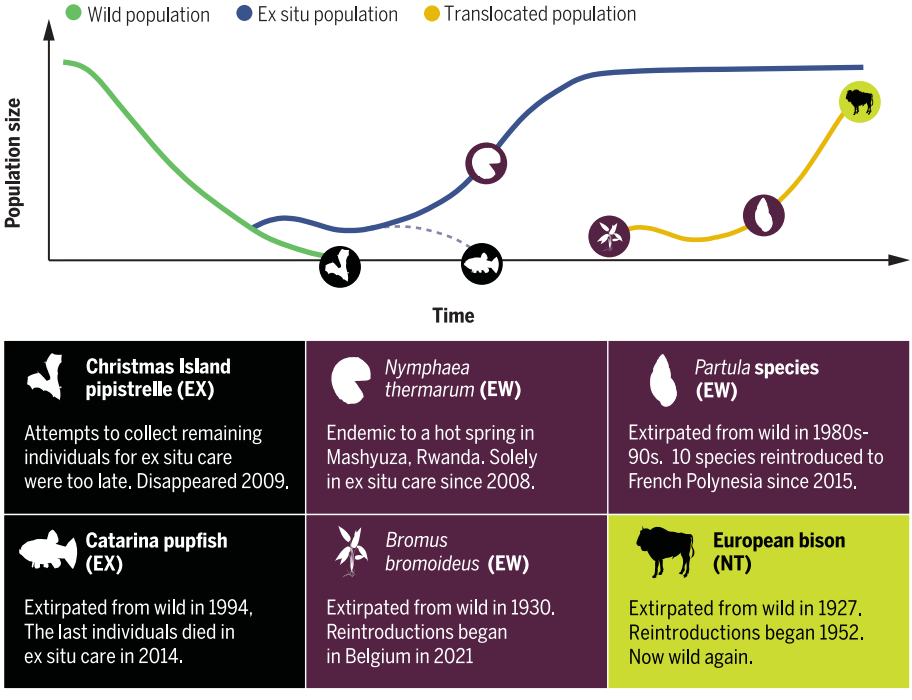
Wild population
Ex situ population
Translocated population
Population size
Time
Christmas Island pipistrelle (EX)
Attempts to collect remaining individuals for ex situ care were too late. Disappeared 2009.
Nymphaea thermarum (EW)
Endemic to a hot spring in Mashyuza, Rwanda. Solely in ex situ care since 2008.
Partula species (EW)
Extirpated from wild in 1980s-90s. 10 species reintroduced to French Polynesia since 2015.
Catarina pupfish (EX)
Extirpated from wild in 1994. The last individuals died in ex situ care in 2014.
Bromus bromoideus (EW)
Extirpated from wild in 1930. Reintroductions began in Belgium in 2021
European bison (NT)
Extirpated from wild in 1927. Reintroductions began 1952. Now wild again.

Ex situ care on the brink of extinction. Ex situ care can save species with declining wild populations from outright extinction. However, populations extirpated to ex situ care are in a precarious state and require growth and careful management to mitigate the risks of genetic deterioration and extinction. These populations can be crucial in species' long-term recovery through translocations back to the wild.

The list of author affiliations is available in the full article online.
*Corresponding author. Email: donal.smith@ioz.ac.uk
Cite this article as D. Smith *et al.*, *Science* **379**, eadd2889 (2023). DOI: 10.1126/science.add2889

READ THE FULL ARTICLE AT
https://doi.org/10.1126/science.add2889

REVIEW

CONSERVATION BIOLOGY

Extinct in the wild: The precarious state of Earth's most threatened group of species

Donal Smith[1]*, Thomas Abeli[2,3], Emily Beckman Bruns[4,5], Sarah E. Dalrymple[3,6], Jeremy Foster[4,5,7], Tania C. Gilbert[3,8,9], Carolyn J. Hogg[3,10], Natasha A. Lloyd[3,11], Abby Meyer[4], Axel Moehrenschlager[3,11,12], Olivia Murrell[4,5,7], Jon Paul Rodriguez[13,14], Paul P. Smith[15], Andrew Terry[16], John G. Ewen[1,3]

Extinct in the Wild (EW) species are placed at the highest risk of extinction under the International Union for Conservation of Nature Red List, but the extent and variation in this risk have never been evaluated. Harnessing global databases of ex situ animal and plant holdings, we report on the perilous state of EW species. Most EW animal species—already compromised by their small number of founders—are maintained at population sizes far below the thresholds necessary to ensure demographic security. Most EW plant species depend on live propagation by a small number of botanic gardens, with a minority secured at seed bank institutions. Both extinctions and recoveries are possible fates for EW species. We urgently call for international effort to enable the latter.

A crisis of species loss unprecedented in human history continues to intensify (*1*, *2*). Over the past century, extinctions in well-understood groups such as vertebrates have far exceeded what would be considered a normal background rate based on the fossil record (*3*). The bulk of extinctions lie largely ahead: The proportion of species threatened with extinction among the most comprehensively assessed speciose groups ranges from 13% in birds to 42% in gymnosperms (*4*), and patterns of decline and extinction in poorly known taxa may be even more severe (*5*, *6*). However—despite the failure to meet similar commitments in the 2010 Aichi Biodiversity Targets (*7*)—the 2022 Kunming-Montreal Global biodiversity targets for halting extinctions and recovering species (*8*) should be regarded as achievable. This is because the field of conservation biology is continuing to demonstrate that the status of threatened species can be improved and that extinctions in the wild can be prevented and even reversed. The conservation status of the world's vertebrates, though deteriorating, would be significantly worse were it not for conservation interventions (*9*). Indeed, 28 to 48 extant bird and mammal species would have gone extinct between 1993 and 2020 were it not for actions such as habitat protection, translocation, and ex situ conservation using breeding facilities and zoos (*10*). Ex situ conservation using botanic gardens and seed banks has also been used to support the restoration of at least eight plant species and populations that had disappeared from their indigenous range (*11*). Among these endeavors is a category of species representing a nexus of responsibility, vulnerability, and opportunity—those species that, having been entirely extirpated in the wild, exist solely in zoos, aquariums, botanical gardens, or seed banks and consequently qualify for the International Union for Conservation of Nature (IUCN) Red List of Threatened Species (Red List) category of extinct in the wild (EW) (*4*). This category is applied to any species "known only to survive in cultivation, in captivity or as a naturalized population (or populations) well outside the past range" (*12*).

Species restricted to ex situ care arrived there through a variety of means; in some cases, individuals were collected from highly threatened populations with the specific aim of species conservation. The lizard fauna native to Christmas Island in the Indian Ocean, for example, suffered significant declines starting in the 1970s as a result of habitat modification and the effects of introduced species (*13*). In response to the crisis, two endemic lizard species were rescued into ex situ care in 2009, providing refuge from outright extinction before the last individuals were recorded in the wild in 2012 (*13*). In other cases, species were collected for scientific or hobbyist interest and only acquired conservation relevance once the situation in the wild became dire. For example, in 1925, 17 Socorro doves (*Zenaida graysoni*) were collected from Socorro Island in the Pacific Ocean and transported to an aviculturist in California in the USA (*14*), forming the basis for an ex situ collection that is today distributed in small numbers in captive facilities across North America and Europe (*15*). On its native Socorro, however, the dove entered an abrupt decline sometime after 1958 and was last seen in the wild in 1972 (*15*, *16*). In other instances, collection into ex situ maintenance is itself the principal driver of extinction in the wild. Wild populations of Southern African cycad species such as the escarpment cycad (*Encephalartos brevifoliolatus*) and Heenan's cycad (*Encephalartos heenanii*) have disappeared because of collection for the trade in ornamental plants (*17*, *18*), yielding ex situ collections that nonetheless represent potential sources for eventual recovery in the wild. Though the circumstances surrounding their procurement are diverse, all of these species share a dependence on human care, combined with a wild context that—at least historically—has presented threats sufficiently severe to lead to their extirpation.

EW species occupy an overlooked space in the Red List, the framework for evaluating and comparing species' risk of extinction. The assessment process evaluates states and trends in the geographic ranges and populations of species as well as their threats and allocates categories of extinction risk accordingly. These categories range in increasing risk from "least concern" through "near threatened," "vulnerable," "endangered," "critically endangered," "extinct in the wild," and "extinct." Species in the vulnerable, endangered, and critically endangered categories are classed as "threatened" with extinction. EW species are not included in this group, despite being categorized as facing higher extinction risk. In fact, because the Red List process concerns itself solely with wild populations, the populations of EW species—whether thriving or on the brink—are not subject to assessment. The broader conservation community has consequently largely ignored the extent of and variation in extinction risk among the very group of species for which humans are most responsible and whose futures are among the least assured.

Harnessing global ex situ databases and academic and gray literature, we reveal the dynamic and often perilous state occupied by EW species, assessing their current populations as well as summarizing the journeys and fates of all species known to have been restricted to ex situ care since 1950. Extending our analysis beyond the introduction in

[1]Institute of Zoology, Zoological Society of London, London, UK. [2]Department of Science, University of Roma Tre, Roma, Italy. [3]IUCN SSC Conservation Translocation Specialist Group, Calgary, Canada [4]Botanic Gardens Conservation International-US, San Marino, CA, USA. [5]Chicago Botanic Gardens, Chicago, IL, USA. [6]School of Biological and Environmental Sciences, Liverpool John Moores University, Liverpool, UK. [7]Northwestern University, Evanston, IL, USA [8]Marwell Wildlife, Hampshire, UK. [9]School of Biological Sciences, University of Southampton, Southampton, UK. [10]Faculty of Science, School of Life and Environmental Sciences, The University of Sydney, Sydney, Australia. [11]Wilder Institute / Calgary Zoo, Calgary, Canada. [12]Department of Biological Sciences, University of Calgary, Canada. [13]IUCN Species Survival Commission, Caracas, Venezuela. [14]Instituto Venezolano de Investigaciones Científicas, and Provita, Caracas, Venezuela. [15]Botanic Gardens Conservation International, Surrey, UK. [16]Zoological Society of London, London, UK.
*Corresponding author. Email: donal.smith@ioz.ac.uk

1994 of the EW category (*19*), we chose 1950 to approximate the beginning of the modern era of species conservation (*20*). This time window enabled us to build a comprehensive list of species in a comparable context, minimizing the risk of biasing our selection toward well-known cases.

Our dataset therefore included assessments of the 84 species (40 animals and 44 plants) categorized as EW on Red List version 2022-2 (*4*). Of these, two (both animals) have gone extinct since their most recent assessment (Table 1). The assessments of a further 10 appear erroneous: Two are extinct having never been in ex situ care, three are likely extant in the wild having never been extirpated, three are synonyms of species that remain extant in the wild, and the statuses of two are unknown (table S1). We added a further 21 species that were ex situ–restricted at some point since 1950, but now occupy a different state (i.e., they are either extinct or considered wild again). These species were identified through a review of the IUCN summary statistics for genuine status changes, the Red List narrative texts of extinct species, and the assessments of extant species with populations indicated as originating from reintroductions or assisted colonizations (*21*). Twelve of these additional species are now wild again (Table 2), and a further nine have gone extinct (Table 1). In total we identified and summarized the conservation history and statuses of 95 species (52 animals and 43 plants) known to have been EW or restricted to ex situ care since 1950, 72 of which (33 animals and 39 plants) are considered to remain in this state as of 2022.

For each species, we collected information on the history of the collection, ex situ maintenance, and conservation of each. Namely: the periods over which founders of the ex situ population were collected from the wild; the number of individuals collected to initiate the ex situ population; the number of founder lineages represented in the present population (where this is noted as a separate number); the year the species was last recorded in the wild; and the timing and status of any attempts to reestablish the species in the wild through conservation translocations. The status of the ex situ populations of currently EW species was assessed by quantifying the number of institutions holding them; the type of institution for plants (i.e., botanical garden or seed bank); the total ex situ population size for animals (this is not generally quantified or reported for plants); whether an animal species was subject to metapopulation management or had a studbook; and whether any population viability analyses had been carried out for ex situ populations. Data was collated primarily from Red List assessments, supplemented where necessary using recovery project documentation, academic literature, targeted Google and Google News searches, and contact with relevant taxon experts and conservation practitioners (*21*). Information on ex situ populations of currently EW species was derived from Species360's Zoological Information Management System (*22*), Association of Zoos and Aquariums' database of species survival programs (SSPs) (*23*), the European Association of Zoos and Aquaria (EAZA)'s list of ex situ programmes (EEPs) (*24*), Australasia's Zoo Aquarium Association's list of Species Management Programs (SMPs) (*25*), and the World Association of Zoos and Aquariums' list of Global Species Management Plans (*26*) (for animal species), and Botanic Gardens Conservation International's PlantSearch (*27*) (for plant species).

The varied and worrying state of EW species

We found considerable variation and concerning deficiencies among EW species in factors critical to their long term recovery. A minimum number of individuals between 30 and 50 is recommended to found an ex situ population to capture an adequate representation of the genetic diversity of the wild population (*28*, *29*). Most currently EW animal populations for which such information is available (8 of 13) were founded by <30 individuals, and among the less well documented plants we report that at least 7 of 40 EW populations were founded by just a single individual (Table 3). Most ex situ populations of EW species were thus imperiled to begin with and require population growth to enhance demographic security and reach a size at which loss through drift of the genetic diversity that remains is at a tolerably low level (Fig. 3A).

Of the 30 EW animal species currently maintained in ex situ institutions for which we could find data, only 6 have populations exceeding 1500 individuals, and half are below 500 (Fig. 1). Given that botanic gardens often hold just one or a few individuals of each species (*30*), we expect that the populations of EW plant species may be extremely small. What constitutes a viable population size is highly context-specific, depending on the biology of the species, aspects of its management and environment, as well as varying definitions of "viable" (*31*). Viability can be expressed in demographic terms, for example the population size needed to have a specific probability of persistence over a specific period of time or number of generations. Meta analyses of minimum viable population sizes calculated across hundreds of species have reported medians of 1377 (for a 90% probability of persistence over 100 years across 1198 animal and plant species) (*32*), 4169 (standardized to a 99% probability of persistence over 40 generations across 212 animal and plant species) (*33*), and 5816 (for a 99% probability of persistence over 40 generations across 102 vertebrate species) (*34*), with wide and positively skewed distributions. Most EW species for which data on population sizes are available are well below these estimates. Though population viability analyses were at some point carried out for at least eight currently EW species (all animals), we are only aware of three that currently use these tools to inform management (table S2).

Managers of ex situ populations must also consider the effect population size has on retention of genetic diversity. In situations such as those faced by EW species, where supplementation of populations with individuals from elsewhere (i.e., the wild) is impossible, an effective population size (N_e) of at least 500 is thought to be required for even well-founded populations to avert the loss of genetic diversity, and it has been argued that N_e = 1000 is a better approximation to maintain evolutionary potential (*35*). N_e corresponds to the number of individuals contributing to the next generation and is generally considerably smaller than the total number of individuals in the population, the census population size (N). In ex situ populations of threatened animals, the ratio of effective population size to census population size (N_e/N) has been estimated to average 0.26 (*36*), implying that most populations should exceed 1900 individuals at the very least to maintain genetic diversity (*37*). Of known populations, 80% of EW animals fall below this level, and half have census population sizes below even the minimum recommended N_e. These figures do not represent universal thresholds delineating viable populations from lost causes, but rather standards that enable us to highlight populations that may be at risk. In this light, the shortfall for EW species is stark.

Holding species across multiple collections provides a buffer against institutional-level risks such as disease outbreaks, catastrophes, and the financial insecurity and logistical challenges deepened by global crises such as the COVID-19 pandemic (*38*, *39*). Most EW animal species are reported at four or fewer institutions (Fig. 2 and table S2). The median number of holders for an EW plant species is eight, but we note that six EW plant species are reported at just a single institution (Fig. 2 and table S2). However, it is not the same few institutions holding these species: The 43 species with <10 holders are spread across 93 institutions (53 zoological and 40 botanical). Overall, EW species are held by at least 501 institutions globally (239 zoological and 262 botanical).

However, distributing an EW species across several holders brings with it the potential for fragmenting an already compromised population into a set of smaller isolated groups. For animal species, breeding and transfer between different institutions comprising ex situ metapopulations can be managed regionally under

Table 1. Species that have gone extinct after having been ex situ–restricted since 1950.

Scientific name	Common name	Kingdom	Class	Year last recorded in wild	Extinction year	Published Red List assessments	Notes	Additional references
Aylacostoma stigmaticum		Animals	Gastropoda	1996	2011	EW (2000)	Collected from the wild into ex situ care in 1993 before filling of a reservoir in its native habitat. The last known wild population disappeared by 1996. This species became extinct outright in 2011 following a disease outbreak in ex situ facilities; the causal agent was unidentified but was suspected to be viral.	
Chelonoidis abingdonii	Pinta giant tortoise	Animals	Reptilia	1972	2012	EX (2016); EW (1996, as *Geochelone nigra abingdoni*)	The last known individual of the species, known as Lonesome George, survived in ex situ care following his collection in 1972 until his death in 2012 marked the extinction of the species.	
Emoia nativitatis	Christmas Island whiptail-skink	Animals	Reptilia	2010	2014	EX (2017); CR (2010)	Declines in wild first reported 1998, likely driven by introduced species. Three females were caught in 2009 with the intention of captive breeding, but the last known individual died ex situ in 2014.	(*13*)
Melamprosops phaeosoma	Po'Ouli	Animals	Aves	2004	2004	EX (2019); CR (1994, 1996, 2000, 2004, 2007, 2008, 2009, 2012, 2013, 2016, 2018); T (1988)	By 1997, only three individuals were known. The last sightings for two of these were in December 2003 and January 2004. The last known individual was captured in September 2004, but died in captivity 78 days later in November 2004.	(*72*)
Megupsilon aporus	Catarina pupfish	Animals	Actinoperygii	1994	2014	EX (2019); EW (1996); E (1994, 1990, 1988, 1986)	This species was endemic to Potosi Spring, which dried out because of groundwater extraction. The species was difficult to maintain in captivity, being sensitive to environmental conditions and vulnerable to infection. Serious declines occurred in 2013, and its scattered distribution across multiple holders likely inhibited full appreciation of the significance of these. The last remaining individual died in 2014.	(*57*)
Nesiota elliptica	St. Helena olive	Plants	Magnoliopsida	1994	2003	EX (2016, 2004); EW (2003, 1998)	This species, native to St. Helena, was rediscovered in the remnants of its native habitat in 1977. This last known wild individual died in 1994, but seeds and cuttings taken from the tree led to attempts to cultivate the species ex situ. It proved difficult to maintain, and fungal infections killed the remaining seedlings and cuttings in 2003.	(*73*)

Scientific name	Common name	Kingdom	Class	Year last recorded in wild	Extinction year	Published Red List assessments	Notes	Additional references
Partula arguta		Animals	Gastropoda	1991	1995	EX (1996, 2009); EN (1994)	Endemic to Huahine, Society Islands; as is the case for the other *Partula* species covered by this study, this species was collected into ex situ care prior to extirpation from the wild following introduction of the carnivorous snail *Euglandina rosea*. The last known individual died ex situ in 1995.	(*42*, *74*, *75*)
Partula aurantia	Moorean viviparous tree snail	Animals	Gastropoda	1981	1991	EX (2019, 2009, 2006); EN (1994)	Endemic to Moorea, Society Islands. As is the case for the other *Partula* species covered by this study, this species was collected into ex situ care prior to extirpation from the wild following introduction of *E. rosea*. The last individual died in ex situ care in 1991.	(*76*–*78*)
Partula clarkei (Reclassified from *P. turgida*)		Animals	Gastropoda	1991	1996	EX (1994, 1996, 2009)	Endemic to Raiatea, Society Islands. As is the case for the other *Partula* species covered by this study, this species was collected into ex situ care before extirpation from the wild following introduction of *E. rosea*. Last known individual died ex situ in 1996 after abrupt population declines attributed to microsporidian parasites (*70*), but the causal agent has since been questioned (*14*).	(*42*, *79*)
Partula faba		Animals	Gastropoda	1994	2015	EW (2009, 1996); E (1994)	Endemic to Raiatea and Tahaa, Society Islands. As is the case for the other *Partula* species covered by this study, this species was collected into ex situ care before extirpation from the wild following introduction of *E. rosea*. The last individual died in ex situ care in 2015.	(*42*)
Partula labrusca		Animals	Gastropoda	1992	2002	EX (2009); EW (1996); E (1994)	Endemic to Raiatea, Society Islands. As is the case for the other *Partula* species covered by this study, this species was collected into ex situ care before extirpation from the wild following introduction of *E. rosea*. The last individual died in ex situ care in 2002.	(*42*)

Not all species were listed on the Red List as EW; see "published Red List assessments" column for details. Key to Red List categories: CR, Critically Endangered; E, Endangered (pre-1994 category); EN, Endangered; EX, Extinct; EW, Extinct in the Wild; NT, Near Threatened; T, Threatened (pre-1994 category); VU, Vulnerable

formalized breeding programs: EAZA EEPs in Europe, SSPs predominantly in North America, and SMPs in Australasia. Global captive management programs (GCMPs) have been proposed in recognition of the need for overarching global management, but these have struggled to gain traction and no EW species has a GCMP despite the fact that at least eight are held across multiple regions (*26*). Despite their benefits, we find that SSPs are absent for 50% (5 of 10) of those held at North American institutions, whereas EEPs are absent for 18% (5 of 22) of EW animal species held at European institutions (table S2). Even for species covered by a cooperative breeding program, implementation of management decisions can be challenging. Based on logistical, husbandry, demographic, or genetic factors, SSPs issue recommendations to transfer individuals between institutions or for individuals to breed with a specific mate or mates.

Table 2. Species that have regained IUCN wild status after having been ex situ–restricted since 1950.

Scientific name	Common name	Kingdom	Class	Last reported in wild	Number of individuals collected (of which, number of founders)	Year conservation translocations started (R, Reintroduction; AC, Assisted Colonization)	Published Red List assessments	Notes	Additional references
Acanthobrama telavivensis	Yarkon bream	Animals	Actinopterygii	1999	150	R: 2002	VU (2014); EW (2006).	Native to coastal streams of Israel, this species declined throughout the second half of the 20th century until a severe drought in 1999 dried out the last remnants of its habitat. To secure the future of the species, 150 fish were brought into ex situ care in the days prior to extirpation. Reintroduction attempts followed 3 years later which were further refined in subsequent years alongside habitat restoration. The species now has a growing population in the wild again.	(*80*)
Bison bonasus	European bison	Animals	Mammalia	1927	54 (12)	R: 1952	NT (2020); VU (2008); EN (2000, 1996); V (1994, 1990, 1988); "Very rare but believed to be stable or increasing" as *B. b. bonasus* (1965)	Once distributed across western, central, and southeastern Europe, this species declined in response to human expansion with its associated hunting pressure and ecosystem alteration. It was finally extirpated from the wild in 1927 but survived in European zoos. A breeding project commenced in Białowieża, Poland, in 1929, leading to the first reintroductions back into the wild in 1952. Wild populations have grown to the point of the current categorization of near threatened, though the species still depends on conservation management.	(*81*, *82*)

Scientific name	Common name	Kingdom	Class	Last reported in wild	Number of individuals collected (of which, number of founders)	Year conservation translocations started (R, Reintroduction; AC, Assisted Colonization)	Published Red List assessments	Notes	Additional references
Canis rufus	Red wolf	Animals	Mammalia	1980	14 (12)	R:1987	CR (2018, 2004, 1996); E (1994, 1990, 1988, 1986, 1982)	Once common in the eastern USA, the red wolf declined as a result of human persecution and hybridization with coyotes (*Canis latrans*). Between 1973 and 1980, 400 individuals were collected from the wild, and from these, the last fourteen putatively pure red wolves were selected to initiate an ex situ population.	(*83*)
Chelonoidis hoodensis	Española giant tortoise	Animals	Reptilia	1974	15 (15)	R: 1975 AC: 2015	CR (2017, 2016, 1994 as *Geochelone nigra hoodensis*)	Endemic to Española, the Galápagos Islands, exploitation for human consumption and habitat degradation drove the wild population to only 14 in 1974, at which point all remaining individuals were removed to establish an ex situ population (joined by an additional male already present in San Diego Zoo). Reintroductions commenced the following year. Used as an ecological replacement for a now-extinct tortoise species on Santa Fe island from 2015.	(*84*, *85*)
Diplotaxis siettiana	Jaramago de Alborán	Plants	Magnoliopsida	1974	Not reported	R: 1999	CR (2011, 2006); EX (1998)	Endemic to the island of Alborán, Spain. Extensive human modification of habitat, particularly the introduction of cattle, likely led to declines. Species was not seen after 1974. Reintroductions commencing in 1999 established a self-sustaining population.	(*11*)

Scientific name	Common name	Kingdom	Class	Last reported in wild	Number of individuals collected (of which, number of founders)	Year conservation translocations started (R, Reintroduction; AC, Assisted Colonization)	Published Red List assessments	Notes	Additional references
Equus ferus	Takhi; Przewalski's Horse	Animals	Mammalia	1969	53 (12)	R: 1997	EN (2015, 2011); CR (2008); EW (1996)	Ranged across the Eurasian steppe from Russia east to northern China and Mongolia until the 1800s, when it began to decline. Remnant populations persisted until the last wild individual was recorded in the Dzungarian Gobi Desert in 1969. 11 of 12 founders contributing to the present population had been captured into ex situ care between 1899 and 1902, with 1 additional mare caught in 1947. Reintroductions commenced in Mongolia in the 1990s.	(*86*)
Gymnogyps californianus	California condor	Animals	Aves	1987	22 (14)	R: 1992 and 1994	CR (2020, 2018, 2017, 2016, 2015, 2013, 2012, 2010, 2009, 2008, 2006, 2004, 2000, 1996, 1994); T (1988)	Precipitous population declines in the 20th century driven largely by persecution and poisoning due to consumption of carcasses containing lead shot. The last known individuals of the species were collected from the wild by 1987 to initiate an ex situ population. Reintroductions started 1992. All reintroduced individuals were collected back into captivity in 1994 as a result of behavioral problems. Reintroductions recommenced 1995.	(*87*)
Hibiscadelphus giffardianus		Plants	Magnoliopsida	1930	1	R: 1951	CR (1998); E (1978)	Only one individual of this small tree native to Hawai'i was ever known. This individual died in 1930, but seeds were collected and the species was propagated ex situ. Replanted in original habitat between 1951 and 1964.	(*88*)

Scientific name	Common name	Kingdom	Class	Last reported in wild	Number of individuals collected (of which, number of founders)	Year conservation translocations started (R, Reintroduction; AC, Assisted Colonization)	Published Red List assessments	Notes	Additional references
Hypotaenidia owstoni	Ko'ko'; Guam Rail	Animals	Aves	1987	22	AC: 1989 R: 1998	CR (2019); EW (2016); EW (2012, 2010, 2008, 2004, 2000, 1996, 1994, as *Gallirallus owstoni*); T (1988, as *Rallus owstoni*)	Extirpation from Guam in 1987 driven largely by brown tree snakes. Conservation translocations started on the island of Rota (outside of native range) in 1989; however, despite evidence of breeding here, this population is not considered to be self-sustaining due to the continued release efforts required to ensure its persistence. A 1998 release into a snake-controlled area in Guam failed as a result of destruction of the snake barrier by a typhoon in 2002. Releases on the island of Cocos starting in 2010 have seen breeding (by 2014), and this population is now considered self-sustaining and was the basis for downlisting to CR in 2019.	(*89*, *90*)
Oryx leucoryx	Arabian oryx	Animals	Mammalia	1972	≥17 (17)	R: 1982	VU (2017, 2011); EN (2008, 2003, 1996); E (1994, 1990, 1988, 1986); "Very rare and believed to be decreasing in numbers" (1965)	Once distributed across the Arabian Peninsula, this species experienced steep population declines in the 20th century and was last reported in the wild in 1972. A captive program was commenced in 1962 to 1963 in the USA with nine individuals, at least three of which were wild-caught for conservation purposes. In parallel to this, a collection was established in Riyadh containing additional animals from Saudi Arabia and Qatar, as well as individuals from the USA herd. In 1993, the global population was reported to be derived from 17 wild-caught founders.	(*91*)

Scientific name	Common name	Kingdom	Class	Last reported in wild	Number of individuals collected (of which, number of founders)	Year conservation translocations started (R, Reintroduction; AC, Assisted Colonization)	Published Red List assessments	Notes	Additional references
Mustela nigripes	Black-footed Ferret	Animals	Mammalia	1987	18 (7)	R: 1991	EN (2015, 2008); EW (1996); E (1994, 1990, 1988, 1986, 1982); "Very rare and believed to be decreasing in numbers" (1965)	Once distributed across west central North America from southern Canada to northern Mexico, tightly linked to the habitat of its principal prey, prairie dogs (*Cynomys* spp.) Habitat conversion, persecution of prairie dogs as an agricultural pest, and sylvatic plague led to precipitous ferret declines across the 20th century. The species was thought lost in the 1970s until discovery of a declining small population in 1981. The last known individuals were captured into ex situ care in 1987. Multiple reintroductions starting in 1991 have resulted in at least three self-sustaining wild populations.	(*92*)
Zoogoneticus tequila	Tequila splitfin	Animals	Actinoperygii	2013	6	R: 2015	EN (2019); CR (2009)	Endemic to the upper Río Ameca in Jalisco, Mexico, this species was extirpated in 2013, probably due to the impacts of introduced species and habitat degradation. Reintroductions started in 2015, establishing a population that is currently growing.	

Not all species were listed on the Red List as EW, see "published Red List assessments" column for details. Key to Red List categories: CR, Critically Endangered; E, Endangered (pre-1994 category); EN, Endangered; EX, Extinct; EW, Extinct in the Wild; NT, Near Threatened; T, Threatened (pre-1994 category); VU, Vulnerable.

However, a recent analysis has found that SSP recommendations to transfer individuals between institutions were fulfilled just 57% of the time, and the fulfilment rate of recommendations for specific individuals to breed was even lower at 20% (*40*).

Genetic management is informed by a reliable understanding of the pedigree of individuals within a population, generally recorded in a studbook. We were unable to find any indication of studbooks for 31% (10 of 32) of EW animal species managed ex situ (table S2).

Table 3. Number of individuals initiating ex situ populations and—where reported—number of founder lineages currently represented, of animal (left) and plant (right) EW species.

Animal species	Number of individuals collected (of which, number of founders)	Plant species	Number of individuals collected
Alagoas curassow	5 (3)	*Abutilon pitcairnense*	1
Ameca shiner	6	*Cyanea pinnatifida*	1
Wyoming toad	10	*Encephalartos relictus*	1
ʻAlalā (or Hawaiian crow)	10 (9)	*Encephalartos woodii*	1
Spix's macaw	17 (7)	*Kokia cookei*	1
Socorro dove	17	*Sophora toromiro*	1
Milu (or Père David's deer)	18 (11)	*Cyanea superba*	3
Sihek (or Guam kingfisher)	29 (16)	*Diplazium laffanianum*	5
Lister's gecko	43		
Golden skiffia	<50		
Scimitar-horned oryx	48 to 60		
Blue-tailed skink	66		
Kihansi spray toad	499		

Species missing studbooks were fish, amphibians, and invertebrates, taxa typically housed and bred in groups, a situation in which individual pedigrees are generally unavailable. However, such species can still be subject to genetic management using population genetic models and group-level information (*41*), as is deployed for ex situ populations of Polynesian tree snails (*36*, *42*). Management of ex situ plant collections is hampered by poor knowledge of the provenance of populations, a limited ability to track them at an individual level, and a lack of coordination across institutions (*30*). Efforts to address these problems and develop pedigree-based metapopulation management techniques for plants are currently underway (*30*, *43*).

For some plant species, storage of propagules in seed banking facilities offers an opportunity to pause generational turnover, and thus circumvent many of the processes that compromise genetic viability of ex situ populations over time. Though not suitable for all species (*44*), this technique—which can retain seed viability for potentially hundreds of years (*45*)—will be crucial in ensuring that at least 75% of threatened plant species are maintained ex situ (target 8 of the Global Strategy for Plant Conservation) (*46*). Using a seed storage prediction model (*21*, *47*), we found that ~89% (31 of 35 species modeled, see table S5) of EW plant species are predicted to produce desiccation-tolerant seeds suitable for seed banking. Although it is possible that some accessions from living collections may refer to seeds, it is notable that only 28% (11 of 39) of EW plant species are reported by dedicated seed banks (Fig. 2).

Beyond loss of diversity through genetic drift, maintaining species in ex situ care across multiple generations brings the risk of adaptation to the conditions in which the species is kept (*48*), a risk that increases with population size and genetic diversity (*38*). Further, even optimal ex situ care cannot prevent in situ change: Plants and animals held separate from wild environments for extended periods may not be well adapted to the shifting ecosystems to which we would like to return them (*49*).

The state of EW species should thus be regarded with a sense of urgency. With small founder and population sizes and a modest number of holding institutions, most risk genetic deterioration, declines, and extinction under our care. Ex situ conservation has been an instrumental tool in preventing extinction in these species, but it cannot forestall it indefinitely. Reestablishment in the wild is a crucial step toward recovery.

Contrasting fates: extinctions versus returns to the wild

We find that conservation translocations back to wild settings have been undertaken much less commonly for plant than animal species: only 26% (11 of 43) of historically (1950 to 2022) ex situ–restricted and 23% (9 of 39) of currently EW plant species, compared with the majority of both historically ex situ–restricted (32 of 53, 60%) and currently EW (22 of 33, 67%) animal species (Fig. 3, Table 2, and tables S2 and S4). The rate of translocations of plants from ex situ collections has been previously observed to be low (*11*), perhaps partly attributable to a lower level of attention and available resources accorded to the conservation of plants when compared with that of animals (*50*). Although the rate among animals is encouraging, we are still left with 41 extant EW species (30 plants and 11 animals) that have never been subject to an attempted return to the wild. The Socorro dove (*Zenaida graysoni*), for example, collected from the wild in 1925 (*14*), is approaching a century—approximately 37 generations—in ex situ care.

The EW state can nevertheless represent a crucial waypoint on the pathway to recovery. There are 12 species (10 animals and 2 plants) that were once extirpated from the wild but are now considered to have wild populations again (Fig. 3 and Table 2). These include the Jaramago de Alborán (*Diplotaxis siettiana*), now categorized as critically endangered on the red list; the Yarkon bream (*Acanthobrama telavivensis*), which has been downlisted to vulnerable; and the European Bison (*Bison bonasus*), which has recovered from the threatened to near threatened categories. But less fortunate fates are also possible: 11 species have gone extinct after existing only in ex situ care (Fig. 3 and Table 1). These include the St. Helena olive (*Nesiota elliptica*) and the Pinta giant tortoise (*Chelonoidis abingdonii*), both lost in the past decade.

The need for an improved system of assessing ex situ–restricted taxa

Though we expanded our investigation of historically ex situ–restricted species beyond those assessed on the Red List as EW, we have deferred to the Red List in confirming present day extinction from the wild (*21*). This likely underrepresents the true number of species that currently merit the status or are approaching it. For example, a further 58 species (46 plants and 12 animals) currently assessed as critically endangered have been tagged as "possibly extinct in the wild" (*4*, *51*). In addition, the often slow pace of changes in Red List status (*52*), combined with a conservative approach to declaring extinction (*53*), together produce a considerable lag between a species last being seen in the wild and initially being listed as EW; we find 11 years to be the median interval. Bearing in mind the threat of an oncoming wave of extinctions over the coming decades (*54*), a considerable number of ex situ–restricted species may therefore be accumulating with no reliable way of identifying them. Species that have recently been claimed to likely qualify as EW but are not yet assessed as such include the ʻālula (*Brighamia insignis*) (*43*), a shrub native to Hawaii, the Vietnam pheasant (*Lophura edwardsi*) (*55*), and the Javan pied starling (*Gracupica jalla*) (*56*), all of which are currently classified as critically endangered. However, only the first bears the "possibly extinct in the wild" tag.

It is clear, however, that designation as EW would not facilitate the evaluation of extinction risk or recovery potential. As demonstrated in this study, the single EW category contains

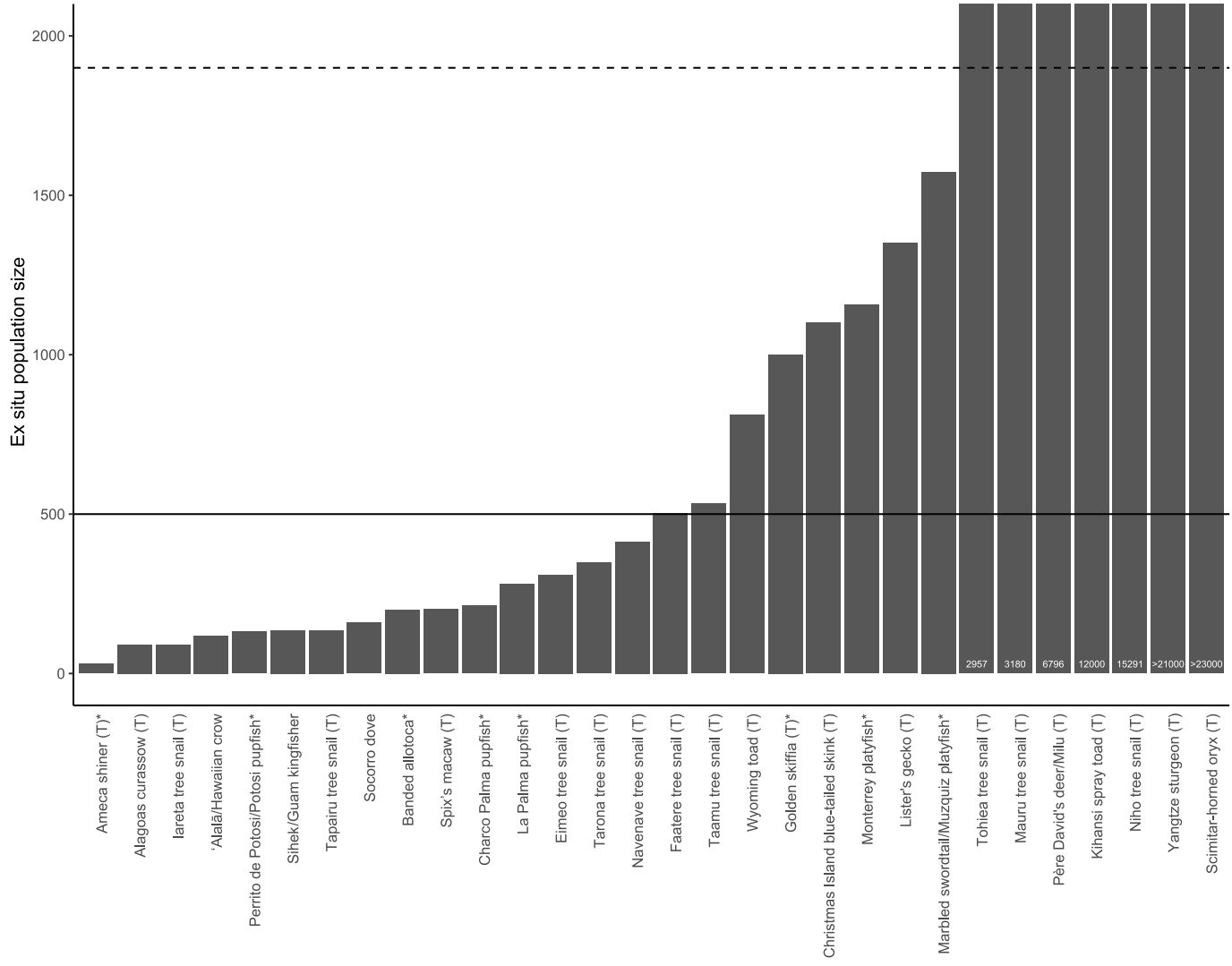

Fig. 1. Estimated ex situ population sizes of EW animal species. Solid horizontal line, Minimum N_e recommended to minimize loss of genetic diversity (500). Dashed horizontal line, minimum census population size expected to ensure effective population size of 500 (1900 individuals) (*37*). Where population sizes are >2000, the total size is denoted at the base of the bar. Population estimates are for 30 of the 32 EW animal species held ex situ and were compiled using Zoological Information Management System (ZIMS) (*22*), a database representing the real-time holdings of more than 1100 zoological and aquarium collections globally, combined with academic and gray literature, and advice from relevant taxon experts and conservation practitioners. Species marked with an asterisk may have additional individuals kept by hobbyists. Species marked with "T" have additional in situ populations as a result of conservation translocations but are not yet considered wild under the Red List.

such variability in the viability of its species (and efforts to quantify that viability) as to potentially conceal the plight of the least secure. Might the Catarina pupfish (*Megupsilon aporus*) be with us today had its precarious status in the years running up to its demise been better characterized and communicated (*57*)? It is certainly not credible to place this species in the same category of extinction risk as one such as the milu (Père David's deer, *Elaphurus davidianus*) which, after over 35 years of reintroductions and conservation management, numbers more than 9000 individuals of varying degrees of "wildness" distributed across its native range in China (*58*), although still being assessed as EW. An improved system for assessing the health and progress of EW species would be both beneficial and—given that the global databases that could inform such surveillance are already established—feasible.

Recommendations

The cases we depict chart more than 70 years of attempts to use ex situ conservation to prevent extinction and facilitate the recovery of species on the very brink, highlighting both the fragility of this status and the potential for success despite that fragility. Ensuring that the fortunes of EW species continue to bend away from extinction requires a redoubling of effort and a collective realization—in the minds of the conservation community, legislators, and the public—of their existence and plight. In response, the IUCN World Conservation Congress 2020 called for the reestablishment of current EW species in the wild by 2030 (*59*). This should be coupled with the identification of additional currently threatened species whose recovery could be achieved through ex situ care. We urge a forward-looking approach to rescue, revitalize, release, and reinforce populations: rescue suitable species close to extinction into ex situ care, revitalize and strengthen current ex situ populations to ensure continued

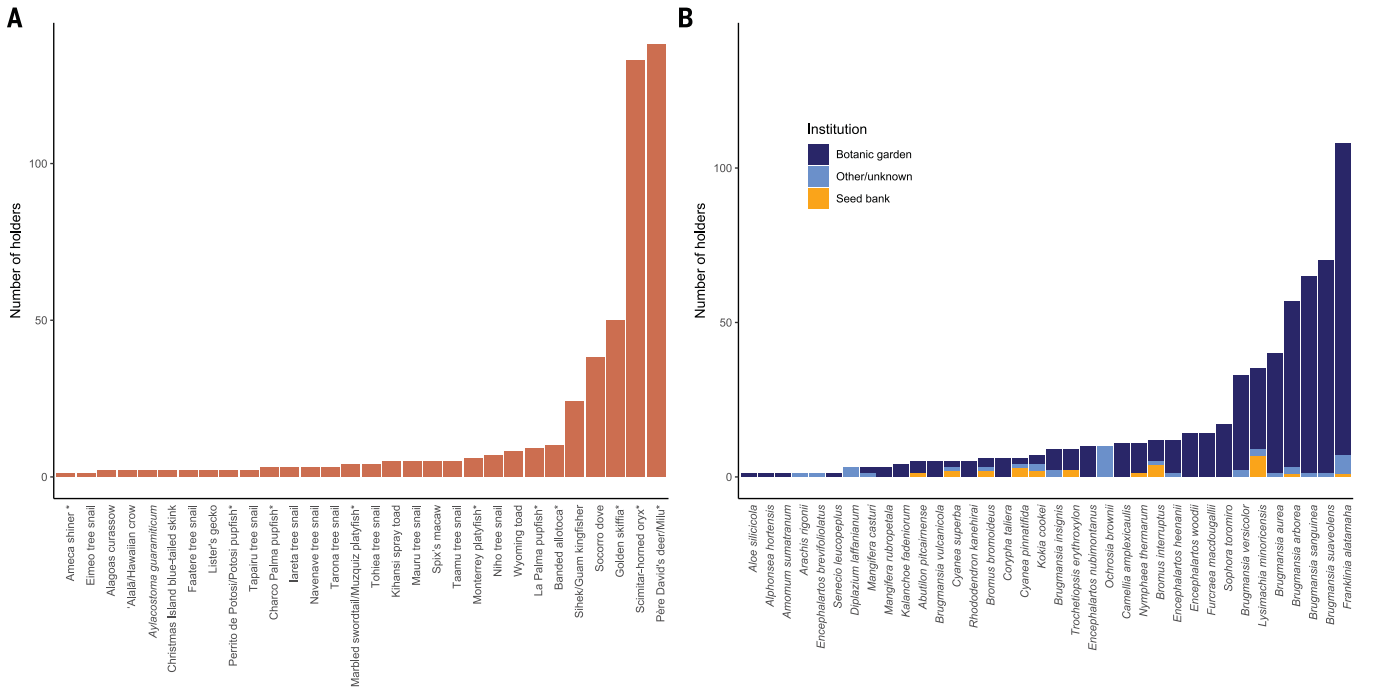

Fig. 2. Holders of ex situ EW species. (**A**) Estimated number of holders for 30 of the 32 EW animal species held ex situ. Estimates were produced as in Fig. 1. Species marked with an asterisk may have additional individuals kept by hobbyists. (**B**) Estimates of number and type (botanical garden, seed bank, or unknown) of ex situ holders of 36 of the 39 EW plant species; compiled using PlantSearch, a database reporting the living plant, seed, and tissue holdings of more than 1100 botanical collections globally (*27*), combined with academic and gray literature, and advice from relevant taxon experts and conservation practitioners.

viability, engage in ambitious and innovative release programs to return species to the wild, and drive recovery of released populations through continued reinforcement and management.

Deciding where, when, and whether to rescue species is not a trivial task and is confounded by risky (that is, uncertain) outcomes. From a biological perspective, the removal of a species to ex situ care may be challenging as the attempt may accelerate extinction in the wild, and, combined with downstream consideration of the likelihood of successful wild releases from ex situ care, should be weighed against in situ alternatives (*60*). Decisions about rescue will always go beyond biological perspectives to include a mix of financial, ethical, social, and cultural considerations. For example, at least four Hawaiian forest bird species face extinction in the coming decade as a result of avian malaria (*61*). The immediate removal of individuals into ex situ care, and thus the likely creation of EW populations, is seen as the management action with the highest probability of extinction avoidance for at least one of these species, the 'akikiki (*Oreomystis bairdi*), with an estimated wild population in 2021 of just 45 individuals (*61*). The location of ex situ facilities must balance Native Hawaiians' preference not to remove birds from Hawai'i (*61*). Such multiobjective decisions are inevitable in conservation and influence what alternatives are available and how the best one may be selected. We encourage adopting a transparent and deliberative approach to decision making on a case-by-case basis, such that values are clearly identified and decisions are rationally made in light of these (*62*). We must be bold and take urgent risky action, but this does not mean abandoning critically important recognition of values and drawing on available science to inform what this action is and how we should best implement it. We wish to avoid cases such as the Christmas Island pipistrelle (*Pipistrellus murrayi*), for which ex situ care was proposed and eventually agreed upon but through delay and indecision, inaction and extinction were inadvertently chosen instead (*63*).

Similarly, ex situ institutions such as zoos and botanic gardens must balance multiple values, of which EW species conservation is just one. In most cases, revitalization of ex situ EW populations will require significant additional resources: More individuals require more space, infrastructure, and staff time. This must be balanced with the contributions ex situ institutions also play in non-EW species conservation, education, visitor experience, and the space and financial constraints required to deliver these. Although we are indebted to such institutions for being the only thing standing between EW species and extinction, we encourage a much more strategic approach to EW species ex situ care whereby decision science is used to develop unified management plans informed, at the least, by population viability analysis and genetic management. In addition, we call on funders to support the delivery of ex situ care and consequent recovery in the wild through release and reinforcement.

As recovery in the wild ought to be an ultimate objective for all EW species, management plans for ex situ populations should be integrated with in situ planning, as is envisaged in the IUCN's "One Plan Approach" (*64*), which has not, as far as we can identify, been adopted for any EW species. There are many reasons why some EW species have never been released into the wild. For some plants, such as the seven EW *Brugmansia* species native to South America, historic wild localities are simply not known (*65*). For some species, such as the sihek (or Guam kingfisher, *Todiramphus cinnamominus*), their indigenous range remains inhospitable to their return. However, reasoned and bold actions may allow wild recovery either through proactive removal of in situ extinction drivers or releases beyond indigenous range (*66*, *67*). For example, Christmas Island blue-tailed skinks (*Cryptoblepharus egeriae*) have been released to the wild on the Cocos (Keeling) islands (*68*) and proposals for sihek releases on Palmyra Atoll are under consideration (*69*). Although release is a landmark moment—and is rightly celebrated—this should typically mark the beginning of a long-term commitment to recover the species in situ. Pioneering work has returned 10 formerly extirpated Polynesian tree snail species to the Society Islands,

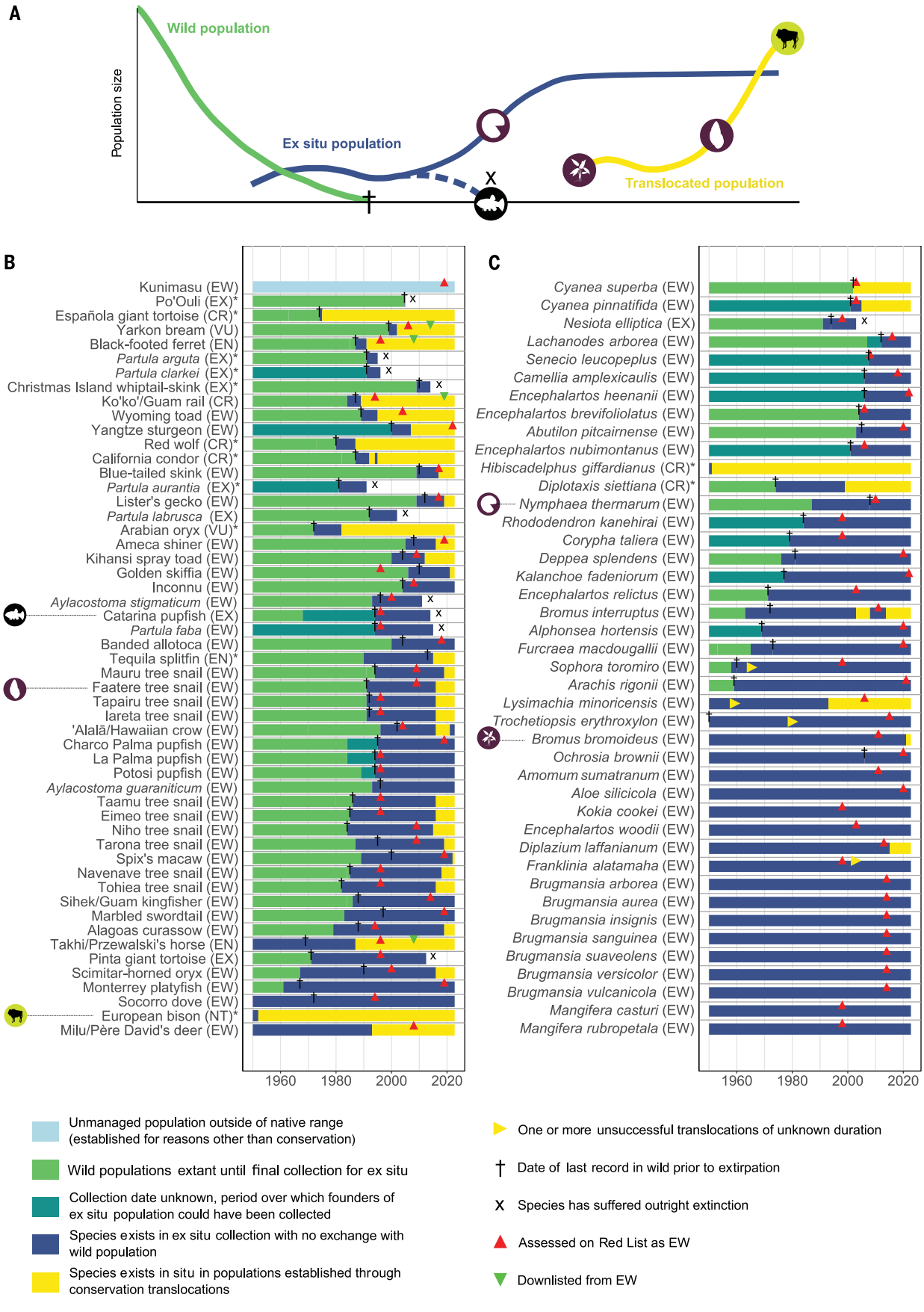
A
Wild population
Population size
Ex situ population
Translocated population
B
Kunimasu (EW)
Po'Ouli (EX)*
Española giant tortoise (CR)*
Yarkon bream (VU)
Black-footed ferret (EN)
Partula arguta (EX)*
Partula clarkei (EX)*
Christmas Island whiptail-skink (EX)*
Ko'ko'/Guam rail (CR)
Wyoming toad (EW)
Yangtze sturgeon (EW)
Red wolf (CR)*
California condor (CR)*
Blue-tailed skink (EW)
Partula aurantia (EX)*
Lister's gecko (EW)
Partula labrusca (EX)
Arabian oryx (VU)*
Ameca shiner (EW)
Kihansi spray toad (EW)
Golden skiffia (EW)
Inconnu (EW)
Aylacostoma stigmaticum (EW)
Catarina pupfish (EX)
Partula faba (EW)
Banded allotoca (EW)
Tequila splitfin (EN)*
Mauru tree snail (EW)
Faatere tree snail (EW)
Tapairu tree snail (EW)
Iareta tree snail (EW)
'Alalā/Hawaiian crow (EW)
Charco Palma pupfish (EW)
La Palma pupfish (EW)
Potosi pupfish (EW)
Aylacostoma guaraniticum (EW)
Taamu tree snail (EW)
Eimeo tree snail (EW)
Niho tree snail (EW)
Tarona tree snail (EW)
Spix's macaw (EW)
Navenave tree snail (EW)
Tohiea tree snail (EW)
Sihek/Guam kingfisher (EW)
Marbled swordtail (EW)
Alagoas curassow (EW)
Takhi/Przewalski's horse (EN)
Pinta giant tortoise (EX)
Scimitar-horned oryx (EW)
Monterrey platyfish (EW)
Socorro dove (EW)
European bison (NT)*
Milu/Père David's deer (EW)
1960
1980
2000
2020
C
Cyanea superba (EW)
Cyanea pinnatifida (EW)
Nesiota elliptica (EX)
Lachanodes arborea (EW)
Senecio leucopeplus (EW)
Camellia amplexicaulis (EW)
Encephalartos heenanii (EW)
Encephalartos brevifoliolatus (EW)
Abutilon pitcairnense (EW)
Encephalartos nubimontanus (EW)
Hibiscadelphus giffardianus (CR)*
Diplotaxis siettiana (CR)*
Nymphaea thermarum (EW)
Rhododendron kanehirai (EW)
Corypha taliera (EW)
Deppea splendens (EW)
Kalanchoe fadeniorum (EW)
Encephalartos relictus (EW)
Bromus interruptus (EW)
Alphonsea hortensis (EW)
Furcraea macdougallii (EW)
Sophora toromiro (EW)
Arachis rigonii (EW)
Lysimachia minoricensis (EW)
Trochetiopsis erythroxylon (EW)
Bromus bromoideus (EW)
Ochrosia brownii (EW)
Amomum sumatranum (EW)
Aloe silicicola (EW)
Kokia cookei (EW)
Encephalartos woodii (EW)
Diplazium laffanianum (EW)
Franklinia alatamaha (EW)
Brugmansia arborea (EW)
Brugmansia aurea (EW)
Brugmansia insignis (EW)
Brugmansia sanguinea (EW)
Brugmansia suaveolens (EW)
Brugmansia versicolor (EW)
Brugmansia vulcanicola (EW)
Mangifera casturi (EW)
Mangifera rubropetala (EW)
1960
1980
2000
2020
Unmanaged population outside of native range (established for reasons other than conservation)
Wild populations extant until final collection for ex situ
Collection date unknown, period over which founders of ex situ population could have been collected
Species exists in ex situ collection with no exchange with wild population
Species exists in situ in populations established through conservation translocations
One or more unsuccessful translocations of unknown duration
Date of last record in wild prior to extirpation
Species has suffered outright extinction
Assessed on Red List as EW
Downlisted from EW

Fig. 3. The conservation history of all species known to have met the definition of EW since 1950. (**A**) Schematic showing stages in the process of recovery of highly threatened species through collection for ex situ care, ex situ population growth and maintenance, and return to the wild through translocations. Pathways through these stages or towards extinction are illustrated with icons representing example species in (**B** and **C**). Timelines representing the history of this process for all animal (B) and plant (C) species that would have met the definition of EW since 1950. Colors represent the population status and activity over the time period depicted. Species are listed in ascending order of time spent in ex situ care experiencing no exchange with wild populations (using the minimum possible duration where this is not known with certainty). The present Red List status is listed in parentheses after the common name (animals) or scientific name (plants). Species marked with an asterisk have never been listed as EW on the Red List.

but considerable obstacles to the recovery of these species remain in part due to the ongoing threats posed by the non-native predatory New Guinea flatworm (*Platydemus manokwari*) (*70*). Those involved in Polynesian tree snail recovery are learning how to best attempt new releases and reinforce all wild populations. With sustained support and adaptive management, Polynesian tree snails and other EW species can emulate the successful paths to recovery in the wild forged by species such as the Yarkon bream and European bison. Real opportunities to prevent extinction and return previously lost species to the wild abound, and we must take them.

REFERENCES AND NOTES

1. H. M. Pereira *et al*., Scenarios for global biodiversity in the 21st century. *Science* **330**, 1496–1501 (2010). doi: 10.1126/science.1196624; pmid: 20978282
2. Secretariat of the Convention on Biological Diversity, "Global Biodiversity Outlook 5" (GBO-5, 2020).
3. G. Ceballos *et al*., Accelerated modern human-induced species losses: Entering the sixth mass extinction. *Sci. Adv.* **1**, e1400253 (2015). doi: 10.1126/sciadv.1400253; pmid: 26601195
4. International Union for Conservation of Nature, IUCN Red List Threatened Species Version 2022-2 (IUCN, 2022); https://www.iucnredlist.org/en.
5. R. Dirzo *et al*., Defaunation in the Anthropocene. *Science* **345**, 401–406 (2014). doi: 10.1126/science.1251817; pmid: 25061202
6. C. Régnier *et al*., Mass extinction in poorly known taxa. *Proc. Natl. Acad. Sci. U.S.A.* **112**, 7761–7766 (2015). doi: 10.1073/pnas.1502350112; pmid: 26056308
7. G. Ceballos, P. R. Ehrlich, P. H. Raven, Vertebrates on the brink as indicators of biological annihilation and the sixth mass extinction. *Proc. Natl. Acad. Sci. U.S.A.* **117**, 13596–13602 (2020). doi: 10.1073/pnas.1922686117; pmid: 32482862
8. UN Environment Program, Convention on Biological Diversity, Kunming-Montreal Global biodiversity framework (2022); https://www.cbd.int/doc/c/e6d3/cd1d/daf663719a03902a9b116c34/cop-15-l-25-en.pdf.
9. M. Hoffmann *et al*., The impact of conservation on the status of the world's vertebrates. *Science* **330**, 1503–1509 (2010). doi: 10.1126/science.1194442; pmid: 20978281
10. F. C. Bolam *et al*., How many bird and mammal extinctions has recent conservation action prevented? *Conserv. Lett.* **14**, (2020). doi: 10.1111/conl.12762
11. T. Abeli *et al*., Ex situ collections and their potential for the restoration of extinct plants. *Conserv. Biol.* **34**, 303–313 (2020). doi: 10.1111/cobi.13391; pmid: 31329316
12. International Union for Conservation of Nature, IUCN Red List Categories and Criteria: Version 3.1 (IUCN, Second edition, 2012).
13. P. Andrew *et al*., Somewhat saved: A captive breeding programme for two endemic Christmas Island lizard species, now extinct in the wild. *Oryx* **52**, 171–174 (2016). doi: 10.1017/S0030605316001071
14. E. W. Gifford, Grayson's Pigeon (Zenaidura graysoni) in Captivity. *Auk* **44**, 513–519 (1927). doi: 10.2307/4074841
15. BirdLife International, International Union for Conservation of Nature, "Zenaida graysoni" (IUCN Red List of Threatened Species, 2020); https://dx.doi.org/10.2305/IUCN.UK.2020-3.RLTS.T22690740A178409463.en.
16. L. F. Baptista, Socorro Dove Breeding/Release Program. *AFA Watchb.* **18**, 15–16 (1991).
17. J. D. W. Bösenberg, "Encephalartos brevifoliolatus" (IUCN Red List of Threatened Species, 2022); https://dx.doi.org/10.2305/IUCN.UK.2022-1.RLTS.T41882A50824805.en.
18. J. D. W. Bösenberg, "Encephalartos heenanii" (IUCN Red List of Threatened Species, 2022); https://dx.doi.org/10.2305/IUCN.UK.2022-1.RLTS.T41888A51055983.en.
19. B. Groombridge, G. M. Mace, G. Rabb, 1994 IUCN red list of threatened animals (World Conservation Monitoring Centre, 1994).
20. H. R. Akçakaya *et al*., Quantifying species recovery and conservation success to develop an IUCN Green List of Species. *Conserv. Biol.* **32**, 1128–1138 (2018). doi: 10.1111/cobi.13112; pmid: 29578251
21. Materials and methods are available as supplementary materials.
22. Species360 Zoological Information Management System (ZIMS) (2022); https://www.species360.org/.
23. Association of Zoos and Aquariums, Animal Program Database, (2022); https://ams.aza.org/eweb/DynamicPage.aspx?Site=AZA&WebKey=8f652949-31be-4387-876f-f49a2d7263b2.
24. European Association of Zoos and Aquariums, Specialist Programmes (2023); https://www.eaza.net/conservation/programmes/##TAGSandBP.
25. Zoo Aquarium Association Australasia, Species Programs (2022) https://zooaquarium.org.au/public/Public/Conservation/Species-Programs.aspx.
26. World Association of Zoos and Aquariums, Global Species Management (WAZA, 2022); https://www.waza.org/priorities/conservation/conservation-breeding-programmes/global-species-management-plans/.
27. Botanic Gardens Conservation International, PlantSearch (BGCI, 2022); https://www.bgci.org/resources/bgci-databases/plantsearch/.
28. F. W. Allendorf, G. Luikart, *Conservation and the Genetics of Populations* (Wiley, 2009).
29. R. Frankham, J. D. Ballou, D. A. Briscoe, *Introduction to Conservation Genetics* (Cambridge Univ. Press, ed. 2, 2010) https://www.cambridge.org/core/books/introduction-to-conservation-genetics/696B4E558C93F7FBF9C33D6358EA7425.
30. J. Wood *et al*., Applying the zoo model to conservation of threatened exceptional plant species. *Conserv. Biol.* **34**, 1416–1425 (2020). doi: 10.1111/cobi.13503; pmid: 32233087
31. R. C. Lacy, Lessons from 30 years of population viability analysis of wildlife populations. *Zoo Biol.* **38**, 67–77 (2019). doi: 10.1002/zoo.21468; pmid: 30585658
32. B. W. Brook, L. W. Traill, C. J. A. Bradshaw, Minimum viable population sizes and global extinction risk are unrelated. *Ecol. Lett.* **9**, 375–382 (2006). doi: 10.1111/j.1461-0248.2006.00883.x; pmid: 16623722
33. L. W. Traill, C. J. A. Bradshaw, B. W. Brook, Minimum viable population size: A meta-analysis of 30 years of published estimates. *Biol. Conserv.* **139**, 159–166 (2007). doi: 10.1016/j.biocon.2007.06.011
34. D. H. Reed, J. J. O'Grady, B. W. Brook, J. D. Ballou, R. Frankham, Estimates of minimum viable population sizes for vertebrates and factors influencing those estimates. *Biol. Conserv.* **113**, 23–34 (2003). doi: 10.1016/S0006-3207(02)00346-4
35. R. Frankham, C. J. A. Bradshaw, B. W. Brook, Genetics in conservation management: Revised recommendations for the 50/500 rules, Red List criteria and population viability analyses. *Biol. Conserv.* **170**, 56–63 (2014). doi: 10.1016/j.biocon.2013.12.036
36. R. Frankham, J. D. Ballou, D. A. Briscoe, *Introduction to Conservation Genetics* (Cambridge Univ. Press, 2002).
37. C. M. Lees, J. Wilcken, Sustaining the Ark: The challenges faced by zoos in maintaining viable populations. *Int. Zoo Yearb.* **43**, 6–18 (2009). doi: 10.1111/j.1748-1090.2008.00066.x
38. R. Frankham, Genetic adaptation to captivity in species conservation programs. *Mol. Ecol.* **17**, 325–333 (2008). doi: 10.1111/j.1365-294X.2007.03399.x; pmid: 18173504
39. A. Trask *et al*., Extinct-in-the-wild species' last stand. *Science* **369**, 516–516 (2020). doi: 10.1126/science.abd4560; pmid: 32732417
40. L. J. Faust, S. T. Long, K. Perišin, J. L. Simonis, Uncovering challenges to sustainability of AZA Animal Programs by evaluating the outcomes of breeding and transfer recommendations with PMCTrack. *Zoo Biol.* **38**, 24–35 (2019). doi: 10.1002/zoo.21470; pmid: 30614074
41. J. Wang, Monitoring and managing genetic variation in group breeding populations without individual pedigrees. *Conserv. Genet.* **5**, 813–825 (2004). doi: 10.1007/s10592-004-1982-6
42. D. Clarke, EAZA Best Practice Guidelines for Partula snails (EAZA, 2019); https://www.eaza.net/assets/Uploads/CCC/BPG-2019/2019-Partula-sp-EAZA-Best-Practice-Guidelines-Approved.pdf.
43. J. A. Foster, S. K. Walsh, K. Havens, A. T. Kramer, J. B. Fant, Supporting long-term sustainability of ex situ collections using a pedigree-based population management approach. *Appl. Plant Sci.* **10**, e11491 (2022). doi: 10.1002/aps3.11491; pmid: 36258785
44. S. V. Wyse, J. B. Dickie, K. J. Willis, Seed banking not an option for many threatened plants. *Nat. Plants* **4**, 848–850 (2018). doi: 10.1038/s41477-018-0298-3; pmid: 30390079
45. K. O'Donnell, S. Sharrock, The contribution of botanic gardens to *ex situ* conservation through seed banking. *Plant Divers.* **39**, 373–378 (2017). doi: 10.1016/j.pld.2017.11.005; pmid: 30159531
46. S. Sharrock, Secretariat of the Convention on Biological Diversity, "Plant Conservation Report 2020: A review of progress in implementation of the Global Strategy for Plant Conservation 2011-2020" (CBD Technical Series No. 95, 2020); https://www.cbd.int/doc/publications/cbd-ts-95-en-hr.pdf.
47. S. V. Wyse, J. B. Dickie, Taxonomic affinity, habitat and seed mass strongly predict seed desiccation response: A boosted regression trees analysis based on 17 539 species. *Ann. Bot.* **121**, 71–83 (2018). doi: 10.1093/aob/mcx128; pmid: 29267906
48. R. Rauschkolb, L. Szczeparska, A. Kehl, O. Bossdorf, J. F. Scheepens, Plant populations of three threatened species experience rapid evolution under ex situ cultivation. *Biodivers. Conserv.* **28**, 3951–3969 (2019). doi: 10.1007/s10531-019-01859-9
49. D. J. Schoen, A. H. D. Brown, The Conservation of Wild Plant Species in Seed Banks: Attention to both taxonomic coverage and population biology will improve the role of seed banks as conservation tools. *Bioscience* **51**, 960–966 (2001). doi: 10.1641/0006-3568(2001)051[0960:TCOWPS]2.0.CO;2
50. V. Negrón-Ortiz, Pattern of expenditures for plant conservation under the Endangered Species Act. *Biol. Conserv.* **171**, 36–43 (2014). doi: 10.1016/j.biocon.2014.01.018
51. S. H. Butchart, A. J. Stattersfield, T. M. Brooks, Going or gone: Defining "Possibly Extinct" species to give a truer picture of recent extinctions. *Bull. Br. Ornithol. Club* **126**, 7 (2006).
52. S. H. M. Butchart *et al*., Measuring global trends in the status of biodiversity: Red list indices for birds. *PLOS Biol.* **2**, e383 (2004). doi: 10.1371/journal.pbio.0020383; pmid: 15510230
53. S. H. M. Butchart *et al*., Which bird species have gone extinct? A novel quantitative classification approach. *Biol. Conserv.* **227**, 9–18 (2018). doi: 10.1016/j.biocon.2018.08.014
54. M. J. Monroe, S. H. M. Butchart, A. O. Mooers, F. Bokma, The dynamics underlying avian extinction trajectories forecast a wave of extinctions. *Biol. Lett.* **15**, 20190633 (2019). doi: 10.1098/rsbl.2019.0633; pmid: 31847745
55. N. J. Collar, Preparing captive-bred birds for reintroduction: The case of the Vietnam Pheasant Lophura edwardsi. *Bird Conserv. Int.* **30**, 559–574 (2020). doi: 10.1017/S0959270920000039
56. S. Bas van Balen, N. J. Collar, The Vanishing Act: A History and Natural History of the Javan Pied Starling Gracupica jalla. *Ardea* **109**, 41–54 (2021). doi: 10.5253/arde.v109i1.a1

57. R. da Silva *et al*., Assessing the conservation potential of fish and corals in aquariums globally. *J. Nat. Conserv.* **48**, 1–11 (2019). doi: 10.1016/j.jnc.2018.12.001
58. Z. Cheng *et al*., Reintroduction, distribution, population dynamics and conservation of a species formerly extinct in the wild: A review of thirty-five years of successful Milu (Elaphurus davidianus) reintroduction in China. *Glob. Ecol. Conserv.* **31**, 01860 (2021). doi: 10.1016/j.gecco.2021.e01860
59. International Union for Conservation of Nature, 119 - Improving process and action to identify and recover 'Extinct in the Wild' species (IUCN, 2020); https://www.iucncongress2020.org/motion/119.
60. S. Canessa *et al*., Planning for ex situ conservation in the face of uncertainty. *Conserv. Biol.* **30**, 599–609 (2016). doi: 10.1111/cobi.12613; pmid: 26306549
61. E. H. Paxton, M. Laut, S. Enomoto, M. Bogardus, "Hawaiian forest bird conservation strategies for minimizing the risk of extinction: biological and biocultural considerations" (Univ. of Hawai'I, Hawai'i Cooperative Studies Unit Technical Report HCSU-103, 2022); http://hdl.handle.net/10790/5386.
62. V. Hemming *et al*., An introduction to decision science for conservation. *Conserv. Biol.* **36**, e13868 (2022). doi: 10.1111/cobi.13868; pmid: 34856010
63. T. G. Martin *et al*., Acting fast helps avoid extinction. *Conserv. Lett.* **5**, 274–280 (2012). doi: 10.1111/j.1755-263X.2012.00239.x
64. O. Byers, C. Lees, J. Wilcken, C. Schwitzer, The One Plan Approach: The philosophy and implementation of CBSG's approach to integrated species conservation planning. *WAZA Mag.* **14**, 2–5 (2013).
65. A. Hay, "Brugmansia aurea" (IUCN Red List of Threatened Species, 2014); https://www.iucnredlist.org/species/38124/58906215.
66. International Union for Conservation of Nature, Species Survival Commission, Guidelines for reintroductions and other conservation translocations. (IUCN, 2013); https://www.iucn.org/resources/publication/guidelines-reintroductions-and-other-conservation-translocations.
67. J. F. Brodie *et al*., Global policy for assisted colonization of species. *Science* **372**, 456–458 (2021). doi: 10.1126/science.abg0532; pmid: 33926936
68. Parks Australia, Christmas Island National Park, Basking on tropical oasis after decade in captivity (2021); https://parksaustralia.gov.au/christmas/news/basking-on-tropical-oasis-after-decade-in-captivity/.
69. Federal Register, Endangered and Threatened Wildlife and Plants; Establishment of a Nonessential Experimental Population of the Guam Kingfisher, or Sihek, on Palmyra Atoll, USA (Federal Register, 2022); https://www.federalregister.gov/documents/2022/08/31/2022-18571/endangered-and-threatened-wildlife-and-plants-establishment-of-a-nonessential-experimental.
70. T. Coote, G. Garcia, D. Clarke, Fourth year of Partula species reintroductions into natural habitat on Tahiti and Moorea. *Tentacle*, **26**, 35–38 (2018). doi: 10.1525/auk.2010.127.4.958
71. D. Smith *et al*., Extinct in the Wild data, Version Number, Zenodo (2023); doi: 10.5281/zenodo.7534501
72. E. VanderWerf, The Race to Save the World's Rarest Bird: The Discovery and Death of the Po'ouli. *Auk* **127**, 958–959 (2010). doi: 10.1525/auk.2010.127.4.958
73. Royal Botanic Gardens Kew, "Nesiota elliptica (Roxb.) Hook.f." (2023); https://powo.science.kew.org/taxon/urn:lsid:ipni.org:names:717646-1.
74. J. Gerlach, The Huahine tiny Partula, (2023); https://islandbiodiversity.com/arguta.htm.
75. J. Randerson, End of the trail for Polynesia's star snails. *New Sci.* **178**, 10–10 (2003). pmid: 14686412
76. J. Murray, E. Murray, M. S. Johnson, B. Clarke, The extinction of Partula on Moorea *Pac Sci.* **42**, 150–153 (1988). pmid: 14686412
77. S. Wells, The IUCN Species Survival Commission, "The extinction of endemic snails (genus Partula) in French Polynesia: is captive breeding the only solution" in *The Conservation Biology of Molluscs*, E. A. Kay, Ed. (IUCN SSC, 1995), ch. 3, pp. 25–28.
78. S. Tonge, Q. Bloxam, A review of the captive-breeding programme for Polynesian tree snails Partula spp. *Int. Zoo Yearb.* **30**, 51–59 (1991). doi: 10.1111/j.1748-1090.1991.tb03465.x
79. A. A. Cunningham, P. Daszak, Extinction of a Species of Land Snail Due to Infection with a Microsporidian Parasite. *Conserv. Biol.* **12**, 1139–1141 (1998). doi: 10.1046/j.1523-1739.1998.97485.x
80. M. Goren, Saving critically endangered fish species–utopia or practical idea? The story of the Yarqon bleak–Acanthobrama telavivensis (Cyprinidae) as a test case. *Aqua Int. J. Ichthyol.* **15**, 1–12 (2009).
81. Z. Pucek, International Union for Conservation of Nature, IUCN/SSC Bison Specialist Group, *European Bison: Status Survey and Conservation Action Plan* (IUCN, 2004).
82. M. Tokarska, C. Pertoldi, R. Kowalczyk, K. Perzanowski, Genetic status of the European bison Bison bonasus after extinction in the wild and subsequent recovery. *Mammal Rev.* **41**, 151–162 (2011). doi: 10.1111/j.1365-2907.2010.00178.x
83. J. W. Hinton, M. J. Chamberlain, D. R. Rabon Jr., Red Wolf (Canis rufus) Recovery: A Review with Suggestions for Future Research. *Animals* **3**, 722–744 (2013). doi: 10.3390/ani3030722; pmid: 26479530
84. J. P. Gibbs, E. A. Hunter, K. T. Shoemaker, W. H. Tapia, L. J. Cayot, Demographic outcomes and ecosystem implications of giant tortoise reintroduction to Española Island, Galapagos. *PLOS ONE* **9**, e110742 (2014). doi: 10.1371/journal.pone.0110742; pmid: 25350744
85. W. Tapia, H. B. Goldspiel, J. P. Gibbs, Introduction of giant tortoises as a replacement "ecosystem engineer" to facilitate restoration of Santa Fe Island, Galapagos. *Restor. Ecol.* **30**, e13476 (2022). doi: 10.1111/rec.13476
86. S. Wakefield, J. Knowles, W. Zimmermann, M. Dierendonck, *Status and Action Plan for the Przewalski's Horse (Equus ferus przewalskii)*. (2002).
87. J. R. Walters *et al*., Status of the California Condor(Gymnogyps californianus) and Efforts to Achieve Its Recovery. *Auk* **127**, 969–1001 (2010). doi: 10.1525/auk.2010.127.4.969
88. T. Belfield, T. Tunison, J. Chase, S. McDaniel, "Rare plant stabilization projects at Hawaii Volcanoes National Park, 1998-2008" (Technical Report 174, Pacific Cooperative Studies Unit, Univ. of Hawai`i, Honolulu, Hawai`i, 2011), p. 121.
89. M. K. Brock, G. M. Beauprez, The Rail Road To Recovery. *Endanger. Species Update* **18**, S6–S6 (2001); https://go.gale.com/ps/i.do?id=GALE%7CA75707011&sid=googleScholar&v=2.1&it=rissn=10813705&p=AONE&sw=w&userGroupName=anon~ff78efe0
90. US Fish & Wildlife Service, ETWP; Determination of Experimental Population Status for an Introduced Population of Guam Rails on Rota in the Commonwealth of the Northern Mariana Islands; 54 FR 43966 43970 (FWS, 1989); https://www.fws.gov/species-publication-action/etwp-determination-experimental-population-status-introduced-0.
91. A. Spalton, A brief history of the reintroduction of the Arabian oryx Oryx leucoryx into Oman 1980–1992. *Int. Zoo Yearb.* **32**, 81–90 (1993). doi: 10.1111/j.1748-1090.1993.tb03519.x
92. US Department of the Interior, US Geological Survey, J. Roelle, B. Miller, J. Godbey, D. Biggins, Recovery of the black-footed ferret: Progress and continuing challenges. (Scientific Investigations Report 2005-5293, 2005).

ACKNOWLEDGMENTS

We are very grateful to the three anonymous reviewers for their thorough review of this manuscript, and insightful and constructive guidance in improving it. We thank the following taxon experts for providing advice on the conservation history and present status of species we investigated: M. Böhm, I. Burfield, A. Cliffe, J. Donaldson, J.-P. Emery, J. Gerlach, F. Howarth, M. Koeck, C. Lugarini, D. Mallon, B. Masuda, T. Pearce, P. Pearce-Kelly, S. Putney, M. G. Quintana, M. Savage, S. Stadler, and A. Trask. Species icons are all public domain and were obtained from phylopic.org and were produced by T. G. Barnes, M. Michaud, E. Moody, F. Vaux, and S. Traver. **Funding:** D.S. and J.G.E. acknowledge funding from Research England. A.b.M. acknowledges funding from US Botanic Gardens and National Geographic Society (grant NGS-57037C-19). **Author contributions:** Conceptualization: D.S., T.A., S.D., J.G.E., T.G., C.J.H., N.A.L., Ax.M., J.P.R., and P.P.S. Methodology: D.S., T.A., S.D., J.G.E. Investigation: D.S., T.A., E.B.B., S.D., J.F., Ax.M., O.M. Supervision: J.G.E. Writing – original draft: D.S., T.A., J.G.E., T.G., C.J.H., N.A.L., Ax.M., J.P.R., P.P.S., A.T., Writing – review and editing: D.S., T.A., J.G.E., T.G., C.J.H., N.A.L., Ax.M. J.P.R., P.P.S., and A.T. **Competing interests:** Ax.M. is also affiliated with Clemson University (USA), Oxford University (UK), and University of Canterbury (NZ). **Data and materials availability:** All data are available in the main text, the supplementary materials, and the dataset archived at DOI: 10.5281/zenodo.7534501 (*71*). **License information:** Copyright © 2023 the authors, some rights reserved; exclusive licensee American Association for the Advancement of Science. No claim to original US government works. https://www.sciencemag.org/about/science-licenses-journal-article-reuse

SUPPLEMENTARY MATERIALS

science.org/doi/10.1126/science.add2889
Materials and Methods
Tables S1 to S5
References (*93*–*137*)

Submitted 8 June 2022; accepted 19 January 2023
10.1126/science.add2889

TECHNICAL COMMENT

PLANT SCIENCE

Comment on "Soybean photosynthesis and crop yield are improved by accelerating recovery from photoprotection"

Thomas Sinclair[1]*, James Specht[2], Kenneth Cassman[2], Larry Purcell[3], Thomas Rufty[4]

De Souza *et al.* (Research Articles, 19 Aug 2022, adc9831) recently claimed major soybean yield increases resulting from transformation of the nonphotochemical quenching mechanism of photosynthesis. However, there is little basis for the premise that such a transformation would result in yield increase. The field experiment was flawed and does not provide evidence for increases in crop yield.

The recent article titled "Soybean photosynthesis and crop yield are improved by accelerating recovery from photoprotection" by De Souza *et al.* (*1*) generated considerable media attention. Its promise of large crop yield increases by transforming a few genes was proposed as an important advance in increasing human food production. However, the article does not provide reliable experimental evidence to support claims of increased yields.

This photosynthesis project, funded in part by the Bill and Melinda Gates Foundation, has generated publications arguing that modification of the nonphotochemical quenching (NPQ) mechanism of photosynthesis will greatly increase photosynthetic productivity. The hypothesis is that the NPQ system is slow "to relax following the frequent sun-shade transitions that occur within crop canopies." Indeed, the article demonstrates that the time constant for "fast" and "moderate" relaxing components in wild-type plants is about 1.5 and 20 min, respectively.

We previously commented (*2*) on two fundamental premises of an earlier study (*3*) leading to the current report (*1*): (i) photosynthetic rates limit crop yield and (ii) relaxation times of the NPQ mechanism are limiting under field conditions. Extensive investigations for more than 50 years have not provided support for the first premise. For example, a major study in soybean (*Glycine max* L. Merr.) selected lines with up to 35% variation in photosynthetic rates but the lines showed no differences in seed yield (*4*). Most recently, a study of a genetically diverse population of soybean found leaf photosynthetic capacity was negatively correlated with seed yield (*5*). Overall soybean yields have doubled in the past 80 years (*6*) yet maximum photosynthetic capacity does not differ among older and newer cultivars (*7*). The failure to achieve increased yield in most major crop species by increasing photosynthesis capacity has been noted in several recent reviews (*8*–*10*). Ultimately, the limitation on crop yield is not carbon per se. Instead, for most regions globally, the availability of water and nutrient resources are inadequate to support construction of seed components to achieve higher grain yield (*11*).

The NPQ relaxation time argument is not consistent with the dominate source of light fluctuations, which are a result of wind-driven leaf movements that occur in crop canopies. For example in maize (*Zea mays* L.) canopies, the frequency of fluctuation between direct and shaded radiation levels was measured to be in the range of 10 to 50 seconds per cycle (*12*). In the experimental approach taken by De Souza *et al.* (*1*), transformed lines still had time constants of 5 min for the high-to-low light level transition. Due to this slow response time there would be very infrequent shifts to the low-light level status for the NPQ system, making the NPQ transformation essentially irrelevant in field production.

Ultimately, translating any proposed approach to increasing crop yield requires rigorous field experiments. The field experiment reported by De Souza *et al.* (*1*) did not meet several long-standing criteria established for conducting valid genotype yield comparisons. These criteria include (i) measured yield in multiple environments (a combination of locations and years), (ii) multiple-row field plots so that harvested rows are bordered, (iii) rows of sufficient length so that at least 0.5 m at the end of the harvested rows can be discarded, and (iv) yield is directly measured per unit land area. Field trials to determine potential yield differences between genotypes generally are found to require observations in at least 15 environments; even more in regions with high weather variability across years (*13*). De Souza *et al.* (*1*) obtained data in only two years at one location, and the nonsignificant results from the second year were ignored in their conclusion that transformed plants had higher yields. Further, the results in the single year are shown with symbols for significant differences that are inconsistent with common usage.

Single-row plots as used by De Souza *et al.* (*1*) meant no bordering of the harvested area by plants of the same genetic makeup and stature. Yield performance in single rows is dependent on neighboring rows. A neighboring row that grows differently for any number of reasons will influence the yield of adjacent rows. Single-row studies are only viewed as usable in preliminary field screens of major phenotypic characteristics, which must be followed by multiple-row and multiple-environments field plot trials to establish claims about yield. The single rows used by De Souza *et al.* (*1*) were only 0.56-m long (17 sown seeds), which is clearly inadequate for discarding at least 0.5 m at each end of the row.

We also question the method used to determine seed yield in De Souza *et al.* (*1*). While total seed weight of individual rows was apparently measured, this value was not reported as the yield. Instead, yield per plant was determined for each row and then multiplied by a common plant density of 24.7 plants m^{-2}, which was only 65% of the seed density at sowing. Calculation of seed yield based on constant plant density appears to have been an attempt to account for highly variable plant population among rows, which would greatly confound individual plant yield. Further, the derived yields of several transgenic lines were reported as 6 to 7 t ha^{-1}. If accurate, this would be among the highest scientifically based soybean yields ever reported in the US Midwest. Further, it would have occurred although their crop suffered an apparent plant population much lower than optimum (*14*) and a cutworm attack.

We conclude that the questionable premises for the study and the invalid field protocol offer no factual basis for concluding that a yield gain would occur with the NPQ transformation as claimed by De Souza *et al.* (*1*). We still see no evidence that crop yield can be substantially increased by alteration of crop photosynthesis.

[1]Agricultural Research Service, USDA, Gainesville, FL. [2]Dep Agronomy and Horticulture, University of Nebraska, Lincoln, NE. [3]Crop Science Research Center, University of Arkansas, Fayetteville, AR. [4]Crop and Soil Sciences Dep, North Carolina State University, Raleigh, NC.
*Corresponding author. Email: trsincla@ncsu.edu

REFERENCES AND NOTES

1. A. P. De Souzas *et al.*, *Science* **377**, 851–854 (2022).
2. T.R. Sinclair, T.W. Rufty, *Science eLetters* 14 December 2016.
3. J. Kromdijk *et al.*, *Science* **354**, 857–861 (2016).
4. D. M. Ford, R. Shibles, D. E. Green, *Crop Sci.* **23**, 517–520 (1983).
5. C. M. Montes *et al.*, *Genetics* **221**, iyac065 (2022).
6. K. Rincker *et al.*, *Crop Sci.* **54**, 1419–1432 (2014).
7. R. P. Koester, B. M. Nohl, B. W. Diers, E. A. Ainsworth, *Plant Cell Environ.* **39**, 1058–1067 (2016).
8. T. R. Sinclair, T. W. Rufty, R. S. Lewis, *Trends Plant Sci.* **24**, 1032–1039 (2019).

9. J. B. Passioura, *Crop Pasture Sci.* **71**, 517–528 (2020).
10. J. L. Araus, R. Sanchez-Bragado, R. Vicente, *J. Exp. Bot.* **72**, 3936–3955 (2021).
11. N. D. Mueller *et al*., *Nature* **490**, 254–257 (2012).
12. R. L. Desjardins, T. R. Sinclair, E. R. Lemon, *Agron. J.* **65**, 904–908 (1973).
13. T. R. Sinclair, A. Soltani, H. Marrou, M. Ghanem, V. Vadez, *Crop Sci.* **60**, 700–708 (2020).
14. M. Epler, S. Staggenborg, *Crop Manag.* **7**, 1–13 (2008).

ACKNOWLEDGMENTS

Competing Interests: The authors declare no competing interests. **License information:** Copyright © 2023 the authors, some rights reserved; exclusive licensee American Association for the Advancement of Science. No claim to original US government works. https://www.sciencemag.org/about/science-licenses-journal-article-reuse

Submitted 12 September 2022; accepted 26 January 2023
10.1126/science.ade8506

TECHNICAL RESPONSE

PLANT SCIENCE

Response to Comments on "Soybean photosynthesis and crop yield is improved by accelerating recovery from photoprotection"

Amanda P. De Souza[1], Steven J. Burgess[1], Lynn Doran[1], Lusya Manukyan[1], Jeffrey Hansen[1], Nina Maryn[2], Lauribel Leonelli[1], Krishna K. Niyogi[2,3], Stephen P. Stephen[1]*

We recently demonstrated that accelerating the relaxation of nonphotochemical quenching leads to higher soybean photosynthetic efficiency and yield. In response, Sinclair *et al*. assert that improved photosynthesis cannot improve crop yields and that there is only one valid experimental design for proving a genetic improvement in yield. We explain here why neither assertion is valid.

We recently demonstrated that the overexpression of *At*VDE, *At*PsbS, and *At*ZEP in soybeans accelerated the nonphotochemical quenching (NPQ) relaxation with a concomitant improvement in photosynthesis under fluctuating light, and that this improvement corresponded to an increase in yield in 1 year of a 2-year field experiment (*1*). Sinclair *et al*. (*2*) disputed that improvement in photosynthesis could lead to increased crop yields. Their principal claims are: (i) photosynthesis is not limiting to crop yields; (ii) speed of NPQ relaxation cannot impact yield, and (iii) the experimental design is flawed.

The argument that photosynthesis does not limit productivity claimed by Sinclair *et al*. (*2*) ignores an increasing body of work that demonstrates a strong link between photosynthesis and crop yield (*3*–*8*). As an example of that, figure 1 of the 3-year study by Koester *et al*. (*9*) does show a significant positive relationship between the daily integral of leaf photosynthetic CO_2 uptake per unit leaf area and cultivar release date. That means that the more recent higher yielding cultivars show higher leaf photosynthesis over the course of a day. This is in contrast to Sinclair *et al*.'s citation of this study to support their contention that photosynthesis has no relationship with improved soybean yields. More importantly, hundreds of studies of crop yield under elevated [CO_2] have already demonstrated the capacity of photosynthesis to enhance yield in C_3 crops (*10*, *11*). Artificial elevation of [CO_2] around C_3 crops has two direct physiological effects: (i) increase in the rate of photosynthetic CO_2 assimilation by the acceleration of carboxylation and competitive inhibition of photorespiration, and (ii) decreased stomatal conductance, which would be beneficial in water-limited conditions. Even if one claims that the main observed response is related to improved water relations, there are many field experiments under well-watered conditions that show a large yield increase across a wide range of C3 crops when [CO_2] is elevated (*11*). Most notably, some of the largest yield responses to elevated CO_2 are observed in paddy rice which is flooded with water throughout its growth cycle (*10*). This is commensurate with the observation that up-regulation of the primary photosynthetic carboxylase, Ribulose-1:5-bisphosphate carboxylase/oxygenase by a single gene manipulation, increased photosynthesis and yield in rice over four years of field trials with different levels of N nutrition (*3*). This all provides a wealth of experimental evidence showing that where photosynthesis is increased so are crop yields. We were not, as implied by Sinclair *et al*. (*2*), arguing that water and nutrient contents are unimportant. Rather, we were showing at this central location in the major soybean production area of North America, that photosynthesis can be improved to result in yield gains.

Leaves typically transmit about 10% of the light they receive, so when a portion of a leaf goes into the shade of another leaf, light level may drop by 90% of full sunlight due to absorption by the overlying leaf (*12*). In this situation, photosynthesis is strongly light-limited, and yet, a large portion of that energy will be "wasted" through continuing dissipation by NPQ. Therefore, any acceleration in the relaxation of NPQ will be beneficial to photosynthetic efficiency, no matter how short the duration of shading. High-frequency light fluctuation resulting from wind-driven leaf movements is not the only cause of light fluctuation in crop canopies. The continuous change in sun-leaf geometry through the day causes fluctuations throughout the canopy at intervals from a few minutes to hours (*13*, *14*), and intermittent cloud cover is also on such time scales. Computational modeling of these fluctuations in light and its effects on canopy carbon gain through photosynthesis provide a strong theoretical rationale for accelerating NPQ kinetics (*14*) and the benefits have already been demonstrated in practice (*15*).

Sinclair *et al*. (*2*) assert that a claim of improved yield potential could only be made with multiyear and multilocation field trials with 4-row plots and that we ignored our second year of data. The results of the second year were not ignored with full results for both years provided with the publication. A significant discussion was made on reporting the different environmental conditions of the two years and how this may have affected the outcome. We agree that these experiments were initial screenings and that establishing multilocation trials to test the impact across environments is the next necessary step. "Violated several long-standing criteria" are those of Sinclair *et al*. (*2*) and not absolute requirements. Criteria to determine yield differences between genotypes greatly vary among studies. Martin *et al*. (*16*), for instance, recommend that the evaluation of progenies of soybean plants should be done using short-row plots in two or three locations but only with a single replication. Moreira *et al*. (*17*) used a single-row plot size without replication and in a single year to determine yield in soybean progeny. Bruns (*18*) compared soybean yield using single-row plots versus twin-row plots over two locations and three years and did not observe differences in seed weight between the experimental designs. These studies exemplify that there is no one way to evaluate yield performance in soybeans. Indeed, single-row evaluation even without any replication is considered a reliable indicator of yield potential for a diverse number of soybean breeding programs (*19*).

A fundamental requirement of any experiment is that risk of systematic bias is eliminated, usually by randomization and replication. As reported, our experiment consisted of 15 experimental blocks each containing one row of the 8 transgenic lines plus one row of the nontransformed control (wildtype, WT). Positions within the block were randomized so that no genotype would be adjacent to the same genotype repeatedly. The most critical measure is the comparison between the WT from which the transgenic events were derived and propagated, in parallel with the transformants tested. We accept that there is a risk in single-row plots that if the adjacent row is shorter, then a faster growing row would intercept more light and any production

[1]Departments of Plant Biology and of Crop Sciences, Carl R Woese Institute for Genomic Biology, University of Illinois at Urbana-Champaign, Urbana, IL, USA. [2]Howard Hughes Medical Institute, Department of Plant and Microbial Biology, University of California, Berkeley, CA, USA. [3]Molecular Biophysics and Integrated Bioimaging Division, Lawrence Berkeley National Laboratory, Berkeley, CA, USA.
*Corresponding author. Email: slong@illinois.edu

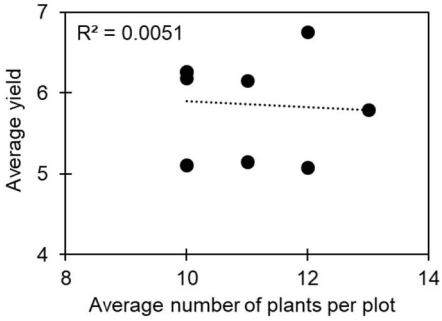

Fig. 1. Correlation between the number of plants per plot and yield. Data points represent the correlation between the average number of plants per plot and average yield (n = 15) for each transgenic line plus WT.

difference might be amplified. However, we did not find significant differences in height between the genotypes tested (fig. S19) (*1*). Further, our experimental design with 15 replicated blocks and a randomized row assignment for each line would largely cancel out any influence of neighboring rows on the performance of specific lines.

As noted in (*1*) there were losses due to cutworms in the first experiment. Those losses, however, did not significantly alter the average number of plants per plot per line (P = 0.688), eliminating the risk of any systematic error. There was no correlation between the average number of plants per plot with the yield results (R^2 = 0.005; Fig. 1), indicating that the differences observed in yield were not due to differences in plant population per plot. We accept that basing yield per hectare on single plant yields at this reduced density likely exaggerated absolute yield, but the proportionate increase of the transgenic events over the WT remains. Further, it is very common for small plot trials to deliver higher projected yields per hectare than observed at the farm scale (*20*, *21*).

In conclusion, our experimental design did not violate the principle underlying all comparisons of different lines, and eliminated sources of systematic bias. Therefore, it can be considered a demonstration that bioengineering of photosynthesis improves productivity in soybeans.

REFERENCES AND NOTES

1. A. P. De Souza *et al*., *Science* **377**, 851–854 (2022).
2. T. R. Sinclair, J. E. Specht, K. Cassman, L. Purcell, T. W. Rufty, Comment on "Soybean photosynthesis and crop yield are improved by accelerating recovery from photoprotection" (Science, 2022); 10.1126/science.ade8506.
3. D.-K. Yoon *et al*., *Nat. Food* **1**, 134–139 (2020).
4. X. Li *et al*., *Commun. Biol.* **3**, 151 (2020).
5. J.-H. Chen *et al*., *Nat. Plants* **6**, 570–580 (2020).
6. J. Wu *et al*., *Proc. Natl. Acad. Sci. U.S.A.* **116**, 23850–23858 (2019).
7. N. Friedland *et al*., *Sci. Rep.* **9**, 13028 (2019).
8. B. Wang *et al*., *Front. Plant Sci.* **9**, 709 (2018).
9. R. P. Koester, B. M. Nohl, B. W. Diers, E. A. Ainsworth, *Plant Cell Environ.* **39**, 1058–1067 (2016).
10. E. A. Ainsworth, S. P. Long, *Glob. Change Biol.* **27**, 27–49 (2021).
11. B. A. Kimball, *Agron. J.* **75**, 779–788 (1983).
12. R. A. Slattery, A. K. Grennan, M. Sivaguru, R. Sozzani, D. R. Ort, *J. Exp. Bot.* **67**, 4697–4709 (2016).
13. R. Pearcy, *Annu. Rev. Plant Physiol. Plant Mol. Biol.* **41**, 421–453 (1990).
14. X. G. Zhu, D. R. Ort, J. Whitmarsh, S. P. Long, *J. Exp. Bot.* **55**, 1167–1175 (2004).
15. J. Kromdijk *et al*., *Science* **354**, 857–861 (2016).
16. S. Martin, B. Dye, B. McBlain, *Crop Sci.* **30**, 74–79 (1990).
17. F. F. Moreira, A. A. Hearst, K. A. Cherkauer, K. M. Rainey, *Plant Methods* **15**, 139 (2019).
18. H. A. Bruns, *Agron. J.* **103**, 702–708 (2011).
19. J. Hegstad, G. Bollero, C. D. Nickell, *Crop Sci.* **39**, 1671–1675 (1999).
20. K. Gomez, S. De Datta, *Exp. Agric.* **7**, 87–92 (2008).
21. A. Probst, *Agron. J.* **35**, 662–666 (1943).

ACKNOWLEDGMENTS

Competing Interests: As noted in the original manuscript, L.L., K.N., and S.L., are inventors on a patent "Transgenic plants with increased photosynthesis efficiency and growth" WO2017205834A1.
License information: Copyright © 2023 the authors, some rights reserved; exclusive licensee American Association for the Advancement of Science. No claim to original US government works. https://www.sciencemag.org/about/science-licenses-journal-article-reuse

Submitted 19 October 2022; accepted 26 January 2023
10.1126/science.adf2189

By **Yana Suchikova**

A year of war

On 23 February 2022, I talked with the university rector about opening a new laboratory for nanomaterial synthesis. We planned to begin its implementation the next day. But our plans were shattered by powerful explosions on 24 February, as Russia's invasion of my country began. We sat in the rector's office and were silent. It was the loudest silence, as we wondered: What to do? How to work? What is next?

Three days later, Russian troops entered our city, Berdyansk, Ukraine, and we were under occupation. University activities were suspended; only we, the university management, went to work. A few days later, the Russian occupiers came to the university and took the rector at gunpoint, suggesting he go over to their side and head the new Russian Berdyansk University. He categorically refused, of course, and thankfully they let him go. But after that, we knew we could no longer safely work at the university.

We begin to meet in the park on a bench—a kind of university without walls, under the open sky. There is no mobile connection or internet. Meetings must be arranged in advance, changing the location each time. Everyone wanders around the city in search of Wi-Fi to catch the network for a minute and read the news: What is out there, in unoccupied Ukraine? Is the war still going on? Which side has the advantage?

Three months into the occupation, we are hiding in other people's apartments because it is dangerous to be in our own. At any minute people with assault rifles can come and take us "to the basement" because of our work with the university. I am afraid for my son, that when they come for me he will be at home and see it. He goes to live with my parents.

I am no longer afraid; the main thing is to be focused and to work. Work helps us escape the numbness and despair. We work to help Ukraine endure, and we work for its postwar recovery. I write scientific articles and process experimental data obtained before the war. A new kind of work is also added: taking care of the students who stayed in the dormitory. We find and bring them food, ensure the availability of drinking water, and conduct briefings in case of a nuclear attack.

"We have lost everything. But we have not lost faith in Ukraine."

Eventually, the rector is able to transfer the university's charter and seal to a new address in territory controlled by Ukraine and move the website to the cloud, because our servers were stolen by the occupiers. But all other property of the university remains in Berdyansk.

There is only one road left from the occupied city, which is called the Road of Death because many don't survive the shelling and abuse from the occupiers. Finally, my family and I manage to evacuate. I rent an apartment in a town 1000 kilometers from home. But I will stay in Ukraine. I am needed here and must work for the preservation of our university.

I write this article at dawn. There is no light or internet; the apartment is dark and cold. However, I have hot tea and the laptop will last for a few more hours. And then the lights will turn on. Behind darkness always comes light.

At 9 o'clock in the morning the light and internet appear. An air raid alarm sounds outside the window, which means there may be a massive missile attack today. I finish editing as quickly as possible and send off the article while there is still electricity.

Then the working day begins—meetings, research, writing scientific reports and grant applications. It will take place here in the kitchen because we do not have administrative premises. Still, I will be in a beautiful working dress and hairstyle, with makeup and perfume; we all try to look our best. We have nothing, we have lost everything. But we have not lost faith in Ukraine, the importance of our work, the hope for a bright future that will come after dark. We hold the scientific front. We are unbroken. We will survive. ■

Yana Suchikova is vice rector for scientific work of the Berdyansk State Pedagogical University. Send your career story to SciCareerEditor@aaas.org.

ILLUSTRATION: ROBERT NEUBECKER

2022 AAAS Fellows approved by the AAAS Council

In October 2022, the AAAS Council elected 505 members as Fellows of AAAS. Election as a Fellow honors members whose efforts on behalf of the advancement of science or its applications in service to society have distinguished them among their peers and colleagues. Presented by section affiliation, they are:

Section on Agriculture, Food, and Renewable Resources

Bryan William Brooks, *Baylor University*

John Chandler Cushman, *University of Nevada, Reno*

David M. Eissenstat, *Penn State University*

Gerrit Hoogenboom, *University of Florida*

Rupa S. Iyer, *Tarleton State University*

Wenbo Ma, *The Sainsbury Laboratory (United Kingdom)*

Maeli Melotto, *University of California, Davis*

Rosamond Lee Naylor, *Stanford University*

Cheryl Ann Palm, *University of Florida*

Bala Rathinasabapathi, *University of Florida*

Douglas D. Rhoads, *University of Arkansas*

M. A. Saghai Maroof, *Virginia Tech*

José Eduardo Portela Santos, *University of Florida*

Shin-Han Shiu, *Michigan State University*

Whendee L. Silver, *University of California, Berkeley*

Dominique Van Der Straeten, *Ghent University (Belgium)*

Doreen Ware, *US Department of Agriculture*

Yinong Yang, *Penn State University*

Yanhai Yin, *Iowa State University*

Yunde Zhao, *University of California, San Diego*

Section on Anthropology

Patricia Louise Crown, *University of New Mexico*

Eduardo Fernandez-Duque, *Yale University*

David Allen Himmelgreen, *University of South Florida*

Katie Hinde, *Arizona State University*

Sarah B. Hrdy, *University of California, Davis*

Lynne A. Isbell, *University of California, Davis*

William A. Lovis, *Michigan State University*

Theodore G. Schurr, *University of Pennsylvania*

Chet C. Sherwood, *George Washington University*

Michael R. Waters, *Texas A&M University*

Amber Wutich, *Arizona State University*

Section on Astronomy

Catherine C. Espaillat, *Boston University*

Gary Joseph Ferland, *University of Kentucky*

Catharine D. Garmany, *National Optical-Infrared Astronomy Research Laboratory*

Saurabh W. Jha, *Rutgers, The State University of New Jersey*

Priyamvada Natarajan, *Yale University*

Joel Parriott, *National Science Foundation*

Rita Maria Sambruna, *NASA Goddard Space Flight Center*

Robert J. Scherrer, *Vanderbilt University*

Ellen R. Stofan, *Smithsonian Institution*

Tommaso Treu, *University of California, Los Angeles*

Ethan Tecumseh Vishniac, *Johns Hopkins University*

Dennis Zaritsky, *University of Arizona*

Nicolle E. B. Zellner, *Albion College*

Section on Atmospheric & Hydrospheric Sciences

Jennifer M. Collins, *University of South Florida*

José D. Fuentes, *Penn State University*

Mae Sexauer Gustin, *University of Nevada, Reno*

Atul K. Jain, *University of Illinois Urbana-Champaign*

Xiaohong Liu, *Texas A&M University*

Gordon McBean, *Western University (Canada)*

Stephen A. Montzka, *National Oceanic and Atmospheric Administration*

Carlos A. Nobre, *University of São Paulo (Brazil)*

Lorenzo M. Polvani, *Columbia University in the City of New York*

Robert G. M. Spencer, *Florida State University*

Hang Su, *Max Planck Institute for Chemistry (Germany)*

Rashid Ussif Sumaila, *University of British Columbia (Canada)*

Peter E. Thornton, *Oak Ridge National Laboratory*

Roger M. Wakimoto, *University of California, Los Angeles*

Section on Biological Sciences

Nihal Ahmad, *University of Wisconsin-Madison*

Evangelyn C. Alocilja, *Michigan State University*

Carol Arnosti, *University of North Carolina at Chapel Hill*

Avi Ashkenazi, *Genentech*

Alfred Ayala, *Brown University Warren Alpert Medical School/Rhode Island Hospital*

Melinda A. Beck, *University of North Carolina at Chapel Hill*

Linda S. Birnbaum, *NIH National Institute of Environmental Health Sciences*

Patricia L. R. Brennan, *Mount Holyoke College*

Stuart Brody, *University of California, San Diego*

Emilio Miguel Bruna, *University of Florida*

Vivian Budnik, *University of Massachusetts Chan Medical School*

Stephen Buratowski, *Harvard Medical School*

Andrea L. Case, *Kent State University*

Patricia A. Champion, *University of Notre Dame*

Shiuan Chen, *Beckman Research Institute of City of Hope*

Xin Chen, *Johns Hopkins University*

Lars Chittka, *Queen Mary University of London (United Kingdom)*

Michael L. Collyer, *Chatham University*

Liza S. Comita, *Yale University*

Paul R. Copeland, *Rutgers New Jersey Medical School*

Anita H. Corbett, *Emory University*

Gail A. Cornwall, *Texas Tech University Health Sciences Center*

Jorge Cortes Nuñez, *University of Costa Rica*

Christopher Ashley Cullis, *Case Western Reserve University*

Sandra M. Davern, *Oak Ridge National Laboratory*

Goggy Davidowitz, *University of Arizona*

Valérie de Crécy-Lagard, *University of Florida*

Enrique M. De La Cruz, *Yale University*

David G. Drubin, *University of California, Berkeley*

David Cameron Duffy, *University of Hawai'i at Mānoa*

Lee A. Dyer, *University of Nevada, Reno*

Aimee L. Edinger, *University of California, Irvine*

J. Erika Jeannine Edwards, *Yale University*

Edward H. Egelman, *University of Virginia*

Michael S. Engel, *University of Kansas*

Vanessa O. Ezenwa, *Yale University*

W. Chris Funk, *Colorado State University*

Raghavendra Gadagkar, *Indian Institute of Science (India)*

Richard H. Gomer, *Texas A&M University*

Michael Allen Gore, *Cornell University*

Miriam L. Greenberg, *Wayne State University*

Brian D. Gregory, *University of Pennsylvania*

Steven B. Haase, *Duke University*

C. Drew Harvell, *Cornell University*

Rebecca Wright Heald, *University of California, Berkeley*

Oleh Khalimonchuk, *University of Nebraska-Lincoln*

Jan K. Kitajewski, *University of Illinois Chicago*

Heather M. Leslie, *University of Maine*

David B. Lindenmayer, *Australian National University*

Mary S. Lipton, *Pacific Northwest National Laboratory*

Zhenkun Lou, *Mayo Clinic*

David Lyden, *Weill Cornell Medicine*

Jian Ma, *Carnegie Mellon University*

Stanley Maloy, *San Diego State University*

John M. Marzluff, *University of Washington*

Mitch McVey, *Tufts University*

David Dudley Moore, *University of California, Berkeley*

Leonie C. Moyle, *Indiana University Bloomington*

Robert G. Moyle, *University of Kansas*

Aindrila Mukhopadhyay, *Lawrence Berkeley National Laboratory*

George F. Muschler, *Cleveland Clinic Lerner Research Institute*

Kenneth A. Nagy, *University of California, Los Angeles*

Irene Lucile Garcia Newton, *Indiana University Bloomington*

Maria E. Orive, *University of Kansas*

Anna-Lisa Paul, *University of Florida*

Wolfgang Peti, *University of Connecticut Health Center School of Medicine*

Malin L. Pinsky, *Rutgers, The State University of New Jersey*

Ann H. Reid, *National Center for Science Education*

Christina L. Richards, *University of South Florida*

Leslie J. Rissler, *National Science Foundation*

Douglas N. Robinson, *Johns Hopkins University School of Medicine*

Luiz A. Rocha, *California Academy of Sciences*

Alistair Rogers, *Brookhaven National Laboratory*

Remo Rohs, *University of Southern California*

Lijun Rong, *University of Illinois College of Medicine at Chicago*

Kevin Martin Ryan, *The Beatson Institute for Cancer Research (United Kingdom)*

Matthew E. Smith, *University of Florida*

Thomas James Smith, *The University of Texas Medical Branch*

Pamela S. Soltis, *University of Florida*

Joseph W. Spatafora, *Oregon State University*

Lukasz Lech Stelinski, *University of Florida*

Nan-Yao Su, *University of Florida*

S. Joshua Swamidass, *Washington University in St Louis*

Maurice S. Swanson, *University of Florida College of Medicine*

Robert Tjian, *University of California, Berkeley*

Elizabeth J. Tran, *Purdue University*

M. Stephen Trent, *University of Georgia*

Neil Durie Tsutsui, *University of California, Berkeley*

Daniel Wall, *University of Wyoming*

Xiu-Feng (Henry) Wan, *University of Missouri-Columbia*

Nian Wang, *University of Florida*

Richard Megumi Watanabe, *University of Southern California Keck School of Medicine*

Katrina M. Waters, *Pacific Northwest National Laboratory*

Marta L. Wayne, *University of Florida*

Virginia M. Weis, *Oregon State University*

Claus O. Wilke, *The University of Texas at Austin*

Carmen J. Williams, *NIH National Institute of Environmental Health Sciences*

Loren Dean Williams, *Georgia Institute of Technology*

Susan H. Williams, *Ohio University*

Richard A. Wilson, *University of Nebraska-Lincoln*

Rachael Winfree, *Rutgers, The State University of New Jersey*

De-Yu Xie, *North Carolina State University*

Wei Xu, *University of Wisconsin-Madison*

Bing Yang, *University of Missouri-Columbia/Donald Danforth Plant Science Center*

Howard A. Young, *NIH National Cancer Institute*

Xiaoxi Zhuang, *University of Chicago*

Section on Chemistry

Rufina G. Alamo, *Florida Agricultural and Mechanical University/Florida State University*

Lane A. Baker, *Texas A&M University*

Vahe Bandarian, *University of Utah*

Matthew C. Beard, *National Renewable Energy Laboratory*

Eric R. Bittner, *University of Houston*

Jon P. Camden, *University of Notre Dame*

Paul Chirik, *Princeton University*

Kyoung-Shin Choi, *University of Wisconsin-Madison*

Michael T. Crimmins, *University of North Carolina at Chapel Hill*

Ana de Bettencourt-Dias, *University of Nevada*

Ram Devanathan, *Pacific Northwest National Laboratory*

Alexander C. Drohat, *University of Maryland School of Medicine*

Annaliese K. Franz, *University of California, Davis*

Arturo J. Hernández-Maldonado, *University of Puerto Rico-Mayagüez*

Malika Jeffries-EL, *Boston University*

Kurt Wolfgeng Kolasinski, *West Chester University*

Elizabeth A. Komives, *University of California, San Diego*

Carol Korzeniewski, *Texas Tech University*

Stosh A. Kozimor, *Los Alamos National Laboratory*

Audrey L. Lamb, *The University of Texas at San Antonio*

James W. Leahy, *University of South Florida*

Juliette T. J. Lecomte, *Johns Hopkins University*

Gina MacDonald, *James Madison University*

John A. McLean, *Vanderbilt University*

Liviu M. Mirica, *University of Illinois Urbana-Champaign*

Rangachary (Mukund) Mukundan, *Los Alamos National Laboratory*

Teri W. Odom, *Northwestern University*

Frank E. Osterloh, *University of California, Davis*

Tanja Pietraß, *Los Alamos National Laboratory*

Adam Madison Rawlett, *Army Research Laboratory*

V. Prakash Reddy, *Missouri University of Science and Technology*

Garry Rumbles, *National Renewable Energy Laboratory*

Aaron D. Sadow, *Iowa State University*

Eric J. Schelter, *University of Pennsylvania*

Norbert F. Scherer, *University of Chicago*

Eric W. Schmidt, *University of Utah*

Wendy J. Shaw, *Pacific Northwest National Laboratory*

Jennifer S. Shumaker-Parry, *University of Utah*

Yi Tang, *University of California, Los Angeles*

Sergei Tretiak, *Los Alamos National Laboratory*

Lisa Marie Utschig, *Argonne National Laboratory*

Akos Vertes, *George Washington University*

Marcus Weck, *New York University*

Section on Dentistry and Oral Health Sciences

Azeez Butali, *University of Iowa*

Marcelo Freire, *J. Craig Venter Institute*

Purnima S. Kumar, *University of Michigan*

Daniel Malamud, *New York University*

Pamela Crotty Yelick, *Tufts University School of Dental Medicine*

Section on Education

Angela Marie Calabrese Barton, *University of Michigan*

Ann M. L. Cavallo, *The University of Texas at Arlington*

Shuchismita Dutta, *Rutgers, The State University of New Jersey*

James Steven Fairweather, *Michigan State University (Emeritus)*

Patrick Hamilton, *Science Museum of Minnesota*

Sharon M. Homer-Drummond, *Tri-County Technical College*

Cheryl L. B. Manning, *Northern Illinois University*

Jeffrey T. Olimpo, *The University of Texas at El Paso*

Donna J. Petersen, *University of South Florida*

Ainissa G. Ramirez, *Author/Science Writer*

Sandra L. Richardson, *National Science Foundation*

Marion C. Usselman, *Georgia Institute of Technology*

Margaret A. Waterman, *Southeast Missouri State University*

Jason R. Wiles, *Syracuse University*

Section on Engineering

Linda M. Abriola, *Brown University*

Burcu H. Akinci, *Carnegie Mellon University*

Stelios T. Andreadis, *State University of New York at Buffalo*

John H. Booske, *University of Wisconsin-Madison*

Jonathan Cagan, *Carnegie Mellon University*

Peter J. Delfyett, *University of Central Florida*

Ronald F. DeMara, *University of Central Florida*

Lily (Ageliki) Elefteriadou, *University of Florida*

Gregory L. Fenves, *Emory University*

Shubhra Gangopadhyay, *University of Missouri-Columbia*

Tryphon T. Georgiou, *University of California, Irvine*

Keisuke Goda, *The University of Tokyo (Japan)*

Vivek K. Goyal, *Boston University*

Samuel Graham, *University of Maryland, College Park*

Carol A. Handwerker, *Purdue University*

Yih-Fang Huang, *University of Notre Dame*

Bahram Javidi, *University of Connecticut*

Shaoyi Jiang, *Cornell University*

Ahsan Kareem, *University of Notre Dame*

Joerg Lahann, *University of Michigan*

Ajay P. Malshe, *Purdue University*

Diana Marculescu, *The University of Texas at Austin*

Prabhat Mishra, *University of Florida*

Massoud Pedram, *University of Southern California*

John H. Perepezko, *University of Wisconsin-Madison*

Kristin Aslaug Persson, *University of California, Berkeley*

Pengyu Ren, *The University of Texas at Austin*

Fabio H. Ribeiro, *Purdue University*

Carlos M. Rinaldi-Ramos, *University of Florida*

M. Taher A. Saif, *University of Illinois Urbana-Champaign*

Julie M. Schoenung, *University of California, Irvine*

Charles M. Schroeder, *University of Illinois Urbana-Champaign*

Warren D. Seider, *University of Pennsylvania*

Sindee L. Simon, *North Carolina State University*

Abraham D. Stroock, *Cornell University*

Jeanne M. VanBriesen, *Carnegie Mellon University*

Tza-Huei (Jeff) Wang, *Johns Hopkins University*

Jennifer L. West, *University of Virginia*

Karen I. Winey, *University of Pennsylvania*

Fengqi You, *Cornell University*

Section on General Interest in Science and Engineering

Anthony Theodore Chronopoulos, *University of Texas San Antonio*

Valeri Roxanne Bogucka, *The University of Texas at Austin*

Timir Datta, *University of South Carolina*

Kara (Villamil) Gavin, *University of Michigan*

William K. Hallman, *Rutgers, The State University of New Jersey*

Deborah L. Illman, *University of Washington (Retired)*

Larry Klein, *LK Productions*

Asheley R. Landrum, *Texas Tech University*

Sunshine Menezes, *University of Rhode Island Metcalf Institute*

Kathryn (Kate) Moran, *University of Victoria/Ocean Networks Canada*

Czerne M. Reid, *University of Florida*

Section on Geology and Geography

Laurie C. Anderson, *South Dakota School of Mines and Technology*

Lori Ann Bettison-Varga, *Natural History Museums of Los Angeles County*

Rónadh Cox, *Williams College*

Steven L. D'Hondt, *University of Rhode Island*

Nicholas P. Dunning, *University of Cincinnati*

Doug Erwin, *Smithsonian National Museum of Natural History*

Carmala N. Garzione, *University of Arizona*

Robert T. Gregory, *Southern Methodist University*

Laura A. Guertin, *Penn State Brandywine*

David W. Hyndman, *The University of Texas at Dallas*

Wendy Elizabeth Jepson, *Texas A&M University*

Kirk R. Johnson, *Smithsonian National Museum of Natural History*

Robert E. Kopp, *Rutgers, The State University of New Jersey*

Melinda Jean Laituri, *Colorado State University*

Jei (Jackie) Li, *University of Michigan*

Dorothy Marie Peteet, *NASA Goddard Space Flight Center/ Columbia University*

Dar A. Roberts, *University of California, Santa Barbara*

Kevin M. Rosso, *Pacific Northwest National Laboratory*

Blaire Van Valkenburgh, *University of California, Los Angeles*

Peter Daniel Wilf, *Penn State University*

Section on History and Philosophy of Science

Erik M. Conway, *NASA Jet Propulsion Laboratory*

Amy Lauren Fairchild, *The Ohio State University*

Alan C. Love, *University of Minnesota*

Roberta L. Millstein, *University of California, Davis*

Section on Industrial Science and Technology

Anice Anderson, *Private Engineering, Consulting, and Philanthropy*

Raymond G. Beausoleil, *Hewlett Packard Enterprise*

Antonio J. Conejo, *The Ohio State University*

Laurie E. Locascio, *National Institute of Standards and Technology*

KC Morris, *National Institute of Standards and Technology*

John C. Wagner, *Idaho National Laboratory*

Ji-Cheng (JC) Zhao, *University of Maryland, College Park*

Section on Information, Computing, and Communication

Scott Aaronson, *The University of Texas at Austin*

Remzi H. Arpaci-Dusseau, *University of Wisconsin-Madison*

Valerie B. Barr, *Bard College*

Mitra Basu, *National Science Foundation*

Yiran Chen, *Duke University*

Marie desJardins, *desJardins Consulting*

Kevin Fu, *Northeastern University*

Yun Fu, *Northeastern University*

Lise Getoor, *University of California, Santa Cruz*

Stephen Marshall Goodnick, *Arizona State University*

Deborah Gracio, *Pacific Northwest National Laboratory*

Mohammad Taghi Hajiaghayi, *University of Maryland, College Park*

Haym Hirsh, *Cornell University*

Srikanth V. Krishnamurthy, *University of California, Riverside*

James F. Kurose, *University of Massachusetts*

Insup Lee, *University of Pennsylvania*

Keqin Li, *State University of New York at New Paltz*

David J. Love, *Purdue University*

Dana S. Nau, *University of Maryland, College Park*

Padma Raghavan, *Vanderbilt University*

Grigore Rosu, *University of Illinois Urbana-Champaign*

Valerie E. Taylor, *Argonne National Laboratory*

Jaideep S. Vaidya, *Rutgers, The State University of New Jersey*

XiaoFeng Wang, *Indiana University Bloomington*

Alexander L. Wolf, *University of California, Santa Cruz*

Mohammed J. Zaki, *Rensselaer Polytechnic Institute*

Section on Linguistics and Language Science

Emily M. Bender, *University of Washington*

Alec Marantz, *New York University*

D. Kimbrough Oller, *University of Memphis*

Elisabeth O. Selkirk, *University of Massachusetts Amherst*

Laura Wagner, *The Ohio State University*

Section on Mathematics

Abba B. Gumel, *University of Maryland, College Park*

Brendan Hassett, *Brown University*

Hans G. Kaper, *Georgetown University*

Irena Lasiecka, *University of Memphis*

Talitha M. Washington, *Clark Atlanta University/Atlanta University Center*

Peter Winkler, *Dartmouth College*

Section on Medical Sciences

Zvia Agur, *Institute for Medical BioMathematics (Israel)*

Ross Andel, *Arizona State University*

Avery August, *Cornell University*

Danika L. Bannasch, *University of California, Davis, School of Veterinary Medicine*

William Anthony Beltran, *University of Pennsylvania*

John A. Blaho, *City University of New York*

Gerard Conrad Blobe, *Duke University*

Atul Butte, *University of California, San Francisco*

Thomas E. Carey, *University of Michigan*

Peter C. Dedon, *Massachusetts Institute of Technology*

Marina Pasca di Magliano, *University of Michigan*

Cynthia E. Dunbar, *NIH National Heart, Lung, and Blood Institute*

Eric A. Engels, *NIH National Cancer Institute*

Giamila Fantuzzi, *University of Illinois Chicago*

Mark W. Feinberg, *Harvard Medical School/Brigham and Women's Hospital*

Bettina C. Fries, *Renaissance School of Medicine at Stony Brook University*

Elodie Ghedin, *NIH National Institute of Allergy and Infectious Diseases*

Kathy K. Griendling, *Emory University School of Medicine*

Johann Eli Gudjonsson, *University of Michigan Medicine*

Tobias M. Hohl, *Memorial Sloan Kettering Cancer Center*

M. Luisa Iruela-Arispe, *Northwestern University*

Reshma Jagsi, *Emory University*

Donald L. Jarvis, *University of Wyoming*

Thirumala-Devi Kanneganti, *St. Jude Children's Research Hospital*

Stephen Y. Lai, *The University of Texas MD Anderson Cancer Center*

Pamela J. Lein, *University of California, Davis, School of Veterinary Medicine*

Pu Paul Liu, *NIH National Human Genome Research Institute*

Benjamin Alan Lopman, *Emory University Rollins School of Public Health*

Carolyn Cidis Meltzer, *University of Southern California Keck School of Medicine*

Peter Nagele, *University of Chicago*

Lisa Kay Nolan, *University of Georgia*

Asma Nusrat, *University of Michigan*

Cliona O'Farrelly, *Trinity College Dublin (Ireland)*

Ghislain Opdenakker, *Rega Institute for Medical Research at KU Leuven (Belgium)*

Timothy P. Padera, *Massachusetts General Hospital*

Charles A. Parkos, *University of Michigan*

Wellington Pham, *Vanderbilt University School of Medicine*

Rajini Rao, *Johns Hopkins University*

Antony Rosen, *Johns Hopkins University School of Medicine*

Mark A. Rubin, *University of Bern (Switzerland)*

Arnold Schwartz, *University of Cincinnati College of Medicine*

Randy J. Seeley, *University of Michigan*

Cullen M. Taniguchi, *The University of Texas MD Anderson Cancer Center*

Victor J. Torres, *New York University Grossman School of Medicine*

Apostolia M. Tsimberidou, *The University of Texas MD Anderson Cancer Center*

Anthony T. Vella, *University of Connecticut, UCONN Health, School of Medicine*

Donata Vercelli, *University of Arizona*

Harel Weinstein, *Weill Cornell Medicine*

Lee Scott Weinstein, *NIH National Institute of Diabetes and Digestive and Kidney Diseases*

David S. Weiss, *Emory University School of Medicine*

Jianhua Yu, *City of Hope National Medical Center and Beckman Research Institute*

Lynn Zechiedrich, *Baylor College of Medicine*

Elias A. Zerhouni, *Johns Hopkins University (Emeritus)/National Institutes of Health (Retired)*

Section on Neuroscience

Gregory Kent Bergey, *Johns Hopkins University School of Medicine*

Cornelia Christine Bergmann, *Cleveland Clinic Lerner Research Institute*

Karen Faith Berman, *NIH National Institute of Mental Health*

William A. Carlezon, *Harvard Medical School/McLean Hospital*

Kenneth C. Catania, *Vanderbilt University*

Geert J. de Vries, *Georgia State University*

Xinzhong Dong, *Johns Hopkins University School of Medicine/ Howard Hughes Medical Institute*

Barry John Everitt, *University of Cambridge (United Kingdom)*

Maria Laura Feltri, *University at Buffalo*

Bonnie Lynne Firestein, *Rutgers, The State University of New Jersey*

David J. Freedman, *University of Chicago*

Christian L. Lorson, *University of Missouri-Columbia*

Donna M. Martin, *University of Michigan Medicine*

Christopher J. McBain, *NIH Eunice Kennedy Shriver National Institute of Child Health and Human Development*

Michelle M. Mielke, *Wake Forest School of Medicine*

Guo-Li Ming, *University of Pennsylvania*

Bruce Ovbiagele, *University of California, San Francisco*

Murali Prakriya, *Northwestern University*

John Huntington Reynolds, *Salk Institute for Biological Studies*

Julie H. Simpson, *University of California, Santa Barbara*

Georg F. Striedter, *University of California, Irvine*

Joni Wallis, *University of California, Berkeley*

Section on Pharmaceutical Sciences

Donna M. Huryn, *University of Pittsburgh School of Pharmacy*

Scott Harold Kaufmann, *Mayo Clinic*

Ikhlas A. Khan, *University of Mississippi*

Sanjay K. Srivastava, *Texas Tech University Health Sciences Center*

Sean D. Sullivan, *University of Washington*

Changquan Calvin Sun, *University of Minnesota*

Duxin Sun, *University of Michigan*

John Richard Traynor, *University of Michigan Medicine*

Paul Workman, *Institute of Cancer Research (United Kingdom)*

Wen Xie, *University of Pittsburgh School of Pharmacy*

Section on Physics

Mark John Bowick, *University of California, Santa Barbara*

Alexander Chernyshev, *University of California, Irvine*

Michael (Misha) Chertkov, *University of Arizona*

Roy Clarke, *University of Michigan*

Massimiliano Di Ventra, *University of California, San Diego*

James N. Eckstein, *University of Illinois Urbana-Champaign*

Jason Stewart Gardner, *Oak Ridge National Laboratory*

James Alexander Glazier, *Indiana University Bloomington*

David Goldhaber-Gordon, *Stanford University*

Philippe Guyot-Sionnest, *University of Chicago*

Thomas C. Killian, *Rice University*

Lena F. Kourkoutis, *Cornell University*

Wolfgang Losert, *University of Maryland, College Park*

William H. Matthaeus, *University of Delaware*

John F. Mitchell, *Argonne National Laboratory*

David A. Muller, *Cornell University*

Howard A. Padmore, *Lawrence Berkeley National Laboratory*

Christopher J. Palmstrøm, *University of California, Santa Barbara*

Raghuveer Parthasarathy, *University of Oregon*

Lois Pollack, *Cornell University*

Mohit Randeria, *The Ohio State University*

Robert Rosner, *University of Chicago*

Jennifer L. Ross, *Syracuse University*

Dan M. Stamper-Kurn, *University of California, Berkeley*

Rebecca Surman, *University of Notre Dame*

Yuri Suzuki, *Stanford University*

Alessandro Vespignani, *Northeastern University*

Robert L. Willett, *Nokia Bell Labs*

Jennifer J. Wiseman, *NASA Goddard Space Flight Center*

Xiaoqin Zou, *University of Missouri-Columbia*

Section on Psychology

Christine Dunkel Schetter, *University of California, Los Angeles*

Kara D. Federmeier, *University of Illinois Urbana-Champaign*

Jean E. Fox Tree, *University of California, Santa Cruz*

Barbara L. Fredrickson, *University of North Carolina at Chapel Hill*

Susan A. Gelman, *University of Michigan*

Jill Martine Harkavy-Friedman, *American Foundation for Suicide Prevention*

Gregory Scott Hickok, *University of California, Irvine*

Sheri L. Johnson, *University of California, Berkeley*

Grazyna Kochanska, *University of Iowa*

David J. Lewkowicz, *Yale University*

James S. Magnuson, *University of Connecticut/Basque Center on Cognition, Brain, and Language*

Richard E. Mayer, *University of California, Santa Barbara*

Rodolfo Mendoza-Denton, *University of California, Berkeley*

Mary C. Murphy, *Indiana University Bloomington*

Linda A. Teplin, *Northwestern University Feinberg School of Medicine*

Section on Social, Economic, and Political Sciences

Judith D. Auerbach, *University of California, San Francisco*

Trudy Ann Cameron, *University of Oregon*

Richard Dembo, *University of South Florida*

Sonalde Desai, *University of Maryland, College Park*

Amos Golan, *American University*

Joseph C. Hermanowicz, *University of Georgia*

Matthew O. Jackson, *Stanford University*

Walter Richard Mebane, *University of Michigan*

Wendy A. Naus, *Consortium of Social Science Associations*

Gary Orfield, *University of California, Los Angeles*

Joshua L. Rosenbloom, *Iowa State University*

Juliet B. Schor, *Boston College*

Ronald L. Simons, *University of Georgia*

Marjorie S. Zatz, *University of California, Merced*

Section on Societal Impacts of Science and Engineering

Gillian Bowser, *Colorado State University*

Ali Douraghy, *US Department of Energy*

Mónica Ivelisse Feliú Mójer, *Ciencia Puerto Rico/Science Communication Lab*

David M. Hart, *George Mason University*

Kristin M. Omberg, *Pacific Northwest National Laboratory*

Joanne Padrón Carney, *American Association for the Advancement of Science*

Deborah D. Stine, *Science and Technology Policy Academy*

Kate E. Stoll, *American Association for the Advancement of Science*

Section on Statistics

Catherine A. Calder, *The University of Texas at Austin*

Jacqueline M. Hughes-Oliver, *North Carolina State University*

Marek Kimmel, *Rice University*

Ping Ma, *University of Georgia*

Wendy L. Martinez, *US Census Bureau*

Dionne L. Price, *US Food and Drug Administration*

Peihua Qiu, *University of Florida*

Hui Zou, *University of Minnesota*

Call for nomination of 2023 Fellows

The Executive Office invites groups of three previously elected AAAS Fellows in good standing to nominate eligible AAAS members for election as Fellows. The 2023 Fellows nomination cycle is open from 31 January to 25 April, 2023 at 11:59 p.m. Eastern time.

A member whose efforts on behalf of the advancement of science or its applications are scientifically or socially distinguished and who has been a continuous member for the 4-year period leading up to the year of nomination may, by virtue of such meritorious contribution, be elected a Fellow by the Council.

Examples of areas in which nominees may have made significant contributions are research; teaching; technology; services to professional societies; administration in academe, industry, and government; and communicating and interpreting science to the public. Fellows are elected annually by the AAAS Council from the list of approved nominations from the Section Steering Committee. AAAS encourages diverse nominations that include a fair representation of women, minorities, and persons with disabilities. Fellows are expected to uphold the commonly held standards of professional ethics and scientific integrity.

AAAS will only accept nominations through our online submission portal. We will no longer accept mailed or emailed nomination materials. More information, including the submission portal, can be found at: https://www.aaas.org/programs/fellows/current-nomination-cycle.